# CFD Simulation of Advanced Diesel Engines

**Andreas Peter Kleemann**

Thesis submitted for the degree of
Doctor of Philosophy of the University of London
and for the
Diploma of Imperial College

Mechanical Engineering Department
Imperial College of Science, Technology and Medicine
London SW7 2BX

February 2001

# Abstract

This study uses CFD methodology to simulate an advanced Diesel engine operated at higher than conventional peak cylinder pressures. The existing mathematical models for Diesel combustion, pollutant formation and wall heat transfer are improved and validated for this operating range.

The fluid flow is described via the gas-phase Favre-averaged transport equations, governing the conservation of mass, chemical species, momentum and energy, based on the Eulerian continuum framework. These equations are closed by means of the $k-\varepsilon$ turbulence model. The liquid phase uses the Lagrangian approach, in which parcels, representing a class of droplets, are described by differential equations for the conservation of mass, momentum and energy. The numerical solution of the gas phase is obtained by the finite volume method applied to unstructured meshes with moving boundaries. Diesel ignition is modeled via a reduced kinetics mechanism, coupled with a characteristic timescale combustion model. Additionally, $NO_x$ and soot emissions are simulated.

For the elevated cylinder temperatures and pressures, the behaviour of the thermophysical properties of the gases and liquids involved is critically examined. A near-wall treatment is applied accounting for the large gradients of thermophysical properties in the vicinity of the wall. Furthermore an alternative combined combustion and emissions modelling approach, RIF, based on the laminar flamelet concept is tested.

The methodology is validated by reference to experimental data from a research engine, a constant volume pressure chamber and a high-pressure DI Diesel engine at various operating conditions. The modified near-wall treatment gives better agreement with the heat transfer measurements. The methodology predicts Diesel combustion evolution reasonably well for the elevated pressures. Best agreement was achieved using the LATCT combustion model combined with a $NO_x$ and soot model. The predictions of emissions show encouraging trends especially regarding the soot/$NO_x$ tradeoff, but require tuning of model coefficients.

## Acknowledgements

I would like to express my sincere gratitude to my supervisor, Prof. A.D. Gosman, for his expert guidance and the motivation and inspiration throughout the duration of the study. I also would like to thank him for the fruitful discussions and thorough, constructive criticism which provided me with a fundamental understanding of Computational Fluid Dynamics and diesel engine modelling strategies.

I wish to thank in particular Mr. H.G. Weller for the numerous and helpful discussions which provided me with a better insight into the complexity of CFD modelling. In this respect I am also indebted to Mr. F. Lange, Mr. M. Islam, Dr. E. Ikonomou, Dr. C. Bai, Mr. A. Ghobadian and Mr. S. Weston. Further I would like to express my gratitude to Mr. K. Kummer and Prof. D. Hountalas for the provision of experimental data and the many discussions regarding the novel diesel engine concept.

Many thanks also to Mrs. N. Scott-Knight for the reliable and efficient arrangement of many essential administrative matters.

Furthermore I take the opportunity to acknowledge the financial support provided by the Commission of the European Community.

I am greatly indebted to the present and previous group members in particular Ms. N.R. Saber, Mr. G.M. Bennett, Mr. H.L. Tang, Mr. C. Chasos and Mr. H. Delavier for their moral support and the memorable times throughout my PhD studies.

Finally I wish to thank my parents, my brother and all the friends that sincerely supported me during my studies.

# Contents

**List of Tables** 19

**List of Figures** 30

**Nomenclature** 31

**1 Introduction** 38

1.1 Background . . . . . 39

1.2 The Diesel Engine Process . . . . . 44

1.2.1 Experimental methods . . . . . 45

1.2.2 Diesel engine cycle . . . . . 47

1.2.2.1 Intake stroke . . . . . 47

1.2.2.2 Compression stroke . . . . . 48

1.2.2.3 Combustion stroke . . . . . 50

1.2.2.4 Exhaust stroke . . . . . 54

1.3 Effect of High Peak Pressure Operation . . . . . 55

1.3.1 Thermodynamics . . . . . 56

1.3.1.1 Gas phase . . . . . 56

1.3.1.2 Liquid phase . . . . . 57
1.3.2 Ignition and combustion . . . . . 58
1.3.3 Pollutant formation . . . . . 59
1.3.4 Wall heat transfer . . . . . 60
1.3.5 Conclusion . . . . . 61
1.4 Present Contribution . . . . . 61
1.5 Thesis Outline . . . . . 62

**2 Previous Modelling of Diesel Engine Processes 64**

2.1 Introduction . . . . . 64
2.2 Modelling Categories . . . . . 64
2.2.1 Phenomenological models . . . . . 65
2.2.2 Multidimensional models . . . . . 66
2.3 Modelling of Diesel Subprocesses . . . . . 68
2.3.1 Turbulence . . . . . 68
2.3.2 Spray . . . . . 70
2.3.3 Ignition and combustion . . . . . 74
2.3.3.1 Chemical kinetics . . . . . 74
2.3.3.2 Reaction mechanism . . . . . 75
2.3.3.3 Pre-ignition phase . . . . . 76
2.3.3.4 Post-ignition phase . . . . . 78
2.3.4 Pollutants . . . . . 82
2.3.4.1 $NO_x$ modelling . . . . . 82

2.3.4.2 Soot modelling . . . . . 84
2.3.5 Wall heat transfer modelling . . . . . 92
2.3.5.1 Introduction . . . . . 92
2.3.5.2 Correlation-based engine heat transfer approaches . . 93
2.3.5.3 Theory-based engine heat transfer approaches . . . . 97
2.4 Closure . . . . . 102

**3 Mathematical Modelling** **104**

3.1 Introduction . . . . . 104
3.2 Instantaneous Governing Equations . . . . . 105
3.2.1 Mass conservation . . . . . 106
3.2.2 Momentum conservation . . . . . 106
3.2.3 Energy conservation . . . . . 107
3.2.4 Chemical species conservation . . . . . 109
3.2.5 Constitutive relations . . . . . 109
3.2.6 Study of equation of state . . . . . 112
3.2.6.1 Cubic equations of state . . . . . 113
3.2.6.2 Tests for high pressure and temperature condition . . 113
3.2.6.3 Test for high pressure and low temperature condition 115
3.2.6.4 Conclusions . . . . . 117
3.2.7 Study of thermophysical properties . . . . . 118
3.2.7.1 Molecular viscosity . . . . . 118
3.2.7.2 Thermal conductivity . . . . . 119

3.2.7.3 Heat capacity . . . . . 120
3.2.7.4 Diffusion coefficient . . . . . 122
3.2.7.5 Conclusions . . . . . 123
3.2.8 General instantaneous transport equation . . . . . 124
3.3 Ensemble-Averaged Governing Equations . . . . . 124
3.3.1 Ensemble-averaging . . . . . 124
3.3.2 Favre-averaged transport equation . . . . . 126
3.3.3 Favre-averaged constitutive relations . . . . . 127
3.3.4 General Favre-averaged transport equation . . . . . 129
3.3.5 Turbulence model . . . . . 129
3.3.5.1 Turbulence kinetic energy equation . . . . . 130
3.3.5.2 Turbulence dissipation rate equation . . . . . 131
3.4 Spray Model . . . . . 131
3.4.1 Nozzle model . . . . . 132
3.4.2 Droplet-gas interaction . . . . . 132
3.4.2.1 Atomisation . . . . . 133
3.4.2.2 Droplet trajectory and momentum exchange . . . . . 133
3.4.2.3 Droplet energy and mass balance and contribution to gas phase . . . . . 135
3.4.2.4 Droplet breakup . . . . . 138
3.4.3 Droplet-droplet interaction . . . . . 140
3.4.4 Droplet-wall interaction . . . . . 141
3.4.5 Study of liquid thermophysical properties . . . . . 141

3.4.5.1 Liquid density . . . . . 142
3.4.5.2 Liquid viscosity . . . . . 143
3.4.5.3 Liquid thermal conductivity . . . . . 144
3.4.5.4 Liquid heat capacity . . . . . 145
3.4.5.5 Surface tension . . . . . 146
3.4.5.6 Vapour-liquid equilibrium . . . . . 148
3.4.5.7 Enthalpy of vapourisation . . . . . 151
3.4.5.8 Single droplet evaporation . . . . . 153
3.4.5.9 Conclusions . . . . . 157
3.5 Combustion Model . . . . . 158
3.5.1 Pre-ignition phase . . . . . 159
3.5.1.1 Shell ignition model . . . . . 159
3.5.1.2 4-step ignition model . . . . . 162
3.5.1.3 Implementation . . . . . 165
3.5.2 Ignition criterion . . . . . 165
3.5.3 Post-ignition phase . . . . . 166
3.5.3.1 LATCT combustion model . . . . . 166
3.5.3.2 RIF model . . . . . 170
3.6 Pollutant Formation . . . . . 180
3.6.1 $NO_x$ model . . . . . 180
3.6.2 Soot model . . . . . 182
3.6.2.1 Soot formation model . . . . . 183
3.6.2.2 Soot oxidation model . . . . . 183

3.6.2.3 Implementation . . . . . 185
3.7 Summary of Governing Equations . . . . . 186
3.8 Boundary Conditions . . . . . 187
3.8.1 Walls . . . . . 187
3.8.1.1 Standard wall function approach . . . . . 188
3.8.1.2 Validity of standard wall function approach . . . . . 193
3.8.1.3 Modified wall function approach . . . . . 200
3.8.2 Inflow and outflow boundaries . . . . . 204
3.8.3 Symmetry planes . . . . . 205
3.8.4 Cyclic boundaries . . . . . 206
3.9 Initial Conditions . . . . . 206
3.10 Closure . . . . . 207

**4 Numerical Approach** **209**

4.1 Introduction . . . . . 209
4.2 Discretisation Technique . . . . . 210
4.2.1 Finite volume method . . . . . 210
4.2.1.1 General concept . . . . . 210
4.2.1.2 Notation . . . . . 211
4.2.1.3 Gauss' divergence theorem . . . . . 213
4.2.2 Spatial and temporal discretisation . . . . . 214
4.2.2.1 Unsteady term . . . . . 215
4.2.2.2 Convection/diffusion term . . . . . 215

4.2.2.3 Source term . . . . . 217
4.2.2.4 Convective flux differencing scheme . . . . . 217
4.2.3 Discretised general transport equations . . . . . 218
4.2.4 Boundary conditions . . . . . 219
4.2.4.1 Wall boundaries . . . . . 219
4.2.4.2 Inflow and outflow surfaces . . . . . 221
4.2.4.3 Symmetry planes . . . . . 221
4.2.4.4 Cyclic boundaries . . . . . 222
4.3 Solution Procedure . . . . . 222
4.3.1 General concept . . . . . 222
4.3.2 Solution sequence . . . . . 223
4.3.3 Solution of linear algebraic equations . . . . . 226
4.3.3.1 Partial differential equations . . . . . 226
4.3.3.2 Ordinary differential equations . . . . . 228
4.4 Closure . . . . . 230

**5 Description of Test Cases** **231**

5.1 RWTH Aachen Engine . . . . . 232
5.1.1 Experimental setup . . . . . 232
5.1.2 Computational setup . . . . . 235
5.2 Aachen Pressure Chamber . . . . . 237
5.2.1 Experimental setup . . . . . 237
5.2.2 Computational setup . . . . . 240

5.3 HPP Prototype Engine . . . . . 243
5.3.1 Experimental setup . . . . . 244
5.3.2 Computational setup . . . . . 248
5.4 Closure . . . . . 251

**6 Results and Discussion** **253**

6.1 RWTH Aachen Engine . . . . . 253
6.1.1 Flow field . . . . . 254
6.1.2 In-cylinder pressure and temperature . . . . . 265
6.1.3 Wall heat transfer . . . . . 266
6.1.4 Summary . . . . . 274
6.2 Aachen Pressure Chamber . . . . . 275
6.2.1 Fuel vapour and liquid penetration . . . . . 275
6.2.2 Fuel vapour concentration . . . . . 280
6.2.3 Combustion . . . . . 282
6.2.4 Soot concentration . . . . . 290
6.2.5 Summary . . . . . 297
6.3 HPP Prototype Engine . . . . . 299
6.3.1 Motored case . . . . . 299
6.3.1.1 In-cylinder pressure . . . . . 299
6.3.1.2 Wall heat transfer . . . . . 300
6.3.2 Fired case . . . . . 307
6.3.2.1 Modified initial conditions . . . . . 308

6.3.2.2 Combustion . . . . . 310
6.3.2.3 Wall heat transfer . . . . . 320
6.3.2.4 Emissions . . . . . 334
6.3.3 Summary . . . . . 342
6.4 Closure . . . . . 344

**7 Closure** **348**
7.1 Conclusions . . . . . 348
7.2 Recommendations and Suggestions for Future Work . . . . . 352
7.3 Closure . . . . . 354

**A Overview of Heat Transfer Correlations** **355**

**B Soot Modelling** **356**
B.1 Overview of Soot Modelling Approaches . . . . . 356
B.2 Soot Model Parameters . . . . . 358

**C Correlations for Thermodynamic Properties** **360**
C.1 Gas-Phase Thermophysical Correlations . . . . . 360
C.1.1 Molecular viscosity . . . . . 360
C.1.1.1 Sutherland correlation . . . . . 360
C.1.1.2 Chung *et al.* correlation . . . . . 360
C.1.1.3 Lucas correlation . . . . . 362
C.1.2 Thermal conductivity . . . . . 362
C.1.2.1 Modified Eucken correlation . . . . . 362

C.1.2.2 Chung *et al.* correlation . . . . . 363
C.1.2.3 Ely and Hanley correlation . . . . . 364
C.1.3 Heat capacity . . . . . 365
C.1.4 Diffusion coefficient . . . . . 366
C.1.4.1 Chapman and Enskog correlation . . . . . 366
C.1.4.2 Fuller *et al.* correlation . . . . . 367
C.1.4.3 Wilke and Lee correlation . . . . . 367
C.2 Liquid-Phase Thermophysical Correlations . . . . . 368
C.2.1 Density . . . . . 368
C.2.1.1 Hankinson-Brobst-Thomson correlation . . . . . 368
C.2.1.2 Simple thermodynamic correlation . . . . . 369
C.2.2 Viscosity . . . . . 369
C.2.2.1 Andrade and Letsou-Stiel correlation . . . . . 369
C.2.2.2 Chung *et al.* correlation . . . . . 371
C.2.2.3 Brulé and Starling correlation . . . . . 371
C.2.2.4 Simple thermodynamic correlation . . . . . 371
C.2.3 Thermal conductivity . . . . . 371
C.2.3.1 Latini correlation . . . . . 371
C.2.3.2 Sato and Riedel correlation . . . . . 372
C.2.3.3 Missenard and Riedel correlation . . . . . 372
C.2.3.4 Simple thermodynamic correlation . . . . . 373
C.2.4 Heat capacity . . . . . 373
C.2.5 Surface tension . . . . . 374

C.2.5.1 Macleod and Sugden correlation . . . . . 374
C.2.5.2 Brock and Bird correlation . . . . . 374
C.2.5.3 Simple thermodynamic correlation . . . . . 374
C.2.6 Vapour pressure . . . . . 375
C.2.7 Enthalpy of vapourisation . . . . . 375
C.2.7.1 Majer and Svoboda correlation . . . . . 375
C.2.7.2 Simple thermodynamic correlation . . . . . 376
C.2.7.3 Real gas latent heat of vapourisation . . . . . 376
C.3 Vapour-Liquid Equilibrium . . . . . 376

**D Surface Temperature and Wall Heat Flux** **379**

**Bibliography** **381**

# List of Tables


1.1 Emission standards for the European Union (EU) for heavy-duty Diesel engines (from [93, 412]). European Stationary Cycle. Quantities in [g/kWh] (Smoke in [$m^{-1}$]). . . . . 42

1.2 Effects of increasing gas pressure on spray behaviour. . . . . 58

2.1 Coefficients for Woschni correlation in Eq. (2.13). . . . . 95

3.1 Constants for cubic equations of state taken from [358]. . . . . 113

3.2 Initial values for the adiabatic compression. . . . . 114

3.3 Properties of air taken from [358]. . . . . 115

3.4 Initial conditions for high pressure and low temperature case (subscript $\infty$ indicates initial values). . . . . 116

3.5 Properties of dodecane taken from [358]. . . . . 116

3.6 Prandtl and Schmidt numbers derived from experiments for scalar variables; taken from [38, 268]. . . . . 129

3.7 Model coefficients in the $k-\varepsilon$ turbulence model (from [246, 305]). . . 131

3.8 Coefficients for drag correlations. . . . . 134

3.9 Coefficients for Reitz-Diwakar breakup model. . . . . 140

3.10 Coefficients proposed by various researchers for Reitz-Diwakar breakup model. . . . . 140

3.11 Input parameters for single droplet evaporation study. . . . . 153

3.12 Thermophysical property correlations used in the single droplet evaporation study. . . . . 154

3.13 Influence of relative velocity on droplet lifetime. . . . . 157

3.14 Kinetic constants of Shell autoignition model (taken from [152, 425]). Pre-exponentials in units of [cm], [mol], [s]; activation energies in [J/mol]. . . . . 161

3.15 Reaction parameters for 4-step ignition model (taken from [308]). . . 164

3.16 Rate parameters for $n$-heptane and $n$-dodecane single-step quasi-global reaction (from [458]). Units in [cm], [s], [mole], [J] and [K]. . . 168

3.17 Lower heating value of various fuels (from [85, 248]). . . . . 170

3.18 Rate coefficients for extended Zeldovich mechanism (from [37]). . . . 181

3.19 Model coefficients of standard wall functions (from [259]). . . . . 191

3.20 Reference values with respect to intake for order of magnitude analysis. 195

3.21 Geometric information for single-cylinder DI Diesel engine and air properties. . . . . 195

3.22 Gradients and maximum quantities for order of magnitude analysis. . 195

3.23 Order of magnitude for terms in boundary layer momentum equation. 195

3.24 Order of magnitude for terms in boundary layer enthalpy equation. . 195

4.1 Normalisation factors and thresholds for transport equation residuals (from [410]). . . . . 229

5.1 Geometrical information and operating condition of RWTH Aachen engine (from [190, 252]). . . . . 232

5.2 Location of monitoring points for LDA measurement of RWTH Aachen engine (from [190]). . . . . 234

5.3 Maximum standard deviation for measurement quantities for RWTH Aachen engine (from [190]). . . . . 235

5.4 Inlet conditions of RWTH Aachen engine case (see also [252]). . . . . 236

5.5 Initial conditions and computational parameters for Aachen engine calculation. . . . . 236

5.6 Dimensions and maximum capacity of Aachen chamber [393]. . . . . 237

5.7 Injector specification and injection parameters of Aachen chamber (from [243]). . . . . 238

5.8 Measurement locations for fuel vapour mass fraction. $z$ is direction downstream of nozzle in direction of spray axis and $r$ is radial offset from spray axis. . . . . 239

5.9 Standard deviation due to pulse-to-pulse variations for Aachen pressure chamber. . . . . 240

5.10 Spray submodels used for Aachen pressure chamber. . . . . 242

5.11 Ignition and combustion submodel coefficients for Aachen pressure chamber. . . . . 242

5.12 Soot model parameters for Aachen pressure chamber. $A$ is pre-exponential factor and $E$ is activation energy. . . . . 243

5.13 Initial conditions and computational parameters for Aachen pressure chamber calculation. . . . . 243

5.14 Geometrical information and operating condition of DI Diesel engine at HTW Dresden (from [168, 248, 391]). . . . . 244

5.15 Injector specifications for HPP prototype engine. . . . . 246

5.16 Various operating points investigated for HPP prototype engine. . . . 246

5.17 Maximum standard deviation for measurement quantities for DI Diesel engine (from [248]). . . . . 248

5.18 Spray submodels and parameters used for HPP prototype engine. . . 249

5.19 Ignition and combustion submodel coefficients for HPP prototype engine simulation. . . . . 250

5.20 Soot model parameters for HPP prototype engine. $A$ is pre-exponential factor and $E$ is activation energy. . . . . 251

5.21 Wall temperatures for various wall sections for HPP prototype engine. 251

6.1 Comparison of measured and predicted ignition delay for pressure chamber case. . . . . 288

6.2 Time required by different combustion models to burn specific percentage of total injected fuel mass. . . . . 290

6.3 Estimation of peak heat flux compared to measurements at measurement points on piston surface (− and + indicate under- and overestimation, respectively). . . . . 304

6.4 Measured and predicted peak pressure and ignition delay for EOP1. . 314

6.5 Measured and predicted peak pressure and ignition delay for EOP4. . 319

6.6 Pre-exponential factors used in the phenomenological soot models for HPP engine. . . . . 338

A.1 Authors and model parameters for convective heat transfer correlations according to Eq. (2.8). $T_{\text{bulk}}$ is the bulk temperature, given by Eq. (2.11), $\overline{v}_p$ is the mean piston speed and $V_{\text{cyl}}$ is the cylinder volume.355

B.1 Selected soot models for hydrocarbon diffusion flames. . . . . 357

B.2 Summary of parameters for Nagle Strickland-Constable soot oxidation model. . . . . 358

B.3 Soot density and diameter provided in literature. . . . . 358

B.4 Summary of parameters for semi-empirical soot oxidation model. . . . 359

C.1 Chung *et al.* correlation: Coefficients for $E_i$. . . . . 362

C.2 Chung *et al.* correlation: Coefficients for $B_i$. . . . . 364

C.3 Coefficients for polynomials from Chemkin and JANAF database. . . 365

C.4 Pure component parameters for Hankinson-Brobst-Thomson correlation. . . . . 369

C.5 Parameters for Andrade equation. . . . . 370

C.6 Brulé and Starling correlation for liquid viscosity: coefficients for $E_i$. . 371

C.7 Missenard correction factor $Q$ for high-pressure liquid thermal conductivities. . . . . 373

C.8 Parameters to estimate heat capacity at constant pressure for ideal gas state. . . . . 374

D.1 Surface thermocouple probe specifications [190, 248]. . . . . 380

# List of Figures


1.1 Direct injection Diesel combustion system (from [167]). . . . . 40

1.2 Indirect injection Diesel combustion system (from [167]). . . . . 40

1.3 Turbulent intake jet showing eddies of various length scale (from [139]). $l$ integral length scale, $\lambda$ Taylor microscale, $\eta$ Kolmogorov microscale. 48

1.4 Mean kinetic energy distribution prediction for small bore engine with bowl-in-piston chamber (from [20]). . . . . 49

1.5 Typical schematic of DI Diesel engine heat-release rate (from [146]). 51

1.6 Pollutant species formation as function of equivalence ratio $\phi$ (from [412]). . . . . 52

1.7 Conceptual schematic of Diesel flame during diffusion burning (from [88]). . . . . 53

1.8 Effect of boost pressure on in-cylinder pressure and temperature at SOI for HPP prototype engine (data obtained from [248]). . . . . 55

1.9 Generalised compressibility chart (from [358]). The compressibility $Z$ is plotted over reduced pressure defined as gas pressure over critical pressure. $Z$ equals unity for ideal gases. . . . . 56

1.10 Effect of temperature $T_i$ and pressure $p_i$ on ignition delay (from [298]). Ignition delay is comprised of the physical delay $\tau_1$ and the chemical delay $\tau_2$. . . . . 59

2.1 Flowchart for phenomenological models (from [167]). . . . . 65

2.2 Schematic of relative velocity computed between gas phase and liquid phase (from [247]). $v_{gas}$ is local gas velocity, $v_{num}$ is averaged gas velocity in cell, $v_{real}$ is gas velocity seen by the drop and $v_{drop}$ is drop velocity. . . . . 73

2.3 Comparison between predictions and experiments for Shell ignition model at various pressures for iso-octane at equivalence ratio 0.9 (from [152]). Pressures increase from top line to bottom line as 0.7, 1.0, 1.4, 2.0 bar. . . . . 77

2.4 Comparison between predictions and experiments for a reduced 14-step ignition mechanism for an *n*-heptane/air mixture at unity equivalence ratio (from [342]). . . . . 77

2.5 Schematic of processes involved leading to soot particles (from [27]). 85

2.6 Schematic of various processes taken into account in the soot model of Balthasar *et al.* (from [89]). . . . . 91

2.7 Comparison of HTCs for a test engine using different approaches of [14, 99, 321, 336, 467] (from [467]). . . . . 96

3.1 Temperature versus pressure trace for adiabatic compression. . . . . 115

3.2 Compressibility factor for various EOS at high pressures and variable temperatures with 10% dodecane in mixture. . . . . 117

3.3 Variation of molecular viscosity predicted by correlations without pressure correction. . . . . 119

3.4 Variation of molecular viscosity predicted by Chung *et al.* with pressure correction. . . . . 119

3.5 Variation of thermal conductivity predicted by correlations without pressure correction. . . . . 120

3.6 Variation of thermal conductivity predicted by Chung *et al.* correlation with pressure correction. . . . . 120

3.7 Variation of heat capacity at constant pressure for adiabatic compression. . . . . 121

3.8 Variation of air/dodecane binary diffusion coefficient for adiabatic compression predicted by low-pressure correlations. . . . . 123

3.9 Variation of air/dodecane binary diffusion coefficient for adiabatic compression predicted by high-pressure correlation. . . . . 123

3.10 Liquid density versus temperature for dodecane. . . . . 142

3.11 Liquid viscosity versus temperature for dodecane by correlations without pressure correction. . . . . 144

3.12 Liquid viscosity versus temperature for dodecane by correlations with pressure correction. . . . . 144

3.13 Liquid conductivity versus temperature for dodecane without pressure correction. . . . . 145

3.14 Liquid conductivity versus temperature for dodecane with pressure correction. . . . . 145

3.15 Liquid heat capacity versus temperature for dodecane. . . . . 146

3.16 Predicted surface tension versus temperature for dodecane with low-pressure correlation. . . . . 147

3.17 Predicted surface tension versus temperature for dodecane with high-pressure correlation. . . . . 147

3.18 Vapour-liquid equilibrium calculation using different EOS. Mole fraction of *n*-heptane at interface for varying temperature at gas/liquid interphase. . . . . 150

3.19 Latent heat of vapourisation versus temperature of *n*-heptane/nitrogen system at high pressures. . . . . 152

3.20 Droplet diameter history for high-pressure evaporation. . . . . 155

3.21 Droplet temperature history for high-pressure evaporation. . . . . 155

3.22 Droplet diameter history for different ambient temperatures in a high pressure environment using high-pressure correlations. . . . . 156

3.23 Schematic of linkage between CFD and RIF codes. . . . . 176

3.24 Schematic of velocities at wall boundary. . . . . 189

3.25 Measured and calculated turbulent Prandtl number distribution in thermal boundary layer (from [221]). $Pr_t$ is turbulent Prandtl number. Data taken from [48, 181, 221, 233]. . . . . 198

3.26 Schematic of valve region including the valve curtain. . . . . 205

4.1 Cell notation in FVM. . . . . 212

4.2 Interpolation factors for the estimation of cell face values. . . . . 213

4.3 Schematic of cyclic boundary. . . . . 222

4.4 Flow chart of numerical solution algorithm. . . . . 224

5.1 RWTH Aachen motor and measurement locations for three probes (from [190, 252]). . . . . 233

5.2 Valve lift curve for RWTH Aachen engine. . . . . 234

5.3 Discharge coefficient for different valve lifts. . . . . 234

5.4 Coarse mesh for Aachen engine at 90° CA. . . . . 235

5.5 Fine mesh for Aachen engine at 90° CA. . . . . 235

5.6 Aachen pressure chamber (from [393]). . . . . 238

5.7 Volumetric injection rate history for Aachen chamber [243]. . . . . 239

5.8 Computational mesh of Aachen pressure chamber. . . . . 241

5.9 Diagram of HPP prototype engine (from [168]). . . . . 245

5.10 Injector position and injection axes. 1,...,8 indicate spray axes of each hole. . . . . 245

5.11 Volumetric injection rate histories for HPP prototype engine. . . . . 247

5.12 Sensor locations for HPP prototype engine. . . . . 247

5.13 One-eighth wedge-shaped computational mesh for HPP prototype engine at 400° CA. . . . . 248

6.1 Velocity distribution at horizontal and vertical cross-sections for 90° CA and 120° CA using coarse mesh. . . . . 255

6.2 Velocity distribution at horizontal and vertical cross-sections for 180° CA and 300° CA using coarse mesh. . . . . 255

6.3 Velocity distribution at horizontal and vertical cross-sections for 90° CA and 120° CA using fine mesh. . . . . 256

6.4 Velocity distribution at horizontal and vertical cross-sections for 180° CA and 300° CA using fine mesh. . . . . 256

6.5 Comparison of axial velocity distribution at 90° CA. . . . . 257

6.6 Comparison of axial velocity distribution at 120° CA. . . . . 257

6.7 Comparison of axial velocity distribution at 150° CA. . . . . 257

6.8 Comparison of axial velocity distribution at 210° CA. . . . . 257

6.9 Calculated in-cylinder mass history for RWTH Aachen engine test case. . . . . 259

6.10 Comparison of axial velocity component at measurement point P3. . 259

6.11 Turbulence kinetic energy distribution at horizontal and vertical cross-sections for 90° CA and 120° CA using fine mesh. . . . . 261

6.12 Turbulence kinetic energy distribution at horizontal and vertical cross-sections for 180° CA and 300° CA using fine mesh. . . . . 261

6.13 Comparison of axial RMS velocity at measurement point P3. . . . . 263

6.14 Comparison of integral length scale at measurement point P2. . . . . 263

6.15 Calculated and measured pressure variations. . . . . 266

6.16 Calculated and measured bulk temperature variations. . . . . 266

6.17 Heat flux distributions for 90° CA and 180° CA using SWF approach. 267

6.18 Heat flux distributions for 90° CA and 180° CA using MWF approach. 267

6.19 Heat flux distributions for 300° CA and 360° CA using SWF approach. 268

6.20 Heat flux distributions for 300° CA and 360° CA using MWF approach. 268

6.21 Comparison of local heat flux at measurement point HT1. . . . . 269

6.22 Comparison of local heat flux at measurement point HT2. . . . . 269

6.23 Comparison of local heat flux at measurement point HT3. . . . . 270

6.24 Average turbulence kinetic energy in near-wall region. . . . . 270

6.25 Summary of heat flux measurements at three locations on cylinder head. . . . . 271

6.26 Summary of heat flux predictions using modified wall function approach. . . . . 271

6.27 Comparison of heat transfer coefficients between calculations and global heat transfer models. . . . . 272

6.28 Comparison of total heat transfer between predictions and global heat transfer correlations. . . . . 272

6.29 Fuel mass fraction for LATCT/NSC model at times 0.5 – 2.5 ms. . . 276

6.30 Fuel mass fraction for RIF approach at times 0.5 – 2.5 ms. . . . . 276

6.31 Comparison of liquid penetration. . . . . 277

6.32 Sauter mean diameter for calculation using RIF approach. . . . . 277

6.33 Comparison of axial fuel vapour penetration. . . . . 279

6.34 Fuel vapour mass fraction at $P_{34}$. . . . . 280

6.35 Fuel vapour mass fraction at $P_{40}$. . . . . 281

6.36 Fuel vapour mass fraction at $P_{44}$. . . . . 281

6.37 Fuel vapour mass fraction at $P_{50}$. . . . . 281

6.38 Fuel vapour mass fraction at $P_{54}$. . . . . 281

6.39 Burnt fuel mass fraction for LATCT/NSC model at times 1.5 – 1.9 ms. 283

6.40 Burnt fuel mass fraction for RIF approach at times 1.1 – 1.5 ms. . . 283

6.41 Distribution of scalar dissipation rate for RIF approach at times 1.1 – 1.5 ms. . . . . 284

6.42 Temperature distribution for LATCT/NSC model at times 1.5 – 1.9 ms. . . . . 285

6.43 Temperature distribution for LATCT/NSC model at times 2.0 – 4.0 ms. . . . . 285

6.44 Temperature distribution for RIF approach at times 1.1 – 1.5 ms. . . 287

6.45 Temperature distribution for RIF approach at times 2.0 – 4.0 ms. . . 287

6.46 Heat release rate for different combustion approaches. . . . . 288

6.47 Scalar dissipation rate history for RIF approach. . . . . 288

6.48 Evaporated, unburnt and burnt fuel mass for LATCT/NSC model. . 290

6.49 Evaporated, unburnt and burnt fuel mass for RIF approach. . . . . 290

6.50 Measured iso-contours of soot mass concentration at times 2.0 – 4.0 ms. 291

6.51 Iso-contours of soot mass concentration for LATCT/Hiroyasu model at times 2.0 – 4.0 ms. . . . . 291

6.52 Iso-contours of soot mass concentration for LATCT/NSC model at times 2.0 – 4.0 ms. . . . . 292

6.53 Iso-contours of soot mass concentration for RIF approach at times 2.0 – 4.0 ms. . . . . 292

6.54 Distributions of fuel/air equivalence ratio for LATCT/NSC model at times 2.0 – 4.0 ms. . . . . 294

6.55 Distributions of fuel/air equivalence ratio for RIF approach at times 2.0 – 4.0 ms. . . . . 294

6.56 Soot concentration comparison at $P_{30}$. . . . . 295

6.57 Soot concentration comparison at $P_{40}$. . . . . 295

6.58 Soot concentration comparison at $P_{50}$. . . . . 295

6.59 Soot concentration comparison at $P_{60}$. . . . . 295

6.60 Soot concentration comparison at $P_{70}$. . . . . 296

6.61 Chamber-averaged soot mass fraction for RIF approach. . . . . 296

6.62 Comparison of measured and predicted pressure. . . . . 300

6.63 Heat flux distribution on cylinder head at 360° CA using SWF approach. . . . . 301

6.64 Heat flux distribution on cylinder head at 360° CA using MWF approach. . . . . 301

6.65 Heat flux distribution on piston surface at 360° CA using SWF approach. . . . . 301

6.66 Heat flux distribution on piston surface at 360° CA using MWF approach. . . . . 301

6.67 Tangential velocity distribution at 360° CA using MWF approach. . 302

6.68 Radial velocity distribution at 360° CA using MWF approach. . . . 302

6.69 Comparison of heat flux on piston surface at eight measurement locations. . . . . 303

6.70 Average turbulence kinetic energy in near-wall region using MWF approach. . . . . 304

6.71 Collection of heat flux histories from measurements on piston surface.305

6.72 Collection of heat flux histories predicted using MWF approach. . . 305

6.73 Comparison of heat transfer coefficients between calculations and global heat transfer models. . . . . 306

6.74 Comparison of total heat transfer between calculations and global heat transfer models. . . . . 306

6.75 Soot imprint on piston after test cycles including combustion. . . . . 308

6.76 Polished piston with traces due to flame impingement. . . . . 308

6.77 Swirl number for intake stroke predicted using original and refined port geometries of HPP engine. . . . . 309

6.78 Temperature distributions along spray axis for 355° to 370° CA using LATCT model, $R_s = 0.5$. . . . . 311

6.79 Temperature distributions along spray axis for 380° to 410° CA using LATCT model, $R_s = 0.5$. . . . . 311

6.80 Temperature distributions mid-way between spray axes for 370° to 405° CA using LATCT model, $R_s = 0.5$. . . . . 312

6.81 Temperature distributions along spray axis for 355° to 370° CA using RIF model, $R_s = 0.5$. . . . . 313

6.82 Temperature distributions along spray axis for 380° to 410° CA using RIF model, $R_s = 0.5$. . . . . 313

6.83 Comparison of measured and predicted cylinder pressure histories for EOP1. . . . . 314

6.84 History of scalar dissipation rate in RIF calculation for EOP1. . . . 314

6.85 Heat release rate comparison for EOP1, $R_s = 0.5$. . . . . 317

6.86 Burnt fuel mass fraction comparison for EOP1, $R_s = 0.5$. . . . . 317

6.87 History of predicted $CO$, $CO_2$ and consumed fuel mass using RIF for EOP1. . . . . 318

6.88 Comparison of measured and predicted pressure for EOP4. . . . . 318

6.89 Heat release rate comparison for EOP4. . . . . 319

6.90 Burnt fuel mass fraction comparison for EOP4. . . . . 319

6.91 Heat flux distribution on piston surface using LATCT model for 370° to 400° CA, $R_s = 0.5$. . . . . 320

6.92 Comparison of heat flux on piston surface at eight measurement locations using standard and modified wall function approaches; LATCT combustion model, $R_s = 0.5$. . . . . 322

6.93 Comparison of heat flux on piston surface at eight measurement locations using LATCT combustion model and RIF with MWFs. . . 324

6.94 Comparison of heat flux on piston surface at eight measurement locations for various swirl levels; LATCT combustion model and MWFs. . . . . 327

6.95 Comparison of heat flux on piston surface at eight measurement locations for various characteristic droplet breakup time coefficients; LATCT combustion model and MWFs, $R_s = 0.5$. . . . . 329

6.96 Comparison of heat flux on piston surface at eight measurement locations for various degrees of nozzle blockage; LATCT combustion model and MWFs, $R_s = 0.5$. . . . . 331

6.97 Comparison of measured and calculated pressure history for various degrees of nozzle blockage. . . . . 332

6.98 Comparison of heat transfer coefficients between calculations and global heat transfer models. . . . . 334

6.99 Comparison of total heat transfer between calculations and global heat transfer models. . . . . 334

6.100 Soot distribution using NSC model for 360° to 395° CA. . . . . 335

6.101 Soot distribution using RIF model for 360° to 395° CA. . . . . 335

6.102 $NO_x$ distribution using NSC model for 360° to 395° CA. . . . . 337

6.103 $NO_x$ distribution using RIF model for 360° to 395° CA. . . . . 337

6.104 Cylinder-averaged soot concentration using various approaches for 2.85 bar boost pressure and 1420 RPM. . . . . 338

6.105 Cylinder-averaged gas temperature history, predicted using various soot modelling approaches. . . . . 338

6.106 Cylinder-averaged fuel/air equivalence ratio using phenomenological soot models. . . . . 339

6.107 $NO_x$ prediction using various soot modelling approaches. . . . . 340

6.108 Soot/$NO_x$ tradeoff prediction using LATCT/NSC model. . . . . 341

C.1 Takahashi high-pressure correction for low-pressure diffusivities (from [421]). . . . . 367

# Nomenclature

## Latin characters

| | |
|---|---|
| $\mathcal{A}$ | coefficient matrix |
| $\mathbf{A}$ | coefficient matrix |
| $A$ | area, Arrhenius pre-exponential factor |
| $a$ | coefficient, velocity gradient |
| $B$ | cylinder bore |
| $\mathbf{b}$ | source term of vector equation |
| $b$ | coefficient, source term of scalar equation |
| $\mathcal{C}$ | convective flux |
| $\mathbf{C}$ | work of external surface forces vector |
| $C$ | coefficient, molar heat capacity |
| $C_D$ | discharge coefficient |
| $C_\mu$ | constant in the $k-\varepsilon$ turbulence model |
| Co | Courant number |
| $c$ | coefficient, heat capacity, progress variable |
| $\mathcal{D}$ | diffusion flux coefficient |
| $\mathbf{D}$ | rate-of-strain tensor |
| $D$ | coefficient, diameter |
| $\mathbf{d}$ | diffusion flux vector |
| $d$ | distance |
| $E$ | energy, constant in the wall functions |
| $e$ | coefficient, specific internal energy |
| $\mathcal{F}$ | factor proposed by El Wakil *et al.* [103] for Stefan flow |
| $\mathbf{F}$ | boundary flux vector |
| $F$ | factor |
| $f$ | fugacity, rate coefficient, delay coefficient, fraction |
| $f()$ | function of () |
| $G$ | factor, turbulence generation |
| $\mathbf{g}$ | vector of gravitational acceleration |
| $g$ | coefficient |
| $H$ | factor |
| $h$ | factor, convective heat transfer coefficient, specific enthalpy |
| $\mathbf{I}$ | unity tensor |
| $\mathbf{j}$ | diffusion flux vector |
| $\mathcal{K}$ | Boltzmann constant, $1.38 \times 10^{-23}$ J/K |
| $k$ | thermal conductivity, turbulence kinetic energy, reaction rate constant |
| $\overline{k_{ij}}$ | binary interaction coefficient |

| | |
|---|---|
| $L$ | coefficient, length, length scale, latent heat of vapourisation |
| Le | Lewis number |
| $l$ | length scale |
| $\mathcal{M}$ | third body species |
| $M$ | molecular weight, chemical symbol of a species |
| ${}^{s}M$ | soot moment |
| $m$ | coefficient, mass, number of moles |
| $\mathcal{N}$ | discretised nabla ($\nabla$) operator |
| $N$ | number of (cells, components, droplets, etc.), engine speed, number density |
| Nu | Nusselt number |
| $\mathbf{n}$ | normal vector |
| $n$ | coefficient, index, number of moles |
| Oh | Ohnesorge number |
| $\mathcal{P}$ | parachor |
| $P$ | probability density function |
| $P\left(\frac{\sigma_h}{\sigma_{h,t}}\right)$ | P-function, inertial sublayer resistance factor |
| Pe | Peclet number |
| $p$ | pressure, parameter |
| $\dot{Q}$ | energy flux, volumetric flow rate |
| $Q$ | exothermicity per cycle, factor |
| $\mathbf{q}$ | heat flux vector |
| $q$ | heat flux, parameter |
| Re | Reynolds number |
| $\mathbf{R}$ | rotation matrix |
| $R$ | specific gas constant, reaction steps, radius, residual, ratio |
| $\mathcal{R}$ | universal gas constant = 8.314 $\frac{\mathrm{J}}{\mathrm{mol\,K}}$ |
| $\mathbf{r}$ | position vector |
| $r$ | radius, stoichiometric ratio, index |
| $\mathcal{S}$ | surface vector |
| $\mathbf{S}$ | source term of vector equation |
| $S$ | source term of scalar equation, surface area |
| Sh | Sherwood number |
| $\mathbf{T}$ | tensor field |
| $T$ | temperature |
| $t$ | time |
| $\mathbf{u}$ | velocity vector |
| $u$ | velocity |
| $V$ | volume |
| $v$ | velocity, specific volume |
| We | Weber number |
| $w$ | specific work, weighting factor |
| $\mathbf{x}$ | position vector |
| $x$ | coordinate in x-direction, mole fraction in liquid, ratio |
| $Y$ | species mass fraction |
| $y$ | coordinate in y-direction, mole fraction in vapour |
| $Z$ | compressibility factor, mixture fraction |
| $z$ | coordinate in z-direction, dimensionless mass transfer rate |

## Greek characters

| | |
|---|---|
| $\alpha$ | coefficient, angle, crank angle, void fraction |
| $\beta$ | coefficient, constant of thermocouple material |
| $\Gamma$ | diffusivity coefficient, gamma function |
| $\gamma$ | ratio of specific heats $c_p/c_v$, ratio |
| $\Delta$ | difference |
| $\delta$ | Dirac function |
| $\varepsilon$ | turbulence dissipation rate, emissivity, energy |
| $\eta$ | Kolmogorov scale, wall-normal coordinate |
| $\Theta$ | temperature, shape factor |
| $\vartheta$ | void fraction |
| $\kappa$ | von Kármán constant, ignition-to-combustion switch |
| $\lambda$ | second viscosity coefficient, interpolation factor, tolerance, Taylor microscale |
| $\mu$ | dynamic viscosity, chemical potential |
| $\nu$ | kinematic viscosity, stoichiometric coefficient |
| $\xi$ | inverse viscosity |
| $\rho$ | density |
| $\sigma$ | Prandtl/Schmidt number, surface tension, Stefan-Boltzmann constant ($5.67 \times 10^{-8}\ \frac{\mathrm{W}}{\mathrm{m^2 K^4}}$), characteristic length |
| $\boldsymbol{\tau}$ | shear stress vector |
| $\tau$ | shear stress, timescale |
| $\boldsymbol{\phi}$ | vector of general fluid property |
| $\Phi$ | fugacity coefficient, shape factor |
| $\varphi$ | crank angle |
| $\phi$ | general fluid field property |
| $\chi$ | scalar dissipation rate, ratio |
| $\Psi$ | factor |
| $\psi$ | variable for chemical species, velocity |
| $\Omega$ | collision integral |
| $\dot{\omega}$ | reaction rate |
| $\omega$ | angular velocity, acentric factor, dissipation per unit turbulence kinetic energy |

## Subscript and Superscript

| | |
|---|---|
| $A$ | site A in NSC soot oxidation model, species |
| $a$ | activation |
| $B$ | site B in NSC soot oxidation model, species |
| $b$ | backward, burned, exponent, breakup, boundary, boiling |
| $CG$ | related to conjugate gradient method |
| $CN$ | related to cetane number |
| $c$ | critical, cycle, characteristic, carbon, cross, cell, convergence |
| $comb$ | combustion |
| $cyl$ | cylinder |
| $\mathcal{D}$ | diffusion |
| $d$ | displacement, droplet |

| | |
|---|---|
| $e$ | energy |
| $eff$ | effective |
| $evap$ | evaporation |
| $f$ | fuel, forward, film, formation, cell face |
| $g$ | gas |
| $HV$ | lower heating value |
| $h$ | convective, enthalpy |
| $i$ | index (i = 1,2,...) |
| $ign$ | ignition |
| $j$ | index |
| $k$ | conductive, turbulence kinetic energy |
| $L$ | liquid |
| $LT$ | related to LATCT combustion model |
| $l$ | liquid, laminar |
| $m$ | microscopic, mass, mixture, molar |
| $mix$ | mixture |
| $mot$ | motored |
| $N$ | related to point N |
| $NN$ | related to point NN |
| $n$ | normal, normalised |
| $nom$ | nominal mean |
| $o$ | oxidation, old |
| $\mathcal{P}$ | linear part of source term |
| $P$ | point, polarity effect |
| $p$ | pressure, piston, droplet parcel, reaction product |
| $pad$ | paddle wheel |
| $Q$ | quantum effect |
| $r$ | reduced, radiative, reaction, relative |
| $reac$ | reaction |
| $ref$ | reference |
| $res$ | residual |
| $SL$ | saturated liquid |
| $s$ | surface, soot, swirl, Sutherland, saturated |
| $spec$ | species |
| $st$ | stable, stoichiometric |
| $T$ | thermal annealing |
| $t$ | turbulent, total |
| $tot$ | total |
| $\mathcal{U}$ | proportional part of source term |
| $\mathbf{u}$ | momentum |
| $V$ | vapour |
| $v$ | vapour, volume |
| $vp$ | vapour pressure |
| $W$ | wall |
| $Y$ | species mass fraction |
| $Z$ | mixture fraction, adsorption and desorption |
| 0 | reference value |
| 1,2 | indices |
| $*$ | dimensionless quantity, wall-parallel component |
| $+$ | dimensionless near-wall quantity, low-pressure value |
| $'$ | fluctuating quantity about Reynolds average, dimensionless quantity |
| $''$ | fluctuating quantity about Favre average |

| | |
|---|---|
| $\infty$ | external, freestream, initial |
| $\alpha$ | rotation |
| $\varepsilon$ | turbulence dissipation rate |
| $\tau$ | friction |
| $\overline{\Phi}$ | Reynolds mean value |
| $\tilde{\Phi}$ | Favre mean value |
| $\hat{\Phi}$ | instantaneous value, domain-averaged value |
| $\langle\Phi\rangle$ | conditionally averaged turbulent mean value |
| $\phi$ | dependent variable |
| $\psi$ | species |
| $^\circ$ | ideal gas |

## Abbreviations

| | |
|---|---|
| ALS | Andrade and Letsou-Stiel |
| BDC | Bottom Dead Centre |
| BTDC | Before TDC |
| BiCG | Bi-Conjugate Gradient |
| CA | Crank Angle |
| CARS | Coherent Anti-Stokes Raman Spectroscopy |
| CAS | Cross-sectionally Averaged Spray |
| CCD | Charge Coupled Device |
| CG | Conjugate Gradient |
| CI | Compression Ignition |
| CFD | Computational Fluid Dynamics |
| CN | Cetane Number |
| CV | Control Volume |
| D | Dimensional |
| DDM | Discrete Droplet Method |
| DI | Direct Injection |
| DISI | Direct Injection Spark Ignition |
| DNS | Direct Numerical Simulation |
| EBU | Eddy BreakUp |
| EC | European Commission |
| EGR | Exhaust Gas Recirculation |
| EOI | End Of Injection |
| EOP | Engine Operating Point |
| EOS | Equation Of State |
| EU | European Union |
| EVO | Exhaust Valve Opening |
| Eq. | Equation |
| FDM | Finite Difference Method |
| FEM | Finite Element Method |
| FFM | Full Field Modelling |
| FFT | Fast Fourier Transform |
| FVM | Finite Volume Method |
| HACA | H-Abstraction and $C_2H_2$-Addition |
| HBT | Hankinson-Brobst-Thomson |

| | |
|---|---|
| HC | HydroCarbon |
| HEDE | High fuel-Efficient Diesel Engine |
| HPP | High Peak Pressure |
| HRA | Heat Release Analysis |
| HRR | Heat Release Rate |
| HT | Heat Transfer |
| HTC | Heat Transfer Coefficient |
| HTW | Hochschule für Technik und Wirtschaft |
| HV | Heating Value |
| HWA | Hot Wire Anemometry |
| ICCG | Incomplete Cholesky Conjugate Gradient method |
| IDI | InDirect Injection |
| IVC | Intake Valve Closure |
| IVO | Inlet Valve Opening |
| LATCT | Laminar And Turbulent Characteristic Timescale |
| LDA | Laser Doppler Anemometry |
| LEA | Laser Extinction/Absorption |
| LES | Large Eddy Simulation |
| LHF | Locally Homogeneous Flow |
| LHS | Left-Hand Side |
| LIEF | Laser-Induced Exciplex Fluorescence |
| LIF | Laser-Induced Fluorescence |
| LII | Laser-Induced Incandescence |
| LIS | Laser-Induced Scattering |
| LMS | Lorenz-Mie Scattering |
| MARS | Monotone Advection and Reconstruction Scheme |
| MEOP | Motored Engine Operating Point |
| MDM | MultiDimensional Model |
| MWF | Modified Wall Function |
| NS | Navier-Stokes |
| NSC | Nagle Strickland-Constable |
| NTU | National Technical University |
| ODE | Ordinary Differential Equation |
| PAH | Polycyclic Aromatic Hydrocarbon |
| PCP | Peak Cylinder Pressure |
| PDA | Phase Doppler Anemometry |
| PDE | Partial Differential Equation |
| PDF | Probability Density Function |
| PISO | Pressure Implicit with Splitting of Operators |
| PIV | Particle Image Velocimetry |
| PLIF | Planar Laser-Induced Fluorescence |
| PM | Particulate Matter |
| PR | Peng-Robinson |
| PSL | Parabolic Sublayer Scheme |
| pvT | Pressure-Volume-Temperature |
| RHS | Right-Hand Side |
| RIF | Representative Interactive Flamelet |
| RK | Redlich-Kwong |
| RMS | Root Mean Square |
| RON | Research Octane Number |
| RPM | Revolutions-Per-Minute |
| RS | Rayleigh Scattering |
| RWTH | Rheinisch-Westfälische Technische Hochschule |

| | |
|---|---|
| SF | Separated Flow |
| SI | Spark Ignition |
| SMD | Sauter Mean Diameter |
| SOI | Start Of Injection |
| SRK | Soave-Redlich-Kwong |
| SRS | Spontaneous Raman Scattering |
| SWF | Standard Wall Function |
| TDC | Top Dead Centre |
| TVD | Total Variation Diminishing |
| VC | Valve Closure |
| VLE | Vapour-Liquid Equilibrium |

# Chapter 1

# Introduction

In 1892 Rudolf Diesel presented a new type of internal combustion engine that differed in principle and design from the already existing Otto engine. Over the past century the use of Diesel engines as a power-generating device has become increasingly popular and its significance as a promising technology for the forthcoming decades has been acknowledged by engine manufacturers. Nowadays compression ignition (CI) engines can be found in a variety of environments ranging from power plants, ships and locomotives to road vehicles. One of the key fields of application is the automotive industry. While the Diesel engine is already the major propulsion technology for heavy-duty trucks [394, 395], its market potential in Europe for passenger cars is predicted to rise up to approximately 25% within the next few years [162, 300, 338].

The Diesel engine concept offers advantageous characteristics in comparison to the gasoline engine. Better fuel economy is achieved through controlled injection, which is important due to the rising cost of fossil fuels. As a consequence of lower fuel consumption, the amount of $CO_2$ emissions is reduced, therefore minimising the contribution to the greenhouse effect. Diesel engines can utilise oil fractions as fuels that arise early in the oil refinery process and are therefore less expensive. Also alternative fuels such as methanol and compressed or liquefied natural gas

can be used. Higher compression ratios and the introduction of direct injection technology lead to higher thermal efficiencies of about 30% in comparison to the spark ignition (SI) engine [162, 338]. A remarkable thermodynamic efficiency of 50% is viable [162, 218, 482]. Despite the advent of the much acclaimed direct injection spark ignition (DISI) engine, the Diesel engine will be able to defend its market position in the future due to a higher thermal efficiency, particularly at full load, leading to favourable cost-effectiveness [412].

## 1.1 Background

Two types of automotive Diesel engines exist, classified by the respective injection location (see Figures 1.1 and 1.2). In direct injection (DI) Diesel engines fuel is injected through a multiple-hole nozzle into the main chamber, while for indirect injection (IDI) engines a single-hole injector supplies the fuel into a pre-combustion chamber that is linked through a narrow connecting passage to the main chamber. The purpose of the latter configuration is to create vigorous air motion and hence turbulence for the mixture preparation. This is needed in particular for smaller engine sizes.

Generally, direct injection technology offers important advantages compared to the indirect injection system, such as a 15 – 20% reduction in fuel consumption and comparatively lower heat losses [395, 412]. Thus the application of the IDI principle was traditionally limited to small-sized, high speed engines, although recently it has also been replaced by DI designs. In addition, the DI Diesel engine allows higher air charging, producing a higher specific power output. The sooting tendency is also reduced [162]. It is therefore not surprising that the DI Diesel engine has achieved substantial market penetration in Europe in commercial vehicles. As for passenger vehicles, the future low-emission, so-called 3-litre car is most likely to be equipped with a small DI Diesel engine [162]. For these reasons the present research, which

is part of a European Commission funded project, is focused on DI Diesel engines for heavy-duty trucks supplied to the European market.

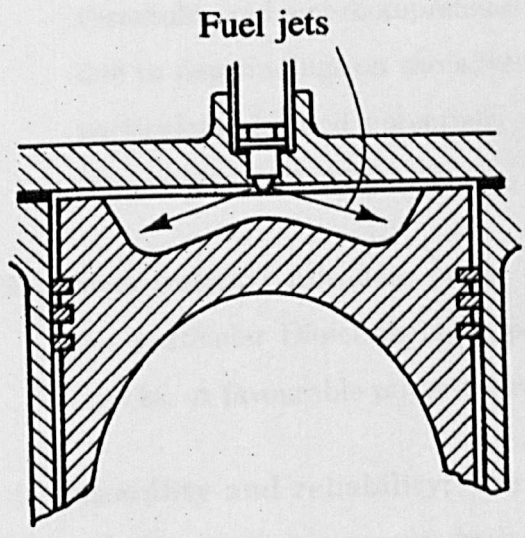



**Figure 1.1:** Direct injection Diesel combustion system (from [167]).

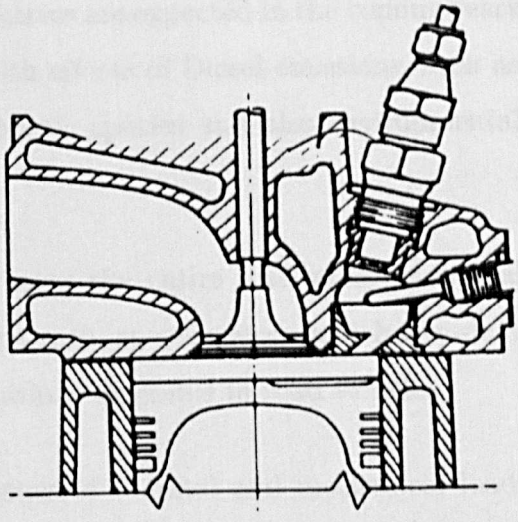


**Figure 1.2:** Indirect injection Diesel combustion system (from [167]).

For CI engines to maintain their position as a leading power generating device for heavy-duty vehicles, four major requirements have to be met:

1. **Engine efficiency:** The oil crisis in the 1970s, with its rocketing fuel prices, raised customer awareness with respect to engine thermal efficiency. Concern was also built up about the long-term availability of crude petroleum. Nowadays, optimistic estimates expect the oil reserves to last for at least another 40 years. However, due to continuously rising fuel prices and customer demands for cost effectiveness with respect to other possible power sources, fuel conversion efficiency has emerged as one of the main criteria for engine design.

2. **Emission regulations:** In recent years, the increasingly stringent emission regulations worldwide (see e.g. Table 1.1 for Europe) require adequate combustion technology to cope with the limits set forth in specific regulated test cycles [185, 300, 338, 394]. For Diesel engines, these comprise, above all, $NO_x$[†] and particulate matter (PM) emissions, since they are known to con-

[†] $NO_x$ comprises the species NO and $NO_2$.

tribute to urban smog, global warming, acid rain and ozone depletion in the stratosphere [56, 148, 167, 372, 434]. Further reductions in exhaust emission thresholds and more comprehensive directives are expected in the coming years due to new findings on the adverse health effects of Diesel emissions, such as particulate size and potentially carcinogenic species and also environmental impact [236, 372, 389, 412].

3. **Power output:** Adequate power output over the entire load range is crucial for particular Diesel engine applications such as generators and heavy-duty trucks. A favourable power-to-weight ratio is desirable in road vehicles.

4. **Durability and reliability:** The challenges of thermal and mechanical loads on the system components have to be addressed appropriately to prevent failure of vital parts. Also, due to differences in fuel quality in different countries, the reliable operation within a reasonable range of fuel types must be guaranteed.

Extensive research on the complex and interactive in-cylinder processes in Diesel engines has resulted in a number of key technologies being introduced in the past. The most important ones are[†] [344]:

**Supercharging and intercooling of intake air:** In comparison to naturally aspirated engines the maximum power output and fuel economy is increased by these measures [167]. Furthermore, since more air is entering the combustion chamber, oxidation of soot is facilitated due to higher oxygen levels, reducing smoke emissions at peak loads [162, 294]. Depending on the amount of intercooling, $NO_x$ levels are lowered as a consequence of lower combustion temperatures. A negative side-effect of supercharging is increased mechanical and thermal loading resulting from higher chamber pressures and temperatures [294].

[†]A lot of effort has also been put into improving fuel quality. Further information can be found e.g. in [441].

**Enhanced injection systems:** Advanced injection systems, notably common rail technology [412], using centrally located multi-hole nozzles give high injection velocities. Turbulent mixing is enhanced, allowing reduction of combustion noise and particulate emissions [162, 414]. Retarded injection start has the potential to reduce $NO_x$ levels, but results in higher smoke emissions. For early injection the converse holds true. This is commonly known as the particulates-$NO_x$ tradeoff [412].

**Exhaust gas recirculation (EGR):** Recirculated exhaust gas leads to a richer mixture of higher heat capacity with lower oxygen levels. Hence, the flame temperature is reduced, resulting in decreased $NO_x$ levels [162]. Soot levels, however, increase with higher EGR due to less oxidation, limiting the EGR rate to 30 - 50% [162]. The optimal amount of EGR introduced decreases with load and speed and is linked to fuel consumption rates [412].

As seen above, the key technologies necessitate careful design and tuning of the combustion process in order to meet market demands and exhaust legislation in Europe. To date, for heavy-duty vehicles, the conflicting targets of emission limits, outlined by the Euro II and III standards, and fuel consumption have been addressed by means of high injection pressures using multi-hole nozzles and supercharging [441]. Due to the tighter $NO_x$ threshold in the directives for 2005 (Euro IV) and 2008 (Euro V) (see Table 1.1) this strategy would imply a penalty in terms of an increased fuel consumption of around 10% [168].

| Standard | Date | CO | HC | $NO_x$ | PM | Smoke |
|---|---|---|---|---|---|---|
| Euro II | 1996 | 4.0 | 1.1 | 7.0 | 0.25 | — |
| | 1998 | 4.0 | 1.1 | 7.0 | 0.15 | — |
| Euro III | 2000 | 2.1 | 0.66 | 5.0 | 0.1 | 0.8 |
| Euro IV | 2005 | 1.5 | 0.46 | 3.5 | 0.02 | 0.5 |
| Euro V | 2008 | 1.5 | 0.46 | 2.0 | 0.02 | 0.5 |

**Table 1.1:** Emission standards for the European Union (EU) for heavy-duty Diesel engines (from [93, 412]). European Stationary Cycle. Quantities in [g/kWh] (Smoke in [$m^{-1}$]).

One solution to this problem would be a significant increase of the peak cylinder

pressure (PCP) which would offer beneficial engine efficiency. Three combustion strategies exist to achieve increased combustion pressures. The first option includes a higher compression ratio which, however, restricts injection timing and yields no significant increase in efficiency [171]. Alternatively the combination of supercharging and EGR allows to reach the Euro IV standards with a reduced specific fuel consumption at full load. Yet, at part load the PM target cannot be met due to high hydrocarbon (HC) emissions [169]. Considerably higher injection pressures are required with advanced start of injection (SOI) to satisfy both higher efficiency and emissions limits [170]. These injection pressures necessitate an injection system that is currently not available in series truck engines [45]. At present the last option is the most promising variant. It combines supercharging to achieve higher efficiencies with both an advanced injection timing to reduce PM emissions and an external $NO_x$-reduction measure such as cooled EGR or Selective Catalytic Reduction. Thus the abovementioned conflict between $NO_x$ and fuel consumption can be separated. A fuel saving of up to 15% based on Euro II is within reach [168].

The research described in this thesis was conducted within a larger EC-funded project called HEDE (High Fuel-Efficient Diesel Engine with Significantly Increased Peak Pressure) that included several European partners (AVL List, DaimlerChrysler, Federal Mogul, HTW Dresden, Imperial College, NTU Athens). The focus of the project was on the understanding and characterisation of the effect of significantly increased PCPs on engine operation and emissions. The research was based on a prototype engine which combines supercharging with air intercooling to obtain improved fuel efficiency while supplying higher power output. The increased charge density leads to PCPs of up to 23 MPa, well above those of standard engines, which range up to 12 MPa [218]. These severe operating conditions entail higher component stresses due to the pressure and thermal loads such that the knowledge of the distribution of wall heat transfer is crucial to the component design. In addition, the elevated operating conditions affect in-cylinder gas motion, the spray, combustion evolution and emissions.

All these effects can, in principle, be studied using Computational Fluid Dynamics (CFD), provided that the methodology yields predictions of sufficient accuracy for the conditions of interest. Thus the contribution of the present work toward this new engine concept, as documented in this thesis, included the refinement and extension of an existing engine simulation CFD code to enable the calculation of the performance, emissions and heat loads of the prototype engine operating at elevated peak pressures. These results in turn were validated by comparison with available measurements†, including cylinder pressure, heat transfer and exhaust emissions for several engine operating points.

*Computational Fluid Dynamics* has become an increasingly powerful engineering tool in the early engine design process to reduce the time and costs of development and provide information difficult to obtain by other means. The utilisation of CFD has been driven by the rapid rise in computer power, measured in terms of computational speed and storage capacity.

In what follows a general introduction into the physical processes of the Diesel engine is presented. Then an overview is given of the influence of increased peak cylinder pressure on these processes.

## 1.2 The Diesel Engine Process

Over the past decades many researchers have contributed to the fundamental understanding of the phenomena involved in Diesel engines. Progress is made difficult owing to the small dimensions involved and the extreme, highly transient pressures and temperatures. This section first introduces experimental methods which have largely contributed to our current understanding of the Diesel engine process.

†Note that the effect of EGR under these operating conditions was not studied, since measurements were not available. For the interested reader further insight into the influence of EGR on the Diesel engine cycle can be found in [387, 412].

Thereafter the conventional Diesel engine cycle is characterised.

### 1.2.1 Experimental methods

Experimental methods for engines can be subdivided into local, global and visualisation techniques. While *global* methods provide overall trends representative for the entire cylinder (i.e. pressure trace), *visualisation* techniques give qualitative insight into flow and combustion phenomena. By contrast, *local* measurements extract quantitative in-cylinder information at discrete points and thus are crucial for CFD model development validation.

To date, among both local and visualisation techniques laser-based methods are paramount since they allow non-intrusive in situ measurements of high spatial and temporal resolution. However, optical access via a transparent piston or liner becomes necessary, requiring considerable modifications to the original layout of the combustion chamber. Limitations on peak pressure and engine speed then result.

The following part summarises the major experimental methods used in Diesel engine measurements. Detailed information and recommendations for each technique are found in the provided references and in Chigier [70].

**1. Gas phase**

- The mean flow *velocity* and *turbulence* intensities are captured by hot wire anemometry (HWA) and laser Doppler anemometry (LDA) [47, 67, 409]. While HWA faces calibration problems and directional ambiguity, LDA is widely-applied since it does not suffer from these, nor interferes with the flow field. In addition, high-speed films or CCD cameras are used, often in combination with flow seeding (e.g. see particle image velocimetry (PIV) [460]) to visualise the *flow field* and flame propagation. High-speed photography is also applied to detect autoignition sites besides $OH$ chemiluminescence [22, 162].

- Cylinder *pressure* is measured via a piezo-electric pressure transducer [186].
- The local *gas temperature* is derived from molecular density measurements employing an equation of state by the two-colour method, spontaneous Raman scattering (SRS), Rayleigh scattering (RS) and Lorenz-Mie scattering (LMS) [47, 67, 211]. High-speed photography using CCD cameras is similarly applied to extract flame temperatures [485].
- For local *species concentration* profiles SRS, RS, coherent anti-Stokes Raman spectroscopy (CARS), laser-induced fluorescence (LIF), planar LIF (PLIF) and dual wavelength laser extinction/absorption (LEA) are used [67, 83, 485]. The fast gas sampling valve technique represents an alternative technique which, however, cannot resolve highly transient processes [162]. Quantitative *soot distribution* is provided through self-luminescence, laser-induced scattering (LIS), laser-induced incandescence (LII) and light extinction methods [162, 217, 439, 484]. LII is particularly suitable to obtain two-dimensional soot imaging since background noise from droplets can be easily eliminated, unlike in LIS.

**2. Liquid phase**

- High-speed imaging techniques combined with laser schlieren and shadowgraphy measurements are suitable to characterise *spray propagation*, *liquid penetration* and *spray angle* [162]. Imaging has also been applied to observe *cavitation* in the nozzle [23, 65, 112]. Simultaneous information of liquid and vapour phase locations are achieved by laser-induced exciplex fluorescence (LIEF) [217, 485].
- *Droplet velocities* are measured using LDA and phase Doppler anemometry (PDA) [47]. However, PDA can only extract information in the less dense region of the spray.
- Detailed information about *droplet size distribution* is provided by PDA, LMS and dual wavelength LEA.

- *Droplet species concentrations* are obtained from scattering techniques (e.g. SRS).

**3. Gas/wall interface**

- Surface temperatures and heat fluxes are commonly measured by surface and embedded thermocouples [54, 105, 267]. These local temperatures are the basis for determining the local *wall heat flux.*

## 1.2.2 Diesel engine cycle

The four-stroke Diesel engine cycle is subdivided into four periods based on piston motion: intake, compression, expansion and exhaust stroke. Each period involves events that are different in nature.

### 1.2.2.1 Intake stroke

During the intake stroke, air is drawn into the cylinder due to the existing pressure difference across the valves. For high-speed, small-bore CI engines swirl about the valve axis is generated by the port geometry (i.e. helical port) providing initial angular momentum to the flow field. This produces a higher turbulence intensity towards the end of compression when the fuel vapour mixes with air [167]. Enhanced mixing promises better fuel and temperature distributions, resulting in lower particulate emissions [441]. However, more rapid mixing increases $NO_x$ production [441]. This is the reason why for large bore engines almost no swirl is introduced and mixing is controlled mainly via the injection process.

As the valves open, the incoming charge separates from the valve seat and lip and produces a highly turbulent, annular jet with large velocity gradients at its boundaries. The flow interacts with the cylinder walls and moving piston creating a complex flow structure composed of recirculation regions beneath the valve head

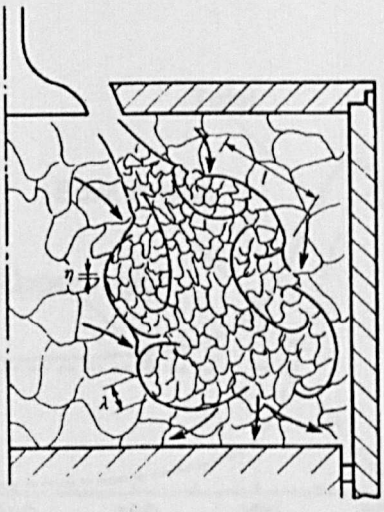



**Figure 1.3:** Turbulent intake jet showing eddies of various length scale (from [139]). $l$ integral length scale, $\lambda$ Taylor microscale, $\eta$ Kolmogorov microscale.

and corners between chamber wall and cylinder head and large-scale circumferential flow patterns initiating the swirl around the cylinder axis. The inflow jet is highly turbulent containing eddies roughly the size of the local thickness of the jet. Those largest vortices break down to small-scale turbulence and essentially contribute to turbulence production (see Figure 1.3) [184, 371]. When the piston velocity decreases the intake flow slows down and the swirl and turbulence distribution over cylinder height evens out.

#### 1.2.2.2 Compression stroke

As soon as the induction period has finished at intake valve closure (IVC), the cylinder charge is compressed by the upward piston movement reaching cylinder pressures and temperatures of the order of 4 – 12 MPa and 1000 – 1200 K, respectively [218]. In bowl-in-piston configurations swirl motion is enhanced toward top dead centre (TDC) as the result of the restricted geometry and conservation of angular momentum. However, due to wall friction and turbulent dissipation 1/4 – 1/3 of the initial momentum is lost at TDC [167]. Similarly, as the temperatures rise, the increasing gas viscosity contributes to energy dissipation; but this effect is very small. Furthermore, owing to rising temperatures the wall heat transfer increases.

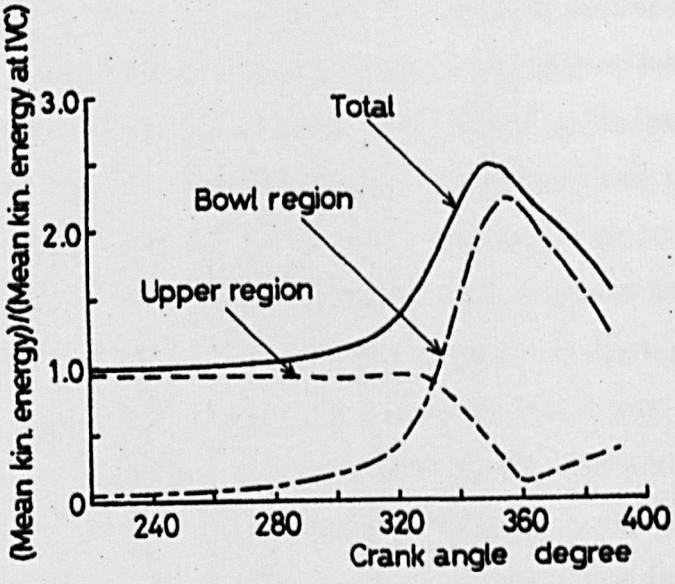



**Figure 1.4:** Mean kinetic energy distribution prediction for small bore engine with bowl-in-piston chamber (from [20]).

Towards TDC the swirling mass is transferred from the upper cylinder into the bowl region, substantially augmenting the swirl velocities in the bowl. The kinetic energy in the upper part diminishes. Squish flow in radial direction is initiated with maximum velocities around 10° CA before TDC [167] which causes the kinetic energy in the bowl region to increase further, as seen in Figure 1.4. Experimental evidence has shown that the turbulence intensity due to the squish-induced shear flow rises up to five-fold depending on the shape of the bowl lip, as in the case of a re-entrant piston bowl [110]. A link of this design shape to lower particulates has been established, since the higher turbulence levels result in better mixture formation [61, 222].

Depending on the engine load fuel injection starts a few crank angles (CAs) before TDC. Rapid mixing is desirable for the optimal distribution of the fuel vapour in the combustion chamber, which can be achieved through small-scale turbulence originating either from the decay of macroscopic flow structures remaining from the intake stroke or from the nature of the injection process. Modern heavy-duty Diesel engines use a centred injector with 4 – 12 nozzle holes of diameters less than 200 $\mu$m [300, 362, 441]. To provide adequate spray momentum so that the spray

penetrates sufficiently across the chamber, the injection pressures can be as high as 200 MPa, producing droplet velocities of up to 600 m/s at full load [362]. The large velocity gradients between the spray and ambient gas induce small-scale turbulent motion that greatly enhances the radial spreading of fuel vapour in between the jets and improves air entrainment [139]. This is known to lower particulate emissions [194, 218, 441]. Despite the close to sonic injection velocities the spray liquid core penetrates only 20 – 30 mm into the bowl as the liquid jet breaks up almost instantly into droplets with diameters of around 10 $\mu$m [162, 218]. These comparatively small droplets rapidly evaporate at the high surrounding chamber temperatures [441]. In this respect, injection systems in heavy-duty engines are generally designed such that spray wall impingement is avoided, as the latter is attributed to flame quenching and thus to increased particulate and unburnt hydrocarbon emissions [218, 372, 441].

#### 1.2.2.3 Combustion stroke

While the fuel vapour propagates through the bowl and hot air is entrained, a number of chemical reactions take place breaking down large hydrocarbons into smaller components and causing further reactions between them and with the surrounding gases. Despite the initial cooling of the gas and consequent drop in local mixture temperature due to evaporative cooling, the pre-combustion reactions produce enough thermal energy to sustain the reactions and to initiate combustion. At regions where the mixture is close to stoichiometric, spontaneous autoignition occurs with a time lag (i.e. ignition delay) of the order of a millisecond after SOI, which corresponds to 0.5° – 1° CA [162, 167, 335, 441]. Subsequently, as seen from the heat release profile in Figure 1.5, combustion is initiated as a partially-premixed flame depleting the fuel in areas where during the ignition delay period a mixture in the combustible limits has been formed. This combustion phase is characterised by a short and rapid increase in heat release which accelerates the evaporation process. The resulting instantaneous rise in cylinder pressure has a critical impact on

combustion noise and dynamic loading of the cylinder components. Therefore the control over the factors which influence this combustion phase is important. The fuel burnt in premixed mode is found to be proportional to the engine speed and ignition delay [7] and therefore to the injected fuel mass during the ignition delay [218].

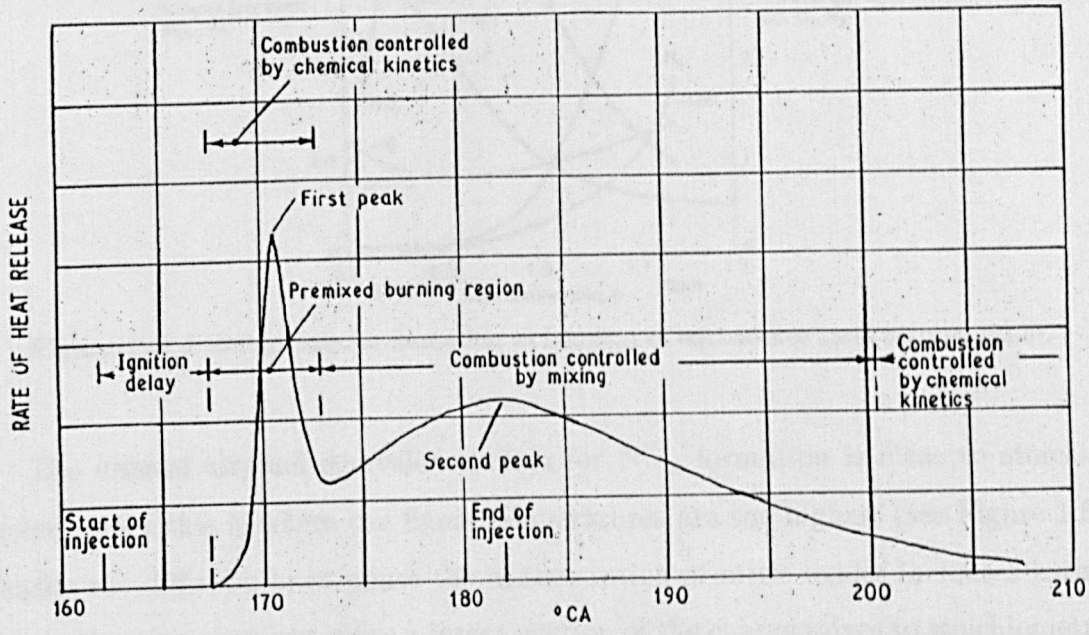



**Figure 1.5:** Typical schematic of DI Diesel engine heat-release rate (from [146]).

While the premixed fuel is being depleted — the spray core being too rich, the spray periphery being to lean for combustion to occur — burning slows down, and the second phase of combustion is entered. Here the reaction rate is controlled by the speed of diffusion-controlled mixing of air and fuel vapour to form a combustible mixture, as the chemical time scales are 500 – 2300 times smaller than the turbulent mixing rate [344]. In the first period of this phase spray entrainment effects still have a strong influence on air/fuel mixing, while later, after end of injection (EOI), turbulent mixing becomes the dominant process. Plee *et al.* [344] determined the characteristic timescales involved in the DI Diesel combustion process and concluded that most of the fuel is consumed in diffusion mode, since the mixture has more time to form a combustible mixture during the diffusion burning period than during the ignition delay.

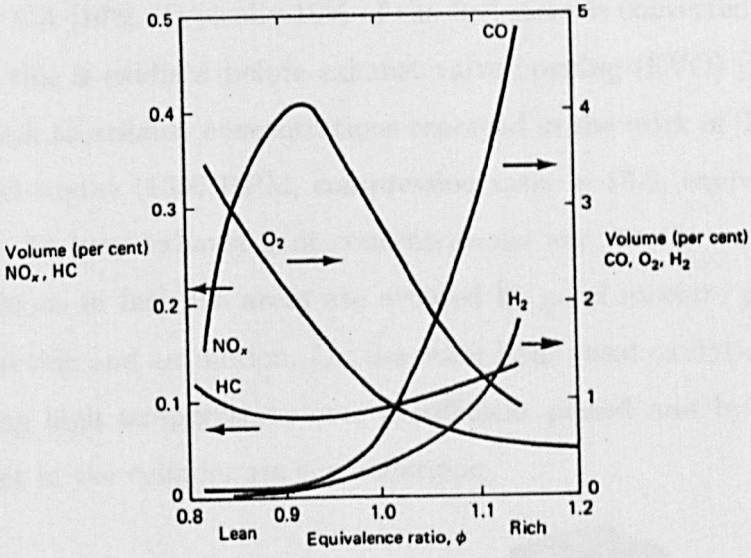



**Figure 1.6:** Pollutant species formation as function of equivalence ratio $\phi$ (from [412]).

The critical air/fuel equivalence ratio for $NO_X$ formation is close to stoichiometric, since this is where the flame temperatures are the highest (see Figure 1.6). During the diffusion burn phase the concentration of nitric oxides increases within the combustion chamber, since a larger portion of the charge mixes to stoichiometric state in comparison to the premixed phase [16]. However, there is strong evidence that $NO_X$ is formed early during the first 20° CA after start of combustion, primarily from products of the premixed burn phase due to the rapid heat release and associated temperature increase during this period [372, 441]. Hence, to control $NO_X$ formation an optimised initial injection profile is necessary. During the expansion stroke the $NO_X$ reactions slow down and finally freeze in the late combustion stage as the gas temperatures drop and dilution of hotter regions with cooler air takes place. As a consequence of the $NO_X$ formation reactions being strongly dependent on local gas temperature, measures to lower the flame temperature like EGR are beneficial [162].

The onset of soot formation occurs early in the burning process. Soot is formed at temperatures between 1000 – 2800 K and pressures between 5 – 10 MPa for air/fuel ratios below 0.6 [50, 167]. Rapid soot formation is followed by oxidation

over 30° – 40° CA [162]. Typically 10% of the fuel mass is converted into soot, but about 90% of this is oxidised before exhaust valve opening (EVO) [162, 372]. The ratio of the peak to exhaust concentrations reported in the work of Tree *et al.* [431] for a DI Diesel engine (1300 RPM, compression ratio = 15.5, equivalence ratio = 0.3) was 282. To keep exhaust soot concentrations low, on the one hand, highly sooting conditions in fuel-rich areas are avoided by good mixture preparation via controlled injection and air motion. On the other hand, soot oxidation is facilitated by maintaining high temperatures over a sufficient period and by increasing the oxygen content in the cylinder via supercharging.

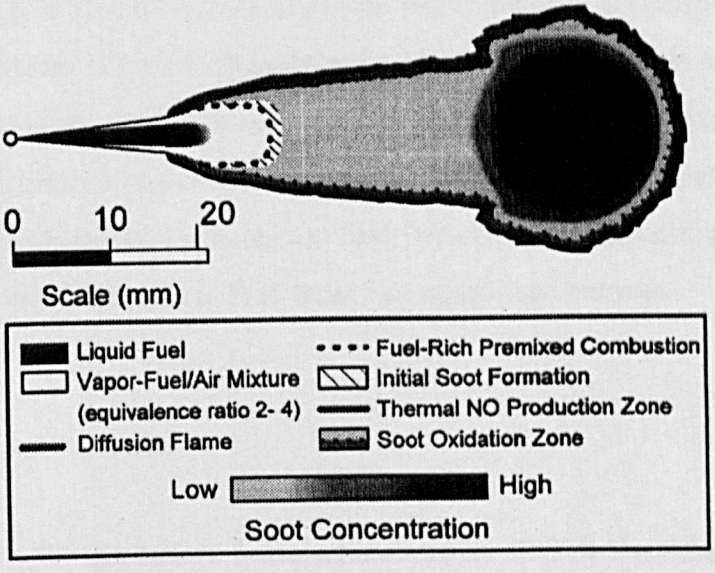



**Figure 1.7:** Conceptual schematic of Diesel flame during diffusion burning (from [88]).

A conceptual schematic of a representative Diesel flame shown in Figure 1.7 for the period after the premixed burn and before EOI was deduced from laser imaging techniques by Dec and coworkers [86, 87, 88]. Around the liquid core an air/fuel mixture of equivalence ratio between two and four is formed. As air is entrained, a rich premixed combustion zone is formed downstream, where initial soot particles are generated. Subsequent growth of soot particles caused by coagulation and collision takes place, while the particles are convected downstream to the flame tip. There the particle size is the largest and the soot concentration is the highest. Oxidation of soot and products of the premixed burn region is enabled by the presence of

molecular oxygen and the $OH$ radicals close to the diffusion combustion region at the periphery of the flame. Thermal $NO$ is found on the lean side of stoichiometric mixture at the flame boundary, where the temperatures are the highest.

After EOI the upstream portion of the flame gradually disappears, while the downstream part reaches the bowl wall. The flame spreads along the walls and folds back towards the centre of the bowl. During this period the soot-filled pocket at the flame tip shrinks, as soot is oxidised.

Unburnt HCs in Diesel engines originate from fuel that is completely unburnt or only partially burnt. This condition results either from excessive mixing as locally the mixture is overlean and therefore will not autoignite, or from flame quenching at the walls and in crevice regions such that combustion is incomplete. Another source for unburnt HCs is due to under-mixed fuel, injected near the end of combustion or from fuel that vapourises after EOI from the nozzle sac volume.

#### 1.2.2.4 Exhaust stroke

At around 40° – 60° CA before bottom dead centre (BDC) the exhaust valves open. At this point the majority of burning has ended and the cylinder temperatures have decreased considerably. Due to the large pressure difference between the cylinder and the exhaust system the burnt mixture flows out of the chamber. To improve scavenging the inlet valves open approximately 10° – 20° CA before TDC exhaust to allow positive air flow through the engine. At high load this is additionally beneficial owing to more efficient cooling of critical parts like the exhaust valves. Volumetric efficiency is thereby enhanced [167]. However, as the cylinder pressure decreases, reverse flow into the inlet port occurs which can promote port fouling. During the expansion process and in the exhaust system the remaining soot particles coalesce with heavy hydrocarbons and sulfates before being released into the environment. The exhaust valves typically close between 8° – 20° CA after TDC.

## 1.3 Effect of High Peak Pressure Operation on Diesel Engine Processes

The present high peak pressure (HPP) Diesel engine concept utilises a supercharger in conjunction with an air intercooler. For this, the dependence of mixture pressure and temperature at SOI on intake pressure is illustrated in Figure 1.8.

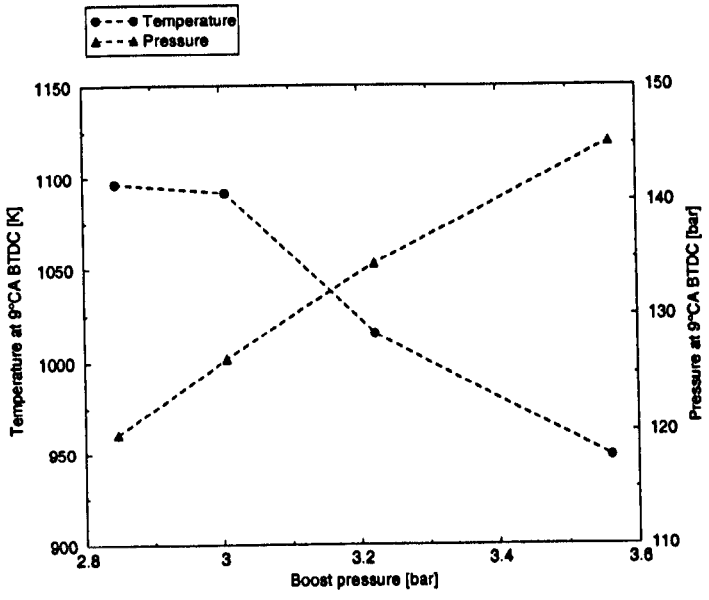



**Figure 1.8:** Effect of boost pressure on in-cylinder pressure and temperature at SOI for HPP prototype engine (data obtained from [248]).

As the boost pressure is increased, the cylinder pressure at SOI is augmented approximately linearly, but the cylinder-averaged mixture temperature at SOI decreases by a similar proportion. Thus cooling of intake air results in gas temperatures during the intake stroke that are considerably lower than without this measure, resulting in reductions in mean gas temperature of the order of 30% at SOI, assuming isentropic compression. In addition, the increased charge density necessitates more thermal energy during the combustion period to heat up the larger cylinder mass causing lower mean combustion temperatures compared to without supercharging and intercooling. The effect of these charged pressure and temperature levels on the Diesel engine process is summarised next.

### 1.3.1 Thermodynamics

#### 1.3.1.1 Gas phase

As illustrated in Figure 1.9 with increasing pressures the gas thermodynamic state, defined by pressure, volume and temperature, changes its characteristics found at low pressures, usually described by the ideal gas law [133, 358]. The extent to which the state departs from the ideal gas behaviour is related to the critical properties of the fluid and is particularly large for high pressure and low temperature conditions (see Figure 1.9). The HPP engine operates under reduced pressures $p_r$ between 0.1 and 6 and reduced temperatures $T_r$ between 2 and 13. The implications of high cylinder pressures with respect to the ideal gas law is studied in detail in Section 3.2.6.

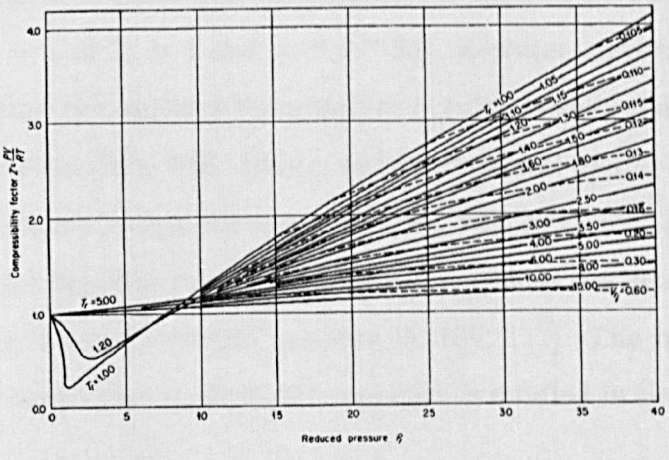



**Figure 1.9:** Generalised compressibility chart (from [358]). The compressibility $Z$ is plotted over reduced pressure defined as gas pressure over critical pressure. $Z$ equals unity for ideal gases.

In addition, the thermophysical properties (e.g. viscosity and conductivity) are affected by the high pressures in the cylinder. In this regime they are found not only to strongly vary with temperature, but also with gas pressure [358]. The behaviour of transport properties under these conditions in turn influences interactive processes between gas and liquid phase, and gas phase and wall, respectively. This is studied for the HPP concept in Section 3.2.7.

#### 1.3.1.2 Liquid phase

##### Thermophysical properties

As the gas pressure increases, the liquid thermophysical properties become dependent on pressure as well as temperature [358]. Also anomalies occur close to the critical point [133]. This influences the characteristics of droplet behaviour and properties like vapourisation, phase equilibrium, transport properties and solubility of gases in the droplets [144, 472]. A significant change in the behaviour of thermophysical properties is attained when the mixture critical point is exceeded, known as supercritical conditions. This results in the gas and liquid densities being of the same order of magnitude such that the gas/liquid interface vanishes. The gas and liquid are essentially of the same phase. This regime is attained only for a combination of ambient reduced quantities (defined as the ratio of actual to critical value) of $T_r > 2$ and $p_r > 1$, or $T_r > 1$ and $p_r > 2$ [133]. However, in droplet clouds it has been recognised that the ambient temperature is substantially reduced due to cooling from vapourisation [208, 209]. Hence, the supercritical regime is not reached for the majority of droplets within the spray core [96, 208, 209, 404]. In addition due to increasing gas solubility into the liquid, critical conditions are attained at pressures much higher than the fuel's critical pressure [5, 107, 111]. The implications of the HPP concept on liquid thermophysical properties is studied in Section 3.4.5.

##### Spray

A summary of the observed trends in sprays documented in the literature with increasing gas pressure is given in Table 1.2. At increased gas pressures, the spray angle increases. Additionally the axial droplet spacing is reduced resulting in higher collision and coalescence rates, which in turn increase the mean droplet diameter. Aerodynamically-induced droplet deformation is increased due to the diminishing liquid surface tension as gas pressures are rising. Also when the liquid surface tension decreases breakup is facilitated, resulting in shorter breakup length and

time. Consequently, the liquid penetration length is reduced. Since gas heat transfer depends on the mixture Reynolds number (see Eq. (3.70a)) which in turn depends on pressure, the heat transfer rates between the liquid and gas phases are enhanced when the chamber pressures increase. Thus in this case the evaporation rate becomes faster.

| Parameter | Effect[a] | Reference |
|---|---|---|
| Spray angle | ↑ | [179, 310, 359, 360, 486] |
| Breakup length and time | ↓ | [18, 78, 112, 131, 179, 329, 359] |
| Evaporation rate | ↑ | [5, 189, 284, 388, 432] |
| SMD | ↑ | [177, 329, 419, 486] |
| Spray tip penetration | ↓ | [18, 177, 265, 310] |
| Axial droplet spacing | ↓ | [78] |
| Droplet coalescence and collision | ↑ | [359, 364] |
| Droplet deformation | ↑ | [78] |

[a] ↑ increase, ↓ decrease

**Table 1.2:** Effects of increasing gas pressure on spray behaviour.

The influence of increased pressures is studied for a simplified single droplet evaporation case in Section 3.4.5.8. Further in-depth studies of the effect of liquid thermophysical properties for elevated pressure and temperature conditions on evaporation are found in [81, 82, 90, 144, 188, 205, 206, 210, 301, 348, 432, 436, 437, 487].

### 1.3.2 Ignition and combustion

For a rapid compression machine, Miwa *et al.* [298] studied the effect of pressure and temperature on ignition delay as a function of both the chemical and mixing characteristics. Figure 1.10 displays the findings. An increase in either gas temperature or pressure results in shorter delays (see also [5, 146, 381]). Further, as the pressure is increased, the ignition delay becomes less sensitive to variations in the temperature level. Moreover, a change in ignition behaviour was observed at around 800 K. Below this temperature physical processes like evaporation and air/fuel mixing were found to determine ignition delay while above this temperature the chemical delay seemed to control its duration. Generally it was found that the ignition phenomena

are strongly influenced by spray-related processes such as evaporation and air/fuel mixing [5].

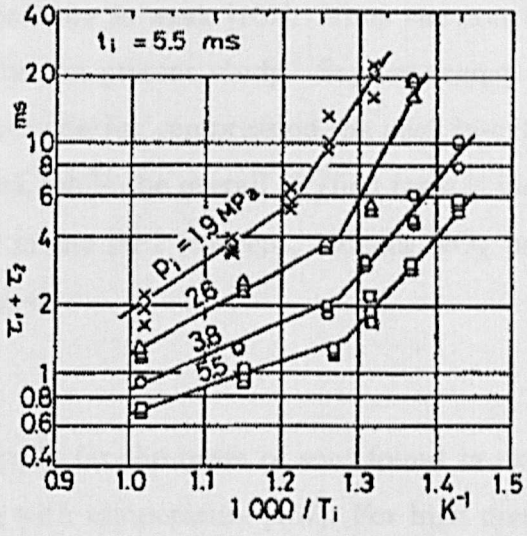



**Figure 1.10:** Effect of temperature $T_i$ and pressure $p_i$ on ignition delay (from [298]). Ignition delay is comprised of the physical delay $\tau_1$ and the chemical delay $\tau_2$.

The chemical reaction rate depends significantly on pressure as the chemical processes are influenced directly by the partial pressure of oxygen [435, 464]. This is already taken into account in the conventional combustion modelling practice. Single droplet combustion was investigated by several researchers under high pressures [60, 133, 175, 385, 433]. Their findings reveal that with increasing pressure the burning rate accelerates, reaching a maximum near the fuel's critical pressure. For supercritical pressures the burning rate tends to decrease with rising pressure, since the combustion is mainly governed by diffusion processes rather than evaporation [84, 109, 133, 216, 472]. However, as said before, the majority of the spray droplets, subject to the high pressure environment, do not reach the supercritical state.

### 1.3.3 Pollutant formation

Since the emission regulations for $NO_x$ and soot are most critical, only these pollutants are considered in this section.

Nitric oxide formation in Diesel engines is strongly influenced by local mixture temperature, as described by the Zeldovich mechanism, and oxygen concentration. The dependence on pressure is weak [167]. Thus the conventional $NO_x$ model is sufficiently accurate for the present study. Supercharging without intercooling is particularly critical, since during compression the peak in-cylinder temperatures are significantly augmented, while the overall air/fuel ratio is increased. Yet, intercooling the intake air, as in the HPP concept, reduces $NO_x$ production, as the peak temperatures are lowered.

The critical C/O ratio for the onset of soot found in experiments lies between 0.5 and 0.8 increasing with temperature [167]. For high pressures soot inception is accelerated in fuel-righ regions where the temperature is high. Due to supercharging a denser mixture is present in the cylinder with higher oxygen content. Therefore soot oxidation is particularly promoted resulting in an overall reduction in soot emissions [5, 220, 225, 372]. The effect of pressure on soot formation and oxidation is already considered in the conventional soot model as described in Section 3.6.2.

### 1.3.4 Wall heat transfer

Wall heat transfer depends on the gas-side turbulent heat transport in the boundary layer that is characterised by steep gradients of temperature particularly during combustion [167]. The gradients, defined by the mixture and wall temperature, subsequently influence the thermophysical properties of the mixture due to their temperature dependence, which in turn affect the boundary layer thickness and wall heat flux, respectively. The influence of increased PCP on wall heat flux is accounted for via the description of mixture thermophysical properties. For the current study, a modified wall heat transfer approach is proposed in Section 3.8.1.3 to capture the steep gradients of transport properties in the boundary layer.

### 1.3.5 Conclusion

The impact of the HPP concept on various engine processes, documented in the literature, has been summarised. Gas/liquid interaction and spray dynamics change considerably as the peak cylinder pressure is augmented. These effects need to be captured appropriately for a numerical simulation. Combustion characteristics, pollutant formation mechanisms and wall heat transfer depend stronger on temperature than on pressure. The influence of temperature on in-cylinder processes is already considered in the conventional CFD engine methodology.

## 1.4 Present Contribution

The objective of this study is to assess and where necessary and feasible modify or extend multidimensional Diesel combustion simulation methodology, embodied in an existing CFD code, to make it applicable to the new increased peak pressure design concept. The specific contributions are as follows:

- **Assessment:** The conventional modelling approach regarding the thermodynamics of the gas and liquid phases have been assessed for the unusually high chamber pressures.

    1. An evaluation of the appropriate equation of state for the pressure and temperature range of the HPP concept has been performed.
    2. The validity of correlations for the gas and liquid thermophysical properties in this regime have been studied.

- **Extension and modification:** The existing state-of-the-art Diesel engine simulation methodology has been modified and extended as follows:

    1. An alternative combustion model of the laminar flamelet type, RIF, was interfaced with an existing CFD code. It includes detailed chemistry for

*n*-heptane fuel ignition and combustion and incorporates $NO_x$ and soot models and particle dynamics.

2. An improved wall heat transfer treatment for the range of operating conditions has been implemented.
3. Phenomenological soot formation and oxidation mechanisms have been added to an existing eddy breakup combustion model which already incorporates a $NO_x$ model.

- **Evaluation:** The revised CFD methodology has been extensively tested by reference to experimental data. The test cases include:

1. RWTH Aachen engine: A motored axisymmetric research engine for flow field and heat transfer evaluation.
2. Aachen pressure chamber: A quiescent constant-volume pressure chamber for spray, combustion and soot comparisons.
3. HPP prototype engine: A high-pressure DI Diesel engine prototype for combustion, emissions and heat transfer comparisons.

## 1.5 Thesis Outline

In the following chapter an overview is given of previous modelling attempts for Diesel engine processes including phenomenological and multidimensional models. The various subprocesses in Diesel engines are then described and the major previous modelling approaches in the CFD framework are outlined. A summary of the most widely-used submodels in CFD Diesel engine modelling is given.

In Chapter 3 the mathematical models used in this study are described. The instantaneous transport equations are derived for the gas phase of a two-phase gas/liquid flow system. They are then ensemble-averaged and additional turbulent transport terms are closed via the $k - \varepsilon$ turbulence model. The Lagrangian discrete droplet method is introduced, incorporating various separate submodels for

the spray processes encountered in Diesel engines. In the light of the HPP concept a study of increased pressures on gas and liquid thermophysical properties has been added. The ignition, combustion and pollutant formation models are presented next. Finally, the boundary and initial conditions are outlined to complete the mathematical description.

The numerical practices applied are provided in Chapter 4. The integration and discretisation of the governing equations are described, employing the finite volume method on general unstructured meshes with a collocated variable arrangement. Additionally the discretised boundary conditions are reproduced. The solution procedure based on the PISO algorithm for solving the discretised governing equations is briefly outlined. The description of numerical solvers using the conjugate gradient method and the relevant convergence criteria concludes the numerical approach.

The following Chapter 5 briefly describes the experimental and computational setup, together with available measurement data. Validation studies for three test cases are discussed in Chapter 6 by comparing predictions with experimental data. The flow field and heat transfer predictions are compared with measured data for a motored research engine. The calculated vapour and spray evolution, ignition delay and soot concentrations are evaluated by comparison to measurements for a pressure chamber under Diesel-like conditions. Finally, the results for combustion characteristics, heat transfer and exhaust concentrations are presented for the HPP prototype engine at several operating points and compared with experimental data.

The findings of the current study are summarised in Chapter 7 along with recommendations for future research.

# Chapter 2

# Previous Modelling of Diesel Engine Processes

## 2.1 Introduction

The previous chapter introduced the trends in Diesel engine development among which the high peak pressure engine concept, investigated in the present work, is a significant contribution. Also, the benefits of this concept and implications on Diesel engine processes were discussed along with the present contributions. This chapter briefly reviews two major modelling categories in Section 2.2. They include phenomenological models and multidimensional modelling approaches. The various modelling approaches for the Diesel engine subprocesses are briefly described in Section 2.3. The closure in Section 2.4 concludes this chapter.

## 2.2 Modelling Categories

In numerical simulations a mathematical framework is used to describe the various physical processes involved in Diesel engines. The existing methodologies can be

grouped into two main categories [167]: *phenomenological* and *multidimensional* models. They are described next.

### 2.2.1 Phenomenological models

The phenomenological category comprises zero- and one-dimensional models in which the thermodynamic and chemical state of the working fluid is described. Zero-dimensional models do not incorporate geometric features nor any flow field description and are therefore used primarily for parametric performance studies of the entire engine as part of cycle simulations [4, 26, 353, 483]. One-dimensional models† introduce spatial information and are often used in connection with a zonal approach, where regions in the cylinder with similar flow pattern (e.g. bowl, cylinder and boundary layer) are taken into account by a separate set of equations. In this case prior knowledge of the flow structure is essential. Each phenomenon is then modeled separately as illustrated in Figure 2.1 including thermodynamics, in- and outflow processes, heat transfer, combustion and emissions. Applications for DI Diesel engines range from predictions of fuel spray penetration [239, 245] to combustion and emissions [244, 250, 253, 302].

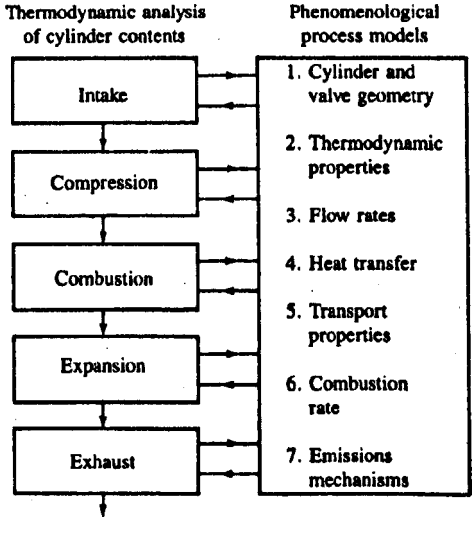



**Figure 2.1:** Flowchart for phenomenological models (from [167]).

†One-dimensional models are also referred to as quasi-dimensional or zonal models [167, 337, 412].

The disadvantages of phenomenological models arise from the necessity to fit their parameters to experiments and their limited insight into detailed physical phenomena like spray behaviour. However, due to their simplicity and capacity to predict overall trends, they remain popular among engine developers [337]. Further reading is provided in [167, 176].

### 2.2.2 Multidimensional models

Multidimensional models (MDMs), which are also known as *Computational Fluid Dynamics*, describe physical phenomena in all three spatial directions and time which renders them more complex and more computationally expensive compared to phenomenological models. However, they are more realistic and provide a fundamental insight into the nature of engine processes. A set of coupled partial differential equations (PDEs) is used to describe the conservation of mass, momentum, energy and species concentration together with an equation of state (EOS) for the fluid. The continuity and momentum equations are usually referred to as *Navier-Stokes* (NS) equations. The solution domain is resolved into a finite number of discrete domains (i.e. computational mesh) and numerical algorithms solve the PDEs expressed as a system of algebraic relations, linking the variables in the discrete domains. Such discretisation approaches comprise the finite difference method (FDM), the finite element method (FEM) and the finite volume method (FVM), which are described in more detail in the works of [118, 443, 456]. The FVM is mostly applied in MDMs, in part because it ensures that the conservation laws are obeyed.

As elucidated in Section 1.2 Diesel engine flows contain highly unsteady turbulent flow with length scales varying over several orders of magnitude. These scales require adequate resolution, but the choice of the appropriate methodology has to balance accuracy, stability and computation cost [337]. Three major approaches have been employed for flow simulations: *direct numerical simulation* (DNS), *full-*

*field modelling* (FFM) and *large eddy simulation* (LES)†.

In DNS the governing equations are solved numerically with sufficient spatial and temporal resolution. Turbulent motion is resolved down to the smallest scales on which viscous forces are active, the so-called Kolmogorov microscale. With this scale being of the order of $10^{-2}$ mm at around SOI due to the injection process [121, 139], a computational mesh with more than $10^{12}$ grid points for a 3-D engine simulation becomes necessary [362, 365]. In addition the small timescales of around $10^{-5}$ s at SOI [139] need to be resolved. This approach would therefore entail a prohibitive computational overhead and thus is unrealistic for engine calculations [118, 167, 337]. To overcome the impractical direct solution of motions of all scales, approximations via statistical averaging have been introduced for the remaining methodologies.

In FFM the flow variable is decomposed into a mean value and its fluctuating component. For engine calculations phase-averaging (or ensemble-averaging) is customary to represent the average of values at a certain instance in an engine cycle. The PDEs of the mean quantities are then solved everywhere in the flow, while additional models are needed to express various averages of turbulence parameters, usually referred to as *Reynolds stresses* and turbulent scalar fluxes, respectively. The models must encompass the contribution of all scales of turbulent motion. This introduces approximations, since the characteristics of large-scale motion are different from small-scale motion; the former being inherently anisotropic (i.e. turbulent motion depends on flow direction) while the latter approach isotropy [371]. Engine simulations are commonly based on FFM.

LES calculates large-scale turbulent flow directly down to a scale of the order of the mesh size. Turbulence of smaller scales is modeled separately through statistical averaging. New unknowns as in the FFM arise, coined *subgrid-scale Reynolds*

†Full-field models are sometimes termed *statistical flux models* while large eddy simulations are occasionally coined *subgrid-scale simulations* [167].

*stresses.* Since small-scale turbulence is isotropic in character, the turbulence modelling in this approach tends to be more accurate [143, 371]. Turbulence in LES is defined as the fluctuations of flow variables about their local average and is therefore related to the current engine cycle. In FFM, on the contrary, it stands for variations at one location and at a specific instant about an average obtained over many engine cycles. LES is generally more computationally expensive than FFM due to higher mesh resolution particularly in the near-wall region [405]. Moreover several engine cycles have to be computed to obtain ensemble-averaged quantities crucial to the engine design. Hence this approach has not routinely been used in engine calculations [160, 371, 443].

## 2.3 Modelling of Diesel Subprocesses

In what follows the modelling approaches for Diesel subprocesses typically used in CFD Diesel engine simulations are briefly reviewed.

### 2.3.1 Turbulence

The turbulence closure completes the ensemble-averaged momentum equations by expressing the Reynolds stresses in terms of the other unknowns of these equations. Three main classes of turbulence models exist: *Algebraic models*, *turbulent viscosity models* and *Reynolds stress models.*

Algebraic and turbulent viscosity models presume the existence of an analogy between the effect of viscous stresses and Reynolds stresses on the mean flow which can be formulated in a Newtonian-type relationship. This approach is known as the *Boussinesq hypothesis* which introduces a ficticious scalar eddy viscosity $\nu_t$. The underlying assumption for both approaches is that the local turbulent viscosity is isotropic, i.e. the ratio between Reynolds stress and mean rate of deformation of

fluid particles is the same in all directions. This assumption is violated in particular for recirculating, separating and stagnation point flows.

Among the turbulence closures the two-equation models which belong to the turbulent viscosity approaches have attracted the largest research effort in the past for engineering flows. They comprise two transport equations for the velocity and length scale, respectively, or related quantities. The eddy viscosity is expressed as a function of both. The effect of transport of turbulence quantities by mean flow and diffusion is catered for and the production and destruction of turbulence is taken into account. The basic assumption made is that the rate of energy dissipation is driven by the decay of large eddies into small-scale dissipative turbulence.

Commonly the velocity scale is given in terms of the turbulence kinetic energy $k$. The second transport equation is expressed in terms of either the length scale $l$ itself, a timescale $\tau$, the dissipation per unit turbulence kinetic energy $\omega$ or the dissipation rate $\varepsilon$. In-depth discussion of each approach is found in [149, 462].

In engine simulations usually the $k-\varepsilon$ turbulence model is employed (see e.g. [13, 155, 195, 204, 320, 366, 453]) due to its compromise between simplicity, accuracy and computational efficiency [167, 443]. The standard $k-\varepsilon$ turbulence model is based on the work of Jones and Launder [212]. Extensions have been included to account for compressibility effects, essential for engine flows [101]. Also modifications have been incorporated to make it applicable to two-phase flows such as in Diesel engines [246]. Further development of this turbulence closure include different model coefficients, extensions to the turbulence transport equations and non-linear $k-\varepsilon$ turbulence models (cf. [443, 462, 470]).

Another turbulence model has been applied to engine calculations, notably the *Reynolds stress transport model.* The model comprises equations for each of the Reynolds stress tensor components, eliminating the assumption of turbulence isotropy as in the turbulent viscosity models. The solution of additional transport

equations greatly increases the computational requirements without the guarantee of substantially better results [443]. This is why only a few validation studies for engine simulations have been carried out in the past (see e.g. [102, 263]).

### 2.3.2 Spray

Two main concepts have emerged to address phase modelling for sprays in Diesel engines. The first concept, the *locally homogeneous flow* (LHF) model, assumes infinitely fast rates of interphase transport compared to flow field timescales. Therefore the local kinematic and thermodynamic equilibrium is maintained. For spray applications this concept is approximated accurately only for sprays with very small droplets having a Sauter mean diameter (SMD) of less than 10 $\mu$m [107, 249]. It was recognised that spray processes under Diesel-like conditions exhibit finite interphase transport rates resulting in significant disagreement with experiments [108, 229]. This was attributed to the fact that in real sprays the relative velocities of the droplet and gas differ partly due to high injection velocities and partly due to larger droplet diameters. The LHF approach has been mainly used for bubbly flows [402, 445] and combustion of sprays [229, 282, 316, 429] and is further documented in the review of Faeth [107] and Kuo [249].

The second concept treats each phase individually and is therefore coined the *separated flow* (SF) model, allowing for finite interphase transport rates of mass, momentum and energy. Generally, processes in the flow field are only resolved in detail down to the drop size due to computational time considerations. This requires that phenomena inside and immediately surrounding the drops be captured via empirical correlations. With regard to the liquid phase, two approaches have been used, namely the *continuous* and *discrete* approach. The former models the liquid phase either as a second continuum, treated in a Eulerian framework [100, 157], or as a droplet cloud whose properties are represented by a multidimensional distribution function [158, 430, 464]. In the latter case a transport equation for this statistical

distribution function is solved at all locations in the flow field for each droplet size subrange, thus creating excessive computational overheads [158].

Sprays in Diesel engines are commonly modeled by the *discrete droplet method* (DDM) [107, 140, 141]. The spray is introduced into the combustion chamber as parcels, each of which characterises a large number of identical droplets, whose state is derived from the solution of conservation equations expressed in Lagrangian formulation. Since the flow phenomena immediately surrounding the droplets are not solved in detail, empirical correlations are used to estimate the interphase transfer rates of mass, momentum and energy between the droplets and the gas phase. In addition, submodels are employed to specify various physical processes within the spray, including:

- Atomisation
- Droplet dynamics (i.e. drag, breakup, collision, coalescence, turbulent dispersion)
- Droplet heating and vapourisation
- Wall impingement (when required)

These submodels have been described and assessed in a number of reviews [1, 71, 77, 107, 141, 362, 398, 441]. In principle, the validity of the individual submodels is extremely difficult to assess due to difficulties of measurements in dense sprays and problems of achieving adequate mesh resolution when solving the Lagrangian equations. As a consequence, it is customary to adjust coefficients of various empirical correlations to obtain satisfactory quantitative agreement with measurements [140, 362].

Significant differences exist between both modelling concepts of the SF approach. The continuous approach solves the spray equations in the entire solution domain,

despite the droplets residing only in a confined sector of the domain. More importantly for each droplet size range a separate set of spray equations has to be solved to adequately represent the Diesel spray. By contrast, the DDM caters for individual droplet sizes without the increase of computational costs. Hence the discrete formulation is overall less computationally expensive.

A more detailed discussion about the pros and cons of the continuum and discrete approach are provided in [43, 80, 150, 261, 305, 397].

Both spray modelling concepts require a very fine mesh in the near-injector region to resolve steep gradients of gas and liquid phase properties. In DDM, however, since the gas phase is described by Eulerian continuum equations for each domain, a grid size larger than the droplets is required such that in each domain the volume fraction for the liquid phase becomes comparatively small. For too large liquid volume fractions numerical instabilities occur. In Diesel sprays a conflicting situation arises in the injector vicinity between the high gradients of thermophysical properties which require a high mesh resolution and the high droplet densities which necessitate a larger mesh spacing. Therefore, the near-injector region is commonly resolved with a coarser grid. Owing to insufficient spatial discretisation of the flow close to the injector nozzle with a resident gas velocity averaged over the cell, the actual relative velocities between the droplets and the gas phase are overestimated. The situation is illustrated in Figure 2.2. Consequently this produces erroneous inputs for the estimation of gas phase source terms and droplet drag which subsequently will lead to the unrealistic prediction of global quantities like liquid and fuel vapour penetration [107, 141, 247, 415]. This in turn may cause autoignition at wrong locations greatly affecting the flame position.

To address this shortcoming of the DDM while maintaining its favourable computational features, a novel concept has emerged based on a two-fluid formulation [247, 446, 447, 448]. The spray region near the injector including the orifice is solved in a separate code using a 1D approximation which averages over the cross-

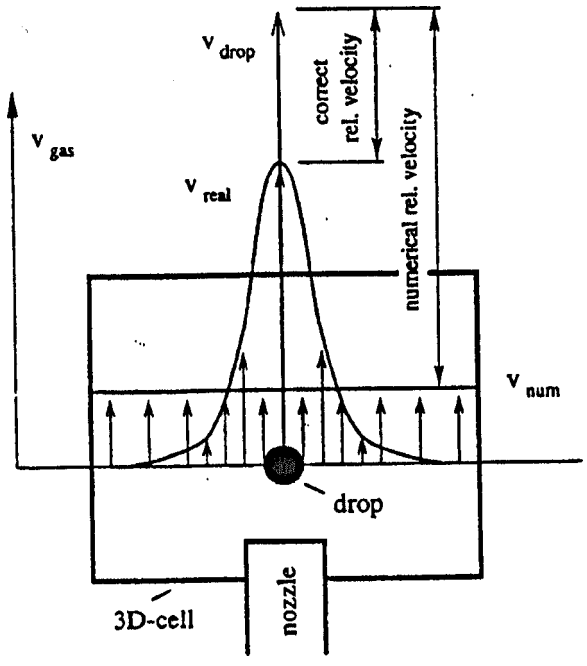



**Figure 2.2:** Schematic of relative velocity computed between gas phase and liquid phase (from [247]). $v_{gas}$ is local gas velocity, $v_{num}$ is averaged gas velocity in cell, $v_{real}$ is gas velocity seen by the drop and $v_{drop}$ is drop velocity.

section of the spray within a predefined cone. Assumptions are made about the profile of flow variables in radial direction and a model has to be specified to account for air entrainment into the cone. The 3D code runs in parallel calculating the gas phase while source terms to and from the gas and liquid phase, respectively, are exchanged between the codes. At a specified distance from the injector, the spray calculation switches from the *cross-sectionally averaged spray* (CAS) to the stochastic particle method as the 1D approximation becomes less accurate in the dilute spray region.

The major impediment to spray modelling is the specification of adequate injector exit conditions from experiments which are a necessary input for the CFD calculation. This is due to the limited optical accessibility of the dense spray region such that insufficient experimental data are available for validation studies [162, 249].

## 2.3.3 Ignition and combustion

### 2.3.3.1 Chemical kinetics

In order to describe the physical state of a chemically reacting system it is essential to take into account the reaction kinetics which depend on various parameters such as the species concentrations, temperature and pressure. In general, a system involving $N$ chemical species and $R$ reaction steps is expressed mathematically as [271]:

$$\sum_{i=1}^{N} \nu'_{ij} M_i \underset{k_{b_j}}{\overset{k_{f_j}}{\rightleftharpoons}} \sum_{i=1}^{N} \nu''_{ij} M_i \quad ; \qquad j = 1, 2, \ldots, R \tag{2.1}$$

where for species $i$ $\nu'_{ij}$ and $\nu''_{ij}$ are the stoichiometric coefficients in reaction $j$ of the reactants and products, respectively, $M$ is the chemical symbol of species $i$ and $k$ is the rate constant for forward and backward direction, denoted by subscripts $f$ and $b$. Of interest in numerical calculations is the reaction rate of each species $i$, $\dot{\omega}_i$, within the system which enters the species conservation equation as source term, given as:

$$\dot{\omega}_i = \sum_{j=1}^{R} \dot{\omega}_{ij}$$

where the individual rate for each reaction $j$, $\dot{\omega}_{ij}$, is expressed as [271]:

$$\dot{\omega}_{ij} = (\nu''_{ij} - \nu'_{ij})\, k_{f_j} \rho^{m_j} \prod_{i=1}^{N} Y_i^{\nu_{ij}} \left(1 - \frac{k_{b_j}}{k_{f_j}} \rho^{(n_j - m_j)} \prod_{i=1}^{N} Y_i^{(\nu''_{ij} - \nu'_{ij})}\right) \tag{2.2}$$

Note that $\rho$ is the density, $Y$ is the species mass fraction, and $m_j$ and $n_j$ are the total numbers of moles of reactants and products, respectively.

Based on collision theory the specific reaction rate constant $k$ is expressed according to the empirical *Arrhenius law* where it is assumed that molecules only react if they acquire an energy level that is higher than the activation energy $E_a$ [249, 464]:

$$k = A \exp\left(-\frac{E_a}{\mathcal{R}T}\right) \tag{2.3}$$

where $A$ is the frequency factor, also termed Arrhenius factor or pre-exponential factor, $\mathcal{R}$ is the universal gas constant and $T$ denotes the temperature. The exponential, called Boltzmann factor, therefore accounts for the probability of collisions

in which reactions can occur. While the activation energy is a constant determined from experiments, the frequency factor may include a weak dependence on $T$ and is often tuned to fit measured rate constants [464].

#### 2.3.3.2 Reaction mechanism

Radicals which are extremely reactive play an important role in pre-ignition and combustion reactions. They are formed and consumed in complex, interdependent reaction mechanisms, so-called *chain reactions.* Chemical reactions are *initiated* with radical-creating elementary reactions which are formed from stable molecules of hydrocarbons and oxygen. Those unstable intermediate species subsequently attack other molecules or radicals. Depending on the number of radicals in the reaction products being unity or greater than one, the reaction is called *chain-propagation* and *chain-branching,* respectively. Chain reactions are *terminated* if radicals are consumed. Chain-branching reactions can accelerate dramatically if they lead to a rapid production of radicals and are simultaneously fed by a rapid heat release, causing *thermal runaway.* This coincides with spontaneous ignition.

For the comprehensive description of a reacting system it is necessary to consider all relevant chemical species and to include all chemical reaction steps with their respective rates. This represents a fundamental obstacle as hydrocarbon combustion involves a large number of significant species and an even larger number of fundamental reactions [441]. To date the detailed reaction mechanisms are known only for a few of the simpler hydrocarbons with considerable uncertainties regarding the reaction rates [271, 464]. In addition, the immense complexity of the full description renders a simulation impractical from the numerical point of view [215, 271, 464]. To address this impediment, it has become customary in engine simulations to introduce a few global reactions which do not represent elementary reaction steps to describe the chemical behaviour. Equation (2.3) then provides the overall rate with coefficients and activation energy fitted to particular conditions [271, 457].

Besides by chemical kinetics the local reaction rate is strongly influenced by turbulence effects, such that the reaction speed slows down. For too high turbulent strain either ignition is prevented or the flame extinguishes. This is due to the heat or radical production not being able to balance diffusive heat losses in the reaction zone.

The approaches for the description of chemical reactions in Diesel engines can be subdivided into two subsequent intervals, depending on the prevailing temperature. The first time interval, called ignition delay or *pre-ignition phase*, extends from start of injection until the appearance of a flame which indicates autoignition. Comparatively low temperatures and low radical concentration exist in the combustion chamber. The second interval, the combustion phase or *post-ignition phase*, begins after autoignition with higher temperatures due to exothermic reactions. Since dominant reaction paths vary considerably with respect to the temperature level, the combustion model may require to switch from one reaction set to another [5]. This has been commonly based on two separate criteria or a combination of both: temperature threshold [35, 152, 328, 365, 390, 449] and temperature gradient [152, 390].

In the following sections the two intervals are summarised and treated separately.

#### 2.3.3.3 Pre-ignition phase

Two main approaches for the MDM modelling of pre-ignition reactions are used. In the first category generic species are introduced in quasi-global reactions to simulate the complex hydrocarbon chemistry. The reactions are selected based on assumptions of the major reaction paths and their rates are tuned such that the important features of experimental data are captured. The most prominent and widely tested member is the multistep 'Shell' ignition model [151, 152] developed for knock modelling in SI engines and extended for Diesel autoignition at high pressures and temperatures by Theobald and Cheng [425]. It reproduces key features of autoignition, e.g. two-stage ignition which refers to the two stages of ignition chemistry: the

chain reactions in the first stage at low temperatures followed by the second stage of accelerated reactions as temperatures increase rapidly. The Shell model will be described in more detail in Section 3.5.1.1. Another such approach is found in [481].

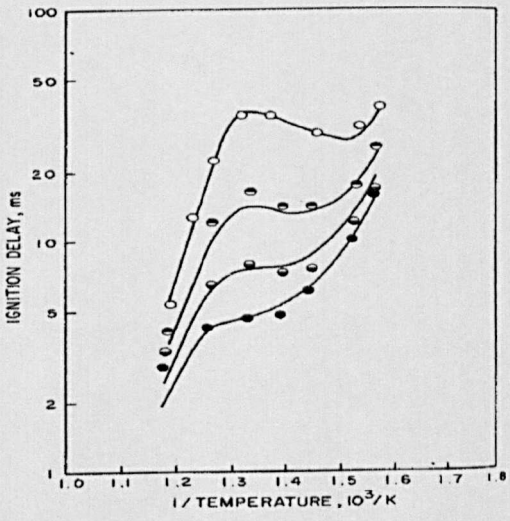



**Figure 2.3:** Comparison between predictions and experiments for Shell ignition model at various pressures for iso-octane at equivalence ratio 0.9 (from [152]). Pressures increase from top line to bottom line as 0.7, 1.0, 1.4, 2.0 bar.

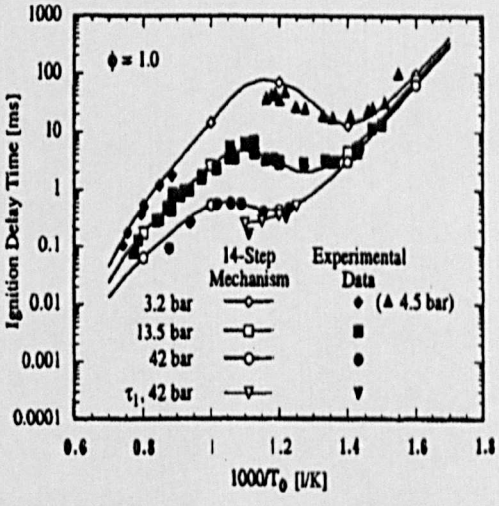



**Figure 2.4:** Comparison between predictions and experiments for a reduced 14-step ignition mechanism for an *n*-heptane/air mixture at unity equivalence ratio (from [342]).

The second category comprises approaches that systematically reduce the comprehensive set of chemical mechanisms through fundamental assumptions. The steady-state approximation is applied to reaction intermediaries such that the number of system equations is reduced. This holds true in particular for chain reactions with little branching. Similarly partial equilibrium is assumed for specific reactions in forward and backward direction reducing the order of the governing equations. Examples for such approaches are found in [49, 51, 308, 334, 342].

Figures 2.3 and 2.4 show the comparison of two autoignition models with experimental data under engine-like conditions for various pressures. Quantitative agreement is excellent.

#### 2.3.3.4 Post-ignition phase

Three major regimes are distinguished for non-premixed, gaseous, turbulent combustion, classified by the respective timescales involved which are the reaction and turbulent mixing timescale [97, 249, 464]. The reaction timescale comprises the period during which species react towards chemical equilibrium. The turbulent mixing time concerns the time for turbulent structures separating fuel and oxidiser to break up and mix such that molecular chemical reactions can occur.

The first combustion regime represents the limit of *finite rate chemistry* where reaction rates have comparatively large timescales compared to the turbulent mixing timescales. The second regime is the limit of *fast chemistry* which is governed by turbulent mixing processes, since the reaction timescales are very small. In the third regime both timescales are of similar order such that the effect of each has to be taken into consideration. For hydrocarbon fuels the key reaction steps that occur at high temperatures are usually significantly faster than transport processes, thus approaching the fast kinetics assumption [215]. In this regime complete combustion is attained as soon as the reactants are mixed. To compute the reaction chemistry, an algorithm for chemical equilibrium such as that in [138] is conventionally used. The solution is commonly based on defining a conserved scalar variable[†] from which the thermodynamic and thermochemical state of the system can be deduced. Reaction rates are no longer needed.

In Diesel combustion many phenomena related to hydrocarbon combustion cannot be approximated by the fast chemistry assumption. They exhibit finite kinetics such as for ignition, flame quenching, incomplete combustion and pollutant formation [215, 249]. Therefore the majority of Diesel combustion processes fall in the third regime and resolve simultaneously mixing and reaction timescales.

[†]The conservation equation for this scalar contains no source term.

Current Diesel combustion models can be categorised into *eddy breakup-based* and *flamelet-based* approaches. They are described next.

### Eddy breakup-based models

This category of combustion models is based on the eddy break-up (EBU) model of Spalding [407, 408] which presumes that the reaction speed is controlled solely by the turbulent dissipation and mixing of small scale eddies. The chemical reaction is assumed to occur infinitely quickly. The mean reaction rate for the fuel is therefore given as:

$$\overline{\dot{\omega}_f} = -\rho C_f \frac{\varepsilon}{k} \sqrt{\overline{Y_f'^2}} \tag{2.4}$$

where $f$ indicates fuel quantities, $C_f$ is an eddy-breakup coefficient, $k$ is the turbulence kinetic energy, $\varepsilon$ denotes the dissipation rate and $\overline{Y_f'^2}$ is the root-mean-square concentration fluctuation. Note that the ratio $\frac{\varepsilon}{k}$ is the eddy breakup rate. Spalding's EBU concept has been successfully applied in highly turbulent premixed combustion [464].

Further development by Magnussen and Hjertager [279] lead to a widely-used variant suitable for premixed or diffusion flames. It still assumes fast chemistry when deriving a rate expression, but therein additionally takes into account the dependence on dissipation rate of eddies containing different species (i.e. fuel and oxygen) and burnt products.

Patterson *et al.* [328] introduced the Magnussen EBU-type Laminar And Turbulent Characteristic Timescale (LATCT) model for Diesel combustion, based on an extension of the characteristic time model of Reitz and Bracco [361], previously developed for SI engines by Abraham *et al.* [2]. It assumes that all species simultaneously react towards the local equilibrium concentration in a characteristic time which consists of the sum of laminar (i.e. chemical kinetic) and turbulent timescales. Therefore the importance of laminar chemistry is recognised in particular during

early flame growth before turbulent mixing becomes predominant. Additionally regions, in which laminar timescales are large such as in the near-injector region compared to turbulent ones due to high injection velocities, are represented more accurately with respect to Magnussen's approach. The laminar timescale is evaluated from an Arrhenius expression which can include residual gas effects and the turbulent counterpart is essentially the same as for the Magnussen model. Further extensions of the initial LATCT model are documented in [241, 469].

Two major shortcomings exist for the EBU-based models. Firstly, the coefficients appearing therein have been assigned different values in the literature, indicating that they need to be adjusted for each combustion system and operating condition [140]. This is not desirable. Secondly, the eddy turnover time $\frac{k}{\epsilon}$ which governs the reaction rate in Eq. (2.4) tends to vanish *at the wall* as the turbulence kinetic energy $k$ goes to zero [454, 455]. This results in infinite flame speeds which are unphysical. In the case of the LATCT model the near-wall reaction rate will be dominated by the laminar timescale, since the turbulent counterpart is negligible. Therefore a less drastic, unphysical increase in flame speed is predicted at the wall.

Despite those deficiencies, the Reitz *et al.* EBU-type combustion models have been extensively tested and used by researchers for truck engines [140, 240, 362]. They will be described in more detail in Section 3.5.3.

### Flamelet-based models

Combustion models that fall under this category are based on the laminar flamelet concept [332]. They describe a turbulent diffusion flame as an ensemble of laminar diffusion flamelets for which chemical timescales are assumed to be much shorter than turbulent mixing scales. Therefore the reaction zone is very thin compared to the integral turbulence scale. However, it is recognised that turbulence may affect the local flame structure via turbulent strain, such that the reaction is either slowed or quenched.

One family of such flamelet-based approaches are the *flame area models* of Dillies *et al.* [94] and Musculus and Rutland [309]. Their models are adaptations of Marble and Broadwell's Coherent Flamelet Model [283] for use in Diesel combustion. Flame surfaces are established (e.g. for flame zones burning in premixed and diffusion mode) for which transport equations are solved. Surface generation due to turbulent strain and surface depletion as a result of quenching and burnout of reactants are accounted for. Thus far there has been limited success in the application of such models for Diesel engines [140] because of the necessity to choose adequately several coefficients therein for each operation mode with only a few studies to guideline their choice.

The most recent flamelet approach is the *Representative Interactive Flamelet* (RIF) method of Peters and coworkers [31, 33, 34, 35, 57, 339, 341, 343, 449], which is based on the fast chemistry assumption. Combustion takes place in the vicinity of the stoichiometric mixture contour and the flamelet structure is understood to extend normal to this surface. Non-equilibrium effects due to turbulent strain are accounted for so that the reactions may not go instantaneously to equilibrium. On the grounds of the assumption that chemical timescales are considerably shorter than turbulent mixing scales it is legitimate to decouple the chemistry from the fluid dynamics. Under certain additional assumptions the laminar flamelets can be calculated separately by unsteady one-dimensional transport equations in mixture fraction space which are relatively inexpensive to solve. Therefore a detailed chemistry mechanism can be incorporated which includes ignition, combustion, pollutant formation and soot reactions. The coupling of flamelet and CFD calculations necessitates the exchange of flamelet parameters (i.e. pressure, oxidiser-side temperature, fuel-side temperature and scalar dissipation rate) from the CFD solution to the RIF, and the flamelet solution in terms of instantaneous reaction extent and heat release to the CFD calculation. The latter quantities concern laminar values which are converted to their turbulent counterparts via the presumed-PDF approach. This alternative approach to the EBU-type models is presented in more detail in Sec-

tion 3.5.3.2.

Despite of simplifications in the flamelet solution, the computing requirements of the detailed chemistry prohibit its application at every grid point. Therefore initially only one flamelet has been solved by the RIF developers requiring spatial averaging of the CFD solution. However, recent effort has lead to the development of the *Eulerian Particle Flamelet Model* which is based on the RIF method with up to 20 flamelets to better represent Diesel combustion. The method is described in detail in [31, 32, 33, 34, 163].

### 2.3.4 Pollutants

In the EBU-type combustion models separate submodels are required to calculate pollutants such as $NO_x$ and soot which are described next.

#### 2.3.4.1 $NO_x$ modelling

Oxides of nitrogen can be formed in four different reaction paths classified as the thermal, prompt, fuel and $N_2O$-intermediate $NO$ formation routes [434]. Generally, the reactions involved are relatively slow and non-energetic compared to fuel oxidation so that the $NO_x$ model is commonly solved after the flame structure has been calculated. The reaction system of the $NO_x$ model is solved in a similar fashion as described in Section 2.3.3.1 employing additional assumptions of partial equilibrium and quasi-steadiness.

*Thermal NO* is thought to be the dominant reaction path for $NO$ formation in Diesel combustion and exhibits a strong temperature dependence. Atmospheric nitrogen is oxidised at high temperatures above 1880 K [434] under locally slightly fuel-lean conditions. Zeldovich [480] introduced a two-step $NO$ reaction mechanism based on nitrogen and oxygen atoms. This system has been extended due to underestimation of $NO$ levels by Lavoie *et al.* [260], which is commonly referred to as

the *extended Zeldovich model*, to include an additional $NO$-creating elementary reaction involving $OH$ radicals. The concentrations of $O$ and $OH$ are estimated using assumptions of partial equilibrium. Studies revealed that thermal $NO$ formation strongly depends on the supply of atomic oxygen which results from the dissociation of molecular oxygen. The latter reaction tends to have a high activation energy and thus is particularly sensitive to temperature levels. The accurate estimation of non-equilibrium $O$-atom levels as found in turbulent diffusion flames is hence crucial to accurate $NO$ predictions [172, 434]. This has led to a large variation in rate coefficients in the Zeldovich mechanism by a factor of up to two for combustion simulations [167, 352]. The extended Zeldovich mechanism will be described in detail in Section 3.6.1.

The second mechanism, the *prompt NO* path, is the reaction of atmospheric nitrogen with hydrocarbon radicals in fuel-rich regions to form $NO$. This mechanism was first established by Fenimore [114] and refined by Miller and Bowman [292]. The prompt $NO$ path is mostly ignored in pollutant modelling, since it represents only a small portion of total $NO$ production in fuel-lean combustion systems like Diesel engines [172].

*Fuel NO* refers to the $NO$ formation from fuel-bound nitrogen such as in coal and fuel oil [92]. This reaction path is of minor importance in Diesel combustion, since the current fuels contain negligible amounts of nitrogen [167].

An additional mechanism has been proposed in the literature involving the $N_2O$ *intermediate* [260]. This route is activated at low temperatures in a fuel-lean environment. There is some evidence that this reaction mechanism may contribute to $NO$ formation in Diesel combustion with increasing pressures [56].

Nitrogen dioxide in Diesel engines ranges from 10% – 30% of total $NO_x$ emis-

sions [167] and is formed from $NO$ in the flame zone due to excess oxygen and in regions of rapid cooling. An $NO_2$ elementary reaction was proposed by Merryman and Levy [290]. Due to the strong dependence of $NO_2$ on $NO$, an overall estimate of $NO$ concentration is commonly regarded as representative for both species and as indicative for the total amount of $NO_x$ formed.

#### 2.3.4.2 Soot modelling

Soot formation in hydrocarbon flames occurs via a complex sequence of homogeneous and heterogeneous reaction mechanisms which are not fully understood yet [226]. However, much progress has been made in the past by experimental and numerical studies to identify the key reaction processes and sequences in sooting flames.

Soot formation and oxidation modelling suitable for MDM can be classified into two categories: *semi-global* and *detailed chemistry* soot models. A short overview of soot formation and oxidation fundamentals is given before various soot models are described. They are also listed in Table B.1 in Appendix B.1. For the interested reader the review papers of Kennedy [226] and Hiroyasu [176] give further detail of attempted soot models.

##### Soot formation and oxidation fundamentals

Soot formation involves two characteristic stages [17, 167]: *gas-phase chemistry* leading to particle nucleation followed by *soot particle dynamics* resulting in particle growth. This is illustrated in the schematic in Figure 2.5.

1. *Gas-phase chemistry:* Hydrocarbons pyrolyse in a high temperature environment to smaller hydrocarbons which include in particular acetylene ($C_2H_2$). First aromatic species are formed based on these aliphatic hydrocarbons. Further addition of either aromatic or smaller alkyl species grows the aromatic hydrocarbons to polycyclic aromatic hydrocarbons (PAH) which, together with

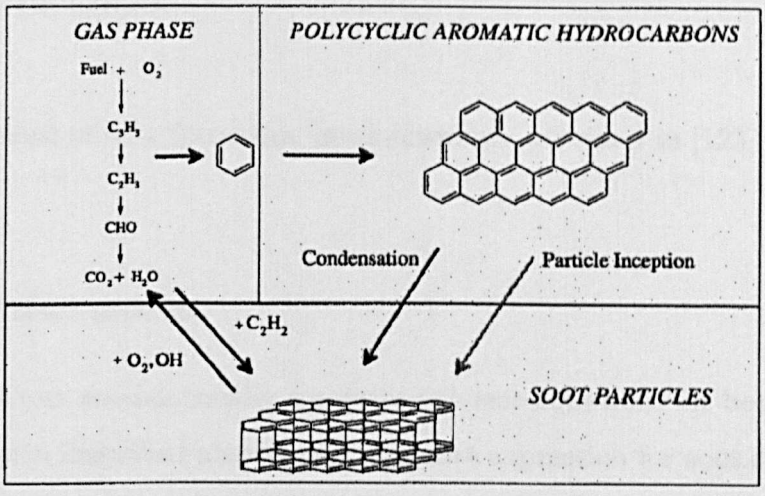



**Figure 2.5:** Schematic of processes involved leading to soot particles (from [27]).

acetylene, are believed to be the main precursors of soot. Through the HACA mechanism [123] (i.e. H-Abstraction and $C_2H_2$-Addition) and subsequent ring closure larger and heavier PAHs are formed. Those finally initiate the smallest soot particles.

2. *Soot particle dynamics:* From soot particle inception onwards, soot growth takes place via two distinct mechanisms. Firstly, when particles collide, larger spheroid particles are created due to coalescence. The second mechanism involves surface growth through chemical reactions mainly with acetylene, PAHs and PAH radicals. Experimental evidence suggests that gas-phase chemical reactions only occur at so-called *active sites*, since surface growth rates are significantly different for particles consisting of the same apparent surface area. As particles increase further in size, chains of carbonaceous spherules are formed. At this stage de-hydrogenation and alignment of polyaromatic layers result in graphitic material that is finally emitted in Diesel engines.

Soot oxidation competes with the soot formation process early in the reaction sequence. The major oxidants are $OH$, $O$ and $O_2$ with the first being important particularly under fuel-rich conditions and the latter in a fuel-lean environment. Other oxidants are $H_2O$ and $CO_2$. Through oxidation of PAHs and soot particles,

$CO$ and $CO_2$ are formed.

Further detail of soot formation mechanism are provided in [123, 125, 167, 226, 281, 374].

### Semi-global soot models

Semi-global soot models mostly comprise two rate equations for both main stages of soot formation described above and a separate expression for soot oxidation. The models usually incorporate a simple chemistry description and are tailored to agree with measurements for specific experiments. Therefore predictive results can only be achieved for conditions that are similar with respect to pressure, fuel type and other relevant parameters.

In this section various soot formation models applicable to Diesel combustion are presented, followed by a selection of typical soot oxidation models.

*I) Soot formation models*

The most popular soot formation model of this category was proposed by Hiroyasu [178] for Diesel application. Soot production is based on an Arrhenius rate expression. The reaction is assumed to depend on local fuel concentration and pressure.

Said *et al.* [384] extended the simple chemistry soot formation model of Kennedy *et al.* [227] for a laminar ethylene/air diffusion flame to make it applicable to a large number of hydrocarbon fuels. Conservation equations for mass fractions of soot and a hypothetical intermediate species were derived. Additionally, an average particle number density was assumed based on experimental findings that in strongly sooting flames particle coagulation is rapid such that the number density decreases very fast. The intermediate species was created by fuel decomposition and was de-

pleted by either oxidation or soot formation. Therefore soot itself was balanced by the conversion of the intermediate species to soot and soot oxidation. The model requires adjustments of a large number of parameters to fit measurement data and has previously been applied to Diesel combustion by Theodossopoulos [427].

Lindstedt [270, 272] developed soot models for laminar and turbulent diffusion flames including a simple chemistry description for soot formation. The gas phase is described by a detailed reaction mechanism for ethylene flames based on work by Warnatz [451] and Jones and Lindstedt [214]. Rate equations were established for soot volume fraction and particle number density. The nucleation rate and surface growth as source terms for the volume fraction equation were assumed to be first order dependent on acetylene concentration. A later extension [273] also included a benzene formation mechanism for soot nucleation. An investigation regarding the relevant surface area for particle surface growth in premixed flames indicated that best agreement with experiments was achieved when relating surface growth with particle number density. The particle number density expression accounted for particle inception and coagulation. This model is not suitable for Diesel combustion due to the significant differences in gas phase reactions using either ethylene or Diesel fuel. In addition, the detailed chemical reactions in the gas phase produce substantial computational overheads.

Several flamelet-based approaches for soot formation modelling in diffusion flames have been derived. One such model is that of Moss *et al.* [303, 304, 418] who solved balance equations for soot volume fraction and particle number density as functions of mixture fraction. Soot volume was assumed to increase due to surface growth and particle nucleation. Surface growth in this approach depended on number densities. Particle number densities were balanced by particle inception and coagulation mechanisms. This soot model was derived for laminar diffusion flames and is therefore not suitable for Diesel engine applications.

A comprehensive flamelet-based soot model was proposed by Young and Moss [478] for turbulent diffusion flames. Favre-averaged transport equations were solved for soot volume fraction and particle number density which were modeled in analogy to Moss' earlier work [303]. The closure of mean source terms presented a major problem due to their non-linear dependence on temperature. This difficulty was solved by applying certain assumptions and by obtaining the mean source terms using a probability density function and integrating over mixture fraction. The radiative heat loss was taken into account due to the strongly sooting nature of the flame investigated. A gas temperature correction was applied.

In Diesel engine combustion simulations the most widely-used semi-global soot formation model is that of Hiroyasu due to its simplicity and successful application to a broad range of operating conditions [362].

*II) Soot oxidation models*

Lee *et al.* [266] derived a simple Arrhenius soot oxidation rate equation from measurements in laminar diffusion flames. $O_2$ is assumed to be the major oxidant. Temperatures in the experiment ranged from 1200 – 1700 K while the oxygen partial pressures extended from 0.04 – 0.12 atm. Both temperature and oxygen partial pressure ranges are below the conditions encountered in Diesel combustion.

Another soot model which solely considers $O_2$ soot oxidation is the widely-used model of Nagle and Strickland-Constable (NSC) [311]. An Arrhenius rate equation was proposed based on pyrographite oxidation for temperatures between 1100 – 2500 K and oxygen partial pressures from 0.1 – 0.6 atm. Carbon oxidation was related to surface chemistry involving more reactive sites $A$ and less reactive sites $B$. For engine calculations the oxygen partial pressure is usually higher than in the experiments of NSC. However, it was concluded that at high enough oxygen partial pressures, soot oxidation behaves in a similar manner as pyrographite due to structural resemblance [167, 399].

Fenimore and Jones [115] derived an oxidation rate expression based on $OH$ attack in diffusion flames for temperatures between 1530 – 1890 K and partial oxygen pressures in the range of 0.04 – 0.3 atm. Their specific ethylene flame resulted in too slow oxidation rates when molecular oxygen was taken alone as the major agent. Oxidation primarily by $OH$ could explain the experimental trends. Diesel engine conditions, however, exceed the temperature and partial oxygen pressure levels studied in these experiments. In addition soot burnout via $O_2$ attack is significant in Diesel combustion [167, 384] which is not captured in this model.

Another popular soot oxidation model was developed by Hiroyasu *et al.* [178] for Diesel soot. It consists of an Arrhenius expression which includes a dependence on local fuel concentration and pressure.

For the conditions relevant to Diesel combustion the soot oxidation models of NSC and Hiroyasu are the most promising approaches.

### Detailed chemistry soot models

Detailed chemistry models include all phenomena in the gas phase and particle stages described above. Such detailed models are generally computationally expensive and sensibly depend on the inclusion of the relevant reaction paths. Critical to these models is the transition from gas-phase kinetics to particle dynamics as both involve processes that are inherently different.

Frenklach [123, 126] has developed a comprehensive soot model that incorporates the most important phenomena of soot formation, growth and oxidation. Gas-phase kinetics aim at the accurate prediction of $H$, $OH$, $O_2$, $C_2H_2$ and benzene concentrations, as they were found critical to soot formation and oxidation. The HACA mechanism is incorporated for PAH formation. The subsequent infinite polymerisation process of PAHs is accompanied by formation of soot particles of different

structure and size. Since the numerical evaluation of each polymerisation step is computationally expensive (the number of steps has to be very large or ideally infinite), the method of *linear lumping* by Frenklach [122] has been proposed. It is assumed that PAH growth can be subdivided into a polymerisation sequence of identical reactions. A statistical description of PAH size distribution is chosen such that only transport equations for the density-weighted statistical moments are solved. An identical approach is used for the size distribution of soot particles. In this framework, soot particle dynamics like nucleation, condensation, coagulation, surface growth and oxidation are expressed as source terms to the moment equations. Soot oxidation is modeled via $O_2$ and $OH$ attack. Impressive agreement with experimental data was achieved for several premixed flames.

Yoshihara *et al.* [476] systematically reduced the methane oxidation and PAH reaction mechanisms of Frenklach and coworkers [125, 126, 127] by identifying key reactions. Additionally steady-state and partial equilibrium assumptions were evoked. Soot oxidation was modeled by the $OH$ attack using a collision efficiency. The model predictions were compared with Diesel engine exhaust measurements. Remarkably good agreement was achieved.

A similar approach for a laminar premixed flame was attempted by Mauss and coworkers [288]. The soot model developed by Mauss *et al.* [285, 289] is used which is an extension of the work of Frenklach and Wang [125]. The formation of benzene and PAHs in fuel-rich conditions is described using the approach of Frenklach and Warnatz [128]. To reduce the numerical effort the PAH polymerisation is assumed to be fast. Thus the PAHs are in a quasi-steady state and their concentrations can be deduced from simple algebraic expressions. This soot model was evaluated against measurements for various premixed flames and showed generally excellent agreement.

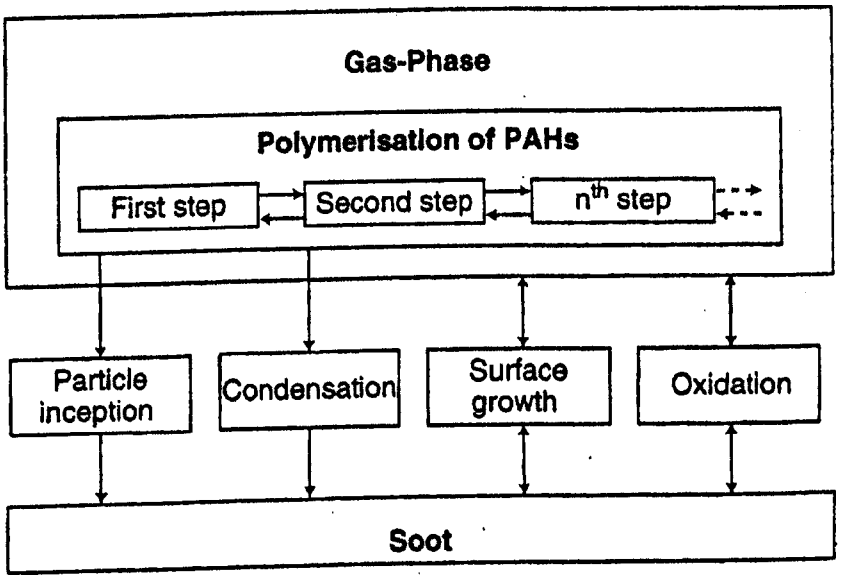



**Figure 2.6:** Schematic of various processes taken into account in the soot model of Balthasar *et al.* (from [89]).

Balthasar and Mauss [27] have adapted the detailed chemistry approach for soot modelling of Frenklach and Mauss [125, 285] to the flamelet framework which was successfully applied to laminar and turbulent diffusion flames [25, 28] and Diesel combustion [89, 220]. A schematic of the different subprocesses of the soot model is displayed in Figure 2.6. It is assumed that the growth of soot particles is slow compared with gas-phase reactions and transport processes in the flame. A transport equation is solved for the soot volume fraction incorporating source terms for particle inception, condensation, surface growth and oxidation. These source terms have been fitted to multi-parameter functions of mixture fraction, scalar dissipation rate, oxidiser temperature and pressure resulting in simple algebraic relations. The parameters then are stored in a flamelet library. This approach resulted in a significant reduction of computational effort, thus being very attractive for engine simulations.

Among the detailed chemistry soot models the approach of Balthasar and Mauss is the most promising one due to the favourable compromise between computational costs and comprehensive soot chemistry description.

## 2.3.5 Wall heat transfer modelling

### 2.3.5.1 Introduction

Three modes of heat transfer exist between a gas and a wall:

**1. Heat convection** The major part of heat exchange in Diesel engines originates from *forced convection* where the fluid is in relative motion with respect to the confining walls, on which thermal boundary layers are formed. Within this thin layer a temperature gradient exists as a consequence of the difference in gas temperature $T$ and wall temperature $T_W$. *Newton's law of cooling* relates the convective heat flux $q_h$ to the temperature difference through the following rate equation:

$$q_h = h\,(T - T_W) \tag{2.5}$$

The variable $h$ is known as the *convection heat transfer coefficient* (HTC). It represents the complex dependence of the heat exchange process upon the flow characteristics in the boundary layer, the spray and combustion effects, the thermodynamics and the thermophysical properties of the gases.

**2. Heat conduction** The local heat flux at the wall surface via heat conduction is given through *Fourier's law* as:

$$q_k = -k \left.\frac{\partial T}{\partial y}\right|_{y=0} \tag{2.6}$$

where $k$ is the thermal conductivity and $y$ is the wall-normal coordinate.

**3. Heat radiation** Radiation heat transfer rates in Diesel engines are closely linked to soot particle formation, since particulate radiation is about five times higher than that from gaseous combustion products [167]. An appreciable amount of radiation occurs only during the heat release period, with a peak after the premixed combustion phase is ended (5° – 10° CA after start of combustion) [54]. In general particulate radiation is modeled similarly to black body radiation as:

$$q_r = \varepsilon_{eff}\,\sigma\left(T_r^4 - T_W^4\right) \tag{2.7}$$

where $\varepsilon_{eff}$ is an effective emissivity determined through measurements and $\sigma$ is the Stefan-Boltzmann constant. An appropriate radiation temperature has to be chosen which will substantially affect the heat flux due to the fourth power dependence.

Approaches for engine wall heat transfer can be grouped into two major categories: *correlation-based* and *theory-based models*. The first type of models have primarily been used to estimate the overall heat loss of an engine. Among those a few approaches are commonly quoted in the engine community and serve as an initial approximation for CFD simulations. These will be briefly described below and used for validation purposes in Chapter 6. The second category comprises models that are derived from analytical solutions including the CFD methodology. A more thorough overview over the variety of models that exist, is given in the review paper of Borman and Nishiwaki [54].

#### 2.3.5.2 Correlation-based engine heat transfer approaches

With the help of a dimensional analysis of engine heat transfer using the characteristic geometrical and physical quantities, a similarity law, i.e. a correlation, for convective heat transfer can be derived in terms of non-dimensional groups:

$$\left(\frac{h\,L}{k}\right) = a\left(\frac{\rho\,v\,L}{\mu}\right)^{m}\left(\frac{c_p\,\mu}{k}\right)^{n} \quad \Longrightarrow \quad \mathrm{Nu} = a\,\mathrm{Re}^{m}\,\sigma_e{}^{n} \tag{2.8}$$

Therein $L$ stands for a characteristic length, $v$ for velocity, $\mu$ for viscosity, and $c_p$ for the specific heat capacity at constant pressure. $a$, $m$ and $n$ are model coefficients, while Nu, Re and $\sigma_e$ are the Nusselt, Reynolds and Prandtl number, respectively. Often a constant value for the Prandtl number is used such that the correlation is redefined using a new constant $c$ as:

$$\mathrm{Nu} = c\,\mathrm{Re}^{m} \tag{2.9}$$

The model coefficients are commonly obtained through curve fitting to match the overall heat balance of engine measurements. To obtain the convective heat flux from the correlation three effective quantities have to be selected:

1. The velocity and characteristic length in the Reynolds number.
2. The temperature at which the gas transport properties are evaluated.
3. The average gas temperature.

Besides convection heat transfer, correlation-based approaches either consider radiation heat transfer separately or include its effect in the convective heat transfer correlation in a lumped form.

In what follows the three widely-quoted correlation-based engine heat transfer modelling approaches are briefly outlined in which an expression is provided for the time-varying global heat transfer. An overview of these approaches is given in Table A.1 in the Appendix. For the interested reader other correlation-based approaches are provided in [54, 167, 176].

### Time-varying global heat transfer correlations

Annand [14] proposed a convection heat transfer correlation by using published experimental data on instantaneous heat flux at cylinder head locations for SI and CI engines and fitted them with the following expression:

$$\mathrm{Nu} = c\,\mathrm{Re}^{0.7} \tag{2.10}$$

where $c$ has an arbitrary value between 0.35 and 0.8 and is related to the intensity of charge motion. Gas properties are evaluated at the cylinder-averaged gas temperature:

$$\overline{T}_g = \frac{pVM}{m\mathcal{R}} \tag{2.11}$$

where $V$ is the volume, $M$ is the molecular weight and $m$ is the mass. The characteristic length in the Reynolds number is the cylinder bore. A separate term for radiation heat transfer according to Eq. (2.7) was specified to obtain the total instantaneous heat flux.

Another widely-used equation for spatially-averaged heat transfer coefficients was developed by Woschni [466, 467, 468]. He took measurements on a four-valve DI Diesel engine without swirl and fitted the experimental results with the following correlation:

$$\mathrm{Nu} = 0.035\,\mathrm{Re}^{0.8} \tag{2.12}$$

where the Reynolds number is based on the mean piston speed and the cylinder bore as the characteristic quantities. Thermophysical properties like conductivity and viscosity were set proportional to the temperature as $k \propto T^{0.75}$ and $\mu \propto T^{0.62}$. The gas temperature at which the gas properties were evaluated was chosen as the bulk mean temperature. On this basis, a spatially averaged HTC was proposed as:

$$h = 0.82\,\frac{p^{0.8}}{B^{0.2}\,T^{0.55}}\left[c_1\overline{v}_p + c_2\frac{V_d\,T_0}{p_0\,V_0}(p - p_{\mathrm{mot}})\right]^{0.8} \tag{2.13}$$

where the values indexed with 0 are reference values taken for instance at IVC or start of combustion, $B$ is the cylinder bore, $\overline{v}_p$ is the mean piston speed, $p_{\mathrm{mot}}$ is the motored pressure and $V_d$ is the displacement volume. The model coefficients are tabulated in Table 2.1. Woschni accounted for the higher turbulence levels and their effect on wall heat transfer during the gas exchange cycle in comparison to the compression and expansion stroke through the coefficient $c_1$. During the combustion period due to higher gas temperatures and radiation heat transfer an additional term is included that increases the HTC and involves the difference in pressure between a motored and fired cycle. Moreover, the influence of swirl on heat transfer is considered through the coefficient $c_1$ with a swirl velocity defined according to $v_{\mathrm{swirl}} = B\,\omega_{\mathrm{pad}}/2$, where $\omega_{\mathrm{pad}}$ is the rotational speed of the paddle wheel taken from

| Period | Coefficients | |
|---|---|---|
| | $c_1$ | $c_2$ |
| Gas exchange | $6.18 + 0.417\,\frac{v_{\mathrm{swirl}}}{\overline{v}_p}$ | 0 |
| Compression | $2.28 + 0.308\,\frac{v_{\mathrm{swirl}}}{\overline{v}_p}$ | 0 |
| Combustion and Expansion | $2.28 + 0.308\,\frac{v_{\mathrm{swirl}}}{\overline{v}_p}$ | $3.24 \times 10^{-3}$ |

**Table 2.1:** Coefficients for Woschni correlation in Eq. (2.13).

a steady-state swirl experiment. Woschni claims that his equation is applicable universally to SI and CI engines. However, the coefficients have to be adjusted for each geometrically different engine.

Various measuring techniques to determine heat transfer were applied by Hohenberg [182]. On the basis of a similarity analysis he developed an expression for the heat transfer coefficient similar to Woschni's:

$$h = c_1 \frac{p^{0.8}}{V^{0.06}\, T^{0.4}} (\overline{v}_p + c_2) \tag{2.14}$$

where $T$ is the bulk gas temperature. The mean values obtained for the coefficients are $c_1 = 130$ and $c_2 = 1.4$ which were obtained by measurements on a number of DI Diesel engines of varying size and combustion system. The major difference to previous correlations is the use of a characteristic length including the cylinder volume, and the lower exponent in the mean gas temperature.

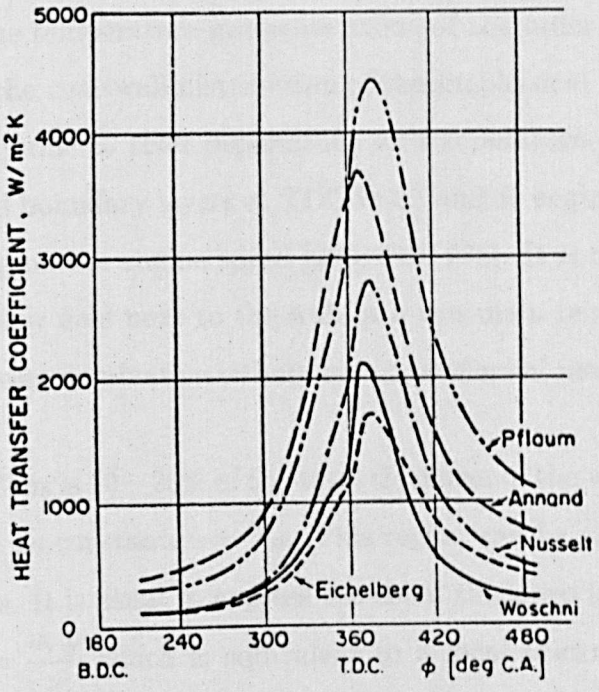



**Figure 2.7:** Comparison of HTCs for a test engine using different approaches of [14, 99, 321, 336, 467] (from [467]).

Woschni compared the predictions of several heat transfer correlations with his own formula as shown in Figure 2.7 using measurement data for a test engine.

Differences by a factor of two are observed, which comes from the fact that the formulæ were derived from a variety of engines at differing operating conditions.

#### 2.3.5.3 Theory-based engine heat transfer approaches

CFD methodology belongs to this category. The various processes in the vicinity of the wall are resolved spatially and temporally to obtain the local wall heat transfer. Effects of gas thermophysical properties, thermodynamics, flow characteristics, turbulence, spray and combustion are all accounted for.

The characteristic size of turbulent eddies as well as turbulent fluctuations decrease towards the wall, leading to a change of transport mechanism from turbulent to viscous dominated processes [392]. This results in steep, non-linear gradients of flow variables in the proximity of the wall within a thin layer, known as the *boundary layer*. Similarly large temperature gradients exist (of the order of 500 K) that appreciably influence the near-wall distribution of thermophysical fluid properties like density and viscosity due to their dependence on temperature. The depths of the velocity and thermal boundary layers at TDC in CI and SI engines is of the order of 1 – 2 mm depending on the engine speed [200, 219, 276]. It is customary to subdivide the turbulent flow field next to the wall into two main regions where different characteristic processes dominate – either viscous or inertial mechanisms [117, 443].

1. **Inner region:** This is 10 – 20% of the total thickness of the wall layer. The shear stress is taken as constant: $\tau = \tau_W$. This region can be subdivided into three different zones. It is usual to express the zonal thickness in a non-dimensional variable $y^+ = \frac{u_\tau y}{\nu}$ which is equivalent to a local thickness-based Reynolds number, where $u_\tau$ is the friction velocity and $\nu$ is the kinematic viscosity.

   - **Viscous or conduction sub-layer:** This is the very thin layer ($y^+ < 5$) where only viscous forces act. A Couette flow is assumed with linear gradients of flow variables. Newton's law of viscosity and Fourier's law

of heat conduction describe the flow field. The instantaneous velocity profile exhibits finite velocity fluctuations caused by the effects of fluid elements from the adjacent layers.

- **Buffer layer:** This is the transitional region ($5 < y^+ < 30$) where viscous and turbulent shear forces are of the same order of magnitude.
- **Log-law or inertial layer:** This is the fully turbulent zone (typically $30 < y^+ < 500$) where turbulent stresses dominate. A logarithmic profile adequately describes the velocity and temperature distribution.

2. **Outer region:** This is the layer where the law-of-the-wake is valid due to the dominance of inertia forces. Turbulent structures and transport are dominant. The viscous transport is negligible.

In engine simulations it has been common practice to ignore the buffer layer and separately treat the inner region within the turbulence model. Within the framework of the $k-\varepsilon$ turbulence model three major practices are found in the literature [256]: the *high Reynolds number* $k-\varepsilon$ *turbulence model*, the *low Reynolds number* $k-\varepsilon$ *turbulence model* and the *two-layer turbulence model*.

### High Reynolds number $k-\varepsilon$ turbulence model

This approach places one control volume within the inner region of the boundary layer such that its cell centre is located at a distance $y^+$ between 30 and 100 normal to the wall [118, 410]. The turbulence and flow variables outside this region are represented by the full transport equations for momentum, enthalpy, turbulence kinetic energy $k$ and dissipation rate $\varepsilon$; however, the inner region is represented by semi-analytical *wall functions*. The "standard" wall functions used in $k-\varepsilon$ modelling were originally proposed by Launder and Spalding [259]. They describe the near-wall flow and temperature profiles and are derived for a one-dimensional Couette flow from the momentum and enthalpy equations assuming steadiness, constant gas properties, no pressure gradients, turbulence equilibrium and no combustion [118].

The use of the standard wall functions to predict wall heat transfer in engines generally leads to an underprediction of heat flux [191, 203, 366]. Several researchers have derived modified versions of wall functions or similarity approaches particularly for wall heat transfer by relaxing some of the assumptions to make them applicable to engine applications. The modified approaches cater for one or several of the following phenomena in the boundary layer:

- Transient effects.
- Variable thermophysical properties.
- Pressure gradients.
- Combustion heat release.

An overview of different formulations of the dimensionless temperature wall function can be found in Spalding [406] and Kays *et al.* [223].

*a) Transient effects*

An analytical solution for the transient variation in wall heat flux has been derived by Yang and Martin [471] based on a similarity approach and a perturbation method. In addition a simple approximate solution was derived by fitting a set of functions to the analytical solutions. This approach has been applied to engine simulations, e.g. by [155, 366, 473, 474]. These studies showed that this methodology is computationally more expensive than the standard wall function approach and does not give superior performance.

Huh *et al.* [191] have proposed a modified temperature wall function including the pressure work and neglecting pressure gradients, heat sources and changes of near-wall gas temperature. The neglect of the last-named was based on the assumption that the gas temperature in the thermal boundary layer varies significantly less than pressure and gas density. Also, constant thermophysical properties in the boundary region were employed. Predictions of heat fluxes in motored and fired

engines did not substantially improve compared to the standard wall function approach.

*b) Variable thermophysical properties*

The variation of density and viscosity in the vicinity of the wall has been accounted for in the modified wall function approach of Angelberger *et al.* [13]. Both properties show a strong temperature dependence and vary substantially in the near-wall region in engines, induced by steep temperature gradients due to compression and combustion. The velocity and temperature law-of-the-wall were derived such that the density variation was included in the expression for the non-dimensional temperature profile, while the viscosity effects were accounted for in the definition of the non-dimensional parameter for the wall-normal distance. This approach will be described in detail in Section 3.8.1.3. Improved results were obtained in [13] for heat flux predictions of a fired SI engine.

Similarly, Han and Reitz [155, 366] proposed a modified temperature wall function that considers density variations in the near-wall region. The predictions showed better agreement compared to the standard wall function approach with respect to heat flux measurements for an SI and Diesel engine under motored and fired conditions. They concluded that the main reason for the underprediction of engine wall heat transfer is the assumption of incompressibility in the boundary layer in the derivation of the laws-of-the-wall.

Other proposals for the redefinition of a non-dimensional variable for the wall-normal distance to include viscosity variation effects in the thermal boundary layer for pipe flows are found in [76, 154].

*c) Pressure gradient*

A modified wall function approach for boundary layer flows including effects of pressure gradients has been derived by Volino and Simon [444]. The method is based on Van Driest's damping function [440] for turbulent transport near the wall and

a subsequent modification by Kays and Crawford [223] to account for velocity lag due to pressure gradients. Better agreement compared to the standard approach was obtained for the velocity and temperature profiles in the boundary layers which were subject to pressure gradients. However, it appears that no validation studies for engine heat transfer using this approach have been performed.

*d) Combustion heat release*

Han and Reitz [155] proposed a modified temperature wall function, including chemical heat release. They concluded that the effects of a heat source in the near-wall region on heat transfer predictions are negligible for a large Diesel engine.

### Low Reynolds number $k - \varepsilon$ turbulence model

In this practice, special low Reynolds number transport equations for $k$ and $\varepsilon$ are solved throughout the computational domain including the wall region [443]. A fine mesh in the vicinity of the wall is necessary to capture gradients of flow variables, with the near-wall grid node typically located at $y^+ \approx 1$ [410]. A great number of low Reynolds number $k - \varepsilon$ variants have emerged in the past for different applications [69, 166, 251, 258, 327]. For engine simulations the higher mesh density close to the wall creates expensive computational overheads. Thus, so far the application of this approach in engine flows has had only limited success [203, 204, 345].

### Two-layer turbulence model

In this approach, the viscosity-influenced inner regions up to a $y^+$ between 60 – 100 [410] is modeled by a zero- or one-equation low Reynolds number turbulence model and in the outer region by the high Reynolds number $k - \varepsilon$ turbulence model. The low Reynolds number turbulence modelling approaches of this category comprise either mixing length models or one-equation turbulence models which calculate $k$ from a transport equation, and obtain the $\varepsilon$ distribution from an algebraic function (see e.g. [159, 462, 465]). The two-layer approach shares similar disadvantages with

respect to computational overheads as the low Reynolds number $k - \varepsilon$ turbulence model and therefore has not been commonly used for engine flows.

Two variants of the two-layer concept have been proposed. Jennings and Morel [203, 204] resolved only the near-wall region, i.e. below $y^+ = 50$, through a finer grid. In this wall layer grid the boundary equations are fully solved including pressure gradient effects. The resulting solution of the wall shear stress and heat flux is inserted in the bulk flow equations as boundary condition and the turbulence field of the grid points of the two meshes that overlap are set by interpolation. Furthermore the slope of the length scale at $y^+ = 50$ is adjusted to ensure a smooth profile from the bulk flow into the near-wall region. The pressure field is only solved in the outer flow region. Good agreement is found for engine flow and heat transfer predictions.

A parabolic sublayer scheme (PSL) is suggested by Iacovides and Launder [193], where the viscous sublayer and buffer layer are resolved by a fine mesh. Pressure variation normal to the wall, i.e. static pressure variation, is neglected, removing the necessity to solve for the pressure field in the thin boundary layer. The velocity components parallel to the wall in the near-wall region are calculated via the momentum equations, the normal velocities are obtained through continuity. The PSL approach reduces computational time and storage requirements [256], but has not been tested for engine flows.

## 2.4 Closure

This chapter reviewed the various modelling approaches for Diesel engine processes. Initially the two main modelling categories were briefly introduced, comprising the phenomenological and multidimensional models. The former are typically used to predict the overall performance of Diesel engines. They, however, require extensive parameter adjustment for different combustion systems and operating conditions. The multidimensional models comprise the CFD methodology which resolve various physical processes in time and space. Commonly full field modelling is used to

describe the turbulent processes in the flow field.

Modelling approaches for several subprocesses in Diesel engines based on the CFD methodology were then briefly outlined. They comprise turbulence, spray, combustion chemistry including pollutant formation and wall heat transfer. For each subprocess a brief overview of possible modelling strategies was given and in turn the most widely-used approaches were identified. These are summarised as follows:

**Turbulence:** High Reynolds number $k - \varepsilon$ turbulence model.

**Spray:** Discrete droplet method with separate modelling of spray and droplet physics subprocesses.

**Autoignition:** 'Shell' autoignition model.

**Combustion:** Eddy breakup-type combustion model like LATCT variant.

**Pollutant formation:** The extended Zeldovich mechanism for $NO$ and a phenomenological model for soot formation and oxidation like that of Hiroyasu and Nagle Strickland-Constable.

**Wall heat transfer:** Extension of $k - \varepsilon$ turbulence model using wall functions in the near-wall region.

In the section for wall heat transfer several empirical models were also described which are commonly quoted in the engine community.

As novel, advanced Diesel engine concepts emerge and increased computing power becomes available, the conventionally used modelling approaches need to be re-evaluated against experimental data and if necessary improved to obtain improved predictions. The choice of modelling approaches for a CFD engine simulation is then guided by a favourable balance between accuracy and computational efficiency.

The following chapter outlines the mathematical foundation of the present Diesel simulation methodology with extensions to make it applicable to the increased peak pressure concept.

# Chapter 3

# Mathematical Modelling

## 3.1 Introduction

After having introduced various modelling approaches of subprocesses of the Diesel engine process in the previous chapter, including the current state of CFD Diesel engine methodology, this chapter provides the mathematical foundation of the current study. The in-cylinder fluid is treated as a continuum which properties and state can be described as continuous functions in space and time based on the Eulerian framework. The spray equations are expressed in Lagrangian formulation and the interactions between gas and liquid phases are taken into account via source terms in the respective system equations.

Conservation equations for mass, momentum, energy and species conservation are solved to describe the state of the gas phase. In addition, constitutive relations and thermophysical properties are defined to close the system equations. All these are assembled in Section 3.2. In addition, a sensitivity study for the appropriate equation of state and correlations for thermophysical properties at elevated pressure and temperature conditions is added in the light of the application to the novel HPP concept.

The highly turbulent flow in engines with a broad spectrum of length and time-

scales would necessitate prohibitive storage requirements and run-times for the direct solution of the governing equations, as explained in Section 2.2.2. To circumvent this shortcoming, statistical averaging is employed: in engines this usually entails ensemble-averaging. As a consequence of averaging, unknown correlations of fluctuating quantities appear which are treated by the $k-\varepsilon$ turbulence model as outlined in Section 3.3.

The liquid phase governing equations for the spray are summarised in Section 3.4. Additionally submodels are described to incorporate various physical processes related to the spray. A separate sensitivity study is performed to assess appropriate correlations of liquid thermophysical properties for the elevated pressure and temperature conditions.

Diesel combustion modelling including the pre-ignition and post-ignition phases are summarised in Section 3.5. In particular the mathematical description of the Representative Interactive Flamelet model as an alternative to the EBU-type combustion model is presented. Furthermore models to capture $NO_x$ and soot formation are presented in Section 3.6.

The mathematical framework is closed by the specification of initial and boundary conditions in Section 3.8. In addition, a modified wall heat transfer approach is derived based on wall functions.

## 3.2 Instantaneous Governing Equations

The instantaneous conservation laws for extensive fluid properties such as mass, momentum and energy are developed from balance equations on a control volume [46, 118]. These are conveniently expressed through differential equations. For a heterogeneous mixture, however, not only has the exchange of extensive fluid properties with the surrounding volume to be accounted for, but also the exchange of such properties within the interior of the control volume. Thus in the gas phase equations for the separated flow approach the volume displaced by the liquid phase is

captured by the void fraction $\vartheta$ and the interaction of mass, momentum, energy and species concentration between the phases is expressed by appropriate source/sink terms in the conservation equations. The void fraction is derived from the general phase fraction equation which is defined as the ratio of component volume $V_i$ per unit volume of mixture [318]:

$$\alpha_i = \frac{V_i}{V} \quad ; \quad \sum_{i=1}^{N} \alpha_i = 1 \tag{3.1}$$

where $i$ is the component index and $N$ is the total number of components. The volume fraction $\vartheta$ is obtained when taking $i$ as the gas phase.

### 3.2.1 Mass conservation

The continuity equation is derived from a mass balance over the control volume and is expressed as [198]:

$$\frac{\partial \rho_m \vartheta}{\partial t} + \nabla \cdot (\rho_m \vartheta \mathbf{u}) = S_m^d \tag{3.2}$$

where $t$ indicates time, $\rho_m$ the effective or microscopic density, $\vartheta$ the void fraction, $\mathbf{u}$ the velocity and $S_m^d$ refers to the source term per unit volume due to droplet evaporation and condensation. The divergence of the mass velocity vector $\nabla \cdot (\rho_m \vartheta \mathbf{u})$ expresses the net rate of mass flux over the control volume boundaries per unit volume. In addition, an effective or macroscopic density can be derived as:

$$\rho = \frac{m_{\text{gas}}}{V_{\text{gas}}} \frac{V_{\text{gas}}}{V} = \rho_m \vartheta \tag{3.3}$$

which will be used from now on.

### 3.2.2 Momentum conservation

The momentum balance over the control volume results in the momentum equation given by [157, 318]:

$$\frac{\partial (\rho \mathbf{u})}{\partial t} + \nabla \cdot (\rho \mathbf{u}\mathbf{u}) = -\vartheta \nabla p + \nabla \cdot (\vartheta \tau) + \rho \mathbf{g} + S_{\mathbf{u}}^d \tag{3.4}$$

where $p$ refers to the thermodynamic gas pressure which is assumed to be locally in equilibrium between the two phases, $\tau$ is the stress tensor, $\mathbf{g}$ the vector of gravitational acceleration and $S_{\mathbf{u}}^{d}$ stands for the momentum contribution due to interaction between the two phases. The first term on the left-hand side (LHS) stands for the net rate of change of momentum per unit volume and the second term represents the efflux of momentum per unit volume by fluid flow. The first two terms on the right-hand side (RHS) give the momentum gain due to external surface forces such as pressure and shear stress, respectively, and the third term on the RHS captures the body forces due to gravity acceleration. Since the viscous and inertial forces dominate in relatively high velocity gas flows, as they occur in engines, it is appropriate to neglect the gravitational body forces [461].

It is noteworthy that the void fraction has not been included in the pressure gradient† following the discussions of Harlow and Amsden [157] and Clerides [77]. In the case of an inhomogeneous distribution of phases and the absence of gravity the momentum equation would not be able to yield static equilibrium of the system, if $\vartheta$ would lie within the gradient operator [157]. This is unphysical.

### 3.2.3 Energy conservation

Energy can be expressed either by internal energy or by the total energy. The total energy is obtained by adding the specific kinetic energy $\frac{1}{2}\mathbf{u}^2$ to the internal energy which is defined as:

$$e = \int_{T_{ref}}^{T} c_v \, dT \tag{3.5}$$

This equation is known as the caloric equation of state. Here $T$ is the absolute temperature and $c_v$ is the specific heat at constant volume, generally a function of temperature and composition.

†Some authors have included the void fraction within the pressure gradient (see e.g. [198]).

By multiplying the momentum equation Eq. (3.4) by $\mathbf{u}$, the specific kinetic energy equation is obtained which is then subtracted from the specific total energy equation (e.g. given in [318]). The result is the conservation equation for specific internal energy. If the body forces and the molecular shear work terms are neglected due to their relatively small contribution to the overall energy balance [246] the resulting internal energy equation is [318]:

$$\frac{\partial \rho\, e}{\partial t} + \nabla\cdot(\rho\, \mathbf{u}\, e) = \nabla\cdot(-\mathbf{q}) - p\nabla\cdot[\vartheta\, \mathbf{u} + (1-\vartheta)\, \mathbf{u}_l] + S_e^d + \kappa\, \dot{Q}_{ign} + (1-\kappa)\, \dot{Q}_{comb} \tag{3.6}$$

Here $\mathbf{q}$ stands for the heat flux only by conduction, since radiation is not taken into account. This decision is made on the basis that in the particular system of gas and liquid considered here on the one hand the droplets are very small and on the other hand, gaseous spectral radiation bands and liquid fuels absorption bands in general do not coincide according to Berlad [41] and Faeth [106].

The pressure work in the gas phase is given as $-p\nabla\cdot(\vartheta\mathbf{u})$ and $-p\nabla\cdot[(1-\vartheta)\mathbf{u}_l]$ accounts for the pressure work of the liquid on the gas phase exerted at the interface. The latter contribution can be derived by expressing the state of the liquid phase in Eulerian formulation and taking the liquid as incompressible. In the case when liquid is introduced into the control volume, thereby diminishing the volume occupied by the gas, the gas phase is compressed. The liquid velocity $\mathbf{u}_l$ appearing in the pressure work due to the liquid phase is not readily available, since the liquid phase is described in the Lagrangian framework. However, the term $\nabla\cdot[(1-\vartheta)\mathbf{u}_l]$ can be substituted by the following expression, derived from the liquid continuity equation in Eulerian formulation assuming an incompressible liquid [77]:

$$\nabla\cdot[(1-\vartheta)\mathbf{u}_l] = \frac{\partial \vartheta}{\partial t} - \frac{S_m^d}{\rho_l} \tag{3.7}$$

where $\rho_l$ is the liquid density.

Since the pressure work due to the liquid phase is taken into account separately, the source term $S_e^d$ solely represents the heat exchange between gas and the liquid

phase. Other source terms stand for energy supply due to pre-ignition reactions $\dot{Q}_{ign}$ and due to combustion reactions $\dot{Q}_{comb}$. A coefficient $\kappa$ is introduced to switch between pre-ignition and post-ignition phases. $\kappa$ is unity for the former phase and vanishes after autoignition.

### 3.2.4 Chemical species conservation

The mass fraction balance per unit volume for chemical species $\psi$, defined as $Y_\psi = \rho_\psi/\rho$, is given as [403]:

$$\frac{\partial \rho Y_\psi}{\partial t} + \nabla\cdot(\rho \mathbf{u} Y_\psi) = \nabla\cdot\mathbf{j} + S^d_{Y_\psi} + \dot{\omega}_{Y_\psi} \tag{3.8}$$

where $\rho_\psi$ is the species density, $\mathbf{j}$ is the species flux due to diffusion, $S^d_{Y_\psi}$ is the source term with respect to the liquid phase (i.e. fuel evaporation and condensation) and $\dot{\omega}_{Y_\psi}$ refers to the species formation and depletion rate due to chemical reactions.

### 3.2.5 Constitutive relations

In the conservation equations presented above, unknown quantities still reside which need additional modelling, referred to as constitutive relations.

#### Newton's law of friction

For a Newtonian fluid the viscous shear stress tensor is expressed as [392]:

$$\boldsymbol{\tau} = 2\mu\mathbf{D} + \lambda\nabla\cdot(\mathbf{u}\,\mathbf{I}) \tag{3.9}$$

where $\mathbf{D}$ expresses the deformation tensor, $\mathbf{I}$ stands for the identity tensor and $\mu$ and $\lambda$ are the dynamic molecular viscosity (i.e. first viscosity coefficient) and second viscosity coefficient, respectively. The symmetric deformation (also rate-of-strain) tensor describes the rate of strain acted upon a fluid element and is given by:

$$\mathbf{D} = \frac{1}{2}[\nabla\mathbf{u} + (\nabla\mathbf{u})^T] \tag{3.10}$$

where the superscript $T$ indicates transposition.

Applying Stokes's hypothesis [411] to the viscosity coefficients the following relation is obtained:

$$\lambda = -\frac{2}{3}\mu \tag{3.11}$$

**Fourier's law of heat conduction and Fick's law of diffusion**

For heat conduction Fourier's law reads [197]:

$$\mathbf{q} = -k\,\nabla T \tag{3.12}$$

with $k$ as the thermal conductivity defined as:

$$k = \frac{\rho\,\nu\,c_p}{\sigma_e} \tag{3.13}$$

Here $\nu$ is the molecular kinematic viscosity and $\sigma_e$ is the molecular Prandtl number. When expressing heat conduction via the internal energy using its definition in Eq. (3.5) and the ratio of specific heats $\gamma = c_p/c_v$, the heat flux vector can be expressed by:

$$\mathbf{q} = -\rho\,\Gamma_e\,\nabla e \tag{3.14}$$

where $\Gamma_e$ refers to the diffusion coefficient of the internal energy which is defined using $\nu$ and $\sigma_e$ as:

$$\Gamma_e = \frac{\nu\,\gamma}{\sigma_e}$$

Note that in Eq. (3.14) the gradient of specific heat $c_v$ with respect to temperature has been neglected despite being dependent on gas temperature and composition $c_v = c_v(Y_\psi, T)$. This decision is based on the fact that its contribution is relatively small compared to the gradient of internal energy [77].

The molecular diffusion flux of species $\psi$ due to concentration gradients is expressed by Fick's law as [197]:

$$\mathbf{j}_\psi = -\rho\,\Gamma_\psi\,\nabla Y_\psi \tag{3.15}$$

Here, $\Gamma_\psi$ represents the diffusion coefficient and is defined by:

$$\Gamma_\psi = \frac{\nu}{\sigma_{Y_\psi}}$$

where $\sigma_{Y_\psi}$ is the molecular Schmidt number.

Note that in this study second-order diffusion effects are neglected. Those comprise the mass diffusion by a temperature gradient (Soret effect) and energy diffusion driven by concentration gradients (Dufour effect). A theoretical description of these effects are found in [46, 145, 277]. Generally, second-order diffusion is negligible and of minor importance [46, 82, 106, 107], in particular due to dominant energy and mass transport in engines caused by turbulence.

### Caloric equation of state

The internal energy is related to the temperature via the caloric equation of state given as:

$$e(Y_\psi, T) = \int_{T_{ref}}^{T} c_v(Y_\psi, T)\, dT \quad ; \quad \psi = 1, \ldots, N \tag{3.16}$$

The specific heat at constant volume $c_v$ is a function of the concentrations of $N$ species and temperature. This equation is used to iteratively obtain $e$ from $T$ and vice versa.

### Equation of state

The EOS relates the variables pressure, specific volume and temperature $(p, v, T)$ to each other. For many gases, like air, the ideal gas equation represents the pvT behaviour well at low pressures and moderate temperatures [450]. Thus, in engineering flows conventionally the working fluid is assumed to be ideal.

The ideal gas law reads [358]:

$$p\, v_m = \mathcal{R}\, T \tag{3.17}$$

where $v_m$ is the molar volume. A gas-composition-dependent gas constant $R$ can be

introduced such that the ideal gas EOS reads:

$$p = \rho_m \, R \, T \tag{3.18}$$

where $R$ is defined for a mixture of $N$ components with molar concentration $y_i$ for species $i$ by:

$$\frac{1}{R} = \sum_{i=1}^{N} \frac{y_i}{R_i} \tag{3.19}$$

For elevated pressures as encountered in the HPP concept the ideal gas equation may deviate considerably from experimental data [358]. To quantify the non-ideality, the compressibility factor $Z$ is introduced as:

$$Z = \frac{p \, v_m}{\mathcal{R} T} \tag{3.20}$$

For an ideal gas $Z$ is unity. If the temperature is augmented simultaneously with the pressure, again the gas tends to closely obey the ideal gas law [358].

To study in detail the validity of the ideal gas assumption in this research, a sensitivity study was performed covering the in-cylinder pressure and temperature range of the new Diesel engine concept. The findings are summarised in the next section.

### 3.2.6 Study of equation of state

Numerous EOS have emerged to cope with the extended pressure and temperature ranges. Among those the cubic EOS of Redlich-Kwong (RK), Soave-Redlich-Kwong (SRK) and Peng-Robinson (PR) are widely accepted, with sufficient coefficients to allow fitting to experimental data and giving a reasonable compromise between simplicity and generality [306, 358]. These three EOS are chosen for this evaluation study.

#### 3.2.6.1 Cubic equations of state

The cubic EOS studied are given below and their coefficients are summarised in Table 3.1.

**Redlich-Kwong EOS [356]:**

$$p = \frac{\mathcal{R}T}{v_m - b} - \frac{\frac{\alpha}{\sqrt{T}}}{v_m(v_m + b)}. \tag{3.21}$$

**Soave-Redlich-Kwong EOS [401]:**

$$p = \frac{\mathcal{R}T}{v_m - b} - \frac{\alpha\left[1 + f(\omega)(1 - \sqrt{\frac{T}{T_c}})\right]^2}{v_m(v_m + b)} \tag{3.22}$$

**Peng-Robinson EOS [330]:**

$$p = \frac{\mathcal{R}T}{v_m - b} - \frac{\alpha\left[1 + f(\omega)(1 - \sqrt{\frac{T}{T_c}})\right]^2}{v_m^2 + 2bv_m - b^2} \tag{3.23}$$

Here $\omega$ is the *acentric factor* which indicates the degree of non-sphericity of a molecule and the quantities with index $c$ designate critical values.

| EOS | b | $\alpha$ | $f(\omega)$ |
|---|---|---|---|
| Redlich-Kwong | $\frac{0.08664\mathcal{R}T_c}{p_c}$ | $\frac{0.42748\mathcal{R}^2T_c^{2.5}}{p_c}$ | — |
| Soave-Redlich-Kwong | $\frac{0.08664\mathcal{R}T_c}{p_c}$ | $\frac{0.42748\mathcal{R}^2T_c^2}{p_c}$ | $0.48 + 1.574\omega - 0.176\omega^2$ |
| Peng-Robinson | $\frac{0.07780\mathcal{R}T_c}{p_c}$ | $\frac{0.45724\mathcal{R}^2T_c^2}{p_c}$ | $0.37464 + 1.54226\omega - 0.26992\omega^2$ |

**Table 3.1:** Constants for cubic equations of state taken from [358].

#### 3.2.6.2 Tests for high pressure and temperature condition

High pressures and temperatures occur at the end of the compression stroke and during the combustion phase. These conditions extend considerably beyond the

critical properties of air. Therefore the first case involves a state change similar to the adiabatic compression of air at Diesel-like conditions. An adiabatic state change represents a more severe condition compared to a compression with heat losses, since the in-cylinder temperatures attain higher levels.

For an adiabatic compression the first law of thermodynamics relates the change of specific internal energy $\Delta e$ to the specific work $w$ as:

$$w = -\Delta e \tag{3.24}$$

With an expression for specific work due to volume change and the internal energy taken as a function of volume and temperature gives:

$$\int p(v)\,dv = -\int \left(\frac{\partial e}{\partial T}\right)\Big|_v dT + \int \left(\frac{\partial e}{\partial v}\right)\Big|_T dv \tag{3.25}$$

The right hand side can be simplified assuming a constant specific heat at constant volume which is a valid approximation under the current conditions [450] and the Maxwell relations:

$$\int p(v)\,dv = -\int c_v\,dT + \int T^2 \left(\frac{\partial\left(\frac{p}{T}\right)}{\partial T}\right)_v dv\Big|_T \tag{3.26}$$

With the EOS and Eq. (3.26), the state change due to compression can be obtained.

The adiabatic compression is computed using geometrical and other data for the HPP Diesel engine prototype which is described later in Section 5.3. The initial temperature was set to the intake value while the initial charge mass was taken from an induction calculation for the engine. The initial values are listed in Table 3.2 and the properties of air are given in Table 3.3.

| $T_0$ [K] | $V_0$ [m$^3$] | $m_0$ [kg] | $v_{m0}$ [m$^3$/kmol] |
|---|---|---|---|
| 315 | $2.112\times10^{-3}$ | $6.285\times10^{-3}$ | 9.73 |

**Table 3.2:** Initial values for the adiabatic compression.

| $c_v$ [J/(mol K)] | $M$ [g/mol] | $\gamma$ [-] | $p_c$ [bar] | $T_c$ [K] | $\omega$ [-] |
|---|---|---|---|---|---|
| 20.68 | 28.96 | 1.4 | 37.365 | 132.41 | 0.03606 |

**Table 3.3:** Properties of air taken from [358].

As shown in the temperature versus pressure plot of Figure 3.1 the three cubic EOS give almost identical results over the range displayed. As the pressure rises due to the contracting volume, the differences between the ideal gas law and the cubic EOS increase. At the maximum expected peak cylinder pressure of about 23 MPa the differences are however below 1.5%. Therefore it can be concluded that the predictions using the ideal gas law for high pressure and temperature conditions show acceptably small departures from the real gas behaviour.

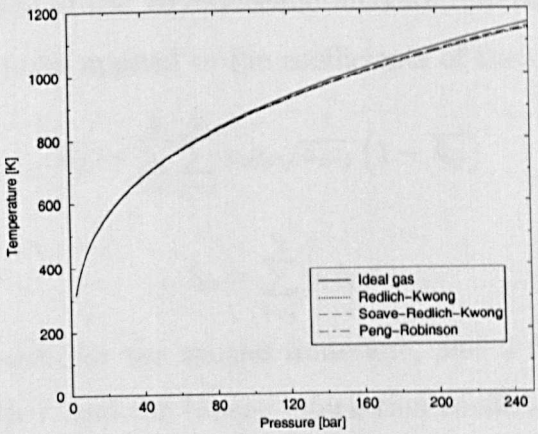



**Figure 3.1:** Temperature versus pressure trace for adiabatic compression.

#### 3.2.6.3 Test for high pressure and low temperature condition

A second test case was chosen for high pressure and low temperature conditions, for which the largest differences from ideal gas behaviour are expected [450]. This situation is encountered in the vicinity of the spray due to evaporative cooling. An air/dodecane mixture was chosen due to the similar properties of dodecane and Diesel fuel [383].

For this test case initial conditions were again selected for the HPP prototype engine. The initial pressure and temperature at a typical SOI (see Table 3.4), obtained from an induction calculation when boosting the intake air to 3.5 bar, were used. The dodecane concentration was fixed at a representative value of 10%† taken from calculations of the spray early after start of injection. The mixture temperature was gradually reduced to the droplet temperature of 350 K while holding the pressure constant.

| $p_{boost}$ [bar] | SOI [° CA] | $y_{C12H26}$ | $p_\infty$ [bar] | $T_\infty$ [K] |
|---|---|---|---|---|
| 3.5 | 351.0 | 10% | 140.7 | 960.1 |

**Table 3.4:** Initial conditions for high pressure and low temperature case (subscript $\infty$ indicates initial values).

To evaluate the state of the air/dodecane mixture, mixing rules obtained from Reid *et al.* [358] have to be applied to the coefficients of the cubic EOS:

$$a_m = \sum_{i=1}^{2}\sum_{j=1}^{2} y_i y_j \sqrt{a_i a_j}\left(1 - \overline{k_{ij}}\right) \tag{3.27}$$

$$b_m = \sum_{i=1}^{2} y_i\, b_i \tag{3.28}$$

where the index 1 stands for the species dodecane, and 2 for air. Here $y_i$ is the mole fraction of species $i$, and the binary interaction coefficient $\overline{k_{ij}}$ has been set to 0, which is a good approximation for hydrocarbons [358]. The properties of air and dodecane are listed in Tables 3.3 and Table 3.5, respectively.

| $M$ [g/mol] | $p_c$ [bar] | $T_c$ [K] | $T_{boil}$ [K] | $\omega$ [-] |
|---|---|---|---|---|
| 170.34 | 18.2 | 658.2 | 489.5 | 0.575 |

**Table 3.5:** Properties of dodecane taken from [358].

The compressibility factors obtained using the three cubic EOS in the temperature range from 350 K to 950 K are shown in Figure 3.2. Over most of the range,

†Note that this is a molar concentration; hence the dodecane mass fraction is considerably higher at around 40% due to its large molecular mass.

they give $Z$ values above unity, which indicates that for given pressure and temperature, the density is predicted to be lower than for an ideal gas. For decreasing temperatures below 600 K the compressibility factor decreases continuously with especially large slopes at low temperatures. The highest departures from an ideal gas of about 9% are predicted at 620 K when using the SRK EOS.

The study shows that the departure from ideal gas behaviour under high pressure and low temperature conditions is less than 10%. Also, it is noteworthy that the differences between the cubic EOS are as large as their deviations from the ideal gas EOS.

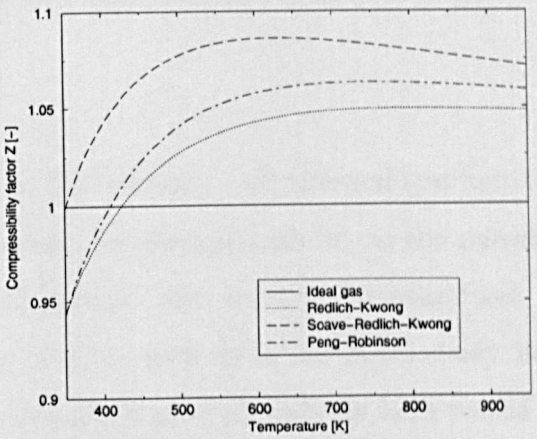



**Figure 3.2:** Compressibility factor for various EOS at high pressures and variable temperatures with 10% dodecane in mixture.

#### 3.2.6.4 Conclusions

The validity of the ideal gas assumption under two critical situations in the range of operation conditions for the new Diesel engine concept has been investigated. As reference three cubic EOS are chosen which have been designed to model pvT behaviour over a wider range of conditions. At high pressures and temperatures the departure from ideal gas behaviour for air is less than 1.5%. For the situation of high pressure and lower temperature the ideal gas law would produce errors less than 10%. In particular for the latter test case, the differences between the cubic

EOS are of the same order as the departures from ideal gas behaviour. Therefore it is concluded that the application of the ideal gas assumption gives acceptably small departures from real gas behaviour under the expected range of operating conditions.

### 3.2.7 Study of thermophysical properties

In the gas phase governing equations the following thermophysical properties appear: molecular viscosity, thermal conductivity, heat capacity, and diffusion coefficient. Here, various correlations for these quantities are examined for their applicability under elevated in-cylinder conditions and their suitability for CFD engine calculations.

Transport properties like viscosity and thermal conductivity are known to vary with temperature. However, for the applicability at the relevant chamber conditions the effects of increased pressure also need to be examined. For this purpose the adiabatic compression of air is used as in the EOS study in Section 3.2.6.2. The correlations chosen in this study have extensively been tested against measurements and are recommended by Reid *et al.* [358]. A summary of the correlations is found in Section C.1 in the Appendix.

#### 3.2.7.1 Molecular viscosity

For the study of molecular viscosity, the correlations of Sutherland [392], Chung *et al.* [74] and Lucas [275] were chosen. The Sutherland correlation is computationally the simplest, but does not include a pressure correction like the latter two. As reference, the molecular viscosity of air at standard atmosphere is $1.81 \times 10^{-5}$ Ns/m$^2$.

Figures 3.3 and 3.4 show the separate variations of molecular viscosity with temperature. The maximum temperature of 1150 K corresponds to a pressure of

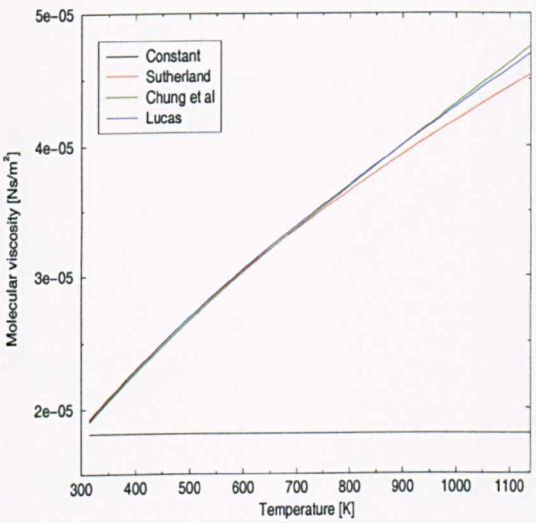



**Figure 3.3:** Variation of molecular viscosity predicted by correlations without pressure correction.

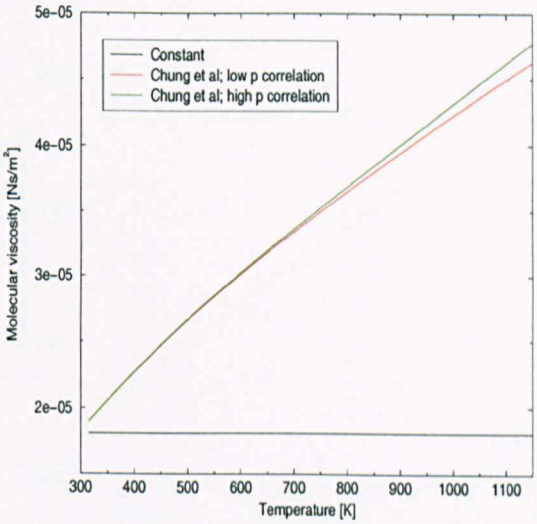



**Figure 3.4:** Variation of molecular viscosity predicted by Chung *et al.* with pressure correction.

around 250 bar. For increasing temperatures the molecular viscosity increases almost linearly to a maximum of about 2.4 times the initial value. As seen in Figure 3.3 the correlations differ negligibly by less than 0.5% over the whole pressure and temperature range shown. The maximum pressure correction, given by the Chung *et al.* correlation, is approximately 3%. For temperatures below 700 K the effect is negligible.

#### 3.2.7.2 Thermal conductivity

To study the effect of temperature and pressure on thermal conductivity under engine-like conditions the modified Eucken correlation [417] and those of Chung *et al.* [75] and Ely and Hanley [104] were chosen. The complexity of the correlation increases significantly from the modified Eucken equation to the Chung *et al.* correlation and that of Ely and Hanley. While the first is strictly valid only for the low-pressure range, the latter two contain corrections for high pressures. As reference, the conductivity of air at standard atmosphere is $2.637 \times 10^{-2}$ W/(mK).

Figures 3.5 and 3.6 display the variation of thermal conductivity with tempera-

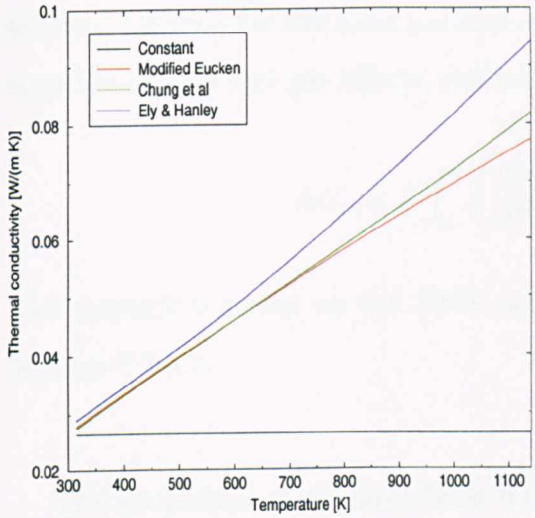



**Figure 3.5:** Variation of thermal conductivity predicted by correlations without pressure correction.

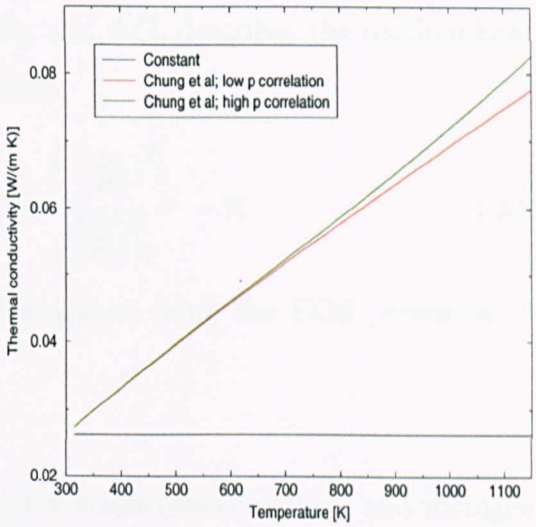



**Figure 3.6:** Variation of thermal conductivity predicted by Chung *et al.* correlation with pressure correction.

ture for adiabatic compression. As the temperatures increase, $k$ increases approximately linearly. At 1150 K it reaches levels that are of the order of three times larger than the initial value. Larger differences of up to 20% can be observed among the methods in particular for high pressures and temperatures as seen in Figure 3.5. The correlation of Ely and Hanley gives consistently the highest values. The difference between considering and neglecting the effects of elevated pressure on thermal conductivity is about 6.5% for pressures up to 230 bar as can be seen from Figure 3.6. For temperatures below 600 K both approaches give similar magnitudes.

#### 3.2.7.3 Heat capacity

The influence of increased pressure and temperature levels on the heat capacity at constant pressure is studied next. The polynomial relationships of the JANAF database [147] are used which assume an ideal gas and express the heat capacity as a function of temperature only. The real gas effects on heat capacity of a pure component due to elevated pressures is given by [358]:

$$C_p = C_p^\circ + \Delta C_p \tag{3.29}$$

where $C_p^\circ$ stands for the ideal gas heat capacity and $\Delta C_p$ describes the residual heat capacity due to real gas effects, defined by [358]:

$$\Delta C_p = T \int_\infty^v \left( \frac{\partial^2 p}{\partial T^2} \right) dv - \frac{T \left( \frac{\partial p}{\partial T} \right)^2 \Big|_v}{\left( \frac{\partial p}{\partial v} \right) \Big|_T} - \mathcal{R} \tag{3.30}$$

The respective terms on the RHS can be calculated using the EOS presented in Section 3.2.6.1.

The properties of air have been obtained for a mixture of oxygen and nitrogen applying the following mixing rule [358]:

$$C_{pm}^\circ = \sum_i y_i \, C_{pi}^\circ \tag{3.31}$$

Here the molar concentrations of oxygen and nitrogen were assumed to be 0.2095 and 0.7905, respectively. As reference, the heat capacity $C_p^\circ$ of air is supplied in the results as 29.18 J/(mol K).

The change in heat capacity at constant pressure for adiabatic compression is shown in Figure 3.7. As temperatures rise the heat capacities increase close to linearly. At 1150 K which corresponds approximately to 250 bar due to compression the ideal gas $C_p$ is about 16% larger than the initial value at 315 K. The real gas $C_p$

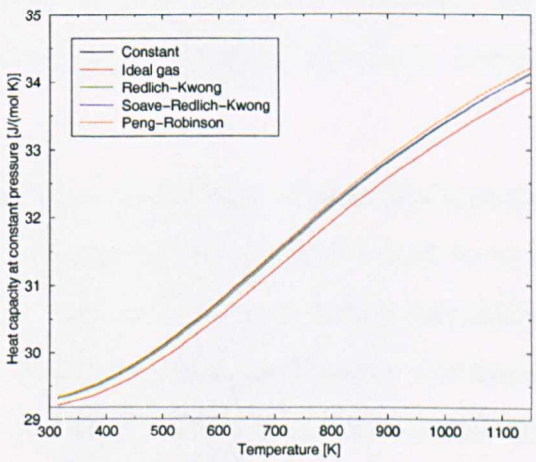



**Figure 3.7:** Variation of heat capacity at constant pressure for adiabatic compression.

values give, compared to the ideal gas values, consistently higher heat capacities that are less than 1% larger for the temperature range shown. Negligible differences exist among the various real gas heat capacities even at high pressures and temperatures.

#### 3.2.7.4 Diffusion coefficient

A similar sensitivity study for adiabatic compression was performed on gas phase binary diffusion coefficients for air/dodecane mixtures. The correlations chosen are those of Chapman and Enskog [63], Fuller *et al.* [129] and Wilke and Lee [463]. The latter are essentially variations of the Chapman and Enskog correlation based on different sets of experimental data. For the high pressure regime, the corrections of Takahashi [421] were applied to the low-pressure diffusivities. The diffusivity was taken to be independent of composition, which is valid for binary gaseous mixtures [46, 358]. Air was assumed to be composed of oxygen and nitrogen with a molar concentration ratio of 0.2095 to 0.7905.

Figures 3.8 and 3.9 show the variation of the diffusion coefficient with temperature for adiabatic compression. As temperatures increase, the molecular diffusivity decreases. The end values at around 1150 K are lower by a factor of around nine than the initial values at 350 K. The differences among the correlations are less than 9%. When applying the high-pressure correction of Takahashi to the previous Chapman and Enskog predictions, negligible differences are found over the entire pressure and temperature range calculated, as seen in Figure 3.9.

Multicomponent mixture diffusivities depend nonlinearly on the concentration gradients of all substances present and therefore need to be specified for each component pair [46]. Their evaluation is thus computationally expensive. However, it is known that turbulence increases significantly the mass transfer compared to molecular transport. Therefore usually a constant diffusivity has been applied for engine calculations to model molecular interphase diffusion of the various species

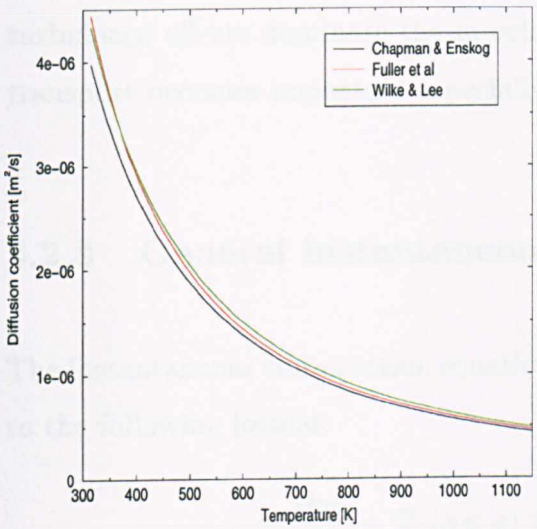



**Figure 3.8:** Variation of air/dodecane binary diffusion coefficient for adiabatic compression predicted by low-pressure correlations.

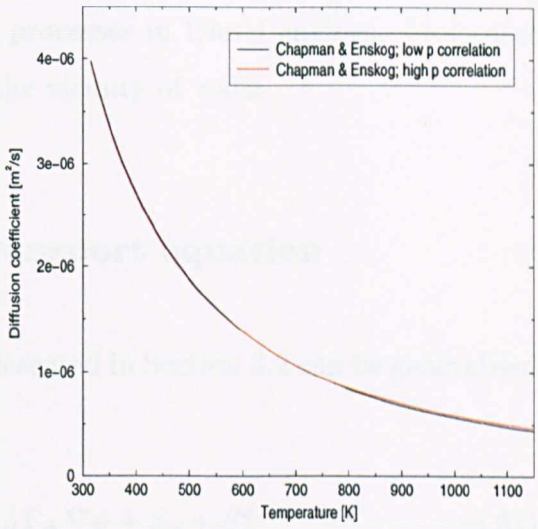



**Figure 3.9:** Variation of air/dodecane binary diffusion coefficient for adiabatic compression predicted by high-pressure correlation.

involved (see e.g. [77, 246, 427]). On this basis it has been decided to employ the last-mentioned practice of constant diffusivities in this research.

#### 3.2.7.5 Conclusions

The previous study indicates that transport properties are largely dependent on temperature. The dependence on pressure for an adiabatic compression was found to be small, up to 6.5%, at the conditions of interest. Thus it was decided to incorporate the temperature effects into molecular viscosity, thermal conductivity and heat capacity at constant pressure. The following correlations are chosen in the present study for each transport property due to their simplicity and capability to reproduce the correct trends:

- *Molecular viscosity:* Sutherland equation.
- *Molecular thermal conductivity:* Modified Eucken equation.
- *Heat capacity at constant pressure:* JANAF polynomials.

Since turbulent transport substantially enhances mass transfer, a constant diffusivity is employed representative for the in-cylinder mixture. In general it is noted that

turbulence effects dominate the in-cylinder processes in Diesel engines. Molecular transport becomes important especially in the vicinity of walls.

### 3.2.8 General instantaneous transport equation

The instantaneous conservation equations presented in Section 3.2 can be generalised to the following format:

$$\frac{\partial \rho\phi}{\partial t} + \nabla\cdot(\rho\,\mathbf{u}\,\phi) = \nabla\cdot\rho\,\Gamma_\phi\,\nabla\phi + S_\phi + S_\phi^d \tag{3.32}$$

where $\phi$ is the dependent variable, $\Gamma_\phi$ refers to the molecular diffusion coefficient, and $S_\phi$ and $S_\phi^d$ represent the source terms related to the gas phase and gas/liquid interphase exchange, respectively.

## 3.3 Ensemble-Averaged Governing Equations

For unsteady, quasi-periodic flows such as in the engine cylinder, *ensemble-averaging* or *phase-averaging* has usually been employed to capture the turbulent nature of the flow field [167]. Other averaging techniques such as time or space averaging are appropriate only for stationary and homogeneous turbulence, respectively, and hence are not suitable for engine simulations.

### 3.3.1 Ensemble-averaging

For ensemble-averaging the transport equations in compressible engine flows, two different approaches have been applied. The first involves an unweighted *Reynolds-averaging* technique [370] , while the second is based on a density-weighted *Favre-averaging* technique [113].

### Reynolds-averaging

The instantaneous value of a variable $\phi$ at location $\mathbf{x}$ and at a specific crank angle $\alpha$ in the cycle can be decomposed into:

$$\phi(\mathbf{x},\alpha) = \overline{\phi}(\mathbf{x},\alpha) + \phi'(\mathbf{x},\alpha) \tag{3.33}$$

where $\overline{\phi}$ indicates the ensemble-averaged mean and $\phi'$ is the fluctuation about the Reynolds mean value, for which by definition $\overline{\phi'} = 0$. The average is obtained ideally over an infinite number of identical cycles, expressed as:

$$\overline{\phi}(\mathbf{x},\alpha) = \lim_{N\to\infty}\left[\frac{1}{N}\sum_{i=1}^{N}\phi(\mathbf{x},\alpha + i\alpha_c)\right] \tag{3.34}$$

Here, $N$ is the number of identically repeated realisations and $\alpha_c$ is the engine cycle.

### Favre-averaging

The following weighted decomposition has been proposed by Favre for the instantaneous $\phi$ at crank angle $\alpha$:

$$\phi(\mathbf{x},\alpha) = \tilde{\phi}(\mathbf{x},\alpha) + \phi''(\mathbf{x},\alpha) \tag{3.35}$$

Here $\phi''$ denotes the fluctuations about the Favre mean value $\tilde{\phi}$, defined by:

$$\tilde{\phi}(\mathbf{x},\alpha) = \frac{1}{\overline{\rho}_m(\mathbf{x},\alpha)}\lim_{N\to\infty}\left[\frac{1}{N}\sum_{j=1}^{N}\rho_m(\mathbf{x},\alpha + i\alpha_c)\;\phi(\mathbf{x},\alpha + i\alpha_c)\right] \tag{3.36}$$

where $\overline{\rho}_m$ stands for the Reynolds mean density.

For compressible and combusting flows Favre-averaging offers advantageous characteristics over Reynolds-averaging. Firstly only a few new terms are introduced as a consequence of averaging in comparison to many new terms in the latter case [462]. Secondly the Favre-averaged transport equations more closely resemble the instantaneous counterparts, so a unique physical interpretation of each term is possible. On this basis it is decided to adopt this technique for the present research.

When applying Favre-averaging on transport equations for multiphase flows where the void fraction accounts for the presence of the dispersed phase, ensemble-averaging of the void fraction becomes necessary. Consequently $\overline{\rho}_m$ in Eq. (3.36) acquires the meaning of microscopic density and several new terms arise in the averaged transport equations involving correlations of mean and fluctuating values of the void fraction, respectively, with other dependent mean variables and their fluctuations, respectively. This renders the governing equations complex. To mathematically reduce the complexity, Favre-averaging is employed by weighing the instantaneous field variables with the *macroscopic* density instead. Therefore the Favre mean variable can be expressed by combining Eqs. (3.34) and (3.36) to:

$$\tilde{\phi}(\mathbf{x},\alpha) = \frac{1}{\overline{\rho}(\mathbf{x},\alpha)}\overline{\rho(\mathbf{x},\alpha)\,\phi(\mathbf{x},\alpha)} \tag{3.37}$$

with a Reynolds-mean macroscopic density given as:

$$\overline{\rho}(\mathbf{x},\alpha) = \overline{\rho_m(\mathbf{x},\alpha)\,\phi(\mathbf{x},\alpha)} \tag{3.38}$$

However, correlations of void fraction fluctuation with other field variable fluctuations exist (e.g. $\overline{\vartheta'\,\nabla p'}$ in the momentum equation). These require further modelling assumptions to express them in terms of known quantities. Since no general modelling approach is readily available and following the practices of previous researchers [77, 196, 246, 427], they will be ignored. For the spray source terms $S_\phi^d{}'$ a similar situation leads to the same practice.

When Favre-averaging the governing equations, additional relations between Reynolds- and Favre-averaged quantities are needed which are given e.g. in [249].

### 3.3.2 Favre-averaged transport equation

When density-weighted ensemble-averaging is applied to the general instantaneous transport equation in Eq. (3.32), the following result is obtained:

$$\frac{\partial\overline{\rho}\tilde{\phi}}{\partial t} + \nabla\cdot\left(\overline{\rho}\tilde{\mathbf{u}}\tilde{\phi}\right) = \nabla\cdot\left(\overline{\rho}\overline{\Gamma}_\phi\nabla\tilde{\phi}\right) - \nabla\cdot\left(\overline{\rho\mathbf{u}''\phi''}\right) + \overline{S}_\phi + \overline{S}_\phi^d \tag{3.39}$$

Here fluctuations of the diffusion coefficient $\Gamma_\phi$ have been neglected on the grounds that in highly turbulent flows, as in engines, the viscous terms become negligible compared to their turbulent counterparts [174, 422].

A new term appears in the above equation, $\rho \mathbf{u}''\phi''$, that is commonly interpreted as representing the turbulent diffusion flux of the variable $\phi$. This needs additional modelling, in order that the system of equations is closed. This is commonly referred to as the *closure problem* [462]. In the present study the closure used is the *Boussinesq approximation* [55] which assumes an analogy between laminar and turbulent flow, summarised below.

### 3.3.3 Favre-averaged constitutive relations

#### Newton's law of friction

The molecular shear tensor of Eq. (3.9) resulting from ensemble-averaging yields:

$$\tilde{\tau} = \overline{\rho}\left(2\overline{\nu}\widetilde{\mathbf{D}} - \frac{2}{3}\overline{\nu}\nabla\cdot\tilde{\mathbf{u}}\mathbf{I}\right) \tag{3.40}$$

Here the fluctuations of $\nu$ have been neglected based on the same reasoning as for the diffusion coefficient $\Gamma_\phi$. Analogously the turbulent diffusion term $\overline{\rho\mathbf{u}''\mathbf{u}''}$, also called Reynolds stress tensor, is modelled using the Boussinesq approximation as:

$$\widetilde{\tau_t} = \overline{\rho\mathbf{u}''\mathbf{u}''} = \overline{\rho}\left(2\nu_t\widetilde{\mathbf{D}} - \frac{2}{3}\nu_t\nabla\cdot\tilde{\mathbf{u}}\mathbf{I}\right) - \frac{2}{3}\overline{\rho}\tilde{k}\mathbf{I} \tag{3.41}$$

where $\nu_t$ is the turbulent or eddy kinematic viscosity. This requires additional modelling via a turbulence closure, because – unlike the molecular kinematic viscosity – $\nu_t$ is not a fluid property and depends on the turbulent flow field properties. Here $\tilde{k}$ is given by:

$$\tilde{k} = \frac{1}{2}\widetilde{\mathbf{u}''\cdot\mathbf{u}''} \tag{3.42}$$

### Fourier's law of heat conduction and Fick's law of diffusion

After ensemble-averaging, Fourier's law of heat conduction and Fick's law of diffusion read:

$$\overline{\mathbf{q}} = -\overline{\rho}\,\overline{\Gamma}_e\,\nabla\tilde{e} \tag{3.43}$$

$$\overline{\mathbf{j}} = -\overline{\rho}\,\overline{\Gamma}_{Y_\psi}\,\nabla\tilde{Y}_\psi \tag{3.44}$$

For the turbulent diffusion of scalar properties in general the application of the Boussinesq hypothesis results in:

$$-\overline{\rho\,\mathbf{u}''\phi''} = \overline{\rho}\,\Gamma_{\phi,t}\,\nabla\tilde{\phi} \tag{3.45}$$

where $\Gamma_{\phi,t}$ stands for the turbulent or eddy diffusion coefficient.

### Caloric equation of state

Favre-averaging the caloric equation of state yields:

$$\tilde{e} = \int_{T_{ref}}^{T} \tilde{c}_v\,d\tilde{T} \tag{3.46}$$

with the averaged specific heat, given as:

$$\tilde{c}_v = c_v\left(\tilde{Y}_\psi, \tilde{T}\right) \tag{3.47}$$

Here the correlation $\overline{\rho\,c_v''T''}$ is assumed to be small enough to be neglected.

### Equation of state

The influence of gas composition fluctuations on the specific gas constant $R$ is assumed to be negligible following the practice of previous researchers [77, 246]. Additionally terms which contain void fraction fluctuations such as $\overline{p'\vartheta'}$ and $\overline{\rho_m'\vartheta'}$ are neglected based on the same arguments as put forward to the omission of the term $\overline{\vartheta'\,\nabla p'}$ in the momentum equation. Thus the density-weighted EOS reads:

$$\overline{p} = \frac{\overline{\rho}\,\overline{R}\tilde{T}}{\overline{\vartheta}} \approx \overline{\rho}_m\overline{R}\tilde{T} \tag{3.48}$$

### 3.3.4 General Favre-averaged transport equation

It is convenient to introduce effective quantities for the kinematic viscosity and diffusion coefficient. Thus the molecular and turbulent transport properties are combined as:

$$\overline{\nu}_{eff} = \overline{\nu} + \nu_t \tag{3.49}$$

$$\overline{\Gamma}_{\phi,eff} = \overline{\Gamma}_{\phi} + \Gamma_{\phi,t} \tag{3.50}$$

Both effective quantities can be related to each other by:

$$\overline{\Gamma}_{\phi,eff} = \frac{\overline{\nu}_{eff}}{\sigma_{\phi}} \tag{3.51}$$

where $\sigma_{\phi}$ is the Prandtl or Schmidt number taken as constant and listed in Table 3.6 for various variables.

| $\phi$ | $Y_{\psi}$ | $e$ | $k$ | $\varepsilon$ |
|---|---|---|---|---|
| $\sigma_{\phi}$ | 1.0 | 0.8 | 1.0 | 1.2 |

**Table 3.6:** Prandtl and Schmidt numbers derived from experiments for scalar variables; taken from [38, 268].

Using Eqs. (3.45) and (3.50) the generalised governing equation (3.39) can now be written as:

$$\frac{\partial \overline{\rho}\tilde{\phi}}{\partial t} + \nabla\cdot(\overline{\rho}\,\tilde{\mathbf{u}}\,\tilde{\phi}) = \nabla\cdot\left(\overline{\rho}\,\overline{\Gamma}_{\phi,eff}\,\nabla\tilde{\phi}\right) + \overline{S}_{\phi} + \overline{S}^{d}_{\phi} \tag{3.52}$$

### 3.3.5 Turbulence model

In this study a version of the $k-\varepsilon$ turbulence model is used which accounts for compressibility effects as derived by El Tahry [101] and extended to two-phase flow by Kralj [246]. In this model the Favre-averaged dissipation rate $\varepsilon$ is defined by:

$$\tilde{\varepsilon} = \frac{1}{\overline{\rho}}\,\overline{\boldsymbol{\tau}' : \nabla\mathbf{u}''} \tag{3.53}$$

The turbulent diffusivity $\Gamma_{\phi,t}$ and kinematic viscosity $\nu_t$ in the definition of the turbulent stresses and turbulent scalar fluxes in Eqs. (3.41) and (3.45) are expressed as [215]:

$$\Gamma_{\phi,t} = \frac{\nu_t}{\sigma_{\phi,t}} \tag{3.54}$$

$$\nu_t = C_\mu \frac{\tilde{k}^2}{\tilde{\varepsilon}} \tag{3.55}$$

where $\sigma_{\phi,t}$ refers to the turbulent Prandtl and Schmidt numbers which are taken as constant, given in Table 3.6. Besides, $C_\mu$ is a model coefficient listed in Table 3.7.

The turbulence parameters $k$ and $\varepsilon$ are obtained by solving their respective transport equations. The full derivation of both equations is covered by Kralj [246] and will not be reproduced here.

#### 3.3.5.1 Turbulence kinetic energy equation

The transport equation for the turbulence kinetic energy is [246]:

$$\frac{\partial \overline{\rho}\tilde{k}}{\partial t} + \nabla\cdot\left(\overline{\rho}\,\tilde{\mathbf{u}}\,\tilde{k}\right) = \nabla\cdot\overline{\rho}\,\Gamma_{k,t}\,\nabla\tilde{k} + G - \overline{\rho}\,\tilde{\varepsilon} + \overline{S}_k^d \tag{3.56}$$

where $\Gamma_{k,t}$ represents the diffusivity of the turbulence kinetic energy. The first term on the RHS stands for the turbulence diffusion and the subsequent two terms represent the generation and viscous dissipation of turbulence energy, respectively. The last term on the RHS is the spray contribution to $k$. The turbulence generation rate is:

$$G = \tilde{\tau}_t : \nabla\tilde{\mathbf{u}} \tag{3.57}$$

For the spray source term the following definition is provided according to Kralj [246]:

$$\overline{S}_k^d = \overline{\mathbf{u}''\cdot\mathbf{S}_\mathbf{u}^d} - \overline{\mathbf{u}''\cdot\mathbf{u}\,S_m^d} + \frac{1}{2}\overline{\mathbf{u}''\cdot\mathbf{u}''S_m^d} \tag{3.58}$$

Here, the first term on the RHS represents the rate of work exchange between eddies and droplets due to drag forces. The next two terms represent the effects of mass transfer (i.e. evaporation) on $k$.

#### 3.3.5.2 Turbulence dissipation rate equation

The transport equation for the turbulence dissipation rate is [246]:

$$\frac{\partial \overline{\rho}\widetilde{\varepsilon}}{\partial t} + \nabla\cdot(\overline{\rho}\,\widetilde{\mathbf{u}}\,\widetilde{\varepsilon}) = \nabla\cdot\overline{\rho}\,\Gamma_{\varepsilon,t}\nabla\widetilde{\varepsilon} + C_{\varepsilon 1}G\frac{\widetilde{\varepsilon}}{\widetilde{k}} - C_{\varepsilon 2}\overline{\rho}\frac{\widetilde{\varepsilon}^2}{\widetilde{k}} + C_{\varepsilon 3}\overline{\rho}\,\widetilde{\varepsilon}\nabla\cdot\widetilde{\mathbf{u}} + \overline{S}_{\varepsilon}^{d} \qquad (3.59)$$

where $\Gamma_{\varepsilon,t}$ stands for the diffusivity of the dissipation rate and $C_{\varepsilon 1}$, $C_{\varepsilon 2}$ and $C_{\varepsilon 3}$ are coefficients, listed in Table 3.7. The first term on the RHS refers to the diffusion of $\varepsilon$, while the second term stands for its generation due to mean shear and self-stretching effects of turbulence. The viscous destruction is accounted for in the third term, followed by terms representing the generation and destruction due to compressibility effects. The final term represents the contribution of the spray to turbulence which is evaluated according to Mostafa and Mongia [305] as:

$$\overline{S}_{\varepsilon}^{d} = C_{\varepsilon 4}\frac{\widetilde{\varepsilon}}{\widetilde{k}}\overline{S}_{k}^{d} \qquad (3.60)$$

Another coefficient $C_{\varepsilon 4}$ appears that was determined by Mostafa and Mongia through matching predictions to measurement data. Its value is provided in Table 3.7.

| $\sigma_k$ | $\sigma_\varepsilon$ | $C_\mu$ | $C_{\varepsilon 1}$ | $C_{\varepsilon 2}$ | $C_{\varepsilon 3}$ | $C_{\varepsilon 4}$ |
|---|---|---|---|---|---|---|
| 1.0 | 1.2 | 0.09 | 1.44 | 1.92 | −0.373 | 1.0 |

**Table 3.7:** Model coefficients in the $k-\varepsilon$ turbulence model (from [246, 305]).

## 3.4 Spray Model

When liquid fuel is injected into the combustion chamber, its initial conditions are determined by the nozzle flow and atomisation processes. Once propagating in the gas mixture, droplets interact with the ambient gas, with neighbouring droplets and, if the penetration is far enough, with the cylinder wall. In the Lagrangian formulation a submodel is provided for each process as outlined below. For a detailed description of each model the reader is referred to the works of Clerides [77] and Kralj [246].

In general simplifying assumptions are made for the spray modelling following Clerides [77]:

1. Droplets are assumed to be spherical.
2. Interphase transport relating to mass, momentum and energy are taken as quasi-steady. Thus they correspond to steady-state rates derived when using the same boundary conditions.
3. Correlations for transfer coefficients of mass, momentum and energy between droplet and ambient mixture are derived from single droplet experiments and are assumed valid for a Diesel spray.

These assumptions idealise the real Diesel spray substantially. However, they are introduced to simplify the mathematical modelling and render the numerical approach affordable [77, 107].

### 3.4.1 Nozzle model

The flow structure in the nozzle greatly influences the injection velocity which subsequently affects the various spray processes. A simple nozzle model was applied that calculates the effective nozzle exit velocity as the ratio of specific volumetric flow rate $\dot{Q}$ and nozzle geometric cross-sectional area $A$ according to:

$$u_{eff} = \frac{\dot{Q}}{A} \tag{3.61}$$

No provisions for cavitation effects have been made available in the nozzle flow model. However, in the present work the effects of cavitation have been studied by reducing the nozzle diameter.

### 3.4.2 Droplet-gas interaction

The liquid jet emerging from the nozzle atomises to the initial droplet field. Thereafter these droplets can break up further to form secondary droplets. While prop-

agating through the chamber, droplet-gas interaction takes place via inter-droplet and interphase exchange of mass, momentum and energy.

#### 3.4.2.1 Atomisation

In the present study the phenomenological atomisation model of Huh and Gosman [192] is applied. Based on an order of magnitude analysis spray atomisation was found to be primarily influenced by the gas inertia forces and the internal turbulent fluid stresses imposed due to nozzle flow. Two stages are identified which lead to atomisation:

(a) The flow through the nozzle hole induces turbulence which generates initial perturbations on the jet surface after injection.

(b) Due to the aerodynamic forces the perturbations increase until a certain level is reached which results in exponential growth. This eventually leads to the formation of small droplets owing to liquid detachment. This process is known as surface wave growth.

From a one-dimensional analysis of the nozzle flow the model derives the initial strength of perturbations. It then applies wave growth theory with other assumptions to estimate the initial droplet size-distribution, initial droplet velocities and spray angle.

#### 3.4.2.2 Droplet trajectory and momentum exchange

The droplet trajectory in terms of the droplet position vector $\mathbf{x}_d$ in global Cartesian coordinates and velocity $\mathbf{u}_d$ is given by [246]:

$$\frac{d\mathbf{x}_d}{dt} = \mathbf{u}_d \tag{3.62}$$

To obtain the droplet velocity, the momentum conservation equation is solved, neglecting gravitational, virtual mass, Basset, Magnus and Saffman forces based on

the findings of [6, 107, 246]. This equation is:

$$\frac{d\mathbf{u}_d}{dt} = \frac{\hat{\mathbf{u}} - \mathbf{u}_d}{\tau_\mathbf{u}} \tag{3.63}$$

Here, $\hat{\mathbf{u}}$ is the instantaneous gas velocity vector and $\tau_\mathbf{u}$ represents the momentum relaxation time that indicates the degree of interaction between gas and liquid phase. $\tau_\mathbf{u}$ is defined by:

$$\tau_\mathbf{u} = \frac{2\, m_d}{\rho\, C_d A_d |\hat{\mathbf{u}} - \mathbf{u}_d|} \tag{3.64}$$

In the above equation $m_d$ is the droplet mass and $A_d$ stands for the cross-sectional area of the droplet, perpendicular to the vector of the relative velocity $|\hat{\mathbf{u}} - \mathbf{u}_d|$. $C_d$ is the droplet drag coefficient that is given by the following empirical expressions, taken from [410, 479]:

$$C_d = \begin{cases} \frac{24}{\mathrm{Re}_d}\left(1 + \alpha\, \mathrm{Re}_d^{\beta}\right) & , \ \mathrm{Re}_d \leq 1000 \\ 0.44 & , \ \mathrm{Re}_d > 1000 \end{cases} \tag{3.65}$$

where the coefficients $\alpha$ and $\beta$ are listed in Table 3.8. The droplet Reynolds number $\mathrm{Re}_d$ is given by:

$$\mathrm{Re}_d = \frac{\rho_m\, |\hat{\mathbf{u}} - \mathbf{u}_d|\, D_d}{\mu_f} \tag{3.66}$$

The dynamic viscosity of the gas $\mu_f$ is evaluated at the *film* temperature $T_f$ and fuel vapour mass fraction $Y_f$. These are defined as:

$$T_f = T_{d,s} + \frac{1}{3}\,(T - T_{d,s}) \tag{3.67a}$$

$$Y_f = Y_{v,s} + \frac{1}{3}\,(Y_v - Y_{v,s}) \tag{3.67b}$$

where $Y_v$ indicates the fuel vapour mass fraction in the ambient gas and the index $s$ denotes properties at the droplet surface.

| Correlation | $\alpha$ | $\beta$ |
|---|---|---|
| Standard [410] | 0.15 | 0.687 |
| Yuen and Chen [479] | 1/6 | 2/3 |

**Table 3.8:** Coefficients for drag correlations.

The interaction of droplets with turbulent eddies is accounted for using the approach of Gosman and Ioannides [142] that applies the stochastic random walk technique.

The droplet momentum contributions to the gas phase are represented as a source term in the momentum equation, Eq. (3.4). It is assumed that the momentum loss from the droplet is entirely absorbed by the gas. The source term is then [246]:

$$S_{\mathbf{u}}^{d}(\mathbf{x}) = -\lim_{\substack{\Delta t\to 0\\ \delta V\to 0}} \frac{1}{\Delta t\,\delta V}\int_{\delta V}\left[\sum_{p=1}^{N_p}\int_{t}^{t+\Delta t}\delta\left(\mathbf{x}-\mathbf{x}_p\right)\frac{d}{dt}\left(m_p\mathbf{u}_p\right)dt\right]dV \tag{3.68}$$

Here $m_p = N_d m_d$ is the mass of a computational parcel that contains $N_d$ droplets of mass $m_d$ and $\delta$ is the Dirac function.

### 3.4.2.3 Droplet energy and mass balance and contribution to gas phase

#### Droplet energy conservation

If the droplet temperature is assumed to be uniform† an overall energy balance gives [46]:

$$m_d\, c_{p,d}\,\frac{dT_d}{dt} = \dot{Q}_{gas} + \dot{Q}_{evap} \tag{3.69}$$

where index $d$ expresses droplet properties. Here, the LHS expresses the net change of internal energy for both the liquid droplet and vapour formed. The terms of the RHS represent the convection heat transfer rate between gas and droplet, and heat extraction due to evaporation, respectively. They are evaluated as:

$$\dot{Q}_{gas} = 4\pi R_d^2\, h\,(T - T_{d,s}) \tag{3.70a}$$

$$\dot{Q}_{evap} = \frac{dm_d}{dt} L(T_{d,s}) \tag{3.70b}$$

†In Diesel engine sprays the assumption of a uniform droplet temperature leads to inaccuracies [77]. However, the analytical solution is prohibitive in terms of computational overheads. A computationally more efficient, semi-analytical method that considers the temperature profile in a droplet has been derived by Clerides [77]. However, due to considerations of computational effort, and based on the findings of Hohmann [183] that the simplifying assumption of a uniform droplet temperature does not result in appreciable differences from real sprays, the latter practice was adopted in this study.

where $R_d$ refers to the instantaneous droplet radius, $d(m_d)/dt = \dot{m}_d$ is the evaporation rate and $L(T_{d,s})$ denotes the latent heat of vapourisation, evaluated at the droplet surface temperature $T_{d,s}$. The heat transfer coefficient $h$ is obtained from:

$$h = \frac{\mathrm{Nu}\, k_f}{D_d} \tag{3.71}$$

Here, $k_f$ refers to the gas thermal conductivity evaluated at the arithmetic film mean temperature $T_f$, i.e.:

$$T_f = \frac{T + T_{d,s}}{2} \tag{3.72}$$

A number of Nu correlations have emerged in the past, derived from different experimental data sets (see e.g. Clerides [77]). Here the correlation of Ranz and Marshall [354, 355] is employed, modified by a factor $\mathcal{F}$ proposed by El Wakil *et al.* [103] to account for the effect of a reduced heat transfer coefficient due to mass transfer, known as Stefan flow or blowing effect:

$$\mathrm{Nu} = (2 + 0.6\, \mathrm{Re}^{\frac{1}{2}}\, \sigma_e^{\frac{1}{3}})\, \mathcal{F} \tag{3.73}$$

Here the droplet Prandtl number $\sigma_e$ is defined by:

$$\sigma_e = \frac{\mu_f\, c_{p,f}}{k_f} \tag{3.74}$$

The mixture properties in the above two equations are evaluated at the arithmetic mean film temperature $T_f$. The factor $\mathcal{F}$ is defined as:

$$\mathcal{F} = \frac{z}{e^z - 1} \tag{3.75}$$

in which $z$ is a dimensionless mass transfer rate:

$$z = -\frac{c_{p,v}\, \dot{m}_d}{\pi D_d\, k_f\, \mathrm{Nu}} \tag{3.76}$$

Here $c_{p,v}$ is the specific heat of fuel vapour at constant pressure. To calculate the droplet temperature, Eq. (3.69) is recast to:

$$\frac{dT_d}{dt} = \frac{T - T_d}{\tau_e} \tag{3.77}$$

where $\tau_e$ is a heat transfer relaxation time, given by:

$$\tau_e = \frac{m_d\, c_{p,d}}{4\pi R_d^2\, h + \frac{\dot{m}_d L(T_d)}{T - T_d}} \tag{3.78}$$

This quantity indicates the heat transfer rate between gas and droplet such that for small values the droplet reaches the ambient temperature rapidly.

### Droplet mass conservation

The evaporation rate for a single-component droplet is given as [53]:

$$\frac{dm_d}{dt} = -\pi\, D_d\, \mathcal{D}_f\, \mathrm{Sh}\, \rho_f\, \ln \frac{1 - y_v}{1 - y_{v,s}} \tag{3.79}$$

where $\mathcal{D}_f$ stands for the mass diffusivity evaluated at the film temperature, Sh is the Sherwood number defined below and $y_{v,s}$ and $y_v$ are the fuel vapour molar concentrations at the droplet surface and in the far-field, respectively. The gas density $\rho_f$ is determined from the ideal gas law, evaluated by using the arithmetic mean of gas properties and those at the droplet surface. Commonly for ideal mixtures the vapour concentration at the droplet surface is obtained from *Raoult's Law* as:

$$y_{v,s} = \frac{p_{v,s}}{p}\, x_{d,s} \tag{3.80}$$

where $p$ is the total pressure in the gas mixture and $p_{v,s}$ and $x_{d,s}$ are the partial vapour pressure and fuel liquid molar concentration at the droplet surface, respectively. It is customary to assume that the gas does not diffuse into the droplet, i.e. $x_{d,s} = 1$.

The Sherwood number Sh is a dimensionless mass transfer coefficient. It is evaluated according to Ranz and Marshall [354, 355] as:

$$\mathrm{Sh} = 2 + 0.6\, \mathrm{Re}^{\frac{1}{2}}\, \sigma_{Y_\psi}^{\frac{1}{3}} \tag{3.81}$$

where $\sigma_{Y_\psi}$ is the Schmidt number, given by:

$$\sigma_{Y_\psi} = \frac{\mu_f}{\rho_m\, \mathcal{D}_f} \tag{3.82}$$

By introducing an evaporation relaxation time $\tau_m$, defined as:

$$\tau_m = \frac{m_d}{\pi D_d\, \mathcal{D}_f\, \mathrm{Sh}\, \rho_f\, \ln \frac{1-y_v}{1-y_{v,s}}} \tag{3.83}$$

Eq. (3.79) can be recast to:

$$\frac{dm_d}{dt} = -\frac{m_d}{\tau_m} \tag{3.84}$$

The evaporation relaxation time influences the evaporation rate such that for small values, evaporation is fast.

### Droplet energy and mass contributions to gas phase

The energy transfer between droplets and gas gives rise to an associated source term in Eq. (3.6) to conserve heat [77]:

$$S_e^d(\mathbf{x}) = -\lim_{\substack{\Delta t\to 0\\ \delta V\to 0}} \frac{1}{\Delta t \delta V}\int_{\delta V}\left\{\sum_{p=1}^{N_p}\int_t^{t+\Delta t}\delta\left(\mathbf{x}-\mathbf{x}_p\right)\frac{d}{dt}\left[m_p c_{p,d}\left(T_p - T_{ref}\right)\right]dt\right\}dV \tag{3.85}$$

where $T_{ref} = 298\,K$ indicates the reference temperature.

Similarly the conservation of mass produces a droplet source term in Eq. (3.2) due to mass transfer between droplet and gas [77]:

$$S_m^d(\mathbf{x}) = -\lim_{\substack{\Delta t\to 0\\ \delta V\to 0}} \frac{1}{\Delta t \delta V}\int_{\delta V}\left[\sum_{p=1}^{N_p}\int_t^{t+\Delta t}\delta\left(\mathbf{x}-\mathbf{x}_p\right)\frac{dm_p}{dt}dt\right]dV \tag{3.86}$$

Finally, in the species concentration balance in Eq. (3.8) the contribution due to droplet evaporation to the species $\psi$ is given by [77]:

$$S_{Y_\psi}^d(\mathbf{x}) = -\lim_{\substack{\Delta t\to 0\\ \delta V\to 0}} \frac{1}{\Delta t \delta V}\int_{\delta V}\left[\sum_{p=1}^{N_p}\int_t^{t+\Delta t}\delta\left(\mathbf{x}-\mathbf{x}_p\right)\frac{dm_{p,\psi}}{dt}dt\right]dV \tag{3.87}$$

#### 3.4.2.4 Droplet breakup

The disintegration of droplets, called breakup, occurs when external aerodynamic forces acting on the surface exceed the stabilising forces due to surface tension. Breakup continues until a stable diameter is reached for which surface tension balances the external forces. According to Hinze [173] and Hsiang and Faeth [187] breakup regimes can be classified by two non-dimensional quantities, the Weber number We and the Ohnesorge number Oh, defined by:

$$\mathrm{We} = \frac{\rho_m\left|\hat{\mathbf{u}}-\mathbf{u}_d\right|^2 D_d}{\sigma_d} \tag{3.88}$$

$$\mathrm{Oh} = \frac{\mu_d}{\sqrt{\rho_d D_d \sigma_d}} \tag{3.89}$$

Here $\sigma_d$ is the surface tension coefficient, We expresses the ratio of inertial to surface tension forces and Oh represents the ratio of viscous to surface tension forces. Two different breakup models have been used in the current study, as follows.

### Reitz-Diwakar model

This model reported by Reitz and Diwakar [359, 363, 364] and based on the work of Nicholls [317] recognises two breakup regimes. They are distinguished by expressions, involving the Weber and droplet Reynolds number. The following criteria are applied:

1. *Bag breakup*, i.e. the non-uniform pressure profile surrounding the droplets produces a bag in the low-pressure wake region which then disintegrates. This occurs when:

$$\mathrm{We} > C_{bag} \tag{3.90a}$$

2. *Stripping breakup*, i.e. liquid is sheared from the droplet surface, when:

$$\frac{\mathrm{We}}{\sqrt{\mathrm{Re}_d}} > C_{strip} \tag{3.90b}$$

The recommended values of $C_{bag}$ and $C_{strip}$ are listed in Table 3.9.

Breakup is initiated if either criterion is reached. The stable droplet diameter is calculated from:

$$D_{st} = \begin{cases} C_{bag}\, \frac{\sigma_d}{\rho_m |\hat{\mathbf{u}}-\mathbf{u}_d|^2} & , \text{ for bag breakup} \\ C_{strip}^2\, \frac{\sigma_d^2}{\rho_m |\hat{\mathbf{u}}-\mathbf{u}_d|^3 \mu_m} & , \text{ for stripping breakup} \end{cases} \tag{3.91}$$

The rate of change of the droplet diameter is expressed as:

$$\frac{dD_d}{dt} = -\frac{D_d - D_{st}}{\tau_b} \tag{3.92}$$

where $\tau_b$ denotes the characteristic breakup time given as:

$$\tau_b = \begin{cases} C_b D_d \sqrt{\frac{\rho_d D_d}{\sigma_d}} & , \text{ for bag breakup} \\ \frac{C_s D_d}{|\hat{\mathbf{u}}-\mathbf{u}_d|} \sqrt{\rho_d \rho_m} & , \text{ for stripping breakup} \end{cases} \tag{3.93}$$

with the coefficients $C_b$ and $C_s$ provided in Table 3.9.

| $C_{bag}$ | $C_{strip}$ | $C_b$ | $C_s$ |
|---|---|---|---|
| 6 | 0.5 | $\pi/4$ | 10 |

**Table 3.9:** Coefficients for Reitz-Diwakar breakup model.

Uncertainties exist regarding the model coefficients, as listed in Table 3.10. In this study values of the model developers, i.e. Reitz-Diwakar [364], were chosen.

After breakup, the droplet velocity is updated to conserve the total energy of the droplet and a droplet momentum loss is added to the gas momentum.

| Researcher | $C_{bag}$ | $C_{strip}$ | $C_s$ |
|---|---|---|---|
| Clerides [77] | 6.0 | 1.0 | 10 |
| Nicholls [317] | – | – | 4 |
| O'Rourke-Amsden [323] | – | – | $\sqrt{3}/2$ |
| Reitz-Diwakar [363] | 3.6 – 8.4 | 0.5 | 1 – 10 |
| Reitz-Diwakar [364] | 6.0 | 0.5 | 10 |

**Table 3.10:** Coefficients proposed by various researchers for Reitz-Diwakar breakup model.

### Hsiang-Faeth model

Hsiang and Faeth [187] recognised only one breakup type for which the stable diameter and characteristic breakup time are given by:

$$D_{st} = 6.2 D_d \left(\frac{\rho_d}{\rho_m}\right)^{1/4} \sqrt{\frac{\mu_d}{\rho_d D_d |\hat{\mathbf{u}} - \mathbf{u}_d|}} \tag{3.94}$$

$$\tau_b = \frac{35}{7 - \mathrm{Oh}} \frac{D_d}{|\hat{\mathbf{u}} - \mathbf{u}_d|} \sqrt{\frac{\rho_d}{\rho_m}} \tag{3.95}$$

The rate of change of the droplet diameter is then calculated from Eq. (3.92).

## 3.4.3 Droplet-droplet interaction

Droplet collision may result in the exchange of mass, momentum and energy between the droplets and can also lead to coalescence. The model of O'Rourke [322] has been used in this study which distinguishes three types of collision results:

1. Separation: Droplets collide and produce smaller droplets.
2. Permanent coalescence: Droplets collide and form a single droplet.
3. Bouncing: Droplets collide and merely exchange momentum.

### 3.4.4 Droplet-wall interaction

The mode at which a droplet jet impinges on the wall is commonly characterised by the incident liquid Weber number and the wall temperature. In this study the model proposed by Chaves and Obermeier [64] that accounts for multiple droplet impacts is applied, which categorises the following impingement modes:

1. *Splashing*: The impinging droplet breaks up into smaller droplets that are reflected from the wall.
2. *Fragmentation*: The impinging droplet is fragmented into smaller droplets that stick to the wall.
3. *Wall sticking*: The impinging droplet remains intact and sticks to the wall.

Effects of wall roughness and curvature on impingement mode are neglected. Also, liquid film formation and heat transfer between the droplet and wall are not taken into account.

### 3.4.5 Study of liquid thermophysical properties

In the liquid phase governing equations and the equations of the spray submodels the following liquid thermophysical properties appear: density, viscosity, thermal conductivity, heat capacity, surface tension and enthalpy of vapourisation. Additionally the thermodynamic conditions at the gas/liquid interface are required to evaluate the evaporation rate. Here, several correlations for the above properties and the treatment to derive the thermodynamic conditions at the interface are examined for their applicability at the elevated pressure conditions of the HPP concept.

In the current study a simple case was chosen to examine the behaviour of liquid properties at the elevated pressures of the HPP engine. Since droplets evaporate very fast under those conditions, a constant pressure was specified while varying the liquid temperature. The pressure was chosen to be the same as for the case discussed in Section 3.2.6.3, i.e. 140.7 bar. Dodecane was chosen as liquid. The correlations examined have extensively been validated against experimental data and were selected based on recommendations of Reid *et al.* [358]. They are summarised in Section C.2 in the Appendix. Due to uncertainties and singularities close to the critical temperature, the graphs only cover the temperature range from 340 K to 620 K.

This section first discusses the results of the correlations for various liquid properties under the relevant conditions. Based on these results, at the end of this section the choice of correlations for the present work is given.

### 3.4.5.1 Liquid density

To estimate liquid densities the technique of Hankinson-Brobst-Thomson (HBT) [153] was chosen that was later extended to the high pressure regime by Thomson *et al.* [428]. In addition, a simple thermodynamic correlation [410] was evaluated.

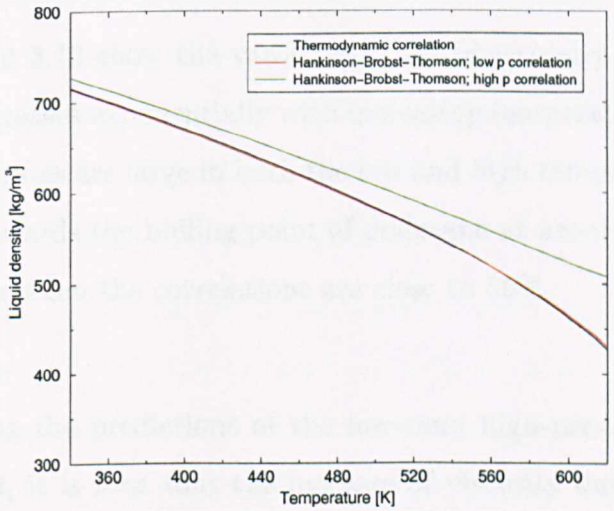



**Figure 3.10:** Liquid density versus temperature for dodecane.

Figure 3.10 shows the variation of liquid densities as predicted by the correlations. The density initially decreases linearly with temperature and declines faster from around 520 K. At the critical point, the liquid and gas densities become equal in magnitude. When comparing the low-pressure correlations, it is apparent that the thermodynamic correlation matches closely the predictions using the HBT method over the temperature range shown. When correcting the HBT correlation for pressure effects, higher liquid densities arise. The difference between low-pressure and high-pressure correlation increases with higher temperature from 1.7% at 350 K to around 18% at 620 K.

#### 3.4.5.2 Liquid viscosity

Liquid viscosities were estimated using the correlations of Andrade [10, 11] and Letsou-Stiel [269] (ALS) which is a combination of two approaches valid for different temperature ranges. Additionally, the approaches of Chung *et al.* [74] for simple hydrocarbons and a variation thereof, proposed by Brulé and Starling [59] for complex hydrocarbons, were used. The latter two correlations are for dense gases, which are applicable to liquids at moderate temperatures [358]. A high-pressure correction to the ALS technique was applied using the method of Lucas [275]. Furthermore predictions of a simple thermodynamic correlation [410] are enclosed.

Figures 3.11 and 3.12 show the variation of liquid viscosity with temperature. Liquid viscosity decreases exponentially with increasing temperature. The difference between the correlations are large in both the low and high temperature ranges with closer agreement towards the boiling point of dodecane at around 490 K. At 620 K the discrepancies between the correlations are close to 50%.

When comparing the predictions of the low- and high-pressure correlations of ALS in Figure 3.12, it is seen that the increase of viscosity due to high pressures is well reproduced. Larger differences of viscosity in terms of absolute values are

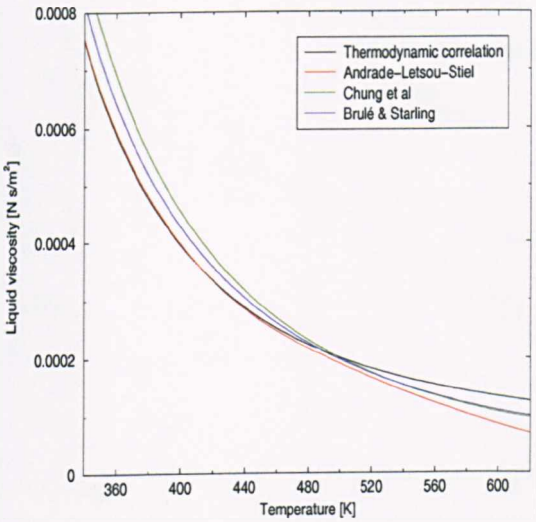



**Figure 3.11:** Liquid viscosity versus temperature for dodecane by correlations without pressure correction.

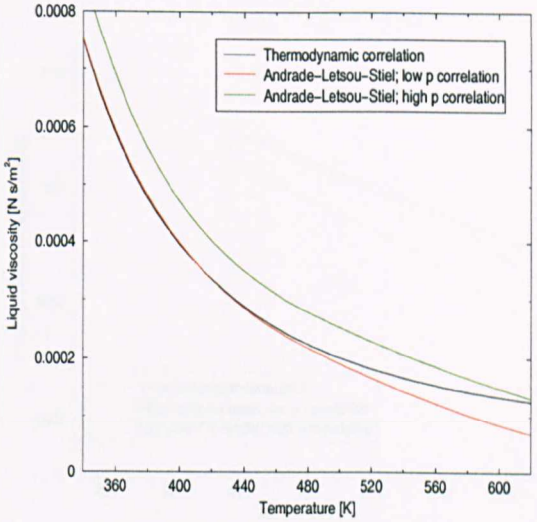



**Figure 3.12:** Liquid viscosity versus temperature for dodecane by correlations with pressure correction.

found at low temperatures. However, at high temperatures the high-pressure correlation predicts viscosities larger by a factor of two than its low-pressure variant. The thermodynamic correlation follows closely the low-pressure variant of ALS at low temperatures while converging towards the high-pressure variant at high temperatures.

#### 3.4.5.3 Liquid thermal conductivity

For the study of liquid thermal conductivities, the correlations of Latini [29, 30], Sato and Riedel [375, 376, 377, 378] and Missenard and Riedel [297, 296] were chosen. The latter two have proposed separate techniques to account for pressure effects [254, 295]. Additionally, a simple thermodynamic correlation [410] was applied.

In Figures 3.13 and 3.14 the trends for liquid thermal conductivity are shown using various correlations. When increasing the liquid temperature, the conductivity decreases almost linearly with a slightly larger slope at high temperatures. The low-pressure correlations of Latini *et al.* and Missenard and Riedel achieve close agreement over the temperature range considered. The prediction of Sato and

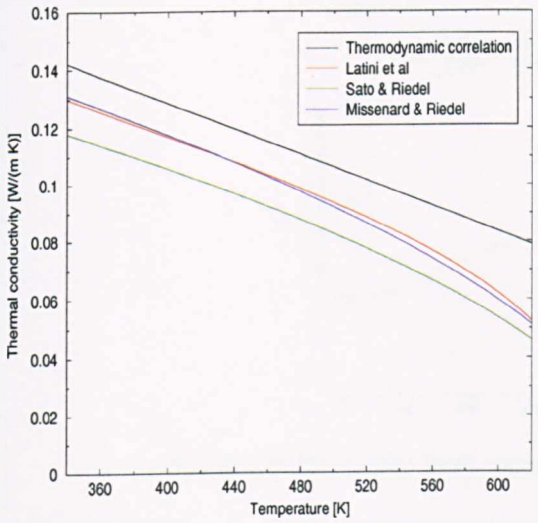



**Figure 3.13:** Liquid conductivity versus temperature for dodecane without pressure correction.

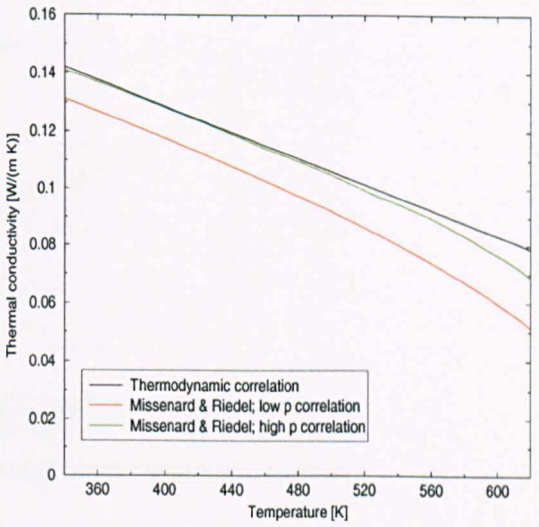



**Figure 3.14:** Liquid conductivity versus temperature for dodecane with pressure correction.

Riedel results overall in lower conductivities of the order of 11% for the entire temperature interval compared to the Latini *et al.* correlation. The thermodynamic correlation gives around 15% larger conductivities compared to Latini *et al.* and does not reflect the slope increase towards higher temperatures.

If the high-pressure correction is applied to the Missenard and Riedel technique, overall around 14% higher thermal conductivities result compared to its low-pressure variant, as seen in Figure 3.14. At 620 K the difference amounts to about 34%. When comparing the thermodynamic correlation with the high-pressure correlation of Missenard and Riedel, close agreement is found up to 480 K with increasing discrepancies towards high temperatures. At 620 K 15% higher conductivities are predicted using the simple thermodynamic correlation.

#### 3.4.5.4 Liquid heat capacity

To estimate liquid heat capacities, the method of Rowlinson and Bondi [52, 380] has frequently been used. No particular pressure correction technique was found in the literature. Furthermore a simple thermodynamic correlation [410] was evaluated.

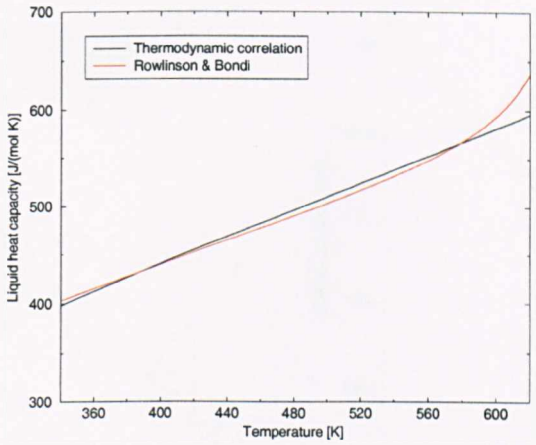



**Figure 3.15:** Liquid heat capacity versus temperature for dodecane.

Figure 3.15 depicts the change in liquid heat capacity with temperature. An almost linear increase is predicted by the Rowlinson and Bondi method with rising temperature. However, the slope becomes steeper towards the critical point, where the liquid heat capacity becomes singular [133]. When applying a thermodynamic correlation for the prediction of the heat capacity, close agreement is found with respect to the correlation. Larger discrepancies occur towards the critical point with lower values for the former of around 6% at 620 K.

#### 3.4.5.5 Surface tension

The surface tension of liquid dodecane has been calculated using the correlations of Macleod and Sugden [278] and Brock and Bird [58]. In addition, a simple thermodynamic correlation [410] has been evaluated.

Figures 3.16 and 3.17 display a close to linear decrease of surface tension with temperature. Towards the critical point it vanishes. The correlations of Macleod and Sugden and Brock and Bird show similar magnitudes at low pressures. At higher temperatures the latter predicts smaller values of the order of 44% at 620 K. The simple thermodynamic correlation agrees well with the above correlations at low temperatures. However, at higher temperatures, the values follow more closely the trend of Brock and Bird, resulting in an about 25% lower surface tension at 620 K.

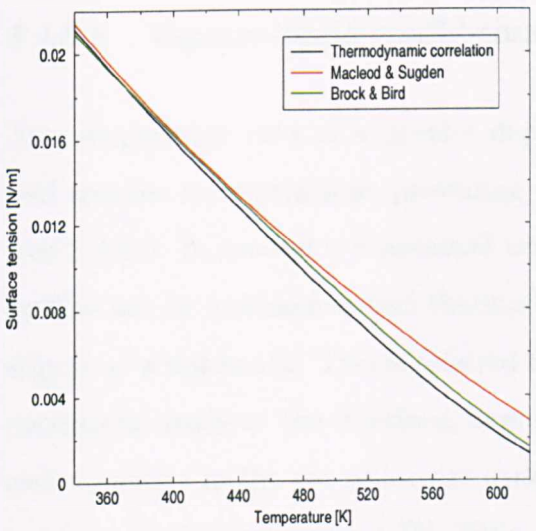



**Figure 3.16:** Predicted surface tension versus temperature for dodecane with low-pressure correlation.

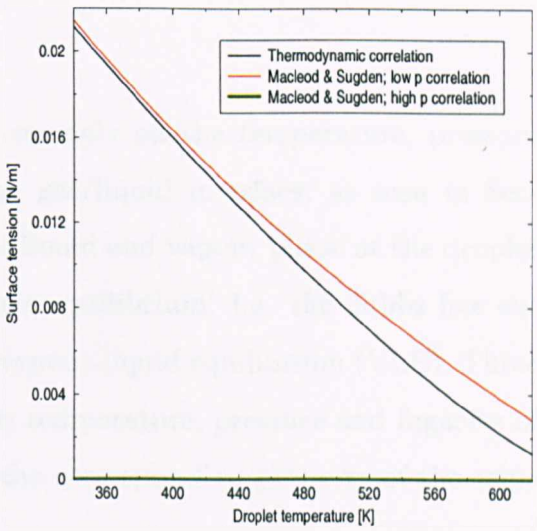



**Figure 3.17:** Predicted surface tension versus temperature for dodecane with high-pressure correlation.

When the PR EOS is used to evaluate the vapour density in the Macleod and Sugden correlation, the predictions show very small values of surface tension over the entire temperature range as seen in Figure 3.17. The low-pressure correlation of Macleod and Sugden and the simple thermodynamic correlation yield significantly larger surface tensions. The surface tension is reduced owing to the fact that the densities of liquid and vapour are of the same order of magnitude at high pressures, therefore reducing the unbalance in the inter-molecular forces acting in the surface layer of the liquid. The result of the high-pressure correlation indicates that droplet breakup, characterised by the Weber and Ohnesorge numbers (see Section 3.4.2.4), is immediate after injection, which is unrealistic. The stable diameter after breakup is very small which would cause very fast evaporation in a high temperature environment, leading to very short droplet lifetimes. This would produce a very short liquid penetration length, which runs counter to experimental observations: a liquid spray is seen of 20 – 30 mm length [162]. Therefore the trend predicted by the high-pressure correlation has to be considered with care. The experimental evidence [162] suggests that the effect of surface tension on breakup in the high pressure environment is overestimated by the high-pressure correlations.

#### 3.4.5.6 Vapour-liquid equilibrium

The evaporation rate of a droplet depends strongly on the temperature, pressure and species concentrations prevailing at the gas/liquid interface, as seen in Section 3.4.2.3. In general it is assumed that the liquid and vapour phase at the droplet surface are in mechanical and thermodynamic equilibrium: i.e. the Gibbs free energy is at a minimum. This is referred to as vapour-liquid equilibrium (VLE). Three conditions apply at the interface, namely the temperature, pressure and fugacity of each species $i$ in the gas phase are equal to the corresponding property of the same species $i$ in the liquid phase [90, 358]:

$$T_s^V = T_s^L \tag{3.96a}$$

$$p_s^V = p_s^L \tag{3.96b}$$

$$f_{s,i}^V = f_{s,i}^L \tag{3.96c}$$

where subscript $s$ denotes surface properties and the superscripts $V$ and $L$ refer to the vapour and liquid phases, respectively. The fugacity $f$ expresses the tendency of a component to diffuse from the phase it currently resides in. It depends on temperature, pressure and composition. To obtain the thermodynamic state at the gas/liquid interface, the fugacity values in Eq. (3.96c) have to be determined. For low pressures and ideal gases, and assuming non-solubility of gas into the liquid phase, a simple solution exists, commonly known as Raoult's Law (see Eq. (3.80)). However, at high pressures, these assumptions become increasingly invalid, such that the solution procedure is more complex.

Reviews of such solution techniques are provided in [72, 73, 306, 358, 386]. Generally two methods are available according to Mühlbauer and Raal [306]: the *combined method* or activity coefficient method and the *direct method* or EOS method. Both methods make use of auxiliary functions to account for the non-idealities of each phase. While the first method uses the activity and fugacity coefficients, the second approach considers the fugacity coefficient only. The activity coefficient is related to

the Gibbs free energy and the fugacity coefficient is defined via a relation involving an EOS.

The VLE has been extensively studied for single droplet evaporation at high ambient pressures (see e.g. [144, 206, 207, 284, 487]). These studies mostly employed the direct method due to its relative simplicity compared to the combined method [306].

A simple, idealised test case, involving the interface of an $n$-heptane liquid and nitrogen gas was chosen to study the VLE[†]. The fuel $n$-heptane has similar properties as Diesel fuel [342] and has extensively been used for Diesel spray and combustion studies [77, 427]. The direct method was used in connection with the cubic EOS presented in Section 3.2.6.1. The main equations used are outlined in Section C.3 in the Appendix. The calculations were performed for a constant pressure of 140.7 bar and the droplet surface temperature was varied. The results are displayed as fuel vapour concentrations at the gas/liquid interface in Figure 3.18, showing the $n$-heptane mole fraction in both the liquid and vapour phase.

In the results for the cubic EOS the branch for the vapour phase extends over the range of mole fractions less than the mole fraction at the critical point of the mixture[††] (i.e. mixture critical mole fraction). By contrast, the branch for the liquid phase extends over a mole fraction range larger than the mixture critical mole fraction. The SRK and PR EOS predict very similar equilibrium compositions over the entire temperature interval displayed. The fuel vapour concentration at the interface is augmented for larger temperatures, indicating a higher vapourisation rate. Also, the nitrogen solubility into the liquid phase is increasing with rising temperatures.

[†]The choice of $n$-heptane instead of dodecane is based on the availability of binary interaction coefficients for all of the EOS (see Section C.3). While they have been tabulated in Knapp *et al.* [238] for $n$-heptane, they have not been reported for dodecane.

[††]The mixture critical point depends on pressure and species concentration and is affected by solubility of ambient gas [358].

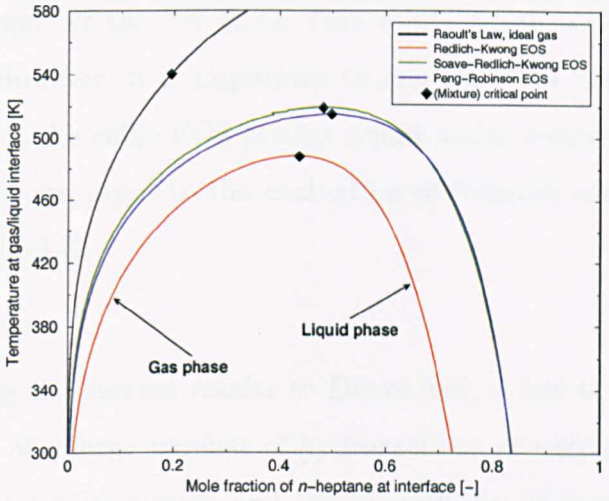



**Figure 3.18:** Vapour-liquid equilibrium calculation using different EOS. Mole fraction of $n$-heptane at interface for varying temperature at gas/liquid interphase.

This can be deduced from the liquid phase fraction of $n$-heptane which is diminishing with increasing temperatures. At the mixture critical point the gas solubility amounts to about 50% according to the cubic EOS. It is apparent that the composition at the interface is strongly sensitive to temperature close to the mixture critical point. Consequently the evaporation rate and thermophysical properties at the gas/liquid interface will be affected significantly. The RK EOS yields higher $n$-heptane vapour fractions and solubility of nitrogen compared to the other EOS implying a higher vapourisation rate. Additionally the mixture critical point is at markedly lower temperatures of the order of 6%.

The results obtained by Raoult's Law assume no solubility of nitrogen in the liquid phase. Moreover the transition to the supercritical regime is not captured well, since changing $n$-heptane vapour concentrations are predicted at temperatures where a mixture of similar nitrogen and $n$-heptane density magnitudes resides. A distinction between liquid and vapour is not possible. Compared to the results of the cubic EOS, similar levels of $n$-heptane vapour are predicted at low temperatures. However, increasingly larger discrepancies are found toward high surface temperatures. In the displayed temperature range the predicted $n$-heptane vapour concentration using Raoult's Law is considerably lower of the order of 60% overall,

compared to the result of the PR EOS. This would entail a significantly reduced evaporation rate. However, it is important to mention that toward critical conditions it is known that the cubic EOS predict liquid molar volumes with errors up to 10% [358]. These are an input to the evaluation of fugacity coefficients and hence affect the estimated VLE.

When comparing the current results to Diesel fuel, it has to be considered that Diesel fuel consists of a large number of hydrocarbons of varying properties. This will affect the critical mixing state and the magnitudes of concentrations in each phase. A substantially higher critical temperature of around 736 K is observed. Additionally with respect to droplet evaporation, due to different volatility differentials among the various Diesel fuel components, sequential vapourisation is reported such that the component with the lowest volatility is depleted first [144, 237, 367].

Finally it is noteworthy that the direct method is computationally expensive and unstable, in particular towards the mixture critical state.

#### 3.4.5.7 Enthalpy of vapourisation

At high pressures the enthalpy of vapourisation not only depends on temperature, but also on pressure. Thus real gas effects become important. As this quantity substantially influences droplet evaporation rates, it is necessary to estimate the extent of non-ideality at the relevant pressure conditions.

As an idealised test case, the $n$-heptane-nitrogen system similar to that of the previous section was used. For a constant pressure of 140.7 bar the gas/liquid interface temperature was varied. To take into account real gas effects, the same cubic EOS were selected as before. In addition, ideal gas predictions using the correlation of Majer and Svoboda [280] and that of a simple thermodynamic correlation [410]

were used. The fundamental equations solved to obtain the latent heat of vapourisation are given in Section C.2.7 in the Appendix.

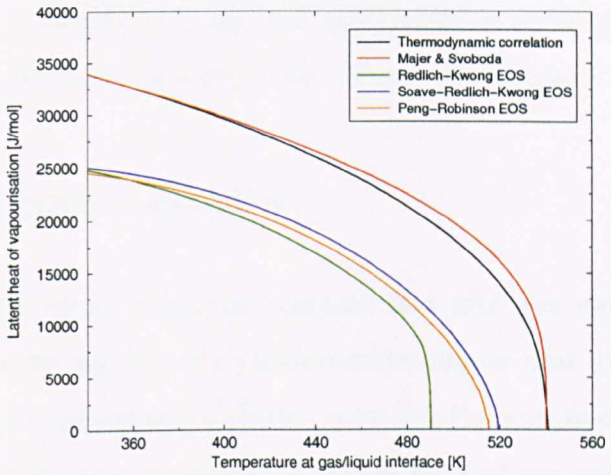



**Figure 3.19:** Latent heat of vapourisation versus temperature of $n$-heptane/nitrogen system at high pressures.

In Figure 3.19 the latent heat of vapourisation is displayed for varying gas/liquid interface temperatures. In general the latent heat decreases with increasing temperatures and vanishes at the mixture critical state. The SRK and PR EOS show similar magnitudes with the latter predicting around 2.5% lower latent heats. The results obtained with the RK EOS initially predict similar levels of latent heat as the other cubic EOS. However, at higher temperatures lower values are achieved. Subsequently a substantially lower mixture critical temperature is estimated, identical to the one in the VLE study. Over the entire temperature range, the difference between the results obtained with the RK EOS and with the PR EOS is about 5% overall.

The ideal gas predictions using the correlation of Majer and Svoboda result in higher enthalpies of vapourisation over the entire temperature range compared to the predictions of the cubic EOS. For instance at 350 K a 38% larger value is calculated. The simple thermodynamic correlation agrees well with the correlation of Majer and Svoboda with slightly larger differences at higher temperatures. The difference between predictions of the thermodynamic correlation and the PR EOS

amounts to about 39% over the temperature range shown.

As with the VLE calculation, the real gas variant is computationally expensive and not always stable, particular near the critical mixing state.

#### 3.4.5.8 Single droplet evaporation

An evaporation study of an $n$-heptane droplet in a nitrogen environment has been performed to assess the validity of a vapourisation model that employs the ideal gas assumption and uses low-pressure correlations for thermophysical properties. As reference a separate model is applied that assumes a real gas and uses high-pressure correlations for thermophysical properties. Typical temperature and pressure levels for the HPP engine are chosen which represent the conditions at SOI. Other input values relate to the HPP prototype engine presented in Section 5.3 and are summarised in Table 3.11. The initial droplet diameter was set to the nozzle hole diameter and the initial droplet temperature was defined as 350 K. In addition:

1. The gas temperature was kept constant.
2. The droplet internal temperature was taken as uniform.
3. Stefan flow was neglected.

The quantities varied included the ambient $n$-heptane mole fraction, the ambient temperature and the relative velocity between the droplet and gas. The mole fraction of $n$-heptane in the gas phase, $y_f$, was chosen as 0% and 10% which corresponds

| | |
|---|---|
| Ambient pressure | 140.7 bar |
| Ambient temperature | 960 K (if not otherwise specified) |
| Ambient $n$-$C_7H_{16}$ mole fraction | 0%, 10% |
| Droplet temperature | 350 K |
| Droplet diameter | 0.2 mm |
| Relative droplet velocity | 100, 200, 300, 400 m/s |
| Time-step | $1 \times 10^{-5}$ s |

**Table 3.11:** Input parameters for single droplet evaporation study.

| Property | Low-pressure method | | High-pressure method | |
|---|---|---|---|---|
| | Liquid | Gas | Liquid | Gas |
| **Equation of state, density** | Hankinson-Brobst-Thomson | Ideal gas law | Hankinson-Brobst-Thomson, high pressure | Peng-Robinson EOS |
| **Viscosity** | Chung *et al.* | Chung *et al.* | Chung *et al.*, high pressure | Chung *et al.*, high pressure |
| **Thermal conductivity** | | Chung *et al.* | | Chung *et al.*, high pressure |
| **Heat capacity** | Rowlinson-Bondi | JANAF | Rowlinson-Bondi | JANAF with PR EOS correction |
| **Diffusion coefficient** | — | Chapman-Enskog | — | Chapman-Enskog, Takahashi correction |
| **VLE** | — | Raoult's Law | — | Equal fugacities, PR EOS |
| **Latent heat** | Majer-Svoboda | — | Ideal gas, PR EOS correction | — |

**Table 3.12:** Thermophysical property correlations used in the single droplet evaporation study.

to 0% and about 36% in terms of mass fraction.

The droplet diameter history and instantaneous droplet temperature were obtained by solving the droplet enthalpy equation, Eq. (3.69), and mass conservation equation, Eq. (3.79). A time-step of $1 \times 10^{-5}$ s was chosen to give time-step independent results. The correlations for the specified thermophysical properties of the gas and the liquid, also used in the earlier thermodynamic studies, are listed in Table 3.12.

Figures 3.20 and 3.21 show the droplet diameter and droplet temperature history, respectively, for a droplet that has a relative velocity of 100 m/s. As time progresses, the droplet temperature rises, causing thermal expansion due to lower liquid density. In all cases the calculation was ended when the mixture critical point was reached. It is seen that by this stage a quasi-steady evaporation regime is not established, where the heat flux to the droplet is balanced by the endothermic evaporation process such that a constant droplet temperature is achieved, the so-called wet-bulb temperature.

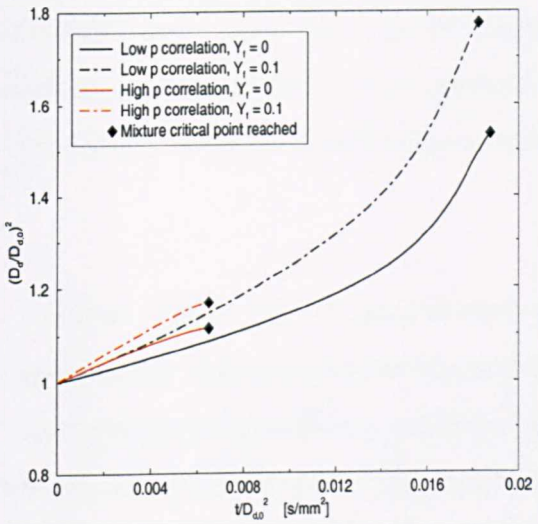



**Figure 3.20:** Droplet diameter history for high-pressure evaporation.

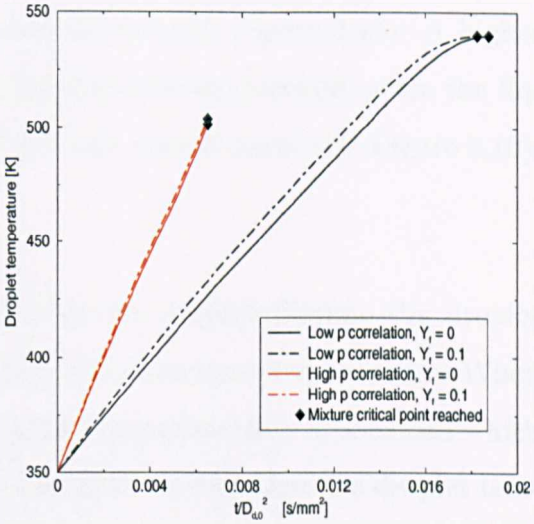



**Figure 3.21:** Droplet temperature history for high-pressure evaporation.

An increase in ambient $n$-$C_7H_{16}$ fraction causes initially condensation onto the cold droplet as seen from Eq. (3.79) and Figure 3.20 such that the droplet diameter increases. This results in slightly faster droplet heating as can be derived from Eq. (3.78) and seen in Figure 3.21. When about two-thirds of the droplet lifetime† has elapsed, condensation ceases and evaporation of the droplet occurs. Due to the more rapid increase in temperature for a higher $n$-heptane fraction in the ambience, the mixture critical point is reached earlier than for a droplet surrounded by pure nitrogen.

When comparing the approach using low-pressure correlations with the equivalent high-pressure model, for the former droplet lifetimes larger by a factor of three are obtained. This is due to the influence of calculated $n$-heptane concentration at the droplet surface which affects evaporation rates in the following way: a lower fuel concentration compared to the high-pressure model results in slower droplet heating (see Eq. (3.78)) and a lower droplet temperature, as seen in Figure 3.21, which subsequently slows the evaporation process. The evaporation rate is addi-

†Here the droplet lifetime is defined as the time between start of calculation and until the point when the droplet has reached the mixture critical point.

tionally retarded owing to lower thermal conductivities (cf. Figure 3.14). A higher maximum droplet diameter is reached with the low-pressure method, since the liquid density is lower in particular towards the mixture critical point (cf. Figure 3.10).

From Figure 3.21 it can be seen that during the droplet lifetime the droplet temperature increases almost linearly up to the critical mixture temperature. When considering real gas effects, a reduced latent heat of vapourisation is obtained which entails less evaporative cooling and faster droplet heating such that the droplet temperatures are higher than when using the low-pressure method.

Figure 3.22 displays the high-pressure model predictions of droplet diameter history when varying the ambient temperature. The same conditions were applied as before, with an ambient fuel vapour fraction of 10%. Similar thermodynamic conditions are encountered by an injected Diesel spray. As the ambient temperature increases, the droplet heating is more rapid resulting in a steeper change in droplet diameter and lower droplet lifetimes. In all of the cases the mixture critical point was reached before complete evaporation.

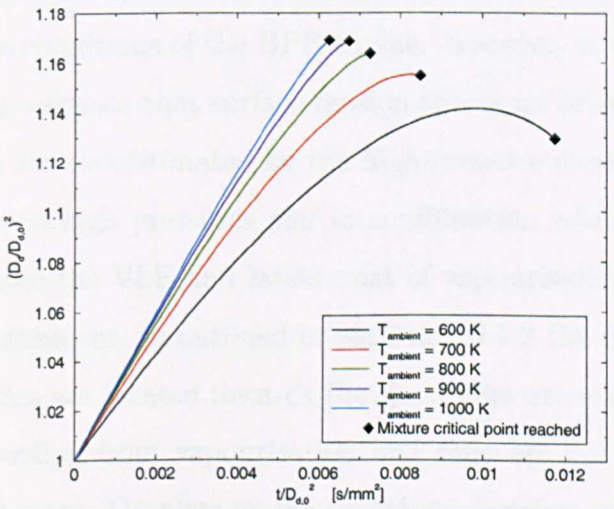



**Figure 3.22:** Droplet diameter history for different ambient temperatures in a high pressure environment using high-pressure correlations.

In Table 3.13 the influence of relative velocity between droplet and gas on droplet lifetime is summarised, when specifying the ambient temperature as 960 K and the fuel vapour fraction as 0.1. The droplet lifetime is reduced considerably when increasing the relative velocity. In addition, the low-pressure approach predicts overall a droplet lifetime that is about three times larger than its high-pressure variant. The droplet lifetime predicted for 400 m/s with the high-pressure method corresponds to slightly less than 1° CA when the engine speed is 1420 RPM.

| Relative velocity [m/s] | Droplet lifetime $t/D_{d,0}^2$ [s/mm$^2$] | |
|---|---|---|
| | Low p method | High p method |
| 100 | 0.01825 | 0.0065 |
| 200 | 0.013 | 0.0045 |
| 300 | 0.0105 | 0.00375 |
| 400 | 0.009 | 0.00325 |

**Table 3.13:** Influence of relative velocity on droplet lifetime.

### 3.4.5.9 Conclusions

The current study reveals that at high temperatures the various properties exhibit an increasingly strong dependence on pressure, such that towards the critical point the largest discrepancies are found between low- and high-pressure correlations. Only the surface tension depends significantly on pressure over the entire range of temperatures at the conditions of the HPP engine. However, it was argued that experimental evidence suggests that surface tension effects on breakup under elevated pressure conditions are overestimated by the high-pressure correlation. In addition real gas effects due to high pressures and in combination with high temperatures substantially influence the VLE and latent heat of vapourisation and consequently evaporation rates. However, as outlined in Section 1.3.1.2 the majority of droplets in Diesel sprays which are located towards the spray core are exposed to lower temperatures due to cooling from vapourisation and thus are not likely to approach the mixture critical state. Droplets at the periphery, however, will experience high ambient temperatures so that the use of low-pressure correlations will yield larger

errors. These droplets are nevertheless subject to high relative velocities which significantly increase droplet heating and breakup, resulting overall in very short droplet lifetimes.

Based on the findings that droplet lifetimes are very short under elevated pressures and temperatures and that the majority of droplets do not reach the mixture critical state where the difference between low-pressure and high-pressure correlations are the largest, it was decided to employ simple thermodynamic correlations for each liquid thermophysical property. They do not incorporate pressure effects and predict closely the trends of the more sophisticated correlations. In this respect it is noteworthy that the latter correlations show large differences among each other. A possible explanation for this is the anomalous behaviour of transport properties close to the critical point which renders the task difficult to find a correlation that accurately predicts both the low and high temperature regions. In addition the VLE calculation is performed assuming an ideal gas which, compared to the high-pressure method, reduces the computational overheads and eliminates the numerical instability of the solution technique in the vicinity of the mixture critical temperature.

It is recognised that high pressure effects on sprays under the conditions of the HPP engine require a more thorough experimental investigation and comprehensive validation studies of modelling approaches that are suitable for Diesel engine simulations. This is beyond the scope of the present work.

## 3.5 Combustion Model

This section briefly introduces the combustion models used in the present study, which are categorised according to the two main reaction phases in Diesel engines.

## 3.5.1 Pre-ignition phase

Two autoignition models were used: the Shell and 4-step models. The former was used for the combustion studies on the HPP prototype engine (see Section 5.3), whereas the latter was applied for the Aachen pressure chamber (see Section 5.2).

### 3.5.1.1 Shell ignition model

The Shell ignition model uses a chain-propagation cycle to predict autoignition of hydrocarbon fuels at high pressures and temperatures. In this, generic molecular species are introduced which represent components of similar role in the ignition chemistry. Despite their different molecular structure, they are treated as a single entity. The reaction mechanisms are specified as follows:

$$RH + O_2 \xrightarrow{k_q} 2R^* \tag{3.97a}$$

$$R^* \xrightarrow{k_p} R^* + P \tag{3.97b}$$

$$R^* \xrightarrow{f_1 k_p} R^* + B \tag{3.97c}$$

$$R^* \xrightarrow{f_4 k_p} R^* + Q \tag{3.97d}$$

$$R^* + Q \xrightarrow{f_2 k_p} R^* + B \tag{3.97e}$$

$$B \xrightarrow{k_b} 2R^* \tag{3.97f}$$

$$R^* \xrightarrow{f_3 k_p} \text{inert products} \tag{3.97g}$$

$$2R^* \xrightarrow{k_t} \text{inert products} \tag{3.97h}$$

Here, the following generic molecules are participating:

| | |
|---|---|
| $RH$ | hydrocarbon fuel of composition $C_nH_{2m}$ |
| $R^*$ | radical formed from the fuel |
| $Q$ | labile intermediate species |
| $P$ | oxidised products, consisting of $CO$, $CO_2$ and $H_2O$ |

The reaction mechanism incorporates the chain-propagation cycle of the branching agent, Eqs. (3.97b) – (3.97f), with one initiation, Eq. (3.97a), and two termination reactions, Eqs. (3.97g) and (3.97h). The reaction chain is propagated by any

of the radical reactions, which, however, are first order dependent on the concentration of the radical involved. In the chemical mechanism the degenerate branching enables the model to capture the cool flame phenomena and two-stage ignition process [240, 362].

Interpretations of the generic species have been proposed based on a review of low temperature hydrocarbon chemistry [40]. The branching agent $B$ is related at low temperatures to hydroperoxides ($RO_2H$) and at high temperatures to hydrogen peroxides ($H_2O_2$). Furthermore the intermediate species $Q$ is thought to represent aldehydes ($RCHO$) in the low temperature ignition branch and the alkylperoxy radical ($HO_2$) and its isomerisation products in the high temperature ignition branch. The inert products are associated with nitrogen.

The rate coefficients in the above reactions are expressed in Arrhenius form as follows:

$$f1 = A_{f1}[O_2]^{x1}[RH]^{y1}\exp\left(-\frac{E_{f1}}{\mathcal{R}T}\right) \tag{3.98a}$$

$$f2 = A_{f2}\exp\left(-\frac{E_{f2}}{\mathcal{R}T}\right) \tag{3.98b}$$

$$f3 = A_{f3}[O_2]^{x3}[RH]^{y3}\exp\left(-\frac{E_{f3}}{\mathcal{R}T}\right) \tag{3.98c}$$

$$f4 = A_{f4}[O_2]^{x4}[RH]^{y4}\exp\left(-\frac{E_{f4}}{\mathcal{R}T}\right) \tag{3.98d}$$

$$k_i = A_i\exp\left(-\frac{E_i}{\mathcal{R}T}\right) \tag{3.98e}$$

where $k_i$ is applicable to $k_{p1}$, $k_{p2}$, $k_{p3}$, $k_q$ and $k_t$. [ ] corresponds to the molar concentration of the respective species. Additionally:

$$k_p = \left(\frac{1}{k_{p1}[O_2]} + \frac{1}{k_{p2}} + \frac{1}{k_{p3}[RH]}\right)^{-1} \tag{3.98f}$$

The kinetic constants in the rate coefficients have been supplied for various fuels in the original work of Halstead *et al.* [152]. They have subsequently been updated by Theobald *et al.* [425] to make them applicable to Diesel autoignition. Here the values for a 70 RON fuel were taken, as provided in Table 3.14.

| Parameter | Arrhenius factor $A$ | Activation energy $E$ | $x_i$ | $y_i$ |
|---|---|---|---|---|
| $f1$ | $1.6 \times 10^{-6}$ | $-6.3 \times 10^4$ | 1.0 | -0.5 |
| $f2$ | $1.8 \times 10^2$ | $-2.9 \times 10^4$ | – | – |
| $f3$ | 0.75 | $4.2 \times 10^4$ | 0.0 | 0.0 |
| $f4$ | $1.21 \times 10^6$ | $1.26 \times 10^5$ | -1.3 | 1.0 |
| $k_{p1}$ | $10^{12}$ | 0.0 | – | – |
| $k_{p2}$ | $10^{11}$ | $6.3 \times 10^4$ | – | – |
| $k_{p3}$ | $10^{13}$ | $3.56 \times 10^3$ | – | – |
| $k_q$ | $6.96 \times 10^{11}$ | $1.46 \times 10^5$ | – | – |
| $k_b$ | $3.35 \times 10^{18}$ | $1.97 \times 10^5$ | – | – |
| $k_t$ | $2.5 \times 10^{12}$ | 0.0 | – | – |

**Table 3.14:** Kinetic constants of Shell autoignition model (taken from [152, 425]). Pre-exponentials in units of [cm], [mol], [s]; activation energies in [J/mol].

Sensitivity studies indicate that the formation of the intermediate species in Eq. (3.97d) is crucial for the formation of the branching agent which subsequently plays an important role in the hot ignition phenomenon. Thus in Diesel autoignition calculations the pre-exponential factor of the formation rate of $Q$ in Eq. (3.98d), $A_{f4}$, is commonly adjusted to match experimental ignition delays [362, 390]. Moreover, *ad hoc* extensions to the Shell model have been proposed to incorporate effects due to fuel composition via a cetane number dependence of the activation energy of reaction (3.97d), $E_{f4}$, and due to residual gases via the pre-exponential factor of the formation rate of $Q$ in Eq. (3.98d), $A_{f4}$ [362]. These have not been applied to the current study.

The mathematical framework for the above reaction set is represented by the following coupled ordinary differential equations (ODEs):

$$\frac{d\overline{Y}_{R^*}}{dt} = \frac{M_{R^*}}{\overline{\rho}} \left\{ 2\left(k_q[RH][O_2] + k_b[B] - k_t[R^*]^2\right) - f_3 k_p[R^*] \right\} \tag{3.99a}$$

$$\frac{d\overline{Y}_B}{dt} = \frac{M_B}{\overline{\rho}} \left\{ f_1 k_p[R^*] + f_2 k_p[Q][R^*] - k_b[B] \right\} \tag{3.99b}$$

$$\frac{d\overline{Y}_Q}{dt} = \frac{M_Q}{\overline{\rho}} \left\{ f_4 k_p[R^*] + f_2 k_p[Q][R^*] \right\} \tag{3.99c}$$

$$\frac{d\overline{Y}_{O_2}}{dt} = \frac{M_{O_2}}{\overline{\rho}} \left\{ -p k_p[R^*] \right\} \tag{3.99d}$$

$$\overline{Y}_{RH} = \frac{M_{O_2}}{M_{RH}} \frac{\overline{Y}_{O_2} - \overline{Y}_{O_2}\big|_{(t=0)}}{p\,m} + \overline{Y}_{RH}\big|_{(t=0)} \tag{3.99e}$$

Due to the nature of the generic species, the equations for the chemical system are not mass-balanced. Therefore it is customary to define appropriate molecular weights of the generic species $B$, $R$, $Q$ and $P$ such that mass is conserved.

The parameter $p$ in Eqs. (3.99d) and (3.99e) is obtained from the overall reaction:

$$C_{n/m}H_2 + p\,O_2 \rightarrow q\,P \tag{3.100a}$$

where:

$$P = \frac{\frac{n}{m}[\gamma\,CO + (1-\gamma)\,CO_2] + H_2O}{q} \tag{3.100b}$$

$$p = \frac{n(2-\gamma)+m}{2m} \tag{3.100c}$$

$$q = \frac{n}{m} + 1 \tag{3.100d}$$

The parameter $\gamma$ defines the ratio of $CO$ to $CO_2$ in the burned products according to:

$$\frac{[CO]}{[CO_2]} = \frac{\gamma}{1-\gamma} \tag{3.101}$$

where $\gamma = 0.67$. The change in system temperature due to chemical reaction is expressed as:

$$\frac{d\overline{T}}{dt} = \frac{1}{\tilde{c}_v\,n_{tot}}\,k_p\,V\,[R^*]\,\overline{Q} \tag{3.102}$$

where $n_{tot}$ is the total number of moles in the volume $V$ and $\overline{Q}$ is the exothermicity per cycle. In the current study, $Q$ has been chosen such that a heat release of Diesel fuel is obtained with a lower heating value of 42.8 MJ/kg.

#### 3.5.1.2 4-step ignition model

A chemical kinetics model for the prediction of autoignition was developed by Müller and Peters [308, 307], based on the full kinetic reaction mechanism of $n$-heptane ignition by Chevalier *et al.* [68], comprising 1011 elementary reactions and 171 chemical species. Through steady-state and partial equilibrium assumptions, a 4-step *ad hoc*

global kinetics model was obtained for high temperature and pressure $n$-heptane autoignition, with adjusted rate coefficients to match the predictions of the full kinetic mechanism. The 4-step ignition model is applicable to the temperature range between 600 – 1500 K and has been extended to incorporate the effects of fuel ignition quality via a cetane number dependence.

The 4-step global kinetics model for $n$-heptane ignition is based on the following reactions:

$$C_7H_{16} \xrightarrow{1} 3C_2H_4 + CH_3 + H \tag{3.103a}$$

$$3C_2H_4 + CH_3 + H + 11O_2 + \mathcal{M} \xrightarrow{2} 7CO_2 + 8H_2O \tag{3.103b}$$

$$C_7H_{16} + 2O_2 \underset{3_b}{\overset{3_f}{\rightleftharpoons}} OC_7H_{13}O_2H + H_2O \tag{3.103c}$$

$$OC_7H_{13}O_2H + H_2O + 9O_2 \xrightarrow{4} 7CO_2 + 8H_2O \tag{3.103d}$$

The intermediate products can be combined into one species such as $X = 3C_2H_4 + CH_3 + H$ in the Eq. (3.103a) and $Y = OC_7H_{13}O_2H + H_2O$ in Eq. (3.103c). Similarly the products in Eqs. (3.103b) and (3.103d) are summarised by $P = 7CO_2 + 8H_2O$. The third body $\mathcal{M}$ is defined as:

$$\mathcal{M} = 3.5\frac{\rho}{M_{mix}} \tag{3.104}$$

where $M_{mix}$ refers to the mean molecular weight of the mixture, expressed as:

$$M_{mix} = \sum_{i=1}^{N_{spec}} y_i M_i \tag{3.105}$$

In the reaction set the first two reactions specify a two-step mechanism for endothermic fuel decomposition into smaller hydrocarbons at high temperatures and the subsequent oxidation into final combustion products. The last two steps model the degenerate chain-branching mechanism at low temperatures that is essential for two-stage ignition. The transition from low temperature to high temperature ignition is achieved by the nature of reaction Eq. (3.103c), where at low temperatures the forward reaction dominates and at temperatures greater than 830 K the backward reaction becomes predominant.

The respective reaction rates are defined as Arrhenius expressions:

$$\dot{\omega}_1 = A_1[C_7H_{16}] \exp\left(\frac{-E_1}{\mathcal{R}T}\right) \tag{3.106a}$$

$$\dot{\omega}_2 = A_2[O_2][X] \exp\left(\frac{-E_2}{\mathcal{R}T}\right) \mathcal{M} \tag{3.106b}$$

$$\dot{\omega}_{3_f} = A_{3_f}[C_7H_{16}][O_2]\ p^{1.75} \exp\left(\frac{-E_{3_f}}{\mathcal{R}T}\right) \tag{3.106c}$$

$$\dot{\omega}_{3_b} = A_{3_b}[Y]\ p^{1.75} \exp\left(\frac{-E_{3_b}}{\mathcal{R}T}\right) \tag{3.106d}$$

$$\dot{\omega}_4 = A_4[O_2][Y] \exp\left(\frac{-E_4}{\mathcal{R}T}\right) \tag{3.106e}$$

where $p$ is in bar and the reaction parameters are provided in Table 3.15.

| Reaction | $A$ | $E$ [J/mol] | $\Delta H_r^\circ$ [kJ/mol] |
|---|---|---|---|
| 1 | 9.0E+08 $s^{-1}$ | 150.0 | 710.5 |
| 2 | 2.0E+15 $cm^3mol^{-1}s^{-1}$ | 60.0 | -5213.0 |
| $3_f$ | 1.0E+20 $cm^3mol^{-1}s^{-1}$ | 160.0 | -54.0 |
| $3_b$ | 5.0E+25 $s^{-1}$ | 310.0 | 54.0 |
| 4 | 1.0E+13 $cm^3mol^{-1}s^{-1}$ | 110.0 | -4447.2 |

**Table 3.15:** Reaction parameters for 4-step ignition model (taken from [308]).

The influence of fuel type was embedded in the reaction rate of the fourth step via a cetane number ($CN$) dependence as follows:

$$\dot{\omega}_{4,CN} = \dot{\omega}_4 \left(\frac{CN}{60}\right)^2 \tag{3.107}$$

In this study the cetane number of $n$-heptane is assumed to be 60.

The mathematical framework for the chemical reactions in Eqs. (3.103a) – (3.103d) consists of the following set of coupled ODEs for the species concentrations and system temperature:

$$\frac{d\overline{Y}_i}{dt} = \frac{M_i}{\overline{\rho}} \sum_{k=1}^{N_{reac}} \dot{\omega}_k\, \nu_{ik} \tag{3.108}$$

$$\frac{d\overline{T}}{dt} = \frac{M_{mix}}{\overline{\rho}\,\tilde{c}_p} \sum_{k=1}^{N_{reac}} -\Delta H^\circ_{r,k}\, \dot{\omega}_k \tag{3.109}$$

where $\dot{\omega}_k$ refers to the reaction rate for reaction $k$, $\nu_{ik}$ is the stoichiometric coefficient for species $i$ in reaction $k$. The heat of reaction $\Delta H^{\circ}_{r,k}$ of reaction $k$ is listed in Table 3.15.

#### 3.5.1.3 Implementation

The mathematical models of the ignition reactions result in local reaction rates for the ignition species and the local heat release. These are then inserted into the transport equations for species and energy via source terms as outlined below.

The transport equation for each species $i$ is given by:

$$\frac{\partial \overline{\rho}\tilde{Y}_i}{\partial t} + \nabla\cdot(\overline{\rho}\,\tilde{\mathbf{u}}\tilde{Y}_i) = \nabla\cdot\left(\overline{\rho}\,\overline{\Gamma}_{Y_i,eff}\nabla\tilde{Y}_i\right) + \overline{S}^{d}_{Y_i} + \overline{S}_{Y_i} \tag{3.110}$$

where $\overline{S}^{d}_{Y_i}$ refers to the fuel droplet source term, relevant only to the fuel species; and the species source term due to ignition given by:

$$\overline{S}_{Y_i} = \overline{\dot{\omega}}_{Y_i} = \frac{d\overline{Y}_i}{dt} \tag{3.111}$$

The RHS of Eq. (3.111) has been specified in Eqs. (3.99a) – (3.99d) and Eq. (3.108) for each ignition model. Note that in the 4-step ignition model only species $C_7H_{16}$, $X$ and $Y$ are solved for. The heat release due to ignition is provided as source term $\overline{\dot{Q}}_{ign}$ in the energy equation Eq. (3.6) according to:

$$\overline{\dot{Q}}_{ign} = \tilde{c}_v\frac{d\overline{T}}{dt} \tag{3.112}$$

Here, $d\overline{T}/dt$ is obtained from Eqs. (3.102) and (3.109) for each ignition model.

### 3.5.2 Ignition criterion

In the current study a global autoignition criterion is applied, as follows. As soon as the ignition criteria are met in one cell, autoignition is assumed to occur in the entire computational domain. Two alternative criteria are defined:

1. Temperature switch:

$$T_{cell} \geq T_{ign} \tag{3.113a}$$

2. Temperature gradient switch:

$$\left(\frac{dT}{dt}\right)_{cell} \geq \left(\frac{dT}{dt}\right)_{ign} \tag{3.113b}$$

where the subscript *cell* and *ign* denote cell values and values of the ignition criterion, respectively. In general, it is customary to determine the values for the ignition criterion by trial and error in order to reproduce the experimental ignition delay.

Once ignition is detected, transition from pre-ignition to post-ignition phase is modeled by setting the ignition-to-combustion switch $\kappa$ as follows:

$$\kappa = \begin{cases} 1 & \text{before autoignition} \\ 0 & \text{after autoignition} \end{cases} \tag{3.114}$$

### 3.5.3 Post-ignition phase

The two combustion models used in this study are presented below. While the Laminar And Characteristic Timescale (LATCT) combustion model belongs to the EBU-type models, the Representative Interactive Flamelet (RIF) model is based on the flamelet concept.

#### 3.5.3.1 LATCT combustion model

Patterson *et al.* [328] proposed an extension of the Magnussen EBU-type combustion model suitable for Diesel combustion simulation. The premise of the combustion model of Magnussen and Hjertager [279] is that the reaction rate is primarily controlled by the rate of intermixing of either fuel and oxygen or hot and cold gases which depends on the turbulent timescale. Thus the chemical reactions are believed to be very fast. In addition it is assumed that the reactions go to completion. By

contrast, the LATCT model assumes that the chemical reactions reach thermodynamic equilibrium; and this state is achieved within a characteristic time which is the sum of the laminar (i.e. chemical) and turbulent timescale. Seven species (i.e. fuel, $O_2, N_2, CO_2, CO, H_2, H_2O$) are considered sufficient by Patterson *et al.* to predict equilibrium temperatures accurately for Diesel combustion. It is assumed that the characteristic time is the same for each species.

### Description of the LATCT combustion model

A variant of the original LATCT combustion model of Patterson *et al.* [328] is used in the present study which has been successfully implemented and tested by Theodossopoulos [427]. Based on the work of Magnussen *et al.* [279] the local reaction rate of fuel consumption is evaluated as follows:

$$\bar{\dot{\omega}}_{Y_f} = \frac{A_{LT}}{\tau_c} \min\left(\tilde{Y}_f, \frac{\tilde{Y}_{O_2}}{r_f}, \frac{B_{LT}\tilde{Y}_p}{1+r_f}\right) \tag{3.115}$$

Here $A_{LT}$ and $B_{LT}$ are model coefficients, $\tau_c$ is the characteristic time, $\tilde{Y}_i$ refers to the local mean mass fractions of fuel, oxygen and reaction products, distinguished by their respective subscripts $f$, $O_2$ and $p$ and $r_f$ is the stoichiometric amount of oxygen required to burn 1 kg of fuel. The chemical reactions are assumed to go to completion. The characteristic time takes into account the varying timescales in Diesel combustion and is defined by:

$$\tau_c = \tau_l + f\tau_t \tag{3.116}$$

where $\tau_l$ and $\tau_t$ are the laminar and turbulent timescales, respectively. The laminar timescale is dominant near the injector region owing to high injection velocities that induce small turbulent timescales, in the vicinity of shear layers generated by the fuel spray and close to the wall. Additionally laminar chemistry is combustion-rate-controlling in the early phase of combustion, when the flame kernel is small compared to the turbulent eddies. Thereafter turbulent mixing effects become more pronounced. This transition from chemical to turbulent mixing controlled combustion is captured via the delay coefficient $f$.

The laminar (or chemical) timescale, $\tau_l$, is obtained from a single-step global reaction representative for the oxidation of hydrocarbons, expressed as [458]:

$$\text{Fuel} + \nu_1 O_2 \rightarrow \nu_2 CO_2 + \nu_3 H_2O \tag{3.117}$$

where $\nu_i$ are the stoichiometric coefficients, given for each fuel. Since this equation combines the elementary reactions of the combustion chemistry, a representative overall reaction rate is defined by [458]:

$$\bar{\omega}_{tot} = A\,T^n \exp\left(\frac{-E_a}{\mathcal{R}T}\right)[\text{Fuel}]^a[\text{Oxidant}]^b \tag{3.118}$$

The empirical constants $A$, $E_a$, $a$, $b$ and $n$ are obtained by comparison of combustion rates of predictions with experimental data. Note that due to the approximations involved in deriving Eq. (3.118), $a$ and $b$ are generally not equivalent to the stoichiometric coefficients in the global reaction. At present the values based on Westbrook and Dryer [458] involving a quasi-global reaction for $n$-heptane and $n$-dodecane fuel are taken, listed in Table 3.16.

| Fuel | $A$ | $E_a$ | $a$ | $b$ | $n$ |
|---|---|---|---|---|---|
| $n$-heptane | 4.3E+12 | 125.25 | 0.25 | 1.5 | 0.0 |
| $n$-dodecane | 2.8E+12 | 125.25 | 0.25 | 1.5 | 0.0 |

**Table 3.16:** Rate parameters for $n$-heptane and $n$-dodecane single-step quasi-global reaction (from [458]). Units in [cm], [s], [mole], [J] and [K].

For the laminar timescale it follows from Eq. (3.118):

$$\tau_l = A^{-1}[\text{Fuel}]^{0.75}[\text{Oxidant}]^{-1.5}\exp\left(\frac{E_a}{\mathcal{R}T}\right) \tag{3.119}$$

The turbulent timescale $\tau_t$ is proportional to the eddy turnover time:

$$\tau_t = C_2\left(\frac{\tilde{k}}{\tilde{\varepsilon}}\right) \tag{3.120}$$

where $C_2 = 0.142$, as specified in [328]. Moreover the delay coefficient $f$ is given as:

$$f = \frac{1 - e^{-c}}{0.632} \tag{3.121}$$

where $c$ is a progress variable, indicating the local extent of combustion. Its values range between 0 and 1 with the following limiting cases:

1. No combustion:

   $c = 0 \quad \longrightarrow \quad f = 0 \quad \longrightarrow \quad \tau_c = \tau_l$

2. Complete consumption of premixed fuel and oxygen:

   $c = 1 \quad \longrightarrow \quad f = 1 \quad \longrightarrow \quad \tau_c = \tau_l + \tau_t$

### Implementation of LATCT model

In Diesel combustion simulations it is more computationally efficient to characterise the inhomogeneous mixture composition by the fuel vapour mass fraction $Y_f$ and a fictitious total fuel mass fraction $Y_{ft}$, equivalent to the mixture fraction. The latter is not influenced by combustion. The transport equations for $Y_{ft}$ and $Y_f$ are:

$$\frac{\partial \overline{\rho}\widetilde{Y}_{ft}}{\partial t} + \nabla\cdot(\overline{\rho}\widetilde{\mathbf{u}}\widetilde{Y}_{ft}) = \nabla\cdot\left(\overline{\rho}\overline{\Gamma}_{Y_{ft},eff}\nabla\widetilde{Y}_{ft}\right) + \overline{S}^d_{Y_{ft}} \tag{3.122}$$

$$\frac{\partial \overline{\rho}\widetilde{Y}_{f}}{\partial t} + \nabla\cdot(\overline{\rho}\widetilde{\mathbf{u}}\widetilde{Y}_{f}) = \nabla\cdot\left(\overline{\rho}\overline{\Gamma}_{Y_{f},eff}\nabla\widetilde{Y}_{f}\right) + \overline{S}^d_{Y_{f}} + \overline{S}_{Y_f} \tag{3.123}$$

where $\overline{S}^d_{Y_{ft}}$, $\overline{S}^d_{Y_f}$ are the local sources of fuel vapour due to droplet evaporation and $\overline{S}_{Y_f}$ is the rate of consumption of fuel, obtained through:

$$\overline{S}_{Y_f} = -\kappa\,\overline{\dot{\omega}}_{Y_{f,ign}} - (1-\kappa)\,\overline{\dot{\omega}}_{Y_{f,comb}} \tag{3.124}$$

The fuel reaction rates due to ignition $\overline{\dot{\omega}}_{Y_{f,ign}}$ and combustion $\overline{\dot{\omega}}_{Y_{f,comb}}$ are given in Eqs. (3.111) and (3.115), respectively.

To obtain the mean reaction progress variable, the burnt mass fraction is defined as:

$$\widetilde{Y}_{fb} = \widetilde{Y}_{ft} - \widetilde{Y}_f \tag{3.125}$$

Thus,

$$\tilde{c} = \frac{\widetilde{Y}_{fb}}{\widetilde{Y}_{ft} - \widetilde{Y}_{f,res}} \tag{3.126}$$

where $\widetilde{Y}_{f,res}$ indicates the local residual fuel at the end of combustion.

The heat release due to combustion is inserted as source term $\overline{\dot{Q}}_{comb}$ in the energy equation Eq. (3.6):

$$\overline{\dot{Q}}_{comb} = \overline{\dot{\omega}}_{Y_{f,comb}} Q_{HV} \tag{3.127}$$

where $Q_{HV}$ denotes the lower heating value of the fuel. This quantity is take from e.g. [9, 85] and is listed in Table 3.17 for the fuels used in the present study.

| Fuel | $n$-Heptane | Diesel |
|---|---|---|
| $Q_{HV}$ [MJ/kg] | 44.92 | 42.8 |

**Table 3.17:** Lower heating value of various fuels (from [85, 248]).

#### 3.5.3.2 RIF model

**Flamelet equations**

The RIF model is based on the laminar flamelet concept and assumes that chemical timescales are considerably shorter than turbulent mixing scales. However, it is recognised that they may not be so short as to allow the reaction to go instantaneously to equilibrium. Turbulent strain effects on the flamelet may rather cause the reactions to slow down or to quench. Hence, combustion is understood to take place in a thin inner reaction zone in the vicinity of the stoichiometric mixture contour, embedded between two chemically inert outer zones in terms of mixture fraction space. Since the flamelet extends normal to this contour, the fast chemistry assumption implies that changes tangential to this surface are negligible while those in normal direction dominate. Thus the flamelet structure can be described via an independent normal coordinate which is the mixture fraction $Z$, defined similar to Eq. (3.126) as:

$$\tilde{Z} = \frac{\tilde{Y}_{ft} - \tilde{Y}_f}{\tilde{Y}_{ft}} \tag{3.128}$$

with the limits for pure oxidiser, $\tilde{Z} = 0$, and pure fuel, $\tilde{Z} = 1$.

To derive the flamelet equations, balance equations for enthalpy and species are taken in which the viscous dissipation term and the spatial pressure gradients are neglected due to the low Mach number approximation. In addition, radiation heat loss is omitted based on the same argument as put forward in Section 3.2.3. Based

on the findings of an order of magnitude analysis and by neglecting the terms of small to leading order [332, 333, 339], the governing equations for temperature and species after a coordinate transformation into $Z$ space are expressed as [31]:

$$\rho\frac{\partial T}{\partial t} - \rho\frac{\chi}{2}\frac{\partial^2 T}{\partial Z^2} - \rho\frac{\chi}{2c_p}\frac{\partial T}{\partial Z}\frac{\partial c_p}{\partial Z} - \sum_i^N \rho\frac{\chi}{2\mathrm{Le}_i}\frac{c_{p_i}}{c_p}\frac{\partial Y_i}{\partial Z}\frac{\partial T}{\partial Z} + \frac{1}{c_p}\sum_i^N \dot{m}_i h_i - \frac{1}{c_p}\frac{\partial p}{\partial t} = 0 \tag{3.129}$$

$$\rho\frac{\partial Y_i}{\partial t} - \rho\frac{\chi}{2\mathrm{Le}_i}\frac{\partial^2 Y_i}{\partial Z^2} - \dot{m}_i + \frac{1}{2}\left[\rho\chi\frac{1}{\mathrm{Le}_i^2}\frac{\partial \mathrm{Le}_i}{\partial Z} + \frac{1}{2}\left(1-\frac{1}{\mathrm{Le}_i}\right)\left(\frac{\partial \rho\chi}{\partial Z} + \rho\chi\frac{c_p}{k}\frac{\partial}{\partial Z}\left(\frac{k}{c_p}\right)\right)\right]\frac{\partial Y_i}{\partial Z} = 0 \tag{3.130}$$

where $N$ denotes the number of chemical species, $\chi$ is the scalar dissipation rate, $\mathrm{Le}_i$, $\dot{m}_i$ and $h_i$ are the Lewis number, the chemical production rate and the enthalpies of species $i$, respectively. The scalar dissipation $\chi$ characterises the non-equilibrium effects in diffusion flames due to turbulent strain. In 3D space the scalar dissipation rate is given by:

$$\chi = 2\mathcal{D}_Z\left(\frac{\partial Z}{\partial \mathbf{x}}\right)^2 \tag{3.131}$$

using the diffusion coefficient of the mixture fraction $\mathcal{D}_Z$ and the spatial coordinate vector $\mathbf{x}$. Usually $\mathcal{D}_Z$ is chosen such that the Lewis number for the mixture fraction becomes unity [31]†. The species Lewis number is defined as:

$$\mathrm{Le}_i = \frac{k}{\rho c_p \mathcal{D}_i} \tag{3.132}$$

where $\mathcal{D}_i$ is the species diffusion coefficient. The species Lewis number is taken as constant and is different for each species, as recommended in [341]. The chemical production rate is:

$$\dot{m}_i = M_i \sum_k \nu_{ik}\,\dot{\omega}_k \tag{3.133}$$

where $\nu_{ik}$ the matrix of stoichiometric coefficients for species $i$ in reaction $k$ and $\dot{\omega}_k$ the reaction rate of reaction $k$.

† $\mathcal{D}_Z$ can be defined arbitrarily. However, it is chosen such that the Lewis number for mixture fraction becomes unity, as recommended by Pitsch and Peters [341] based on a sensitivity study.

In Eqs. (3.129) and (3.130) no convective term appears, since all scalars are assumed to be transported with the same convection velocity as the independent coordinate. However, the last term in Eq. (3.130), which includes the differential diffusion in mixture fraction space, has been associated with convective transport [341].

To obtain an expression for the scalar dissipation rate in mixture fraction space, it is assumed that an analogy exists between the flamelet and a respective laminar flow configuration which was identified by Peters [332] as the counter-flow diffusion flame. For this flow, Kim *et al.* [234] have derived the following relation:

$$\chi(Z) = \frac{a_\infty}{4\pi} \frac{3\left(\sqrt{\frac{\rho_\infty}{\rho}}+1\right)^2}{2\sqrt{\frac{\rho_\infty}{\rho}}+1} \exp\left(-2\left[\mathrm{erfc}^{-1}(2Z)\right]^2\right) \tag{3.134}$$

where the subscript $\infty$ denotes quantities of the external oxidiser stream or at a reference point, $a_\infty$ is the stagnation-point velocity gradient and $\mathrm{erfc}^{-1}$ is the inverse of the complementary error function. In turbulent flows the profile of the scalar dissipation rate is conveniently characterised by a single parameter which has been proposed by Peters [332] as the scalar dissipation rate at stoichiometric conditions $\chi_{st} = \chi(Z_{st})$. This parameter is equivalent to $a_\infty$.

The principal advantage of this flamelet approach is that the flamelet equations are relatively inexpensive to solve. It is therefore possible to incorporate a detailed description of the chemistry. However, for highly turbulent combustion such as in Diesel engines it is important to take into account the unsteadiness [287]. Hence, the flamelet equations are solved interactively with the fluid dynamics equations, usually referred to as the *Representative Interactive Flamelet* concept. In practice, the flamelet code, called "RIF" [379], is run in parallel with the CFD code. The latter provides the pressure, oxidiser-side temperature, fuel-side temperature[†] and scalar dissipation rate to the former. The RIF code returns effectively the instantaneous

[†]The oxidiser-side temperature refers to the mixture temperature at $Z = 0$, whereas the fuel-side temperature denotes the mixture temperature at $Z = 1$.

reaction extent and heat release. This is described in more detail below. The four quantities input into RIF are referred to as *flamelet parameters* and are the necessary initial and boundary conditions for the solution of Eqs. (3.129) and (3.130).

### Flamelet chemistry

The version of the RIF code [379] used in the present study comprises $n$-heptane reaction chemistry of 416 elementary reactions and 42 species. The reaction set is capable of describing the low and high temperature autoignition, fuel decomposition, and fuel oxidation. The $n$-heptane kinetic mechanism is taken from Chevalier *et al.* [68], which kinetic rates have been revised and improved by Baulch *et al.* [36].

$NO_x$ chemistry with 106 reactions and 14 chemical species is included, based on the works of Hewson and Bollig [165] which includes thermal $NO$, prompt $NO$ and nitrous oxide formation. Moreover $NO_x$ reburn via hydrocarbon radicals and amines ($NH_x$) is accounted for.

A complex soot formation and oxidation mechanism is also incorporated. Gas phase chemistry encompasses the formation of soot precursors up to benzene and the formation and growth of small PAHs based on the works of Mauss [285], Frenklach *et al.* [128] and Miller *et al.* [293]. Further growth of PAHs is modeled assuming fast polymerisation up to infinite size such that a steady-state assumption holds. This results in an algebraic set of equations for the PAH concentrations.

Moreover the coagulation of PAHs, the subsequent inception of soot particles, the condensation of PAHs on the soot particle surface, the coagulation of soot particles and the heterogeneous surface reactions are accounted for. These are based on a kinetics model using the method of moments [124]. The coagulation processes obey the Smoluchowski's coagulation equations [400] in the free molecular regime. The surface growth of soot particles is taken from Mauss *et al.* [286] following a similar reaction sequence as the HACA mechanism of Frenklach and Wang [125]. Finally,

soot oxidation is considered by surface attack via hydroxyl radicals and molecular oxygen, as described in [286]. All heterogeneous surface reactions follow the approach of Frenklach and Wang [125], in which the reaction rates are proportional to the number of active sites per unit volume. These in turn are proportional to the soot particle surface.

According to the method of moments, a statistical approach is used to describe the size distribution of soot particles. The moments ${}^{s}M_r$ of the size distribution are defined as:

$$ {}^{s}M_r = \sum_{i=1}^{\infty} i^r N_i \quad ; \quad r = 0, \ldots, \infty \tag{3.135} $$

where $r$ is the order of the moment, $N_i$ is the soot particle number density of size class $i$ with mass $m_i = i m_1$. Here $m_1$ is the mass of the smallest soot particle, assumed to be $C_2$ [343]. The first two moments can be associated with the soot particle number density $N$ and the soot volume fraction $f_v$, such as [27]:

$$ {}^{s}M_0 = \sum_{i=1}^{\infty} N_i = N \tag{3.136} $$

$$ {}^{s}M_1 = \sum_{i=1}^{\infty} i N_i = f_v \frac{\rho_s}{m_1} \tag{3.137} $$

The conservation equation for the moments ${}^{s}M_r$, when assuming that the Lewis numbers of soot are equal to that of the mixture fraction†, read [379]:

$$ \rho \frac{\partial \left( \frac{{}^{s}M_r}{\rho} \right)}{\partial t} - \rho \frac{\chi}{2\mathrm{Le}_1} \frac{\partial^2 \left( \frac{{}^{s}M_r}{\rho} \right)}{\partial Z^2} = S^{i}_{{}^{s}M_r} \tag{3.138} $$

Here $\mathrm{Le}_1$ stands for the Lewis number of the smallest soot particle and $S^{i}_{{}^{s}M_r}$ is the source term due to heterogeneous surface reactions from size class $i$. In general, only the first two moments are solved for due to considerations of computational effort, and since these have a trivial physical meaning [35, 339, 343].

†Equivalent Lewis numbers for soot and mixture fraction reflect equal diffusivities for both quantities. This holds true for relatively small soot particles [343]. Due to reduced computational effort and as the RIF code used in the current study only offers this practice, this approximation was applied.

### Specifications of CFD code setup for linkage with RIF

To obtain the local mean species composition, two additional transport equations in the CFD code for the mean and variance of the mixture fraction, $\tilde{Z}$ and $\widetilde{Z''^2}$, are solved:

$$\frac{\partial\left(\overline{\rho}\tilde{Z}\right)}{\partial t}+\nabla\cdot\left(\overline{\rho}\tilde{\mathrm{u}}\tilde{Z}\right)=\nabla\cdot\left[\frac{\mu_t}{\sigma_{\tilde{Z}}}\nabla\tilde{Z}\right]+\overline{S}_Z^d \tag{3.139}$$

$$\frac{\partial\left(\overline{\rho}\widetilde{Z''^2}\right)}{\partial t}+\nabla\cdot\left(\overline{\rho}\tilde{\mathrm{u}}\widetilde{Z''^2}\right)=\nabla\cdot\left[\frac{\mu_t}{\sigma_{\widetilde{Z''^2}}}\nabla\widetilde{Z''^2}\right]+\frac{2\mu_t}{\sigma_{\widetilde{Z''^2}}}\left(\nabla\tilde{Z}\right)^2-\overline{\rho}\tilde{\chi} \tag{3.140}$$

where $\overline{S}_Z^d$ refers to the mass transfer from spray droplets and $\sigma_{\tilde{Z}}$, $\sigma_{\widetilde{Z''^2}}$ are the Schmidt numbers for the mean and variance of mixture fraction, respectively. The latter two quantities are chosen to be 0.9, following the practice of Peters *et al.* [31, 35, 339].

The scalar dissipation rate for the turbulent flamelet is related to the mixture fraction variance $\widetilde{Z''^2}$ and is evaluated from the following relation according to Jones and Whitelaw [215]:

$$\tilde{\chi}=c_\chi\frac{\tilde{\varepsilon}}{\tilde{k}}\widetilde{Z''^2} \tag{3.141}$$

where $c_\chi=2$. Furthermore the CFD code solves for the chemico-thermal enthalpy, defined as:

$$h=\sum_{i=1}^{N_{spec}}Y_i\,\Delta_f H_i^\circ+\int_{T_0}^{T}c_p\,dT \tag{3.142}$$

where $N_{spec}$ is the total number of species and $\Delta_f H_i^\circ$ stands for the heat of formation of chemical species $i$. The conservation equation for the chemico-thermal enthalpy is:

$$\frac{\partial(\overline{\rho}\tilde{h})}{\partial t}+\nabla\cdot(\overline{\rho}\tilde{\mathrm{u}}\tilde{h})=\nabla\cdot\left(\overline{\rho}\,\overline{\Gamma}_{h,eff}\nabla\tilde{h}\right)-\overline{p}\,\nabla\cdot\left[\vartheta\overline{\mathrm{u}}+(1-\vartheta)\overline{\mathrm{u}}_l\right]+\frac{dp}{dt}+\overline{S}_h^d \tag{3.143}$$

Here $\Gamma_{h,eff}$ is the effective heat diffusivity and $\overline{S}_h^d$ is the heat transfer from the spray droplets to the gas phase. The advantage of solving for the chemico-thermal enthalpy lies in the format of its conservation equation, Eq. (3.143), in which chemical

source terms do not appear. This allows, combined with the fast chemistry assumption, the solution of the CFD governing equations at timescales greater than the chemical timescales which are much smaller during ignition, compared to turbulence timescales.

## Linkage between RIF and CFD code

To make the flamelet solution computationally affordable the RIF developers make the additional assumption that it is adequate to calculate just one or a few flamelets by spatially averaging over the computational domain. In the current work only one flamelet has been solved following the initial practice of the developers. As a consequence of using a limited number of flamelets, the flamelet parameters have to be spatially averaged over the computational domain before being input into the RIF code.

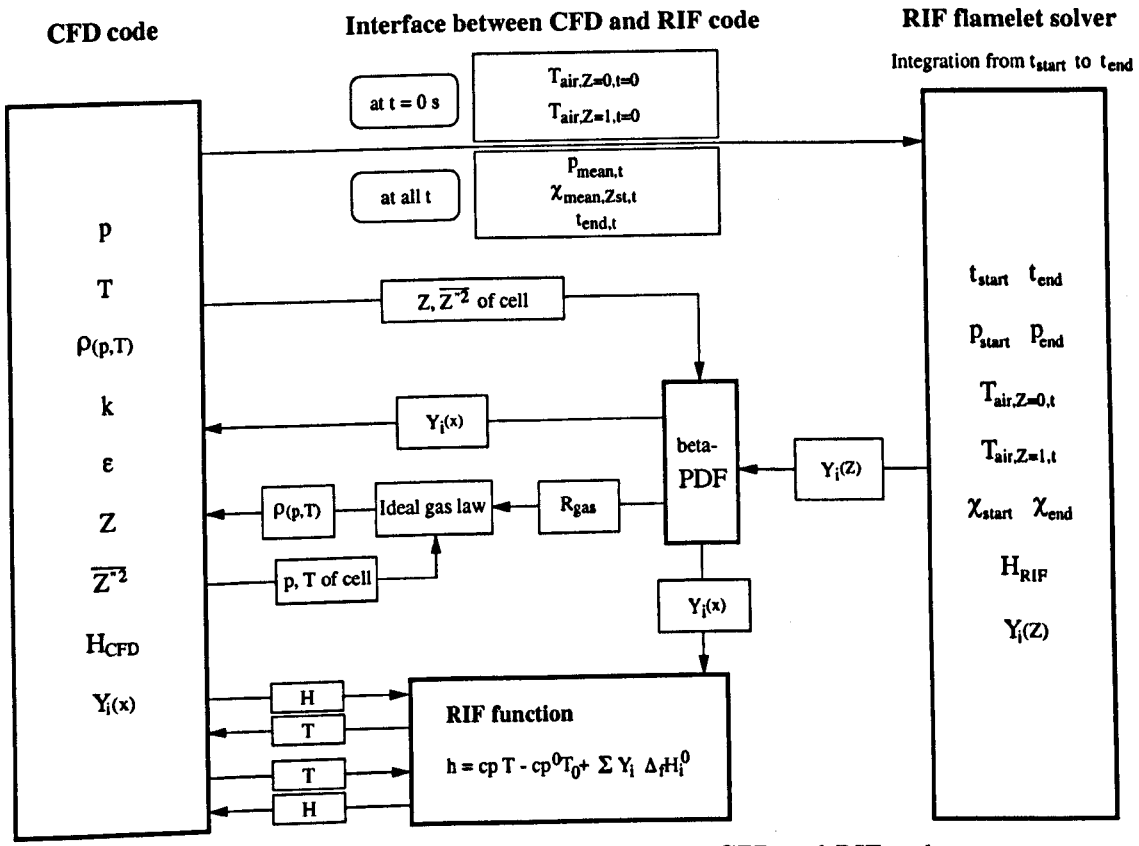



**Figure 3.23:** Schematic of linkage between CFD and RIF codes.

Figure 3.23 summarises the linkage between the CFD and the RIF code. On the left and right side the relevant parameters for the CFD and RIF codes, respectively, are listed, whereas the middle section concerns the interface between both codes, which has been refined by the author. The flamelet calculation is initiated by supplying the flamelet parameters averaged over the computational domain, which is shown at the top of the schematic. Only at the start of the combustion computation, which corresponds to SOI, the oxidiser-side and fuel-side temperatures are input into RIF. At all time-steps the mean pressure, the mean scalar dissipation at stoichiometric mixture fraction and the time-step size are provided. The averaged flamelet parameters are obtained as follows:

1. *Pressure:* The pressure is calculated at each time-step through Reynolds-averaging:

$$\overline{p} = \frac{\sum_{i=1}^{N_{cell}} p_i V_i}{\sum_{i=1}^{N_{cell}} V_i}$$

where $N_{cell}$ is the total number of computational cells and index $i$ denotes the cell number.

2. *Oxidiser-side and fuel-side temperature:* The oxidiser-side temperature is calculated at SOI through Favre-averaging:

$$\widetilde{T}_{oxidiser} = \frac{\sum_{i=1}^{N_{cell}} \rho_i V_i T_i}{\sum_{i=1}^{N_{cell}} \rho_i V_i}$$

The initial fuel-side temperature is taken to be the fuel injection temperature. For the successive time-steps, both oxidiser-side and fuel-side temperatures, known as the *flamelet boundary temperatures*, are evaluated in the RIF code as follows:

$$T^{n+1} = T^n + \frac{1}{\widetilde{c}_p} \Delta \left( \frac{\widetilde{p}}{\widetilde{\rho}} \right)$$

where $T^{n+1}$ and $T^n$ are the temperatures at time-step $n+1$ and $n$, respectively, and $c_p$, $p$ and $\rho$ are evaluated at time-step $n$.

3. *Scalar dissipation rate:* The scalar dissipation rate is conditionally averaged around the stoichiometric mixture fraction contour. Following Pitsch *et al.* [340] the conditional average is:

$$\widehat{\langle \chi_{st} \rangle} = \frac{\int_V \langle \chi_{st} \rangle^{\frac{3}{2}} \overline{\rho} P(Z_{st}) dV'}{\int_V \langle \chi_{st} \rangle^{\frac{1}{2}} \overline{\rho} P(Z_{st}) dV'} \tag{3.144}$$

where $P(Z_{st})$ is the probability density function (PDF) for stoichiometric mixture fraction and $\langle \chi_{st} \rangle$ is the local turbulent mean scalar dissipation rate conditioned at the stoichiometric mixture fraction. The latter is obtained as follows: assume that the instantaneous scalar dissipation rate is expressed as:

$$\chi = \chi_{st} f(Z) \tag{3.145}$$

where $\chi_{st}$ is the scalar dissipation rate at stoichiometric mixture fraction and $f(Z)$ is given by Eq. (3.134)†. Assume also that $\chi_{st}$ and $Z$ are statistically independent, such that the turbulent mean value is:

$$\widetilde{\chi} = \langle \chi_{st} \rangle \widetilde{f(Z)} = \int_{\chi_{st}} \chi'_{st} P(\chi'_{st}) d\chi'_{st} \int_Z f(Z) P(Z) dZ \tag{3.146}$$

Here the integration in $\widetilde{f(Z)}$ ranges from the mixture fraction limit of 0 – 1. Moreover, $P(\chi'_{st})$ and $P(Z)$ denote the probability density functions for stoichiometric scalar dissipation rate and mixture fraction, respectively. Both PDFs are of a beta distribution which has been widely applied in the conserved scalar approach of turbulent reacting flows [44, 201]. The beta-PDF is defined as:

$$P(Z) = \widetilde{Z}^{(\alpha-1)} (1 - \widetilde{Z})^{(\beta-1)} \frac{\Gamma(\alpha + \beta)}{\Gamma(\alpha)\Gamma(\beta)} \tag{3.147}$$

where $\widetilde{Z}$ is the mixture fraction in the current computational cell and $\Gamma$ is the gamma function. The two coefficients $\alpha$ and $\beta$ are calculated from the first two moments of the mixture fraction as:

$$\alpha = \widetilde{Z} \left( \frac{\widetilde{Z}(1 - \widetilde{Z})}{\widetilde{Z''^2}} - 1 \right) \tag{3.148}$$

$$\beta = (1 - \widetilde{Z}) \left( \frac{\widetilde{Z}(1 - \widetilde{Z})}{\widetilde{Z''^2}} - 1 \right) \tag{3.149}$$

†As mentioned earlier, in Eq. (3.134) $a_\infty$ is equivalent to $\chi_{st}$.

Combining Eqs. (3.141) and (3.146), the mean scalar dissipation rate conditioned at the stoichiometric mixture fraction, $\langle \chi_{st} \rangle$, is obtained.

Once the initial and boundary conditions are specified, the RIF flamelet solver integrates the flamelet equations over mixture fraction space up to the end of the CFD time-step. Note that RIF solves at chemical timescales, which during ignition are much smaller than the CFD timescales. For each subsequent CFD time-step, the previous flamelet solution is retained as initial condition for the following integration.

The Favre-averaged species mass fractions are then obtained from the flamelet solution by employing a presumed-PDF approach [249], displayed in the centre of the schematic:

$$\tilde{Y}_i = \int_0^1 Y_i(Z) P(Z) dZ \tag{3.150}$$

To avoid the numerically expensive practice to solve transport equations for all the species within the fluid dynamics code the calculation of the density and the enthalpy-to-temperature conversion is performed outside the CFD code. In the current study only 15 major species were transported in the CFD solution, including the mixture fraction and its variance. The cell density is then calculated via the ideal gas law. Here the pressure and temperature of the cell and the specific gas constant are employed, where the latter depends on the Favre-averaged species concentrations, taken from the RIF solution via the PDF approach.

In order to convert either chemico-thermal enthalpy into temperature and vice versa, a RIF function is employed that performs the conversion according to Eq. (3.142) using the Favre-averaged species concentrations of the flamelet solution via the PDF approach. This is shown at the bottom of the schematic. Since the reference temperature of the RIF and the CFD codes differed, the chemico-thermal enthalpies need to be adjusted before and after the conversion. The value used for adjustment is equivalent to the enthalpy needed to set the enthalpy of the CFD code to zero at the reference temperature of the RIF code, i.e. at 298.12 K.

## 3.6 Pollutant Formation

### 3.6.1 $NO_X$ model

#### Description

In the current study $NO$ formation was accounted for, while the reactions leading to $NO_2$ were neglected. This is based on the findings that $NO$ is the major contributor to overall $NO_X$ levels [459]. With respect to $NO$ formation, the thermal path has solely been considered, since its contribution was found to be dominant in Diesel combustion [167]. It is furthermore assumed that the formation of $NO$ is several orders of magnitude slower than the reactions involving high heat release, such that the formation process is governed by chemical kinetics with finite reaction rates [249]. Moreover, the influence of turbulence has not been considered.

Thermal $NO$ formation has been modeled by using the extended Zeldovich mechanism, defined in the following three reactions:

$$O + N_2 \underset{1b}{\overset{1f}{\rightleftharpoons}} NO + N \tag{3.151}$$

$$N + O_2 \underset{2b}{\overset{2f}{\rightleftharpoons}} NO + O \tag{3.152}$$

$$N + OH \underset{3b}{\overset{3f}{\rightleftharpoons}} NO + H \tag{3.153}$$

The reaction rates employ the Arrhenius equation and are listed in Table 3.18, with the respective coefficients for forward and backward reaction taken from Baulch *et al.* [37]. Due to the high activation energy for the forward reaction in Eq. (3.151) the first reaction is determining the rate of $NO$ formation. Consequently, only at sufficiently high temperatures nitric oxides are produced. Concerning the rate coefficients large uncertainties exist [97, 167, 352]. Heywood [167] attributes an uncertainty factor of two in particular for the reaction in Eq. (3.151) and in engine simulations Reitz *et al.* [240, 328, 362] have introduced a calibration factor to scale the predicted $NO_X$ mass fraction which ranged from 0.78 – 62 [328].

| Reaction index $i$ | Forward rate coefficient $\omega_{if}$ [m$^3$/(kmol s)] | Backward rate coefficient $\omega_{ib}$ [m$^3$/(kmol s)] |
|---|---|---|
| 1 | $1.8 \times 10^{11} \exp\left(\frac{-38370}{T}\right)$ | $3.8 \times 10^{10} \exp\left(\frac{-425}{T}\right)$ |
| 2 | $1.8 \times 10^{7} T \exp\left(\frac{-4680}{T}\right)$ | $3.8 \times 10^{6} T \exp\left(\frac{-20820}{T}\right)$ |
| 3 | $7.1 \times 10^{10} \exp\left(\frac{-450}{T}\right)$ | $1.7 \times 10^{11} \exp\left(\frac{-24560}{T}\right)$ |

**Table 3.18:** Rate coefficients for extended Zeldovich mechanism (from [37]).

The formation rates for $NO$ and $N$ in the above reaction scheme of Eqs. (3.151) – (3.153) are obtained from:

$$\frac{d\overline{Y}_{NO}}{dt} = \frac{M_{NO}}{\rho} (\dot{\omega}_{1f}[O][N_2] + \dot{\omega}_{2f}[N][O_2] + \dot{\omega}_{3f}[N][OH] - \dot{\omega}_{1b}[NO][N] - \dot{\omega}_{2b}[NO][O] - \dot{\omega}_{3b}[NO][H]) \quad (3.154)$$

$$\frac{d\overline{Y}_{N}}{dt} = \frac{M_{N}}{\rho} (\dot{\omega}_{1f}[O][N_2] - \dot{\omega}_{2f}[N][O_2] - \dot{\omega}_{3f}[N][OH] - \dot{\omega}_{1b}[NO][N] + \dot{\omega}_{2b}[NO][O] + \dot{\omega}_{3b}[NO][H]) \quad (3.155)$$

Since the activation energy of the forward reaction in Eq. (3.153) is small, which captures the oxidation of $N$, and due to the relatively small concentration of $N$ compared to other relevant species [167], a quasi-steady assumption for $N$ was applied (i.e. $\frac{d\overline{Y}_N}{dt} = 0$). Thus the instantaneous formation rate of $NO$ is given by:

$$\frac{d\overline{Y}_{NO}}{dt} = \frac{M_{NO}}{\rho} \frac{1}{1 + \frac{\dot{\omega}_{1b}[NO]}{\dot{\omega}_{2f}[O_2] + \dot{\omega}_{3f}[OH]}} \times \left[ 2\dot{\omega}_{1f}[O][N_2] - \frac{2\dot{\omega}_{1b}[NO]}{\dot{\omega}_{2f}[O_2] + \dot{\omega}_{3f}[OH]} (\dot{\omega}_{2b}[NO][O] + \dot{\omega}_{3b}[NO][H]) \right] \quad (3.156)$$

Further assumptions are necessary to estimate the concentration of the radicals $O$, $OH$ and $H$. Since the formation of $NO$ is occurring in the burnt gas region where fuel oxidation reactions are fast, it can be assumed that the species concentrations are close to their equilibrium values [434]. This approximation is particularly valid during the main combustion period which is characterised by high heat release and high temperatures. However, late in the expansion stroke when the temperatures are low and chemical reactions slow down, this assumption becomes increasingly invalid. During this stage the thermal $NO$ path nevertheless is frozen such that

the errors due to the approximation are less significant. The concerning equilibrium reactions are given by:

$$O_2 \rightleftharpoons 2O \tag{3.157}$$

$$O + OH \rightleftharpoons O_2 + H \tag{3.158}$$

$$OH + OH \rightleftharpoons H_2O + O \tag{3.159}$$

The reaction system is solved by the conservation of atomic species involved and the equilibrium constants given by Westenberg [459]. The concentrations of $O_2$ and $H_2O$ are obtained from the combustion calculation.

### Implementation

The following transport equation for the $NO$ mass fraction $Y_{NO}$ is solved:

$$\frac{\partial \overline{\rho}\tilde{Y}_{NO}}{\partial t} + \nabla\cdot(\overline{\rho}\,\tilde{\mathbf{u}}\tilde{Y}_{NO}) = \nabla\cdot\left(\overline{\rho}\,\overline{\Gamma}_{Y_{NO},eff}\nabla\tilde{Y}_{NO}\right) + \overline{S}_{Y_{NO}} \tag{3.160}$$

where the source term $\overline{S}_{Y_{NO}}$ is specified using Eq. (3.156) according to:

$$\overline{S}_{Y_{NO}} = \overline{\dot{\omega}}_{Y_{NO}} = \frac{d\overline{Y}_{NO}}{dt} \tag{3.161}$$

## 3.6.2 Soot model

In the present study a semi-empirical soot model has been implemented, which calculates the two main processes: soot formation and oxidation. It is assumed that the heterogeneous reactions leading to soot particles and their respective growth and oxidation are kinetically controlled due to their small size [167]. The chosen soot submodels have been widely used for engine soot emissions predictions [35, 39, 156, 240, 319, 328].

### 3.6.2.1 Soot formation model

Hiroyasu *et al.* [178] have proposed an approach for soot formation for local gas temperatures between 1000 and 2500 K in which the rate is given by:

$$\frac{d\overline{Y}_{s,f}}{dt} = k_{s,f}\tilde{Y}_f \tag{3.162}$$

where $Y_f$ is the mass fraction of fuel vapour and $k_{s,f}$ is the soot formation rate coefficient. This is calculated from the Arrhenius equation:

$$k_{s,f} = A_{s,f}\sqrt{\overline{p}}\,\exp\left(-\frac{E_{s,f}}{\mathcal{R}\tilde{T}}\right) \tag{3.163}$$

where $A_{s,f}$ and $E_{s,f}$ are the pre-exponential factor and activation energy for soot formation. The values recommended for these coefficients are listed for different applications in Table B.4 in Section B.2 in the Appendix.

### 3.6.2.2 Soot oxidation model

Two phenomenological soot oxidation models have been employed, proposed separately by Hiroyasu [178] and Nagle and Strickland-Constable [311]. The latter model has been applied with most success in Diesel engine simulations [226].

#### Hiroyasu soot oxidation model

Hiroyasu [178] proposed the following soot oxidation model:

$$\frac{d\overline{Y}_{s,o}}{dt} = k_{s,o}\,\chi_{O_2}\,\tilde{Y}_s \tag{3.164}$$

where $\chi_{O_2} = \frac{p_{O_2}}{p}$ stands for the ratio of partial pressure of oxygen $p_{O_2}$ to absolute pressure, $Y_s$ is the soot mass fraction and $k_{s,o}$ is the oxidation rate coefficient. This is given by the Arrhenius equation:

$$k_{s,o} = A_{s,o}\,\overline{p}^{1.8}\,\exp\left(-\frac{E_{s,o}}{\mathcal{R}\tilde{T}}\right) \tag{3.165}$$

Here $A_{s,o}$ and $E_{s,o}$ refer to the pre-exponential factor and activation energy for soot oxidation, listed for various applications in Table B.4 in Section B.2 in the Appendix.

### Nagle Strickland-Constable soot oxidation model

Comparisons of predictions with experiments suggest that at high oxygen partial pressures, soot oxidation can be correlated to oxidation of pyrographite [8, 161, 399]. The semi-empirical soot oxidation model of Nagle and Strickland-Constable is based on such studies of $O_2$ attack on pyrographite rods and is valid for temperatures from 1100 – 2500 K and oxygen partial pressures between 0.1 and 0.6 atm†. The model relates carbon oxidation to the surface chemistry involving more reactive sites $A$ and less reactive sites $B$. Those sites have been identified as basal-carbon and edge-carbon clusters [66]. Three main types of reactions are assumed: the oxidation of type $A$ and $B$ sites and their thermal rearrangement/annealing, expressed as follows:

$$A + O_2 \xrightarrow{1} A + 2CO \tag{3.166}$$

$$B + O_2 \xrightarrow{2} A + 2CO \tag{3.167}$$

$$A \xrightarrow{3} B \tag{3.168}$$

The associated rates are provided as:

$$\bar{\omega}_1 = \frac{k_A\, p_{O_2}}{1 + k_Z\, p_{O_2}}\, x \tag{3.169}$$

$$\bar{\omega}_2 = k_B\, p_{O_2}\, (1 - x) \tag{3.170}$$

$$\bar{\omega}_3 = k_T\, x \tag{3.171}$$

Here $k_A$ and $k_B$ stand for the oxidation rate constants for sites $A$ and $B$, respectively, $k_Z$ is the equilibrium constant for adsorption and desorption, $k_T$ is the rate constant for thermal annealing, and $x$ is the fraction of $A$ sites on the carbon surface. When assuming a stationary value for $x$, the following expression is obtained:

$$x = \frac{1}{1 + \frac{k_T}{k_B\, p_{O_2}}} \tag{3.172}$$

The overall reaction rate is then expressed as:

$$\bar{\omega}_{O_2} = \left(\frac{k_A\, p_{O_2}}{1 + k_Z\, p_{O_2}}\right) x + k_B\, p_{O_2}\, (1 - x) \tag{3.173}$$

†Chen *et al.* [66] have concluded in their studies that the NSC oxidation model correlates soot oxidation adequately for temperatures from 1700 - 4000 K and oxygen partial pressures between 0.05 and 13 atm.

In this mechanism, soot oxidation is first order in oxygen partial pressures for low pressures and becomes independent of $p_{O_2}$ at higher pressures. At a given oxygen pressure, the oxidation rate increases exponentially for lower temperatures and is constant at high temperatures. This is due to the fact that at low temperatures the carbon surface is entirely covered by $A$ sites, while beyond a certain temperature thermal rearrangement becomes predominant favouring the formation of less reactive $B$ sites. Above about 2100 K the oxidation rate is controlled by the $B$ sites [66]. Here the oxidation is first order in oxygen pressure and increases with temperature.

The rate coefficients of Eqs. (3.169) – (3.171) are given by Arrhenius expressions and are listed in Table B.2 in Section B.2 in the Appendix. Also included in the table is a variation proposed by Najjer and Goodger [313] on the original sets of coefficients, to extend predictions to higher oxygen partial pressures.

The soot mass oxidation rate is given by:

$$\frac{d\overline{Y}_{s,o}}{dt} = \frac{6\,M_c}{\rho_s\,D_s}\tilde{Y}_s\,\overline{\dot{\omega}}_{O_2} \tag{3.174}$$

where $M_c$ is the carbon molecular weight, $\rho_s$ is the soot density and $D_s$ is the characteristic soot diameter. The properties of soot used in the literature vary widely and are listed in Table B.3 in Section B.2 in the Appendix. In the present study the values of Yi *et al.* [475] have been employed.

### 3.6.2.3 Implementation

A transport equation for $Y_s$ is solved:

$$\frac{\partial\overline{\rho}\widetilde{Y}_s}{\partial t} + \nabla\cdot\left(\overline{\rho}\tilde{\mathrm{u}}\widetilde{Y}_s\right) = \nabla\cdot\left(\overline{\rho}\overline{\Gamma}_{Y_s,eff}\nabla\widetilde{Y}_s\right) + \overline{S}_{Y_s} \tag{3.175}$$

where the source term is calculated from Eq. (3.162) and Eq. (3.164) or (3.174), respectively, i.e.

$$\overline{S}_{Y_s} = \overline{\dot{\omega}}_{Y_s} = \frac{d\overline{Y}_{s,f}}{dt} - \frac{d\overline{Y}_{s,o}}{dt} \tag{3.176}$$

Soot was assumed to be formed from the local fuel vapour. Moreover, soot burnout was assumed to result in the same heat release as fuel burnout in the LATCT combustion model. Therefore soot formation and oxidation result in the following source terms in the fuel mass fraction $Y_f$ and total fuel mass fraction $Y_{ft}$ equations, respectively:

$$\overline{S}_{Y_f}^{Y_s} = -\frac{d\overline{Y}_{s,f}}{dt} \tag{3.177}$$

$$\overline{S}_{Y_{ft}}^{Y_s} = \frac{d\overline{Y}_{s,o}}{dt} - \frac{d\overline{Y}_{s,f}}{dt} \tag{3.178}$$

It is evident from the above that soot formation causes a change in fuel vapour and total fuel mass fraction, while soot burnout affects the total fuel mass fraction only.

In addition based on experimental evidence that soot formation takes place above around 1000 K [167], the onset of soot production was defined to occur at this temperature level.

## 3.7 Summary of Governing Equations

The governing ensemble-averaged equations for the gas-phase processes are summarised below:

**Mass conservation equation**

$$\frac{\partial\overline{\rho}}{\partial t} + \nabla\cdot(\overline{\rho}\tilde{\mathbf{u}}) = \overline{S}_m^d \tag{3.179}$$

**Momentum conservation equation**

$$\frac{\partial\overline{\rho}\tilde{\mathbf{u}}}{\partial t} + \nabla\cdot(\overline{\rho}\tilde{\mathbf{u}}\tilde{\mathbf{u}}) = -\overline{\vartheta}\nabla\overline{p} + \nabla\cdot\left\{\overline{\rho}\left[\overline{\nu}_{eff}\left(2\widetilde{\mathbf{D}} - \frac{2}{3}\nabla\cdot\tilde{\mathbf{u}}\mathbf{I}\right) - \frac{2}{3}\tilde{k}\mathbf{I}\right]\right\} + \overline{\mathbf{S}}_{\mathbf{u}}^d \tag{3.180}$$

**Energy conservation equation**

$$\begin{aligned}\frac{\partial\overline{\rho}\tilde{e}}{\partial t} + \nabla\cdot(\overline{\rho}\tilde{\mathbf{u}}\tilde{e}) = {} & \nabla\cdot\left(\overline{\rho}\overline{\Gamma}_{e,eff}\nabla\tilde{e}\right) - \overline{p}\nabla\cdot\left[\overline{\vartheta}\overline{\mathbf{u}} + \left(1-\overline{\vartheta}\right)\overline{\mathbf{u}}_l\right] \\ & + \overline{S}_e^d + \kappa\overline{\dot{Q}}_{ign} + (1-\kappa)\overline{\dot{Q}}_{comb}\end{aligned} \tag{3.181}$$

**Chemical species mass fraction conservation equation**

$$\frac{\partial \overline{\rho}\widetilde{Y}_\psi}{\partial t} + \nabla\cdot\left(\overline{\rho}\tilde{\mathbf{u}}\widetilde{Y}_\psi\right) = \nabla\cdot\left(\overline{\rho}\overline{\Gamma}_{Y_\psi,eff}\nabla\widetilde{Y}_\psi\right) + \overline{S}^d_{Y_\psi} + \overline{S}_{Y_\psi} \tag{3.182}$$

**Turbulence kinetic energy equation**

$$\frac{\partial \overline{\rho}\widetilde{k}}{\partial t} + \nabla\cdot\left(\overline{\rho}\tilde{\mathbf{u}}\widetilde{k}\right) = \nabla\cdot\overline{\rho}\overline{\Gamma}_{k,t}\nabla\widetilde{k} + G - \overline{\rho}\widetilde{\varepsilon} + \overline{S}^d_k \tag{3.183}$$

**Turbulence dissipation rate equation**

$$\frac{\partial \overline{\rho}\widetilde{\varepsilon}}{\partial t} + \nabla\cdot(\overline{\rho}\tilde{\mathbf{u}}\widetilde{\varepsilon}) = \nabla\cdot\overline{\rho}\overline{\Gamma}_{\varepsilon,t}\nabla\widetilde{\varepsilon} + C_{\varepsilon 1}G\frac{\widetilde{\varepsilon}}{\widetilde{k}} - C_{\varepsilon 2}\overline{\rho}\frac{\widetilde{\varepsilon}^2}{\widetilde{k}} + C_{\varepsilon 3}\overline{\rho}\widetilde{\varepsilon}\nabla\cdot\tilde{\mathbf{u}} + \overline{S}^d_\varepsilon \tag{3.184}$$

**General transport equation**

$$\frac{\partial \overline{\rho}\widetilde{\phi}}{\partial t} + \nabla\cdot\left(\overline{\rho}\tilde{\mathbf{u}}\widetilde{\phi}\right) = \nabla\cdot\left(\overline{\rho}\overline{\Gamma}_{\phi,eff}\nabla\widetilde{\phi}\right) + \overline{S}_\phi + \overline{S}^d_\phi \tag{3.185}$$

In the following sections, for the sake of simplicity, the symbols '$\overline{\psi}$' and '$\widetilde{\psi}$', representing the Reynolds ensemble-average and Favre ensemble-average values of $\psi$, respectively, are omitted.

The mathematical foundations are complemented by the provision of initial and boundary conditions for each of the dependent variables in the governing equations. They are described next.

## 3.8 Boundary Conditions

In the present study four types of boundaries are applied: walls, inflow and outflow boundaries, symmetry planes and cyclic boundaries. These are described in detail below. Also the derivation of a modified near-wall treatment with allowance for physical property variations is outlined.

### 3.8.1 Walls

In the near-wall region steep gradients of flow properties exist which require a very fine and therefore computation expensive mesh to adequately capture the profiles [256]. Alternatively within the framework of the $k-\varepsilon$ turbulence model, the

*wall function method* is used which bypasses the above shortcomings by employing a coarser near-wall grid and using submodels describing the boundary layers, commonly referred to as *wall functions.* The original work on the wall function method goes back to Launder and Spalding [259] and will be summarised below.

#### 3.8.1.1 Standard wall function approach

**Basis of the standard wall function approach**

The standard wall function approach is derived from a Couette flow analysis which solves the one-dimensional boundary layer equations for momentum, enthalpy, turbulence kinetic energy and its dissipation rate. These are obtained on the assumption that the turbulent boundary layer is very thin, so that the wall-normal velocity is negligible and the gradients of flow properties normal to the wall are much greater than parallel to the wall. In addition, body forces are assumed to be negligible. The Couette equations then read:

$$\frac{\partial \rho u^*}{\partial t} = -\frac{\partial p}{\partial x} + \frac{\partial}{\partial y}\left[\rho(\nu + \nu_t)\frac{\partial u^*}{\partial y}\right] + S_u^d \tag{3.186a}$$

$$\rho c_p \frac{\partial T}{\partial t} = u^* \frac{\partial p}{\partial x} + \frac{dp}{dt} + \frac{\partial}{\partial y}\left[\rho c_p \left(\frac{\nu}{\sigma_e} + \frac{\nu_t}{\sigma_{e,t}}\right)\frac{\partial T}{\partial y}\right] + S_e^d + \dot{Q}_{comb} \tag{3.186b}$$

$$\frac{\partial \rho k}{\partial t} = \frac{\partial}{\partial y}\left[\rho\left(\nu + \frac{\nu_t}{\sigma_k}\right)\frac{\partial k}{\partial y}\right] - \rho\varepsilon + S_k^d \tag{3.186c}$$

$$\frac{\partial \rho \varepsilon}{\partial t} = \frac{\partial}{\partial y}\left[\rho\left(\nu + \frac{\nu_t}{\sigma_\varepsilon}\right)\frac{\partial \varepsilon}{\partial y}\right] - C_{\varepsilon 2}\rho\frac{\varepsilon^2}{k} + S_\varepsilon^d \tag{3.186d}$$

where $y$ is the wall-normal coordinate and $u^*$ is the magnitude of the tangential velocity component of the fluid with respect to the wall normal direction, defined by the wall normal vector $\mathbf{n}$. This is illustrated in Figure 3.24 for the point P. Thus,

$$u^* = |\mathbf{u}^*| \tag{3.187}$$

where

$$\mathbf{u}^* = \mathbf{u} - \mathbf{u}_W - [(\mathbf{u} - \mathbf{u}_W)\cdot\mathbf{n}]\,\mathbf{n} \tag{3.188}$$

Here $\mathbf{u}_W$ refers to the wall velocity, as illustrated in Figure 3.24. The assumptions of

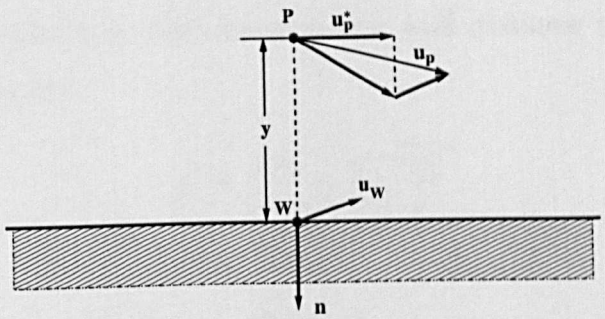



**Figure 3.24:** Schematic of velocities at wall boundary.

quasi-steadiness, no sources due to droplets and combustion, no pressure gradients and therefore constant shear stress and heat flux in the boundary layer further simplify the governing equations:

$$\frac{\partial}{\partial y}\left[\rho\,(\nu+\nu_t)\frac{\partial u^*}{\partial y}\right]=0 \tag{3.189a}$$

$$\frac{\partial}{\partial y}\left[\rho\,c_p\left(\frac{\nu}{\sigma_e}+\frac{\nu_t}{\sigma_{e,t}}\right)\frac{\partial T}{\partial y}\right]=0 \tag{3.189b}$$

$$\frac{\partial}{\partial y}\left[\rho\left(\nu+\frac{\nu_t}{\sigma_k}\right)\frac{\partial k}{\partial y}\right]+\rho\nu_t\left(\frac{\partial u^*}{\partial y}\right)^2-\rho\,\varepsilon=0 \tag{3.189c}$$

$$\frac{\partial}{\partial y}\left[\rho\left(\nu+\frac{\nu_t}{\sigma_\varepsilon}\right)\frac{\partial \varepsilon}{\partial y}\right]+C_{\varepsilon 1}\rho\frac{\varepsilon}{k}\nu_t\left(\frac{\partial u^*}{\partial y}\right)^2-C_{\varepsilon 2}\rho\frac{\varepsilon^2}{k}=0 \tag{3.189d}$$

### Velocity and temperature profiles

Integration of the momentum and enthalpy equations, Eqs. (3.189a) and (3.189b), results in:

$$\rho\left[(\nu+\nu_t)\frac{\partial u^*}{\partial y}\right]=\tau_W \tag{3.190a}$$

$$\rho\,c_p\left[\left(\frac{\nu}{\sigma_e}+\frac{\nu_t}{\sigma_{e,t}}\right)\frac{\partial T}{\partial y}\right]=q_W \tag{3.190b}$$

where the wall shear stress $\tau_W$ and wall heat flux $q_W$, respectively, are given by:

$$\tau_W=\rho\,\nu_{eff}\left.\frac{\partial u^*}{\partial y}\right|_{y=0} \tag{3.191}$$

$$q_W=\frac{\rho\,c_p\,\nu_{eff}}{\sigma_e}\left.\frac{\partial T}{\partial y}\right|_{y=0} \tag{3.192}$$

It is customary to introduce the dimensionless wall distance $y^+$, velocity $u^+$ and viscosity $\nu^+$, defined by:

$$y^+ = \frac{yu_\tau}{\nu} = \frac{y}{\nu}\sqrt{\frac{\tau_W}{\rho}} \tag{3.193}$$

$$u^+ = \frac{u^*}{u_\tau} \tag{3.194}$$

$$\nu^+ = \frac{\nu_t}{\nu} \tag{3.195}$$

Here $u_\tau$ is the friction velocity:

$$u_\tau = \sqrt{\frac{\tau_W}{\rho}} \tag{3.196}$$

The boundary layer momentum and enthalpy equations then take the following form:

$$(1+\nu^+)\frac{\partial u^+}{\partial y^+} = 1 \tag{3.197a}$$

$$\left(\frac{1}{\sigma_e} + \frac{\nu^+}{\sigma_{e,t}}\right)\frac{\partial T^+}{\partial y^+} = 1 \tag{3.197b}$$

where $T^+$ denotes the dimensionless temperature defined by:

$$T^+ = \frac{\rho u_\tau c_p (T_W - T)}{q_W} \tag{3.198}$$

These equations can be integrated analytically by modelling the turbulent transport via a mixing length model, according to Eq. (3.209), as will be outlined later, and assuming negligible thermophysical property variations in the boundary layers and a constant turbulent Prandtl number [223]. The integration limits are taken from the no-slip condition at the wall and when setting the gas-side temperature at the wall to the wall temperature:

$$u^+\Big|_{y^+=0} = 0$$

$$T^+\Big|_{y^+=0} = 0$$

The resulting dimensionless velocity and temperature profiles (i.e. wall functions) for the viscous and inertial sublayers are:

Viscous sublayer:

$$y^+ \leq y_c^+ \Rightarrow \begin{cases} u^+ = y^+ \\ T^+ = \sigma_e u^+ \end{cases} \tag{3.199a}$$

Inertial sublayer:

$$y^+ > y_c^+ \Rightarrow \begin{cases} u^+ = \frac{1}{\kappa} \ln (E y^+) \\ T^+ = \sigma_{e,t} \left[ u^+ + P \left( \frac{\sigma_e}{\sigma_{e,t}} \right) \right] \end{cases} \tag{3.199b}$$

where $y_c^+$ is the wall-normal distance where the laminar and inertial profiles (Eqs. (3.199a) and (3.199b)) intersect, $\kappa$ is the von Kármán constant and the coefficient $E$ accounts for the wall surface roughness [392]. The function $P\left(\frac{\sigma_e}{\sigma_{e,t}}\right)$, called the 'P-function', represents an empirically obtained viscous sublayer resistance factor which is given by Jayatilleke for smooth walls as [202]:

$$P\left(\frac{\sigma_e}{\sigma_{e,t}}\right) = 9.24 \left[ \left( \frac{\sigma_e}{\sigma_{e,t}} \right)^{0.75} - 1 \right] \times \left\{ 1 + 0.28 \exp \left[ -0.007 \left( \frac{\sigma_e}{\sigma_{e,t}} \right) \right] \right\} \tag{3.200}$$

The coefficients in the standard wall functions have been obtained through fitting of the profiles to experimental data [392, 443] and are provided in Table 3.19.

| $\kappa$ | $E$ | $\sigma_e$ | $\sigma_{e,t}$ | $y_c^+$ |
|---|---|---|---|---|
| 0.4187 | 9.793 | 0.7 | 0.9 | 11.63 |

**Table 3.19:** Model coefficients of standard wall functions (from [259]).

When $\tau_W \to 0$ (as at separation and reattachment points), then $y^+ \to 0$, which results in undefined velocity and temperature profiles in the inertial layer according to Eq. (3.199b). To circumvent this singularity, $y^+$ is redefined by replacing $\tau_W$ in Eq. (3.193) by $\rho k \sqrt{C_\mu}$ from Eq. (3.207), giving:

$$y^+ = \frac{C_\mu^{1/4} \sqrt{k}\, y}{\nu} \tag{3.201}$$

### Wall shear stress and heat flux profiles

The wall shear stress and wall heat flux are determined by fitting the velocity and

temperature profiles to Eqs. (3.194) and (3.198):

$$\tau_W = F_W^{\mathbf{u}} \mathbf{u}^* \tag{3.202}$$

$$\mathbf{q}_W = \mathbf{n} F_W^h c_p (T_W - T) = \mathbf{n} F_W^h (h_W - h) \tag{3.203}$$

where $h$ is the enthalpy and $F_W^{\mathbf{u}}$ and $F_W^h$ are obtained from:

Viscous sublayer:

$$y^+ \leq y_c^+ \Rightarrow \begin{cases} F_W^{\mathbf{u}} = -\dfrac{\rho\nu}{y} \\ F_W^h = -\dfrac{\rho\nu}{\sigma_e y} \end{cases} \tag{3.204a}$$

Inertial sublayer:

$$y^+ > y_c^+ \Rightarrow \begin{cases} F_W^{\mathbf{u}} = -\dfrac{\rho\nu}{y} \dfrac{y^+}{\frac{1}{\kappa}\ln\left(Ey^+\right)} \\ F_W^h = -\dfrac{\rho\nu}{\sigma_{e,t}\, y} \dfrac{y^+}{\frac{1}{\kappa}\ln\left(Ey^+\right) + P\left(\frac{\sigma_e}{\sigma_{e,t}}\right)} \end{cases} \tag{3.204b}$$

### Turbulence energy and turbulence dissipation rate profiles

In the log-law sublayer the production and dissipation of the turbulence kinetic energy are assumed to be in equilibrium and the diffusion of the turbulence kinetic energy is taken to be negligible. Thus Eq. (3.189c) reduces to:

$$G = \rho\nu_t \left(\frac{\partial u^*}{\partial y}\right)^2 = \rho\varepsilon \tag{3.205}$$

When combining Eqs. (3.57) with (3.191) and assuming equilibrium, Eq. (3.205), the following relation results:

$$\tau_W^2 = \rho^2 \nu_t \varepsilon \tag{3.206}$$

Substitution of $\nu_t$, as given in Eq. (3.55), into the above results in a uniform turbulence kinetic energy profile in the inertial layer:

$$k = C_\mu^{-\frac{1}{2}} \frac{\tau_W}{\rho} \tag{3.207}$$

Moreover, in the inertial layer it is assumed that the turbulence length scale is proportional to the distance from the wall, based on Prandtl's mixing length theory [223, 392]. Thus,

$$l = \kappa y \tag{3.208}$$

Using this characteristic length scale the turbulent viscosity can be expressed as [443]:

$$\nu_t = \kappa u_\tau y \tag{3.209}$$

When combining Eqs. (3.55), (3.57), (3.191), (3.196) and (3.209), the following equation for the turbulence dissipation rate profile in the inertial sublayer is obtained:

$$\varepsilon = \frac{C_\mu^{3/4} k^{3/2}}{\kappa y} \tag{3.210}$$

This dissipation rate profile replaces its transport equation, Eq. (3.184). The profiles of $k$ and $\varepsilon$ in the inertial sublayer are extended to the viscous layer and are assumed to be defined by Eqs. (3.207) and (3.210) [118]. This treatment leads to inaccuracies, since viscous effects are dominant in the viscous sublayer and the local equilibrium assumption is inadequate. Hence it is customary to avoid placing the near-wall node into the viscous sublayer.

### 3.8.1.2 Validity of standard wall function approach

In this section an assessment of the validity of assumptions of the standard wall function approach is made, including an order of magnitude analysis of the importance of the various physical phenomena involved. Subsequently a modified wall function approach is derived, based on its findings.

#### I.) Order of magnitude analysis

For the purpose of estimating the importance of each term in the boundary layer momentum and enthalpy equations, Eqs. (3.189a) and (3.189b), from which the standard wall functions are derived, an order of magnitude analysis will now be performed, assuming one-dimensionality and neglecting pressure gradients and heat

sources. These assumptions will be scrutinised in more detail in the second part of this section. The momentum and enthalpy equations for these circumstances are:

$$\rho\frac{\partial u^*}{\partial t} = \frac{\partial}{\partial y}\left[\rho(\nu+\nu_t)\frac{\partial u^*}{\partial y}\right] \tag{3.211a}$$

$$\rho c_p\frac{\partial T}{\partial t} = \rho c_p\frac{\partial}{\partial y}\left[\left(\frac{\nu}{\sigma_e}+\frac{\nu_t}{\sigma_{e,t}}\right)\frac{\partial T}{\partial y}\right] + \frac{dp}{dt} \tag{3.211b}$$

These equations are non-dimensionalised by introducing the following (see also [54, 118]):

$$T' = \frac{T}{T_0} \qquad t' = \frac{t}{t_0} \qquad t_0 = \frac{D}{v_0} \qquad y' = \frac{y}{D}$$

$$\mathrm{Re} = \rho v_0\frac{D}{\mu} \qquad \mathrm{Re}_t = \rho v_0\frac{D}{\mu_t} \qquad \mathrm{Re}_u = \rho u^*\frac{D}{\mu} \qquad p' = \frac{p}{p_0}$$

$$\frac{1}{\rho c_p} = \frac{\gamma-1}{\gamma}\frac{T}{p} \qquad \sigma_e = \frac{c_p\mu}{k} \qquad \sigma_{e,t} = \frac{c_p\mu_t}{k_t}$$

where the superscript ' indicates dimensionless quantities and the index 0 designates reference values taken e.g. from intake. Air properties are used in the analysis, and the air is assumed to obey the ideal gas law. The non-dimensionalised equations read:

$$\underbrace{\frac{\partial \mathrm{Re}_u}{\partial t'}}_{\text{transient term}} = \underbrace{\frac{\partial}{\partial y'}\left[\left(\overbrace{\frac{1}{\mathrm{Re}}}^{laminar}+\overbrace{\frac{1}{\mathrm{Re}_t}}^{turbulent}\right)\frac{\partial \mathrm{Re}_u}{\partial y'}\right]}_{\text{diffusion term}} \tag{3.212a}$$

$$\underbrace{\frac{\partial T'}{\partial t'}}_{\text{transient term}} = \underbrace{\frac{\partial}{\partial y'}\left[\overbrace{\frac{1}{\mathrm{Re}\,\sigma_e}}^{laminar}+\overbrace{\frac{1}{\mathrm{Re}_t\,\sigma_{e,t}}}^{turbulent}\right]\frac{\partial T'}{\partial y'}}_{\text{diffusion term}} + \underbrace{\frac{dp'}{dt'}\frac{\gamma-1}{\gamma}\frac{T'}{p'}}_{\text{pressure work term}} \tag{3.212b}$$

The reference values for the order of magnitude analysis, given in Tables 3.20 – 3.22 below, were evaluated for the HPP prototype engine operating under motored conditions, as described in Section 5.3. To estimate the magnitude of each term, the maximum gradients and absolute values of velocity and temperature were taken from simulation results for the engine. The peak pressure was extracted from the experimental data.

The results of the analysis are summarised in Tables 3.23 and 3.24. They clearly demonstrate that the turbulent diffusion term in the inertial sublayer is so large

| Bore $y_0$ [m] | $v_0$ [m/s] | $p_0$ [bar] | $T_0$ [K] | $\rho_0$ [kg/m$^3$] | $\mu_0$ [kg/(m s)] | $t_0$ [s] |
|---|---|---|---|---|---|---|
| 0.13 | 7.1[a] | 49.16[b] | 315 | 1.1 | $2 \times 10^{-5}$ | 0.0183 |

[a] $v_0 = 2LN$, mean piston speed
[b] boost pressure of 2.85 bar × compression ratio of 17.25

**Table 3.20:** Reference values with respect to intake for order of magnitude analysis.

| Bore $D$ [m] | Stroke $L$ [m] | Engine speed $N$ [RPM] | $\sigma_e$ | $\sigma_{e,t}$ | $\gamma$ |
|---|---|---|---|---|---|
| 0.13 | 0.15 | 1420 | 0.7 | 0.9 | 1.3 |

**Table 3.21:** Geometric information for single-cylinder DI Diesel engine and air properties.

| $\left.\frac{du^*}{dt}\right\|_{\max}$ [a] | $\left.\frac{du^*}{dy}\right\|_{\max}$ [b] | $\left.\frac{dT}{dt}\right\|_{\max}$ [a] | $\left.\frac{dT}{dy}\right\|_{\max}$ [c] | $u^*_{\max}$ [a] | $p_{\max}$ [d] | $T_{\max}$ [a] |
|---|---|---|---|---|---|---|
| 21699 m/s$^2$ | 129100 s$^{-1}$ | 82295 K/s | 486620 K/m | 227 m/s | 135 bar | 937 K |

[a] from simulation
[b] based on velocity difference over minimum velocity boundary layer thickness in engines taken as $\delta \approx 1$ mm from [276]
[c] based on temperature difference over minimum thermal boundary layer thickness in engines taken as $\delta \approx 1$ mm from [276]
[d] from experiments

**Table 3.22:** Gradients and maximum quantities for order of magnitude analysis.

that the transient, laminar diffusion and pressure work terms can be neglected in the momentum and enthalpy equations. Although the transient term essentially balances the heat release source during the period when the flame penetrates the boundary layer, this occurs for a very short time, so that the overall prediction error is expected to remain small.

| **Term** | **transient** | **laminar diffusion** | **turbulent diffusion** |
|---|---|---|---|
| **Order of Magnitude** | $10^6$ | $10^5$ | $10^9$ |

**Table 3.23:** Order of magnitude for terms in boundary layer momentum equation.

| **Term** | **transient** | **laminar diffusion** | **turbulent diffusion** | **pressure work** |
|---|---|---|---|---|
| **Order of Magnitude** | 1 | 1 | $10^4$ | 1 |

**Table 3.24:** Order of magnitude for terms in boundary layer enthalpy equation.

### II.) Assumptions of standard wall function approach

The following seven major assumptions, on which the wall functions are based, can now be critically examined with the aid of the above analysis:

**1. Steady state:** The unsteadiness of the boundary layers in an engine originates from the induction process and piston motion, as well as the spray and combustion processes. For the motored case, the velocity and temperature histories are closely bound to the piston motion. In the fired case, especially during the very short period when the spray and/or flame penetrates the boundary layers the related transient effects are especially important. As mentioned earlier in Section 2.3.5.3 a modified wall function approach including transient effects did not show superior performance to the standard model.
A relaxation of the steady-state assumption can be made yielding improved accuracy by assuming a *quasi-steady* situation within the flow field [13, 155, 167]. In this approach the pressure work term in the energy balance is taken into account. However, from the order of magnitude analysis it is clear that this term is relatively small compared to the turbulent diffusion term.

**2. One-dimensionality:** The turbulent flow field in an engine is essentially three-dimensional. Turbulence is initially generated during the induction stroke with flow separation occurring at the valves and recirculation areas located in the corners of the combustion chamber [167, 371]. During this phase the 1D assumption is violated specifically at locations along the walls close to separation and reattachment zones, where strong gradients of velocity and temperature are found. However, these regions cover only a small section of the chamber walls and the gradients decay rapidly due to swirl. In addition, during this period the chamber temperatures are low resulting in comparatively small wall heat fluxes. Therefore during this period the effect of prediction error on overall friction loss and heat transfer when applying the 1D assumption is negligible. During the compression stroke, when gas temperatures

and heat transfer increase, the turbulence intensity reduces and the velocity field becomes increasingly uniform over the chamber cross-section [167]. This is due to the fact that for swirl-dominated flows as encountered in modern Diesel engines the very thin boundary layers generally tend to be more homogeneous in lateral directions, thus approaching one-dimensionality [167], i.e. normal gradients dominate in the near-wall region.

The 1D assumption is most seriously violated when impingement of droplets or the flame on the wall occurs. In large truck engines spray impingement is not common. Despite the flame reaching the boundary layers up to a quench distance inducing velocities due to burned gas expansion, the interaction period is very short.

**3. Constant fluid properties:** In the thin thermal boundary layer the temperature distribution exhibits steep gradients resulting from compression and combustion of the in-cylinder gases and cooling of the wall. Variations of temperature close to the wall can occur over the engine cycle of more than 2000 K and are strongest near TDC [167]. As a consequence, those fluid thermophysical properties that depend strongly on local temperature change considerably during this stage. Kays *et al.* [223] give the following dependencies for air in the range of $600\,\mathrm{K} < T < 1600\,\mathrm{K}$:

$$\rho \sim T^{-1} \qquad \mu \sim T^{0.7} \qquad c_p \sim T^{0.19} \qquad k = \frac{\mu c_p}{\sigma_e} \sim T^{0.85} \qquad \sigma_e \sim T^{0.04}$$

The assumptions of constant thermophysical properties in the boundary layers obviously are particularly in error with respect to density and viscosity. Hence, the assumption will produce significant prediction errors both in the velocity and temperature profiles.

**4. Constant turbulent Prandtl number $\sigma_{e,t}$:** The turbulent Prandtl number is defined as the ratio of momentum to thermal eddy diffusivity and varies according to the flow characteristics. Measurements suggest that the value of $\sigma_{e,t}$ increases considerably towards the wall, while being approximately constant in the outer layer [181, 416]. By contrast, DNS calculations predict no appreciable rise in

turbulent Prandtl number towards the wall with a wall-value of about 1.1 [221, 233], as seen in Figure 3.25. From the experimental and DNS results it can be concluded that for the region in which the wall functions are applied to (i.e. $30 < y^+ < 100$) $\sigma_{e,t}$ remains approximately constant. Thus the overall error of a constant $\sigma_{e,t}$ on turbulent heat transfer is small.

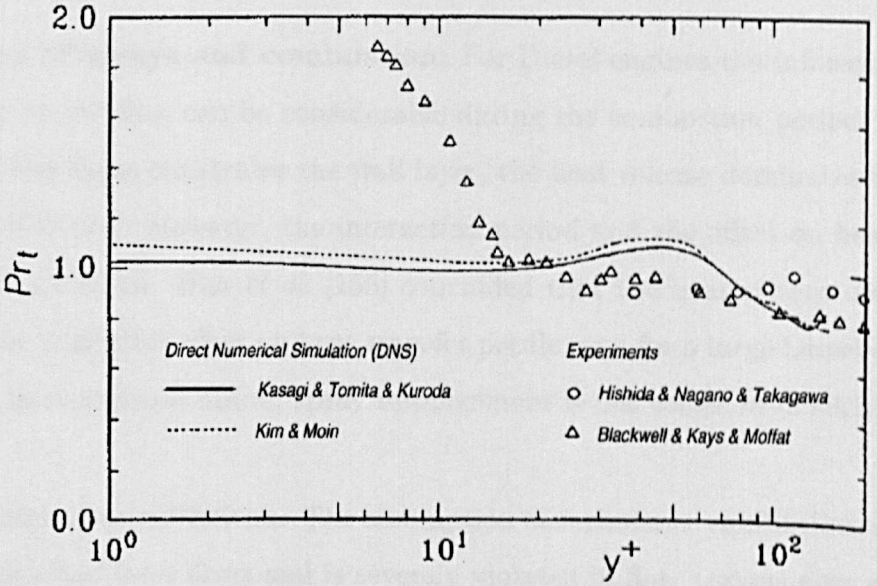



**Figure 3.25:** Measured and calculated turbulent Prandtl number distribution in thermal boundary layer (from [221]). $Pr_t$ is turbulent Prandtl number. Data taken from [48, 181, 221, 233].

**5. Pressure gradients:** In complex flows that exhibit recirculation, stagnation or separation regions streamwise pressure gradients along the walls can be large. Neglecting those gradients could cause large errors in predicted wall shear stress and heat flux [257]. However, these complex flow structures in engines are mainly present during the induction period and decay rapidly towards TDC, promoted by swirl [167, 371]. In addition, they are confined to relatively small portions of the chamber walls and occur when heat transfer levels are low. Flame-induced velocities can cause strong local pressure gradients. However, as mentioned above, the flame/wall interaction time span is very short, resulting in small effects with respect to overall friction loss and heat transfer. Attempts have been made to include pressure gradient effects on wall functions as outlined in Section 2.3.5.3. How-

ever, this practice would not give appreciable improvements in accuracy, because it has been demonstrated that the high Reynolds number $k-\varepsilon$ turbulence model itself cannot resolve the turbulence characteristics of flows with large pressure gradients [166, 424, 443]. Hence, it is concluded that the overall effect of prediction errors when neglecting pressure gradients is acceptable.

**6. Effects of sprays and combustion:** For Diesel engines the influence of spray and flame on the flow can be considerable during the combustion period. In particular once the flame penetrates the wall layer, the heat release dominates the energy balance [320, 474]. However, the interaction period and the effect on heat transfer coefficient are small. Han *et al.* [155] concluded that the heat release due to combustion has negligible effect on heat transfer predictions for a large Diesel engine. In addition, as mentioned above, spray impingement is not common in such engines.

**7. Turbulence equilibrium:** The assumption of turbulence equilibrium is valid for simple boundary layer flows and is severely violated in flow regions near separation and reattachment [213, 223]. As outlined for the assumption of pressure gradients this situation occurs mainly during the induction period and such regions are usually confined to a comparatively small section of the chamber wall. In addition, the turbulent boundary layer generally tends to approach equilibrium rapidly [223]. To obtain improved accuracy, the full boundary layer turbulence equations would have to be solved. However, this would significantly increase the computational overheads and such approaches have not sufficiently been validated for engine flows [143, 256].

## Conclusion

The present order of magnitude analysis of the boundary layer momentum and enthalpy equations concludes that the turbulent diffusion processes clearly dominate the transport of momentum and heat in the turbulent boundary layers. Seven major assumptions for the derivation of the standard wall function approach were

examined. A quasi-steady assumption was concluded to give sufficiently accurate predictions. For the assumptions of one-dimensionality, pressure gradients and turbulence equilibrium it was argued that the effect of the prediction errors were acceptable for the present study. Spray effects were estimated to be negligible, since in truck engines spray/wall interaction is not common. The effect of combustion in the thermal boundary layer on heat transfer was concluded to remain small due to the relatively short interaction period. The assumption of constant thermophysical fluid properties was found to be unacceptable. In particular for the operating conditions envisaged for the present application, large gradients of temperature across the boundary layer are expected to significantly influence the wall shear force and heat flux via the thermophysical properties. A constant turbulent Prandtl number across the region, where the wall functions are employed, was found to be justified. Based on the present findings a modified wall function approach will be derived next.

#### 3.8.1.3 Modified wall function approach

In this section the derivation of the modified near-wall approach of Angelberger *et al.* [13] is reconstructed via a one-dimensional Couette flow analysis in the same way as for the standard functions, apart from allowing for variable transport properties.

##### Velocity and temperature profiles

A new non-dimensional distance $\eta^+$ is introduced to allow for variable viscosity, thus:

$$d\eta^+ = \frac{\nu_W}{\nu} dy^+ \quad ; \quad y^+ = \frac{u_\tau y}{\nu_W} \tag{3.213}$$

where the friction velocity is defined as $u_\tau = \sqrt{\frac{\tau_W}{\rho_W}}$. The kinematic viscosity, defined as $\nu = \frac{\mu}{\rho}$, can be expressed in terms of temperature via the following dependences of density and molecular viscosity on the latter, taken from the ideal gas law and [167, 223]:

$$\frac{\mu}{\mu_W} = \left(\frac{T}{T_W}\right)^{0.7} \tag{3.214}$$

$$\frac{\rho}{\rho_W} = \left(\frac{T_W}{T}\right) \tag{3.215}$$

New non-dimensional forms for velocity, $\psi^+$, and temperature, $\Theta^+$, are also introduced,

$$d\psi^+ = \rho^+ du^+ \tag{3.216}$$

$$d\Theta^+ = \rho^+ dT^+ \tag{3.217}$$

to include allowance for density variations. Here $\rho^+ = \frac{\rho}{\rho_W}$. The transport equations for mean momentum and energy, Eqs. (3.190a) and (3.190b), take the form:

$$(1+\nu^+)\frac{d\psi^+}{d\eta^+} = 1 \tag{3.218a}$$

$$\left(\frac{1}{\sigma_e} + \frac{\nu^+}{\sigma_{e,t}}\right)\frac{d\Theta^+}{d\eta^+} = 1 \tag{3.218b}$$

These equations can be integrated analytically, similar as in the case of the standard wall functions, when modelling the turbulent transport via a mixing length model† and assuming a constant turbulent Prandtl number. The following integration limits are applied, obtained from the no-slip condition at the wall and when setting the gas-side temperature at the wall to the wall temperature:

$$\psi^+\Big|_{\eta^+=0} = 0$$

$$\Theta^+\Big|_{\eta^+=0} = 0$$

The results of the integration are:

Viscous sublayer:

$$\eta^+ \le \eta_c^+ \Rightarrow \begin{cases} \psi^+ = \eta^+ \\ \Theta^+ = \sigma_e \psi^+ \end{cases} \tag{3.219a}$$

Inertial sublayer:

$$\eta^+ > \eta_c^+ \Rightarrow \begin{cases} \psi^+ = \frac{1}{\kappa}\ln(E\eta^+) \\ \Theta^+ = \sigma_{e,t}\left[\psi^+ + P\left(\frac{\sigma_e}{\sigma_{e,t}}\right)\right] \end{cases} \tag{3.219b}$$

†This approach follows the practice of Angelberger *et al.* [13] and is further discussed below.

where $\eta_c^+$ is taken to be identical to $y_c^+$[†] and the model coefficients are provided in Table 3.19. The above equations can be transformed to ones for velocity and temperature by integrating Eqs. (3.216) and (3.217) from the wall to an arbitrary location within the boundary layer, to give the relation:

$$\psi^+ = \rho^+ u^+ \tag{3.220}$$

$$\Theta^+ = \frac{\rho_W u_\tau c_p T_W}{q_W} \ln \frac{T_W}{T} \tag{3.221}$$

By comparing Eqs. (3.199) with (3.219) it is seen that the modified wall laws resemble the standard formulation. However, the dimensionless temperature $\Theta^+$ in Eq. (3.221), which reflects the density variations in the thermal boundary layer, involves the logarithm of the temperature ratio of the wall to the gas rather than the arithmetic difference between both as in the definition for $T^+$ in Eq. (3.198). Examining Eqs. (3.213), (3.214) and (3.215), it is seen that for increasing temperatures with wall-normal distance the kinematic viscosity $\nu$ increases, producing lower $\eta^+$ values. Since the value of $y^+$ is fixed by the properties at the wall, this physically means that the viscous sublayer thickness is increased with a variable viscosity in comparison to the quasi-isothermal case. The impact of variable density and viscosity on shear stress and heat flux will be discussed below.

To avoid the singularity in the velocity and temperature profiles in the inertial layer when $\tau_W \to 0$, the non-dimensional distance is redefined as for the standard wall function approach by replacing $\tau_W$ from Eq. (3.226) in Eq. (3.213) to give:

$$\eta^+ = \frac{C_\mu^{1/4} \sqrt{k} y}{\nu} \tag{3.222}$$

where $k$ is obtained from Eq. (3.226).

### Wall shear stress and heat flux profiles

The wall shear stress and wall heat flux are obtained by fitting the velocity and

[†]This transition value is chosen arbitrarily. Commonly it is determined from experiments. However, no measurements are available for engine flows to guide the choice of $\eta_c^+$ [155].

temperature profiles to Eqs. (3.220) and (3.221):

$$\boldsymbol{\tau}_W = F_W^{\mathbf{u}} \mathbf{u}^* \tag{3.223}$$

$$\mathbf{q}_W = \mathbf{n} F_W^h c_p T \ln\left(\frac{T_W}{T}\right) = \mathbf{n} F_W^h (h_W - h) \tag{3.224}$$

where $F_W^{\mathbf{u}}$ and $F_W^h$ are given by:

Viscous sublayer:

$$\eta^+ \leq \eta_c^+ \Rightarrow \begin{cases} F_W^{\mathbf{u}} = -\dfrac{\rho\nu}{y} \\ F_W^h = -\dfrac{\rho\nu}{\sigma_e y} \end{cases} \tag{3.225a}$$

Inertial sublayer:

$$\eta^+ > \eta_c^+ \Rightarrow \begin{cases} F_W^{\mathbf{u}} = -\dfrac{\rho\nu}{y} \dfrac{\eta^+}{\frac{1}{\kappa}\ln\left(E\eta^+\right)} \\ F_W^h = -\dfrac{\rho\nu}{\sigma_{e,t} y} \dfrac{\eta^+}{\frac{1}{\kappa}\ln\left(E\eta^+\right) + P\left(\frac{\sigma_e}{\sigma_{e,t}}\right)} \end{cases} \tag{3.225b}$$

where $\rho$ and $\nu$ are evaluated using the relations given in Eqs. (3.214) and (3.215).

When comparing Eqs. (3.202), (3.203), (3.223) and (3.224) together with the definition of the factors $F_W^{\mathbf{u}}$ and $F_W^h$, the influence of constant and variable density/viscosity, respectively, on shear stress and wall heat flux can be studied separately. In case of the non-isothermal assumption in the boundary layer the density decreases and the viscosity increases with increasing wall-normal distance. Thus a variable density would yield a lower shear stress and heat flux, whereas a variable viscosity would increase both quantities, compared to the case of constant thermophysical properties. Since the shear stress is closely linked to the turbulence parameters $k$ and $\varepsilon$, as seen from Eqs. (3.226) and (3.227), the turbulence field is similarly affected by the non-isothermal assumption. Furthermore the turbulence parameters in turn influence the velocity and temperature profiles via the dimensionless distance $\eta^+$, given in Eq. (3.222).

### Turbulence energy and dissipation rate profiles

The literature about the effects of variable transport properties in the boundary layer on turbulence quantities is limited, heuristic in nature and not very conclusive [62, 76, 366, 396]. Therefore the assumptions used for the standard wall function approach are also employed for the modified wall function method. It is assumed that turbulence equilibrium is sustained in the inertial layer, and this is enforced by setting the diffusion of $k$ in the boundary layer equation to zero. The turbulence length scale is set proportional to the distance from the wall. The turbulence kinetic energy and its dissipation rate are then obtained as:

$$k = C_\mu^{-\frac{1}{2}} \frac{\tau_W}{\rho_W} \tag{3.226}$$

$$\varepsilon = \frac{C_\mu^{3/4} k^{3/2}}{\kappa y} \tag{3.227}$$

## 3.8.2 Inflow and outflow boundaries

In IC engines, the gas flow to and from the cylinder during intake and exhaust strokes are governed by the inlet and exhaust valves. Inflow and outflow conditions for the mixture need to be specified. These can, in theory, be described in any cross-sectional area of the flow. The input data for the inflow and outflow boundaries are generally obtained from experiments.

### Pressure boundary

For engine flows it is customary to define the pressure boundary conditions in the intake or exhaust system sufficiently up- and downstream, respectively, where the flow field is close to uniform across the boundary cross-section [118]. According to the local pressure gradient the flow direction (i.e. in- or outflow) is determined. In case of inflow the histories of temperature, turbulence parameters and species concentrations at the boundary are to be specified [443]. The velocity magnitude and direction are then obtained from the local pressure gradient and when assuming

a zero velocity gradient along mesh lines that intersect the boundary plane. In case of outflow the distribution of flow variables on the boundary plane are extrapolated from upstream conditions, assuming zero gradients along the mesh lines intersecting this plane. The velocity magnitude and direction are obtained as for inflow conditions. This approach is used for the computation of the induction and compression stroke of the HPP engine, described in Section 5.3.

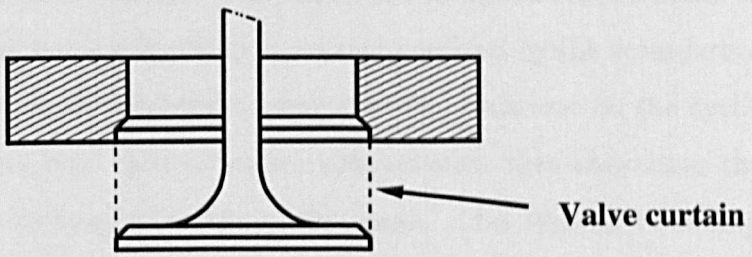



**Figure 3.26:** Schematic of valve region including the valve curtain.

### Valve flow

An alternative inlet and outlet boundary condition can be specified at the valve curtain, which is defined by the circumferential area of the fictitious cylinder formed by the valve head and its projection onto the cylinder head, as shown in Figure 3.26. The inflow and outflow conditions are specified for the following properties as a function of time:

- Gas velocity components.
- Gas pressure, temperature, turbulence parameters, i.e. $k$ and $\varepsilon$, and mixture composition.

The mass flux across the boundary is then obtained by the orifice equation. This approach is used for the simulation of the research engine, presented in Section 5.1.

## 3.8.3 Symmetry planes

If the engine flow is essentially symmetric to a plane in the cylinder, it is appropriate to reduce the computational domain by half. At symmetry planes the normal veloc-

ity component and the normal gradients of all flow variables vanish. This boundary condition is used for the Aachen pressure chamber, presented in Section 5.2.

### 3.8.4 Cyclic boundaries

If the flow repeats itself at a pair of geometrically identical planes in the cylinder, cyclic boundary conditions can be applied. This allows the computational domain to be reduced and the CFD solution involves only the sector confined by the boundaries. The magnitude of fluxes and flow variables at corresponding locations on the cyclic boundaries are equal, while vector quantities are rotated such that they have the same relative orientation with respect to the cyclic plane. This type of boundary condition is used for the HPP engine, described in Section 5.3.

## 3.9 Initial Conditions

In unsteady problems, initial conditions for all flow variables need to be specified in the solution domain. This is required due to the parabolic nature of the system equations with respect to time. Since the engine flow is periodic from cycle to cycle, the influence of initial conditions becomes less pronounced the more cycles are calculated. For practical engine simulations, however, considerations of computational time usually limit the number of computed cycles to one. Therefore adequate initial conditions become necessary which should be realistic and require thermodynamic consistency. They can be estimated from physical reasoning, previous experience, measurement data or specifications obtained from a phenomenological engine simulation tool.

Engine simulations usually start shortly before inlet valve opening (IVO), since during induction the in-cylinder flow is primarily governed by the incoming flow. Hence, the influence of the initial conditions on the flow solution becomes less pronounced. For the simulation of the HPP engine the residual gases from the previous

cycle have not been considered, since typically in Diesel engines their levels are very low due to the overall lean mixture [167].

## 3.10 Closure

This present chapter summarises the governing equations of the multiphase flow generated by the injection and burning of a liquid fuel in an engine. The mathematical description of the gas phase was assembled including constitutive relations such as the ideal gas equation of state, Newton's law of viscosity, Fourier's law of conductivity and Fick's law of diffusivity. A study for the appropriate EOS and thermophysical properties of the gas under the elevated pressure and temperature conditions has also been performed. It was found that under the expected range of operating conditions the ideal gas assumption is appropriate for the present study. Moreover the gas-phase thermophysical properties show a strong dependence on temperature, but small dependence on pressure.

The instantaneous gas-phase equations were averaged using the density-weighted (Favre) ensemble-averaging technique. To take into account the presence of the liquid phase, a macroscopic density was introduced in these ensemble-averaged equations in lieu of the microscopic density. Additional unknown terms arising due to the averaging procedure were modeled by the $k-\varepsilon$ turbulence model.

The mathematical description of the discrete phase was briefly introduced. The spray physics submodels used in the present study were specified, including atomisation, breakup, droplet-droplet and droplet-wall interaction. In addition, a study of liquid thermophysical properties at high temperatures and pressures and a simplified single droplet evaporation case were provided. It was found that at high temperatures, close to the critical temperature, the liquid thermophysical properties show a strong dependence on pressure. Moreover under these conditions real gas effects substantially influence the VLE, latent heat of vapourisation and evaporation rates. However, it was concluded that the majority of droplets are exposed to lower tem-

peratures and evaporate very fast such that in the present study only correlations are used which neglect pressure effects.

Diesel combustion-specific submodels were introduced to account for autoignition, combustion and pollutant formation (i.e. $NO_x$ and soot). Two combustion approaches were presented, of the eddy breakup and flamelet types.

Finally, boundary and initial conditions were defined to close the gas-phase equations. In specific the standard wall function approach was derived and the underlying assumptions were critically assessed, including an order of magnitude analysis of the importance of the various physical phenomena involved. The assumptions for the standard wall function approach were found to be acceptable, except for the assumption of constant thermophysical fluid properties across the boundary layer. A modified wall function approach was proposed based on the work of Angelberger *et al.* [13] which accounts for density and viscosity variations in the near-wall region. Besides, inflow and outflow boundaries were presented next to symmetry planes and cyclic boundaries.

The next chapter describes the discretisation practice applied for the governing equations. A solution algorithm for solving the discretised equation set is also provided.

# Chapter 4

# Numerical Approach

## 4.1 Introduction

The previous chapter has summarised the mathematical foundation of the current study, based on conservation equations for the gas and liquid phases. Additional mathematical models for Diesel autoignition, combustion and pollutant formation have been described along with turbulence equations and constitutive relations. All these equations including their boundary and initial conditions, form a closed system of non-linear, coupled differential equations that cannot be solved analytically. Thus, a numerical solution procedure must be employed.

The present numerical approach uses a discretisation method, the finite volume method, that approximates the continuous function of a dependent variable $\phi$ in a differential equation by a discrete function, defined at a finite number of locations in space and time.

The discretisation technique which is used in the present work is presented in Section 4.2; it results in a set of non-linear, coupled algebraic relations. The solution procedure for these algebraic equations is outlined in Section 4.3. This includes the solution sequence and algorithm for the linear algebraic equations, which arise from the discretisation. The convergence criteria for the iterative methods used are also

outlined. The closure in Section 4.4 concludes the chapter.

## 4.2 Discretisation Technique

### 4.2.1 Finite volume method

The FVM has enjoyed widespread success in the field of computational fluid dynamics. This is due to advantageous features compared to other discretisation techniques (see e.g. [118]) which comprise the enforcement of conservation laws on arbitrary grids of any complex geometrical shape [118].

#### 4.2.1.1 General concept

The discretisation is performed with respect to space and time. The computational domain is divided into a finite number of contiguous, non-overlapping control volumes (CVs) or cells, commonly of tetrahedral or hexahedral shape. In the present work, an unstructured mesh is used, based on hexahedrons. The collocated storage arrangement is used, in which all variables are located at nodes lying at the cell centres to reduce computational storage requirements and to simplify the numerical implementation [118, 331]. They are allowed to distort in time to account for the motion of boundaries to which they are attached. Temporal discretisation is also employed, in which the time domain is divided into a finite number of time intervals, also called *time-steps*.

The discretisation of the governing transport equations is based on approximations of each term by algebraic relations which approximate the variation of the dependent variables between neighbouring nodes in space and time. Via interpolation using these relations the cell face values of each dependent variable $\phi$ are obtained. The set of algebraic equations for each control volume forms a closed system, for which the number of unknown dependent variables is equal to the number

of available discretised equations. The accuracy of the numerical solution is dependent upon the spatial and temporal resolution, but can be increased evidently by reducing the sizes of the cells and time-steps.

Three main approximation schemes for the temporal discretisation have been proposed: the explicit, implicit and semi-implicit technique. Explicit differencing is known to suffer from a numerical time-step restriction due to stability and convergence problems. This is usually defined by the Courant-Friedrichs-Lewy condition $\mathrm{Co} \leq 1$ [79, 118]. Here the Courant number Co is defined as:

$$\mathrm{Co} = \frac{\mathbf{u}\Delta t}{\Delta x} \tag{4.1}$$

where $\Delta x$ refers to the cell size and $\Delta t$ is the time-step size. For a given mesh, this condition therefore dictates the maximum allowable time-step size such that stability is ensured. Semi-implicit differencing may yield oscillatory and hence physically unrealistic solutions [326]. Therefore the Euler implicit technique has been adopted in this study, which guarantees physically meaningful results and is not subject to stability- and convergence-imposed time-step limitations, but for accuracy reasons still requires that Co be not too large. More detail on various aspects of the FVM are found in [118, 325, 443].

#### 4.2.1.2 Notation

A typical cell arrangement and underlying notation are illustrated in Figure 4.1.

The letters $P$, $N$ and $NN$ refer to the considered cell node, a nearest neighbour and the neighbour of $N$ other than $P$, respectively. For the cell $P$, $\mathcal{S}_f^P$ is the cell face vector pointing outwards on cell face $f$. Thus, $f$ can take the values $\{\pm 1, \pm 2, \pm 3\}$, where $f$ and $-f$ designate pairs of opposite faces.

Eight vertices define each cell, whose positions are given by the space vector $\mathbf{r}_i$, $(i = 1, \ldots, 8)$, in the global Cartesian coordinate system. The position vectors $\mathbf{r}_P$

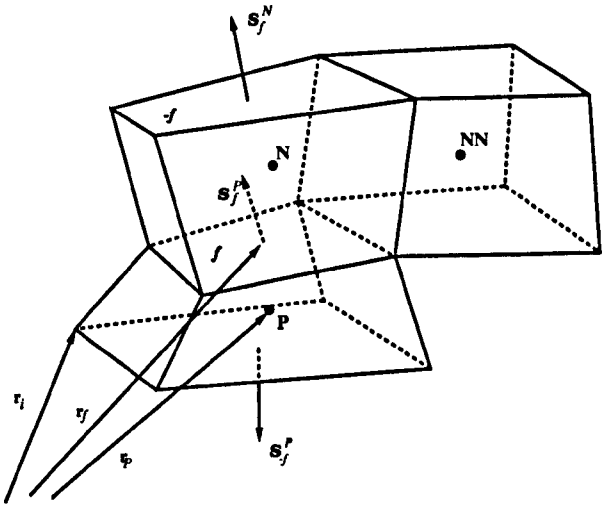



**Figure 4.1:** Cell notation in FVM.

and $\mathbf{r}_f$ refer to the nodal point $P$ at the cell centre and to the centre of the face $f$, respectively. These are respectively given as the arithmetic means of the position vectors of all cell face vertices, thus:

$$\mathbf{r}_P = \frac{1}{8} \sum_{\{i\}_P} \mathbf{r}_i \tag{4.2a}$$

$$\mathbf{r}_f = \frac{1}{4} \sum_{\{i\}_f} \mathbf{r}_i \tag{4.2b}$$

The cell face vector $\mathcal{S}_f^P$ is determined by the vector product of the two face diagonals and always points outwards. Furthermore the cell volume $V_P$ is assembled from the subvolumes of six pyramids whose bases are the respective cell faces and whose apexes coincide at the cell centre $P$, i.e.:

$$V_P = \frac{1}{3} \sum_{\{f\}_P} \mathcal{S}_f^P \cdot (\mathbf{r}_f - \mathbf{r}_P) \tag{4.3}$$

where $\sum_{\{f\}_P}$ indicates the summation over all six directions in cell $P$.

The estimation of the cell face values of dependent variables, $\phi$, and other gas properties such as density uses a spatial interpolation scheme as [443]:

$$\phi_f = \lambda_f^P \phi_P + \left(1 - \lambda_f^P\right) \phi_N \tag{4.4}$$

where $\phi_P$ and $\phi_N$ represent values of $\phi$ at cells $P$ and $N$, respectively, and $\lambda_f^P$ is a geometrical interpolation factor for cell $P$ in the direction $f$, defined by:

$$\lambda_f^P = \frac{d_f^N}{d_f^P + d_f^N} \tag{4.5a}$$

$$\lambda_f^P + \lambda_{-f}^N = 1 \tag{4.5b}$$

Here $d_f^P$ and $d_f^N$ are distances, defined in Figure 4.2.

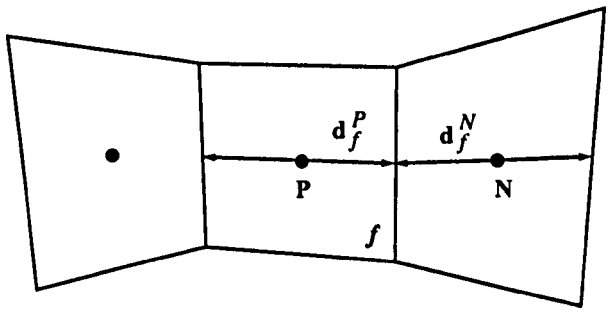



**Figure 4.2:** Interpolation factors for the estimation of cell face values.

#### 4.2.1.3 Gauss' divergence theorem

Gauss' divergence theorem relates the volume integral of the divergence of a vector to the sum of fluxes of the vector quantity over all surfaces of the volume. Thus for a vector field $\mathbf{u}$ it reads [118, 443]:

$$\int_V \nabla \cdot \mathbf{u}\, dV = \int_S d\mathcal{S} \cdot \mathbf{u} \tag{4.6a}$$

where $\mathcal{S}$ indicates the total surface of the volume $V$. Thus, for a typical cell:

$$\nabla \cdot \mathbf{u} \approx \frac{1}{V} \sum_{\{f\}} \mathcal{S}_f \cdot \mathbf{u}_f \tag{4.6b}$$

Applying Gauss' theorem to the gradient of an arbitrary scalar field $\phi$, the divergence and gradient of a vector field $\mathbf{u}$ and the divergence of a tensor field $\mathbf{T}$, considering Eq. (4.4), the following are obtained:

$$\begin{aligned}(\nabla\phi)_P &\approx (\mathcal{N}\phi)_P \\ &= \frac{1}{V_P} \sum_{\{f\}_P} \mathcal{S}_f^P \left[\lambda_f^P \phi_P + \left(1 - \lambda_f^P\right) \phi_N\right]\end{aligned} \tag{4.7a}$$

$$(\nabla\cdot\mathbf{u})_P \approx (\mathcal{N}\cdot\mathbf{u})_P = \frac{1}{V_P}\sum_{\{f\}_P} \mathcal{S}_f^P\cdot\left[\lambda_f^P\mathbf{u}_P + \left(1-\lambda_f^P\right)\mathbf{u}_N\right] \tag{4.7b}$$

$$(\nabla\mathbf{u})_P \approx (\mathcal{N}\mathbf{u})_P = \frac{1}{V_P}\sum_{\{f\}_P} \mathcal{S}_f^P\left[\lambda_f^P\mathbf{u}_P + \left(1-\lambda_f^P\right)\mathbf{u}_N\right] \tag{4.7c}$$

$$(\nabla\cdot\mathbf{T})_P \approx (\mathcal{N}\cdot\mathbf{T})_P = \frac{1}{V_P}\sum_{\{f\}_P} \mathcal{S}_f^P\cdot\left[\lambda_f^P\mathbf{T}_P + \left(1-\lambda_f^P\right)\mathbf{T}_N\right] \tag{4.7d}$$

### 4.2.2 Spatial and temporal discretisation

The general transport equation, Eq. (3.185), in integral form for the cell or control volume $V$ is expressed as:

$$\int_V \frac{\partial\rho\phi}{\partial t}\,dV + \int_V \nabla\cdot\rho\mathbf{u}\phi\,dV - \int_V \nabla\cdot\rho\Gamma_{\phi,eff}\nabla\phi\,dV = \int_V \left(S_\phi + S_\phi^d\right)\,dV \tag{4.8}$$

When applying Gauss' divergence theorem, Eq. (4.6a), this yields:

$$\int_V \frac{\partial\rho\phi}{\partial t}\,dV + \int_S d\mathcal{S}\cdot\rho\mathbf{u}\phi - \int_S d\mathcal{S}\cdot\rho\Gamma_{\phi,eff}\nabla\phi = \int_V \left(S_\phi + S_\phi^d\right)\,dV \tag{4.9}$$

In solution domains with moving boundaries and therefore moving meshes, the control volume must obey the *space conservation law*, which dictates, using Gauss' theorem [91, 118, 452]:

$$\frac{d}{dt}\int_V \rho\phi\,dV = \int_V \frac{\partial\rho\phi}{\partial t}\,dV + \int_S d\mathcal{S}\cdot\rho\,\mathbf{u}_b\,\phi \tag{4.10}$$

with $\mathbf{u}_b$ as the velocity of the boundary of the control volume. Substituting Eq. (4.10) into the general transport equation, Eq. (4.9), the conservation law in the Eulerian/Lagrangian reference frame is defined as:

$$\frac{d}{dt}\int_V \rho\phi\,dV + \int_S d\mathcal{S}\cdot(\rho\mathbf{u}_r\phi - \rho\Gamma_{\phi,eff}\nabla\phi) = \int_V \left(S_\phi + S_\phi^d\right)\,dV \tag{4.11}$$

Here $\mathbf{u}_r$ stands for the relative velocity between the local gas velocity $\mathbf{u}$ and the cell face velocity $\mathbf{u}_b$:

$$\mathbf{u}_r = \mathbf{u} - \mathbf{u}_b \tag{4.12}$$

In what follows, each term of the general transport equation will be discretised in turn.

#### 4.2.2.1 Unsteady term

For the discretisation of the unsteady term, it is assumed that [118]:

$$\int_{V_P} \rho\phi \, dV = (\rho\phi V)_P \approx (\rho V)_P \, \phi_P \tag{4.13}$$

The local rate of change of $\phi$ can be approximated by the mean change during the finite time-step $\Delta t$, such that the unsteady term in Eq. (4.11) becomes:

$$\frac{d}{dt}\int_{V_P} \rho\phi \, dV \approx \frac{(\rho V)_P \, \phi_P - (\rho V)_P^o \, \phi_P^o}{\Delta t} \tag{4.14}$$

where superscript '$o$' denotes the values of the *old* time-step.

#### 4.2.2.2 Convection/diffusion term

The total flux of $\phi$ through the overall cell surface $S_P$ is represented by the second term on the LHS in Eq. (4.11). It is expressed as the sum of the fluxes over all cell faces of cell $P$:

$$\int_{S_P} d\mathcal{S}\cdot(\rho\mathbf{u}_r\phi - \rho\Gamma_{\phi,eff}\nabla\phi) = \sum_{\{f\}_P}\int_{S_f} d\mathcal{S}\cdot(\rho\mathbf{u}_r\phi - \rho\Gamma_{\phi,eff}\nabla\phi) = \sum_{\{f\}_P} F_f \tag{4.15}$$

The total flux $F_f$ of $\phi$ through the face $f$ is approximated by the surface-averaged flux through the face and some representative average values of $\phi$ and $\nabla\phi$. The flux $F_f$ which falls on a boundary face is expressed by the boundary fluxes, specified in Section 4.2.4. Hence [118],

$$F_f \approx \mathcal{S}_f\cdot\left[(\rho\mathbf{u}_r\phi)_f - (\rho\Gamma_{\phi,eff}\nabla\phi)_f\right] \tag{4.16}$$

The convective flux of $\phi$ can be expressed as:

$$\begin{aligned}\mathcal{S}_f\cdot(\rho\mathbf{u}_r\phi)_f &\approx \mathcal{S}_f\cdot(\rho\mathbf{u}_r)_f\,\phi_f \\ &\approx C_f\left[w_f\phi_P + (1-w_f)\,\phi_N\right]\end{aligned} \tag{4.17}$$

where $C_f$ is the mass flux, defined by:

$$C_f = \mathcal{S}_f\cdot(\rho\mathbf{u}_r)_f \tag{4.18}$$

and $w_f$ represents a weighting factor defined by the choice of convective differencing scheme (see e.g. [77]).

The diffusion flux vector $(\rho\Gamma_{\phi,eff}\nabla\phi)_f$ is separated into the *normal diffusion*, $\mathbf{d}_f^n(\phi)$, and *cross diffusion*, $\mathbf{d}_f^c(\phi)$, components as [426]:

$$(\rho\Gamma_{\phi,eff}\nabla\phi)_f = \mathbf{d}_f^n(\phi) + \mathbf{d}_f^c(\phi) \tag{4.19}$$

The normal diffusion component considers only the contributions to the diffusive flux across the faces $+f$ and $-f$ and is approximated as:

$$\mathbf{d}_f^n(\phi) \approx \overline{\mathcal{S}_f}^P (\phi_N - \phi_P) \tag{4.20}$$

where

$$\overline{\mathcal{S}_f}^P = \lambda_f^P \left(1 - \lambda_f^P\right) \left[\left(\mathcal{S}_f^P - \mathcal{S}_{-f}^P\right) \left(\frac{\rho\Gamma_{\phi,eff}}{V}\right)_P + \left(\mathcal{S}_f^P + \mathcal{S}_f^N\right) \left(\frac{\rho\Gamma_{\phi,eff}}{V}\right)_N\right] \tag{4.21}$$

The above expression, Eq. (4.20), requires the values of $\phi$ at $P$ and its neighbour $N$ only, such that a fully implicit treatment of the normal diffusion term is applicable without an increase in the number of nodes involved. In the approximation of the cross diffusion term, however, the values of $\phi$ at selected neighbours $NN$ of $N$ are also needed, thus:

$$\begin{aligned}\mathbf{d}_f^c(\phi) \approx{}& \lambda_f^P \left(\frac{\rho\Gamma_{\phi,eff}}{V}\right)_P \sum_{\{l\neq\pm f\}_P} \mathcal{S}_l \left[\lambda_l\phi_P + (1-\lambda_l)\,\phi_N\right] \\ &+ \left(1 - \lambda_f^P\right) \left(\frac{\rho\Gamma_{\phi,eff}}{V}\right)_N \sum_{\{l\neq\pm f\}_N} \mathcal{S}_l \left[\lambda_l\phi_N + (1-\lambda_l)\,\phi_{NN}\right]\end{aligned} \tag{4.22}$$

An explicit solution technique is applied to circumvent this problem by using the currently available values of $\phi_{NN}$ in the cross diffusion term, Eq. (4.22). Combination of Eqs. (4.16) – (4.22), gives the total flux through the cell face $f$ as:

$$F_f \approx \left(\mathcal{C}_f w_f + \mathcal{D}_f^{\phi,n}\right)\phi_P - \left[\mathcal{C}_f\left(w_f - 1\right) + \mathcal{D}_f^{\phi,n}\right]\phi_N - \mathcal{D}_f^{\phi,c} \tag{4.23a}$$

where

$$\mathcal{D}_f^{\phi,n} = \mathcal{S}_f \cdot \overline{\mathcal{S}_f}^P \tag{4.23b}$$

$$\mathcal{D}_f^{\phi,c} = \mathcal{S}_f \cdot \mathbf{d}_f^c(\phi) \tag{4.23c}$$

#### 4.2.2.3 Source term

The source term in Eq. (4.11), $S_\phi$, may in general be a non-linear function of $\phi$, so linearisation is commonly performed to enhance numerical stability and give a diagonally dominant matrix [325, 443]. The form used is:

$$\int_{V_P} S_\phi \, dV \approx \left(S_U^\phi\right)_P + \left(S_P^\phi\right)_P \phi_P \tag{4.24}$$

Analogously, the spray source term is expressed by:

$$\int_{V_P} S_\phi^d \, dV \approx \left(S_U^{\phi,d}\right)_P + \left(S_P^{\phi,d}\right)_P \phi_P \tag{4.25}$$

To ensure numerical stability and physically realistic solutions, the coefficient $S_P^\phi$ must be negative. Note that $S_P$ is always a scalar, whereas, $S_U$ must be a tensor of the same order as $\phi$.

#### 4.2.2.4 Convective flux differencing scheme

The choice of the interpolation practice, the *differencing scheme*, is crucial to the successful application of the FVM to fluid dynamics problems [325]. The scheme must preserve fundamental characteristics such as physically realistic results, consistency between the discretised and differential equations, numerical stability and boundedness [38, 443].

A large number of schemes can be found in the literature (e.g. [118, 180, 325, 443]). In the present study the Monotone Advection and Reconstruction Scheme (MARS) [410] was adopted: it is a conservative, second-order-accurate differencing scheme. It proceeds in two separate steps: initially a set of monotone gradients are calculated based on a Total Variation Diminishing (TVD) scheme [118] which is second-order-accurate in space. This is referred to as reconstruction. The reconstructed cell face values of the dependent variables are then used to evaluate the face fluxes for all advected properties with the help of a monotone and bounded advection scheme.

### 4.2.3 Discretised general transport equations

Substitution of Eqs. (4.14), (4.23a), (4.24) and (4.25) into Eq. (4.11) yields:

$$\begin{aligned}&\frac{(\rho V)_P \phi_P - (\rho V)_P^o \phi_P^o}{\Delta t} \\ &+\sum_N \left\{ \left[ \mathcal{C}_f w_f + \mathcal{D}_f^{\phi,n} \right] \phi_P - \left[ \mathcal{C}_f (w_f - 1) + \mathcal{D}_f^{\phi,n} \right] \phi_N - \mathcal{D}_f^{\phi,c} \right\} \\ &= \left( S_u^\phi \right)_P + \left( S_P^\phi \right)_P \phi_P + \left( S_u^\phi \right)_P^{\mathrm{S}} + \left( S_u^{\phi,d} \right)_P + \left( S_P^{\phi,d} \right)_P \phi_P \end{aligned} \tag{4.26}$$

where the summation over $N$ refers to the values of the neighbour across the face $f$ and $\left(S_u^\phi\right)_P^{\mathrm{S}}$ is the source term which results from the explicit treatment of the cross diffusion term, Eq. (4.22) [77]. The mass conservation equation, Eq. (3.179), after discretisation reads:

$$\frac{(\rho V)_P}{\Delta t} = \frac{(\rho V)_P^o}{\Delta t} - \sum_N \mathcal{C}_f + \left( S_m^d \right)_P \tag{4.27}$$

Multiplication of the above equation by $\phi_P$ and insertion into Eq. (4.26) gives:

$$\begin{aligned}&\frac{(\rho V)_P^o \phi_P - (\rho V)_P^o \phi_P^o}{\Delta t} \\ &+\sum_N \left\{ \left[ \mathcal{C}_f (w_f - 1) + \mathcal{D}_f^{\phi,n} \right] \phi_P - \left[ \mathcal{C}_f (w_f - 1) + \mathcal{D}_f^{\phi,n} \right] \phi_N - \mathcal{D}_f^{\phi,c} \right\} \\ &= \left( S_u^\phi \right)_P + \left( S_P^\phi \right)_P \phi_P + \left( S_u^\phi \right)_P^{\mathrm{S}} + \left( S_u^{\phi,d} \right)_P + \left( S_P^{\phi,d} \right)_P \phi_P - \left( S_m^d \right)_P \phi_P \end{aligned} \tag{4.28}$$

Equations of the above type can be assembled for all $N_c$ cells in the solution domain, resulting in a system of $N_c$ non-linear algebraic equations. These are generally expressed in compact form as [118, 443]:

$$\mathcal{A}_P^\phi \phi_P = \sum_N \mathcal{A}_N^\phi \phi_N + b_P^\phi \quad ; \quad P = 1, \ldots, N_c \tag{4.29a}$$

where $\mathcal{A}_P^\phi$ and $\mathcal{A}_N^\phi$ stand for the diagonal and off-diagonal coefficients of the system, respectively, and $b_P^\phi$ is the source term, given by:

$$\mathcal{A}_P^\phi = \sum_N \mathcal{A}_N^\phi + \frac{(\rho V)_P^o}{\Delta t} - \left( S_P^\phi \right)_P - \left( S_P^{\phi,d} \right)_P + \left( S_m^d \right)_P \tag{4.29b}$$

$$\mathcal{A}_N^\phi = \left[ \mathcal{C}_f (w_f - 1) + \mathcal{D}_f^{\phi,n} \right] \tag{4.29c}$$

$$b_P^\phi = \frac{(\rho V)_P^o}{\Delta t} \phi_P^o + \sum_N \mathcal{D}_f^{\phi,c} + \left( S_u^\phi \right)_P + \left( S_u^\phi \right)_P^{\mathrm{S}} + \left( S_u^{\phi,d} \right)_P \tag{4.29d}$$

Eq. (4.29a) can be recast in matrix form as [118]:

$$\mathbf{A}^{\phi}\boldsymbol{\phi} = \mathbf{b}^{\phi} \tag{4.30}$$

where $\mathbf{A}^{\phi}$ is an $N_c \times N_c$ sparse and in general unbanded coefficient matrix and $\boldsymbol{\phi}$ and $\mathbf{b}^{\phi}$ are the column vectors of the unknowns and the source, respectively.

The full expressions for the individual discretised governing equations for both gas phase and liquid phase are found elsewhere [77, 246] and will not be repeated here.

### 4.2.4 Boundary conditions

The discretised source terms appearing in the above governing equations are representative for internal cells only. For cells adjacent to the boundary a modified treatment is necessary. The boundary fluxes $F^b$ are imposed directly on the boundary faces and replace the convection/diffusion fluxes $F_f$ for that face, given in Eq. (4.16).

Two types of boundary conditions can be distinguished:

1. *Dirichlet-type boundary condition:* The value of the dependent variable is given, such that the boundary face fluxes are evaluated from these values and those at the nodes adjacent to the boundary.

2. *Neumann-type boundary condition:* The fluxes of the dependent variable are given, such that they are imposed directly on the cell face adjacent to the boundary.

In what follows, the practices for each boundary type are outlined in turn.

#### 4.2.4.1 Wall boundaries

The different wall boundary conditions presented in Section 3.8 require separate implementation as given below.

### Velocity

Combining Eqs. (3.188) and (3.202) the wall shear stress in tangential direction with respect to the wall creates a boundary flux defined by:

$$(\mathbf{F}^{\mathbf{u}})_P^b = -(F_W^{\mathbf{u}})_P \left\{ \mathbf{u}_P - \mathbf{u}_W - \left[ (\mathbf{u}_P - \mathbf{u}_W) \cdot \frac{\mathcal{S}_b}{|\mathcal{S}_b|^2} \mathcal{S}_b \right] \right\} |\mathcal{S}_b| \tag{4.31}$$

where $\mathcal{S}_b$ denotes the cell face vector at the boundary.

### Energy

The wall heat flux, Eq. (3.203), is defined via the boundary flux as:

$$\begin{aligned} (F^e)_P^b &= \mathcal{S}_b \cdot \mathbf{q}_W \\ &= |\mathcal{S}_b| \left(F_W^h\right)_P (h_W - h_P) \end{aligned} \tag{4.32}$$

In case of an adiabatic wall, $(F^e)_P^b$ is set to zero.

### Turbulence parameters

In the turbulence kinetic energy equation, Eq. (3.183), the average turbulence energy dissipation rate over the control volume for a wall cell is evaluated using the wall functions. Hence,

$$\varepsilon_P^k = \frac{1}{V_P} \int_{V_P} \varepsilon \, dV \approx C_\mu^{3/4} k_P^{3/2} \frac{u_P^+}{y_P} \tag{4.33}$$

where $u_P^+$ is given by Eq. (3.199). In case of the modified wall function approach $u_P^+$ is replaced by $\psi_P^+$, which is defined in Eq. (3.219). Furthermore the generation term for turbulence kinetic energy is affected by the wall shear stress which requires adequate modelling. According to Eqs. (3.191) and (3.205) the generation rate in the cell adjacent to the wall, $(G_W)_P$, is defined for the control volume $V_P$ by:

$$(G_W)_P = \int_{V_P} \tau_W \frac{\partial u_P^*}{\partial y} \, dV \tag{4.34}$$

Evaluating $\tau_W$ from Eq. (3.202) and inserting in the above formula using an approximation [246], gives:

$$(G_W)_P \approx -\frac{F_W^{\mathbf{u}}}{y_P} \mathbf{u}_P^* \cdot \mathbf{u}_P^* V_P \tag{4.35}$$

The diffusion flux of $k$ for the wall cells is assumed to be zero [259]. Hence,

$$\left(F^k\right)_P^b = 0 \tag{4.36}$$

The dissipation rate in the near-wall cells using Eq. (3.210) reads:

$$\varepsilon_P = \frac{C_\mu^{3/4} k_P^{3/2}}{\kappa y_P} \tag{4.37}$$

In order to enforce this value at the boundary, the boundary flux is specified as:

$$(F^\varepsilon)_P^b = L\varepsilon_P - L\frac{C_\mu^{3/4} k_P^{3/2}}{\kappa y_P} \tag{4.38}$$

where $L \gg \varepsilon_P$. In this study following [77, 443] a value of $L = 10^{30}$ is used.

#### 4.2.4.2 Inflow and outflow surfaces

It is assumed that the mass flow rate $\dot{m}_b$ through the inflow or outflow boundaries is known. Thus for cells adjacent to such boundaries the boundary fluxes are given as:

Inflow ($\dot{m}_b \leq 0$):

$$\left(F^\phi\right)_P^b = \dot{m}_b(\phi_b - \phi_P) \tag{4.39a}$$

Outflow ($\dot{m}_b > 0$):

$$\left(F^\phi\right)_P^b = 0 \tag{4.39b}$$

where $\phi = Y_\psi$, $\mathbf{u}$, $e$, $k$, $\varepsilon$ and $\phi_b$ is the value of $\phi$ at the cell face $b$.

#### 4.2.4.3 Symmetry planes

The fluxes at symmetry planes are zero such that the boundary fluxes for all variables $\phi = Y_\psi$, $\mathbf{u}$, $e$, $k$, $\varepsilon$ vanish:

$$\left(F^\phi\right)_P^b = 0 \tag{4.40}$$

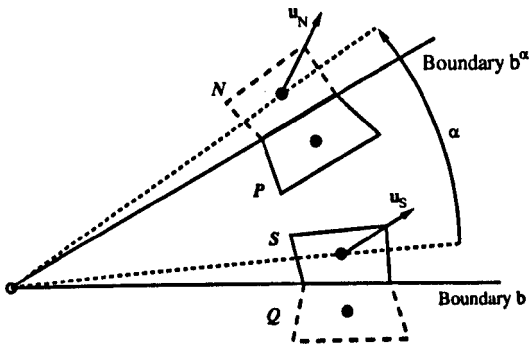



**Figure 4.3:** Schematic of cyclic boundary.

#### 4.2.4.4 Cyclic boundaries

A schematic of the cyclic boundary is given in Figure 4.3. Cell $P$ at the boundary is treated as a regular cell, when a fictitious cell $N$ is added as its neighbour across the boundary $b^\alpha$. $N$ then contains identical scalar properties as cell $S$ and gas velocities that are obtained from velocities in $S$, rotated by the angle $\alpha$. Thus for $\phi = Y_\psi$, $e$, $k$, $\varepsilon$:

$$\phi_N = \phi_S \tag{4.41}$$

$$\mathbf{u}_N = \mathbf{R}^\alpha \cdot \mathbf{u}_S \tag{4.42}$$

where $\mathbf{R}^\alpha$ is a rotation matrix. Similarly the cell $S$ is treated, taking a ficticious cell $Q$ that has the same scalar properties as cell $P$, while the gas velocities are equal to those in cell $P$ rotated by the angle $-\alpha$.

## 4.3 Solution Procedure

### 4.3.1 General concept

The solution of the system of algebraic equations, derived in the previous sections, are based on a solution sequence that is characterised by two main stages. First the governing equations are solved in a predictor-corrector sequence, including spray and combustion equations. Then turbulence parameters are calculated together

with droplet/droplet interactions and pollutant formation.

The core of the solution algorithm is based on the non-iterative PISO (Pressure Implicit with Splitting of Operators) algorithm of Issa [199] which has been extended to include spray and combustion processes [410]. The PISO algorithm uses an operator splitting technique to temporarily decouple the flow equations from each other, to allow sequential solution. These equations are linearised via the assumption that their coefficients, obtained from the currently available values of the relevant properties, are constant. This leads to an initial approximation of all dependent variables in the predictor stage. Thereafter a corrector sequence is applied by taking into account the coupling between the equations. This results in updated coefficients for each governing equation. Herein mass conservation is enforced by solving a pressure correction equation that is generated by combining the continuity and momentum equations. The corrector sequence is repeatedly performed until the specified convergence criteria are satisfied.

The solver for the system of algebraic equations is based on the conjugate gradient method with pre-conditioning and respective convergence criteria. It is briefly described below.

### 4.3.2 Solution sequence

The solution sequence for a typical engine calculation is summarised in the flow chart in Figure 4.4. It includes the following blocks:

1. **Initialisation:** All dependent variables at the beginning of the calculation, $t = t_0$, are set to their initial values.

2. **Mesh motion:** The vertices of the mesh are moved in a prescribed fashion to account for piston/valve motion. Removal or addition of cell layers occurs at

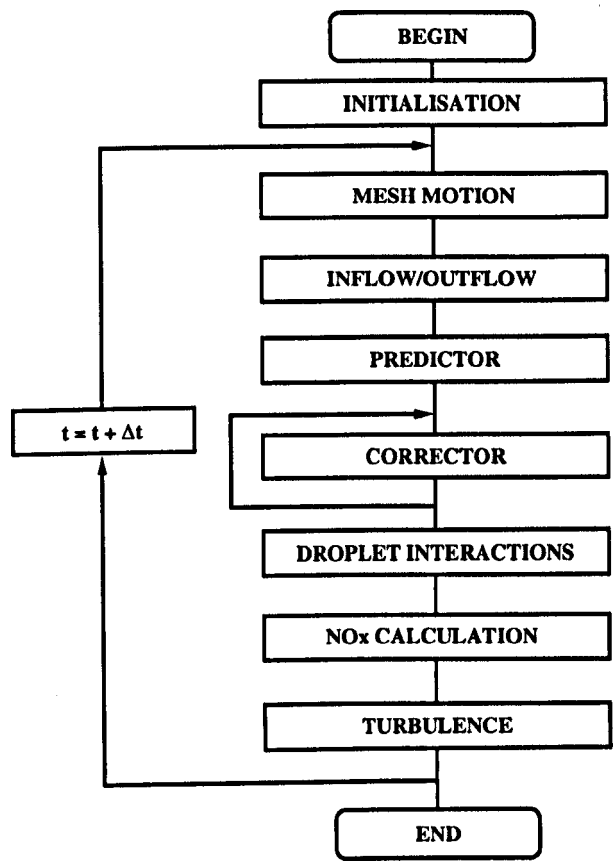



**Figure 4.4:** Flow chart of numerical solution algorithm.

predefined times to avoid extreme values of aspect ratio. Properties related to the mesh, such as cell volumes, cell face area vectors and spatial interpolation factors are evaluated.

3. **Inflow/Outflow:** The inflow/outflow mass and energy fluxes across the respective boundaries are calculated from the boundary conditions. All the flow properties at the inflow/outflow boundaries, i.e. $\mathbf{u}$, $p$, $\rho$, $T$, $Y_\psi$, $k$ and $\epsilon$, are set according to the input data.

4. **Predictor:** The predictor step incorporates both the spray and gas predictor. In the spray predictor, the spray equations are solved using temporal subcycling, resulting in the void fraction field, $\vartheta^{(1)}$, and source terms, which describe the spray contribution to the gas phase. Here, the superscript '(1)' denotes values updated in the predictor step. During the spray predictor phase the gas field properties are kept unaltered. In the gas predictor, initially the mass

fluxes and density, $\rho^{(1)}$, are updated, taking into account the source terms due to boundary fluxes and spray source terms. Moreover the equations for the chemical model, i.e. autoignition or combustion, are solved, to obtain source terms for the chemical species mass fraction and the energy. Then the coefficient matrices of the conservation equations for the chemical species mass fraction and energy are assembled and solved implicitly. The results of the spray predictor and chemical model are considered, so that $Y_\psi^{(1)}$ and $e^{(1)}$ are obtained. In addition, the pressure is evaluated, taking into account the presence of the liquid phase, yielding $p^{(1)}$. Based on the currently available values of pressure, density, mass fluxes and turbulence parameters, the velocity field $\mathbf{u}^{(1)}$ is determined.

5. **Corrector:** Mass conservation is enforced by solving iteratively the pressure correction equation. The spray contributions to the gas phase are corrected and the pressure field is evaluated using the pressure correction. Thereafter new mass fluxes and densities $\rho^{(2)}$ are calculated to estimate the gas velocities $\mathbf{u}^{(2)}$. Finally the chemical species mass fraction and energy equations are solved to give $Y_\psi^{(2)}$ and $e^{(2)}$. The local pressure is then updated as in the predictor step to account for the compression provoked by the liquid phase, yielding $p^{(2)}$. The corrector sequence is repeated until the convergence criteria given in Section 4.3.3.1 are met.

6. **Droplet interactions:** The droplet/droplet interactions are calculated in this step. While the gas-phase properties remain unaltered, the liquid-phase properties are adjusted.

7. **$NO_x$ calculation:** In the case of the EBU-type combustion model the equations for the $NO_x$ mechanism are solved to yield source terms for the relevant species transport equation. The solution of the transport equation for $NO_x$ finally gives the $NO_x$ mass fraction. During this step it is assumed that the gas-phase properties are not affected by the $NO_x$ formation, since the concentration of nitric oxides is very low compared to other species and the

contribution to the system's energy change is negligible [97, 352].

8. **Turbulence:** At this stage all field variables satisfy the governing equations apart from the turbulence parameters. The $k$ and $\varepsilon$ equations are solved within a separate predictor-corrector sequence. Thereby the influence of spray on turbulence parameters is also accounted for.

After completion of the solution sequence, the numerical solution of the governing equations is found which are then used as initial values of the next time-step. The solution sequence is repeated until the specified total number of simulation time-steps is reached.

### 4.3.3 Solution of linear algebraic equations

For the simultaneous solution of a system of linear algebraic equations many different methods have been proposed in the literature (see e.g. [118, 382, 443]). The choice between methods is based on the characteristics of the coefficient matrix $\mathbf{A}^{\phi}$ in Eq. (4.30). In this study two variants of the same solver type are used, which are briefly introduced.

#### 4.3.3.1 Partial differential equations

**Conjugate gradient method**

The conjugate gradient (CG) method was proposed by Hestenes and Stiefel [164] for the solution of a symmetric system of $N_{CG}$ linear equations. The technique starts with an arbitrary initial solution and is capable to converge to the *exact* solution in at most $N_{CG}$ iterations [118, 134]. Many extensions to the CG method have been developed to make them applicable to asymmetric systems [118, 357, 382]. In the present study the bi-conjugate gradient (BiCG) method of Fletcher [120] is employed to solve all transport equations except for the pressure correction equation. The BiCG technique is reported to be able to handle the system of linear equations

of a variety of flow problems and is therefore robust [118].

In a CFD calculation, $N_{CG}$ is typically of the order of $10^4 - 10^5$ such that the number of required iterations is too large and the solution technique becomes impractical. To render the solver more efficient, while maintaining its characteristics, *pre-conditioning* is used. It can be shown that the convergence rate depends on the *spectral condition number*, which is the ratio of the largest to the smallest eigenvalue, and the dispersion of the eigenvalues in the matrix $\mathbf{A}^{\phi}$ [118]. Thus, by reducing the condition number, the convergence rate increases. Pre-conditioning is usually achieved by transforming an asymmetric problem to a symmetric one. As a consequence, the new linear system possesses a smaller condition number, resulting in faster convergence. In the present study diagonal pre-conditioning was used. Further details of CG-type solvers and their variants are found in [118, 134, 350, 382, 438].

The pressure correction equation, which is symmetric, is solved by a variant of the CG method (ICCG), which uses pre-conditioning via incomplete Cholesky decomposition [228]. For more detail, the reader is referred to [118, 268, 426].

### Convergence criteria

In non-linear coupled systems of equations it is customary to solve the system sequentially. Thus for each equation in the PISO predictor-corrector sequence only a single unknown is calculated while the other variables are fixed to the currently available values. In this manner all equations are solved first before the cycle is repeated until the equations are satisfied to a predefined tolerance. This procedure is necessary to resolve the non-linearities in the system. Two types of iterations are therefore distinguished: inner iterations and outer iterations. While the inner iterations are performed on individual equations within the PISO loop, the outer iterations refer to the correction cycles to satisfy the entire equation set. For each type of iteration a different convergence criterion applies.

(a) *Inner iteration*

In the present study the convergence criterion of the inner iteration is satisfied, if the normalised sum of the absolute residual over all cells, $R^{\phi}$, with respect to the normalisation factor, $R_n^{\phi}$, is below a specified level $\lambda$ from its initial value at the current time-step:

$$\frac{R^{\phi}}{R_n^{\phi}} < \lambda \tag{4.43}$$

Here the absolute residual is given by:

$$R^{\phi} = \sum_{P=1}^{N_c} |R_P^{\phi}| \tag{4.44}$$

where

$$R_P^{\phi} = \sum_N \mathcal{A}_N^{\phi}\phi_N + b_P^{\phi} - \mathcal{A}_P^{\phi}\phi_P \tag{4.45}$$

The normalisation factors and the respective threshold for the residuals of the transport equation are listed in Table 4.1. As default the normalisation factor is based on the inflow rate. Once pressure boundaries are used, the factor is dynamically adjusted at each iteration, reflecting the variation in the incoming mass flow.

(b) *Outer iteration*

The convergence criteria in the PISO iteration loops are normalised with respect to the absolute residual sum in the pressure correction equation at the beginning of each corrector step. Convergence is reached in the $k^{th}$ corrector iteration, when the following relation holds true:

$$\frac{\left(R^{p^*}\right)^{(k)}}{R_n^{p^*}} < \lambda_c \tag{4.46}$$

where $p^*$ designates the pressure correction and the tolerance is set to $\lambda_c = 0.15$.

#### 4.3.3.2 Ordinary differential equations

ODEs used in the present study to incorporate chemical kinetics mechanisms (e.g. autoignition) are known to be stiff [249]. A stiff differential equation generally involves an exponential term, such as $Ce^{bx}$ with $b > 0$, where $C$ is related to the

| $\phi$ | $R_n^\phi$ | $\lambda$ |
|---|---|---|
| u | $\sum_{in} \dot{m}_i \sqrt{\overline{u}_i^2 + \overline{v}_i^2 + \overline{w}_i^2}$ | 0.01 |
| $p$ | $\sum_{in} \dot{m}_i$ | 0.001 |
| $e$ | $\max\{(e_{in} - e_{ref}), (e_{out} - e_{ref})\}$ | 0.01 |
| $Y_\psi$ | $\max\left\{\sum_{in} \dot{m}_i Y_\psi, \sum_{out} \dot{m}_i Y_\psi\right\}$ | 0.01 |
| $k$ | $\sum_{in} \dot{m}_i \sqrt{\overline{u}_i^2 + \overline{v}_i^2 + \overline{w}_i^2}$ | 0.01 |
| $\varepsilon$ | $\dfrac{\sum_{in} \dot{m}_i \sqrt{\overline{u}_i^2 + \overline{v}_i^2 + \overline{w}_i^2}}{L/v_{nom}}$ | 0.01 |

In the above:

| | | |
|---|---|---|
| $\dot{m}$ | = | total mass flow through boundary $i$ |
| $\sum_{in}, \sum_{out}$ | = | summation over all inflow and outflow boundaries, respectively |
| $\phi_i$ | = | average value of $\phi$ over boundary $i$ |
| $e_{out}$ | = | $\sum_{out} \dot{m}_i \left(c_v T + \sum_j Y_{\psi,j}\, e_j\right)_i$ |
| $e_{ref}$ | = | $\sum_{in} \dot{m}_i \left(c_v T_{ref} + \sum_j Y_{\psi,j}\, e_j\right)_i$, $T_{ref} = 273K$ |
| $L$ | = | characteristic length of the flow domain, $V_{ref}^{1/3}$ |
| $v_{nom}$ | = | mean inlet velocity |

**Table 4.1:** Normalisation factors and thresholds for transport equation residuals (from [410]).

concentration of species $\psi$. In situations when the species $\psi$ has decayed and $C = 0$, numerical truncation or round-off errors can produce a solution with $C \neq 0$ which creates a stability problem [132]. Therefore the numerical algorithm should be robust and stable by damping out any errors. In addition, due to a rapid change of species concentrations and temperature close to thermal runaway, it is desirable that the solution algorithm can accommodate this situation by automatically selecting the time-step for integration.

At present, the equations describing the autoignition models are solved using the well-known Gear method [130]. This method employs a multi-step predictor-corrector sequence and determines the time-step by limiting the local truncation error to a given error tolerance per integration step. Thus the method is stable and capable in coping with systems of first-order ODEs. Further information on ODE solvers is found in [98, 249].

## 4.4 Closure

This chapter summarises the numerical practice adopted in this study to discretise the governing gas transport equations outlined in Chapter 3. The conservative FVM was used and applied to an arbitrary unstructured mesh comprised of hexahedral cells. The dependent variables are stored in the collocated arrangement to reduce storage requirement. The temporal discretisation is based on a fully-implicit treatment that is capable to yield physically plausible results for an arbitrary time-step size. The final description of the discretised general transport equation was derived followed by the treatment of the boundary conditions.

The solution procedure and sequence of an engine simulation were outlined for solving the discretised system of algebraic equations. The sequence consists of two main parts. The iterative solution of the gas- and liquid-phase variables is obtained in the predictor-corrector sequence. Therein the $NO_x$ mass fraction and turbulence parameters are not treated, which are solved for at the end of the time-step.

To solve the system of algebraic equations for each gas dependent variable, the BiCG method with diagonal pre-conditioning is used. The pressure correction equation in the PISO loop sequence is solved by the ICCG method. In addition, the solver for ODEs, which describe the chemistry mechanism as in autoignition, is specified. They are solved by Gear's method.

With this chapter the mathematical and numerical foundations for the present study are described. The following chapters focus on the description of the test cases and the validation of the methodology and its various submodels.

# Chapter 5

# Description of Test Cases

This chapter describes the three test cases used for the application of the CFD methodology. For each test case the experimental and computational setup are explained, including the available experimental data.

The first test case, introduced in Section 5.1, deals with a nominally axisymmetric research engine under motored conditions. While the pressures are considerably lower than for the HPP concept, the temperatures are approximately in the same level. Measurements of the flow field and wall heat transfer are provided.

The second test case concerns the pulsed injection of fuel into a constant-volume pressure chamber followed by autoignition and combustion, as described in Section 5.2. The conditions are similar to those prevailing in Diesel engines near start of injection. Experimental data are available for spray evolution, autoignition and soot mass concentration.

Finally in Section 5.3 the HPP prototype engine is described for which the complete CFD methodology is assessed including flow, spray, ignition, combustion, pollutant formation and wall heat transfer. Several operating conditions are investigated, one under motored and four under fired conditions. Experimental data are available for in-cylinder pressure, exhaust concentrations and wall heat transfer.

The closure of this chapter is given in Section 5.4.

# 5.1 RWTH Aachen Engine

The nominally axisymmetric research engine at the RWTH Aachen is used to study the in-cylinder flow and heat transfer under motored conditions.

## 5.1.1 Experimental setup

### Description

The motored four stroke single-cylinder research engine with one centrally located valve and a pancake combustion chamber has been used for extensive experimental studies at the RWTH Aachen. The geometrical data and operating conditions are summarised in Table 5.1. Optical access is provided via three quartz glass windows of 16 mm diameter in the cylinder liner below the cylinder head, offset by 90° along the circumference. Additionally, measurement probes can be inserted at three locations in the cylinder head as seen in Figure 5.1 in case of heat transfer measurements.

| | |
|---|---|
| Bore | 100 mm |
| Stroke | 105 mm |
| Connecting rod length | 179.8 mm |
| Compression ratio | 7.78 |
| Engine speed | 1000 RPM |
| *Valve:* | |
| Diameter | 40 mm |
| Maximum lift | 10 mm |
| Opening | 540° CA |
| Closing | 220° CA |

**Table 5.1:** Geometrical information and operating condition of RWTH Aachen engine (from [190, 252]).

The incoming air is heated to 328.15 K and passes through straightening blades before entering the chamber via the central valve. The valve acts as intake and exhaust valve depending on the piston motion. The valve lift curve is reproduced in Figure 5.2.

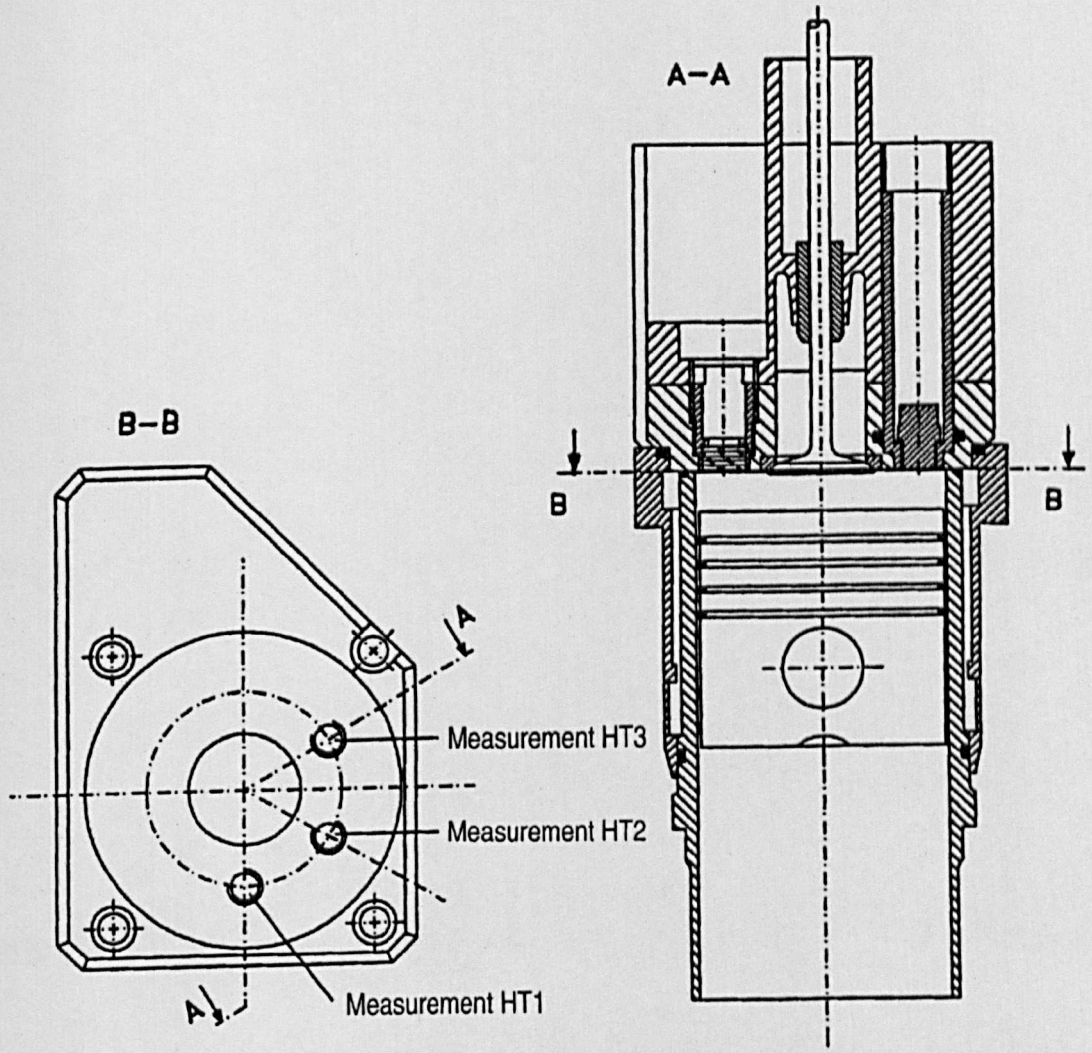



**Figure 5.1:** RWTH Aachen motor and measurement locations for three probes (from [190, 252]).

### Measurements

The velocity distribution in the valve curtain for five valve lifts was measured under steady flow conditions at several points in the valve gap and at five equally-spaced circumferential positions [252]. Also the discharge coefficient $C_D$ was determined at the same valve lifts, shown in Figure 5.3.

Local LDA velocity and turbulence intensity measurements were made at three monitoring locations as defined in Table 5.2. In addition, during the intake period the axial velocities at a distance of 8 mm from the cylinder head were measured at radial distances from 10 to 45 mm.

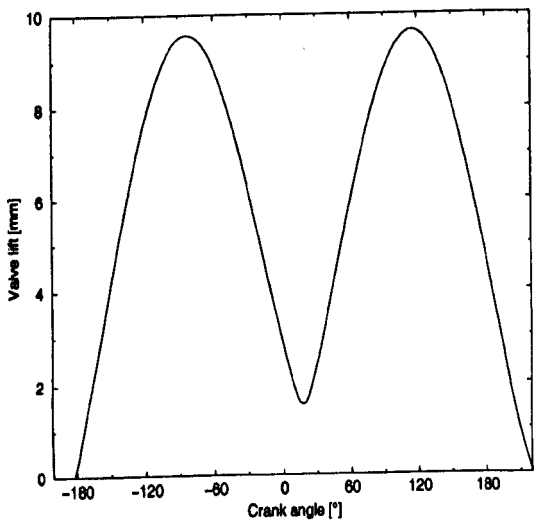



**Figure 5.2:** Valve lift curve for RWTH Aachen engine.

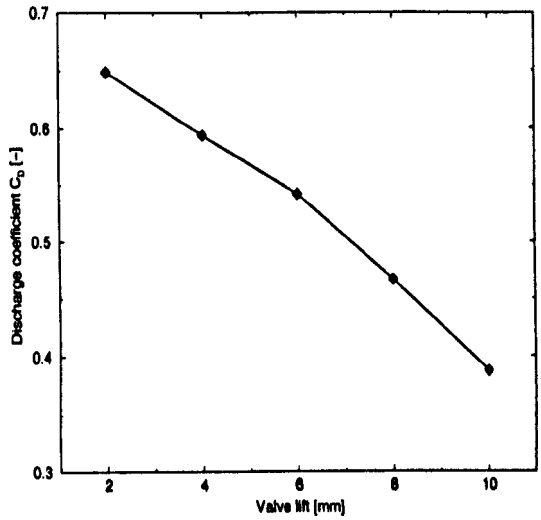



**Figure 5.3:** Discharge coefficient for different valve lifts.

| Measurement Point | Distance from cylinder axis and head | | |
|---|---|---|---|
| | x [mm] | y [mm] | z [mm] |
| **P1** | 38 | 0 | 7 |
| **P2** | 45 | 0 | 7 |
| **P3** | 40 | 0 | 10 |

**Table 5.2:** Location of monitoring points for LDA measurement of RWTH Aachen engine (from [190]).

The pressure was obtained by a pressure transducer and the bulk gas temperature was measured by cold-wire technique. Both measurement probes can be inserted in any of the three locations in the cylinder head as seen in Figure 5.1.

The cylinder head surface temperature was measured via surface thermocouples at three locations offset by 60° at a radius of 35 mm as indicated by the labels HT1,...,HT3 in Figure 5.1. The instantaneous wall heat flux can be derived from a heat conduction analysis as described in Appendix D. The experimental results have been ensemble-averaged over about 200 cycles with a mean of 12 data points and a maximum of 40 data points per °CA. The maximum experimental error for each measured quantity is summarised in Table 5.3. Further details about the experimental setup and the operating conditions can be found in [190, 252, 345] and [368].

| Quantity | Peak pressure | Axial velocity | | RMS velocity | Integral length scale | Surface temperature |
|---|---|---|---|---|---|---|
| | | Compression | Expansion | | | |
| **Standard deviation** | 0.3% | 48% | 68% | 3–6% | 8% | 10% |

**Table 5.3:** Maximum standard deviation for measurement quantities for RWTH Aachen engine (from [190]).

### 5.1.2 Computational setup

Two computational grids were generated for the current study, following recommendations of mesh sensitivity studies of Lange [252], who simulated the same experiment. They are displayed in Figures 5.4 and 5.5. The moving mesh and cell layer removal/addition features were used to keep an approximately constant grid density. Thus, the coarse mesh employs 65888 cells at BDC and 12096 cells at TDC, while the fine mesh incorporates 161936 cells at BDC and 32112 cells at TDC. The removal and addition of cell layers is done to prevent highly-squashed or elongated cells which can affect the stability of the numerical algorithm [426]. During this procedure, all the extensive gas properties are conserved. The main difference between both meshes is the higher resolution of the latter in circumferential direction by a factor of three.

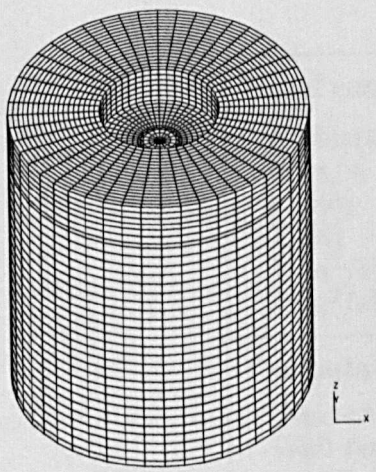


**Figure 5.4:** Coarse mesh for Aachen engine at 90° CA.

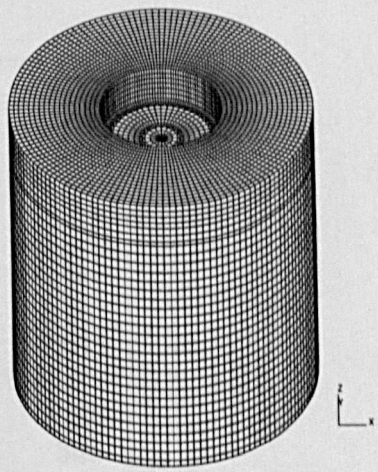


**Figure 5.5:** Fine mesh for Aachen engine at 90° CA.

| | |
|---|---|
| Temperature | 328.15 K |
| Pressure | $1 \times 10^5$ Pa |
| Density | 1.0614 kg/m$^3$ |
| Turb. intensity | 0.0135 |
| Turb. length scale | 0.03 × valve lift |

**Table 5.4:** Inlet conditions of RWTH Aachen engine case (see also [252]).

To obtain the inflow velocities, the measured inflow velocity components in the valve curtain were linearly interpolated in both time and space and scaled to produce the correct mass flow rate at a given crank angle, calculated from the pressure drop across the valve from the orifice equation and the measured discharge coefficient. Due to the absence of experimental data, the incoming turbulence conditions were estimated from data for a geometrically similar engine test case, reported in the literature [143]. The inlet conditions are summarised in Table 5.4.

The initial conditions and the computational parameters are listed in Table 5.5. Uniform initial temperature and pressure at the start of the calculation (0° CA) are assumed in the quiescent cylinder. Since the wall temperatures are reported to fluctuate by a maximum of 3 K they were taken to remain constant at 343 K [252]. The calculation time-step was chosen as 0.125° CA to ensure the mean Courant number stayed below unity.

| Initial conditions | |
|---|---|
| Ambient gas | air |
| $\mathbf{u}$ [m/s] | 0 |
| $p$ [bar] | 1 |
| $T$ [K] | 328 |
| $k$ [m$^2$/s$^2$] | 0 |
| $\varepsilon$ [m$^2$/s$^3$] | 0 |
| **Computational parameters** | |
| Time-step size [° CA] | 0.125 |
| Wall temperature [K] | 343 |

**Table 5.5:** Initial conditions and computational parameters for Aachen engine calculation.

## 5.2 Aachen Pressure Chamber

The Aachen pressure chamber is used to investigate the liquid and fuel vapour penetration, autoignition, combustion and pollutant formation under Diesel-like conditions.

### 5.2.1 Experimental setup

#### Description

Figure 5.6 shows the constant-volume pressure chamber used by researchers at the Rheinisch Westfälische Technische Hochschule (RWTH) Aachen. The dimensions are listed in Table 5.6, along with the maximum global temperature and pressure operating conditions. Optical access is provided via up to four quartz glass windows of 100 mm length and 40 mm width. The chamber walls are adiabatic. At the top of the chamber, compressed air can enter via two heaters and straightening blades. The mean velocity before injection was measured as below 0.1 m/s, so the chamber can be considered quiescent compared to the axial velocities of the fuel jet [393]. Further detail on the geometry of the chamber is found in [393].

| | |
|---|---|
| Length [mm] | 200 |
| Diameter [mm] | 100 |
| Max. temperature [K] | 900 |
| Max. pressure [bar] | 60 |

**Table 5.6:** Dimensions and maximum capacity of Aachen chamber [393].

The injection system includes an in-line injection pump and a Bosch commercial, water-cooled single-hole nozzle. The injector is located at the centre of the top wall and injects downwards along the chamber axis. Specifications of the injector are given in Table 5.7 and are found in [243].

For the present study *n*-heptane is used, injected at a temperature of 295 K. This represents in fact an estimated value, as it was not measured [77]. The injection parameters are summarised in Table 5.7. Figure 5.7 reproduces the volumetric

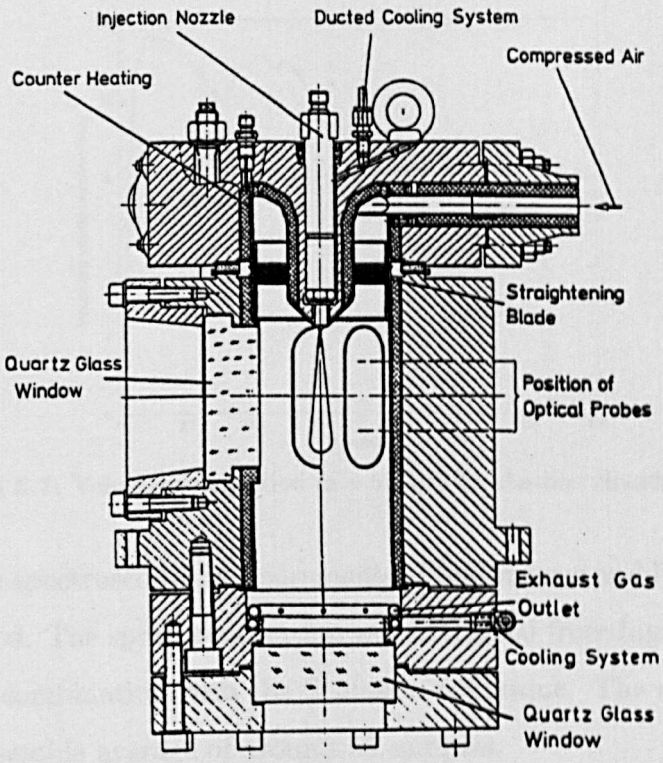



**Figure 5.6:** Aachen pressure chamber (from [393]).

| | |
|---|---|
| *Injector specification* | |
| Length [mm] | 0.8 |
| Diameter [mm] | 0.2 |
| Discharge coefficient | 0.66 |
| *Injection parameters* | |
| Fuel type | $n$-heptane |
| Injection temperature [K] | 295 |
| Injection quantity [mg] | 6 |
| Injection start [ms] | 0 |
| Injection end [ms] | 1.26 |

**Table 5.7:** Injector specification and injection parameters of Aachen chamber (from [243]).

injection flow rate, deduced by Koss *et al.* [243] from the measured needle lift, injection-line pressure and the nozzle discharge coefficient. The latter has been measured at a constant pressure difference of 100 bar as a function of the needle lift.

### Measurements

The fuel vapour mass fraction at five locations, as defined in Table 5.8, were ob-

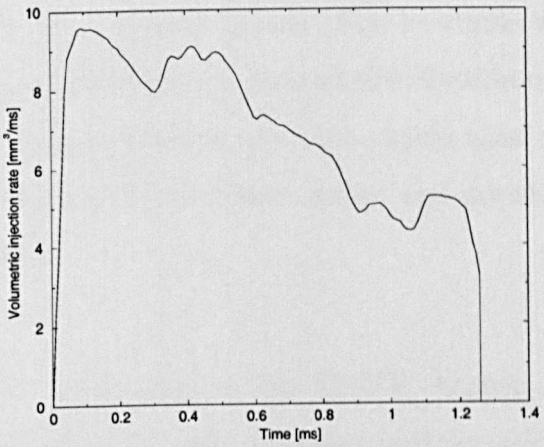



**Figure 5.7:** Volumetric injection rate history for Aachen chamber [243].

tained by Raman spectroscopy. Measurements of fuel vapour and liquid penetrations were also obtained. The spray penetration was extracted from high-speed cinematographic films in combination with the Schlieren technique. The experimental data represent the ensemble average of around 50 samples.

| Location | $z$ [mm] | $r$ [mm] |
|---|---|---|
| $P_{34}$ | 30 | 4 |
| $P_{40}$ | 40 | 0 |
| $P_{44}$ | 40 | 4 |
| $P_{50}$ | 50 | 0 |
| $P_{54}$ | 50 | 4 |

**Table 5.8:** Measurement locations for fuel vapour mass fraction. $z$ is direction downstream of nozzle in direction of spray axis and $r$ is radial offset from spray axis.

Ignition was detected by a photomultiplier using three stacked optical probes each covering a view angle of 20° such that the entire spray could be observed. Ignition was detected by the steep rise in the photomultiplier signal. For the present case, the ignition location was reported to be about 30 mm downstream of the nozzle in the direction of the spray axis and 5 mm radially offset from the chamber axis. The average ignition delay over 256 injection cycles was measured to be 1.63 ms.

Average soot mass concentrations over 32 injection cycles are measured via the light extinction method at five locations downstream of the nozzle on the spray axis

from $z = 30$ mm to 70 mm, spaced 10 mm. The locations will be denoted as $P_{30}$, $P_{40}$, $P_{50}$, $P_{60}$ and $P_{70}$. In addition, the spatial distribution of soot concentration is available at five time instances across the observation area of the chamber. These were assembled from several measurement points and are shown as iso-contours of soot mass concentration.

The measurements were taken at the RWTH Aachen by Bäcker and Wiartalla [24] and are reported in [242, 243]. The standard deviation due to pulse-to-pulse variations for ignition delay and soot concentrations at two locations are listed in Table 5.9.

| Quantity | Standard deviation |
|---|---|
| Ignition delay | 6% |
| Soot intensity: | |
| at $P_{40}$ | 68.3% |
| at $P_{60}$ | 164.9%[a] |

[a]The standard deviation is so large, since soot was not detected here at every cycle.

**Table 5.9:** Standard deviation due to pulse-to-pulse variations for Aachen pressure chamber.

### 5.2.2 Computational setup

The computational domain is a longitudinal wedge section of the pressure chamber, as displayed in Figure 5.8. The mesh consists of 2400 computational cells within a 30° sector with one cell in angular direction, 40 cells in radial direction and 60 cells in axial direction. The experimental results show a spray penetration less than 100 mm in axial and less than 10 mm in radial direction and a flame spread less than 80 mm in axial and less than 20 mm in radial direction. This is taken into account in the mesh design such that a fine mesh is used close to the injector in both the radial and axial directions, whereas a coarser mesh is used in the remaining part of the domain. In addition, due to the experimental observations of spray and flame spread, it can be assumed that the walls are unlikely to influence the

spray and flame evolution. The mesh is structured in accordance with results of mesh sensitivity studies of Kralj [246] and Clerides [77] who simulated the same experiment for validation studies of the spray methodology.

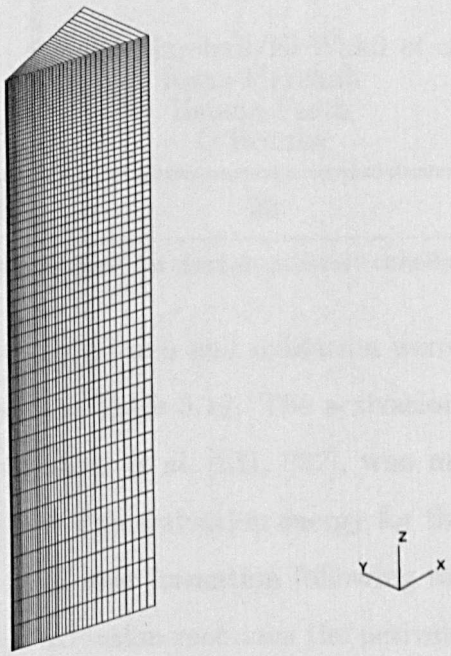



**Figure 5.8:** Computational mesh of Aachen pressure chamber.

The spray submodels and parameters used in the present study are summarised in Table 5.10 and follow the recommendations of spray sensitivity studies of the same experiments by Clerides [77]. An *ad hoc* reduction of 25% to the nozzle diameter was made to represent blockage effects due to cavitation in the nozzle. Better agreement of measured and predicted fuel vapour concentrations at the above measurement locations was achieved by this measure. In addition, the turbulent Prandtl and Schmidt numbers were set to 0.7 following recommendations of Clerides [77] and Faeth [107].

The choice of the autoignition and combustion model follow Theodossopoulos [427] who simulated the same experiment. Parameters concerning the autoignition and LATCT combustion models are given in Table 5.11. As ignition criterion the temperature rate of change criterion was set such that the experimental ignition

| Spray process | Submodel/correlation |
|---|---|
| Nozzle flow | Orifice equation |
| Nozzle $D$ [mm] | 0.15 |
| Atomisation | Huh |
| $C_D$ | 0.66 |
| Drag coefficient | Yuen-Chen |
| Evaporation: | |
| Nu correlation | Ranz-Marshall/El Wakil *et al.* |
| Sh correlation | Ranz-Marshall |
| Breakup | Hsiang-Faeth |
| Collision | O'Rourke |
| Parcel inj. rate [$1/\mu$s] | 20 |

**Table 5.10:** Spray submodels used for Aachen pressure chamber.

delay was achieved. Models for soot formation and oxidation were also activated, taking the model coefficients as given in Table 5.12. The activation energy for the soot formation expression is that of Khan *et al.* [231, 232], who modeled soot exhaust concentrations of Diesel engines. The activation energy for the Hiroyasu soot oxidation model is set equal to that of soot formation following recommendations of Kennedy [226]. For the NSC soot oxidation reactions the activation energies are chosen similar to the values specified by the model developers. The rate coefficients for soot formation and oxidation are chosen such that overall best qualitative and quantitative agreement with the measured soot concentration distribution was achieved.

Calculations were also performed with the alternative RIF model with the coefficient setting recommended by the developers.

| | |
|---|---|
| Ignition model | 4-step |
| $CN$ | 60 |
| Ignition criterion | |
| $dT/dt$ [K/s] | 4555 |
| Combustion model | LATCT |
| $A_{LT}$ | 5.0 |
| $B_{LT}$ | 1.0 |

**Table 5.11:** Ignition and combustion submodel coefficients for Aachen pressure chamber.

| Parameter | Hiroyasu model | | Hiroyasu soot formation/NSC soot oxidation | | | | |
|---|---|---|---|---|---|---|---|
| | $k_{s,f}$ | $k_{s,o}$ | $k_{s,f}$ | $k_A$ | $k_B$ | $k_T$ | $k_Z$ |
| $A$ [1/s] | 620000 | 260000 | 295000 | 0.02 | $4.46\times10^{-5}$ | 151000 | 21.3 |
| $E$ [J/mol] | 164431 | 164431 | 164431 | 147277 | 63597 | 405848 | 17154 |

**Table 5.12:** Soot model parameters for Aachen pressure chamber. $A$ is pre-exponential factor and $E$ is activation energy.

The simulation covered a 5 ms period from start of injection. For the setup using the 4-step autoignition and LATCT combustion the time-step size was chosen as 0.5 $\mu$s, as shown in Table 5.13. For the RIF approach the setting was the same, apart from the period between 0.7 and 1.2 ms which required a smaller time-step of 0.05 $\mu$s in order to cope with the rapid heat release after autoignition. The initial conditions are listed in Table 5.13, following the practice of Clerides [77] and Theodossopoulos [427].

| Initial conditions | |
|---|---|
| Ambient gas | air |
| $\mathbf{u}$ [m/s] | 0 |
| $p$ [bar] | 50 |
| $T$ [K] | 800 |
| $k$ [m$^2$/s$^2$] | $10^{-3}$ |
| $\varepsilon$ [m$^2$/s$^3$] | $7\times10^{-4}$ |
| **Computational parameter** | |
| Time-step size [ms] | $5\times10^{-4}$ |

**Table 5.13:** Initial conditions and computational parameters for Aachen pressure chamber calculation.

## 5.3 HPP Prototype Engine

The HPP prototype engine is used to investigate the spray, combustion, pollutant formation and wall heat transfer under elevated chamber pressures.

### 5.3.1 Experimental setup

#### Description

The single-cylinder DI Diesel engine investigated at the HTW Dresden as part of the HEDE project is a variant of the series OM500 heavy-duty truck engines, developed by DaimlerChrysler. It is suitable for peak cylinder pressures of up to 23 MPa. A summary of the geometrical data and operating conditions is listed in Table 5.14.

| | |
|---|---|
| Bore | 130 mm |
| Stroke | 150 mm |
| Connecting rod length | 273 mm |
| Compression ratio | 17.25 |
| Boost pressure | 2.85/3.5 bar |
| Engine speed | 1420 RPM |
| *Intake valve:* | |
| Diameter | 45.5 $mm^2$ |
| Opening | 670° CA |
| Closing | 340° CA |
| *Exhaust valve:* | |
| Diameter | 41 $mm^2$ |
| Opening | 395° CA |
| Closing | 75° CA |
| *Eight-hole nozzle injector:* | |
| Injection pressure | 120 MPa |
| Injection temperature | 350 K |

**Table 5.14:** Geometrical information and operating condition of DI Diesel engine at HTW Dresden (from [168, 248, 391]).

A drawing of the prototype engine is displayed in Figure 5.9. The incoming air passes through a supercharger and intercooler before entering into the cylinder via swirl ports. The bowl-in-piston chamber is fitted with two inlet and two exhaust valves and features an eight-hole nozzle injector, which is offset by 1.25 mm from the centre of the cylinder axis, as illustrated in Figure 5.10. The injector specifications are listed in Table 5.15. The discharge coefficients for the holes were not measured. The value chosen in the present study is derived from a detailed injector flow analysis performed at the NTU Athens under the HEDE project by matching the predicted injection pressure with measured values [169]. The distance of the hole exit from

the cylinder head varies between 1.5 mm and 1.3 mm with the former for an odd and the latter for an even hole number, as defined in Figure 5.10.

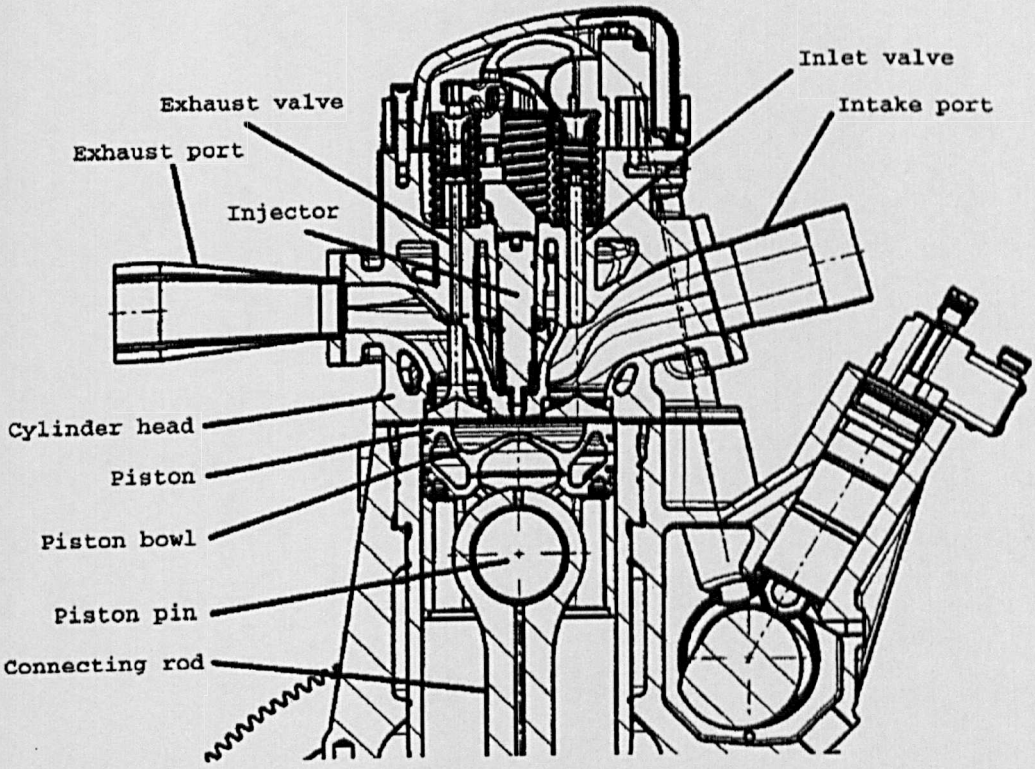



**Figure 5.9:** Diagram of HPP prototype engine (from [168]).

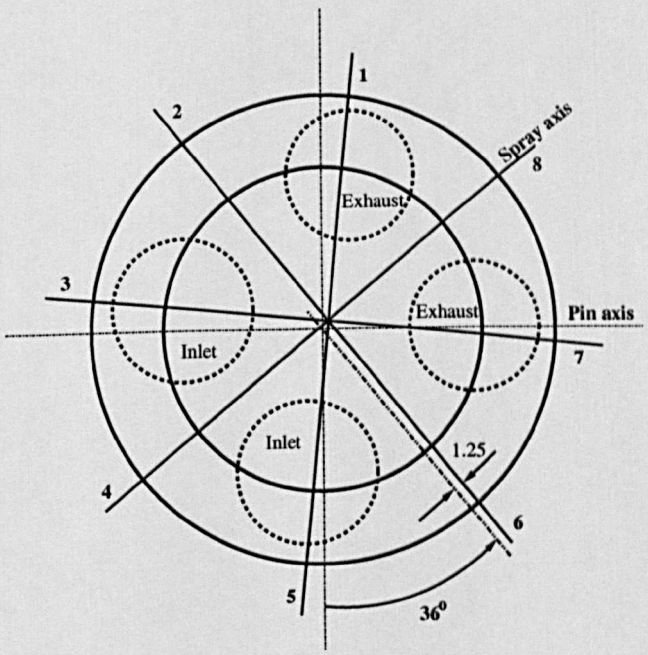



**Figure 5.10:** Injector position and injection axes. $1, \ldots, 8$ indicate spray axes of each hole.

| | |
|---|---|
| Length [mm] | 1.0 |
| Diameter [mm] | 0.2 |
| Discharge coefficient | 0.7 |
| Inclination angle | 77° |

**Table 5.15:** Injector specifications for HPP prototype engine.

A range of different operating conditions has been covered as summarised in Table 5.16. They comprise one motored case (MEOP) and four fired cases (EOP1,...,EOP4) for which standard Diesel fuel (DIN EN 590) is used. All the cases are at a fixed engine speed of 1420 RPM and in case of combustion, full load is considered with variations in injection timing† and boost pressure. The injection rate history, seen in Figure 5.11 for one hole, was determined from the pressure difference across the nozzle using the measured injector pressure and the measured total injected fuel mass, using a conventional orifice equation with fixed discharge coefficient.

| Test case[a] | Start of injection [° CA] | | | Boost pressure [bar] | | Injected mass [g] |
|---|---|---|---|---|---|---|
| | 6.5 | 8.8 | 12.8 | 2.85 | 3.5 | |
| MEOP | | | | • | | – |
| EOP1 | | • | | • | | 80.38 |
| EOP2 | • | | | • | | 82.01 |
| EOP3 | | | • | • | | 78.41 |
| EOP4 | | •[b] | | | • | 77.18 |

[a] • indicates cases/conditions investigated.
[b] Actual start of injection is 9° CA before TDC.

**Table 5.16:** Various operating points investigated for HPP prototype engine.

## Measurements

The in-cylinder pressure was measured by a pressure transducer located in the cylinder head. Instantaneous surface temperature measurements via thermocouples are taken at eight locations on the piston surface (HT1,...,HT4 and HTO1,...,HTO4) along two radii as indicated in Figure 5.12. Additionally, the time-average temperature on the piston crown is measured at five locations (A,...,E, G) and at various

† The start of injection was determined from the needle lift and injector pressure data [248].

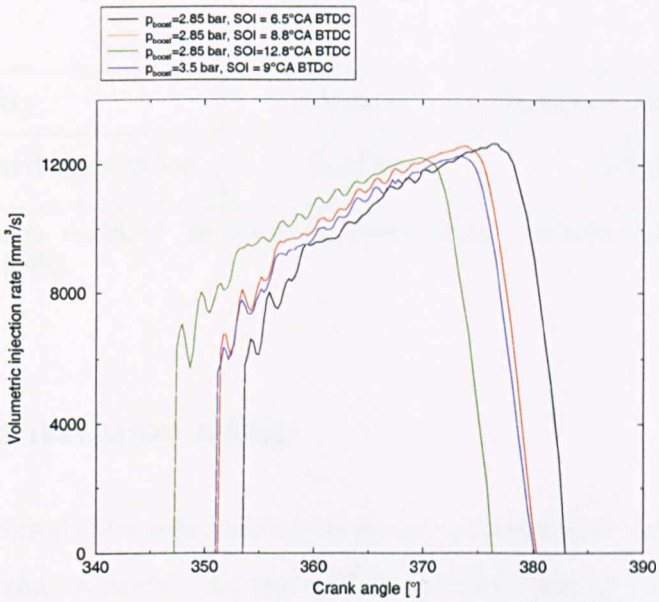



**Figure 5.11:** Volumetric injection rate histories for HPP prototype engine.

depths (F, H,...,J) inside the piston. The instantaneous wall heat flux is derived from a heat conduction analysis, described in Appendix D. Exhaust $NO_x$ concentrations are available for operating points EOP1 to EOP3 and soot concentrations for operating points EOP1, EOP3 and EOP4. The experimental data are ensemble-averaged over 100 cycles with a resolution of 0.25° CA. The maximum experimental errors for pressure and surface temperature are provided in Table 5.17.

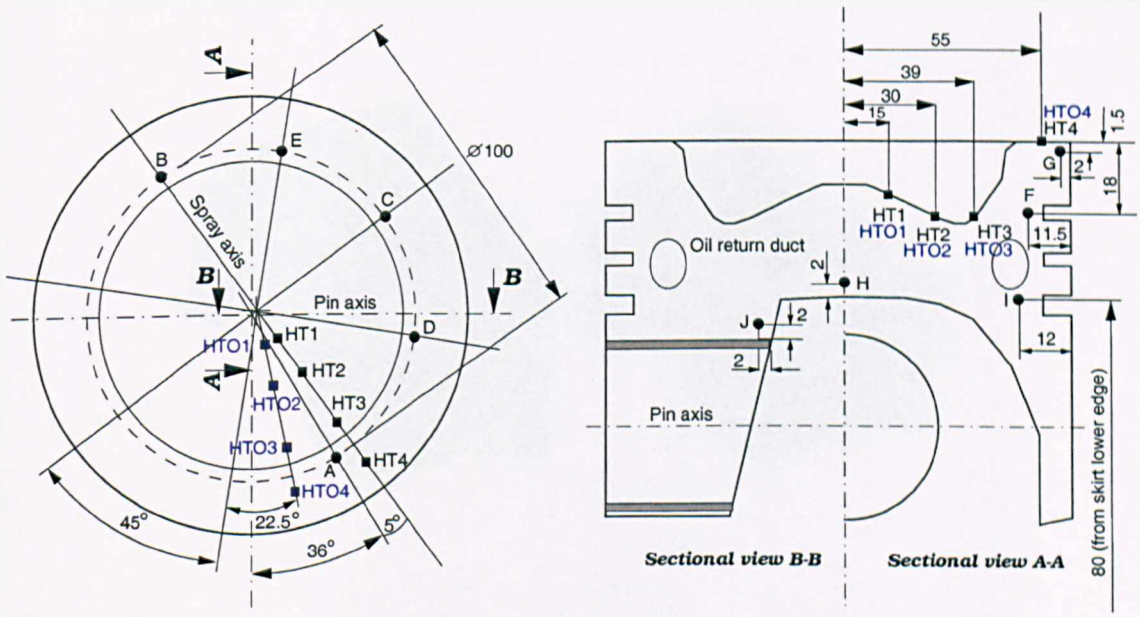



**Figure 5.12:** Sensor locations for HPP prototype engine.

| **Quantity** | Pressure | Surface temperature |
|---|---|---|
| **Standard deviation** | 0.24% | 0.69% |

**Table 5.17:** Maximum standard deviation for measurement quantities for DI Diesel engine (from [248]).

### 5.3.2 Computational setup

A full induction simulation was performed using the measured pressure histories in the intake and exhaust ports. As the calculated flow field is observed to become nearly axisymmetric by the start of injection, the spray and combustion calculations are performed on a one-eighth wedge-shaped calculation domain as seen in Figure 5.13. It contains just one of the eight spray jets. The offset of the spray injector was not considered in the calculations. This decision was based on the very small distance involved and the assumption that the spray evolution in all eight spray directions is therefore similar, which can be confirmed by the soot imprints on the

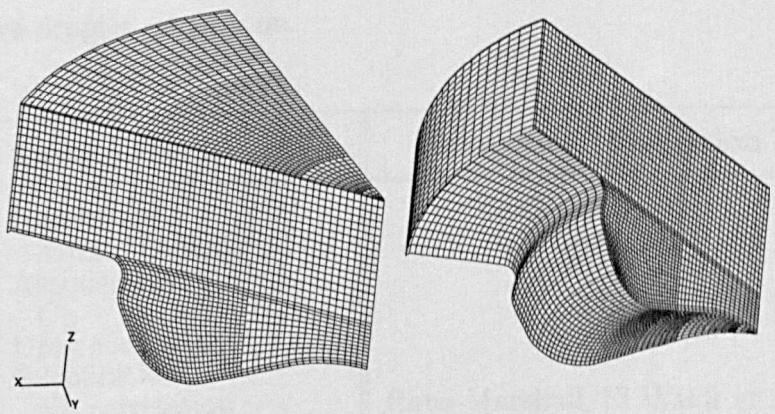



**Figure 5.13:** One-eighth wedge-shaped computational mesh for HPP prototype engine at 400° CA.

piston in Figure 6.75. Periodic boundary conditions are applied on the wedge faces. It is assumed that the processes occurring in the wedge are representative for all of the others. The reduced computational domain was chosen due to the lower computing overheads. The moving mesh features with cell layer addition and removal were employed to keep an approximately constant grid density as in the RWTH Aachen engine case. The computational mesh follows a similar design as for another engine of the same OM500 series simulated under the PRIDE project [346, 347]. It employs 60477 cells at BDC and 17004 cells at TDC.

The spray submodels and injection parameters, used in the present study, are summarised in Table 5.18 and follow the model choice for the simulation of an engine of the same series under the PRIDE project [346, 347]. A parametric study was attempted, taking into account the blockage in the nozzle due to cavitation via the reduction of the nozzle diameter (see Section 6.3.2.3). A variation of the characteristic breakup time in the Reitz-Diwakar breakup model was also performed by modification of the coefficients $C_b$ and $C_s$ in Eq. (3.93) to improve liquid spray penetration, as presented in Section 6.3.2.3. The parcel injection rate was based on recommendations of Dukowicz [95] and Tabrizi [420]. It was chosen such that it would not lead to excessive computing overheads and still produce a statistically representative droplet population.

| Spray process | Submodel/correlation |
|---|---|
| Nozzle flow | Orifice equation |
| Nozzle $D$ [mm] | 0.2, 0.18, 0.16 |
| Atomisation | Huh |
| $C_D$ | 0.7 |
| Drag coefficient | Standard |
| Evaporation: | |
| Nu correlation | Ranz-Marshall/El Wakil *et al.* |
| Sh correlation | Ranz-Marshall |
| Breakup | Reitz-Diwakar |
| Parcel inj. rate [1/° CA] | 200 |

**Table 5.18:** Spray submodels and parameters used for HPP prototype engine.

Two combustion modelling approaches were applied. The first comprises the Shell autoignition model and LATCT combustion model which were combined with pollutant submodels. This combination is frequently employed for Diesel engine simulations (see e.g. [240, 328, 362, 365]). The model parameters for the autoignition and combustion models are listed in Table 5.19. They were selected such that good agreement with experimental ignition delay and pressure history was achieved. The soot model parameters are listed in Table 5.20 and follow closely Patterson *et al.* [328] and the values specified by the developers of the NSC model. The pre-exponential factors for the Hiroyasu soot formation and oxidation model have been adjusted to reach agreement with measured exhaust soot concentrations, as outlined in Section 6.3.2.4. The second combustion model is RIF. In this approach, due to the different fuel type (i.e. *n*-heptane) the injected fuel mass was corrected such that the same total chemical heat release as in the experiments would be yielded.

| Ignition model | Shell |
|---|---|
| Ignition criterion | |
| $T$ [K] | 1100 |
| $dT/dt$ [K/s] | 10000 |
| Combustion model | LATCT |
| $A_{LT}$ | 9.0 |
| $B_{LT}$ | 0.65 |

**Table 5.19:** Ignition and combustion submodel coefficients for HPP prototype engine simulation.

The calculations start at SOI and end at EVO, i.e. 440° CA. The time-step size was held at 0.01° CA for the period until 395° CA which is after EOI to resolve the highly turbulent flow field due to the interaction between the high-speed liquid jet and the surrounding gas. Most of the fuel combustion has taken place up to this point. According to Beshay *et al.* [42] and Clerides [77], who performed parametric studies of the influence of time-step size on spray predictions, the present time-step would yield time-step independent results. For the remainder of the calculation the time-step was set to 0.1° CA to reduce the computational overheads.

| Parameter | Hiroyasu model | | Hiroyasu soot formation/NSC soot oxidation | | | | |
|---|---|---|---|---|---|---|---|
| | $k_{s,f}$ | $k_{s,o}$ | $k_{s,f}$ | $k_A$ | $k_B$ | $k_T$ | $k_Z$ |
| $A$ [1/s] | 750 | 3500 | 150 | 20 | $4.46\times10^{-3}$ | 151000 | 21.3 |
| $E$ [J/mol] | 52300 | 58576 | 52300 | 125520 | 63597 | 405848 | 17154 |

**Table 5.20:** Soot model parameters for HPP prototype engine. $A$ is pre-exponential factor and $E$ is activation energy.

The initial conditions are based on the solution of the induction calculation using the full mesh including ports and valves which is transferred onto the wedge section. A parametric study of swirl level at SOI is performed as discussed in Section 6.3.2.3. The wall temperatures were held constant in time and over entire sections of the wall, as seen in Table 5.21, and are derived by averaging the surface temperature measurements. The assumption of constant wall temperatures over the engine cycle entails minor errors in wall heat transfer, since the measured wall temperature amplitudes of 17 K are relatively small compared to the changes in gas temperature of around 550 K.

| Case | $T_{cyl.\ head}$ [K] | $T_{cyl.\ wall}$ [K] | $T_{piston}$ [K] |
|---|---|---|---|
| MEOP | 410 | 400 | 465 |
| EOP1 | 500 | 475 | 580 |
| EOP2 | 500 | 475 | 585 |
| EOP3 | 490 | 460 | 595 |
| EOP4 | 500 | 470 | 570 |

**Table 5.21:** Wall temperatures for various wall sections for HPP prototype engine.

## 5.4 Closure

This chapter summarised the three test cases used for validation studies of the present CFD methodology. For each case the experimental and computational setups have been described in detail.

The first test case is based on a motored research engine for which flow field and wall heat transfer measurements are available. The computational setup was

described, including the two calculation grids that use moving mesh features with cell layer addition and removal.

The next test case concerns a constant-volume pressure chamber under Diesel-like conditions, for which ignition, fuel vapour and soot concentration measurements are available. The CFD methodology used for this study is outlined including the computational mesh, the choice of CFD submodels and computational parameters.

The last test case is used to validate the Diesel engine CFD methodology under conditions of the increased peak pressure concept. An HPP prototype engine is simulated at various operating points including motored and fired operation. In-cylinder pressure, wall heat transfer and exhaust concentration measurements are available. The CFD methodology for this study is presented, including the mesh. The mathematical submodels employed and their parameters are also specified.

# Chapter 6

# Results and Discussion

The previous chapter described the experimental setup and the available measurement data for the three test cases chosen for validation studies of the present Diesel engine CFD methodology. In addition, the computational setup including the computational grid and the choice of submodels and their parameters were outlined.

This chapter presents the results of the validation studies. The computational results for the RWTH Aachen engine are presented in Section 6.1 which are compared against flow field and heat transfer measurements. The predictions for the Aachen pressure chamber are discussed in Section 6.2 including comparisons with measured fuel vapour distribution, spray penetration and soot concentrations. Finally, Section 6.3 summarises the evaluation of the complete Diesel engine CFD methodology against available experimental data for the HPP prototype engine. The discussion comprises the comparison of predicted pressure history, $NO_x$ and soot exhaust concentrations and wall heat transfer with measurements. Each section summarises the findings. Section 6.4 closes the chapter.

## 6.1 RWTH Aachen Engine

In this test case two computational grids were employed, referred to as *coarse* and *fine* meshes, respectively. The standard (SWF) and the modified wall function

(MWF) approaches were employed.

### 6.1.1 Flow field

The velocity fields for four crank angles predicted with the coarse mesh are shown in Figures 6.1 and 6.2. The standard and modified wall function approaches resulted in identical velocity profiles due to the low temperatures in the cylinder during the intake period and hence only the results for the latter approach are provided. As illustrated by the icon at the bottom right, the vertical cross-section divides the cylinder into two halves in the (x,z) plane, and the horizontal cross-section slices mid-way through the cylinder in the (x,y) plane. During intake a ring vortex is formed below the cylinder head between the valve and the cylinder liner. A slightly asymmetrical flow field is predicted. A helical ring vortex is found between the valve and the piston surface. The inflow stream that is reflected at the piston shows a predominantly upward motion in the centre of the cylinder especially towards BDC (cf. Figure 6.2).

During the compression stroke the upward velocity originating from the piston displacement largely determines the charge motion. The vortex between the valve and the piston collapses, leaving a predominantly vertical motion, as seen at 300° CA in Figure 6.2. The experiments show the collapse at around 270° CA [190] which agrees approximately with the numerical results.

Figures 6.3 and 6.4 display the results at the same instances for the fine mesh. In general the flow field characteristics largely resembles the ones of the coarse mesh. During intake the flow structure and velocity magnitudes are nearly identical. At BDC the fine mesh produces larger axial velocities and the corner vortex is located closer to the cylinder head compared with the coarse mesh. At 300° CA higher velocities are observed in the fine mesh close to the far-side cylinder wall, whereas the predictions of the coarse mesh give the highest velocities close to the cylinder axis.

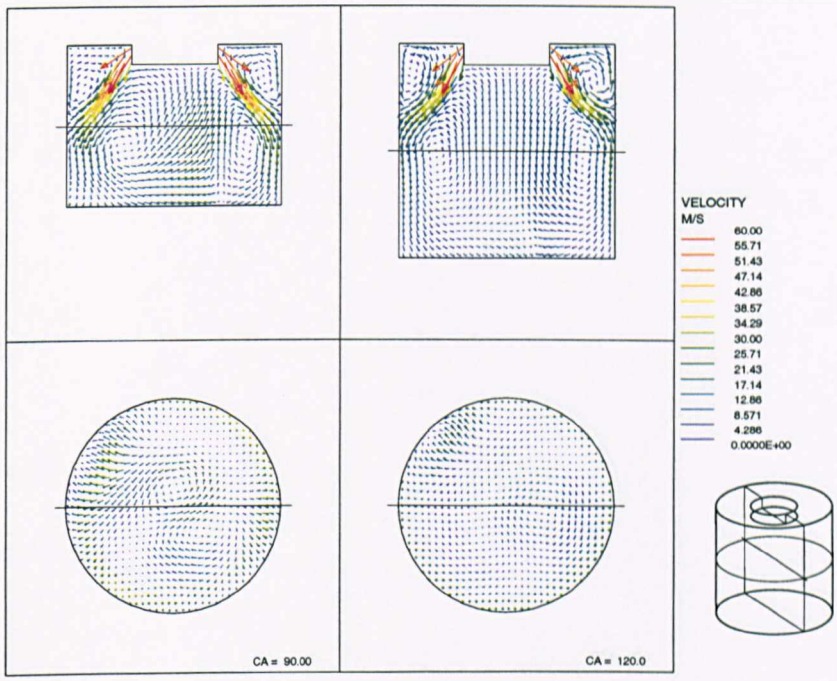



**Figure 6.1:** Velocity distribution at horizontal and vertical cross-sections for 90° CA and 120° CA using coarse mesh.

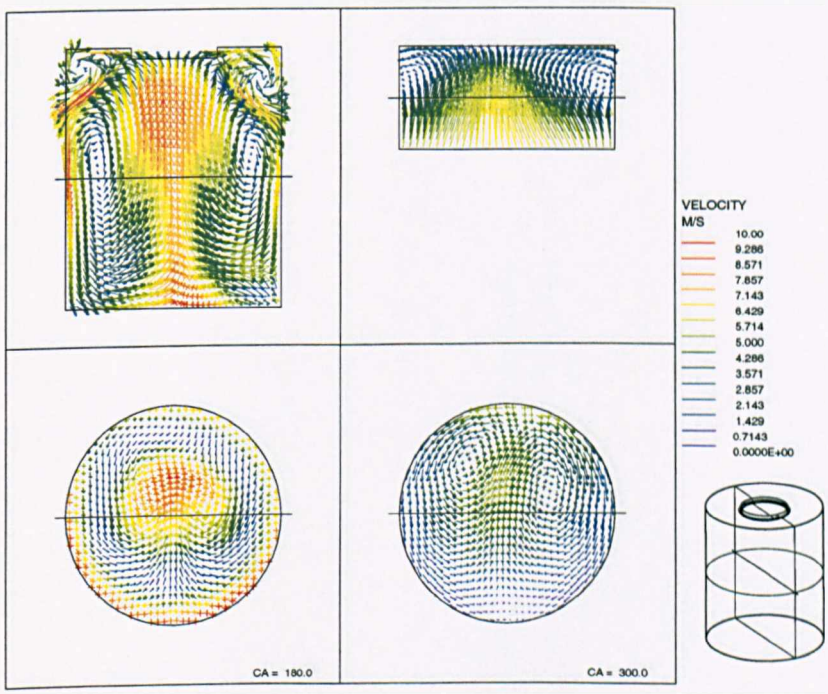



**Figure 6.2:** Velocity distribution at horizontal and vertical cross-sections for 180° CA and 300° CA using coarse mesh.

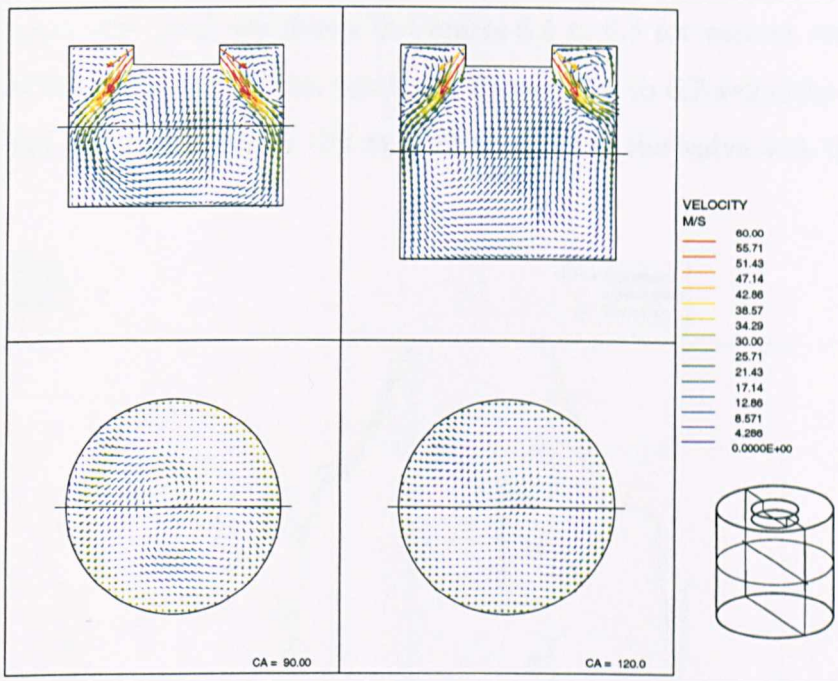



**Figure 6.3:** Velocity distribution at horizontal and vertical cross-sections for 90° CA and 120° CA using fine mesh.

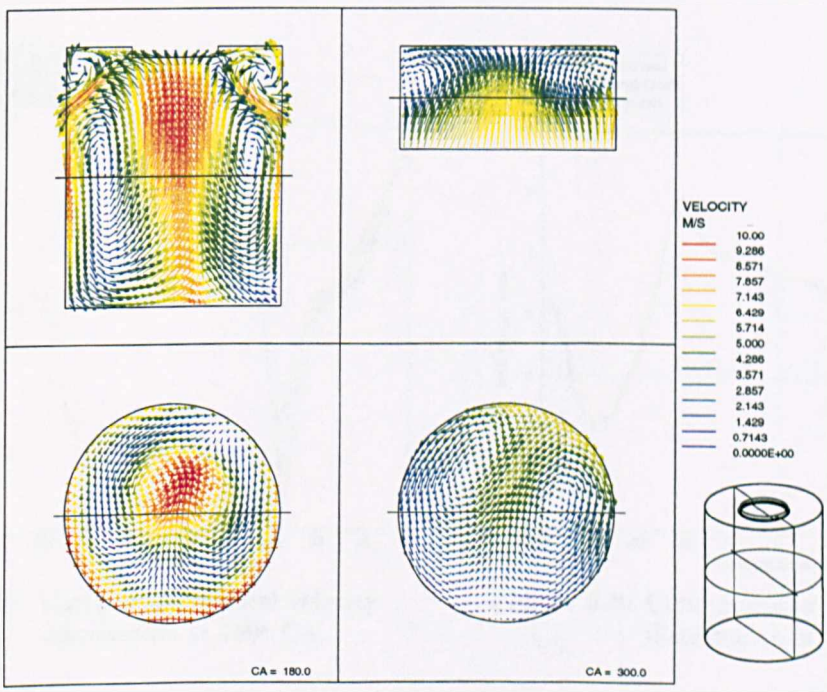



**Figure 6.4:** Velocity distribution at horizontal and vertical cross-sections for 180° CA and 300° CA using fine mesh.

The predicted and measured axial velocity distributions at a distance of 8 mm below the cylinder head are shown in Figures 6.5 to 6.8 for various crank angles. In the numerical and experimental results in Figures 6.5 to 6.7 velocities are not given for a radial distance between -20 and 20 mm, since the valve was located in this region.

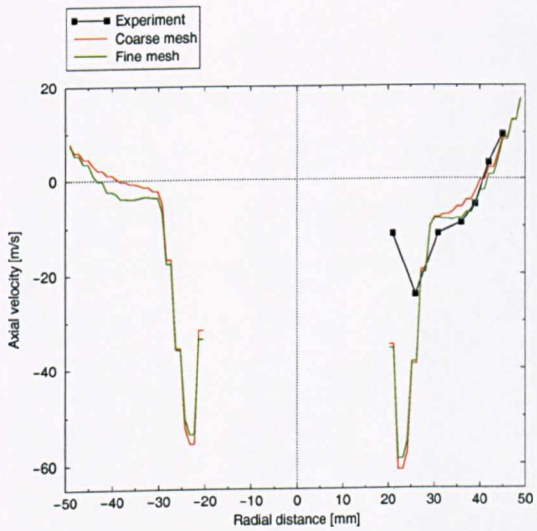



**Figure 6.5:** Comparison of axial velocity distribution at 90° CA.

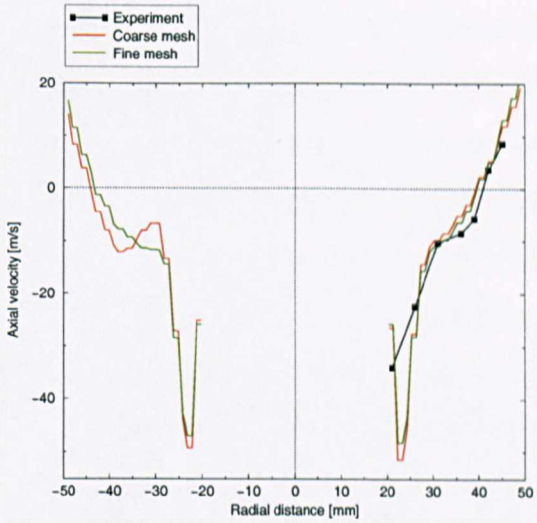



**Figure 6.6:** Comparison of axial velocity distribution at 120° CA.

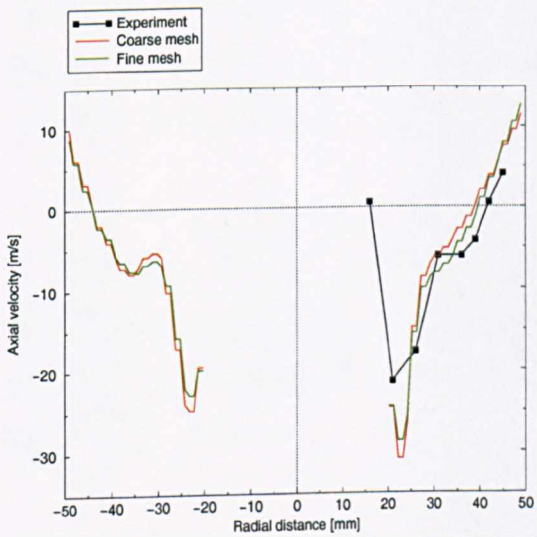



**Figure 6.7:** Comparison of axial velocity distribution at 150° CA.

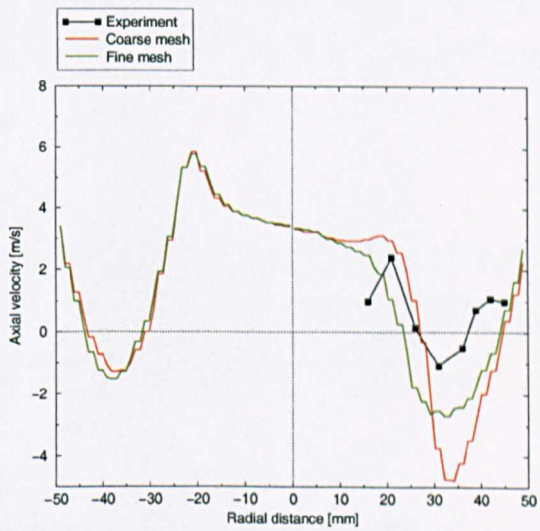



**Figure 6.8:** Comparison of axial velocity distribution at 210° CA.

The incoming charge shapes the flow field next to the valve with measured axial velocities up to 34 m/s at 120° CA. A ring vortex structure in the corner toward the

cylinder liner is seen in the experiments with its centre located at around 40 mm. At 210° CA (Figure 6.8) the valve is almost closed, resulting in fairly low axial velocities. In the centre of the cylinder the upward motion is dominant, since the incoming flow is reflected by the piston. This causes outward flow into the manifold.

The axial velocity profile is predicted quite well, particularly for the first three crank angles shown. The highest differences between measurements and predictions occur next to the valve tip. For instance, at 90° CA the calculations predict velocities up to 60 m/s, around three times higher than measured. However, the general flow structure with ring vortices in the corners towards the cylinder liner is captured well in this cross-section. The change of flow direction in the measured axial velocity at around 40 mm is matched closely. Inaccuracies of the predicted inflow process can be attributed to the boundary condition used, where the inflow direction and velocity magnitudes were derived from steady-state experiments which do not consider dynamic effects. These will also influence the flow field persisting after valve closure (VC). Generally, slightly better agreement with the measurements is achieved when using the fine grid. This is especially true for the distribution at 210° CA. Other sources of error include the modelling of turbulence and inaccuracies originating from the insufficient resolution of the flow processes.

The numerical results show a slightly asymmetric inflow distribution and a similar axial velocity profile is calculated. Higher peak velocities by 5.9% are estimated with the coarser mesh for the first three crank angles considered. Larger differences are found for 210° CA.

Figure 6.9 shows the calculated history of cylinder mass. It is seen that both meshes give very similar magnitudes, with the coarse mesh giving a 0.4% lower trapped mass than the fine mesh. Negligible differences are observed between the results using the standard and modified wall function approach, respectively.

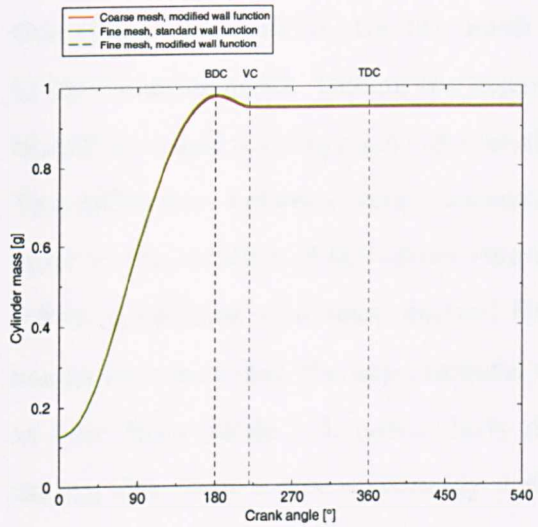



**Figure 6.9:** Calculated in-cylinder mass history for RWTH Aachen engine test case.

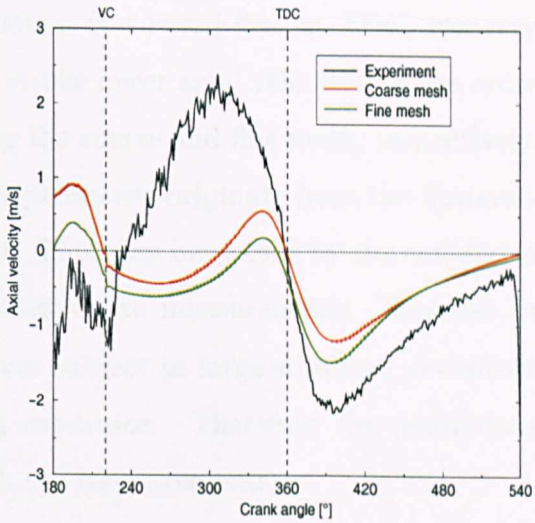



**Figure 6.10:** Comparison of axial velocity component at measurement point P3.

In Figure 6.10 the axial velocity component at measurement point P3 is displayed†. This location is close to the centre of the corner vortex, as can be deduced from Figures 6.5 to 6.8. Therefore this comparison between measurements and predictions represents a severe test case for the estimation of local velocities in a highly variable flow region.

The experiments suggest negative axial velocities throughout the open valve period with a change in slope at around 192° CA and shortly after VC. The flow induced by piston displacement is superimposed on the charge motion towards TDC and clearly determines the flow in the expansion stroke when the velocities in the horizontal plane are almost uniform. At around TDC no mean flow is seen.

Large discrepancies between calculated and measured axial velocities are found during the compression period. While shortly after VC at around 240° CA upward flow is observed in the experiment, the calculations predict positive axial velocities only after 309° CA and 327° CA for the coarse and fine mesh, respectively. Consequently the peak axial velocity is substantially underpredicted during the compres-

†The measured axial velocity history was only available for this measurement point.

sion stroke. In addition, the fine mesh predicts a downward flow at TDC, contrary to the measurements. During the expansion stroke lower axial velocities of the order of 0.55 m/s and 0.43 m/s are calculated using the coarse and fine mesh, respectively. The differences between computations and experiments originate from the disagreement in the location of the corner ring vortex. This may be caused by the calculated inflow conditions that were derived from steady-state measurements. However, it has to be noted that the experimental data are subject to large standard deviations as seen from Table 5.3, particularly during expansion. Therefore the predictions during this phase agree reasonably well with the measurements.

Both simulations predict a qualitatively similar axial velocity history. Differences in magnitude are found particularly during the compression stroke where the axial velocities of the coarse mesh are offset by 0.34 m/s on average towards positive velocities compared to the fine mesh. This is caused by the difference in position of the corner ring vortex below the cylinder head as seen when comparing Figure 6.2 with Figure 6.4. During the expansion stroke the differences between both are of the order of 18%.

In Figures 6.11 and 6.12 the predicted fine-mesh turbulence kinetic energy at selected crank angles is shown. The shear layers in between the upper and lower ring vortices generate large turbulence next to the inflowing stream (see plot at 180° CA in Figure 6.12). A similarity exists between the contour plots of turbulence kinetic energy and velocity vectors shown above. The asymmetry observed from the velocity plots is also present in this distribution. During the compression stroke the turbulence levels decrease, producing an increasingly uniform profile with slightly higher values in the core of the cylinder.

The experimental RMS velocities were determined by two independent methods based on the evaluation of the mean value. Firstly, fluctuations were calculated around an ensemble-averaged value. By this method, the ensemble-averaged RMS

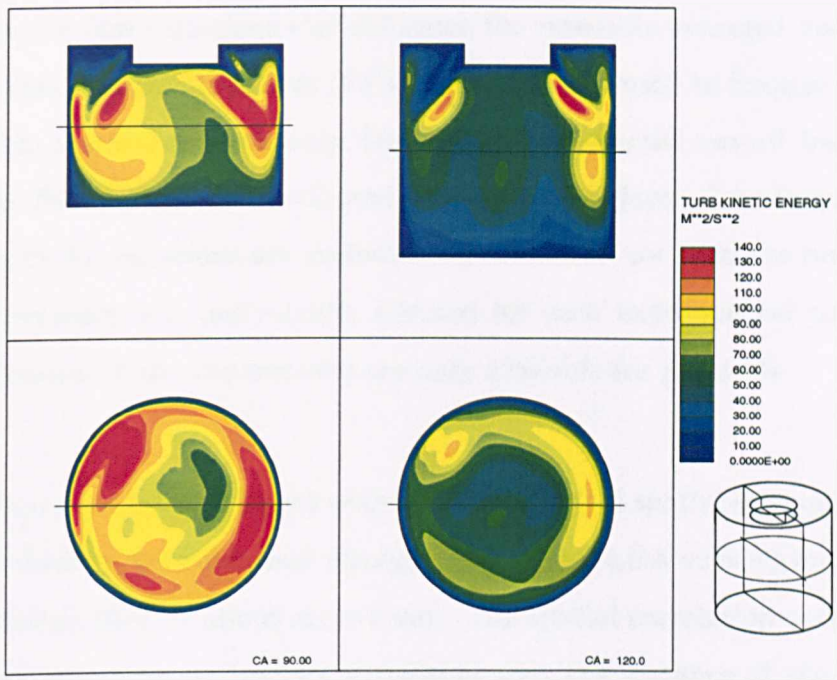



**Figure 6.11:** Turbulence kinetic energy distribution at horizontal and vertical cross-sections for 90° CA and 120° CA using fine mesh.

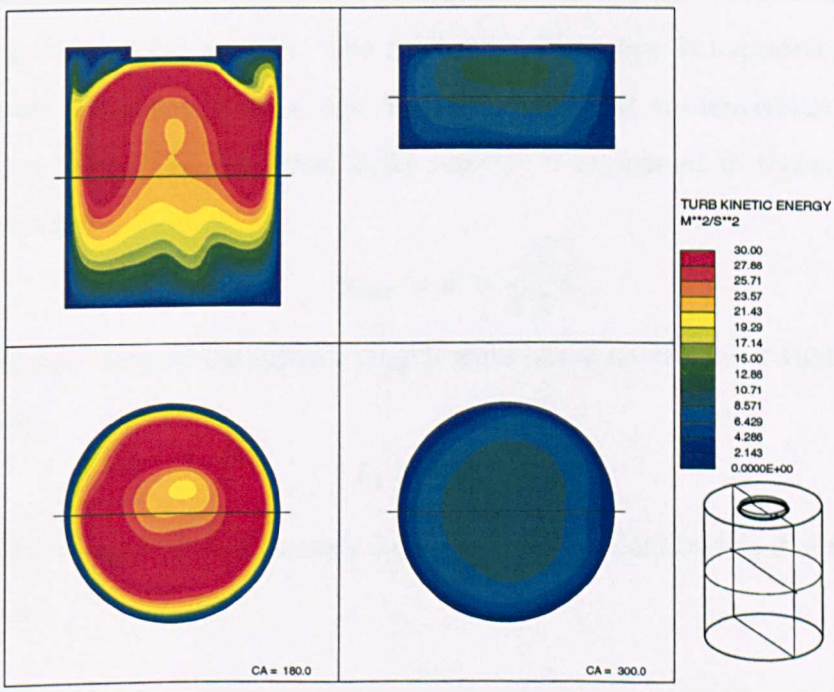



**Figure 6.12:** Turbulence kinetic energy distribution at horizontal and vertical cross-sections for 180° CA and 300° CA using fine mesh.

velocities are larger than the actual instantaneous turbulent fluctuations due to cycle-to-cycle flow variations that influence the ensemble-averaged mean [167]. Secondly, a Fast Fourier Transform (FFT) algorithm was used to frequency analyse the data. This method substantially depends on the selected cut-off frequency above which the fluctuations are attributed to turbulence effects. Low frequency fluctuations like cyclic variations are excluded and therefore not taken as turbulence. The cut-off frequency was individually selected for each experimental condition [190]. RMS velocities of the experiments are only available for point P3.

To obtain the integral length scale, the longitudinal spatial correlation coefficient of axial velocities were obtained through coincidental LDA velocity measurements at two locations offset by about $\Delta x$ =1 mm. The spatial correlation coefficient is then integrated according to Taylor's hypothesis over the distance of the measurement points. The integral length scale from the experiments is only available for point P2.

Turbulence intensities have been obtained from the predictions on the assumption of isotropy of turbulence. The existence of isotropy is supported by the measured RMS velocities in axial and radial direction at measurement point P2, as reported in [190]. The predicted RMS velocity is expressed in terms of turbulence kinetic energy:

$$u_{\mathrm{RMS}} = u' = \sqrt{\frac{2}{3}k}$$

The predicted integral turbulence length scale based on the $k-\varepsilon$ turbulence model, defined as:

$$L_t = C_\mu^{0.75} \frac{k^{1.5}}{\varepsilon}$$

can only be compared qualitatively with the experimental trends due to the different definitions.

In Figure 6.13 the measured and predicted axial RMS velocity variations at point P3 are given. From the measurements it can be derived that the high turbulence level

caused by the inflow process is gradually dissipated during the compression stroke. A local maximum appears before TDC, mainly as the result of the vortical structure in the cylinder centre collapsing. During expansion no additional turbulence is generated, as seen from the decay of velocity fluctuations.

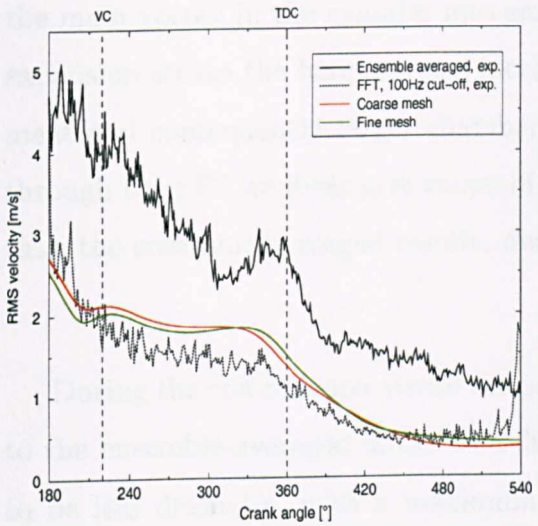



**Figure 6.13:** Comparison of axial RMS velocity at measurement point P3.

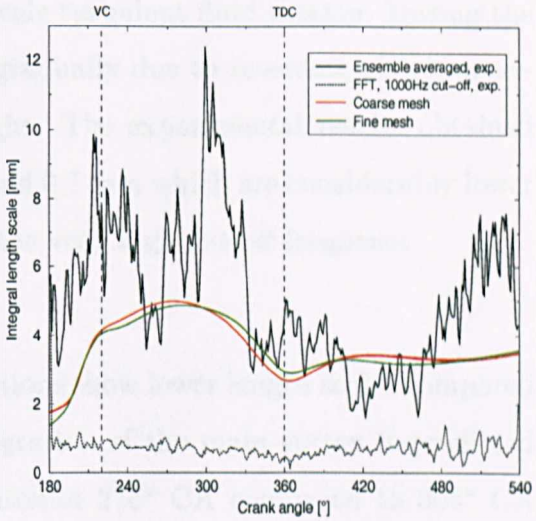



**Figure 6.14:** Comparison of integral length scale at measurement point P2.

The ensemble-averaged results give the highest RMS velocities. The results from FFT give lower quantities by about a factor of two. The difference indicates that the experiments were subject to large cyclic variations.

The predicted curves show qualitatively very good agreement with the experiments. Overall higher axial RMS velocities by 15% and 14% are predicted compared to the FFT results using the coarse and fine mesh, respectively. The calculations show a more rapid disintegration of the macro-structures of the flow field, indicated by an earlier local maximum before TDC and a faster turbulence decay during expansion. This discrepancy can be attributed to the inaccuracies of the turbulence model. The differences between the predictions, of the order of 1%, come from the slight deviation in calculated position of the ring vortex centre close to the measurement point, as discussed before.

The measured integral length scale variations obtained at P2 and the turbulence length scale from the predictions are provided in Figure 6.14. A gradual increase in length scale is observed in the measurements until about 305° CA, after which a sharp drop occurs towards TDC. This behaviour coincides with the disintegration of the main vortex in the cylinder into small-scale turbulent fluid motion. During the expansion stroke the length scales increase gradually due to reversing piston movement and consequently larger chamber height. The experimental results obtained through the FFT analysis give values of around 0.7 mm which are considerably lower than the ensemble-averaged results, due to the very high cut-off frequency.

During the compression stroke the predictions show lower length scales compared to the ensemble-averaged data. The disintegration of the main vortex is predicted to be less dramatic, with a maximum at around 275° CA compared to 305° CA for the measurements. At TDC the integral length scales are around 4 mm for the experiments, which corresponds to 1/4th of the clearance gap. The values for the calculations are 2.66 mm for the coarse mesh and 2.93 mm for the fine mesh, which is about 1/5th of the gap. The continuous increase in integral length scale during the expansion stroke is not captured in the calculations.

Overall the predictions of both meshes for the length scales differ by 0.6%. The deviation of the predictions from the measurements mainly arises from the respective location of the corner vortex which substantially affects the point comparisons.

The computational time increased by about a factor of 2.5 from coarse to fine mesh. Similar qualitative and quantitative agreement was achieved by comparison to experimental data. Marginally better agreement was obtained for the inflow profiles using the fine mesh. Slight deviations in flow field structure, in particular for the compression stroke, could be identified between the two meshes. While the point comparison of axial velocity history differed by 18%, the magnitudes of

trapped mass and turbulence parameters agreed by more than 99%. Further mesh refinement would be computationally expensive and would yield similar accuracies due to the deficiencies in the estimation of inflow velocities as mentioned before. These substantially influence the in-cylinder flow field during the period considered herein. Hence for the remainder of the comparisons for this test case, only the results for the fine mesh are presented.

### 6.1.2 In-cylinder pressure and temperature

In Figure 6.15 the calculated and measured pressure traces are displayed, using for the former both standard and modified wall functions. Quantitative agreement exists up to about 346° CA, which is after VC. This suggests that the trapped mass is correctly predicted. The peak pressure timing for the experiment occurs slightly earlier than for the calculations. The difference in peak pressure is approximately 4.3% and 3.3% for the standard and modified wall function approaches, respectively. Furthermore the pressures during the expansion stroke exceed the measured values. The possible causes for this difference are blowby in the experiments which has not been accounted for in the simulation and larger heat losses to the walls in the research engine compared to the predictions. Overall, the MWF approach performs slightly better with pressures closer to the experiments in comparison to the conventional near-wall treatment. This is thought to be due to increased wall heat transfer which will be discussed further in Section 6.1.3.

The measured and calculated bulk gas temperatures are presented in Figure 6.16. The calculated temperature variation exhibits higher values up to 80 K for the compression stroke, while the peak location occurs earlier than the measured one. The measurement results have been reported to lag behind actual values up to 20° CA [190], which is close to the current discrepancies. In addition, the temperatures at start of compression are lower than the inflow temperature when the valve lift is half the maximum value. This gives further reason to question the accuracy

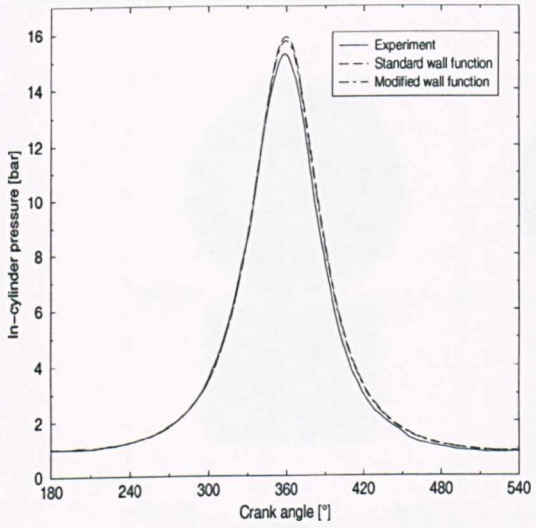



**Figure 6.15:** Calculated and measured pressure variations.

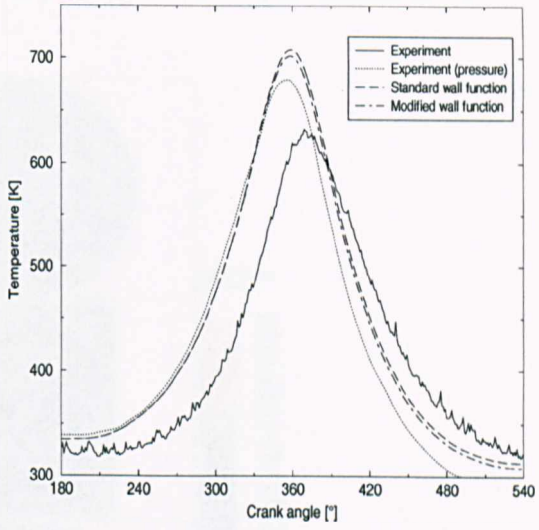



**Figure 6.16:** Calculated and measured bulk temperature variations.

of the experimental data.

As an alternative, the in-cylinder temperature was re-evaluated based on the measured pressure trace and the ideal gas equation. The mass was taken from the CFD calculation and the gas constant was taken as 287.1 J/(kg K). The justification for this approach is that the calculated trapped mass was concluded to match closely the actual value. The numerical solutions follow the derived experimental temperature closely up to TDC. The temperature maximum occurs later for the numerical simulations with larger peak values of around 4.3%, similar to the pressure trace. During expansion the predicted curves are higher. This is because of the assumption of constant trapped mass, whereas the actual mass is affected by blowby.

### 6.1.3 Wall heat transfer

Figures 6.17 – 6.20 display the spatial variations of the calculated heat fluxes on the chamber walls at selected crank angles, obtained via the two wall function approaches. A negative flux indicates heat exchange from the gas to the wall. The upper plot of the figures shows the cylinder head, the middle plot the cylinder liner

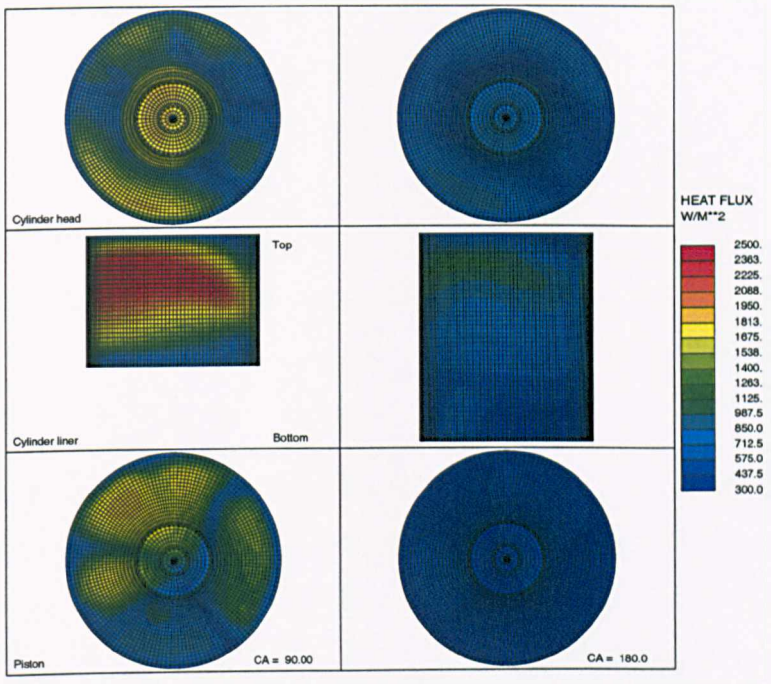



**Figure 6.17:** Heat flux distributions for 90° CA and 180° CA using SWF approach.

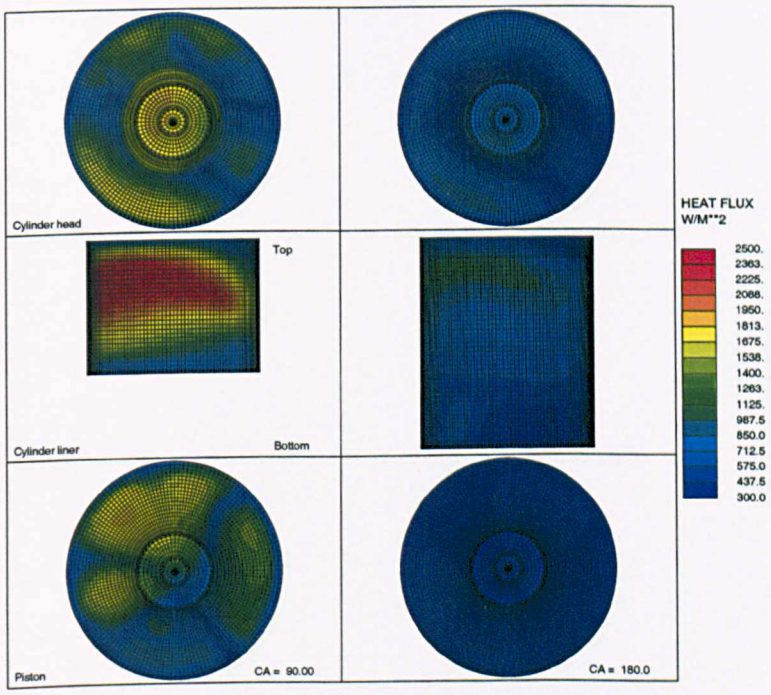



**Figure 6.18:** Heat flux distributions for 90° CA and 180° CA using MWF approach.

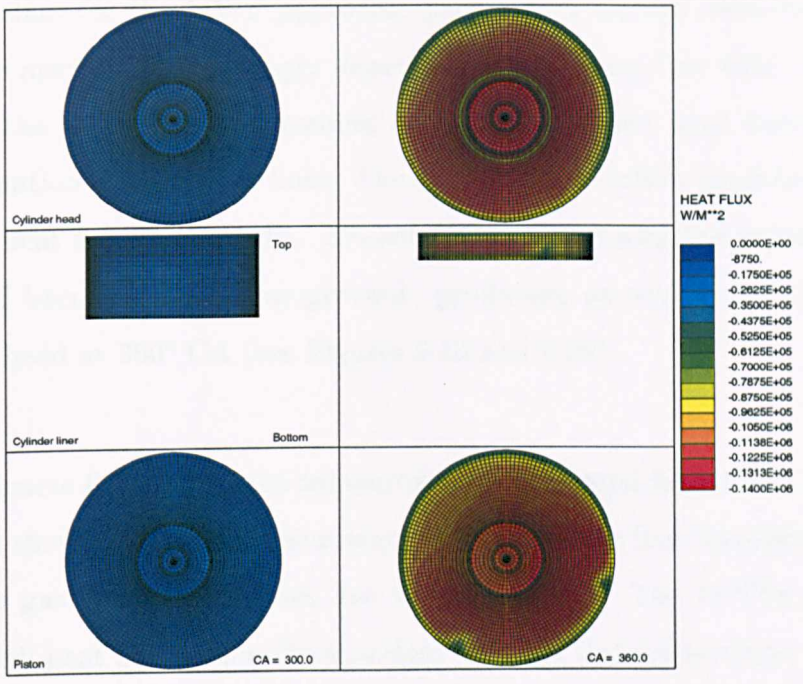



**Figure 6.19:** Heat flux distributions for 300° CA and 360° CA using SWF approach.

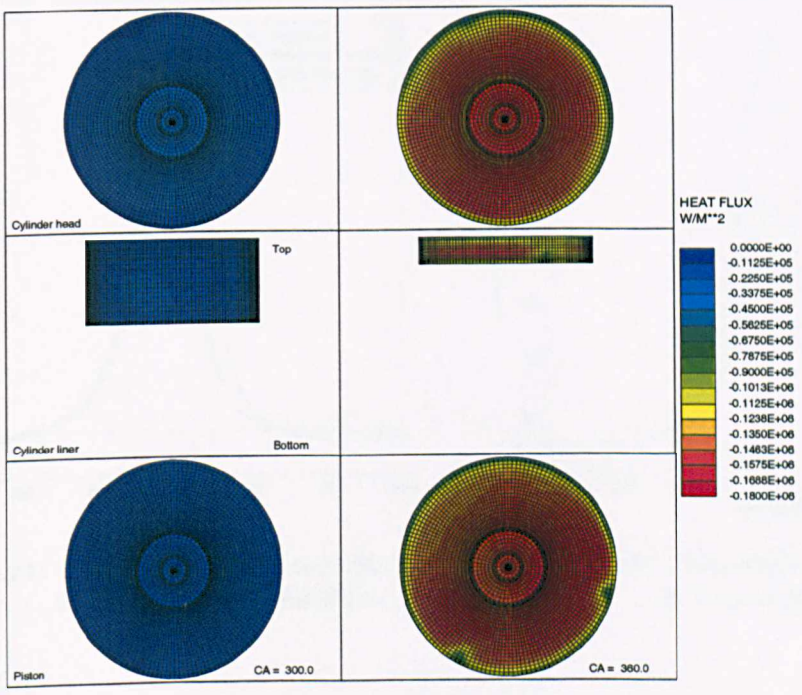



**Figure 6.20:** Heat flux distributions for 300° CA and 360° CA using MWF approach.

and the lower plot the piston surface. Similar distributions are predicted, but with higher values for the MWF approach, particularly during compression. The heat exchange mechanism is strongly dependent on the local flow field. For instance, at 90° CA the effects of the incoming air is seen. Higher heat fluxes occur around the stagnation point on the liner. The asymmetrical inflow conditions cause a non-uniform heat flux at the walls. Towards TDC and during the expansion stroke the flow field becomes more homogeneous, producing an almost uniform level on the cylinder head at 360° CA (see Figures 6.19 and 6.20).

In Figures 6.21 – 6.23 the measured and calculated heat fluxes on the cylinder head are shown for three measurement locations. The flux increases towards TDC, since the gas temperature rises due to compression. The MWFs give about 27% higher wall heat fluxes than the standard versions and are in closer accord with the measurements. Particularly at HT1 quantitative excellent agreement is achieved where the difference for the peak flux amounts to 0.6%. However, the levels at HT2 and HT3 are underpredicted by a maximum of 40% at location HT2.

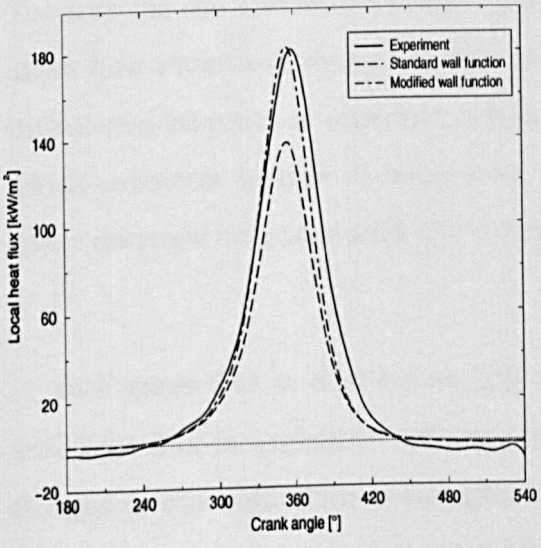



**Figure 6.21:** Comparison of local heat flux at measurement point HT1.

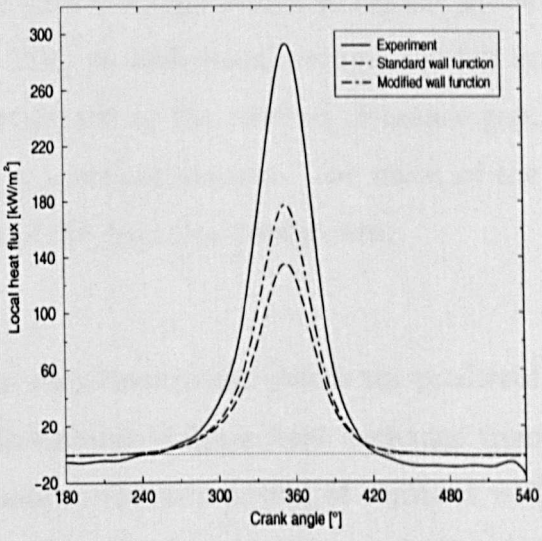



**Figure 6.22:** Comparison of local heat flux at measurement point HT2.

The peak flux timing is predicted earlier than in the measurements, on average by 2.5° CA. The origin of this discrepancy probably lies in the differences between mea-

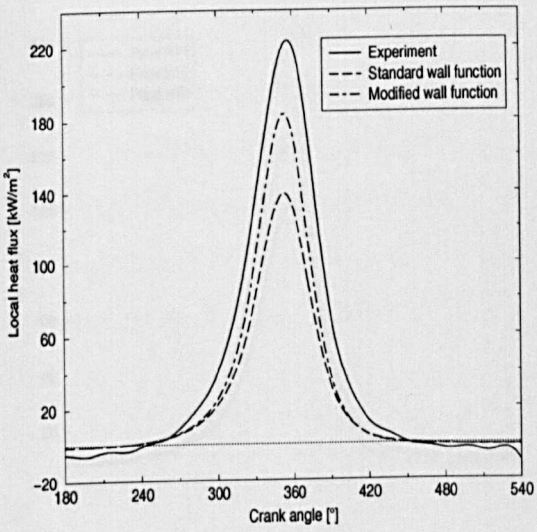



**Figure 6.23:** Comparison of local heat flux at measurement point HT3.

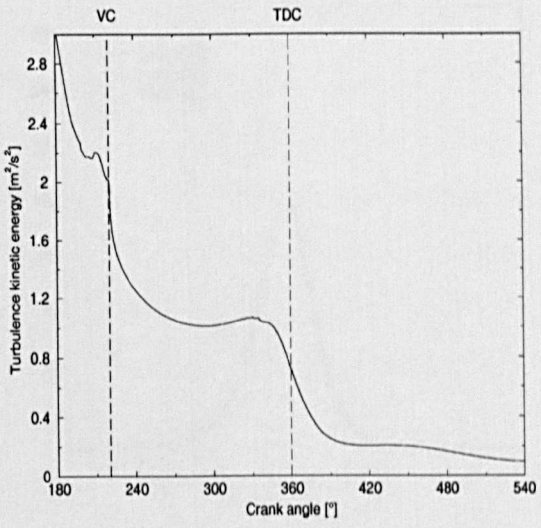



**Figure 6.24:** Average turbulence kinetic energy in near-wall region.

sured and predicted local flow and turbulence fields. As pointed out in Section 2.3.5 and as seen from Eqs. (3.201) and (3.204), the heat transfer characteristics strongly depend on the nature of the flow macro-structure and turbulence. In this respect, Figure 6.24 shows the averaged turbulence kinetic energy in the near-wall region. Towards the end and after VC the turbulence kinetic energy decreases rapidly as the mean flow structures decay. Shortly before TDC an additional, pronounced fall in turbulence intensity is observed, which is attributed to the reduced clearance gap, which promotes further disintegration of flow macro-structures. The onset of the latter decrease coincides with the maximum of the heat flux predictions.

In Figures 6.21 to 6.23 before 240° CA at all measurement points the predicted wall heat flux is negligible, whereas the experiments indicate heat exchange from the gas to the wall. This is thought to be due to the assumption of constant wall temperatures in the calculation. In fact the actual wall temperatures during this period must be higher than the assumed value. The same situation occurs after around 450° CA. However, the energy exchange during these periods is small compared to the peak fluxes so that the effect on the overall heat exchange will be small.

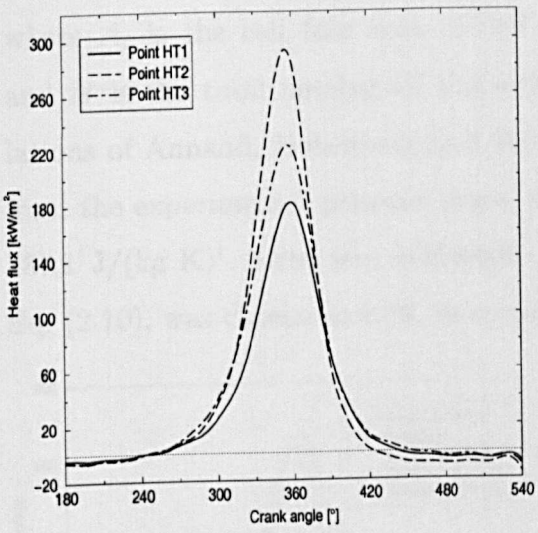



**Figure 6.25:** Summary of heat flux measurements at three locations on cylinder head.

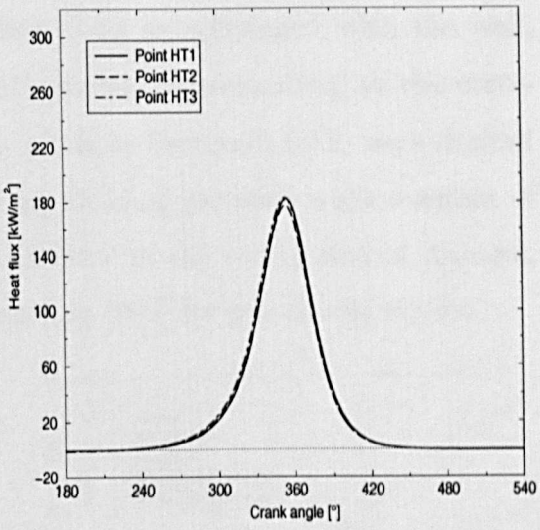



**Figure 6.26:** Summary of heat flux predictions using modified wall function approach.

Collective comparisons between the measured and predicted heat fluxes obtained from the MWF approach are shown in Figures 6.25 and 6.26. The average error in the maximum level is 19%. However, it has to be stated that the surface temperature measurements were subject to a considerable standard deviation of around 10%. The experimental data show a larger variation between the measurement points than the CFD results. This suggests that the near-wall flow structure and turbulence intensity in the experiments differ from the predictions, which consequently affects the wall heat flux. This has been discussed in Section 6.1.1 with respect to axial velocities and turbulence parameters for points P2 and P3. The simulation gives a more uniform velocity and turbulence distribution toward TDC, as seen from Figures 6.4 and 6.12. Furthermore, at crank angles later than 450° CA, the predictions show approximately the same heat flux for all three locations, suggesting homogeneous flow properties. The experimental curves do not exhibit this behaviour.

In Figure 6.27 temporal variations of the surface-average global heat transfer coefficients are shown for compression and expansion strokes. These are defined by:

$$\overline{h}_{\text{area}} = \frac{1}{\sum_i^N A_i} \sum_i^N h\, A_i$$

where $A_i$ is the cell face area of cell $i$, where heat is exchanged with the wall, and $N$ is the total number of wall cells. The curves corresponding to the correlations of Annand, Hohenberg and Woschni, given in Section 2.3.5.2, were derived from the experimental pressure trace, assuming an ideal gas with a gas constant of 287.1 J/(kg K)†. Swirl was neglected. The factor $c$ in the correlation of Annand, Eq. (2.10), was chosen as 0.49, as recommended in [294] for low charge motion.

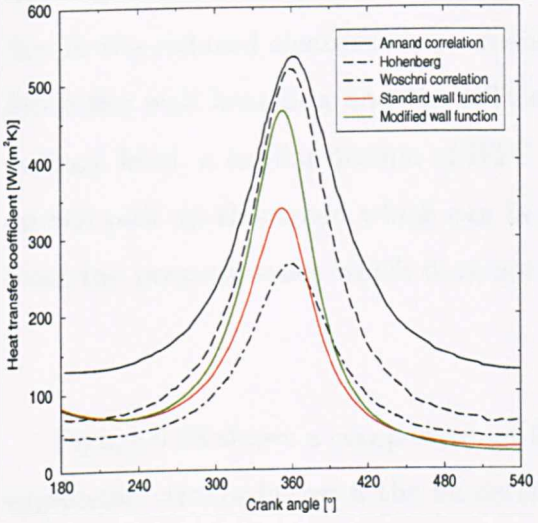



**Figure 6.27:** Comparison of heat transfer coefficients between calculations and global heat transfer models.

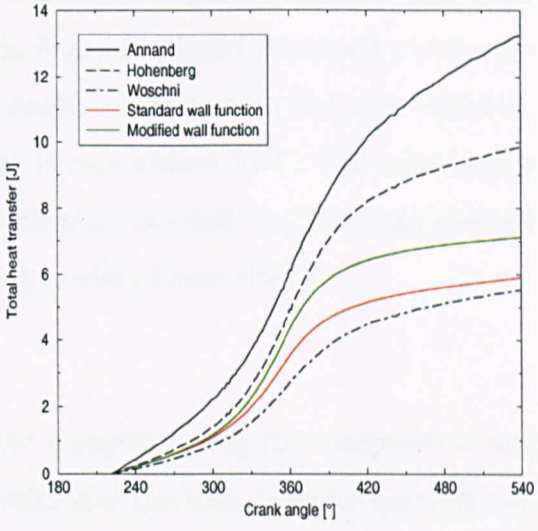



**Figure 6.28:** Comparison of total heat transfer between predictions and global heat transfer correlations.

For the global heat transfer, the results obtained from the MWF approach are taken as the basis for comparisons, since they are thought to best represent the actual heat transfer based on the previous findings. Large variations are seen among the correlation-based heat transfer approaches by more than a factor of two. While the correlation of Hohenberg agrees better with the MWF approach during compression, the correlation of Woschni gives closer values to the latter during late expansion. Overall substantially larger HTCs are calculated with Annand's correlation compared to the MWF results. The peak HTCs are overestimated by the correlations of Annand and Hohenberg by 15.5% and 11.9%, respectively, and underestimated by 43% using Woschni's correlation. The SWF method predicts a 27.2% lower peak

†The gas constant remains approximately constant over the range of pressure and temperature conditions [450].

HTC than the MWF approach and gives similar HTC levels when cylinder temperatures are low, i.e. during early compression and late expansion.

The empirical correlations show a flatter variation than the present predictions, with the peak value occurring about 7° CA later. This shift in peak timing originates from a predicted decay in mean flow structures and turbulence intensity before TDC due to the reduced clearance gap, as shown in Figure 6.24 and discussed previously. Since the wall heat flux and the HTCs are closely connected to the near-wall turbulence level, a similar decline of HTC values occurs before TDC. The correlations do not pick up this trend which can be attributed to the fact that they are derived from the pressure trace which does not seem to reflect these effects.

Figure 6.28 shows a comparison of the heat transfer during the compression and expansion strokes between the numerical results and the heat transfer correlations. This quantity essentially affects the engine efficiency. It is assumed that the total heat transfer vanishes when gas and wall temperatures are identical during the compression stroke. Annand's and Hohenberg's correlations yield the highest total heat transfer at 540° CA which is larger by 86% and 38%, respectively, compared to the modified near-wall treatment. The correlation of Woschni gives total heat transfer levels which closely follow the predictions of the SWF approach, resulting in 23% lower values at 540° CA than the MWF results. 17% smaller total heat transfer is predicted using the standard near-wall treatment in comparison to the modified version. Based on the above comparisons it can be concluded that neither of the empirical correlations yields superior results.

Finally the heat transfer measurements and predictions indicate substantial spatial heat flux and heat transfer coefficient variations. These are not accessible via the empirical heat transfer correlations, which give only the surface-average value.

### 6.1.4 Summary

In this section the flow field and wall heat transfer predictions were assessed for a motored engine.

In general the inflow velocity profile could be well reproduced. However, the predicted peak velocities exceeded the measured ones by a factor of three. Qualitative agreement was achieved for axial velocities at P3 with disagreement in particular during the compression stroke. During expansion the axial velocities were underpredicted at this location overall by 38%. These results were considered reasonably good in particular when considering that the cycle-to-cycle variations in the experiments were up to 68%. The calculated turbulence parameters agreed qualitatively with the measurements. The axial RMS velocities were overpredicted by 14% and the integral length scales were underpredicted by 32%. The cause for the differences between experiments and calculations was in part attributed to the practice of deriving the inflow conditions from steady-state experiments that do not consider dynamic effects. Other sources of error were thought to originate from the turbulence model and inaccuracies from the numerical resolution of the in-cylinder processes. Therefore the calculated position of local flow structures near the cylinder head differed from the experiments, substantially affecting the point comparisons.

Encouraging results were achieved for the cylinder pressure history. Differences between measurements and calculations occurred mainly during expansion. Possible reasons are blowby, which has not been considered in the predictions, and higher actual heat transfer, as seen from the point heat flux comparisons. The peak pressure was overpredicted by about 4%, similar to the gas temperature that was derived from the pressure trace using the ideal gas law.

The point heat transfer comparisons showed that the predicted heat fluxes using the MWFs are on average 19% lower than measured, and the calculated peaks occurred around 2.5° CA earlier than in the experiments. The standard and modified wall function approaches gave similar trends, with the latter achieving 27% higher heat transfer on average. Best agreement was obtained using the modified near-wall

treatment. Disagreement between measurements and simulations were attributed to differences in local flow structures.

Large variations in HTCs were observed from the empirical heat transfer correlations by a factor of two. The predicted curves were on average in between the predictions of Hohenberg's and Woschni's correlations with the former yielding the best agreement among the correlations with respect to the MWF approach. The measurements and CFD results demonstrated that the distribution of heat fluxes varies substantially over the cylinder walls. The empirical correlations are not capable to predict critical levels and regions of heat transfer, since they give only the surface-average estimate.

## 6.2 Aachen Pressure Chamber

### 6.2.1 Fuel vapour and liquid penetration

The vapour mass fraction distributions for several time instances given by calculations with the LATCT/NSC[†] and RIF models are shown in Figures 6.29 and 6.30. The plots are for an 80 × 12 mm region in the top left corner of the calculation domain. In Figure 6.29 it is seen that the vapour propagates along the centreline with the highest concentrations in the core. At 2 ms, which is after the ignition at 1.63 ms, fuel vapour is depleted at the periphery of the vapour plume, leaving a fuel-rich core between 30 and 40 mm downstream of the injector. Nearly all fuel is consumed at 2.5 ms.

The fuel vapour fields in Figure 6.30, obtained with the RIF approach, resemble those for the LATCT combustion model. However, the vapour propagation is faster. Due to the earlier ignition at 1.3 ms, the majority of fuel is consumed at 2 ms and no vapour exists at 2.5 ms.

[†]LATCT/NSC model refers to the LATCT combustion model combined with the Hiroyasu soot formation and NSC soot oxidation model.

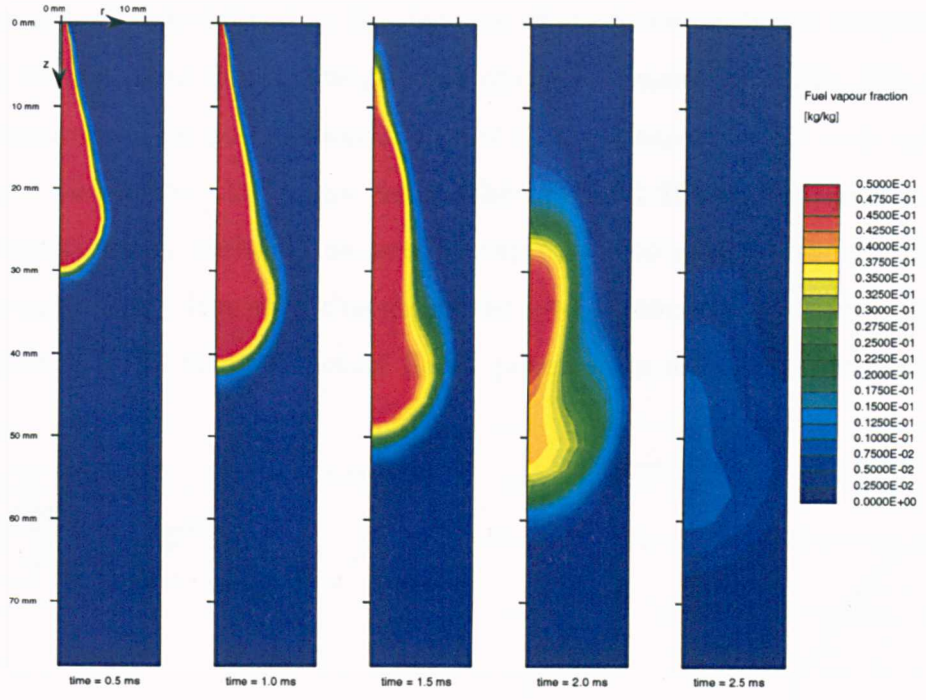



**Figure 6.29:** Fuel mass fraction for LATCT/NSC model at times 0.5 – 2.5 ms.

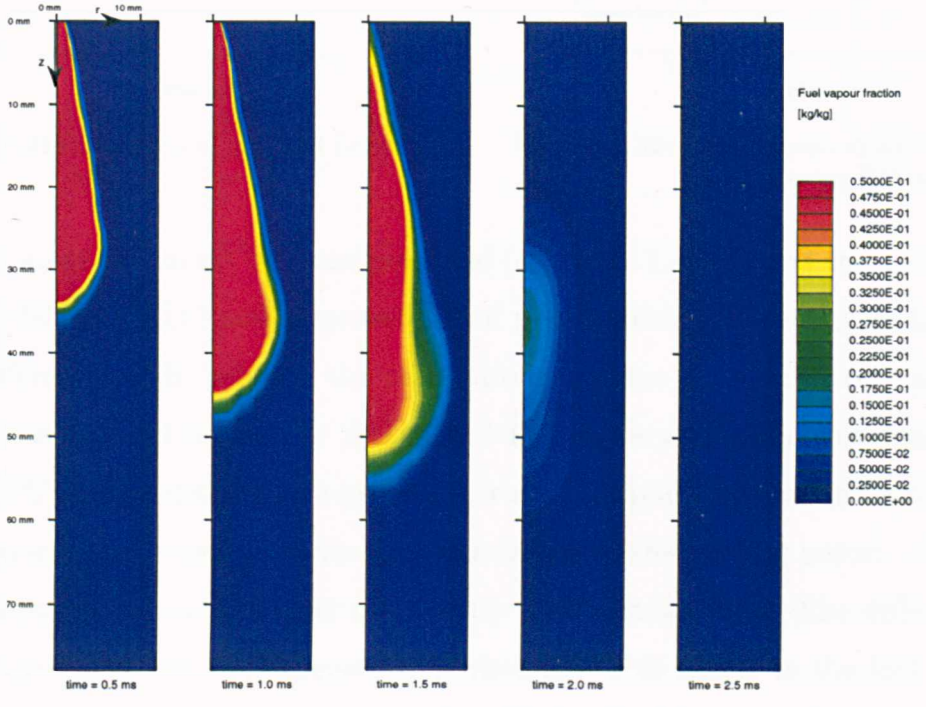



**Figure 6.30:** Fuel mass fraction for RIF approach at times 0.5 – 2.5 ms.

The axial liquid penetration is displayed in Figure 6.31. In the computations, the liquid penetration is defined as the distance of the foremost liquid droplet from the injector location and follows the practice of several researchers [141, 196, 359, 442]. The measured liquid penetration in Figure 6.31 increases to 22.7 mm until 0.3 ms and drops thereafter. At 1.1 ms, before the EOI at 1.26 ms, no liquid is discerned in the experiments, probably because the spray is too dilute to be detected. This trend is unrealistic. However, this shows the level of uncertainty in the experiments and would indicate that the actual liquid penetration may be above the measured values.

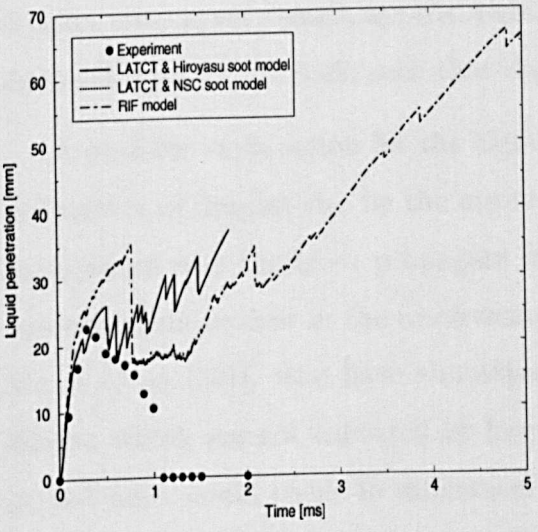



**Figure 6.31:** Comparison of liquid penetration.

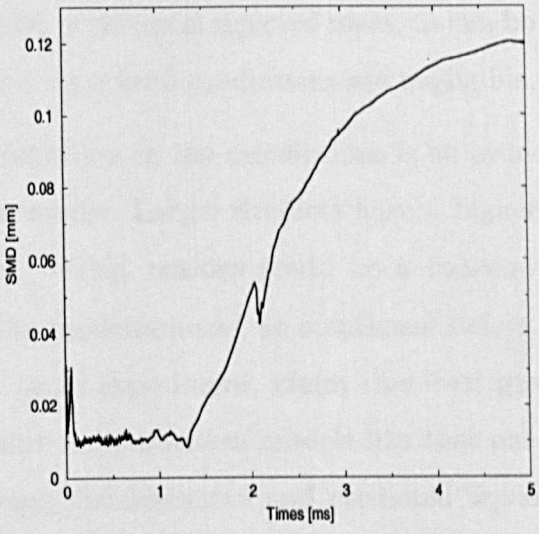



**Figure 6.32:** Sauter mean diameter for calculation using RIF approach.

Very good agreement between predicted (using the LATCT and the two different soot models and RIF) and measured liquid penetrations is observed up to 0.2 ms. The different trends between the calculations are due to the differences in local heat release as will be seen in Section 6.2.3. Contrary to the measurements, the two LATCT calculations give a general increase in liquid penetration up to 37 mm, interspersed with sharp falls due to evaporation of the leading parcel. Complete evaporation is observed at 1.82 ms, shortly after autoignition. The different soot models give identical liquid penetration histories. This is due to the fact that the onset of soot formation only starts after all the liquid fuel has evaporated (see Section 6.2.4).

The RIF model produces higher liquid penetration than the experiments. The spray penetrates steadily up to 35.2 mm for the initial 0.78 ms, after which a sharp drop to 17.6 mm is seen. The latter reflects the heat released by the ignition reactions during this period, as will be seen in Figure 6.46, causing faster droplet evaporation. After 1.4 ms an increase in liquid penetration is again predicted until 5 ms. The corresponding SMD variation, as displayed in Figure 6.32, indicates that due to both enhanced droplet collision and subsequent coalescence and fast evaporation of small droplet the mean droplet diameter increases, causing the evaporation time to be prolonged. Therefore droplets are still present after 5 ms. However, the remaining droplet mass is very small, approximately 0.03% of the total injected mass, as can be deduced from Figure 6.49, such that the effects on overall predictions are negligible.

A possible explanation for the higher penetration in the calculations is an overestimation of droplet size by the atomisation model. Larger droplets have a higher momentum and therefore propagate further. Other reasons could be a too-slow vapourisation process or the uncertainty in the measurements, as mentioned before. Moon *et al.* [301], who have simulated the same experiment, claim that real gas effects, which are not captured by low-pressure vapourisation models like that employed here, could result in differences between the measured and predicted liquid penetrations. This was also outlined in the evaporation study in Section 3.4.5.8. In the simulations of Moon *et al.* overall better agreement with respect to liquid and fuel vapour penetration compared to the low-pressure model was achieved by evaluating the real gas VLE and enthalpy of vapourisation using the cubic EOS of Peng-Robinson. Nevertheless the reduced penetration length in the measurements after 0.3 ms could not be captured. Since no measurements of SMD are available, the cause for the present overpredictions cannot be identified unambiguously.

The axial vapour penetration is displayed in Figure 6.33. In the simulations the vapour penetration is defined as the distance from the injector to the foremost cell on the axis, which contains a fuel mass fraction of larger than $10^{-10}$. Once again both LATCT calculations using different soot models give identical results.

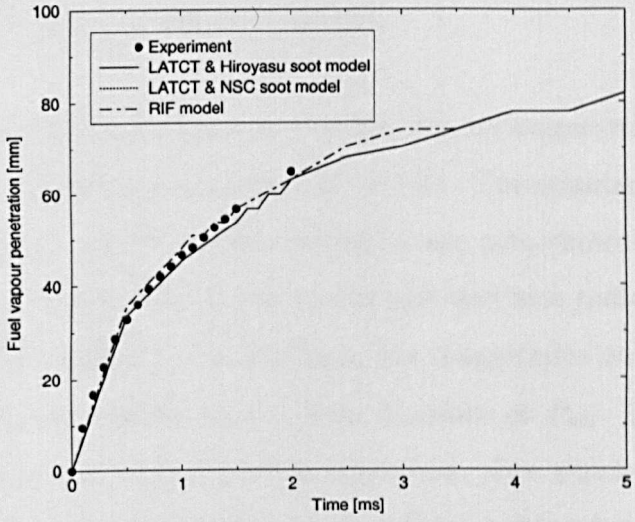



**Figure 6.33:** Comparison of axial fuel vapour penetration.

The experiments show that the vapour follows the liquid during the initial 0.3 ms. Thereafter the propagation slows, as seen from the decreasing slope, until the vapour is mainly convected by the gas. Qualitatively and quantitatively very good agreement is obtained between all calculations and the measurements. The results using the LATCT model are slightly low over the entire period. The RIF approach modestly overpredicts the penetration after around 0.4 ms. This is a consequence of the faster combustion taking place, resulting in locally higher temperatures and thus higher vapourisation rates. From 3.5 ms onwards all three calculations give identical results.

The small underprediction of the vapour penetration using the LATCT approach, which is in accordance with the overprediction of liquid penetration, could be attributed to an underestimate of the evaporation rate. Possible causes for this are either too large droplet diameters due to the atomisation model or a deficiency in the vapourisation model. Moon *et al.* [301] obtained improved results for vapour penetration for this test case, when applying the high-pressure vapourisation model described earlier. This supposition that the discrepancies between predictions and experiments originate primarily from the vapourisation model cannot be confirmed with certainty due to the lack of additional measurements for evaporation rate or SMD.

### 6.2.2 Fuel vapour concentration

The fuel vapour mass fraction histories at the five measurement locations, defined in Table 5.8, are displayed in Figures 6.34 to 6.38. The standard deviations in the measurements due to pulse-to-pulse variations are also shown. The experiments indicate that the vapour arrival times on the axis and at a radial distance of 4 mm from the axis differ negligibly. In addition, the magnitudes on the axis are larger than off axis with the highest vapour mass fractions at $P_{40}$. The vapour fraction initially increases rapidly reaching a first maximum, after which a local minimum is seen followed by a second maximum. At around 1.9 – 2 ms depending on the axial location, the effect of flame arrival is observed, in the form of a rapid depletion of fuel vapour.

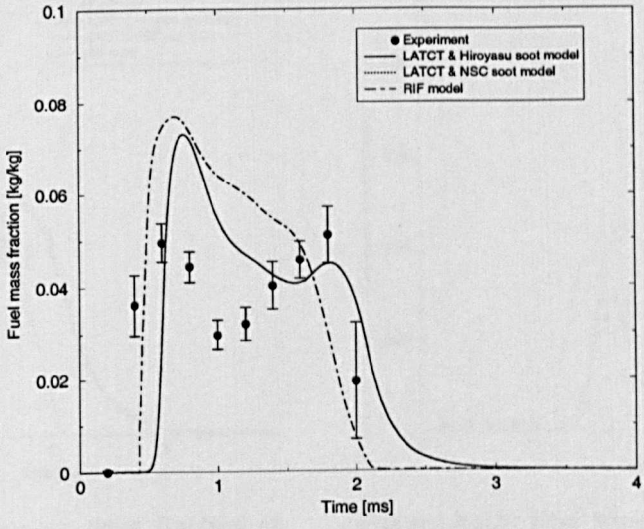



**Figure 6.34:** Fuel vapour mass fraction at $P_{34}$.

The two LATCT variants give nearly coincidental vapour mass fraction histories. The vapour arrival times occur too late at the locations $P_{34}$, $P_{40}$ and $P_{44}$, but good agreement is found at $z = 50$ mm. This confirms the findings of the vapour penetration results. The vapour fraction magnitudes are predicted well at $P_{40}$, but the first maximum and the local minimum are overestimated at the other locations. The second maximum is captured at $P_{34}$, but is absent in the predictions at $P_{44}$ and $P_{50}$.

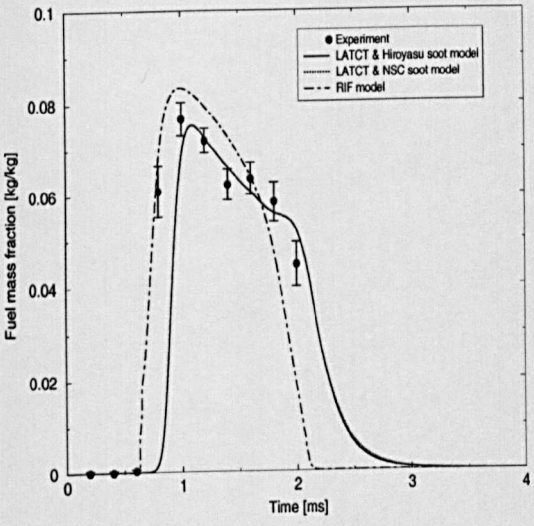



**Figure 6.35:** Fuel vapour mass fraction at $P_{40}$.

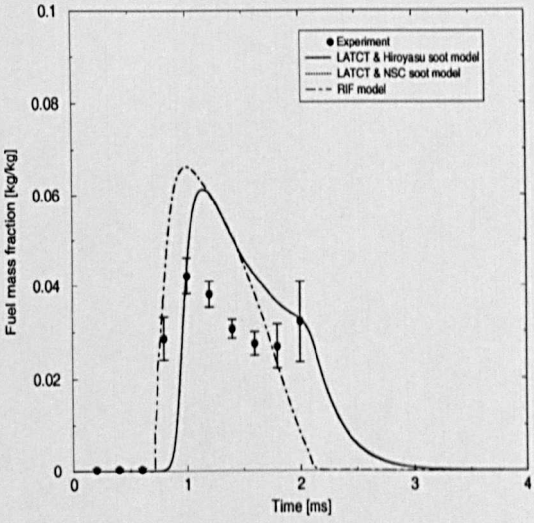



**Figure 6.36:** Fuel vapour mass fraction at $P_{44}$.

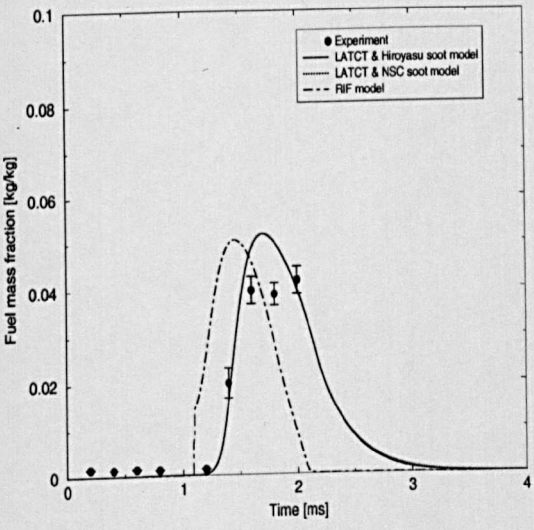



**Figure 6.37:** Fuel vapour mass fraction at $P_{50}$.

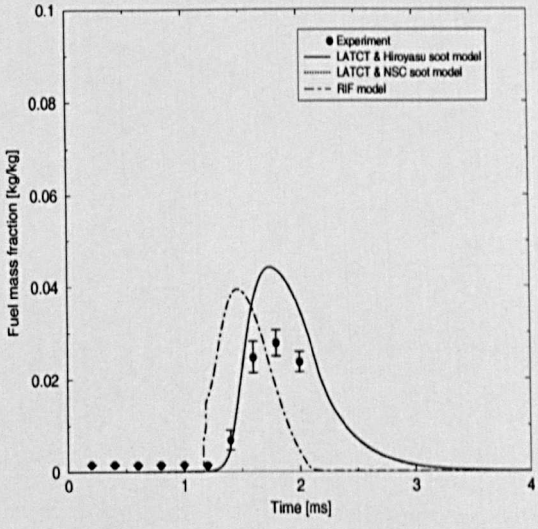



**Figure 6.38:** Fuel vapour mass fraction at $P_{54}$.

The RIF-based results show slightly too late vapour arrival at $P_{34}$, while good agreement is achieved for the locations at $z = 40$ mm. For locations $z = 50$ mm, the vapour arrives about 0.1 ms earlier than in the experiments. The fuel vapour concentrations are overpredicted until 1.7 ms, after which, due to combustion, the local concentration decreases, leading to an underprediction. The RIF approach fails to predict the local minimum and second maximum at all locations, which indicates that the burning rate is too fast. The predicted absence of fuel vapour at

all measurement points after 2.1 ms confirms this conclusion.

The general overestimation of fuel vapour levels prior to ignition can be attributed to underprediction of air/fuel mixing rates such that the rate of spread of fuel vapour is too low. This may point to inaccuracies of the turbulence model. Moreover the evaporation rates may be overpredicted, caused by either an underestimation of the initial droplet sizes or deficiencies in the vapourisation model. This, however, would contradict the supposition of underestimated evaporation rates for the fuel vapour penetration predictions. Additional errors due to insufficient numerical resolution and combustion modelling and experimental uncertainties can contribute to the discrepancies between measurements and calculations. The provided experimental data sets unfortunately do not yield sufficient information to substantiate any of the above possibilities. However, it is noteworthy that other researchers obtained similar levels of overprediction for the same experiments [77, 246, 264].

### 6.2.3 Combustion

Figures 6.39 and 6.40 show the burnt fuel mass fraction distributions for each combustion approach at times close to the occurrence of autoignition. The LATCT model (cf. Figure 6.39) predicts that at 1.6 ms – before autoignition – fuel is consumed near the tip and at the periphery of the vapour plume, with a maximum of burnt fuel mass at around 40 mm in axial and 5 mm in radial direction. Thereafter the burning region extends toward the injector, such that at 1.9 ms it is conical, lying between 5 mm and 30 mm in axial direction.

The RIF model (cf. Figure 6.40) predicts reactions on and near the stoichiometric mixture contour as early as at 1.1 ms. Several locations are observed, where local maxima of burnt fuel exist. The majority are located towards the tip of the vapour plume and at the periphery. This is due to the fact that a fuel-rich mixture exists in the injector region and at the edge of the liquid spray, where similarly high turbulence intensities and therefore high turbulent strains are seen, delaying

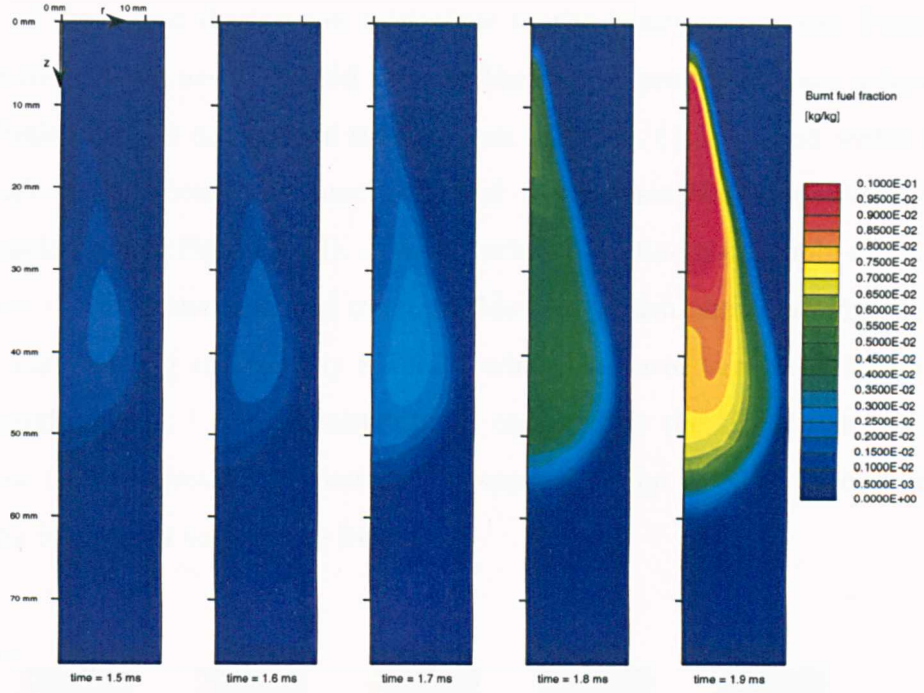



**Figure 6.39:** Burnt fuel mass fraction for LATCT/NSC model at times 1.5 – 1.9 ms.

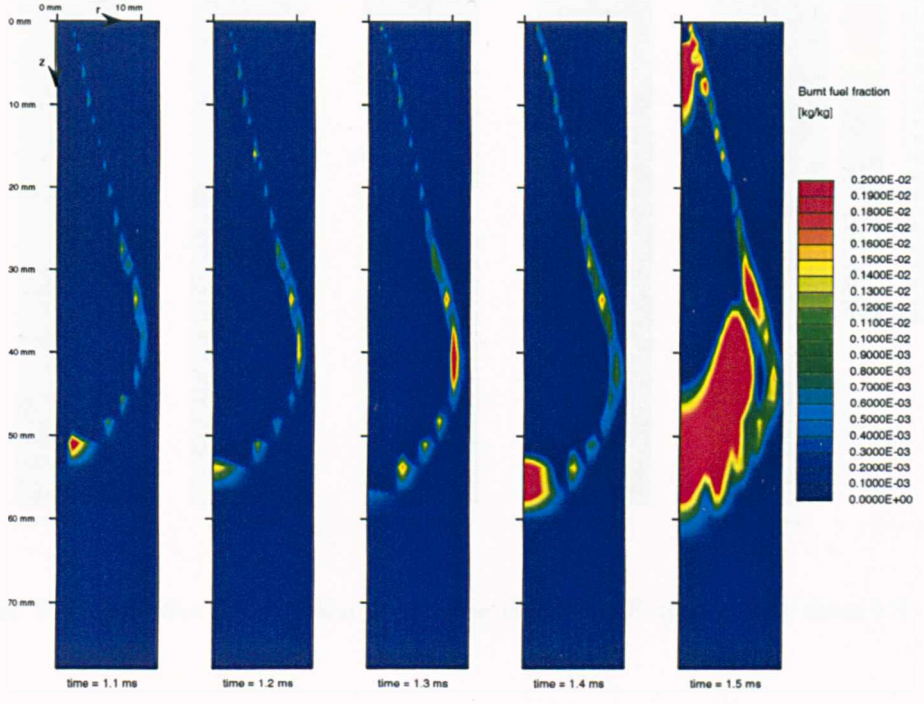



**Figure 6.40:** Burnt fuel mass fraction for RIF approach at times 1.1 – 1.5 ms.

burning in these locations. This is shown in Figure 6.41, which displays the distribution of the scalar dissipation rate. Due to the injection process, high variances of mixture fraction are predicted close to the liquid spray which are proportional to the turbulent scalar dissipation rate, as seen from Eq. (3.141), and which determine the shape of the local PDF function, used to evaluate the Favre-averaged species mass fractions (see Eq. (3.150)). A high variance produces a double $\delta$-function with values of unity at the fuel and oxidiser side [249], such that burning is prevented. Hence, the burning region only spreads, when the local turbulent strain rates are low enough. So at 1.5 ms combustion is confined to the tip of the vapour plume and close to the injector. The core of the vapour plume between 10 mm and 42 mm from the injector is too rich to burn.

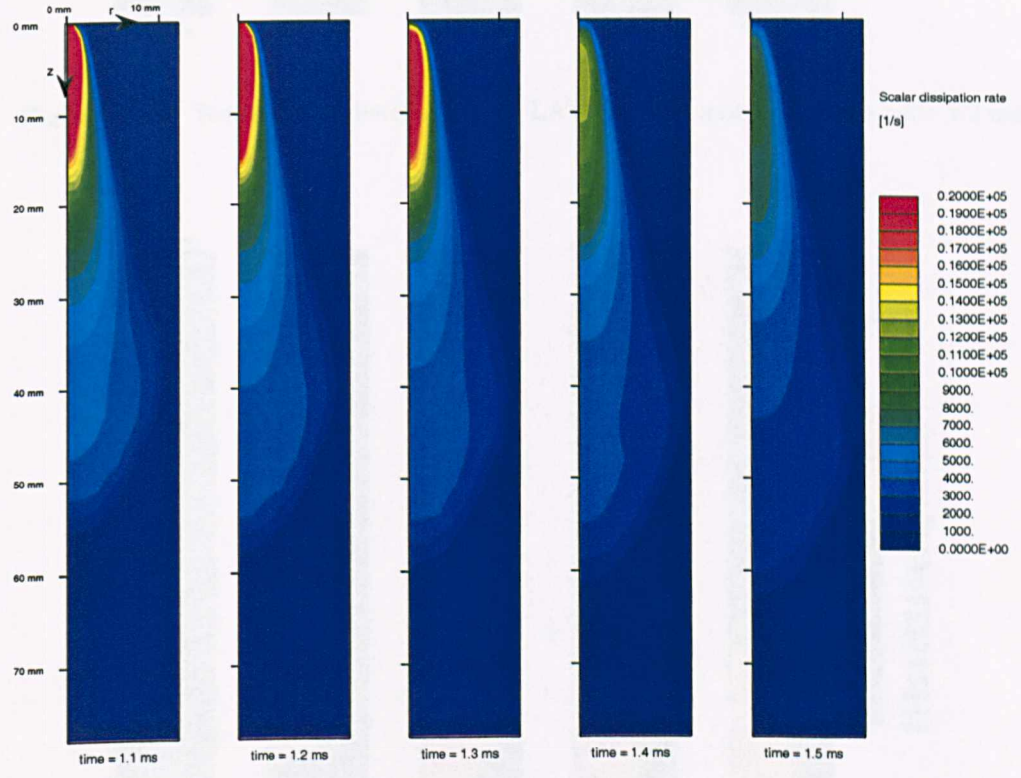



**Figure 6.41:** Distribution of scalar dissipation rate for RIF approach at times 1.1 – 1.5 ms.

In Figures 6.42 and 6.43 the temperature distribution at several instances is shown, predicted with the LATCT combustion model. Prior to autoignition the

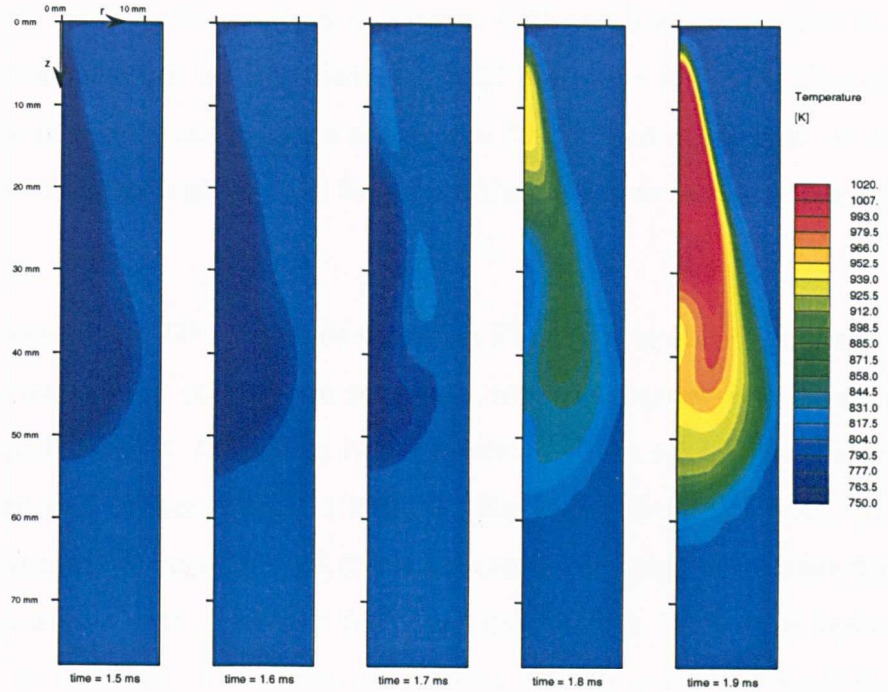



**Figure 6.42:** Temperature distribution for LATCT/NSC model at times 1.5 – 1.9 ms.

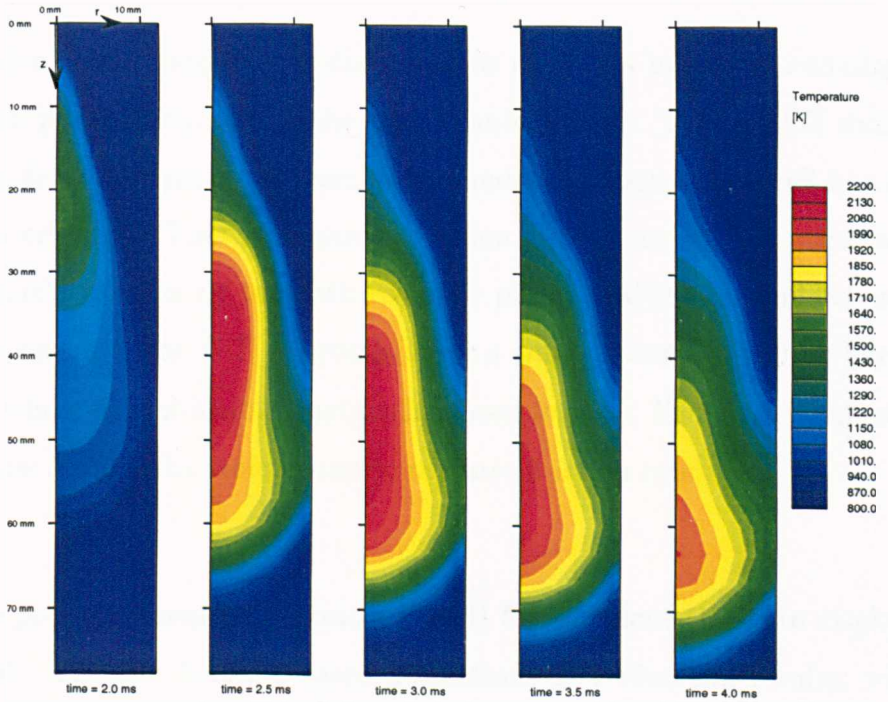



**Figure 6.43:** Temperature distribution for LATCT/NSC model at times 2.0 – 4.0 ms.

temperature field reflects the effects of evaporative cooling in regions where fuel vapour is formed. Comparison of Figures 6.39 and 6.42 shows that at 1.7 ms one autoignition site can be discerned, at $z \approx 32$ mm and $r \approx 7$ mm. This closely agrees with the measured autoignition site at $z = 30$ mm and $r = 4$ mm. At later times a hot core of gas as high as 2300 K is seen, that is convected away from the injector.

In case of the RIF model, as shown in Figures 6.44 and 6.45, low temperatures due to evaporative cooling are seen only within a narrow region along the spray axis, which extends 3.5 mm in radial direction. This reflects the behaviour of the predicted fuel vapour field at 1.0 ms, as illustrated in Figure 6.30. At 1.3 ms the temperature rise occurs around the stoichiometric contour of mixture fraction which is in agreement with the burnt fuel mass distribution. A distinct ignition location cannot be observed. The region of chemical activity spreads toward the spray axis and forms a hot core of temperatures as high as 2260 K. The combustion region then propagates along the spray axis as more fuel is consumed.

Evidently the temperature distributions produced by the two combustion models differ, particularly around the time of autoignition. The LATCT model switches globally from the ignition to combustion model as soon as one cell has reached the ignition criterion. Thus, the burning region extends rapidly to other regions such that shortly afterwards the entire vapour plume undergoes combustion reactions. On the contrary, the RIF approach using a single flamelet predicts burning everywhere, where a combustible mixture has been formed. Therefore combustion is seen in regions around the stoichiometric mixture fraction contour.

The predicted heat release rates (HRR) for all calculations are displayed in Figure 6.46. The two LATCT-based predictions give identical results, with a sharp increase in HRR after ignition, reaching a maximum of 410 kJ/s at around 2.1 ms. This characteristic rise, called the *thermal runaway* phase, is caused by the rapid

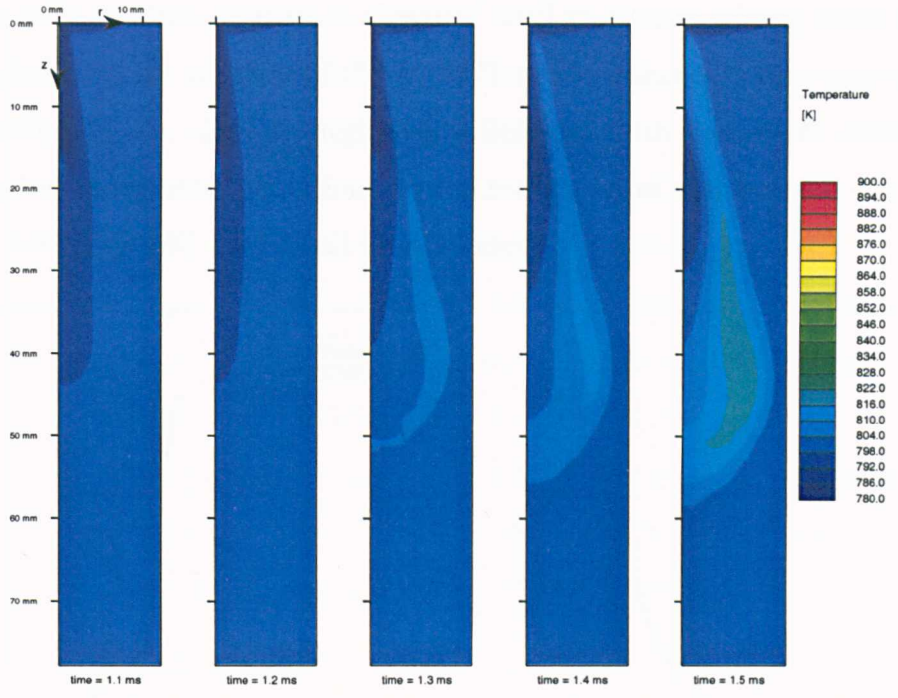



**Figure 6.44:** Temperature distribution for RIF approach at times 1.1 – 1.5 ms.

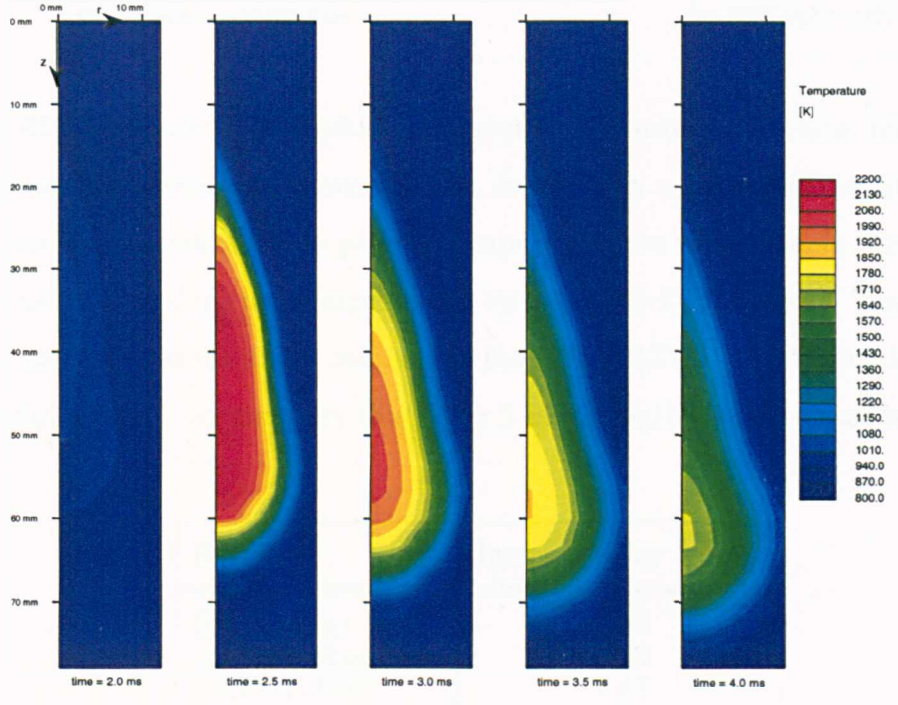



**Figure 6.45:** Temperature distribution for RIF approach at times 2.0 – 4.0 ms.

consumption of the premixed air/fuel mixture, formed during the ignition delay period. A more gradual decrease is observed until at around 4.5 ms, when combustion is completed. Both variants of the LATCT model using different soot models give very similar HRRs. Due to negligible differences with respect to combustion behaviour between both calculations, in the remainder of this section only the results for the LATCT/NSC model will be presented.

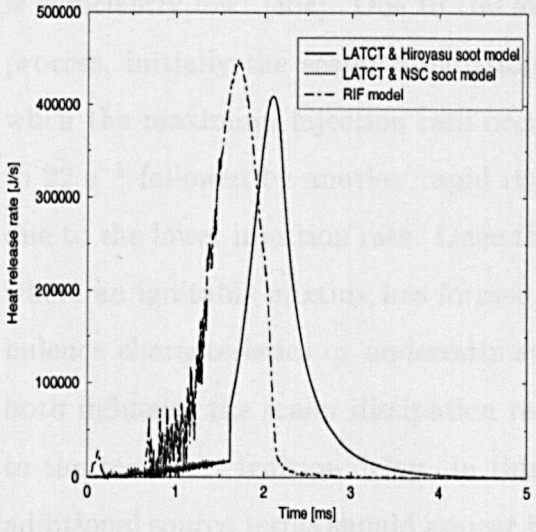



**Figure 6.46:** Heat release rate for different combustion approaches.

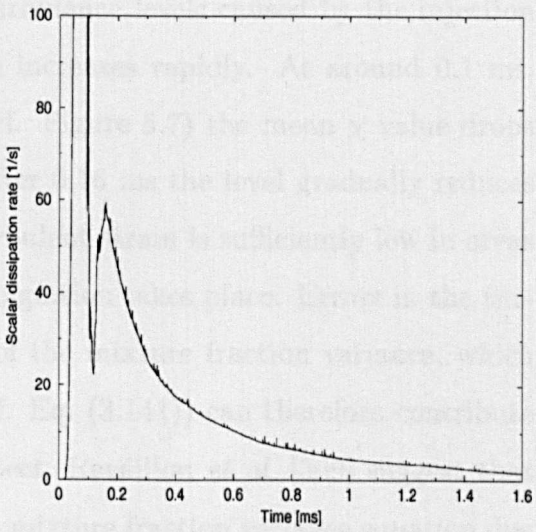



**Figure 6.47:** Scalar dissipation rate history for RIF approach.

The RIF approach does produce a sudden rise in heat release rate, but rather an initially low rise starting at about 0.65 ms, followed by a rapid increase at 1.3 ms, at which point autoignition takes place. Compared to the experiments, the measured ignition delay of 1.63 ms is underpredicted by 0.33 ms (cf. Table 6.1). The maximum HRR of 450 kJ/s occurs at 1.7 ms, earlier than the LATCT result. In addition a far steeper fall in HRR occurs, such that after 3 ms negligible heat release is predicted.

| Result | Ignition delay [°CA] |
|---|---|
| Experiment | 1.63 |
| LATCT/Hiroyasu | 1.63 |
| LATCT/NSC | 1.63 |
| RIF | 1.33 |

**Table 6.1:** Comparison of measured and predicted ignition delay for pressure chamber case.

The too short ignition delay from RIF may point to an underestimation of the scalar dissipation rate, as explained next. The chemical part of ignition delay is determined by the relative levels of heat and radical production via chemical reactions and loss by diffusive transport. In the RIF model the latter depends on the turbulent scalar dissipation rate $\chi$. In Figure 6.47 the history of the value of $\chi$ conditioned at stoichiometric mixture is presented. Ignition occurs, when the level of this quantity is sufficiently low† [464]. Due to the high turbulence levels caused by the injection process, initially the scalar dissipation rate increases rapidly. At around 0.1 ms, when the maximum injection rate occurs (cf. Figure 5.7) the mean $\chi$ value drops to 22 $s^{-1}$ followed by another rapid rise. After 0.16 ms the level gradually reduces due to the lower injection rate. Once the turbulent strain is sufficiently low in areas where an ignitable mixture has formed, autoignition takes place. Errors in the turbulence characteristics or underestimation of the mixture fraction variance, which both influence the scalar dissipation rate (cf. Eq. (3.141)) can therefore contribute to the too short ignition delay. In this respect, Revéillon *et al.* [369] suggest that additional source terms should appear in the mixture fraction variance equation due to evaporation, which will substantially influence ignition behaviour, such that the ignition delay is prolonged. The underpredicted ignition delay can also be caused by inaccuracies in spray and turbulence predictions which affect the distribution of fuel vapour and mixture fraction.

The histories of total fuel evaporated and burned are displayed for both combustion models in Figures 6.48 and 6.49. In the LATCT calculations it is seen that all the fuel has evaporated before autoignition. Prior to this about 4% of the fuel is consumed by the pre-ignition reactions. After ignition, burning is initially fast: then it slows down and the total fuel value is approached asymptotically. Quantitatively, 10% of the fuel is consumed at 1.77 ms, 50% is burnt at 2.12 ms, 90% at 2.67 ms and 99% at 3.8 ms (cf. Table 6.2).

†Barths *et al.* [31] propose a critical scalar dissipation rate of around 23 $s^{-1}$ for their studies of DI Diesel engines. Generally the critical value depends on the fuel type, pressure and temperature of the mixture [449]. Other critical values under Diesel-like conditions are found in [342].

| Model | Time to burn percentage of total injected fuel mass [ms] | | | |
|---|---|---|---|---|
| | 10% | 50% | 90% | 99% |
| LATCT/NSC | 1.77 | 2.12 | 2.67 | 3.80 |
| RIF | 1.40 | 1.70 | 2.00 | 2.41 |

**Table 6.2:** Time required by different combustion models to burn specific percentage of total injected fuel mass.

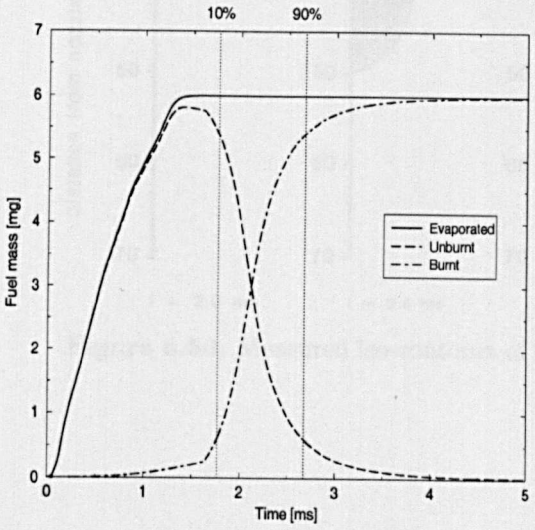



**Figure 6.48:** Evaporated, unburnt and burnt fuel mass for LATCT/NSC model.

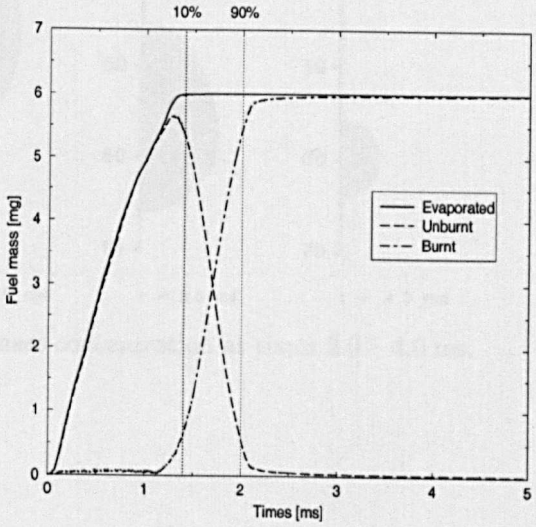



**Figure 6.49:** Evaporated, unburnt and burnt fuel mass for RIF approach.

The RIF approach predicts that during the ignition delay about 1% of the evaporated fuel is consumed. Then the remainder is depleted rapidly after autoignition. The quantitative measures are: 10% of the injected fuel mass is burnt at 1.4 ms, 50% at 1.7 ms, 90% at 2 ms and 99% at 2.41 ms. At 2.1 ms the burning rate rapidly reduces.

### 6.2.4 Soot concentration

The measured and calculated spatial distributions of soot at five times are shown in Figures 6.50 – 6.53. The measurements show a nearly spherical soot cloud that is convected along the spray axis. The highest concentrations of up to 16 g/m$^3$ are found at 2.5 ms.

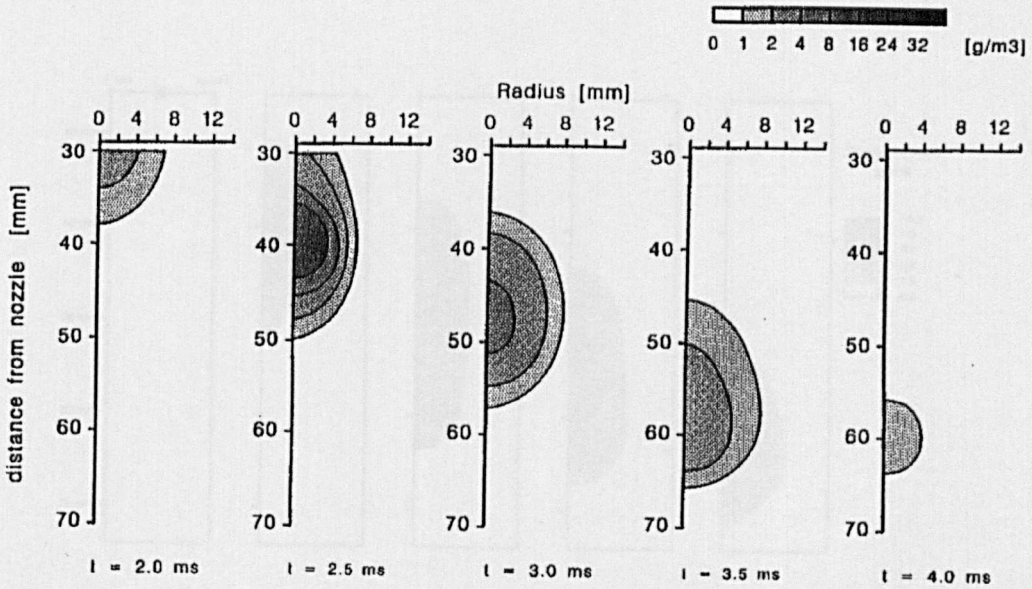



**Figure 6.50:** Measured iso-contours of soot mass concentration at times 2.0 – 4.0 ms.

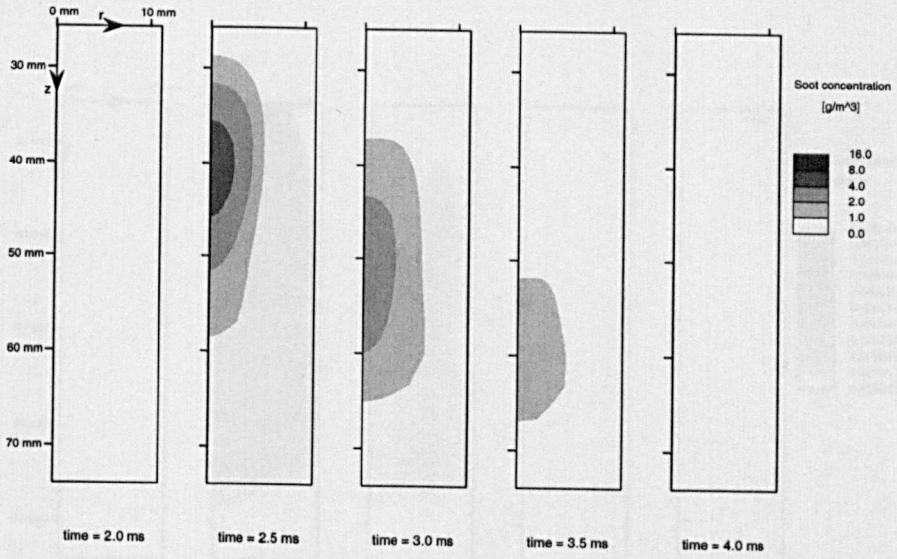



**Figure 6.51:** Iso-contours of soot mass concentration for LATCT/Hiroyasu model at times 2.0 – 4.0 ms.

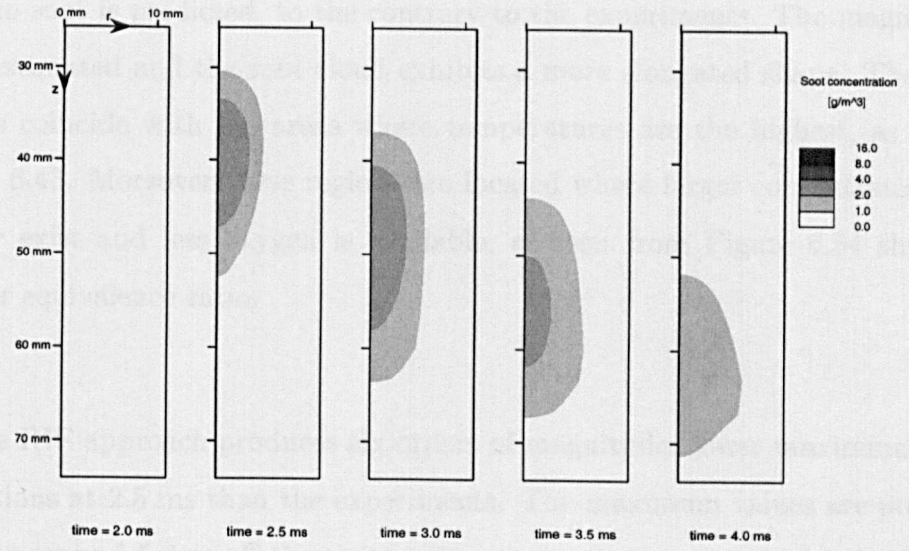



**Figure 6.52:** Iso-contours of soot mass concentration for LATCT/NSC model at times 2.0 – 4.0 ms.

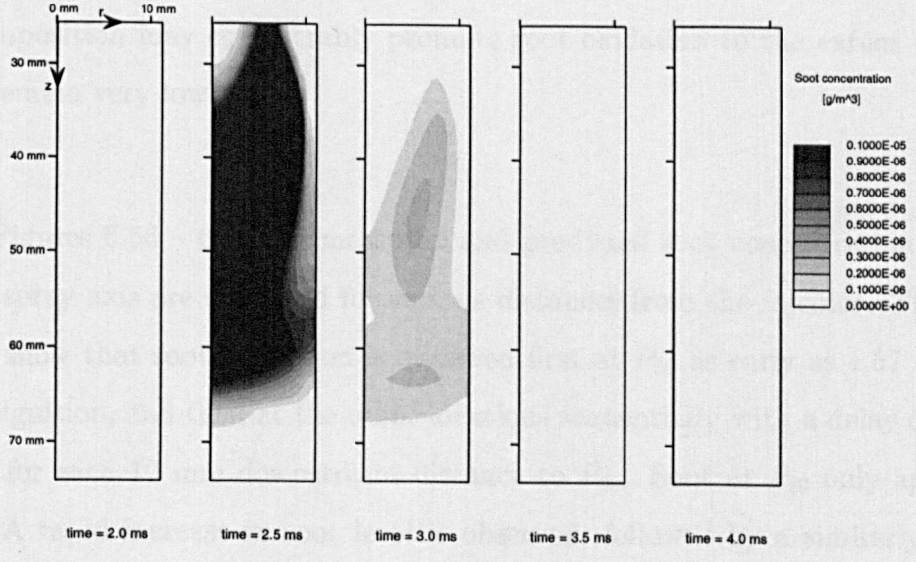



**Figure 6.53:** Iso-contours of soot mass concentration for RIF approach at times 2.0 – 4.0 ms.

The Hiroyasu and NSC models give good agreement with the measurements with respect to the location of maximum concentration. As in the point comparisons, at 2 ms no soot is predicted, to the contrary to the experiments. The magnitudes are underestimated and the soot cloud exhibits a more elongated shape. The soot-rich regions coincide with the areas where temperatures are the highest, as seen from Figure 6.43. Moreover these regions are located where larger concentrations of fuel vapour exist and less oxygen is available, as seen from Figure 6.54 showing the fuel/air equivalence ratio.

The RIF approach produces six orders of magnitudes lower maximum soot concentrations at 2.5 ms than the experiments. The maximum values are predicted to occur at around 5 mm off the spray axis, counter to the measured behaviour. Soot is therefore formed ahead and in the wake of the hot region, seen in Figure 6.45. All of the soot is burnt shortly after 3 ms.

In Figure 6.55 the fuel/air equivalence ratio is shown for RIF. In the core region a richer mixture is observed at 2 ms which is consumed rapidly such that for times later than 2.5 ms a predominantly lean mixture is predicted. The overall very lean gas composition may considerably promote soot oxidation to the extent that soot levels remain very low.

In Figures 6.56 – 6.60 the measured and predicted soot concentration histories on the spray axis are displayed for various distances from the injector. The experiments show that soot formation is observed first at $P_{30}$ as early as 1.57 ms, prior to autoignition, and then at the other locations sequentially with a delay of around 0.5 ms for each 10 mm downstream distance to $P_{60}$. Soot at $P_{70}$ only appears at 4 ms. A rapid increase in soot level is observed, followed by a similarly fast decrease due to oxidation. The highest concentrations of 14.6 g/m$^3$ are found at $P_{40}$, which coincides with the location of the highest fuel mass fractions, illustrated in Figure 6.35.

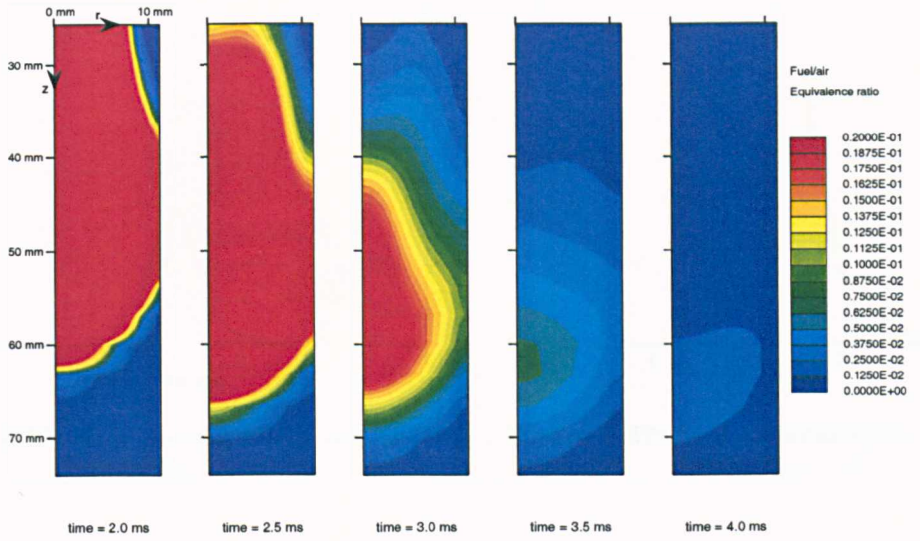



**Figure 6.54:** Distributions of fuel/air equivalence ratio for LATCT/NSC model at times 2.0 – 4.0 ms.

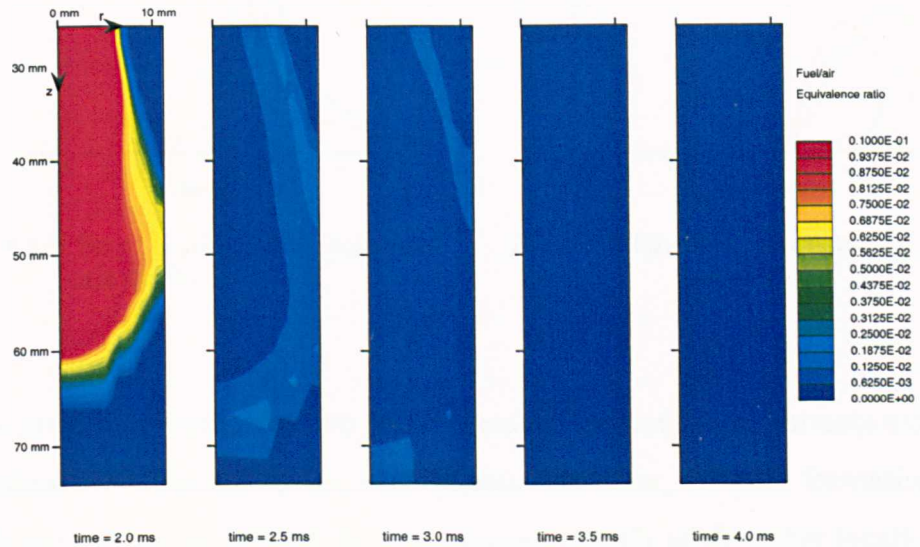



**Figure 6.55:** Distributions of fuel/air equivalence ratio for RIF approach at times 2.0 – 4.0 ms.

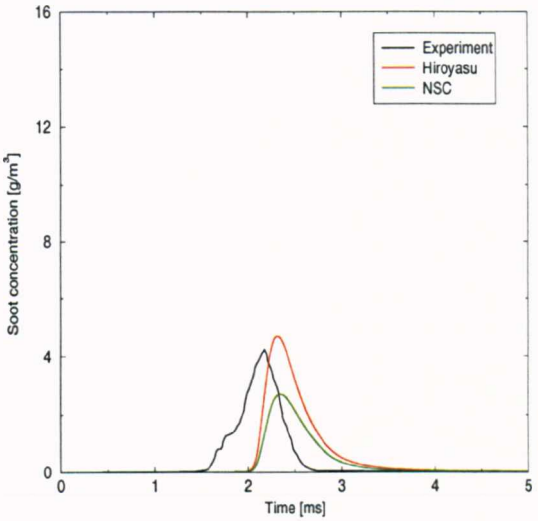



**Figure 6.56:** Soot concentration comparison at $P_{30}$.

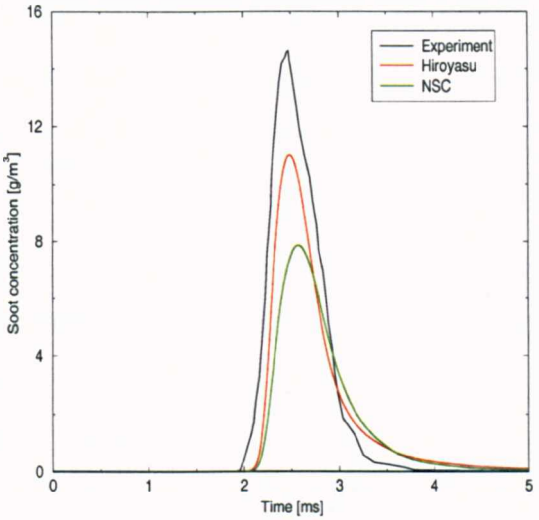



**Figure 6.57:** Soot concentration comparison at $P_{40}$.

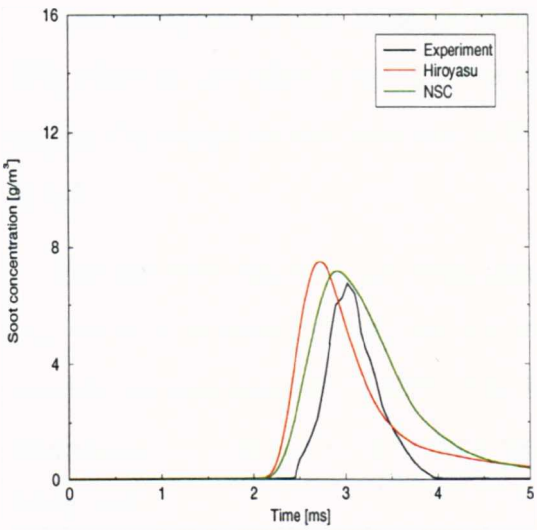



**Figure 6.58:** Soot concentration comparison at $P_{50}$.

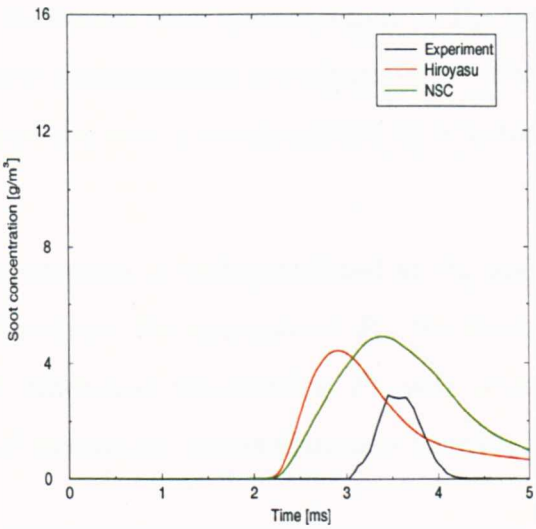



**Figure 6.59:** Soot concentration comparison at $P_{60}$.

The predictions using the two phenomenological soot model variants exhibit similar qualitative behaviour to the experiments. However, the soot formation process is predicted too late at $P_{30}$ and $P_{40}$ and occurs too early at the other locations. Also, the soot oxidation rate is underestimated, so finite levels exist after the soot has entirely been burnt in the measurements. This particularly holds true for locations $P_{50}$, $P_{60}$ and $P_{70}$.

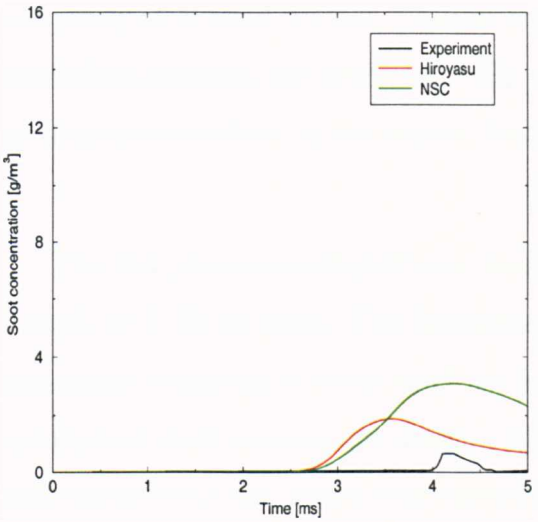



**Figure 6.60:** Soot concentration comparison at $P_{70}$.

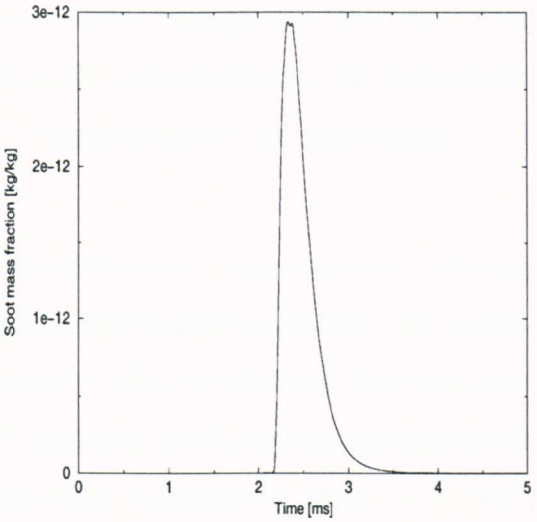



**Figure 6.61:** Chamber-averaged soot mass fraction for RIF approach.

The Hiroyasu model† underpredicts the maximum soot concentration at $P_{40}$ by 25% while at the other locations the maximum concentration is overpredicted. The largest discrepancies are observed at $P_{70}$, where the level is overpredicted by a factor of 2.8.

For the NSC model†† the maximum concentration is underpredicted at $P_{30}$ and $P_{40}$, while it is overpredicted for the other locations. For example at $P_{40}$ the maximum is underestimated by 46%. The largest differences are found at $P_{70}$ with overestimation by a factor of 4.5. The timing of maximum concentration is predicted fairly well.

It is worth noting that considerable pulse-to-pulse variations are observed for locations $P_{40}$ and $P_{60}$ as shown in Table 5.9. Therefore the predicted trends and magnitudes using the phenomenological soot models represent very encouraging results.

The predicted chamber-averaged soot mass fractions using the RIF approach are provided in Figure 6.61. A sharp rise is observed at 2.2 ms, with the peak value

†The combination of Hiroyasu soot formation and oxidation model is referred to as *Hiroyasu model.*

††The combination of Hiroyasu soot formation and NSC soot oxidation model is referred to as *NSC model.*

occurring at around 2.3 ms. Thereafter soot is oxidised rapidly such that after 3 ms negligible amounts are predicted. RIF substantially underestimates the soot levels, as mentioned before, to the extent that local comparisons are not warranted.

The two phenomenological soot models give similar soot concentrations, differing overall by 2.5% at most. The Hiroyasu model predicts higher formation and oxidation rates, resulting in lower levels at 5 ms than the NSC predictions. However, the qualitative distributions are similar. The RIF approach predicts substantially lower soot levels than the latter soot models. It has been reported by Maly *et al.* [281] that the coagulation model of Mauss [285] used in this version of RIF considerably underestimates the soot densities†. Moreover, the RIF calculation estimates a very lean mixture in regions where soot is formed, such that soot oxidation is enhanced. This may lead to low soot concentrations. However, at present it is not clear what causes the significant underestimation of soot quantities due to insufficient information provided in the RIF results about processes leading to soot formation and oxidation. Possible errors may also include inaccuracies in the soot chemistry and gas-phase reactions.

### 6.2.5 Summary

The methodologies for the prediction of the spray processes, fuel/air mixing, autoignition, combustion and soot formation were assessed in this section for injection into a constant volume chamber under high pressures and temperatures.

It was found that the liquid penetration and the vapour arrival times were generally overpredicted, particularly with the LATCT model. Possible reasons for this were postulated to be underprediction of the evaporation rate either due to overestimation of the droplet size or due to real gas effects on the vapourisation process. This explanation was in contrast to the findings of the point vapour measurements

†In the coagulation model of Mauss the assumption of the free molecular regime is made, where coalescence occurs at each collision which holds true for atmospheric pressures. At pressures above 10 bar the coagulation rate has a collision efficiency less than unity, substantially affecting soot formation rates [224, 281].

for the two LATCT calculations in which a too fast evaporation rate seemed to cause higher local vapour concentrations. It was also argued that underprediction of mixing, dependent on the turbulence predictions, could cause discrepancies between simulations and measurements. Additional sources of error include insufficient numerical resolution and inaccuracies in the combustion model.

The RIF approach predicted a different history of fuel vapour at the measurement locations compared to the experiments. Vapour levels were overpredicted. Exothermic chemical reactions are observed as early as 0.65 ms, causing faster evaporation and burning such that after 2.1 ms no fuel vapour was present.

The parameters in the ignition component of the 4-step/LATCT framework were set such that the measured ignition delay was matched. The predicted ignition location agreed very well with the experiments. The RIF model underestimated the ignition delay by 20%. Burning occurred initially at several locations close to the stoichiometric contour, so that the measured ignition location could not be reproduced. The underestimation of ignition delay was thought to come from an underpredicted scalar dissipation rate or inaccuracies of the spray and turbulence models. The RIF model estimated earlier and faster burning compared to the LATCT model variants. At times later than 2.5 ms qualitatively similar temperature distributions were revealed.

Both phenomenological soot model variants were capable of predicting the measured soot concentration trends at all measured locations on the spray axis. Also the soot distribution agreed very well with the experiments especially when considering the large experimental pulse-to-pulse variations. Overpredictions occurred at the further downstream measurement locations by up to a factor of 2.8 and 4.5 for the Hiroyasu and NSC models, respectively. This was attributed to an underestimation of the soot oxidation rate. The two phenomenological soot models showed very similar trends with differences in overall soot concentration of 2.5%. None of both models seemed to be superior.

The RIF approach produced substantially lower maximum soot concentrations

by six orders of magnitude than the measurements. This was partly attributed to the erroneous assumption made in the soot particle coagulation submodel in the present version of the RIF code. Furthermore it was revealed that an overall very lean mixture is predicted which enhances soot oxidation so that very low soot concentrations are yielded. At present the discrepancies between the RIF soot predictions and the measurements cannot be sufficiently explained as more information is needed to analyse the results.

In summary, when reviewing the various numerical results, clearly overall better agreement with experimental data was achieved using the LATCT combustion model combined with the phenomenological soot models.

## 6.3 HPP Prototype Engine

### 6.3.1 Motored case

#### 6.3.1.1 In-cylinder pressure

The in-cylinder pressure variation during the compression and expansion phases is shown in Figure 6.62. The predictions obtained with the two different wall function treatments differ by only 0.2 bar on average, mainly due to differences in overall heat transfer, as will be explained later. At the beginning of the period covered, the pressure is slightly underpredicted due presumably to underestimation of the inducted mass; toward TDC the converse holds. The latter behaviour may be due to blowby, or underestimation of heat losses. In fact, measurements indicate that the blowby is of the order of 0.6% [248] which would reduce the peak pressure by around 0.7%. The predicted pressure overshoot is by 3% and 1.9% for the standard and modified wall function approaches, respectively. The timing of the peak pressures matches the experiments.

Uncertainties, which may also contribute to the aforementioned discrepancies exist about the actual clearance gap. Laufer [255] suggested a gap height between

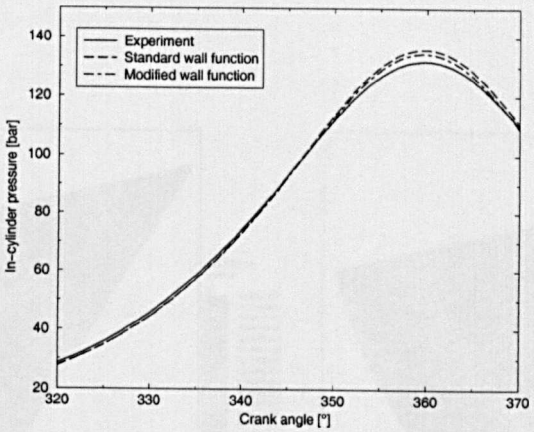



**Figure 6.62:** Comparison of measured and predicted pressure.

1.165 and 1.295 mm, while Kummer [248] estimated the distance to be 1.03 mm. In the calculations the gap was set to a value of 1.62 mm, which gives the quoted compression ratio of 17.25.

#### 6.3.1.2 Wall heat transfer

**Spatial heat flux distribution**

The predicted spatial distributions of heat flux on the cylinder head and piston bowl surfaces for 360° CA, calculated with the two sets of wall functions, are displayed in Figures 6.63 – 6.66. The largest values are found below the piston lip area and on the cylinder head at about a quarter and a half the distance from the cylinder axis to the wall. The results of the two approaches differ more in magnitude rather than distribution; the MWF approach gives considerably higher heat fluxes than the SWF method. The heat flux variation follows closely the pattern of the charge motion, as will be seen below. The changes are predominantly radial and mainly due to swirl.

The distribution of the two main velocity components are shown in Figures 6.67 and 6.68 for the MWF method[†]. Towards TDC the swirl in the chamber becomes an almost stable solid-body rotating flow, as seen in Figure 6.67, which is enhanced

[†]The velocity distribution of the SWF approach differs negligibly from the MWF approach and is therefore not displayed here.

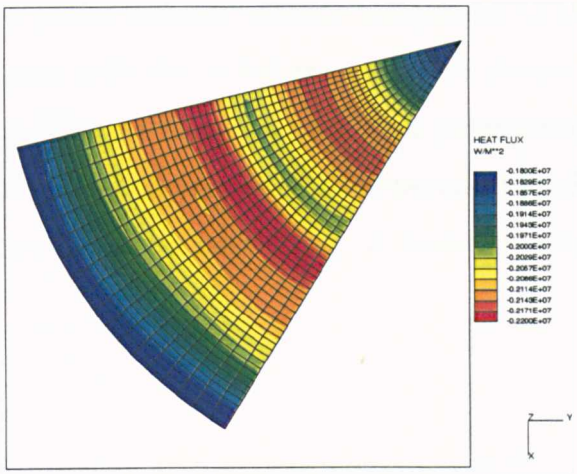



**Figure 6.63:** Heat flux distribution on cylinder head at 360° CA using SWF approach.

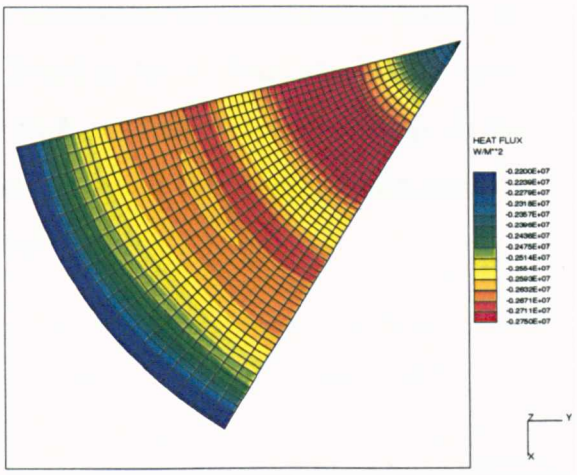



**Figure 6.64:** Heat flux distribution on cylinder head at 360° CA using MWF approach.

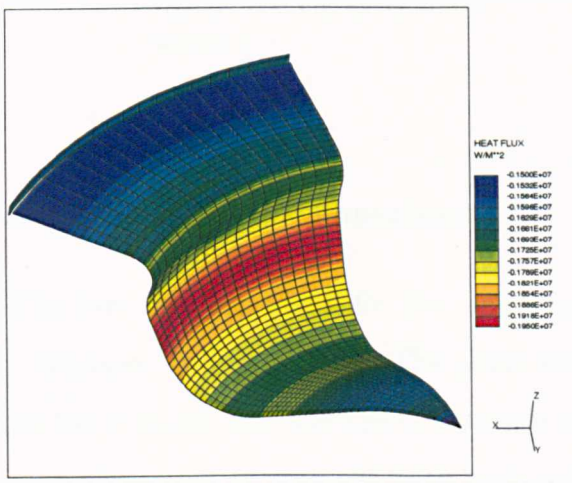



**Figure 6.65:** Heat flux distribution on piston surface at 360° CA using SWF approach.

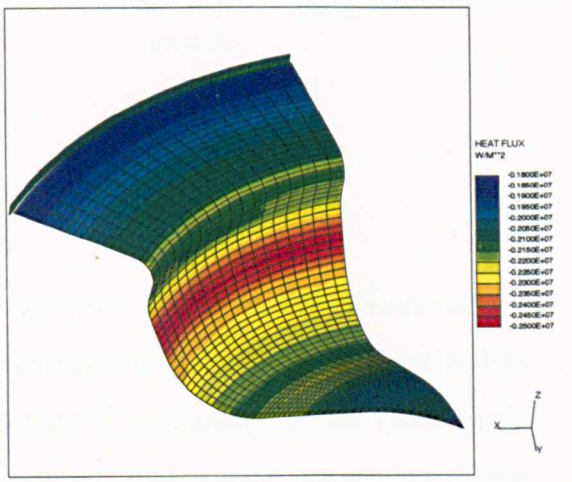



**Figure 6.66:** Heat flux distribution on piston surface at 360° CA using MWF approach.

by compression. High velocity magnitudes occur particularly close to the lip of the bowl. Low velocities are seen toward the centre of the chamber. By comparison, the piston induced velocity component in the $z$-direction is considerably lower. In Figure 6.68 the radial velocities are shown. Fluid is forced from the piston bowl region into the squish area with particularly high gradients around the lip of the bowl. This clearly affects temperature gradients around this region which in turn determine local heat fluxes. A squish flow is not apparent.

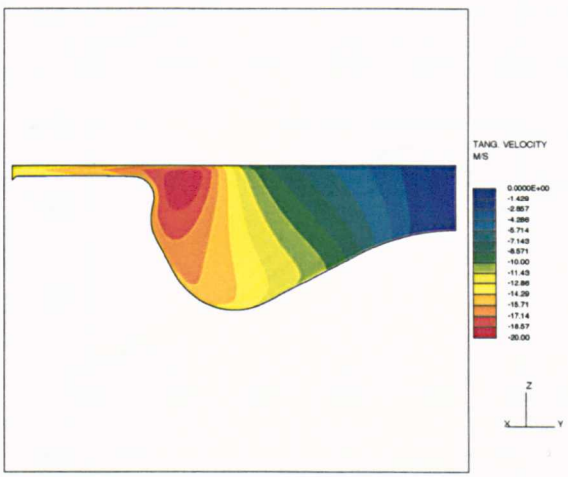



**Figure 6.67:** Tangential velocity distribution at 360° CA using MWF approach.

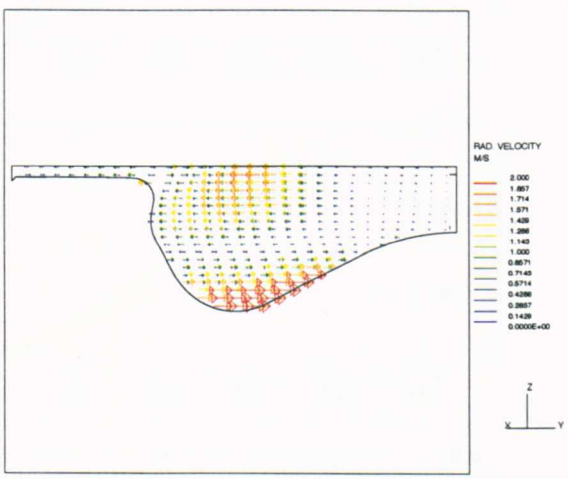



**Figure 6.68:** Radial velocity distribution at 360° CA using MWF approach.

### Point heat transfer comparisons

The heat flux variations for the eight measurement points on the piston surface are displayed in Figure 6.69. The plots are arranged in pairs, each at fixed radius from the cylinder axis and the sequence is in order of increasing radius. Good qualitative agreement is achieved with both sets of wall functions. The timing of the peak value is consistently predicted too early by around 3.95° CA on average. The predicted maxima occur before TDC, while the measured ones occur after.

At the measurement points the SWF method generally underestimates the peak

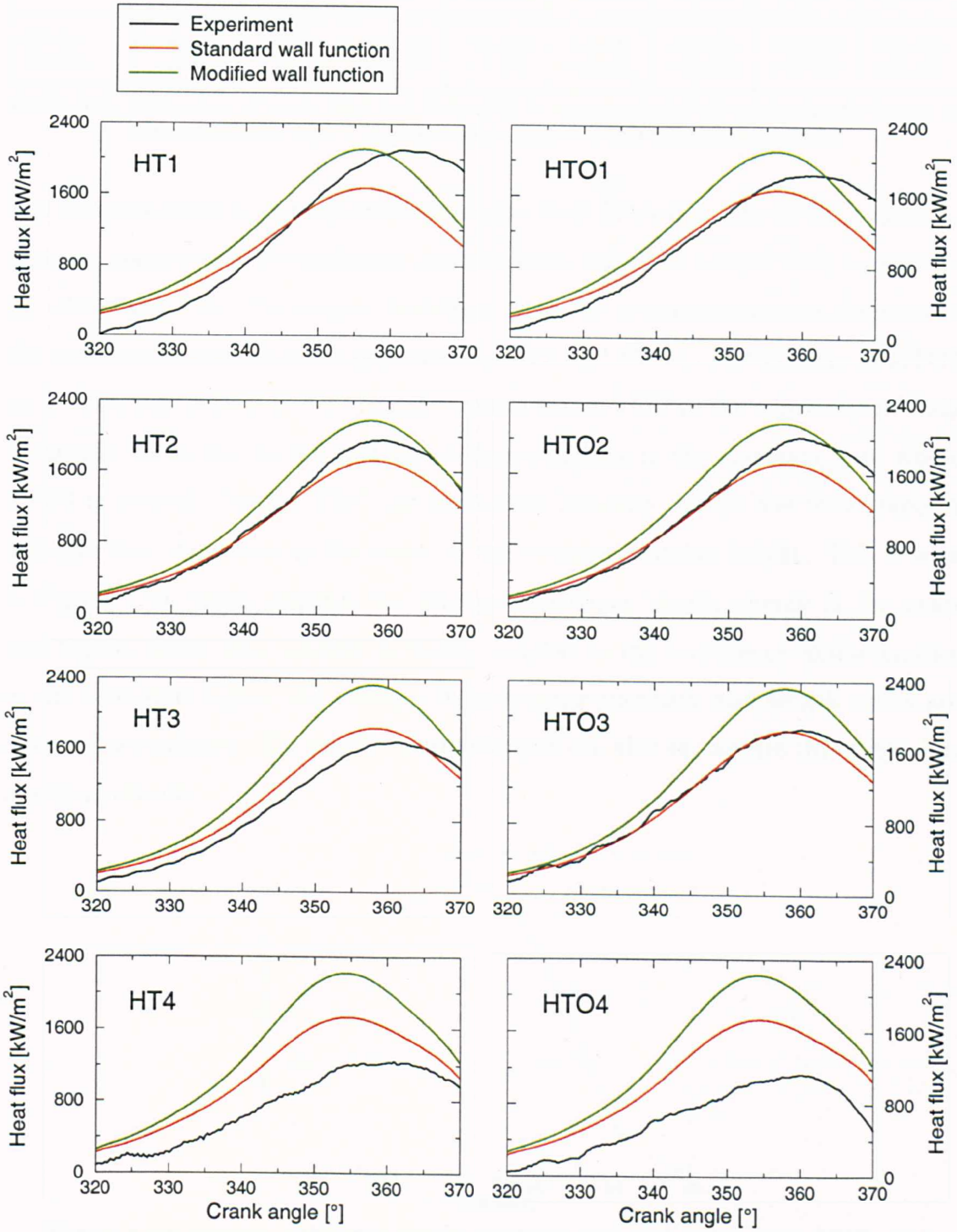



**Figure 6.69:** Comparison of heat flux on piston surface at eight measurement locations.

| Approach | Heat transfer measurement locations | | | | | | | |
|---|---|---|---|---|---|---|---|---|
| | HT1 | HTO1 | HT2 | HTO2 | HT3 | HTO3 | HT4 | HTO4 |
| SWFs | −21.0% | −9.7% | −12.1% | −14.8% | +8.7% | −0.05% | +38.6% | +52.0% |
| MWFs | +0.03% | +14.4% | +11.1% | +7.5% | +38.0% | +24.8% | +77.8% | +95.0% |

**Table 6.3:** Estimation of peak heat flux compared to measurements at measurement points on piston surface (− and + indicate under- and overestimation, respectively).

heat flux compared to the experiments as seen from Table 6.3. The MWF approach, however, consistently overestimates the maximum values by around 34% on average (cf. also Table 6.3). The largest deviations from the measurements are observed at the locations in the clearance gap, notably HT4 and HTO4. Particularly at HTO4 an unusual fast decline in heat transfer occurs before TDC in the experiments. This is thought to be due to the turbulence characteristics in the clearance gap, where HTO4 is located. Toward TDC the turbulence intensity decays due to breakdown of larger flow structures as the result of the reduced chamber height. This is seen in Figure 6.70, which displays the average turbulence kinetic energy in the near-wall region. Since heat transfer is closely coupled to the turbulence characteristics in the near-wall region, the changes in turbulence intensity and length scales are reflected accordingly. The numerical simulations are able to capture this effect, but less dramatically.

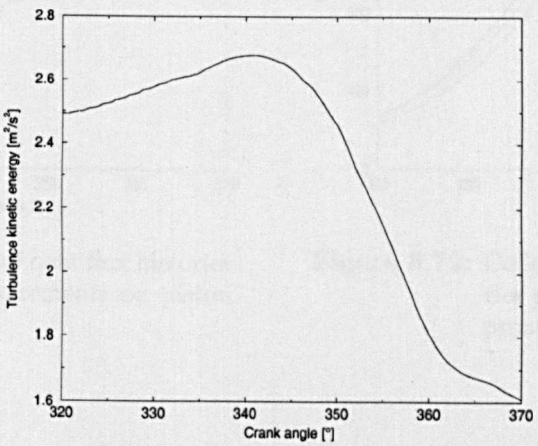



**Figure 6.70:** Average turbulence kinetic energy in near-wall region using MWF approach.

Figures 6.71 and 6.72 show the collective comparisons between measured and

predicted heat fluxes, obtained from the MWF approach. The experimental data show a larger variation between the measurement points than the predictions, similar to the RWTH Aachen test case in Section 6.1.3. Differences in measured and predicted local wall heat flux are caused particularly by differences in the flow and turbulence fields, as indicated for the locations in the clearance gap. These are primarily governed by the inflow process and are affected by numerical resolution and the turbulence modelling. The uncertainty of the clearance gap may also significantly contribute to the discrepancies in predicted and actual heat flux levels at HT4 and HTO4. In addition, errors can originate from the assumption of uniform wall temperatures in the calculations over the piston surface. In this respect it is important to note that the experiments were conducted shortly after cycles including combustion [248]. As a consequence, non-uniform wall temperatures are likely to remain caused by the effects of the spray and flame behaviour.

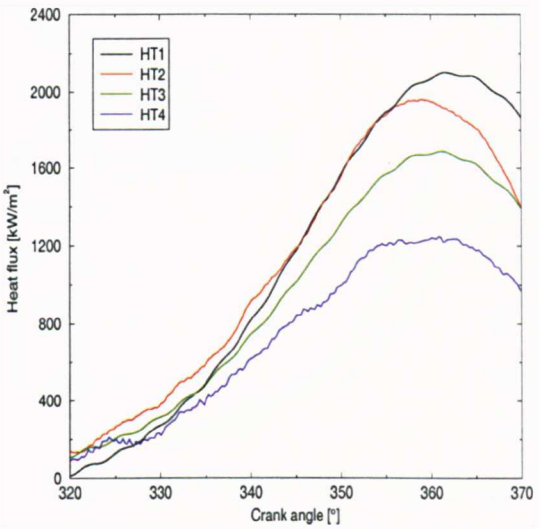



**Figure 6.71:** Collection of heat flux histories from measurements on piston surface.

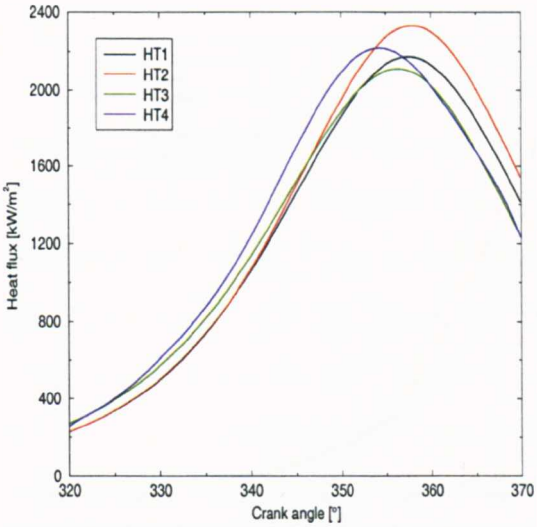



**Figure 6.72:** Collection of heat flux histories predicted using MWF approach.

The MWFs give about 24% larger heat fluxes at all locations than the SWFs. This clearly indicates that density and viscosity variations have a large influence on the heat exchange mechanism. Generally it can be concluded that neither of the near-wall treatments achieves clearly superior agreement with these measurements.

### Surface-averaged HTCs and total heat transfer

Figure 6.73 shows the predicted surface-averaged HTC history obtained from the present calculations and empirical correlations. The parameters in the correlations were chosen as in the RWTH Aachen engine test case. Furthermore the results from the MWFs are taken as reference, since they more adequately represent the actual heat transfer. The range of results from the correlations is quite large, up to around 50%. The Hohenberg correlation gives close agreement with the MWF approach during most of the compression stroke, but overestimates the peak value by 13%. The correlations of Woschni and Annand generally produce lower values compared to the MWF calculation with an around 27% lower peak HTC. By comparison, the SWF method gives 18% lower HTCs on average than the modified near-wall approach.

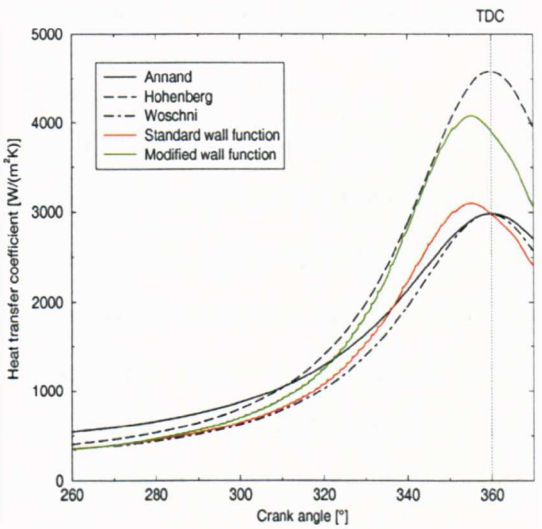



**Figure 6.73:** Comparison of heat transfer coefficients between calculations and global heat transfer models.

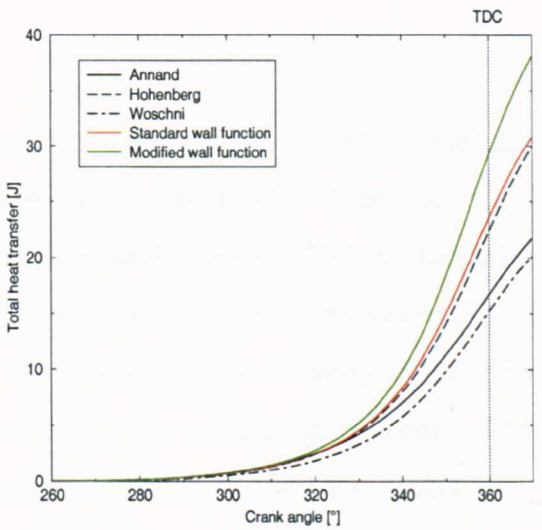



**Figure 6.74:** Comparison of total heat transfer between calculations and global heat transfer models.

Similar to the RWTH Aachen test case a shift in peak location to later crank angles is observed in the correlations in comparison to the calculations. The calculations reflect the rapid decline in turbulence intensity towards TDC in the HTC predictions due to reduced clearance gap, as discussed for Figure 6.70. The corre-

lations do not capture this effect, as they are derived from the pressure trace which does not seem to respond significantly to these changes.

The predicted total heat transfer histories are compared in Figure 6.74. The MWFs give a substantially higher total heat transfer than the correlations. At TDC Annand, Hohenberg and Woschni underestimate the total heat exchange by 43%, 23% and 48%, respectively. By comparison, the SWF approach gives values that are about 19% lower than the modified near-wall treatment. The results for the total heat transfer using Hohenberg's correlation seem in contrast to the global HTC comparisons. While in the former a lower overall heat loss is calculated compared to the CFD calculations, in the latter the HTCs are consistently higher. However, it has to be noted that the instance of zero heat transfer differs between the numerical results and the correlations, yielding differences in the relative sequence of magnitudes for the total heat transfer.

The various heat transfer correlation predictions are subject to substantial differences in magnitude which hints at the necessity to extensively adjust the model parameters for each operating point to achieve reasonable results. The results which more closely compare with the MWF approach are obtained with the correlation of Hohenberg. However, the HTC trend near TDC which is significantly affected by the near-wall flow and turbulence structures cannot be adequately reproduced by the empirical correlations, as seen from the comparisons with the CFD results.

### 6.3.2 Fired case

Several operating conditions have been investigated for the fired case (cf. Table 5.16). In the following the combustion predictions are presented first and compared with the experimental results. This is followed by the evaluation of the heat transfer predictions. Finally the results of the pollutant formation models are presented and compared with measured exhaust gas concentrations.

#### 6.3.2.1 Modified initial conditions

Photographs of the piston surface, shown in Figures 6.75 and 6.76, suggest that on the basis of the "imprints" of the deposits from combustion the swirl number at SOI is about 0.7 [248]. Furthermore, the baseline series OM500 engine is reported to have a characteristic swirl number of 0.5 [346]. However, it is noteworthy that the swirl numbers have not been directly measured in this particular engine and are therefore subject to uncertainty. The swirl numbers predicted in the present study using the measured inlet and exhaust port pressure histories exceeded those numbers by about a factor of two. Since the in-cylinder motion strongly affects the flame propagation and thus the local heat transfer, it was necessary to address this issue to be able to perform meaningful evaluations of the heat transfer and combustion predictions. In fact the results to be presented in Section 6.3.2.3 indicate that the prevailing swirl ratio near TDC is close to zero.

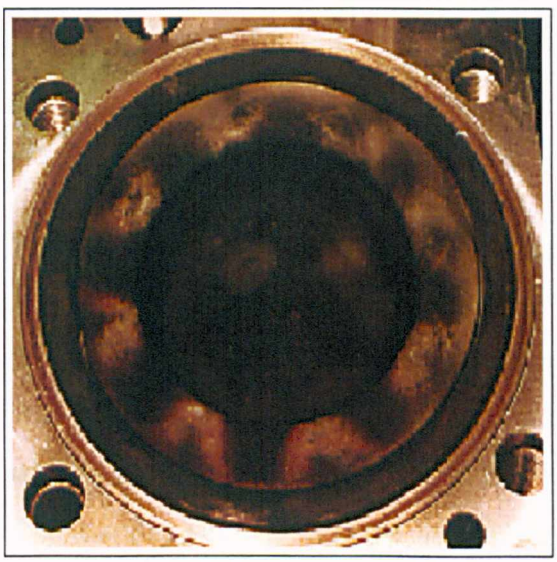


**Figure 6.75:** Soot imprint on piston after test cycles including combustion.

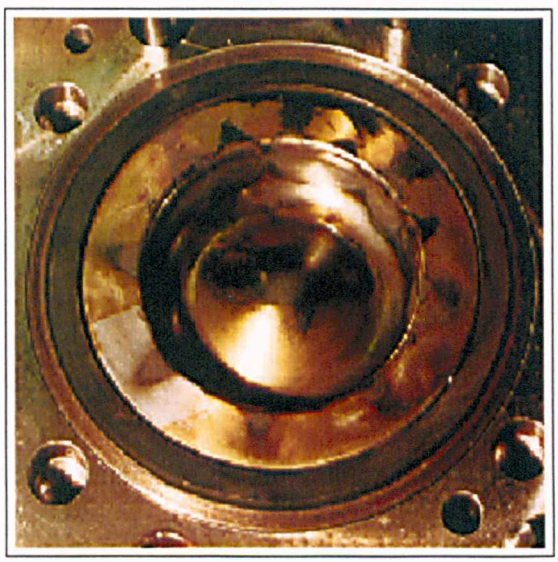


**Figure 6.76:** Polished piston with traces due to flame impingement.

It is known from previous studies that the in-cylinder flow patterns like swirl are greatly influenced by the flow in the intake ports [167]. Therefore a sensitivity study has been performed of the effect of the mesh density in the intake ports. The intake

port was modeled either using a coarse mesh of 37651 cells or a fine mesh of 76057 cells. The intake stroke for both port meshes resulted in negligible change in the predicted swirl levels as seen from Figure 6.77. It was therefore decided to artificially adjust the swirl velocities at SOI to yield a specified swirl number, while keeping the other remaining velocity components and the turbulence field unchanged.

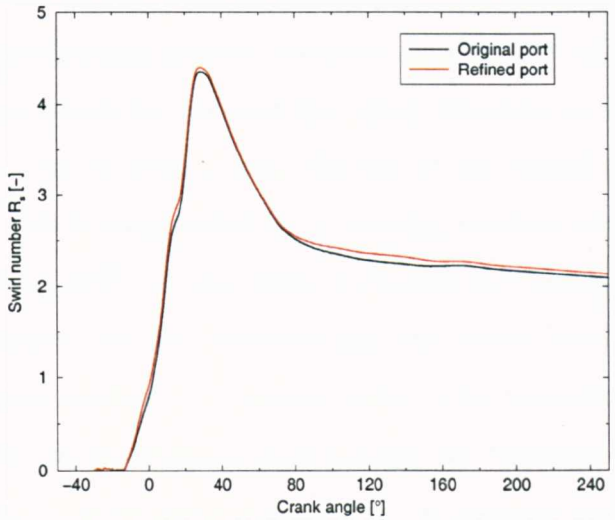



**Figure 6.77:** Swirl number for intake stroke predicted using original and refined port geometries of HPP engine.

The *swirl number* $R_s$ was determined at SOI according to Heywood [167]:

$$R_s = \frac{\omega_s}{2\,\pi\,N} \tag{6.1}$$

where $\omega_s$ is the angular velocity of the in-cylinder charge and $N$ is the engine speed. The angular velocity is given by [167]:

$$\omega_s = \frac{8 \sum_{i=1}^{N} v_{\tan,i}\, r_i}{B^2} \tag{6.2}$$

where the summation is over $N$ cells in the computational domain, $v_{\tan,i}$ is the tangential velocity stored in cell $i$, $r_i$ is the radial distance from the cylinder axis to the cell $i$ and $B$ is the bore.

#### 6.3.2.2 Combustion

**Operating point EOP1 (boost pressure 2.85 bar)**

Figures 6.78 and 6.79 show, for various times, the spatial distributions of temperature for the LATCT model in vertical and horizontal sections containing the spray axis as indicated by the icons on the figures. The swirl number is set to 0.5 at SOI. At 355° CA ignition has already occurred close to the injector nozzle, causing the local gas temperatures to rise and the spray droplets to evaporate faster. A relatively cool rich core is formed near the tip of the liquid spray due to evaporative cooling and this is surrounded by a burning mixture close to stoichiometric conditions. At around 370° CA the flame front hits the piston surface close to the bowl lip and propagates into the clearance gap and piston bowl, respectively. Close to 395° CA the flame reaches the cylinder walls. The temperatures in the regions above the bowl close to the cylinder axis remain low throughout expansion as the mixture there is lean. The droplets displayed in the sections suggest an initial spray penetration of two-thirds the bowl radius. Since gas temperatures surrounding the droplets are not high enough for them to completely evaporate, some droplets travel into the clearance gap after end of injection.

In the horizontal views, the influence of swirl on flame propagation can be observed as the flame plume is rotated in clockwise direction. The regions between two adjacent sprays exhibit considerably lower temperature levels than the core of the flame, indicating that the adjacent flames do not merge.

Figure 6.80 displays the temperature distributions on the vertical mid-plane, mid-way between the spray axes. Here it can be seen that the flame front reaches the piston lip shortly before 375° CA, i.e. later than on the spray axis plane.

In Figures 6.81 and 6.82 the temperature distributions predicted by the RIF model are shown. These are qualitatively similar to the LATCT model predictions,

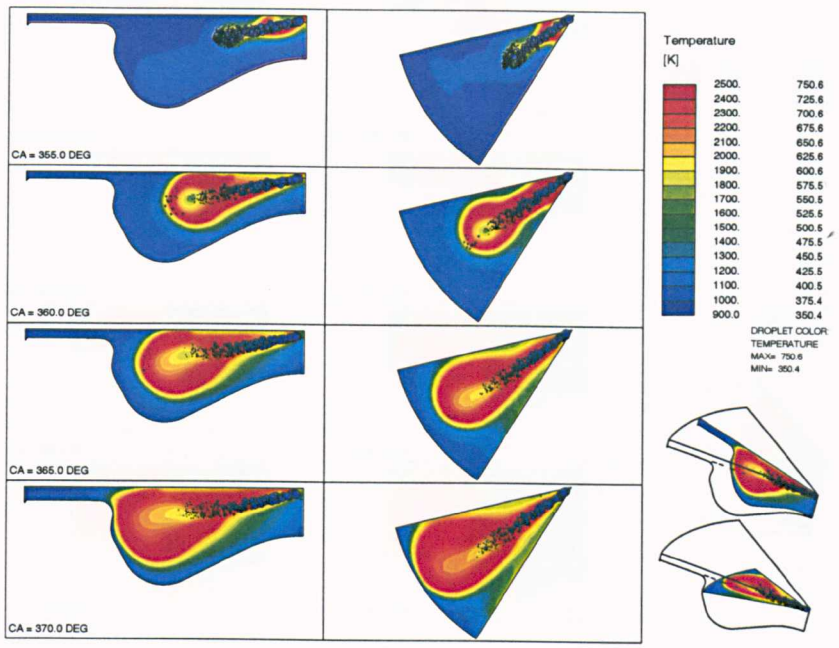



**Figure 6.78:** Temperature distributions along spray axis for 355° to 370° CA using LATCT model, $R_s = 0.5$.

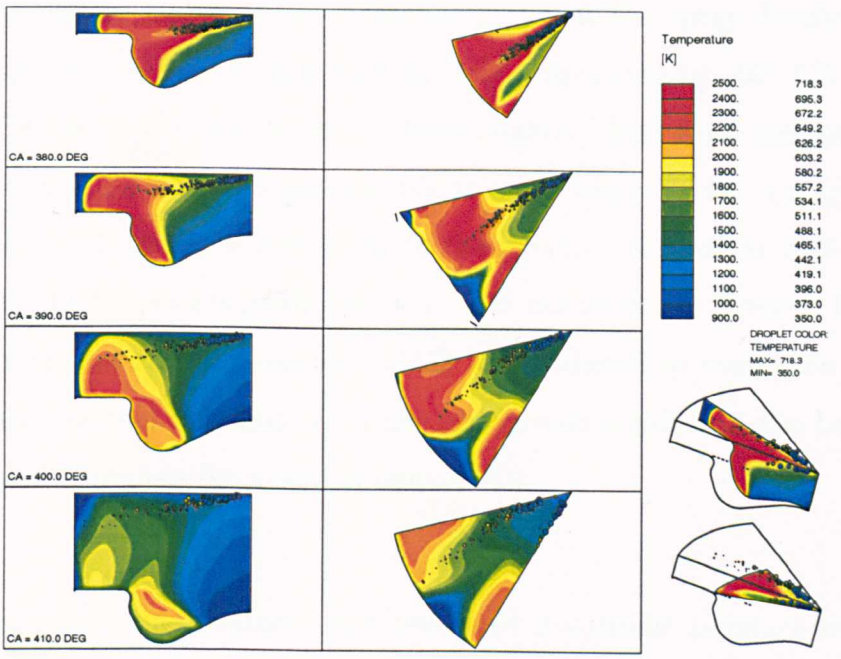



**Figure 6.79:** Temperature distributions along spray axis for 380° to 410° CA using LATCT model, $R_s = 0.5$.

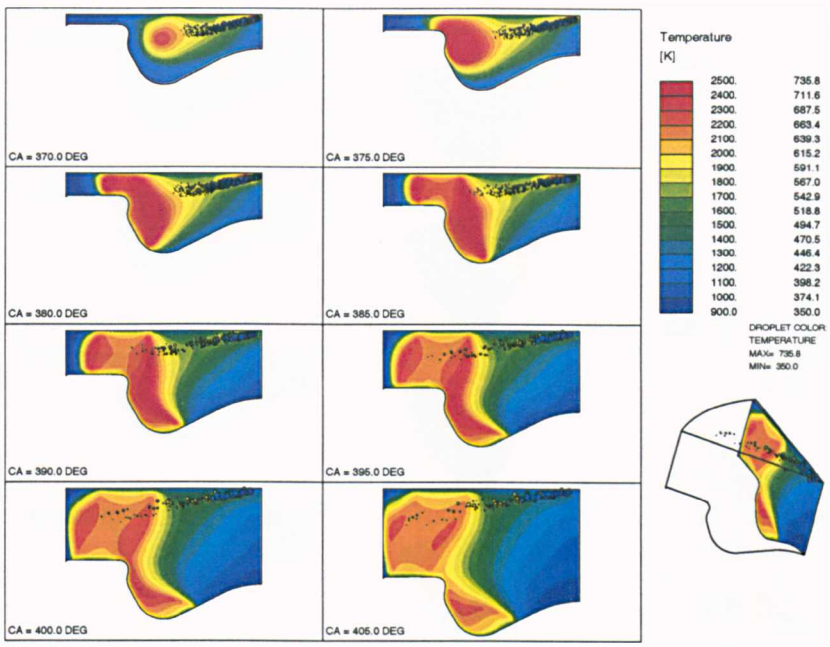



**Figure 6.80:** Temperature distributions mid-way between spray axes for 370° to 405° CA using LATCT model, $R_s = 0.5$.

but here the flame plume at the tip exhibits less radial spreading and the temperature levels are higher. One consequence is that the spray droplets penetrate only to half the bowl radius and have entirely evaporated by 390° CA. Shortly after 370° CA the flame hits the piston bowl slightly offset from the spray axis and propagates into the clearance gap and piston bowl, respectively. A major difference from the LATCT results is seen close to the injector. A burning fuel-rich zone in the vicinity of the nozzle is predicted in the RIF calculations. Towards EOI droplets with lower momentum are injected, which are predicted to evaporate close to the nozzle hole. The fuel-rich mixture in the near-nozzle region has also been observed by the experimentalists for a similar engine [45].

In Figure 6.83 the measured and predicted in-cylinder pressure variations are shown, including for the latter the results with both the LATCT and RIF combustion models. Also shown is the motored pressure history. For the LATCT model at SOI two swirl numbers were investigated, 0.5 and 1.6. The RIF calculation was performed

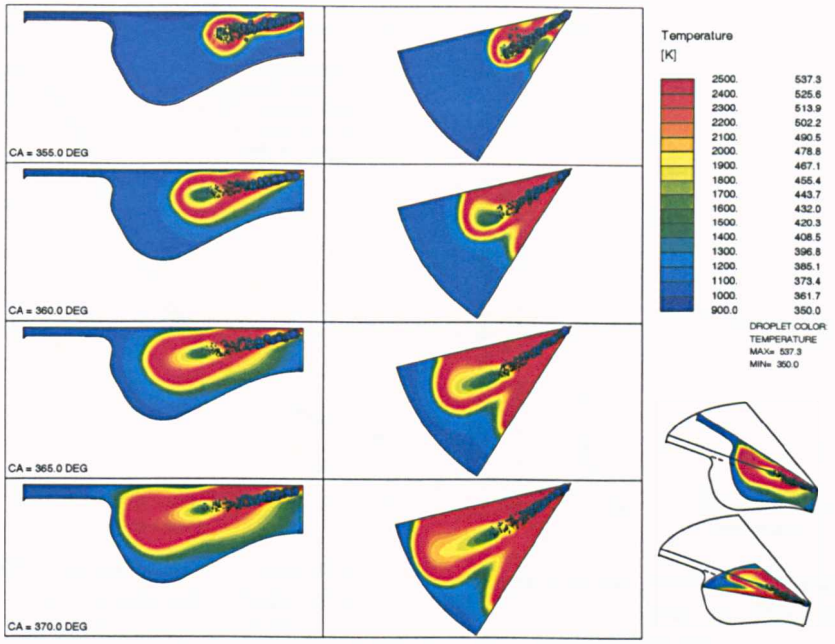



**Figure 6.81:** Temperature distributions along spray axis for 355° to 370° CA using RIF model, $R_s = 0.5$.

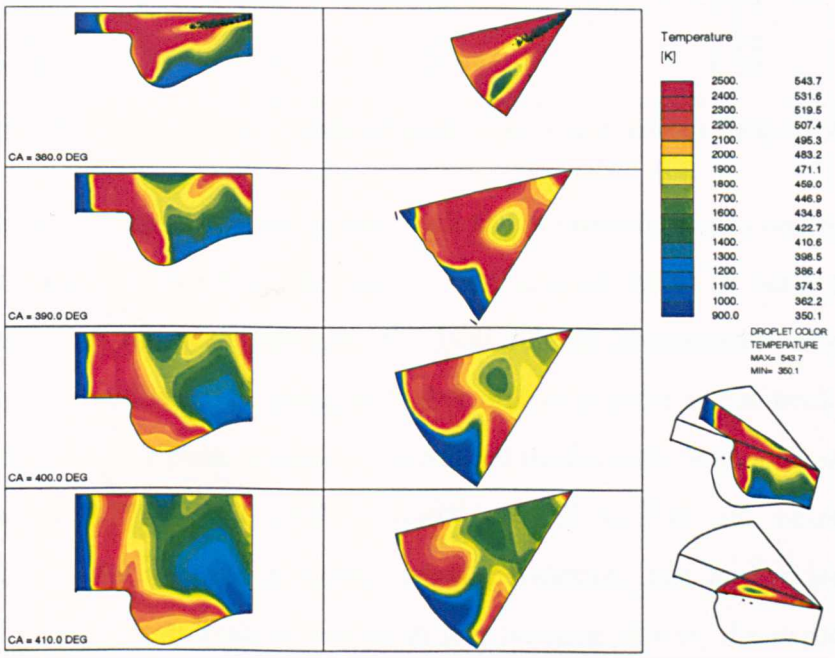



**Figure 6.82:** Temperature distributions along spray axis for 380° to 410° CA using RIF model, $R_s = 0.5$.

for $R_s = 0.5$.

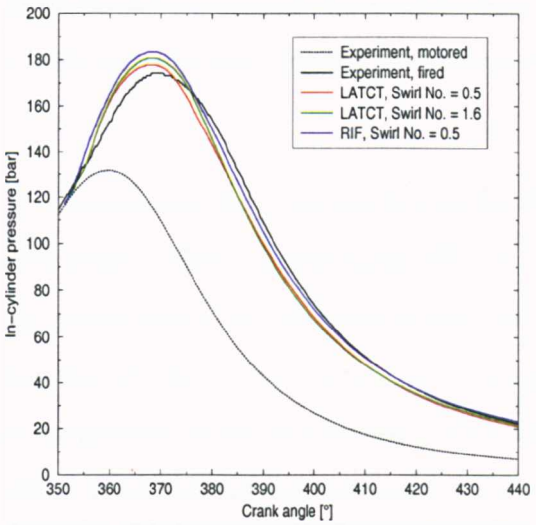



**Figure 6.83:** Comparison of measured and predicted cylinder pressure histories for EOP1.

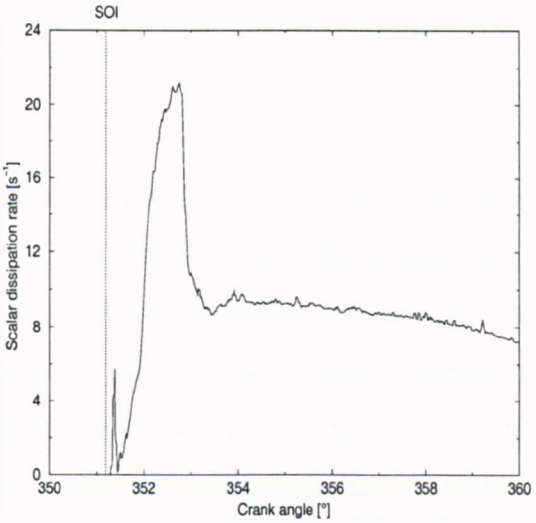



**Figure 6.84:** History of scalar dissipation rate in RIF calculation for EOP1.

| Results | Peak pressure [bar] | Ignition delay [°CA] |
|---|---|---|
| Experiment | 174 | 2.25 |
| LATCT ($R_s = 0.5$) | 178 | 1.77 |
| LATCT ($R_s = 1.6$) | 180 | 1.74 |
| RIF | 183 | 1.77 |

**Table 6.4:** Measured and predicted peak pressure and ignition delay for EOP1.

All the predictions agree fairly well with the measurements in respect of ignition delay†, as seen in Table 6.4, the value being around 0.5° CA early for both the LATCT and RIF models. However, the heat release immediately after ignition is apparently overpredicted, resulting in higher pressures prior to the peak. The timing and magnitude of the peak pressure is predicted moderately well with an error in the latter of about 2.7% for the LATCT model and 5% for RIF (cf. Table 6.4). Since the LATCT model assumes a global one-step reaction, the higher heat release in the initial phase of combustion results in less burning during the expansion stroke. This in turn leads to lower cylinder pressures than the experiments. However, even the RIF model with its detailed finite-rate chemistry modelling predicts slower late

†The ignition delay was based on the change of slope in mean cylinder pressure as outlined in [19, 167].

burning compared to the measurements, particularly between 375° and 385° CA. Towards EVO the numerical and experimental pressure traces converge, staying at a level considerably higher than the motored pressure.

Comparing the pressure traces for different swirl ratios, it is seen that the ignition delay differs by less than 2% (cf. Table 6.4). Differences are discernable later on, particularly in the peak pressures and the pressure levels during the early expansion stroke. The lower swirl ratio produces on the one hand better prediction of maximum pressure (within 1.5%) with respect to the measurements, but on the other hand greater discrepancies to the latter during the early expansion period.

In general, the causes for the discrepancies noted above could stem from modelling and/or measurement uncertainties and are difficult to identify. The error in ignition delay for the LATCT calculations could be attributed to the inaccuracies in mixture preparation which depends on spray evaporation and turbulence intensity. Underestimation of ignition delay in the RIF approach may similarly be due to errors in the spray and turbulence modelling. Discrepancies can also originate from the underprediction of turbulence levels and therefore scalar dissipation rate, as explained for the pressure chamber case in Section 6.2.3. Figure 6.84 displays the history of the turbulent scalar dissipation rate conditioned at stoichiometric mixture. High turbulence levels caused by the injection process are observed shortly after SOI. At around 1.6° CA after SOI the scalar dissipation rate drops sharply below the level at which autoignition takes place. A further source of error in the RIF results may be due to the use of *n*-heptane chemistry, since Diesel fuel was used in the experiments. However, it is noteworthy that the ignition delay is very short and predicted fairly well, so this has a relatively small effect on the subsequent burning characteristics.

The overestimation of initial heat release by both combustion models can be caused by too rapid evaporation compared to the measurements and overpredicted

mixing. Additionally in the LATCT model the global switch from ignition to combustion could cause too rapid early burning. The overprediction of early heat release in the RIF results can also be attributed to the fact that the mixture around the stoichiometric contour ignites simultaneously. This enhances turbulent mixing which in turn promotes rapid burning. Barths *et al.* [31, 32, 34] show that a larger number of flamelets, of the order of 10, improves the predictions around autoignition. A more gradual heat release is observed, as the flamelets ignite consecutively.

Regarding the measurements, there are uncertainties related to the exact SOI and squish height as mentioned earlier [248]. Also cylinder liner deformation owing to the high chamber pressures may have occurred. Despite these differences, the level of agreement is encouraging.

Figure 6.85 displays the apparent HRR of the experiments and the HRR of the calculations for EOP1, for a swirl number of 0.5. The experimental HRR was estimated from a heat release analysis (HRA) according to Heywood [167] using the measured pressure trace and Woschni's correlation for global heat transfer†. Due to simplifying assumptions, like uniform in-cylinder temperatures, negligible effect of crevice flow and uncertainties in burnt gas composition and heat transfer levels, the apparent HRR is only an approximation of the actual rate [167]. The experimental HRR exhibits an initial local peak at around 3° CA after SOI and an overall maximum rate of 2.75 MJ/s at 375° CA. During expansion the HRR reduces gradually and by 430° CA it is nearly zero.

The LATCT results give the initial peak at around 2.2° CA after SOI, followed by an increase to higher levels than the measurements until 360° CA. This overestimation of initial heat release is reflected in the in-cylinder pressure history in Figure 6.83. Thereafter the HRR is underpredicted until 387° CA with a 16% lower peak value, which occurs earlier than in the experiments.

† A substitution of Woschni's correlation by that of Hohenberg did not result in significant differences in apparent HRR.

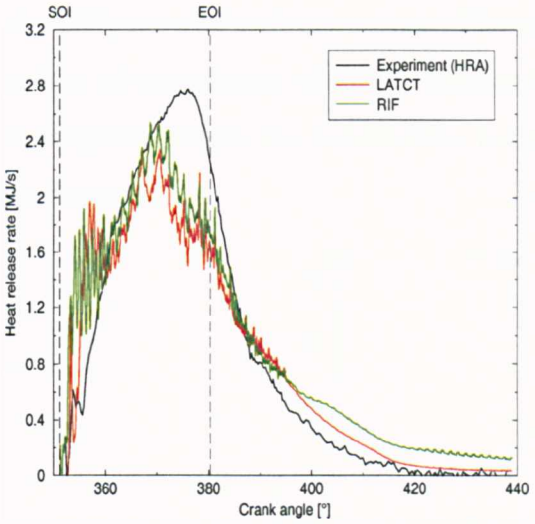



**Figure 6.85:** Heat release rate comparison for EOP1, $R_s = 0.5$.

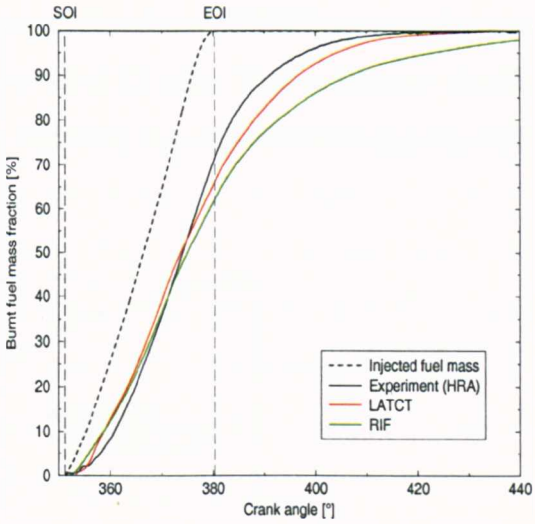



**Figure 6.86:** Burnt fuel mass fraction comparison for EOP1, $R_s = 0.5$.

In the RIF calculation the heat release begins earlier, reaching an initial local peak comparable to the LATCT results. The maximum rate is also below the experimental value by around 9% and is predicted to occur earlier. Later on, the HRR is overpredicted. Somewhat unrealistically RIF predicts appreciable heat release to persist even at EVO.

The abovementioned trends can also be discerned from the burnt fuel mass fraction histories, plotted in Figure 6.86. The experimental curve was deduced from the HRA according to Heywood [167]. While the initial fuel consumption is overpredicted in both calculations, the slope of predicted burnt fuel mass fraction decreases during expansion, indicating slower burning than in the experiments. In the RIF results the combustion is incomplete at EVO, where 2.3% of the total injected fuel is unburned. This is further elucidated in Figure 6.87, which shows the consumed fuel mass history and that of $CO$ and $CO_2$. Initially the majority of the fuel vapour is transformed into $CO$, producing the maximum $CO$ mass around EOI. The $CO$ is then gradually oxidised to $CO_2$. However, near EVO 14% of the peak $CO$ mass remains in the cylinder, corresponding to about 2.7% of the total heat release of the injected fuel. Complete combustion has not been reached at this instance, since

the $CO_2$ mass is still increasing. The predicted $CO$ mass at EVO is greater by two orders of magnitude than the measured value of 0.23 mg. This indicates significant differences in the combustion behaviour between the experiments and the RIF predictions.

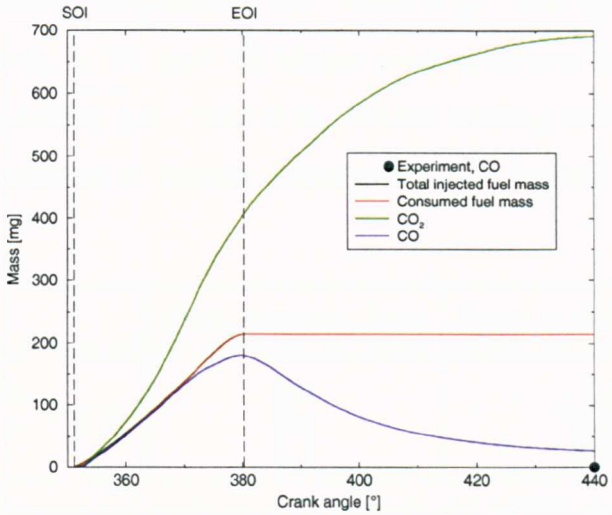



**Figure 6.87:** History of predicted $CO$, $CO_2$ and consumed fuel mass using RIF for EOP1.

### Operating point EOP4 (boost pressure 3.5 bar)

In Figure 6.88 the predicted and measured pressure histories are shown for EOP4 which, as indicated in Table 5.16, features a higher boost pressure of 3.5 bar. A swirl number of 0.5 at SOI was used in the calculations. The experiments give a

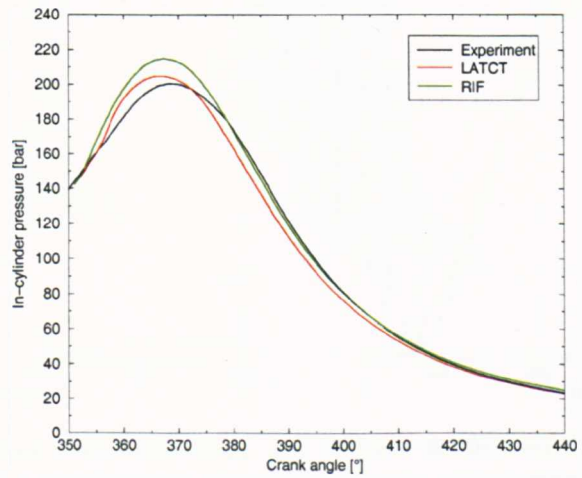



**Figure 6.88:** Comparison of measured and predicted pressure for EOP4.

peak cylinder pressure of 201 bar which is 15% higher than for EOP1. It is seen that even at these elevated chamber pressures, the present CFD methodology is capable to reach predictions of similar accuracy as for EOP1. The calculations predict a shorter ignition delay compared to the experiments by 0.5° and 0.4° CA for the LATCT and RIF model, respectively (cf. Table 6.5). The initial heat release is overpredicted resulting in 2% and 7% higher peak pressures for the LATCT and RIF approach, respectively (cf. Table 6.5). Slower burning is observed during the expansion stroke, resulting in slightly lower pressures. Toward EVO the pressure histories converge.

| Results | Peak pressure [bar] | Ignition delay [°CA] |
|---|---|---|
| Experiment | 201 | 2.2 |
| LATCT ($R_s = 0.5$) | 204 | 1.83 |
| RIF | 215 | 1.76 |

**Table 6.5:** Measured and predicted peak pressure and ignition delay for EOP4.

The apparent HRR and burnt fuel mass fraction histories, deduced from a heat release analysis, are displayed in Figures 6.89 and 6.90. The predicted HRR variations compare similarly to the experiments as for EOP1. Both combustion approaches overestimate the initial heat release rate, yielding higher initial fuel con-

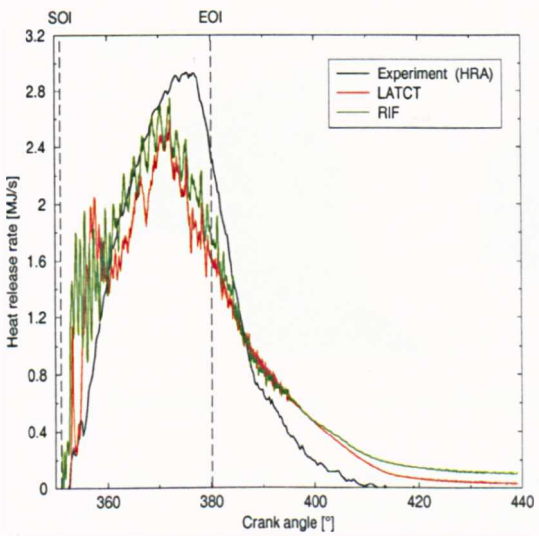



**Figure 6.89:** Heat release rate comparison for EOP4.

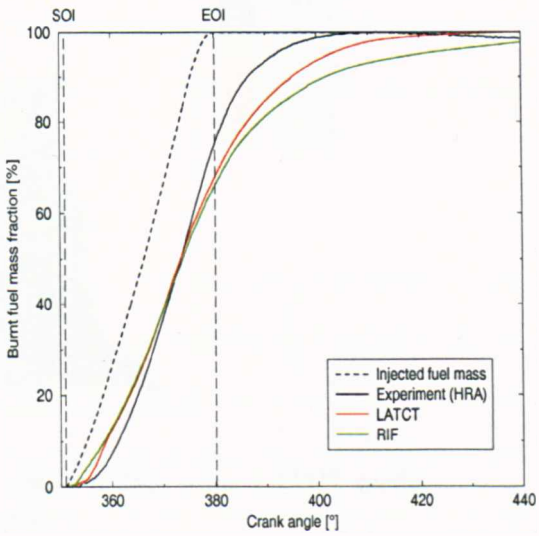



**Figure 6.90:** Burnt fuel mass fraction comparison for EOP4.

sumption than the experiments. During the expansion stroke the HRR is underpredicted until 386° CA, after which the experimental levels are lower than the predictions. The experiments show complete combustion at around 430° CA†. Once again the combustion is not completed in the RIF calculations by EVO.

#### 6.3.2.3 Wall heat transfer

**Base case**

In Figure 6.91 unique information from the present heat transfer predictions is provided in the form of the distribution of heat fluxes on the piston surface at different times, deduced from the results obtained with the LATCT model and the MWF method.

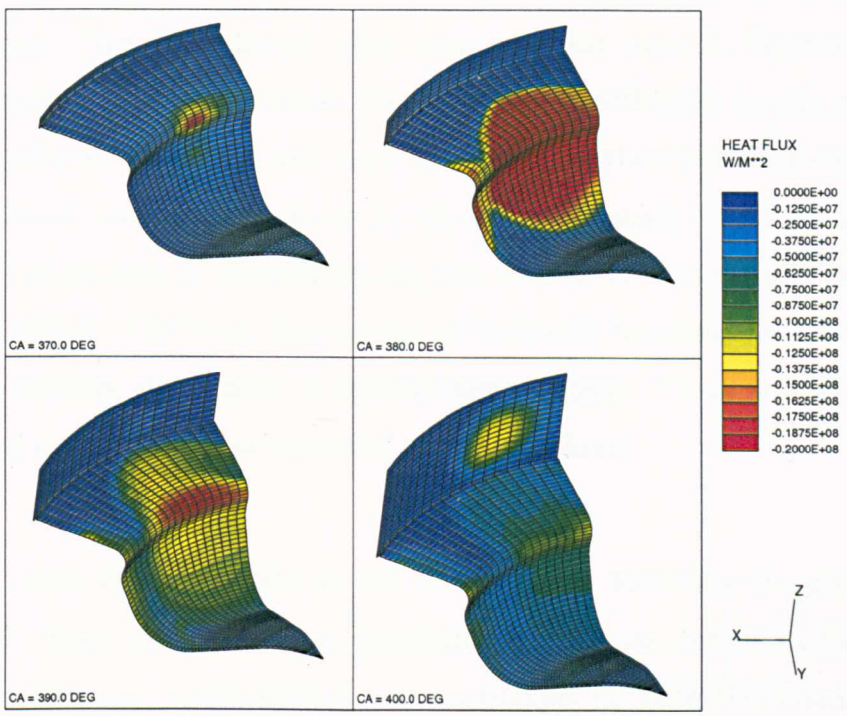



**Figure 6.91:** Heat flux distribution on piston surface using LATCT model for 370° to 400° CA, $R_s = 0.5$.

†The residual unburnt fuel mass fraction in the experimental curve is thought to come from inaccuracies of the heat release analysis, since a negative slope starting at around 420° CA is unphysical.

The flame front reaches the piston lip area at around 370° CA as indicated by the local increase of heat flux. Within a roughly circular area large absolute values up to 24 MW/m$^2$ are found, compared with a mean level elsewhere of around 1 MW/m$^2$. Steep gradients exist around the boundaries. This would indicate high localised thermal loading. By 400° CA the flame has impinged on the cylinder liner, inducing similarly large heat flux levels and gradients there. Relatively cool air is trapped between the flame plumes, resulting in considerably lower fluxes in this region.

It should be noted that the high heat fluxes are due to combined flow and thermal effects. The propagating flame induces high velocities and turbulence levels ahead of the flame front which affect wall heat transfer significantly, once the flame approaches the chamber walls. Moreover the steep temperature gradients in the boundary layer, induced by combustion, influence considerably heat transfer through the variations in the thermophysical properties, which are reflected in the MWF implemented in this study. This is reinforced when comparing the plots in Figures 6.64 and 6.91 for motored and fired operation. The heat flux distribution for the motored case is clearly substantially lower and more uniform than when including combustion. The present heat transfer predictions for the fired operation clearly reveal that for the detailed estimation of thermal loading the concept of heat transfer coefficients is of limited utility. The local distribution of near-wall temperature gradients is necessary to identify the regions of critical thermal loads. These can only be obtained from full combustion simulations of the present kind.

The heat flux variations at the measurement locations are displayed in Figure 6.92. Each plot relates to a particular location, as defined in Figure 5.12, and includes heat flux measurements and predictions for both the standard and modified wall function approaches. The LATCT combustion model was used with a swirl number of $R_s = 0.5$. The MWFs yield considerably higher heat fluxes than the SWFs, by a factor of 4.5 on average. Evidently the steep gradients of thermophysical properties in the near-wall region substantially increase wall heat transfer. The

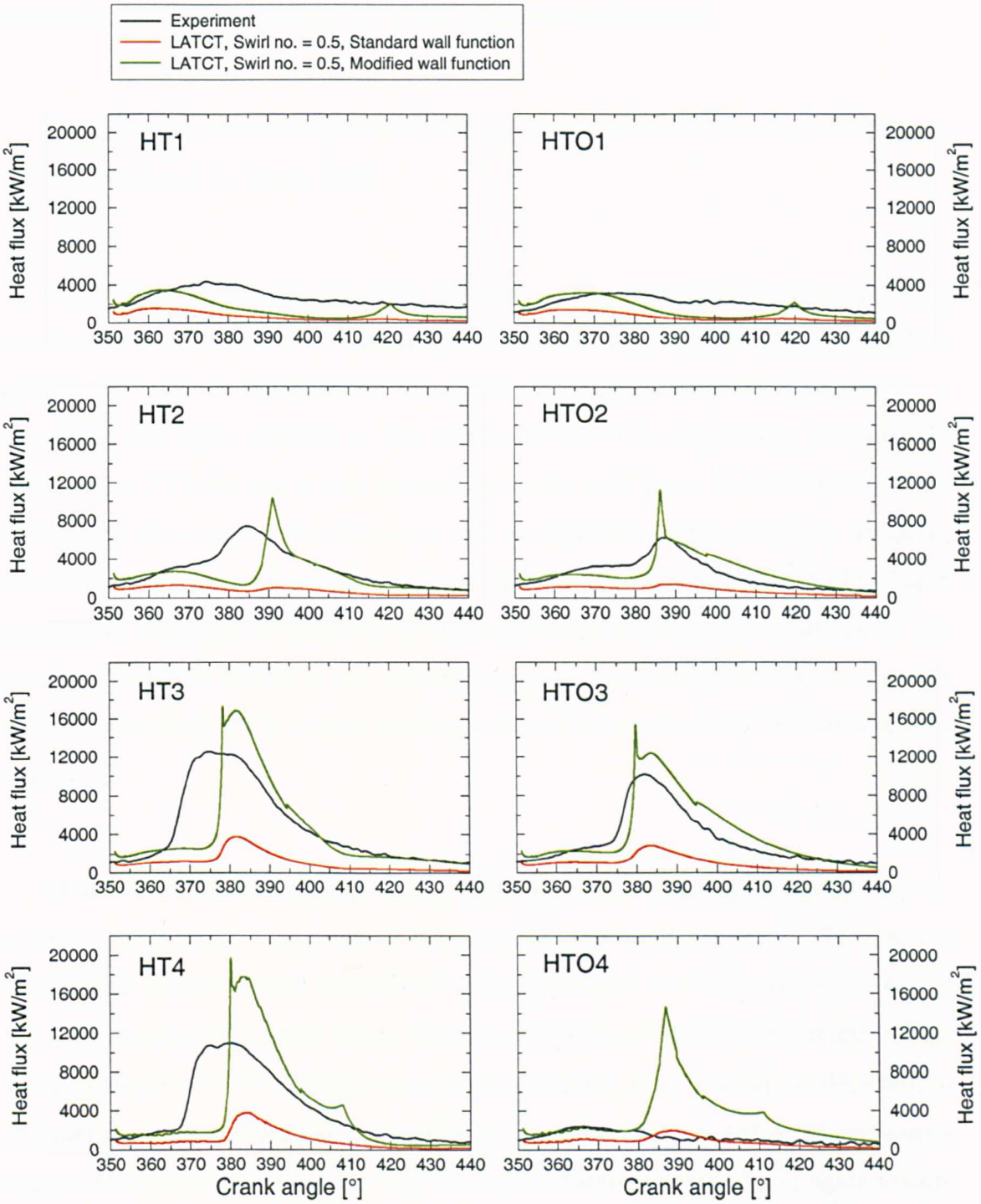



**Figure 6.92:** Comparison of heat flux on piston surface at eight measurement locations using standard and modified wall function approaches; LATCT combustion model, $R_s = 0.5$.

predictions with the MWFs agree better with the experiments. Therefore in the remainder of the section only the MWF approach is discussed.

The heat flux variations obtained with the two combustion models, LATCT and RIF are displayed in Figure 6.93.

For points aligned with the spray axis the results show that the flame initially travels above HT1 and HT2 and arrives at HT3 at around 365° CA and HT4 at around 367° CA, as indicated by the sudden increase in flux. At HT2 there is a somewhat less rapid increase in flux at around 377° CA, suggesting flame arrival then; but at HT1 the rise is very gradual up to the peak level, suggesting that there is no sharp flame front. This behaviour can be explained by the predicted temperature fields in the vertical sections in Figure 6.78 for 360° CA to 370° CA. The flame propagates primarily along the spray axis above the measurement locations on the piston. The radial spread of the burning region towards the piston surface (and in particular towards HT1) occurs gradually, being governed mainly by diffusion processes.

At the "HTO" measurement points, mid-way between two spray axes, sharp increases in heat flux are seen only at HTO3, which the flame reaches at 374° CA and HTO2 with arrival time at around 380° CA. The trend at HTO1 resembles that of the axis location HT1, with about 25% lower heat flux levels. Concerning HTO4, which is situated in the clearance gap, no sharp rise in heat flux can be detected, in contrast to the measurement point HT4 on the axis. Overall, these measurements suggest that the effect of swirl is very low, as the flame appears to propagate mainly along the spray axis. This is what was indicated in the photographs in Figures 6.75 and 6.76, presented earlier.

The predicted fluxes using the LATCT model, MWFs and a swirl number of 0.5

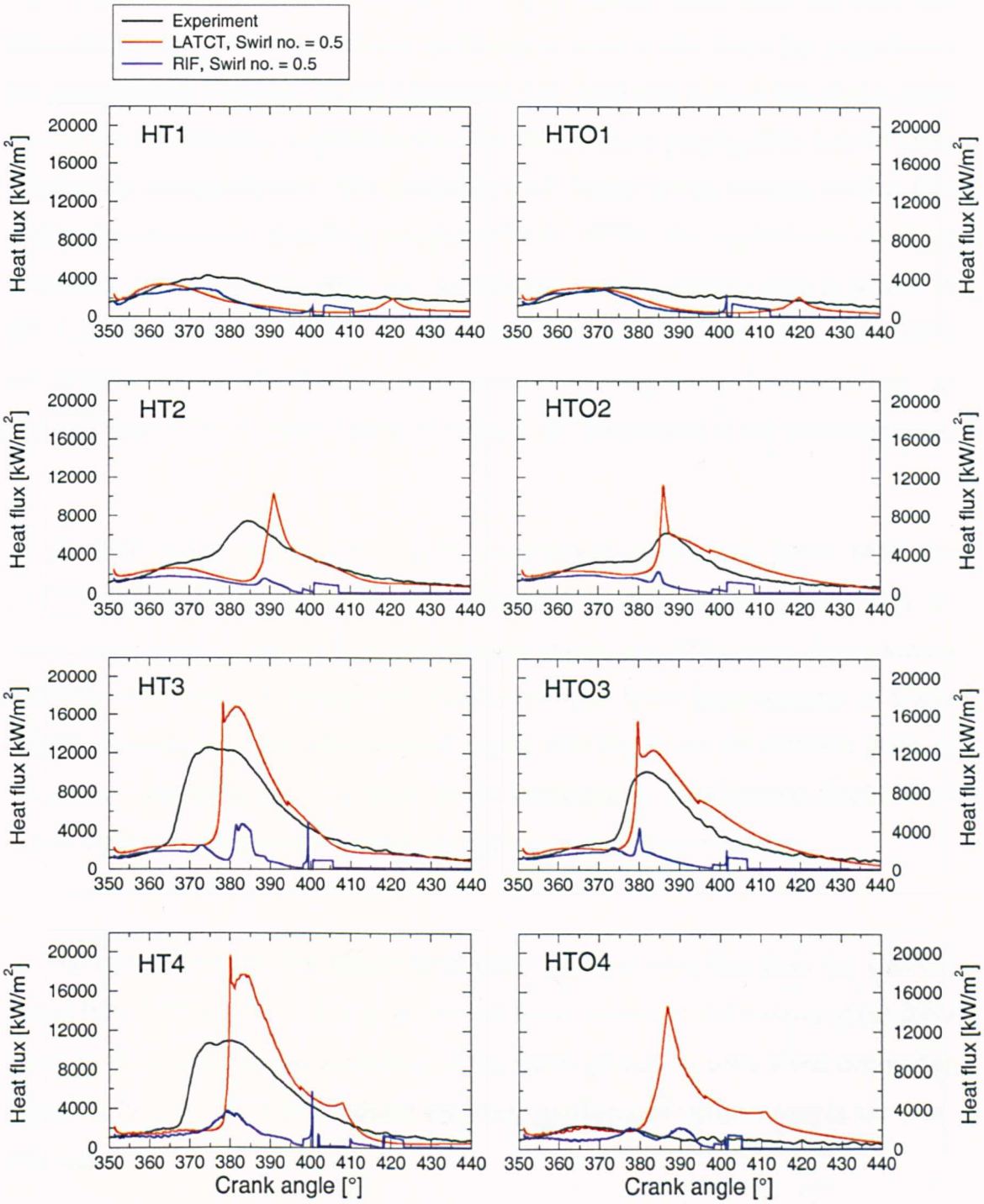



**Figure 6.93:** Comparison of heat flux on piston surface at eight measurement locations using LATCT combustion model and RIF with MWFs.

will now be discussed. The predictions show similar tendencies to the measurements concerning the effect of flame arrival. Due to the sharp flame front the heat flux increases rapidly and then decreases gradually as soon as the flame has passed over the measurement location. In the predictions the rapid rise in heat flux occurs later than in the experiments, suggesting that the rate of flame propagation toward these locations is underpredicted. The predicted peak fluxes are on average within 40% of the measurements, excluding location HTO4. While the experiments show no indication of flame arrival here, the calculations clearly indicate that it occurs at 387° CA. Shortly after 410° CA the simulation predicts flame arrival at points HT1 and HTO1, respectively, due to the hot mixture moving along the piston bowl, as seen in Figure 6.79. A similar steep increase is not discernible in the measurements.

The RIF model using MWFs gives considerably lower heat fluxes than the LATCT model and the measurements. Relatively slow predicted rates of flux increase occur prior to 395° CA at all locations except for HT3, where flame arrival is clearly indicated. At around 400° CA a very thin flame front appears to travel radially inwards over the measurement points, starting from the furthest point in the bowl. This behaviour is evident in the temperature distributions displayed in Figure 6.82. The phenomenon does not appear in the measurements.

The reason that the RIF model gives lower values of heat flux than the LATCT model from 370° to 390° CA (i.e. at around flame arrival at the measurement locations) is the smaller radial spreading of the flame plume, as seen when comparing Figures 6.79 and 6.82, which induces less steep gradients of temperature in the near-wall region.

The published point heat transfer comparisons are probably the first of their kind, as previous evaluation studies have not been able to rely on such detailed information regarding the engine configuration, operating conditions and heat transfer

behaviour. The present study has demonstrated that surface heat flux data provide a much more stringent testing ground for combustion simulation than chamber pressure measurements, due to their high sensitivity to the local flame propagation, as opposed to the global heat release. Given this and the levels of uncertainty in both the modelling and the measurements, the degree of agreement obtained, particularly with the LATCT model and MWFs, should be regarded as encouraging and arguably sufficient to provide a good estimate of the thermal loads on the chamber walls.

In what follows, a sensitivity study is performed for various swirl levels, characteristic breakup time and nozzle blockage. It was attempted to reach overall better agreement with respect to the heat flux measurement.

### Variation of swirl level

The predicted heat fluxes at the measurement locations for various SOI swirl levels are displayed in Figure 6.94. These show that higher swirl generally decreases the maximum heat flux at locations under the spray axis, but increases it at locations mid-way between the sprays. With respect to flame arrival times, a lower swirl velocity reduces the flame arrival time on the spray axis locations and delays it at locations between the axes. The predicted flame arrival times on the spray axis locations correspond best with the experiments for no swirl, but a swirl number of 0.7 gives best agreement mid-way between the axes. However, $R_s = 0$ also gives the largest overpredictions on the spray axis plane, while $R_s = 0.7$ yields the highest peak values mid-way between two sprays. The predictions indicate an especially strong sensitivity to the swirl level at locations in the clearance gap (HT4 and HTO4). At HTO4 only the $R_s = 0$ calculation reproduces the measured indication of no distinct flame arrival. In this respect it has been shown by Yoshizaki *et al.* [477] through experimental investigations on a combustion chamber of a DI Diesel engine that a strong sensitivity exists of flame spread into the clearance region to the height

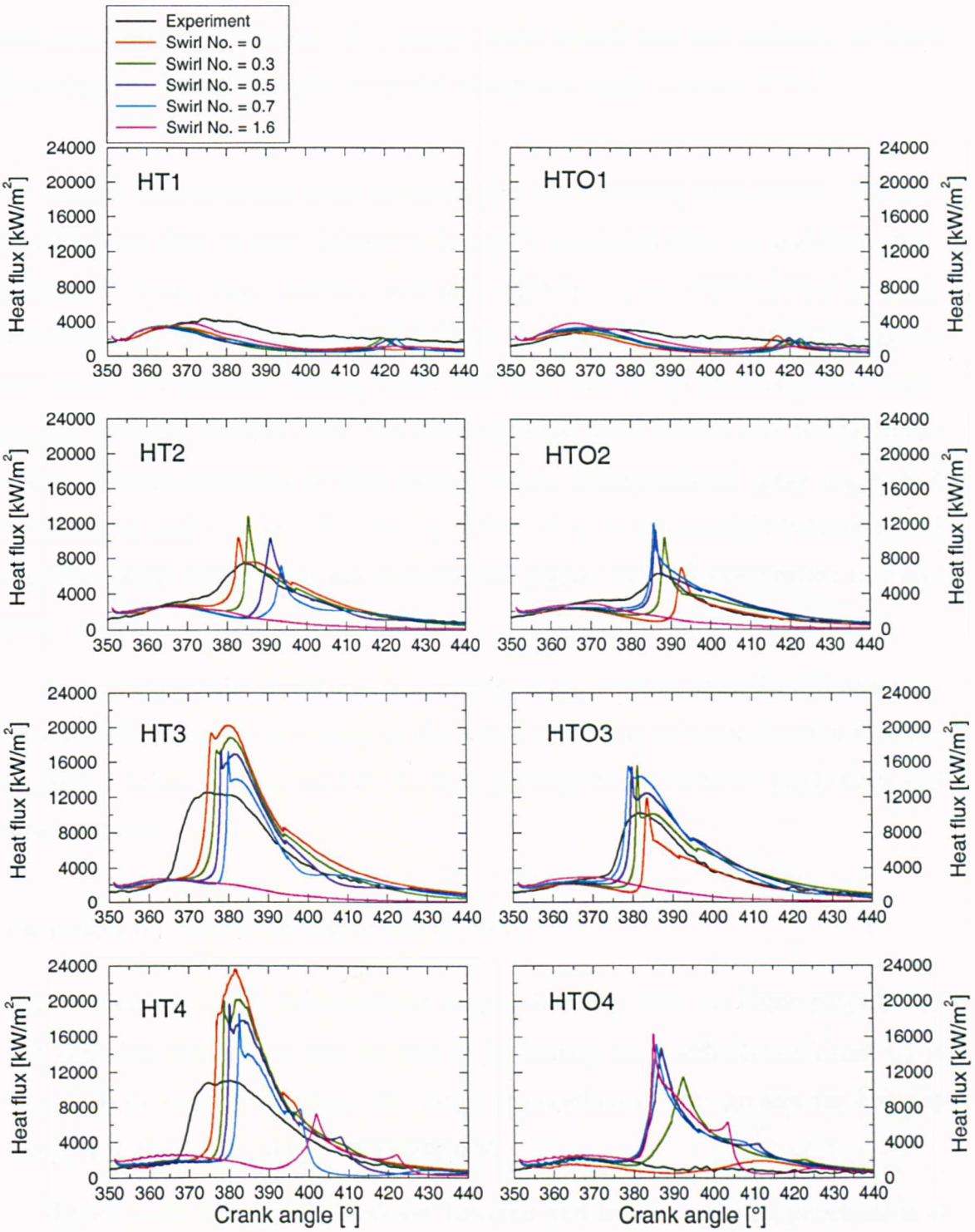



**Figure 6.94:** Comparison of heat flux on piston surface at eight measurement locations for various swirl levels; LATCT combustion model and MWFs.

of the clearance gap. Since for this engine configuration uncertainties exist about the actual height, the absence of a distinct flame arrival may also indicate the flame has quenched before it is able to spread circumferentially towards HTO4.

Overall this sensitivity study indicates that the prevailing swirl ratio is very low, possibly very close to zero. Moreover, it can be concluded that the real flame penetration is faster than predicted and also exhibits a more rapid spread in radial direction. The penetration is controlled by the evaporation rate, vapour penetration speed and turbulent mixing which were also found to be underpredicted in the Aachen pressure chamber case. The reduced radial flame spread may be the consequence of underestimated air/fuel mixing and an underpredicted spray angle. Full modelling of high pressure effects on spray behaviour as discussed in Section 1.3.1.2 would probably improve the calculations with respect to both evaporation rate and spray angle.

Since the heat flux levels are substantially overpredicted when $R_s = 0$ and since uncertainties remain with respect to the actual prevailing swirl, in the present study a nominal value of 0.5 is used in the further comparisons between predictions and measurements.

### Variation of characteristic breakup time

The influence of the characteristic droplet breakup time on flame propagation and heat flux predictions was studied by increasing the coefficients $C_b$ and $C_s$ in Eq. (3.93) by equal proportions (the larger the coefficients, the greater the breakup time). The results are shown in Figure 6.95.

Higher coefficients result in slower breakup and hence increased penetration of the droplets. This results in earlier flame arrival both under the spray axis and between two sprays. In addition a slight increase in peak heat flux is observed. The trends in the clearance gap are less sensitive. None of the calculations reproduces the measured trend at HTO4.

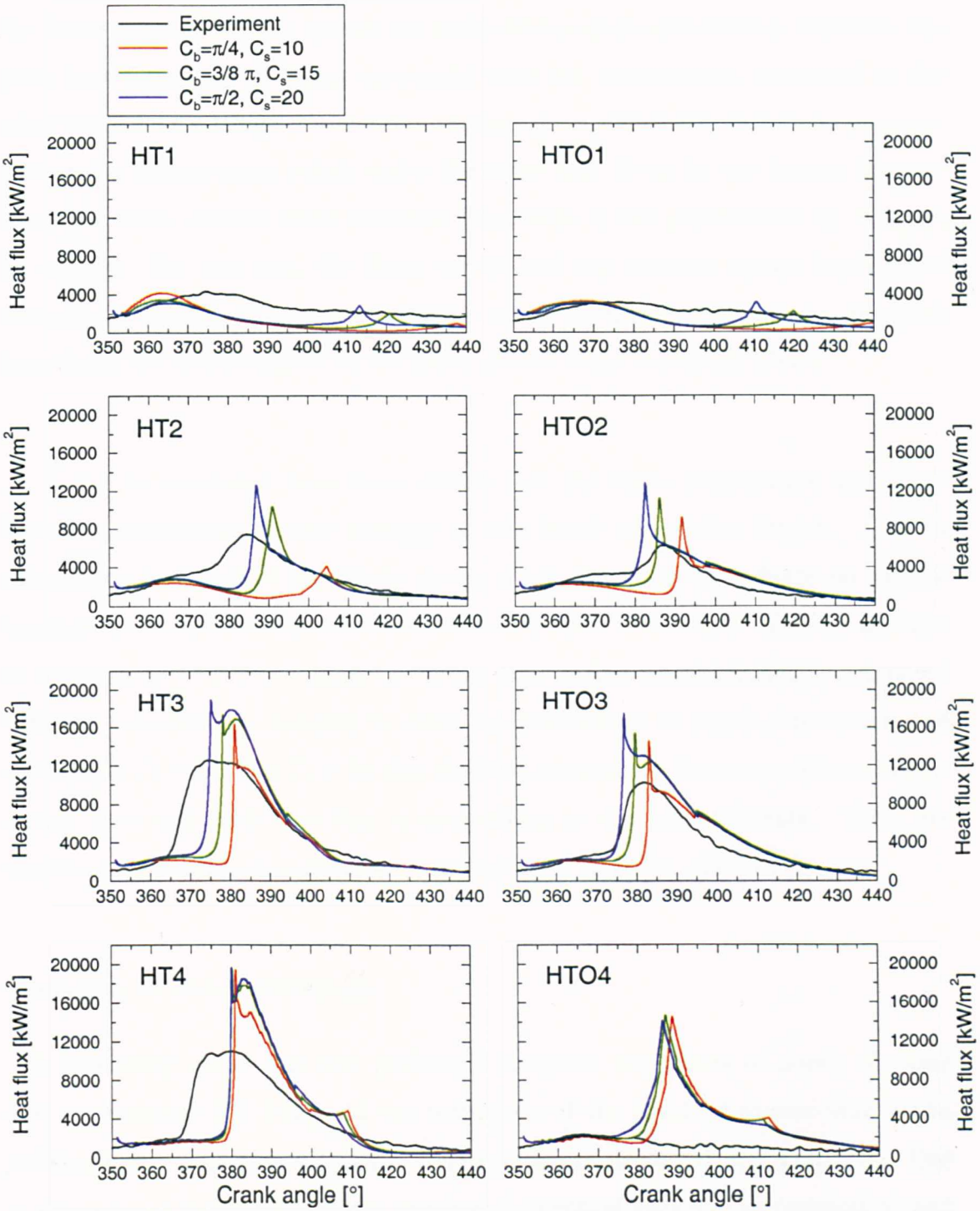



**Figure 6.95:** Comparison of heat flux on piston surface at eight measurement locations for various characteristic droplet breakup time coefficients; LATCT combustion model and MWFs, $R_s = 0.5$.

When using the recommended values for the breakup model ($C_b = \frac{\pi}{4}$, $C_s = 10$) the flame propagation and spread are underestimated at all locations. However, the peak heat fluxes are in better agreement with the experiments, compared to the other coefficient settings. None of the settings gives sufficiently fast flame propagation at the measurement points under the spray axis. Even for the longest breakup time, the flame reaches these locations later than in the experiments by 8.5° CA on average. For this case, the flame arrival mid-way between sprays is predicted correctly at HTO3, while underprediction occurs at HTO2. Furthermore the peak heat fluxes are overpredicted of the order of 58% when excluding HTO4.

It can be concluded from these results that the flame propagation and hence heat flux predictions depend strongly on the liquid penetration length. Also, in comparison to the swirl sensitivity study, a less dramatic dependence on droplet breakup times than on swirl is observed in the heat flux trends. Due to the lack of optical access for this engine, the actual penetration length cannot be compared with the calculations. Keeping in mind the uncertainty in liquid penetration, the coefficients $C_b = \frac{3}{8}\pi$ and $C_s = 15$ give the best compromise between predicted flame arrival time and peak heat flux in comparison to the measurements. These are employed for all calculations shown in the present work for the HPP engine.

### Variation of nozzle blockage

A sensitivity study was also performed to assess the effects of nozzle blockage due to cavitation [65, 141]. *Ad hoc* reductions of the nozzle diameter were made, yielding higher injection velocities. The results are displayed in Figure 6.96. Due to the reduced initial droplet size and higher injection velocity the penetration and evaporation rates are enhanced. This is confirmed by experimental sensitivity studies on a DI Diesel engine reported in [477]. The result is earlier flame arrival at all measurement locations. While a 20% blockage improves flame penetration speed along the spray axis, the flame reaches the locations mid-way between the sprays

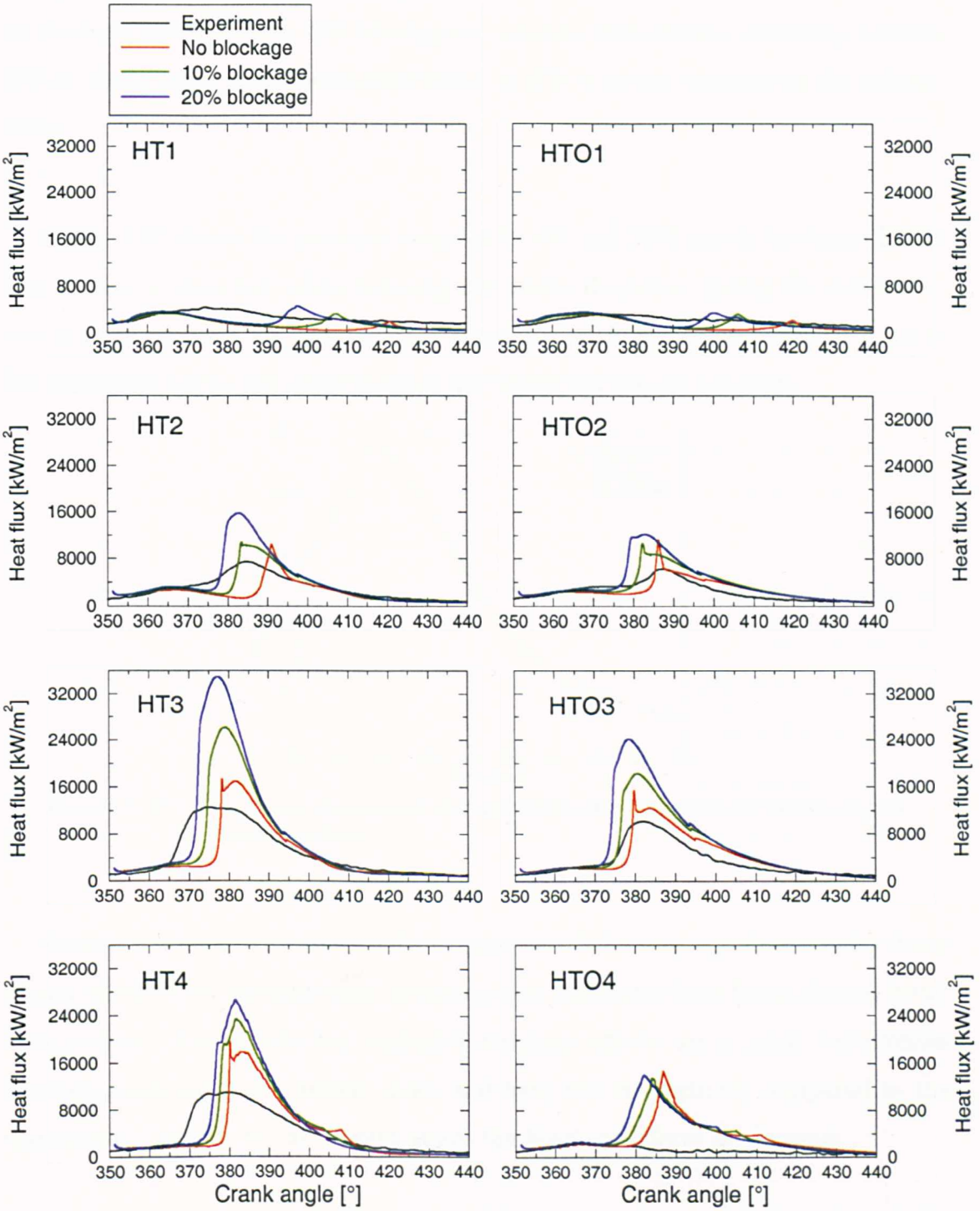



**Figure 6.96:** Comparison of heat flux on piston surface at eight measurement locations for various degrees of nozzle blockage; LATCT combustion model and MWFs, $R_s = 0.5$.

earlier than in the experiments. The peak heat flux is overpredicted by 40% with no blockage and 97% with 20% blockage on average, respectively, excluding location HTO4. Once again the experimental trend at HTO4 is not captured in the calculations.

Figure 6.97 shows the pressure histories for 0% and 20% nozzle blockage. Faster heat release is observed, when reducing the nozzle diameter, giving 9% overprediction of peak pressure for 20% blockage compared with 2% for no blockage. Late in the expansion stroke the experimental and numerical results converge.

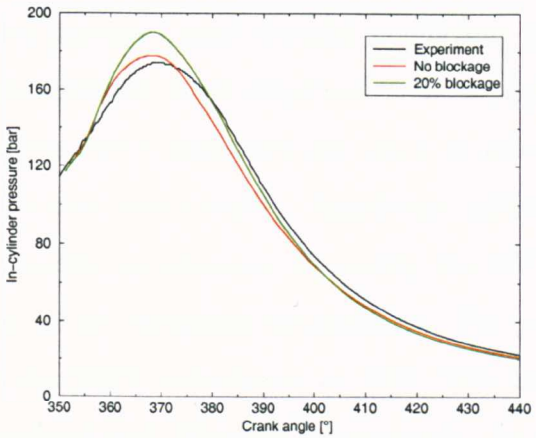



**Figure 6.97:** Comparison of measured and calculated pressure history for various degrees of nozzle blockage.

Overall this sensitivity study indicates that nozzle blockage produces earlier flame arrival times at all measurement locations, and increased heat fluxes due to faster heat release. The results for negligible blockage effects are a good compromise between predicted flame arrival times and heat flux magnitudes compared to the experiments. Hence, in the present study the blockage effects are ignored.

### Conclusion of sensitivity studies

These sensitivity studies have revealed a significant influence of swirl level, liquid penetration length and vapour penetration speed on the heat transfer predictions via their effect on flame propagation. Generally it was seen that the flame propagation

and the radial spread of the flame plume were underestimated in the calculations. In addition, heat transfer measurements indicate negligible swirl which is in contrast to the previous indications, but consistent with the photographs in Figures 6.75 and 6.76. Since none of the tested variations seems to give improvements in both flame arrival times and peak heat flux magnitudes, it is decided to adopt the best compromise regarding both criteria, notably a nominal swirl number of $R_s = 0.5$, the droplet breakup coefficients $C_b = \frac{3}{8}\pi$ and $C_s = 15$ and no nozzle blockage.

### Surface-averaged HTCs and total heat transfer

The predicted surface-averaged heat transfer coefficient history is compared in Figure 6.98 with those obtained from empirical heat transfer correlations. Once again the results using the MWF approach are taken as reference, since they more adequately represent the real heat transfer. Significant differences are observed between the global heat transfer correlations. Generally the MWFs yields considerably larger HTCs compared to the empirical correlations. The peak HTC is underpredicted with respect to the MWF calculation by 53%, 23% and 58% for the correlations of Annand, Hohenberg and Woschni, respectively. By comparison, the SWF method predicts 70% lower HTCs on average than the modified near-wall treatment.

In the CFD simulations the timing of the peak HTC is shifted toward later crank angles, closer to the instance when the bulk gas temperatures are the highest (cf. Figure 6.105). The correlations cannot account for this due to their derivation from the pressure trace which shows a peak around 13° CA earlier (cf. Figures 6.83 and 6.105).

A similar situation as for surface-averaged HTCs is encountered when comparing the total heat transfer, illustrated in Figure 6.99. The MWF approach estimates the highest total heat losses until EVO, which are larger by 2.2, 1.2 and 2.8 compared to Annand, Hohenberg and Woschni. Compared to the modified near-wall treatment the SWF method gives a total heat transfer that is 70% lower.

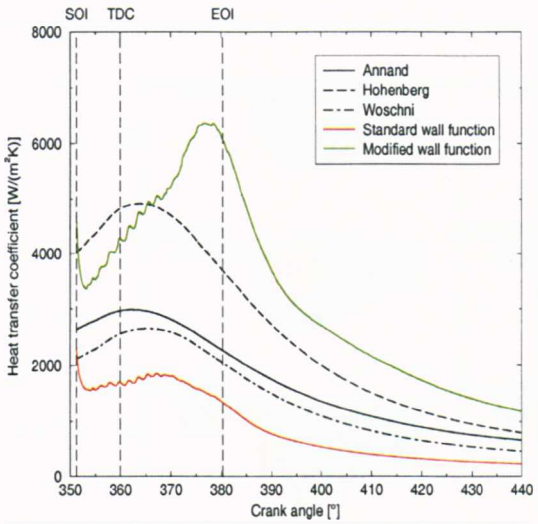



**Figure 6.98:** Comparison of heat transfer coefficients between calculations and global heat transfer models.

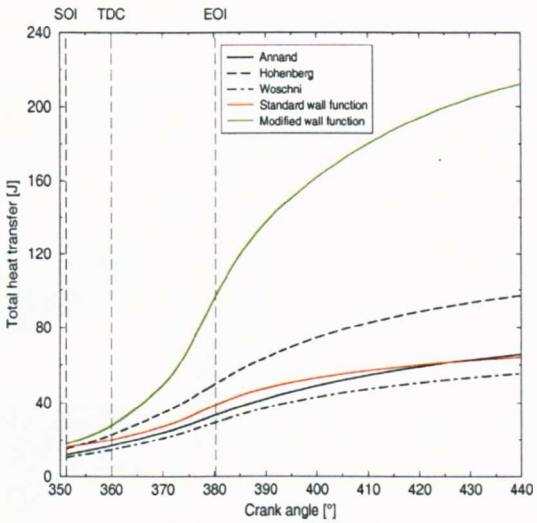



**Figure 6.99:** Comparison of total heat transfer between calculations and global heat transfer models.

It should be noted that the present heat transfer measurements and predictions reveal a substantial influence of combustion and flame propagation on heat transfer. Therefore considerable temporal and spatial variations of heat fluxes are observed over the chamber walls, reaching locally critical magnitudes and gradients. The knowledge of the distribution of critical heat fluxes is vital for the component design. In this respect the heat transfer coefficients fail to estimate critical levels of thermal loading particularly under fired operation, since for the latter the local temperature gradients are required which vary significantly in the combustion chamber. Empirical heat transfer correlations as those studied here therefore fail to adequately estimate the critical temporal and spatial variations of heat transfer.

#### 6.3.2.4 Emissions

**Predicted soot and $NO_x$ fields**

In Figures 6.100 and 6.101 the predicted evolutions of the soot concentration distributions in the vertical section containing the spray axis are shown for the NSC and

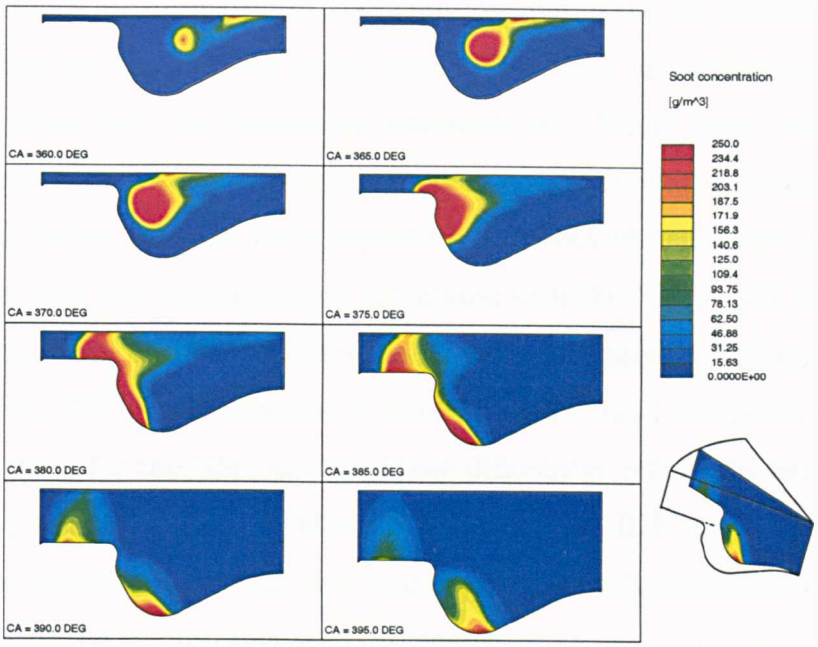



**Figure 6.100:** Soot distribution using NSC model for 360° to 395° CA.

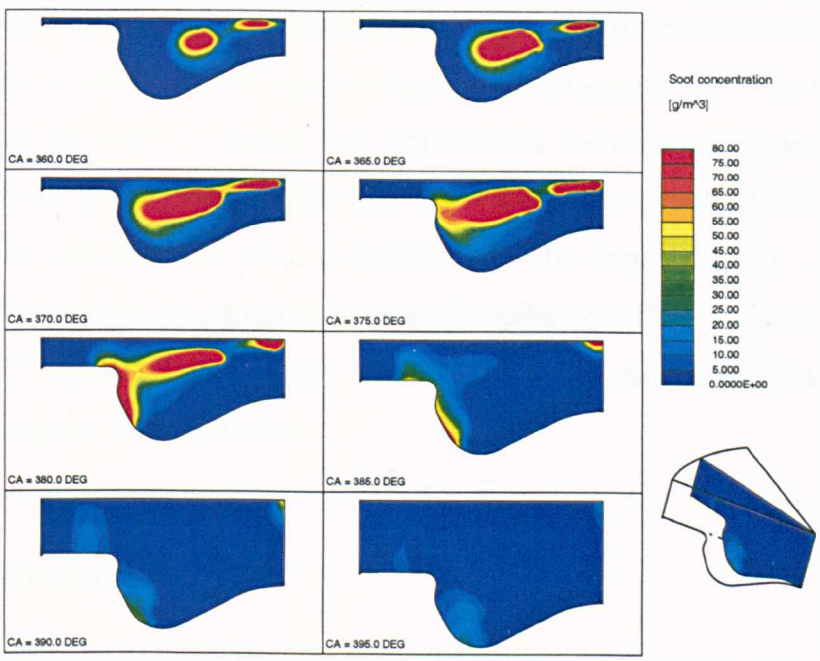



**Figure 6.101:** Soot distribution using RIF model for 360° to 395° CA.

the RIF models, respectively. Both approaches indicate that soon after autoignition soot-rich clouds are formed close to the injector and in the low temperature fuel-rich region within the leading part of the flame. The shape and distribution of the soot cloud conforms with the conceptual schematic of a Diesel flame proposed by Dec and coworkers, previously shown in Figure 1.7. The frontal soot cloud reaches the piston wall before 380° CA and propagates into both the clearance gap and piston bowl. The local soot concentrations calculated with the NSC model are significantly higher than those of the RIF model, as already indicated by the global values. In addition, the RIF model produces a stretched soot cloud compared to the nearly-spherical cloud for the NSC model. These differences reflect the shape of the cool core region seen in Figures 6.78 and 6.81. Since the RIF model predicts burning close to the nozzle even during later crank angles, soot is also found in this location in contrast to the results from the NSC model.

The $NO_x$ concentration field evolutions are displayed in Figures 6.102 and 6.103 for the LATCT model and RIF models, respectively. $NO_x$ is formed on the lean side of the stoichiometric mixture fraction contour where temperatures are the highest and oxygen is entrained. In regions where soot is formed, the $NO_x$ formation rate is low. For the LATCT model the highest $NO_x$ concentrations are found at the bottom of the flame plume, while the RIF model also produces $NO_x$-rich regions close to the cylinder head that propagate into the clearance gap. At later crank angles RIF predicts $NO_x$ formation near the spray axis close to the injector nozzle. The LATCT calculations, however, produces $NO_x$-enriched areas situated mainly in the outer region of the cylinder.

### Soot predictions

In Figure 6.104 the predicted temporal variations of the chamber-averaged soot concentrations for operating point EOP1 are shown, as obtained from the Nagle Strickland-Constable, Hiroyasu and RIF models. For the first two, their empirical

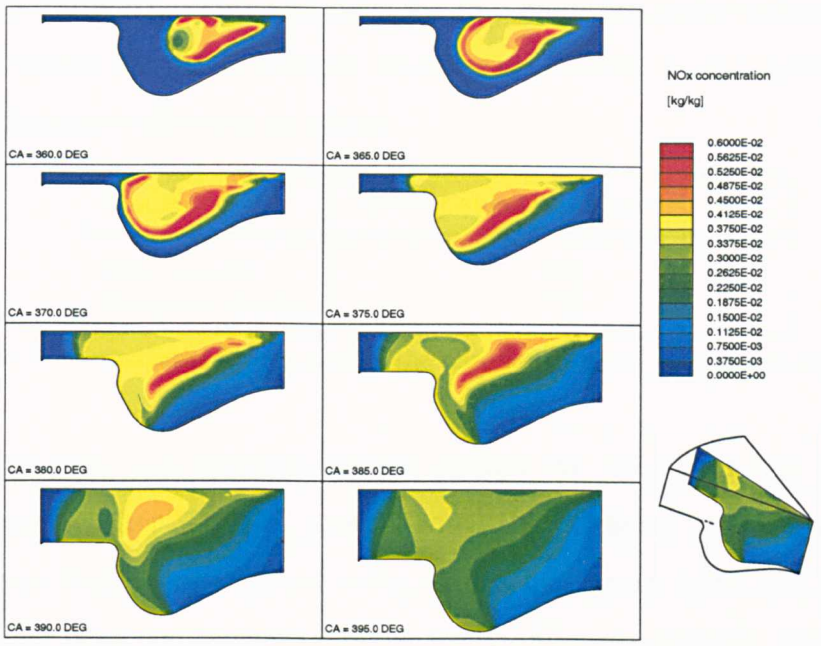



**Figure 6.102:** $NO_X$ distribution using NSC model for 360° to 395° CA.

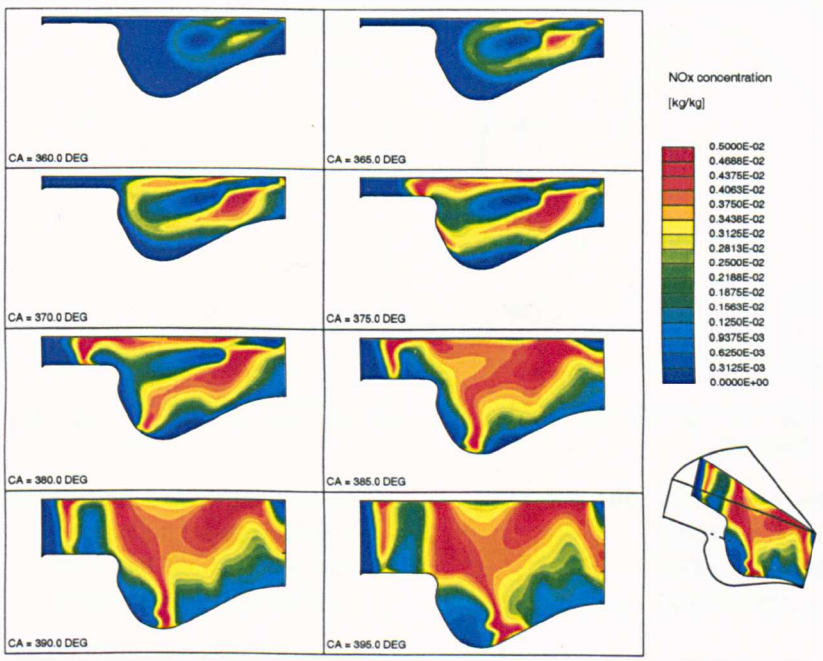



**Figure 6.103:** $NO_X$ distribution using RIF model for 360° to 395° CA.

coefficients have been adjusted to give the correct measured final soot concentration, as listed in Table 6.6. This was done for this operating point only and the same coefficient values were then used for all other conditions. In the case of RIF, there are no analogous coefficients to adjust.

| Model | Pre-exponential factor $A_f$ [$s^{-1}$] |
|---|---|
| NSC model | 350 |
| Hiroyasu model | 750 |

**Table 6.6:** Pre-exponential factors used in the phenomenological soot models for HPP engine.

Both the NSC and Hiroyasu models predict the maximum soot concentration to occur shortly after 380° CA, around when the predicted cylinder-averaged temperature and fuel/air equivalence ratio, shown in Figures 6.105 and 6.106 are the highest. The peak soot concentrations, which differ appreciably between the two models, are substantially larger than the final value, which is consistent with other studies reported in the literature, e.g. [39, 431].

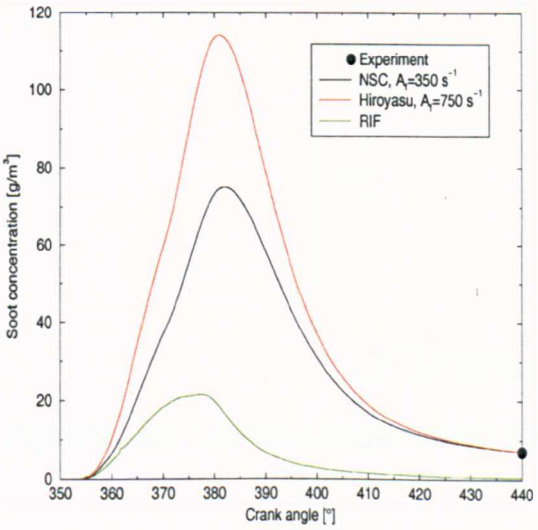



**Figure 6.104:** Cylinder-averaged soot concentration using various approaches for 2.85 bar boost pressure and 1420 RPM.

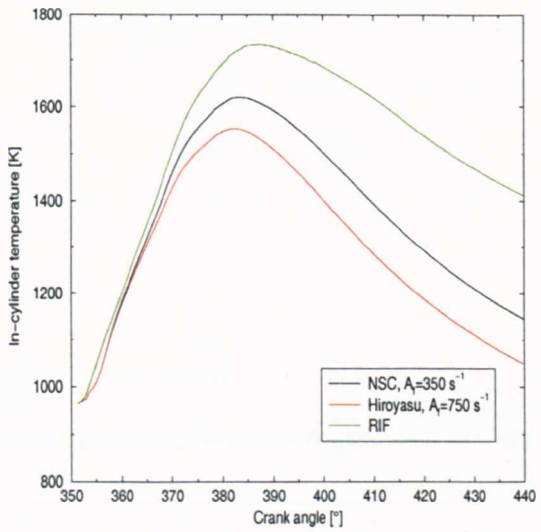



**Figure 6.105:** Cylinder-averaged gas temperature history, predicted using various soot modelling approaches.

The RIF model predicts a somewhat different history, in which slower formation occurs before 380° CA, followed by rapid oxidation, leading to much lower peak and

end values. This underprediction of soot concentrations is similar to the results for the Aachen pressure chamber in Section 6.2.4. However, it is important to keep in mind that the present RIF model is based on $n$-heptane chemistry which produces less soot due to the lower C/H atomic ratio compared to Diesel fuel [299, 312]. Also, as mentioned earlier, the soot coagulation model in the RIF code underestimates soot formation such that soot levels remain low [281].

The cylinder-average temperature histories shown in Figure 6.105 reflect the estimated soot trends. Substantial variations between the various predictions are observed, which have considerable influence on $NO_x$ levels, as will be seen later. As soot is formed the fuel energy is temporarily "stored" in the soot molecules and released as soot is burnt. Therefore a higher soot concentration gives a lower heat release compared to complete combustion, resulting in lower in-cylinder temperatures.

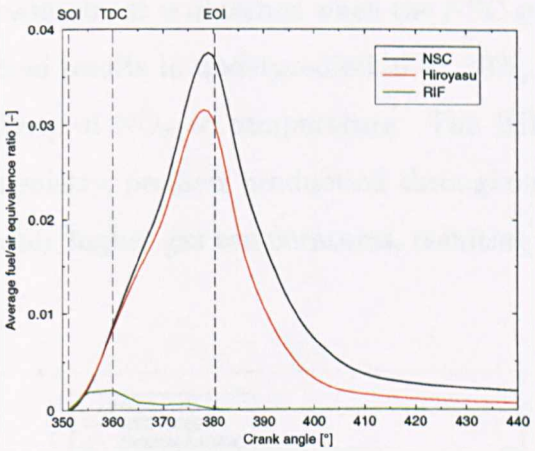



**Figure 6.106:** Cylinder-averaged fuel/air equivalence ratio using phenomenological soot models.

The cylinder-averaged fuel/air equivalence ratio $\phi$ for the LATCT calculations using both phenomenological soot models and RIF are shown in Figure 6.106. In the results of the NSC and Hiroyasu model the mixture is inherently lean with increasing $\phi$ until 378° CA. After EOI the equivalence ratio decreases as fuel is burned. At EVO, i.e. 440° CA, unburnt fuel is observed in both predictions. The NSC model estimates a richer mixture by 34% on average than the Hiroyasu model.

By contrast, the RIF model estimates substantially lower equivalence ratios with a peak at around TDC. This is due to the fact that RIF uses complex gas chemistry, in which fuel is broken down into lighter hydrocarbons and $CO$, as soon as fuel is injected into the combustion chamber. This has been discussed earlier for Figure 6.87 in Section 6.3.2.2. At EVO a negligible amount of fuel remains in the chamber.

### $NO_x$ predictions

Figure 6.107 displays the predicted cylinder-averaged $NO_x$ concentration histories obtained with the different modelling approaches, along with the measured exhaust concentration. The predictions from the extended Zeldovich $NO$ model, when used in conjunction with either the NSC or Hiroyasu soot model (whose effects are felt via their influence on gas temperature, as discussed above) indicate a fast $NO_x$ formation period after ignition, reaching constant levels after about 393° CA. Excellent agreement with the measurement is obtained when the NSC soot model is employed, while the Hiroyasu model results in underprediction by 30%, which is also not bad, considering the sensitivity of $NO_x$ to temperature. The RIF approach, which includes its own $NO_x$ chemistry, predicts production throughout the entire expansion stroke due to considerably higher gas temperatures, resulting in 60% overprediction of the end value.

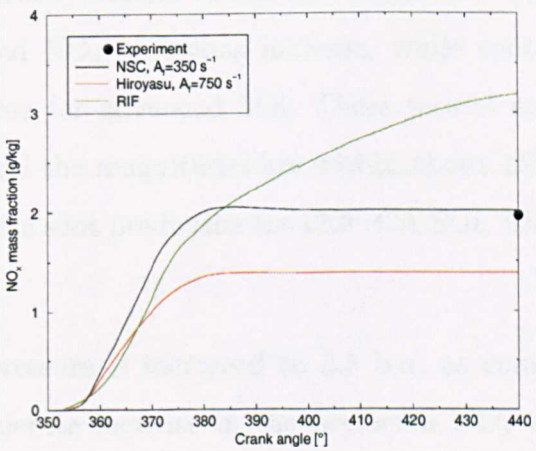



**Figure 6.107:** $NO_X$ prediction using various soot modelling approaches.

### Soot/$NO_x$ tradeoff

Predictions of the levels of soot and $NO_x$ exhaust emissions for the range of operating conditions EOP1 – EOP4, involving changes to injection timing and boost level (see Table 5.16) will now be presented. These were obtained using the LATCT combustion model, the NSC soot model with coefficients tuned for EOP1 as described above, the standard extended Zeldovich *NO* model, and the MWFs. The results are shown, along with the measured data, in Figure 6.108. The numbers beside each plotted point are the SOI timing in degrees before TDC (BTDC).

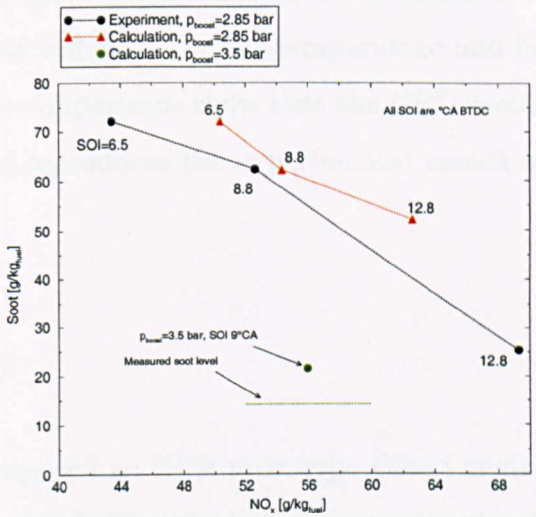



**Figure 6.108:** Soot/$NO_x$ tradeoff prediction using LATCT/NSC model.

As injection is retarded, relative to the 8.8° CA BTDC timing for the base case of EOP1, the predicted $NO_x$ emissions increase, while soot levels are decreased. The converse holds true for advanced SOI. These results are consistent with the experimental trends and the magnitudes are within about 15% for both quantities, with the exception of the soot prediction for 12.8° CA SOI, where the error is larger.

When the boost pressure is increased to 3.5 bar, as compared to 2.85 bar for EOP1, there is a moderate increase in the predicted $NO_x$ emission but the soot level decreases substantially. Both effects are probably the consequence of more oxygen being available, leading to better soot oxidation but also slightly higher

$NO_x$ production. For this case only the soot emissions were measured, the level being 14.14 $g/kg_{fuel}$, as compared with the predicted value of 21.3 $g/kg_{fuel}$.

The degree of agreement obtained for the tradeoff can be regarded as reasonably good, especially when the numerous modelling and measurement uncertainties are taken into account. For example, the soot measurements are only approximate, since the levels are one order of magnitude lower than the scale used on the instrumentation [248, 373]. Similarly, on the modelling side, uncertainties in trapped mass due to blowby or effects of combustion chamber deformation at elevated conditions on temperature can greatly influence the gas temperature and hence $NO_x$ predictions. The present soot/$NO_x$ comparisons show that the CFD methodology used achieves meaningful results and reproduces the experimental trends even at unusually high cylinder pressures.

### 6.3.3 Summary

This last test case comprised an HPP prototype Diesel engine, for which five operating points were examined. They included one motored case and four fired cases with variations in injection timing and boost pressure. Comparisons between predictions and measurements were made for in-cylinder pressure, wall heat transfer on the piston surface and exhaust concentrations of $NO_x$ and soot.

For the motored case the peak pressure was predicted within 3% compared with the measurements, while the peak timing matched the experiments. The disagreement between predictions and measurements were attributed to the uncertainty in clearance gap, the effects of blowby and cylinder deformation, which were not accounted for in the calculations, and underestimation of heat losses.

The wall heat transfer comparisons on the piston surface indicated that the calculations using both the SWFs and the MWFs consistently underpredicted the

peak heat flux timing by around 4° CA. While the modified near-wall treatment yielded larger peak heat fluxes which are within 34% of the experimental data, the SWF approach generally underpredicted the peak heat fluxes by around 20%. The experiments indicated larger variations of heat flux levels between the measurement points than the predictions. The causes for the discrepancies were mainly attributed to the differences in flow and turbulence fields and the spatially non-uniform wall temperatures which were not considered in the simulations.

Large differences were observed among the global heat transfer correlations. The largest heat transfer was predicted by the MWF approach. Hohenberg's correlation was found to most closely agree with the results obtained from the modified near-wall treatment.

For the fired cases, EOP1 and EOP4, the pressure traces were predicted reasonably well using both combustion models, with the peak pressure estimated within 2.7% and 7% for the LATCT and RIF approaches, respectively. The ignition delay was predicted slightly shorter than in the experiments by around 0.5° CA for both combustion variants. Also, the initial heat release was overestimated, while slower late burning was predicted. In this respect even RIF with its complex gas-phase chemistry could not reproduce the correct late burning characteristics. Overall it was concluded that the present CFD methodology is able to achieve predictions of similar accuracy even at the higher cylinder pressures of EOP4 compared to those of EOP1.

The wall heat transfer predictions revealed a strong sensitivity of local heat fluxes to swirl, liquid penetration and vapour penetration speed via their effect on flame propagation. The simulations were able to replicate the qualitative behaviour for most, but not all, of the measurement locations. With the LATCT model, the indicated flame arrival times tended to be too late and the peak fluxes tended to be overpredicted by 40% on average, excluding the locations in the clearance gap. The RIF model predicted significantly lower heat flux levels than the measured values.

However, considering the complexity of the spatial and temporal variations in heat flux and the fact that there were also a number of uncertainties in the measurements (i.e. swirl level), the present results with the LATCT model were regarded as encouraging.

The experiments and CFD results demonstrated that the heat transfer temporal and spatial variations cannot be adequately predicted via the empirical heat transfer correlations. Due to the substantial influence of combustion on heat transfer coefficients, primarily through the high temperature gradients generated in the near-wall region, it was concluded that detailed predictions of the thermal loading on components can only obtained from full combustion simulations. Thus the heat transfer coefficient concept is of limited utility.

The LATCT combustion model combined with the extended Zeldovich *NO* and NSC soot models produced the best agreement with the exhaust gas concentration measurements. The RIF approach underestimates the soot exhaust concentration by 93% and overpredicts the $NO_x$ level at EVO by 60%. These errors can be partly attributed to the underlying *n*-heptane chemistry, and possibly also to the soot coagulation modelling. The soot and $NO_x$ emissions predictions with the LATCT model combinations gave the correct trends with changes to injection timing and boost pressure, but the absolute levels were in error by varying degrees.

The experimental comparisons indicated that of the modelling practices tested in this study, the combination of the MWFs, the LATCT combustion model, the extended Zeldovich *NO* model and the NSC soot model produced the best overall agreement, albeit after some tuning of coefficients in the second- and last-named.

## 6.4 Closure

This chapter presented the assessment of the CFD methodology for Diesel engine simulation presented in previous chapters, by reference to experimental data. Three

test cases were chosen for which measurement data were available.

The RWTH Aachen engine test case was chosen to evaluate the flow field and heat transfer predictions under motored conditions. The inflow velocities and turbulence parameters agreed well with measurements particularly when the large cycle-to-cycle variations in the latter quantities are taken into account. The cylinder pressure history was estimated with encouraging accuracy. The local heat flux trends were predicted satisfactorily, but magnitudes were in general lower than the measured values. The differences between calculations and measurements were attributed to the discrepancies in the local flow and turbulence field predictions, caused by inaccuracies from insufficient numerical resolution or turbulence modelling. Best performance was obtained when using the modified near-wall treatment.

Large differences in the estimation of cylinder-averaged HTCs were found using empirical heat transfer correlations. The CFD predictions lay between those of the correlations. It was demonstrated that the correlations cannot reproduce the substantial variation of thermal loading over the chamber walls.

The Aachen pressure chamber case assessed the prediction of the spray penetrations, fuel vapour distribution, autoignition, combustion and soot formation. The best overall agreement with experiments was achieved with the LATCT combustion model and a phenomenological soot model. The liquid penetration and the vapour arrival times at the measurement locations were generally overpredicted. Possible reasons for this trend were a too low evaporation rate due to an overestimation of droplet size or due to high pressure effects. In addition underprediction of air/fuel mixing dependent on turbulence modelling can contribute to the discrepancies.

For the 4-step/LATCT framework the ignition criterion was set to match the measured ignition delay. The predicted ignition location compared very well to the experiments. The RIF approach predicted a too short ignition delay and several ignition sites.

Both of the phenomenological soot models were found to be capable of predicting the measured soot concentration trends after fitting the model coefficients. The soot oxidation rate was underpredicted, yielding too high levels at the downstream locations. The distributions agreed well with the measurements, in particular when keeping in mind the large pulse-to-pulse variations. The RIF approach yielded substantially lower soot concentrations.

Five operating points were investigated in the simulation of the HPP prototype Diesel engine. The complete CFD methodology was assessed by comparison with measured in-cylinder pressures, wall heat fluxes on the piston surface and exhaust concentrations of $NO_x$ and soot.

The pressure history for the motored case was predicted fairly well, given the uncertainty in clearance gap and the neglect of blowby and cylinder deformation. The wall heat flux trends agreed reasonably well with the measurements. However, the peak heat fluxes occurred earlier in the calculations, and the modified wall function approach overpredicted the magnitudes. The standard near-wall treatment generally underestimated the heat fluxes. In the experiments larger variations in heat flux levels between the measurement locations were observed than in the predictions. The differences between experiments and calculations were mainly attributed to discrepancies in the flow and turbulence fields and non-uniform chamber wall temperatures, which were not considered in the simulations. Furthermore the uncertainty of the clearance gap may significantly contribute to the near-wall turbulence and flow field and hence influence heat transfer.

Once again large differences were found among the empirical heat transfer correlation predictions. The CFD results yielded larger heat losses than any of the correlations.

For fired operation, the experimental comparisons indicated that the combination of the modified wall functions, the LATCT combustion model, the extended Zeldovich *NO* model and the Nagle Strickland-Constable soot model produced the

best overall agreement with the ensemble of measurement quantities. However, this required some tuning of coefficients in the second- and last-named models. The cylinder pressure predictions for two fired operating conditions agreed reasonably well with the experiments, but showed discrepancies in ignition delay and early heat release. The peak cylinder pressures were consequently overpredicted by less than 7%. As for wall heat transfer, the simulations were able to reproduce the qualitative behaviour for most measurement locations. A strong sensitivity of heat fluxes on swirl, liquid penetration and vapour penetration velocity was observed via their influence on flame propagation. Predicted flame arrival times tended to be too late while the peak fluxes were overpredicted. However, considering the complexity of factors that influence heat transfer and the number of uncertainties in the measurements such as swirl level, the present results were regarded as encouraging.

The experiments and CFD results revealed a substantial influence of combustion and flame position on local heat transfer, seen from the considerable temporal and spatial variations of heat fluxes. It was concluded from this that for the prediction of critical thermal loading on components, the local temperature gradients in the vicinity of the wall are required. Since the heat flux can only be derived from the HTCs, if these near-wall temperature gradients are known, the heat transfer correlations fail to adequately predict critical thermal loads. Only CFD combustion simulations of the present kind can provide such information.

The soot and $NO_x$ emissions comparisons indicated that the correct trends were predicted with variations in injection timing and boost pressure when using the LATCT combustion model combined with the extended Zeldovich *NO* and NSC soot model. The absolute magnitudes agreed with the experiments within 35% and 10% on average for soot and $NO_x$, respectively. The RIF approach predicted substantially different pollutant histories with significantly lower soot and larger *NO* concentrations.

The following, final chapter will summarise the main findings and conclusions of the present work and make recommendations for future research.

# Chapter 7

# Closure

This chapter summarises in Section 7.1 the main findings and conclusions drawn from the present study. In addition, suggestions for future research are proposed in Section 7.2.

## 7.1 Conclusions

The main findings of the present work are as follows:

- The current multidimensional Diesel combustion simulation methodology has been assessed and where necessary modified and extended to make it applicable to the increased peak pressure concept. The results have clearly demonstrated that the present methodology is capable of giving reasonable predictions for the elevated temperatures and pressures of the HPP concept. Similar accuracies are obtained even at extremely high pressures for flow, turbulence, spray, combustion, emissions and heat transfer, compared to moderate conditions, as seen when comparing the predictions of the various test cases.

- The best overall agreement with experimental data has been achieved with the LATCT combustion model in combination with the extended Zeldovich *NO*

model, Nagle Strickland-Constable soot model and the modified wall function approach.

- Based on the findings of an order of magnitude analysis and an assessment of the validity of the assumptions leading to the standard wall functions, it was concluded that the assumption of constant thermophysical properties in the boundary layer is unacceptable. A modified near-wall treatment which incorporates variable density and viscosity effects substantially increased heat transfer compared to the standard approach, particularly during fired operation, such that improved predictions could be obtained.

- The heat transfer predictions are regarded as encouraging, particularly when considering the numerous complex factors that influence the heat transfer and the level of uncertainty in the measurements. Wall heat transfer was found to strongly depend on flame propagation, which in turn was substantially influenced by swirl, liquid penetration length and vapour penetration speed. The underprediction of flame propagation speed and radial spread of the flame plume have been identified as the main causes for discrepancies between calculations and measurements in the fired cases. For the motored cases differences in flow structures and turbulence levels were regarded as major sources for the discrepancies.

- It was observed that particularly under fired operation substantial temporal and spatial variations of heat transfer exist. Thus to estimate critical thermal loads from HTCs, as predicted by empirical heat transfer correlations, the near-wall local temperature gradients are required, which are only accessible via a full CFD combustion simulation. Thus the correlations are of limited utility for this purpose.

- The predictions of HTCs using empirical heat transfer correlations varied substantially and considerably underestimated heat losses.

- The point heat transfer comparisons have revealed that surface heat flux data

provide a much more stringent testing ground for combustion simulation than in-cylinder pressure measurements due to their high sensitivity to flame propagation as opposed to global heat release.

- The combustion predictions of the LATCT model agreed fairly well with the experiments. Differences were found between experimental and calculated ignition delay, possibly due to errors from spray and turbulence modelling. The overestimation of early heat release and peak pressure for the HPP engine test case was attributed to discrepancies in air/fuel mixing rates, perhaps due to too rapid evaporation or due to the overpredicted burning rate, caused by assuming complete combustion or when switching globally from ignition to combustion. Moreover as a consequence of too rapid initial burning and complete combustion, the measured late burning characteristics could not be captured.

- Two phenomenological soot models have been successfully implemented in the framework of the LATCT combustion model. Qualitative good agreement using both models has been observed for the spatial distribution of soot concentration under Diesel-like conditions. The soot oxidation rate was underpredicted.

- The Nagle Strickland-Constable soot oxidation model achieved best overall agreement with engine exhaust gas concentrations. It was demonstrated that the correct measured trends of $NO_x$ and soot emissions are predicted with changes to injection timing and boost pressure, once the model coefficients were adjusted only for one operating condition.

- A laminar flamelet-type combustion model, RIF, has been successfully interfaced with the CFD code. The chamber pressure for the HPP prototype engine was predicted moderately well compared to the measurements in respect of magnitude of the peak cylinder pressure. Differences between measured and calculated ignition delay were attributed to underestimation of early air/fuel

mixing and turbulent scalar dissipation rate via turbulence modelling errors. The overprediction of initial heat release and peak pressures was found to be due to the fact that the combustible mixture ignites simultaneously when using only one flamelet, thus promoting turbulence and burning rates. The late burning characteristics of the measurements could not be reproduced. The soot formation rates were significantly underpredicted partly due to the underlying $n$-heptane chemistry as opposed to Diesel fuel chemistry in the experiments and partly due to an erroneous assumption made in the soot particle coagulation model. The $NO_x$ levels were considerably overpredicted, possibly as a consequence of poor late burning predictions. In addition, the heat transfer levels were substantially underestimated as a consequence of less radial spreading of the flame plume.

- The study of equations of state has revealed that the ideal gas law works reasonably well for the temperatures and pressures of interest in the HPP engine.

- The effect of pressure on gas thermophysical properties has been found to be small ($< 6.5\%$) for the range of pressures studied. However, the temperature dependences of the molecular viscosity, thermal conductivity and specific heat at constant pressure must be taken into account which was done in the present work.

- The liquid phase thermophysical properties exhibit a strong dependence on pressure and temperature towards the critical point. In addition, real gas effects substantially influence the vapour-liquid equilibrium and latent heat of vapourisation. The net effect is that the evaporation rate increases, yielding significantly smaller droplet lifetimes. It was argued that the majority of the droplets do not approach the mixture critical conditions and that droplet lifetimes are very short. Hence, in the present study the low pressure correlations were used. This entailed *ad hoc* adjustments to the spray model parameters to improve agreement with the measurements.

- In the present test cases significant experimental uncertainties and cycle-to-cycle variations have been revealed which greatly influence the comparison between measurements and the CFD methodology. In particular the accuracy of initial conditions for the simulations such as inflow conditions at the valve curtain, obtained from experiments, or uncertainties of swirl levels at SOI have a substantial impact on the accuracy of the predictions, as seen especially from the local heat flux comparisons.

## 7.2 Recommendations and Suggestions for Future Work

The present study has shown that there is obviously still a need for further improvement of the CFD methodology. However, the quality of the results obtained should nonetheless encourage further use in its present form.

One of the important impediments to progress in CFD modelling is the limited amount of detailed, accurate and sufficiently complete in-cylinder experimental data available to guide model development. In this respect the local heat transfer measurements obtained for the HPP prototype engine are a valuable addition, because – as demonstrated – they provide a useful testing ground not only for heat transfer models, but also for flow and combustion simulation.

The following tasks are considered as the most important ones for the further development of the methodology:

- Improved modelling of turbulence is needed and its influence on spray, air/fuel mixing, combustion and flame propagation.
- A better and stable numerical approach to resolve the spray processes in the near-nozzle region is required, to account for high injection velocities and to allow for low gas volume fractions.

- Implementation of computationally efficient correlations for the liquid thermophysical properties and appropriate spray submodels which account for high pressure and real gas effects. The new correlations and submodels will require comprehensive validation using experimental data for single droplets as well as sprays at sufficiently high temperatures and pressures.

- More accurate models are necessary that capture the fuel flow in the injector nozzle, including cavitation effects.

- Further extensive studies are needed to assess and improve the modified wall function approach using comprehensive local heat transfer and local shear force measurement data. The necessity to implement wall functions that incorporate the influence of heat release in the near-wall region and pressure gradient effects under Diesel engine conditions should be assessed based on sensitivity studies.

- The spatial variation of surface temperature should be incorporated in future simulations, possibly by solving the 1D heat conduction equation in the wall, when assuming a constant wall temperature at a specified depth below the surface.

- For the LATCT combustion model, an ignition model is needed that accounts for turbulence effects on the ignition process. The development of this should be guided by validation studies using experimental data and/or DNS simulations.

- Source terms for the mixture fraction variance transport equation due to spray evaporation should be considered in the RIF concept to improve ignition predictions. In addition, an improved soot coagulation model is needed to give better agreement with measured soot concentrations. The results of RIF must be further validated against comprehensive experimental data sets including the distribution of species concentrations in the chamber.

- The development and validation is needed of more comprehensive soot formation and oxidation models that include soot chemistry and particle dynamics,

similar to the models proposed by Balthasar *et al.* [27]. They should eliminate the necessity to extensively tune the model coefficients for each application.

- Soot models are required that are capable of predicting the distribution of particle sizes and number densities due to more stringent future particulate emissions policies.

## 7.3 Closure

The present work was aimed at the assessment, improvement and validation of the CFD Diesel engine methodology for engines operating under elevated pressure conditions. In this light the results showed that the proposed methodology can yield meaningful predictions and capture experimental trends even at the high pressures and temperatures of the HPP prototype engine. Although the methodology is not yet fully predictive, it can, when guided by well defined measurement data, give comprehensive insight into the complex and interactive nature of Diesel engine processes. The author hopes that the present contribution will encourage future researchers to further improve the state-of-the-art CFD Diesel engine methodology.

# Appendix A

# Overview of Heat Transfer Correlations

An overview of the different engine heat transfer correlations used in this study has been compiled in the following table. They are all specific forms of the general convective heat transfer formula quoted and arrived at by dimensional analysis:

$$\mathrm{Nu} = a\,\mathrm{Re}^{m}\,\sigma_e{}^{n}$$

The Nusselt and Reynolds numbers are defined as:

$$\mathrm{Nu} = \frac{h\,L}{k}$$

$$\mathrm{Re} = \frac{\rho\,v_{eff}\,L}{\mu}$$

where $v_{eff}$ is the effective velocity and $L$ is the characteristic length. The table also gives the temperature level $T_{eff}$ at which the thermophysical properties are calculated.

| Author | $a$ | $m$ | $n$ | Engine type | $T_{eff}$ | $v_{eff}$ | $L$ |
|---|---|---|---|---|---|---|---|
| Annand [14] | 0.35 – 0.8 | 0.7 | - | CI | $T_{\mathrm{bulk}}$ | $\overline{v}_p$ | Bore |
| Hohenberg [182] | 1.132 | 0.8 | - | DI Diesel | $T_{\mathrm{bulk}}$ | $\overline{v}_p$ | $V_{\mathrm{cyl}}$ |
| Woschni [467] | 0.035 | 0.8 | - | DI Diesel | $T_{\mathrm{bulk}}$ | $\overline{v}_p$ | Bore |

**Table A.1:** Authors and model parameters for convective heat transfer correlations according to Eq. (2.8). $T_{\mathrm{bulk}}$ is the bulk temperature, given by Eq. (2.11), $\overline{v}_p$ is the mean piston speed and $V_{\mathrm{cyl}}$ is the cylinder volume.

# Appendix B

# Soot Modelling

## B.1 Overview of Soot Modelling Approaches

In Section 2.3.4.2 various soot models found in the literature are briefly presented. They can be categorised into two approaches: semi-global and detailed-chemistry soot models. Table B.1 summarises those approaches by providing information on specific characteristic features and on their field of application.

| Author | Variables solved | Chemistry description | Fuel | Application |
|---|---|---|---|---|
| **Semi-global soot models** | | | | |
| Hiroyasu [178] | exhaust soot mass fraction | empirical Arrhenius rate expression | Diesel | Diesel combustion |
| Lindstedt [270, 272, 273] | soot volume fraction, particle number density | simple chemistry for gas-phase, nucleation and surface growth depend on acetylene (and benzene) | methane | laminar counterflow flame |
| Moss *et al.* [303, 304] | soot volume fraction, particle number density | flamelet approach | methane | laminar diffusion flame |
| Said *et al.* [384] | soot volume fraction, average particle number density | constrained equilibrium | ethylene | laminar and turbulent diffusion flame |
| Young and Moss [478] | soot volume fraction, particle number density | flamelet approach | ethylene | turbulent diffusion flame |
| **Detailed chemistry soot models** | | | | |
| Balthasar *et al.* [27] | soot volume fraction | flamelet model with flamelet library for source terms | acetylene | laminar diffusion flame |
| Frenklach [123, 126] | species mass fraction, soot number, size and volume fraction | detailed chemical kinetics and particle dynamics | ethylene | laminar premixed flame |
| Mauss *et al.* [288] | species mass fractions, moments of soot distribution, soot volume fraction | detailed chemical kinetics and particle dynamics | ethylene | laminar premixed flame |
| Yoshihara *et al.* [476] | exhaust soot mass fraction | reduced chemical kinetics, particle dynamics | methane | Diesel combustion |

**Table B.1:** Selected soot models for hydrocarbon diffusion flames.

## B.2 Soot Model Parameters

In Section 3.6.2 the soot models used in the present study are outlined. In these the soot properties have to be specified, along with the coefficients of the Arrhenius rate expression in Eq. (2.3):

$$\dot{\omega} = A \exp\left(-\frac{E_a}{\mathcal{R}T}\right) \tag{B.1}$$

The relevant parameters found in the literature are summarised in the following tables for soot density and diameter, Table B.3, and for the rate coefficients in the semi-global soot models, Tables B.2 and B.4.

| **Nagle Strickland-Constable [311]** | | | | | |
|---|---|---|---|---|---|
| Rate constant | $k_A$ | $k_B$ | $k_T$ | $k_Z$ | Application |
| $A$ [1/s] | 20 | $4.46 \times 10^{-3}$ | 151000 | 21.3 | Pyrographite |
| $E$ [J/mol] | 125520 | 63596.8 | 405848 | 17154.4 | rod |
| **Najjar *et al.* [313]** | | | | | |
| Rate constant | $k_A$ | $k_B$ | $k_T$ | $k_Z$ | Application |
| $A$ [1/s] | 2300 | – | – | 2.13 | Gas turbine, |
| $E$ [J/mol] | 125520 | – | – | 17154.4 | $T < 1800$K |
| **Najjar *et al.* [313]** | | | | | |
| Rate constant | $k_A$ | $k_B$ | $k_T$ | $k_Z$ | Application |
| $A$ [1/s] | 380 | $4.46 \times 10^{-2}$ | 151000 | 5000 | Gas turbine, |
| $E$ [J/mol] | 12552 | 63596.8 | 251040 | 20920 | $T > 1800$K |

**Table B.2:** Summary of parameters for Nagle Strickland-Constable soot oxidation model.

| Author | Soot density [kg/m$^3$] | Soot diameter [m] |
|---|---|---|
| Han *et al.*[156] | 2500 | $2.5 \times 10^{-8}$ |
| Moss *et al.*[304] | 1800 | $3.5 \times 10^{-8}$ |
| Patterson *et al.*[328] | 2000 | $3 \times 10^{-8}$ |
| Reitz [362] | 2000 | $3 \times 10^{-8}$ |
| Said *et al.*[384] | – | $1 \times 10^{-9}$ |
| Theodossopoulos [427] | 1800 | $8 \times 10^{-9}$ |
| Yi *et al.*[475] | 2000 | $2.5 \times 10^{-8}$ |

**Table B.3:** Soot density and diameter provided in literature.

| Author | Pre-exponential Factor $A_{s,f}$ [1/s] | $A_{s,o}$ [1/s] | Activation Energy $E_{s,f}$ [J/mol] | $E_{s,o}$ [J/mol] | Application |
|---|---|---|---|---|---|
| **(1) Approaches based on Hiroyasu soot model** | | | | | |
| Abraham *et al.*[3] | 300 | NSC model | 52300 | NSC model | Diesel engine |
| Aneja *et al.* [12] | 300 | – | 52300 | – | Diesel engine |
| Barths *et al.* [35] | 100 | 30 | 52300 | 58576 | Diesel engine |
| Belardini *et al.* [39] | 100 | 30 | 52300 | 58576 | Diesel engine |
| Patterson *et al.* [328] | 150 | 3500 | 52300 | 58576 | Diesel engine |
| Reitz [362] | 100 | NSC model | 52300 | NSC model | Diesel engine |
| Yi *et al.* [475] | 450 | NSC model | 52300 | NSC model | Diesel engine |
| **(2) Approaches based on other soot model** | | | | | |
| Fenimore *et al.*[115] | – | – | – | 158155 | laminar flame |
| Feugier [119] | | | | 138072 | laminar hydrocarbon flame |
| Kellerer *et al.* [225] | – | | – | 170000 | hydrocarbons in shock tube experiment |
| Khan *et al.* [232] | – | – | – | 164431 | Diesel engine |
| Khan *et al.* [230] | – | – | – | 170000 | Diesel engine |
| Khan *et al.* [231] | – | – | 167360 | 164431 | Diesel engine |
| Kouremenos *et al.* [244] | – | – | 80000 | 120000 | Diesel engine |
| Lee *et al.*[266] | – | – | – | 164431 | laminar flame |
| Linstedt [272] | – | – | – | 163619 | methane air flame |
| Said *et al.* [384] | – | – | 166280 | 220321 | laminar hydrocarbon diffusion flame |
| Tesner *et al.*[423] | – | – | – | 167360 | hydrocarbon diffusion flame |

**Table B.4:** Summary of parameters for semi-empirical soot oxidation model.

# Appendix C

# Correlations for Thermodynamic Properties

## C.1 Gas-Phase Thermophysical Correlations

### C.1.1 Molecular viscosity

#### C.1.1.1 Sutherland correlation [392]

$$\frac{\mu}{\mu_0} = \left(\frac{T}{T_0}\right)^{\frac{3}{2}} \frac{T_0 + C_s}{T + C_s} \tag{C.1}$$

where $\mu_0$ = molecular viscosity at the reference temperature [N s/m$^2$]
$T_0$ = reference temperature [K]
$C_s$ = Sutherland constant

For air, at $T_0 = 273.15$ K, $\mu_0 = 1.716\times10^{-5}$ Ns/(m$^2$). $C_s$ is then taken as 116 [314].

#### C.1.1.2 Chung *et al.* correlation [74]

**Low-pressure correlation**

$$\mu = 40.785 \frac{F_c\sqrt{MT}}{V_c^{\frac{2}{3}}\Omega_v} \tag{C.2}$$

where $\mu$ = viscosity [$\mu$P]
$M$ = molecular weight [g/mol]
$T$ = temperature [K]
$V_c$ = critical molar volume [cm$^3$/mole]
$\Omega_v$ = viscosity collision integral
$F_c$ = $1 - 0.2756\omega + 0.059035\mu_r^4$. Here, $\omega$ is the acentric factor and $\mu_r$ is a dimensionless dipole moment, set to zero.

The collision integral is determined by:

$$\Omega_v = A(T^*)^{-B} + C(\exp(-DT^*) + E\exp(-FT^*) \tag{C.3}$$

where $A = 1.16145$, $B = 0.14874$, $C = 0.52487$, $D = 0.7732$, $E = 2.16178$ and $F = 2.43787$. The dimensionless temperature $T^*$ is defined as:

$$T^* = 1.2593T_r \tag{C.4}$$

### High-pressure correlation

$$\mu = \mu^* \frac{36.344\sqrt{MT_c}}{V_c^{\frac{2}{3}}} \tag{C.5}$$

where $\mu$ = viscosity [$\mu$P]
$M$ = molecular weight [g/mol]
$T_c$ = critical temperature [K]
$V_c$ = critical molar volume [cm$^3$/mole]

The non-dimensional viscosity $\mu^*$ is given as:

$$\mu^* = \frac{\sqrt{T^*}}{\Omega_v}\left[F_c\left(\frac{1}{G_2} + E_6 y\right)\right] + \mu^{**} \tag{C.6}$$

$T^*$ and $F_c$ are already defined in the low-pressure correlation. Additionally the following relations are defined as:

$$y = \frac{\rho V_c}{6} \tag{C.7}$$

$$G_1 = \frac{1 - 0.5y}{(1-y)^3} \tag{C.8}$$

$$G_2 = \frac{E_1\frac{1-\exp(-E_4 y)}{y} + E_2 G_1 \exp(E_5 y) + E_3 G_1}{E_1 E_4 + E_2 + E_3} \tag{C.9}$$

$$\mu^{**} = E_7 y^2 G_2 \exp\left(E_8 + E_9\frac{1}{T^*} + E_{10}\frac{1}{(T^*)^2}\right) \tag{C.10}$$

Here $E_i = a_i + b_i\omega + c_i\mu_r^4$ with its coefficients provided in Table C.1.

| $i$ | $a_i$ | $b_i$ | $c_i$ | $d_i$ |
|---|---|---|---|---|
| 1 | 6.324 | 50.412 | -51.68 | 1189.0 |
| 2 | $1.211\times10^{-3}$ | $-1.154 \times 10^{-3}$ | $-6.257 \times 10^{-3}$ | 0.03728 |
| 3 | 5.283 | 254.209 | -168.48 | 3898.0 |
| 4 | 6.623 | 38.096 | -8.646 | 31.42 |
| 5 | 19.745 | 7.63 | -14.354 | 31.53 |
| 6 | -1.9 | -12.537 | 4.985 | -18.15 |
| 7 | 24.275 | 3.45 | -11.291 | 69.35 |
| 8 | 0.7972 | 1.117 | 0.01235 | -4.117 |
| 9 | -0.2382 | 0.0677 | -0.8163 | 4.025 |
| 10 | 0.06863 | 0.3479 | 0.5926 | -0.727 |

**Table C.1:** Chung *et al.* correlation: Coefficients for $E_i$.

### C.1.1.3 Lucas correlation [275]

$$\mu\xi = [0.807\,T_r^{0.618} - 0.357\exp(-0.449T_r) + 0.340\exp(-4.058T_r) + 0.018]F_P^\circ\,F_Q^\circ \tag{C.11}$$

where $\mu$ = molecular viscosity [$\mu$P]
$\xi$ = inverse viscosity [m$^2$/(N s)]
$F_P^\circ$ = correction factor for polarity effects
$F_Q^\circ$ = correction factor for quantum effects

For hydrocarbons, $F_P^\circ$ and $F_Q^\circ$ are negligible. The inverse viscosity is given by:

$$\xi = 0.176\left(\frac{T_c}{M^3\,p_c^4}\right)^{\frac{1}{6}} \tag{C.12}$$

with $T_c$ in [K], $M$ in [g/mol] and $p_c$ in [bar].

## C.1.2 Thermal conductivity

### C.1.2.1 Modified Eucken correlation [417]

$$\frac{k\,M'}{\mu\,c_v} = 1.32 + \frac{1.77}{c_v/\,\mathcal{R}} \tag{C.13}$$

where $k$ = thermal conductivity [W/(m K)]
$M'$ = molecular weight [kg/mol]
$\mu$ = viscosity [N s/m$^2$]
$c_v$ = heat capacity at constant volume [J/(mol K)]

### C.1.2.2 Chung *et al.* correlation [75]

#### Low-pressure correlation

$$\frac{k\,M'}{\mu\,c_v} = \frac{3.75\,\Psi}{c_v/\mathcal{R}} \tag{C.14}$$

where $k$ = thermal conductivity [W/(m K)]
$\mu$ = low-pressure gas viscosity [N s/m$^2$]
$\Psi$ = factor

Here $\Psi$ is given as:

$$\Psi = 1 + \alpha\frac{0.215 + 0.28288\alpha - 1.061\beta + 0.26665Z}{0.6366 + \beta Z + 1.061\alpha\beta} \tag{C.15}$$

with additional parameters:

$$\alpha = (c_v/\mathcal{R}) - \frac{3}{2} \tag{C.16}$$

$$\beta = 0.7862 - 0.7109\omega + 1.3168\omega^2 \tag{C.17}$$

$$Z = 2.0 + 10.5T_r^2 \tag{C.18}$$

#### High-pressure correlation

$$k = \frac{31.20\,\mu^\circ\Psi}{M'}\left(\frac{1}{G_2} + B_6 y\right) + q\,B_7\,y^2\sqrt{T_r}\,G_2 \tag{C.19}$$

where $k$ = thermal conductivity [W/(m K)]
$\mu^\circ$ = low-pressure gas viscosity [N s/m$^2$]

Besides the parameters already defined in the low-pressure thermal conductivity of Chung *et al.* the following functions are specified:

$$q = 3.586 \times 10^{-3}\sqrt{\frac{T_c}{M'}}/V_c^{\frac{2}{3}} \tag{C.20}$$

$$y = \frac{V_c}{6\,V} \tag{C.21}$$

$$G_1 = \frac{1 - 0.5y}{(1-y)^3} \tag{C.22}$$

$$G_2 = \frac{(B_1/y)[1 - \exp(-B_4 y)] + B_2 G_1 \exp(B_5 y) + B_3 G_1}{B_1 B_4 + B_2 + B_3} \tag{C.23}$$

The coefficients for $B_i = a_i + b_i\omega$ are listed in Table C.2.

| $i$ | $a_i$ | $b_i$ |
|---|---|---|
| 1 | 2.4166 | 0.74824 |
| 2 | -0.50924 | -1.5094 |
| 3 | 6.6107 | 5.6207 |
| 4 | 14.543 | -89.139 |
| 5 | 0.79274 | 0.82019 |
| 6 | -5.8634 | 12.801 |
| 7 | 91.089 | 128.11 |

**Table C.2:** Chung *et al.* correlation: Coefficients for $B_i$.

### C.1.2.3 Ely and Hanley correlation [104]

$$k = k^* + 1.32\frac{\mu^*}{M'}\left(c_v - \frac{3\mathcal{R}}{2}\right) \tag{C.24}$$

where $k$ = thermal conductivity [W/(m K)]

The parameters in this correlation which are being related to methane gas are obtained by following the procedure as outlined below:

**Step 1:** Determine the parameter $T^+$ such that

$$T^+ = T_r \quad T_r \leq 2 \qquad \text{or} \qquad T^+ = 2 \quad T_r > 2 \tag{C.25}$$

**Step 2:** Calculate compound shape factors as:

$$\Theta = 1 + (\omega - 0.011)\left(0.56553 - 0.86276\ln T^+ - \frac{0.69852}{T^+}\right) \tag{C.26}$$

$$\Phi = \left[1 + (\omega - 0.011)(0.3856 - 1.1617\ln T^+)\right]\frac{0.288}{Z_c} \tag{C.27}$$

**Step 3:** Temperature scaling parameters are then defined as:

$$f = \frac{T_c}{190.4}\Theta \tag{C.28}$$

$$h = \frac{V_c}{99.2}\Phi \tag{C.29}$$

**Step 4:** Calculate the equivalent reference temperature $T_0$ to estimated the thermal conductivity and viscosity of the methane reference fluid as follows:

$$T_0 = \frac{T}{f} \tag{C.30}$$

$$\mu_0 = 10^{-7}\sum_{n=1}^{9} C_n T_0^{(n-4)/3} \tag{C.31}$$

$$k_0 = 1944\,\mu_0 \tag{C.32}$$

using the coefficients $C_n$ given as:

$$C_1 = 2.90774 \times 10^6 \quad C_4 = -4.3319 \times 10^5 \quad C_7 = 4.32517 \times 10^2$$
$$C_2 = -3.31287 \times 10^6 \quad C_5 = 7.06248 \times 10^4 \quad C_8 = -1.44591 \times 10^1$$
$$C_3 = 1.6081 \times 10^6 \quad C_6 = -7.11662 \times 10^3 \quad C_9 = 2.03712 \times 10^{-1}$$

**Step 5:** To finally evaluate $k^*$ and $\mu^*$, calculate:

$$k^* = k_0 \, H \tag{C.33}$$

$$\mu^* = \mu_0 \, H \, \frac{M'}{16.04 \times 10^{-3}} \tag{C.34}$$

$$H = \sqrt{\frac{16.04 \times 10^{-3}}{M'}} \, \frac{\sqrt{f}}{h^{\frac{2}{3}}} \tag{C.35}$$

## C.1.3 Heat capacity

According to the JANAF database [147], the heat capacity at constant pressure is expressed as:

$$\frac{c_p}{\mathcal{R}} = \sum_{i=1}^{7} a_i \, T^{i-3} \tag{C.36}$$

where $c_p$ = heat capacity at constant pressure [J/(mol K)]

with the coefficients for different species given in Table C.3.

| Temperature range | Coefficient | $O_2$ | $N_2$ | $n$-$C_7H_{16}$ |
|---|---|---|---|---|
| 200 K – 1000 K | $a_1$ | -3.42556342e+4 | 2.210371497e+4 | -6.12743275e+5 |
| | $a_2$ | 4.84700097e+2 | -3.81846182e+2 | 1.1840854e+4 |
| | $a_3$ | 1.119010961 | 6.08273836 | -7.48718841e+1 |
| | $a_4$ | 4.29388924e-3 | -8.53091441e-3 | 2.918466e-1 |
| | $a_5$ | -6.83630052e-7 | 1.384646189e-5 | -3.41679541e-4 |
| | $a_6$ | -2.0233727e-9 | -9.62579362e-9 | 2.15928521e-7 |
| | $a_7$ | 1.039040018e-12 | 2.519705809e-12 | -5.65585255e-11 |
| 1000 K – 6000 K | $a_1$ | -1.037939022e+6 | 5.87712406e+5 | 1.28153359e+7 |
| | $a_2$ | 2.344830282e+3 | -2.239249073e+3 | -5.41256205e+4 |
| | $a_3$ | 1.819732036 | 6.06694922 | 9.80119459e+1 |
| | $a_4$ | 1.267847582e-3 | -6.1396855e-4 | -1.38270652e-2 |
| | $a_5$ | -2.188067988e-7 | 1.491806679e-7 | 3.43267831e-6 |
| | $a_6$ | 2.053719572e-11 | -1.923105485e-11 | -4.35995372e-10 |
| | $a_7$ | -8.19346705e-16 | 1.061954386e-15 | 2.20016728e-14 |

**Table C.3:** Coefficients for polynomials from Chemkin and JANAF database.

## C.1.4 Diffusion coefficient

### C.1.4.1 Chapman and Enskog correlation [63]

**Low-pressure correlation**

$$\mathcal{D}_{AB} = \frac{0.00266\, T^{\frac{3}{2}}}{p\sqrt{M_{AB}}\,\sigma_{AB}^2\,\Omega_{\mathcal{D}}} \tag{C.37}$$

where $\mathcal{D}_{AB}$ = diffusion coefficient [cm$^2$/s]
$T$ = temperature [K]
$p$ = pressure [bar]
$M_{AB}$ = $2[(1/M_A) + (1/M_B)]^{-1}$
$M_A$ and $M_B$ = molecular weights of species $A$ and $B$
$\sigma_{AB}$ = characteristic length [Å]
$\Omega_{\mathcal{D}}$ = diffusion collision integral

Additionally the following relations are defined:

$$\sigma_{AB} = \frac{\sigma_A + \sigma_B}{2} \tag{C.38}$$

$$\Omega_{\mathcal{D}} = \frac{A}{(T^*)^B} + \frac{C}{\exp(DT^*)} + \frac{E}{\exp(FT^*)} + \frac{G}{\exp(HT^*)} \tag{C.39}$$

$$T^* = \frac{\mathcal{K}T}{\epsilon_{AB}} \tag{C.40}$$

$$\epsilon_{AB} = \sqrt{\epsilon_A\,\epsilon_B} \tag{C.41}$$

where $\mathcal{K}$ is the Boltzmann constant and the coefficients for the collision integral, related to the 12-6 Lennard-Jones potential, are defined according to Neufield *et al.* [315] as:

| | | |
|---|---|---|
| A = 1.06036 | B = 0.1561 | C = 0.193 |
| D = 0.47635 | E = 1.03587 | F = 1.52996 |
| G = 1.76474 | H = 3.89411 | |

The characteristic Lennard-Jones energy $\epsilon$ and length $\sigma$ for each component are given as:

$$\frac{\epsilon}{\mathcal{K}} = 1.15\, T_b \tag{C.42}$$

$$\sigma = 1.18\, V_b^{\frac{1}{3}} \tag{C.43}$$

where $T_b$ is the boiling point temperature at 1 atm and $V_b$ refers to the liquid molar volume evaluated according to the method of Le Bas [262].

### High-pressure correlation

Takahashi [421] has proposed a simple corresponding states method to obtain high-pressure diffusivities from their low-pressure counterparts. A correlation of the following format is provided:

$$\frac{\mathcal{D}_{AB}\, p}{(\mathcal{D}_{AB}\, p)^{+}} = f(T_r, p_r) \tag{C.44}$$

where the superscript + denotes low-pressure values. Figure C.1 displays the correlation in graphical format.

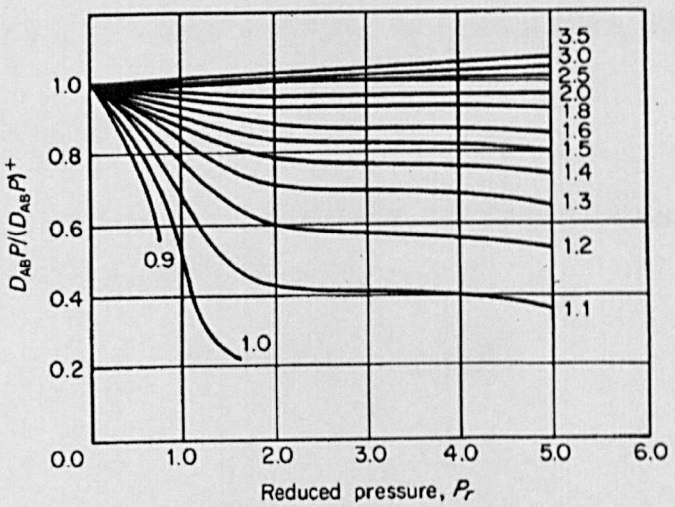



**Figure C.1:** Takahashi high-pressure correction for low-pressure diffusivities (from [421]).

### C.1.4.2 Fuller *et al.* correlation [129]

$$\mathcal{D}_{AB} = \frac{0.00143\, T^{1.75}}{p\sqrt{M_{AB}}\left[(\Sigma_v)_A^{\frac{1}{3}} + (\Sigma_v)_B^{\frac{1}{3}}\right]^2} \tag{C.45}$$

where $\mathcal{D}_{AB}$ = diffusion coefficient [cm$^2$/s]
$\Sigma_v$ = summation over atomic diffusion volumes

### C.1.4.3 Wilke and Lee correlation [463]

$$\mathcal{D}_{AB} = \frac{\left[3.03 - \frac{0.98}{\sqrt{M_{AB}}}\right] 10^{-3} T^{\frac{3}{2}}}{p\sqrt{M_{AB}}\,\sigma_{AB}^2\,\Omega_{\mathcal{D}}} \tag{C.46}$$

where $\mathcal{D}_{AB}$ = diffusion coefficient [cm$^2$/s]

Other parameters in this correlation are evaluated as provided in the Chapman-Enskog correlation.

# C.2 Liquid-Phase Thermophysical Correlations

## C.2.1 Density

### C.2.1.1 Hankinson-Brobst-Thomson correlation [153, 428]

#### Low-pressure correlation

For saturated liquid volumes $V_s$, which are the inverse of the saturated liquid densities, the following expression is given:

$$\frac{V_s}{V^*} = V_R^{(0)}[1 - \omega_{SRK} V_R^{(\delta)}] \tag{C.47}$$

with

$$V_R^{(0)} = 1 - 1.52816(1 - T_r)^{\frac{1}{3}} + 1.43907(1 - T_r)^{\frac{2}{3}} - 0.81446(1 - T_r) + 0.190454(1 - T_r)^{\frac{4}{3}} \tag{C.48}$$

for $0.25 < T_r < 0.95$ and

$$V_R^{(\delta)} = \frac{-0.296123 + 0.386914T_r - 0.0427258T_r^2 - 0.0480645T_r^3}{T_r - 1.00001} \tag{C.49}$$

for $0.25 < T_r < 1.0$. $V^*$ is a pure component characteristic volume listed in Table C.4. The parameter $\omega_{SRK}$ is the acentric factor related to the Soave-Redlich-Kwong equation of state and is also available from Table C.4.

#### High-pressure correlation

The high-pressure modification of the HBT method estimates the liquid volume

| Parameter | $n$-heptane | $n$-dodecane |
|---|---|---|
| $\omega_{SRK}$ [–] | 0.3507 | 0.5807 |
| $V^*$ [L/mol] | 0.4304 | 0.7558 |

**Table C.4:** Pure component parameters for Hankinson-Brobst-Thomson correlation.

according to:

$$V = V_s \left(1 - c \ln \frac{\beta + p}{\beta - p_{vp}}\right) \tag{C.50}$$

where $V_s$ = saturated liquid volume at the vapour pressure $p_{vp}$

The parameters $\beta$ and $c$ are obtained from:

$$\frac{\beta}{p_c} = -1 - 0.9070217(1 - T_r)^{\frac{1}{3}} + 62.45326(1 - T_r)^{\frac{2}{3}} - 135.1102(1 - T_r) + \exp(4.79594 + 0.250047\,\omega_{SRK} + 1.14188\,\omega_{SRK}^2)(1 - T_r)^{\frac{4}{3}} \tag{C.51}$$

and

$$c = 0.0861488 + 0.0344483\,\omega_{SRK} \tag{C.52}$$

### C.2.1.2 Simple thermodynamic correlation [410]

$$\rho = M \frac{0.3333}{(0.24703)^{[1+(1-(\frac{T}{658.2})^{0.286})]}} \tag{C.53}$$

where $M$ = molecular weight [kg/m$^3$]

## C.2.2 Viscosity

### C.2.2.1 Andrade and Letsou-Stiel correlation [10, 11, 269]

#### Low-pressure correlation

The Andrade equation is defined as:

$$\ln \mu_L = A + \frac{B}{T} \tag{C.54}$$

where $\mu_L$ = liquid viscosity [cP]
$T$ = temperature [K]

The parameters $A$ and $B$ are listed in Table C.5, including the temperature range in which the correlation is valid.

| Component | $A$ | $B$ | $\Delta T$ application range [K] |
|---|---|---|---|
| $n$-heptane | -4.325 | 1006 | 183 - 373 |
| $n$-dodecane | -4.562 | 1454 | 268 - 593 |

**Table C.5:** Parameters for Andrade equation.

For higher temperature between $0.76 < T_r < 0.98$, Letsou and Stiel have proposed the following correlation for saturated liquids:

$$\mu_{SL}\,\xi = (\mu_L\,\xi)^{(0)} + \omega\,(\mu_L\,\xi)^{(1)} \tag{C.55}$$

where the additional relations apply:

$$(\mu_L\,\xi)^{(0)} = (2.648 - 3.725T_r + 1.309T_r^2) \times 10^{-3} \tag{C.56}$$

$$(\mu_L\,\xi)^{(1)} = (7.425 - 13.39T_r + 5.933T_r^2) \times 10^{-3} \tag{C.57}$$

The inverse viscosity $\xi$ has already been defined in Eq. (C.12).

### High-pressure correlation

To account for the increase in viscosity with an increase in pressure, Lucas [275] has assembled the following correction to the low-pressure liquid viscosity:

$$\frac{\mu}{\mu_{SL}} = \frac{1 + D\left(\frac{\Delta p_r}{2.118}\right)^A}{1 + C\,\omega\,\Delta p_r} \tag{C.58}$$

where $\mu$ = liquid viscosity at high pressure [cP]
$\mu_{SL}$ = viscosity of saturated liquid at the vapour pressure [cP]
$\Delta p_{vp} = \frac{p - p_{vp}}{p_c}$

The parameters in the correlation are related to the reduced temperature and are expressed as:

$$A = 0.9991 - \frac{4.674 \times 10^{-4}}{1.0523\,T_r^{-0.03877} - 1.0513} \tag{C.59}$$

$$C = -0.07921 + 2.1616\,T_r - 13.404\,T_r^2 + 44.1706\,T_r^3 - 84.8291\,T_r^4$$
$$96.1209\,T_r^5 - 59.8127\,T_r^6 + 15.6719\,T_r^7 \tag{C.60}$$

$$D = \frac{0.3257}{(1.0039 - T_r^{2.573})^{0.2906}} - 0.2086 \tag{C.61}$$

### C.2.2.2 Chung *et al.* correlation [74]

To estimate the liquid viscosity according to Chung *et al.*, the same methodology as outlined in Section C.1.1.2 for high-pressure gas viscosities applies.

### C.2.2.3 Brulé and Starling correlation [59]

Brulé and Starling adopt essentially the same approach as Chung *et al.* for high pressure viscosities. Yet, the coefficients for $E_i$ are modified. They are presented in Table C.6.

| $i$ | $a_i$ | $b_i$ |
|---|---|---|
| 1 | 17.45 | 34.063 |
| 2 | $-9.611 \times 10^{-4}$ | $7.235 \times 10^{-3}$ |
| 3 | 51.043 | 169.46 |
| 4 | -0.6059 | 71.174 |
| 5 | 21.382 | -2.11 |
| 6 | 4.668 | -39.941 |
| 7 | 3.762 | 56.623 |
| 8 | 1.004 | 3.14 |
| 9 | $-7.774 \times 10^{-2}$ | -3.584 |
| 10 | 0.3175 | 1.16 |

**Table C.6:** Brulé and Starling correlation for liquid viscosity: coefficients for $E_i$.

### C.2.2.4 Simple thermodynamic correlation [410]

$$\mu = \exp\left(-20.607 + \frac{1943}{T} + 1.3205 \ln T\right) \tag{C.62}$$

where $\mu$ = liquid viscosity [Pa s]
$T$ = absolute temperature [K]

## C.2.3 Thermal conductivity

### C.2.3.1 Latini correlation [29, 30]

$$k_L = \frac{A(1 - T_r)^{0.38}}{T_r^{\frac{1}{6}}} \tag{C.63}$$

where $k_L$ = thermal liquid conductivity [W/(m K)]
$A = \frac{A^* T_b^\alpha}{M^\beta T_c^\gamma}$
$T_b$ = normal boiling temperature at 1 atm [K]
$M$ = molecular weight [g/mol]

For saturated hydrocarbons the following parameters apply:

$$A^* = 0.0035 \quad \alpha = 1.2 \quad \beta = 0.5 \quad \gamma = 0.167 \tag{C.64}$$

### C.2.3.2 Sato and Riedel correlation [375, 376, 377, 378]

$$k_L = \frac{\frac{1.11}{\sqrt{M}}\left[3 + 20(1 - T_r)^{\frac{2}{3}}\right]}{3 + 20\,(1 - T_{b_r})^{\frac{2}{3}}} \tag{C.65}$$

where $k_L$ = thermal liquid conductivity [W/(m K)]
$T_{b_r}$ = reduced normal boiling point temperature

### C.2.3.3 Missenard and Riedel correlation [297, 296]

#### Low-pressure correlation

$$k_L = \frac{k_L|_{273K}\left[3 + 20(1 - T_r)^{\frac{2}{3}}\right]}{3 + 20[1 - \frac{273}{T_c}]^{\frac{2}{3}}} \tag{C.66}$$

In addition, the following relation is provided:

$$k_L|_{273K} = \frac{8.4 \times 10^{-3}\sqrt{\frac{T_b \rho'}{M}}c'_p}{N^{\frac{1}{4}}} \tag{C.67}$$

where $k_L|_{273K}$ = liquid thermal conductivity at 273 K [W/(m K)]
$\rho'$ = liquid density at 273 K [mol/cm$^3$]
$c'_p$ = liquid heat capacity at constant pressure at 273 K [J/(mol K)]
$N$ = number of atoms in the molecule

#### High-pressure correlation

A simple correlation for liquid thermal conductivities was proposed by Missenard [295] to extend low-pressure conductivities to their equivalent high-pressure values. The proposed equation is:

$$\frac{k_L(p_r)}{k_L(\text{low pressure})} = 1 + Q\,p_r^{0.7} \tag{C.68}$$

where $k_L(p_r)$ = high-pressure liquid thermal conductivity [W/(m K)]
$k_L$(low pressure) = low-pressure thermal conductivity [W/(m K)]

Both conductivities are evaluated at the same temperature. The factor $Q$ is tabulated in Table C.7.

| | Reduced pressure | | | | | |
|---|---|---|---|---|---|---|
| $T_r$ | 1 | 5 | 10 | 50 | 100 | 200 |
| 0.8 | 0.036 | 0.038 | 0.038 | 0.038 | 0.038 | 0.038 |
| 0.7 | 0.018 | 0.025 | 0.027 | 0.031 | 0.032 | 0.032 |
| 0.6 | 0.015 | 0.02 | 0.022 | 0.024 | 0.025 | 0.025 |
| 0.5 | 0.012 | 0.0165 | 0.017 | 0.019 | 0.02 | 0.02 |

**Table C.7:** Missenard correction factor $Q$ for high-pressure liquid thermal conductivities.

### C.2.3.4 Simple thermodynamic correlation [410]

$$k_L = 0.2188 - 2.256 \times 10^{-4} T \tag{C.69}$$

where $k_L$ = liquid thermal conductivity [W/(m K)]
$T$ = absolute temperature [K]

## C.2.4 Heat capacity

Rowlinson and Bondi [52, 380] have proposed a corresponding states method for the estimation of liquid heat capacities, suggesting:

$$\frac{c_{pL} - c_p^\circ}{\mathcal{R}} = 1.45 + \frac{0.45}{1 - T_r} + 0.25\,\omega \left[ 17.11 + \frac{25.2\,(1 - T_r)^{\frac{1}{3}}}{T_r} + \frac{1.742}{T_r} \right] \tag{C.70}$$

where $c_{pL}$ = liquid heat capacity at constant pressure
$c_p^\circ$ = liquid heat capacity at constant pressure for ideal gas state

The heat capacity at constant pressure for the ideal gas state was estimated by fitting a second order polynomial function to the data given in Stull *et al.* [413], defined as:

$$c_p^\circ - c_{p,ref} = A + B\,T + C\,T^2 \tag{C.71}$$

and using a reference liquid heat capacity at 298.15 K. The parameters and reference quantity are listed in Table C.8.

| Component | $A$ | $B$ | $C$ | $c_{p,ref}$ [J/(mol K)] |
|---|---|---|---|---|
| $n$-heptane | 9.205 | 0.5929 | - 0.0002215 | 224 |
| $n$-dodecane | 16.55 | 0.9998 | - 0.0003785 | 376 |

**Table C.8:** Parameters to estimate heat capacity at constant pressure for ideal gas state.

## C.2.5 Surface tension

### C.2.5.1 Macleod and Sugden correlation [278]

$$\sigma^{\frac{1}{4}} = \mathcal{P}\,(\rho_L - \rho_v) \tag{C.72}$$

where $\sigma$ = surface tension [mN/m]
$\mathcal{P}$ = parachor [cm$^3$ g$^{1/4}$ / (s$^{1/2}$ mol)]

The parachor of the liquid was estimated from additive group contribution based on data provided by Quayle [351].

### C.2.5.2 Brock and Bird correlation [58]

Brock and Bird have developed a corresponding states correlation defined as:

$$\frac{\sigma}{p_c^{\frac{2}{3}} T_c^{\frac{1}{3}}} = (0.132\,\alpha_c - 0.279)(1 - T_r)^{\frac{11}{9}} \tag{C.73}$$

where $\sigma$ = surface tension [mN/m]
$\alpha_c$ = Riedel parameter at the critical point

The Riedel parameter has been evaluated according to the suggestion of Miller [291]:

$$\alpha_c = 0.9076\left[1 + \frac{T_{b_r} \ln \frac{p_c}{1.01325}}{1 - T_{b_r}}\right] \tag{C.74}$$

where $T_{b_r}$ is the reduced boiling temperature.

### C.2.5.3 Simple thermodynamic correlation [410]

$$\sigma = 0.055717\,(1 - T_r)^{1.3325} \tag{C.75}$$

where $\sigma$ = surface tension [N/m]

## C.2.6 Vapour pressure

Gomez-Nieto and Thodos [135, 136, 137] have proposed the following expression for the vapour pressure:

$$\ln p_{vp_r} = \beta\left[\frac{1}{T_r^m} - 1\right] + \gamma\left[T_r^7 - 1\right] \tag{C.76}$$

where $p_{vp_r}$ = reduced vapour pressure
$\beta, \gamma, m$ = constants

The constants are defined via additional relations. For nonpolar compounds these are:

$$\gamma = ah + b\beta \tag{C.77}$$

$$a = \frac{1 - \frac{1}{T_{b_r}}}{T_{b_r}^7 - 1} \tag{C.78}$$

$$b = \frac{1 - \frac{1}{T_{b_r}^m}}{T_{b_r}^7 - 1} \tag{C.79}$$

$$h = T_{b_r}\frac{\ln \frac{p_c}{1.01325}}{1 - T_{b_r}} \tag{C.80}$$

$$\beta = -4.267 - \frac{221.79}{h^{2.5}\exp\left(0.0384h^{2.5}\right)} + \frac{3.8126}{\exp\left(\frac{2272.44}{h^3}\right)} \tag{C.81}$$

$$m = 0.78425\exp(0.089315h) - \frac{8.5217}{\exp(0.74826h)} \tag{C.82}$$

## C.2.7 Enthalpy of vapourisation

### C.2.7.1 Majer and Svoboda correlation [280]

Majer and Svoboda suggest a heat of vapourisation in the temperature range of 298.15 K < T < 363 K according to:

$$L = A\exp(-BT_r)(1 - T_r)^C \tag{C.83}$$

where $L$ = latent heat of vapourisation at low pressures [J/mol].

For $n$-heptane the $A = 53660$ and $B = 0.2831$.

### C.2.7.2 Simple thermodynamic correlation [410]

$$L = 4.973 \times 10^4 \, (1 - T_r)^{0.386} \tag{C.84}$$

where $L$ = latent heat of vapourisation at low pressures [J/mol].

### C.2.7.3 Real gas latent heat of vapourisation

The enthalpy required for species $i$ to vapourise into a gas mixture is generally expressed as:

$$L = h_i^V - h_i^L \tag{C.85}$$

where $h_i^V$ = partial molar enthalpy of species $i$ in gas phase [J/mol]
$h_i^L$ = molar enthalpy of species $i$ in liquid phase [J/mol]

The partial molar enthalpy of the vapourising component is related to its ideal gas enthalpy $h_i^\circ$ through:

$$\frac{\Delta h_i^V}{\mathcal{R}T^2} = \frac{h_i^V - h_i^\circ}{\mathcal{R}T^2} = - \left( \frac{\partial \ln \phi_i}{\partial T} \right) \Bigg|_{p,y_i} \tag{C.86}$$

where $\Delta h_i^V$ denotes the deviation between the ideal gas enthalpy and the partial enthalpy at pressure $p$ and species composition $y_i$. The expression involving the fugacity coefficient $\phi_i$ is obtained analytically by using an EOS and necessitates the solution of the vapour-liquid-equilibrium calculation. Such a solution is found e.g. in Reid *et al.* [358]. For an ideal gas $\Delta h_i^V$ is negligible.

Substituting Eq. (C.86) into Eq. (C.85) results finally in:

$$L = h_i^\circ - h_i^L + \Delta h_i^V \tag{C.87}$$

## C.3 Vapour-Liquid Equilibrium

Thermodynamic equilibrium at the gas/liquid interface is expressed as:

$$T_s^V = T_s^L \tag{C.88a}$$

$$p_s^V = p_s^L \tag{C.88b}$$

$$f_{s,i}^V = f_{s,i}^L \tag{C.88c}$$

Alternatively, the last expression can be recast in terms of chemical potentials $\mu$:

$$\mu_{s,i}^V = \mu_{s,i}^L \tag{C.89}$$

The chemical potential is defined by:

$$\mu_i = \mathcal{R}T \ln \frac{f_i}{f_i^\circ} + \mu_i^\circ \tag{C.90}$$

where the superscript '$\circ$' denotes quantities at the standard state. The direct method subsequently introduces a fugacity coefficient $\Phi$ which depends on pressure, temperature and gas composition, given as:

$$\Phi_i = \frac{f_i}{y_i p}, \tag{C.91}$$

where $y_i$ is the molar concentration of species $i$ in the gas phase. The fugacity of each species can be related to the volumetric properties of the mixture through two exact relationships [72, 284, 349]:

$$\mathcal{R}T \ln \Phi_i = \int_V^\infty \left[ \left( \frac{\partial p}{\partial n_i} \right)_{T,V,n_{j\neq i}} - \frac{\mathcal{R}T}{V} \right] dV - \mathcal{R}T \ln Z \tag{C.92}$$

$$\mathcal{R}T \ln \Phi_i = \int_0^p \left[ \left( \frac{\partial V}{\partial n_i} \right)_{T,p,n_{j\neq i}} - \frac{\mathcal{R}T}{p} \right] dp \tag{C.93}$$

where $n_i$ is the number of moles of component $i$ and $V$ is the molar volume. Commonly Eq. (C.92) is used in conjunction with a real gas EOS to solve for the fugacity coefficients in the liquid and vapour phases close to the gas/liquid interface.

An explicit expression for the fugacity coefficient of component $i$ in the gas phase using the Redlich-Kwong and Soave-Redlich-Kwong EOS is expressed by:

$$\ln \Phi_i^V = \ln \frac{V}{V-b} + \frac{b_i}{V-b} - \ln \frac{pV}{\mathcal{R}T} + \frac{ab_i}{\mathcal{R}Tb^2} \left( \ln \frac{V+b}{V} - \frac{b}{V+b} \right)$$

$$- \frac{2\sqrt{a_i} \sum_j y_j \sqrt{a_j}(1-\overline{k_{ij}})}{\mathcal{R}Tb} \ln \frac{V+b}{V} \tag{C.94}$$

where $a, b$ = EOS coefficients of the mixture
$a_i, b_i$ = EOS coefficients of species $i$, defined in Section 3.2.6.1
$\overline{k_{ij}}$ = binary interaction coefficient from Knapp *et al.* [238].

The mixing rules concerning the parameters $a$ and $b$ in the cubic EOS for the gas phase are expressed through:

$$a = \sum_i \sum_j y_i y_j \sqrt{a_i a_j}(1 - \overline{k_{ij}}) \tag{C.95}$$

$$b = \sum_i y_i b_i \tag{C.96}$$

where for $n$-heptane the binary interaction coefficients are 0.1422 for the RK and SRK EOS and 0.1441 for the PR EOS.

The fugacity coefficient for the Peng-Robinson EOS is analogously given as:

$$\begin{aligned} \ln \Phi_i^V = {} & \ln \frac{V}{V-b} + \frac{b_i}{V-b} - \ln \frac{pV}{\mathcal{R}T} \\ & + \frac{ab_i}{b^2 \mathcal{R}T} \left( \frac{\sqrt{2}}{4} \ln \frac{V + b(1+\sqrt{2})}{V + b(1-\sqrt{2})} - \frac{bV}{V^2 + 2bV - b^2} \right) \\ & - \frac{\sqrt{2}}{2} \frac{\sqrt{a_i}}{b\mathcal{R}T} \sum_j y_j \sqrt{a_j}(1 - \overline{k_{ij}}) \ln \frac{V + b(1+\sqrt{2})}{V + b(1-\sqrt{2})} \end{aligned} \tag{C.97}$$

To obtain the liquid phase fugacity coefficients, the equivalent liquid species concentrations $x_i$ have to be inserted instead of $y_i$.

The VLE calculation for a given temperature and pressure is usually known as the *flash problem*. Solution procedures are found e.g. in [21, 235, 358, 386].

# Appendix D

# Surface Temperature and Wall Heat Flux

Since the wall temperature swings caused by the unsteady thermal boundary layer are damped out within a small wall distance of around 1–2 mm [54, 116, 167, 190, 274], to measure surface temperatures the sensing element of the probe has to be placed if possible at the surface, while its thickness should be in the range of micrometers [54, 167]. In both engine experiments, described in the present study, surface thermocouples have been chosen to record the instantaneous surface temperatures and a second thermocouple has been located below the surface to measure the quasi-steady wall temperature.

The instantaneous local heat flux into the chamber walls can be obtained through the assumption of one-dimensional unsteady heat conduction:

$$\frac{\partial T}{\partial t} = \frac{1}{\rho c}\frac{\partial}{\partial x}\left(k\frac{\partial T}{\partial x}\right) \tag{D.1}$$

The solution to this can be represented by a Fourier series [15, 167, 324]:

$$T_W(t) = \overline{T} + \sum_{i=1}^{N}\left[A_i \cos(i\omega t) + B_i \sin(i\omega t)\right] \tag{D.2}$$

where $\overline{T}$ is the cycle-averaged surface temperature, $A_i$, $B_i$ are the Fourier coefficients and $\omega$ is half the engine speed. Differentiation of the above gives the wall heat flux as:

$$q_W(t) = q_0 + \sum_{i=1}^{N} \sqrt{\frac{i\omega}{2}}\,\beta\,[(A_i + B_i)\cos(i\omega t) + (B_i - A_i)\sin(i\omega t)] \qquad \text{(D.3)}$$

where $\beta = \sqrt{\rho c k}$ is a wall thermal property indicating the amount of damping of the temperature oscillations inside the wall. The quantity $q_0$ is the heat flux at the instance when the gas-side and wall temperatures are equal. In general, it is noteworthy that the surface thermocouples measure the total heat flux, including the convective and radiant parts. Table D.1 gives some information about the surface thermocouple probes used in both experiments.

| **Engine case** | Material | Thickness of hot junction [$\mu$m] | $\beta = \sqrt{\rho c k}$ $\left[\frac{W\sqrt{s}}{m^2K}\right]$ | Depth of 2nd element [mm] |
|---|---|---|---|---|
| **RWTH Aachen HPP Prototype** | Nickel<br>High alloy cast iron | 0.3<br>5 - 10 | 11000<br>8800 | 10<br>4 |

**Table D.1:** Surface thermocouple probe specifications [190, 248].

# Bibliography


[1] Abraham J. *What is Adequate Resolution in the Numerical Computations of Transient Jets?* SAE Technical Paper Series, No. 970051, 1997.

[2] Abraham J., Bracco F.V. and Reitz R.D. *Comparisons of Computed and Measured Premixed Charge Engine Combustion.* Combustion and Flame, Vol. 60, pp. 309–322, 1985.

[3] Abraham J., Venkatraman I., Magi V. and Fujita N. *An Evaluation of a Discrete Particle Model for Soot Formationl, Growth, Transport and Oxidation in Diesel Engines.* In The Fourth International Symposium on Diagnostics and Modeling of Combustion in Internal Combustion Engines, COMODIA 98, Kyoto, Japan, Engine Systems Division, The Japan Society of Mechanical Engineers, pp. 155–160, 20-23 July, 1998.

[4] Abu-Qudais M. *Instantaneous Exhaust-Gas Temperature and Velocity for a Diesel Engine.* Applied Energy, Vol. 56, No. 1, pp. 59–70, 1997.

[5] Aggarwal S.K. *A Review of Spray Ignition Phenomena: Present Status and Future Research.* Progress in Energy and Combustion Science, Vol. 24, pp. 565–600, 1998.

[6] Aggarwal S.K. and Peng F. *A Review of Droplet Dynamics and Vaporization Modeling for Engineering Calculations.* ASME Journal of Engineering for Gas Turbines and Power, Vol. 117, pp. 453–461, July, 1995.

[7] Alkidas A.C. *On the Premixed Combustion in a Direct-Injection Diesel Engine.* ASME Journal of Engineering for Gas Turbines and Power, Vol. 109, No. 2, pp. 187–192, 1987.

[8] Amann C.A. and Siegla D.C. *Diesel Particulates — What They are and Why.* Aerosol Science and Technology, Vol. 1, pp. 73–101, 1982.

[9] American Petroleum Institute (API). *Technical Data Book - Petroleum Refining,* 1981.

[10] Andrade da Costa E.N. *The Viscosity of Liquids.* Nature, Vol. 125, pp. 309–310, 1930.

[11] Andrade da Costa E.N. *The viscosity of liquids.* Endeavour, Vol. 13, pp. 117–127, 1954.

[12] Aneja R. and Abraham J. *Comparison of Computed and Measured Results of Combustion in a Diesel Engine.* SAE Technical Paper Series, No. 980786, 1998.

[13] Angelberger C., Poinsot T. and Delhaye B. *Improving Near-Wall Combustion and Wall Heat Transfer Modeling in SI Engine Computations.* SAE Technical Paper Series, No. 972881, 1997.

[14] Annand W.J.D. *Heat Transfer in the Cylinders of Reciprocating Internal Combustion Engines.* Proceedings of the Institution of Mechanical Engineers, Vol. 177, No. 36, pp. 973–990, 1963.

[15] Annand W.J.D. *Heat Transfer in the Cylinder and Porting.* In The Thermodynamics and Gas Dynamics of Internal Combustion Engines, Oxford, J. Horlock and D. Winterbone, editors, Vol. 2, Clarendon Press, pp. 773–805, 1986.

[16] Aoyagi Y., Kamimoto T., Matsui Y. and Matsuoka S. *A Gas Sampling Study on the Formation Processes of Soot and NO in a DI Diesel Engine.* SAE Technical Paper Series, Vol. 89, No. 800254, 1980.

[17] Appel J., Bockhorn H. and Frenklach M. *Kinetic Modeling of Soot Formation with Detailed Chemistry and Physics: Laminar Premixed Flames of $C_2$ Hydrocarbons.* Combustion and Flame, Vol. 121, pp. 122–136, 2000.

[18] Arai M., Tabata M., Hiroyasu H. and Shimizu M. *Disintegrating Process and Spray Characterization of Fuel Jet Injected by a Diesel Nozzle.* SAE Technical Paper Series, No. 840275, 1984.

[19] Arcoumanis C., Nagwaney A. and Whitelaw J.H. *Effect of EGR on Combustion Development in a 1.9L DI Diesel Optical Engine.* SAE Technical Paper Series, No. 950850, 1995.

[20] Arcoumanis C., Begleris P. and Gosman A.D. *Measurements and Calculations of the Flow in a Research Diesel Engine.* SAE Technical Paper Series, No. 861563, 1986.

[21] Assael M.J., Trusler J.P.M. and Tsolakis T.F. *Thermophysical Properties of Fluids: An Introduction to their Prediction.* Imperial College Press, London, UK, 1996.

[22] Astarita M., Corcione F.E., Vaglieco B.M. and Valentino G. *Optical diagnostics of temporal and spatial evolution of a reacting diesel fuel jet.* Combustion Science and Technology, Vol. 148, No. 1, pp. 1–16, 1999.

[23] Badock C., Wirth R., Fath A. and Leipertz A. *Investigation of cavitation in real size diesel injection nozzles.* International Journal of Heat and Fluid Flow, Vol. 20, pp. 538–544, 1999.

[24] Bäcker H. and Wiartalla A. *Pressure Chamber Measurement Data.* Additional report, Rheinisch Westfälische Technische Hochschule, Aachen, December, 1992.

[25] Bai X.S., Balthasar M., Mauss F. and Fuchs L. *Detailed Soot Modeling in Turbulent Jet Diffusion Flames.* Twenty-Seventh Symposium (International) on Combustion, The Combustion Institute, pp. 1623–1630, 1998.

[26] Baker D.M. and Assanis D.N. *A methodology for coupled thermodynamic and heat transfer analysis of a diesel engine.* Applied Mathematical Modelling, Vol. 18, pp. 590–601, 1994.

[27] Balthasar M. *Detailed Soot Modelling in Turbulent Diffusion Flames.* Licensiat thesis, Lund Institute of Technology, Lund, Sweden, 1999.

[28] Balthasar M., Heyl A., Mauss F., Schmitt F. and Bockhorn H. *Flamelet modeling of soot formation in laminar ethyne/air-diffusion flames.* Twenty-Sixth Symposium (International) on Combustion, The Combustion Institute, pp. 2369–2377, 1996.

[29] Baroncini C., Di Filippo P., Latini G. and Pacetti M. *Thermal conductivity of liquids: comparison of predicted values with experimental results at different temperatures.* High Temperatures – High Pressures, Vol. 11, No. 5, pp. 581–586, 1979.

[30] Baroncini C., Di Filippo P. and Latini G. *Comparison between Predicted and Experimental Thermal Conductivity Values for the Liquid Substances and the Liquid Mixtures at Different Temperatures and Pressures.* In Workshop on Thermal Conductivity Measurement, IMEKO, Budapest, 14-16 March, 1983. Paper presented.

[31] Barths H., Antoni C. and Peters N. *Three-Dimensional Simulation of Pollutant Formation in a DI Diesel Engine Using Multiple Interactive Flamelets.* SAE Technical Paper Series, No. 982459, 1998.

[32] Barths H., Hasse C. and Peters N. *Three-Dimensional Modeling of Pollutant Formation in a DI-Diesel Engine.* In 10th International Multidimensional Engine Modeling User's Group Meeting, Detroit, Michigan, USA, March 5, 2000.

[33] Barths H., Peters N., Brehm N., Mack A., Pfitzner M. and Smiljanovski V. *Simulation of Pollutant Formation in a Gas-Turbine Combustor Using Unsteady Flamelets.* Twenty-Seventh Symposium (International) on Combustion, The Combustion Institute, pp. 1841–1847, 1998.

[34] Barths H., Pitsch H. and Peters N. *3D Simulation of DI Diesel Combustion and Pollutant Formation Using a Two-Component Reference Fuel.* Oil & Gas Science and Technology – Revue de l'Institut Français du Pétrole, Vol. 54, No. 2, pp. 233–244, 1999.

[35] Barths H., Pitsch H. and Peters N. *Comparison of the Representative Interactive Flamelet Model and the Magnussen Model for Combustion and Pollutant Formation in DI-Diesel Engines to Experiments.* In Proceedings of the 3rd International Conference on High Performance Computing in the Automotive Industry, M. Sheh, editor, Cray Research, Inc., pp. 423–443, 1997.

[36] Baulch D.L., Cobos C.J., Cox R.A., Frank P., Hayman G., Just T., Kerr J.A., Murrells T., Pilling M.J., Troe J., Walker R.W. and Warnatz J. *Evaluated Kinetic Data for Combustion Modeling.* Journal of Physical and Chemical Reference Data, Vol. 21, pp. 411–429, 1992.

[37] Baulch D.L., Drysdall D.D., Horne D.G. and Lloyd A.C. *Evaluated Kinetic Data for High Temperature Reactions.* Butterworth, 1973.

[38] Begleris P. *Three-Dimensional Flow Predictions in Motored Diesel Engines.* Ph.D. thesis, Imperial College of Science, Technology & Medicine, University of London, December, 1986.

[39] Belardini P., Bertoli C., Ciajolo A., D'Anna A. and Del Giacomo N. *Three-Dimensional Calculations of DI Diesel Engine Combustion and Comparison With In Cylinder Sampling Valve Data.* SAE Technical Paper Series, No. 922225, 1992.

[40] Benson S.W. *The Kinetics and Thermochemistry of Chemical Oxidation with Application to Combustion and Flames.* Progress in Energy and Combustion Science, Vol. 7, No. 2, pp. 125–134, 1981.

[41] Berlad A. and Hibbard R. *Effect of radiant energy on vaporization and combustion of liquid fuels.* RME-52109, NACA, 1952.

[42] Beshay K.R. *Computer Modelling of Diesel Spray Dispersion and Evaporation.* Ph.D. thesis, Imperial College of Science, Technology & Medicine, University of London, 1985.

[43] Beshay K.R., Gosman A.D. and Watkins A.P. *Assessments of Multidimensional Diesel Spray Predictions.* SAE Technical Paper Series, No. 861570, 1986.

[44] Bilger R.W. *Chapter 3: Turbulent Flows with Nonpremixed Reactants.* In Turbulent Reacting Flows, P. Libby and F. Williams, editors, Vol. 44 of Topics in Advanced Physics, pp. 65-113. Springer-Verlag, Berlin, 1980.

[45] Binder K. and Schnabel M. *Private Communication.* DaimlerChrysler, HEDE Project Meeting in Bradford, 23-24 March, 2000.

[46] Bird R.B., Stewart W.E. and Lightfoot E.N. *Transport Phenomena.* John Wiley & Sons, Inc., Wisconsin, USA, 1960.

[47] Black D.L., McQuay M.Q. and Bonin M.P. *Laser-based techniques for particle-size measurement: a review of sizing methods and their industrial applications.* Progress in Energy and Combustion Science, Vol. 22, pp. 267–306, 1996.

[48] Blackwell B.F., Kays W.M. and Moffat R.J. *The Turbulent Boundary Layer on a Porous Plate: An Experimental Study of the Heat Transfer Behavior with Adverse Pressure Gradients.* Report HMT-16, Mechanical Engineering Department, Stanford University, Stanford, CA, 1972.

[49] Bockhorn H. *Sensitivity analysis based reduction of complex reaction mechanisms in turbulent non-premixed combustion.* Twenty-Third Symposium (International) on Combustion, The Combustion Institute, pp. 767–774, 1990.

[50] Bönig M., Feldermann C., Jander H., Lüers B., Rudolph G. and Wagner H.G. *Soot Formation in Premixed $C_2H_4$ Flat Flames at Elevated Pressure.* Twenty-Third Symposium (International) on Combustion, The Combustion Institute, Vol. 23, pp. 1581–1587, 1990.

[51] Bollig M., Pitsch H., Hewson J.C. and Seshadri K. *Reduced n-Heptane Mechanism for Non-Premixed Combustion with Emphasis on Pollutant-Relevant Intermediate Species.* Twenty-Sixth Symposium (International) on Combustion, The Combustion Institute, pp. 729–737, 1996.

[52] Bondi A. *Estimation of the heat capacity of liquids.* Industrial and Engineering Chemistry Fundamentals, Vol. 5, No. 4, pp. 442–449, 1966.

[53] Borman G.L. and Johnson J.H. *Unsteady Vaporization Histories and Trajectories of Fuel Droplets Injected into Swirling Air.* SAE Technical Paper Series, No. 598C, 1962.

[54] Borman G. and Nishiwaki K. *Internal-Combustion Engine Heat Transfer.* Progress in Energy and Combustion Science, Vol. 13, pp. 1–46, 1987.

[55] Boussinesq J. *Essai sur la théorie des eaux courantes.* Mémoires présentés par divers savants à l'Académie des Sciences Paris, Vol. 23, No. 1, pp. 1–660, 1877.

[56] Bowman C.T. *Control of combustion-generated nitrogen oxide emissions: technology driven by regulation.* Twenty-Fourth Symposium (International) on Combustion, The Combustion Institute, pp. 859–878, 1992.

[57] Bray K.N.C. and Peters N. *Chapter 2: Laminar Flamelets in Turbulent Flames.* In Turbulent Reacting Flows, P. Libby and F. Williams, editors. Academic Press, London, 1994, pp. 63–113.

[58] Brock J.R. and Bird R.B. *Surface tension and the principle of corresponding states.* AIChE Journal, Vol. 1, No. 2, pp. 174–177, 1955.

[59] Brulé M.R. and Starling K.E. *Thermo-Physical Properties of Complex-Systems – Applications of Multiproperty Analysis.* Industrial and Engineering Chemistry: Process Design Development, Vol. 23, pp. 833–845, 1984.

[60] Canada G.S. and Faeth G.M. *Combustion of Liquid Fuels in a Flowing Combustion Gas Environment at High Pressures.* Fifteenth Symposium (International) on Combustion, The Combustion Institute, pp. 419–428, 1974.

[61] Cartellieri W.P. and Wachter W.F. *Status Report on a Preliminary Survey of Strategies to meet US-1991 HD Diesel Emission Standards without Exhaust Gas Aftertreatment.* SAE Technical Paper Series, No. 870342, 1987.

[62] Catris S. and Aupoix B. *Density corrections for turbulence models.* Aerospace Science and Technology, Vol. 4, No. 1, pp. 1–11, 2000.

[63] Chapman S. and Cowling T.G. *The Mathematical Theory of Nonuniform Gases,* $2^{nd}$ ed. Cambridge University Press, London, 1952.

[64] Chaves H., Hentschel W., Obermeier F., Schindler K.P. and Weiss D. *Fuel Spray in Diesel Engines, Part II: Spray Propagation and Wall Interaction.* In Proceedings of the $3^{rd}$ International Conference: Innovation and Reliability in Automotive Design and Testing, Florence, Italy, Vol. 2, Associazione Tecnica dell' Automobile (ATA) & Dipartimento di Meccanica e Tecnologie Industriali (DMTI), pp. 761–772, April, 1992.

[65] Chaves H., Knapp M. and Kubitzek A. *Experimental Study of Cavitation in the Nozzle Hole of Diesel Injectors using Transparent Nozzles.* SAE Technical Paper Series, No. 950290, 1995.

[66] Chen W.-Y., Kulkarni A., Milum J.L. and Fan L.T. *Stochastic Modeling of Carbon Oxidation.* AIChE Journal, Vol. 45, No. 12, pp. 2557–2570, December, 1999.

[67] Chen G., Mazumder M.M., Chang R.K., Swindal J.C. and Acker W.P. *Laser diagnostics for droplet characterization: application of morphology dependent resonances.* Progress in Energy and Combustion Science, Vol. 22, pp. 163–188, 1996.

[68] Chevalier C., Louessard P., Müller U.C. and Warnatz J. *A Detailed Low-Temperature Reaction Mechanism of n-Heptane Auto-Ignition.* In Proceedings of the International Symposium on Diagnostics and Modeling of Combustion in Internal Combustion Engines, COMODIA 90, Kyoto, Japan, Engine Systems Division, The Japan Society of Mechanical Engineers, pp. 93–97, 3-5 September, 1990.

[69] Chien K.-Y. *Predictions of Channel and Boundary-Layer Flows with a Low-Reynolds-Number Turbulence Model.* AIAA Journal, Vol. 20, No. 1, pp. 33–38, 1982.

[70] Chigier N.A. *Combustion measurements.* Hemisphere, New York, 1991.

[71] Chiu H.H. *Advances and challenges in droplet and spray combustion. I. Toward a unified theory of droplet aerothermochemistry.* Progress in Energy and Combustion Science, Vol. 26, pp. 381–416, 2000.

[72] Chueh P.L. and Prausnitz J.M. *Vapor-liquid Equilibria at High Pressures. Vapor-Phase Fugacity Coefficients in Non-Polar and Quantum-Gas Mixtures.* Industrial and Engineering Chemistry. Fundamentals, Vol. 6, No. 4, pp. 492–498, 1967.

[73] Chueh P.L. and Prausnitz J.M. *Calculation of high-pressure vapor-liquid equilibria.* Industrial and Engineering Chemistry, Vol. 60, No. 3, pp. 34–52, 1968.

[74] Chung T.H., Ajlan M., Lee L.L. and Starling K.E. *Generalized Multiparameter Correlation for Nonpolar and Polar Fluid Transport Properties.* Industrial & Engineering Chemistry Research, Vol. 27, No. 4, pp. 671–679, 1988.

[75] Chung T.H., Lee L.L. and Starling K.E. *Applications of Kinetic Gas Theories and Multiparameter Correlation for Prediction of Dilute Gas Viscosity and Thermal Conductivity.* Industrial & Engineering Chemistry, Fundamentals, Vol. 23, No. 1, pp. 8–13, 1984.

[76] Chyou S.-W. and Sleicher C.A. *Can One- and Two-Equation Turbulence Models Be Modified To Calculate Turbulent Heat Transfer with Variable Properties?* Industrial & Engineering Chemistry. Research, Vol. 31, pp. 756–759, 1992.

[77] Clerides D. *Numerical Simulation of Spray Processes in Diesel Engines.* Ph.D. thesis, Imperial College of Science, Technology & Medicine, University of London, May, 1997.

[78] Connon C.S. and Dunn-Rankin D. *Droplet Stream Dynamics at High Ambient Pressure.* Atomization and Sprays, Vol. 6, No. 4, pp. 485–497, 1996.

[79] Courant R., Friedrichs O. and Lewy H. *Über die partiellen Differenzgleichungen der mathematischen Physik.* Mathematische Annalen, Vol. 100, pp. 32–74, 1928.

[80] Crowe C.T. *Review – Numerical Models for Dilute Gas-Particle Flows.* ASME Journal of Fluids Engineering, Vol. 104, pp. 297–303, 1982.

[81] Curtis E.W. and Farrell P.V. *Droplet Vaporization in a Supercritical Microgravity Environment.* Acta Astronautica, Vol. 17, No. 11/12, pp. 1189–1193, 1988.

[82] Curtis E.W. and Farrell P.V. *A Numerical Study of High-Pressure Droplet Vaporization.* Combustion and Flame, Vol. 90, pp. 85–102, 1992.

[83] Daily J.W. *Laser induced Fluorescence spectroscopy in flames.* Progress in Energy and Combustion Science, Vol. 23, pp. 133–199, 1997.

[84] Daou J., Haldenwang P. and Nicoli C. *Supercritical Burning of Liquid Oxygen (LOX) Droplet with Detailed Chemistry.* Combustion and Flame, Vol. 101, pp. 153–169, 1995.

[85] Daubert T.E. and Danner R.P. *Data Compilation tables of properties of pure compounds.* Design Institute for Physical Property Data, American Institute of Chemical Engineers (AIChE), 1985.

[86] Dec J.E. *A Conceptual Model of DI Diesel Combustion Based on Laser-Sheet Imaging.* SAE Technical Paper Series, No. 970873, 1997.

[87] Dec J.E. and Canaan R.E. *PLIF Imaging of NO Formation in a DI Diesel Engine.* SAE Technical Paper Series, No. 980147, 1998.

[88] Dec J.E. and Kelly-Zion P.L. *The Effects of Injection Timing and Diluent Addition on Late-Combustion Soot Burnout in a DI Diesel Engine based on Simultaneous 2-D Imaging of OH and Soot.* SAE Technical Paper Series, No. 2000-01-0238, 2000.

[89] Dederichs A.S., Balthasar M. and Mauss F. *Modeling of $NO_x$ and Soot Formation in Diesel Combustion.* Oil & Gas Science and Technology – Revue de l'Institut Français du Pétrole, Vol. 54, No. 2, pp. 245–249, 1999.

[90] Delplanque J.-P. and Sirignano W.A. *Numerical Study of the Transient Vaporization of an Oxygen Droplet at Sub- and Super-Critical Conditions.* International Journal of Heat and Mass Transfer, Vol. 36, No. 2, pp. 303–314, 1993.

[91] Demirdžić I. and Perić M. *Space Conservation Law in Finite Volume Calculations of Fluid Flow.* International Journal for Numerical Methods in Fluids, Vol. 8, pp. 1037–1050, 1988.

[92] DeSoete G.G. *Overall reaction rates of NO and $N_2$ formation from fuel nitrogen.* Fifteenth Symposium (International) on Combustion, The Combustion Institute, pp. 1093–1102, 1975.

[93] Dieselnet. *Emission Standards: European Union. Heavy-Duty Diesel Truck and Bus Engines.* Taken from the Internet URL = http://www.dieselnet.com/standards/eu/hd.html, 1999.

[94] Dillies B., Marx K., Dec J. and Espey C. *Diesel Engine Combustion Modelling Using the Coherent Flame Model in Kiva-II.* SAE Technical Paper Series, No. 930074, 1993.

[95] Dukowicz J.K. *A Particle-Fluid Numerical Model for Liquid Sprays.* Journal of Computational Physics, Vol. 35, pp. 229–253, 1980.

[96] Dwyer H.A., Stapf P. and Maly R. *Unsteady Vaporization and Ignition of a Three-Dimensional Droplet Array.* Combustion and Flame, Vol. 121, pp. 181–194, 2000.

[97] Eaton A.M., Smoot L.D., Hill S.C. and Eatough C.N. *Components, formulations, solutions, evaluation, and application of comprehensive combustion models.* Progress in Energy and Combustion Science, Vol. 25, pp. 387–436, 1999.

[98] Edelson D. *Computer Simulation in Chemical Kinetics.* Science, Vol. 214, pp. 981–986, 1981.

[99] Eichelberg G. *Some new investigations on old combustion engine problems.* Engineering, Vol. 148, pp. 463–446,547–560, 1939.

[100] Elghobashi S.E., Abou-Arab T.W. and Mostafa A. *Prediction of the Particle-Laden Jet with a Two-Equation Turbulence Model.* International Journal of Multiphase Flow, Vol. 10, pp. 697–710, 1984.

[101] El Tahry S.H. $k-\epsilon$ *Equation for Compressible Reciprocating Engine Flows.* AIAA Journal of Energy, Vol. 7, No. 4, pp. 345–353, 1983.

[102] El Tahry S.H. *A Comparison of Three Turbulence Models in Engine-Like Geometries.* In International Symposium on Diagnostics and Modeling of Combustion in Reciprocating Engines, COMODIA 85, Tokyo, Japan, The Japan Society of Mechanical Engineers, pp. 203–213, 4-6 Sept., 1985.

[103] El Wakil M.M., Uyehara O.A. and Myers F.S. *A Theoretical Investigation of the Heating-Up Period of Injected Fuel Droplets Vaporizing in Air.* Technical Note 3179, NACA, 1954.

[104] Ely J.F. and Hanley H.J.M. *Prediction of Transport Properties - 2. Thermal Conductivity of Pure Fluids and Mixtures.* Industrial & Engineering Chemistry, Fundamentals, Vol. 22, No. 1, pp. 90–97, 1983.

[105] Enomoto Y., Nagano H., Hagihara Y. and Koyama T. *Thermal load in D.I. diesel engine under EGR operation – measurements of steady state temperature of combustion chamber wall surface and intake gas temperature.* JSAE Review, Vol. 18, No. 3, pp. 225–231, 1997.

[106] Faeth G.M. *Current status of droplet and liquid combustion.* Progress in Energy and Combustion Science, Vol. 3, pp. 191–224, 1977.

[107] Faeth G.M. *Evaporation and Combustion of Sprays.* Progress in Energy and Combustion Science, Vol. 9, pp. 1–76, 1983.

[108] Faeth G.M. *Spray Combustion: A Review.* In Proceedings of The Second International Conference on Multiphase Flow '95, Kyoto, Japan, Vol. 1, 3–7 April, 1995.

[109] Faeth G.M., Dominicis D.P., Tulpinsky J.F. and Olson D.R. *Supercritical Bipropellant Droplet Combustion.* Twelfth Symposium (International) on Combustion, The Combustion Institute, pp. 9–18, 1968.

[110] Fansler T.D. and French D.T. *Cycle resolved laser-velocimetry measurements in a re-entrant-bowl-in-piston engine.* SAE Technical Paper Series, No. 880377, 1988.

[111] Farrell P.V. and Peters B.D. *Droplet Vaporization in Supercritical Pressure Environments,.* Acta Astronautica, Vol. 13, No. 11/12, pp. 673–680, 1986.

[112] Fath A., Fettes C. and Leipertz A. *Investigation of the Diesel Spray Break-Up Close to the Nozzle at Different Injection Conditions.* In The Fourth International Symposium on Diagnostics and Modeling of Combustion in Internal Combustion Engines, COMODIA 98, Kyoto, Japan, Engine Systems Division, The Japan Society of Mechanical Engineers, pp. 429–434, 20-23 July, 1998.

[113] Favre A. *Equations des Gaz Turbulents Compressibles.* Journal de Méchanique, Vol. 4, No. 3, pp. 361–390, 1965.

[114] Fenimore C.P. *Formation of nitric oxide in premixed hydrocarbon flames.* Thirteenth Symposium (International) on Combustion, The Combustion Institute, pp. 373–380, 1971.

[115] Fenimore C.P. and Jones G.W. *Oxidation of Soot by Hydroxyl Radicals.* Journal of Physical Chemistry, Vol. 71, No. 3, pp. 593–597, 1967.

[116] Ferguson C.R. *Internal Combustion Engines, Applied Thermosciences.* John Wiley & Sons, Inc., New York, USA, 1986.

[117] Fernholz H.-H. *External Flows.* In Turbulence, P. Bradshaw, editor, Vol. 12 of Topics in Applied Physics, Springer-Verlag, Berlin, pp. 45–107, 1978.

[118] Ferziger J.H. and Perić M. *Computational Methods for Fluid Dynamics,* 2nd ed. Springer-Verlag, Berlin, 1997.

[119] Feugier A. *Soot oxidation in Laminar Hydrocarbon Flames.* Combustion and Flame, Vol. 19, pp. 249–256, 1972.

[120] Fletcher R. *Conjugate gradient methods for indefinite systems.* Lecture Notes in Mathematics, Vol. 506, pp. 773–789, 1976.

[121] Fraser R.A., Felton P.G. and Bracco F.V. *Preliminary Turbulence Length Scale Measurements in a Motored I.C. Engine.* SAE Technical Paper Series, No. 860021, 1986.

[122] Frenklach M. *Computer Modeling of Infinite Reaction Sequences — a Chemical Lumping.* Chemical Engineering Science, Vol. 40, No. 10, pp. 1843–1849, 1985.

[123] Frenklach M., Clary D.W., Gardiner W.C.Jr. and Stein S.E. *Detailed kinetic modeling of soot formation in shock-tube pyrolysis of acetylene.* Twentieth Symposium (International) on Combustion, The Combustion Institute, pp. 887–901, 1984.

[124] Frenklach M. and Harris S.J. *Aerosol Dynamics Modeling Using the Method of Moments.* Journal of Colloid and Interface Science, Vol. 118, No. 1, pp. 252–261, 1987.

[125] Frenklach M. and Wang H. *Detailed modeling of soot particle nucleation and growth.* Twenty-Third Symposium (International) on Combustion, The Combustion Institute, pp. 1559–1566, 1990.

[126] Frenklach M. and Wang H. *Detailed mechanism and modeling of soot particle formation.* In Soot Formation in Combustion, Berlin, H. Bockhorn, editor, Springer-Verlag, pp. 162–190, 1994.

[127] Frenklach M., Wang H. and Rabinowitz M.J. *Optimization and analysis of large chemical kinetic mechanisms using the solution mapping method - combustion of methane.* Progress in Energy and Combustion Science, Vol. 18, No. 1, pp. 47–73, 1992.

[128] Frenklach M. and Warnatz J. *Detailed Modeling of PAH Profiles in a Sooting Low-Pressure Acetylene Flame.* Combustion Science and Technology, Vol. 51, pp. 265–283, 1987.

[129] Fuller E.N., Schettler P.D. and Giddings J.C. *A new method for prediction of binary gas-phase diffusion coefficients.* Industrial and Engineering Chemistry, Vol. 58, No. 5, pp. 18–27, 1966.

[130] Gear W.C. *Numerical Initial Value Problems in Ordinary Differential Equations.* Prentice-Hall Series in Automatic Computation. Prentice-Hall, Inc., New Jersey, 1971.

[131] Gelfand B.E. *Droplet Breakup Phenomena in Flows with Velocity Lag.* Progress in Energy and Combustion Science, Vol. 22, pp. 201–265, 1996.

[132] Gerald C.F. and Wheatly P.O. *Applied Numerical Analysis*, 3rd ed. Addison-Wesley Publishing Company, Reading, Massachusetts, 1984.

[133] Givler, S.D.; Abraham J. *Supercritical Droplet Vaporization and Combustion Studies.* Progress in Energy and Combustion Science, Vol. 22, pp. 1–28, 1996.

[134] Golub G.H. and van Loan C. *Matrix computations.* Johns Hopkins University Press, Baltimore, 1990.

[135] Gomez-Nieto M. and Thodos G. *Generalized Treatment for the Vapor Pressure Behavior of Polar and Hydrogen-Bonding Compounds.* Canadian Journal of Chemical Engineering, Vol. 55, pp. 445–449, 1977.

[136] Gomez-Nieto M. and Thodos G. *A New Vapor Pressure Equation and Its Application to Normal Alkanes.* Industrial and Engineering Chemistry Fundamentals, Vol. 16, pp. 254–259, 1977.

[137] Gomez-Nieto M. and Thodos G. *Generalized Vapor Pressure Equation for Nonpolar Substances.* Industrial and Engineering Chemistry Fundamentals, Vol. 17, No. 1, pp. 45–51, 1978.

[138] Gordon S. and McBride B.J. *Computer Program for Calculation of Complex Chemical Equilibrium Composition and Applications.* NASA Reference Publication 1311. National Aeronautics and Space Administration, October, 1994.

[139] Gosman A.D. *Flow Processes in Cylinders.* In The Thermodynamics and Gas Dynamics of Internal Combustion Engines, Oxford, J. Horlock and D. Winterbone, editors, Vol. 2, Clarendon Press, pp. 616–772, 1986.

[140] Gosman A.D. *State of the Art of Multi-Dimensional Modeling of Engine Reacting Flows.* Oil & Gas Science and Technology – Revue de l'Institut Français du Pétrole, Vol. 54, No. 2, pp. 149–159, 1999.

[141] Gosman A.D. and Clerides D. *Diesel Spray Modelling: A Review.* In International Institute for Liquid Atomization and Spray Systems (ILASS), Europe Annual Meeting, Florence, Italy, 9-11 July, 1997.

[142] Gosman A.D. and Ioannides E. *Aspects of Computer Simulation of Liquid-Fuelled Combustors.* AIAA Journal of Energy, Vol. 7, No. 6, pp. 482–490, 1983.

[143] Gosman A.D., Johns R.J.R. and Watkins A.P. *Development of Prediction Methods for In-Cylinder Processes in Reciprocating Engines.* In Proceedings of the Symposium on Combustion Modeling in Reciprocating Engines held 6-7 November, 1978 at the General Motors Research Laboratories, Warren, Michigan, New York, J. Mattavi and C. Amann, editors, Plenum Press, pp. 69–129, 1980.

[144] Gradinger T.B. and Boulouchos K. *A zero-dimensional model for spray droplet vaporization at high pressures and temperatures.* International Journal of Heat and Mass Transfer, Vol. 41, No. 19, pp. 2947–2959, 1998.

[145] Grew K.E. and Ibbs T.L. *Thermal Diffusion in Gases.* University Press, Cambridge, 1952.

[146] Grigg H.C. and Syed M.H. *The problem of predicting rate of heat release in Diesel engines.* Proceeding of the Institution of Mechanical Engineers, Vol. 184, Part 3J, Paper 18, pp. 192–202, 1969-70.

[147] Gurvich L.V., Veyts I.V. and Alcock C.B. *Thermodynamic Properties of Individual Substances*, $4^{th}$ ed., Vol. 1, Part 1-2. Hemisphere Publishing Corporation, New York, 1989.

[148] Haagen-Smit A.J. *Chemistry and Physiology of Los Angeles Smog.* Industrial Engineering Chemistry, Vol. 44, pp. 1342–1346, 1952.

[149] Hallbäck M., Johansson A.V. and Burden A.D. *The basics of turbulence modelling.* In Turbulence and Transition Modelling; Lecture notes from the ERCOFTAC/IUTAM Summerschool held in Stockholm, 12–20 June, 1995, M. Hallbäck, D. Henningson, A. Johansson, and P. Alfredsson, editors, ERCOFTAC Series. Kluwer Academic Publishers, Dordrecht, 1996, Chapter 3, pp. 81–154.

[150] Hallmann M., Scheurlen M. and Wittig S. *Computation of turbulent evaporating sprays: Eulerian versus Lagrangian approach.* ASME Journal of Engineering for Gas Turbines and Power, Vol. 117, No. 1, pp. 112–119, 1995.

[151] Halstead M.P., Kirsch L.J., Prothero A. and Quinn C.P. *A Mathematical Model for Hydrocarbon Autoignition at High Pressures.* Proceedings, of the Royal Society, Vol. A 346, pp. 515–538, 1975.

[152] Halstead M.P., Kirsch L.J. and Quinn C.P. *The Autoignition of Hydrocarbon Fuels at High Temperatures and Pressures - Fitting of a Mathematical Model.* Combustion and Flame, Vol. 30, pp. 45–60, 1977.

[153] Hankinson R.W. and Thomson G.H. *A New Correlation for Saturated Densities of Liquids and Their Mixtures.* AIChE Journal, Vol. 25, No. 4, pp. 653–663, 1979.

[154] Hanna O.T. and Sandall O.C. *Heat Transfer in Turbulent Pipe Flow for Liquids Having a Temperature-Dependent Viscosity.* ASME Journal of Heat Transfer, Vol. 100, pp. 224–229, 1978.

[155] Han Z. and Reitz R.D. *A Temperature Wall Function Formulation for Variable-Density Turbulent Flows with Application to Engine Convective Heat Transfer Modeling.* International Journal of Heat and Mass Transfer, Vol. 40, No. 3, pp. 613–625, 1997.

[156] Han Z., Uludogan A., Hampson G.J. and Reitz R.D. *Mechanism of Soot and $NO_x$ Emission Reduction using Multiple-Injection in a Diesel Engine.* SAE Technical Paper Series, No. 960633, 1996.

[157] Harlow F.H. and Amsden A.A. *Numerical Calculation of Multiphase Fluid Flow.* Journal of Computational Physics, Vol. 17, pp. 19–52, 1975.

[158] Haselman L.C. and Westbrook C.K. *A Theoretical Model for Two-Phase Fuel Injection in Stratified Charge Engines.* SAE Technical Paper Series, No. 780318, 1978.

[159] Hassid S. and Poreh M. *A Turbulent Energy Dissipation Model for Flows With Drag Reduction.* ASME Journal of Fluids Engineering, Vol. 100, pp. 107–112, 1978.

[160] Haworth D.C. and Jansen K. *Large-eddy simulation on unstructured deforming meshes: towards reciprocating IC engines.* Computers & Fluids, Vol. 29, No. 5, pp. 493–524, 2000.

[161] Haynes B.S. and Wagner H.G. *Soot Formation.* Progress in Energy and Combustion Science, Vol. 7, pp. 229–273, 1981.

[162] Hentschel W. *Modern Tools for Diesel Engine Combustion Investigation.* Twenty-Sixth Symposium (International) on Combustion, The Combustion Institute, pp. 2503–2515, 1996.

[163] Hergart C., Barths H. and Peters N. *Using Representative Interactive Flamelets in Three-Dimensional Modeling of the Diesel Combustion Process Including Effects of Heat Transfer.* In 10th International Multidimensional Engine Modeling User's Group Meeting, Detroit, Michigan, USA, March 5, 2000.

[164] Hestenes M.R. and Stiefel E.L. *Method of Conjugate Gradients for Solving Linear Systems.* National Bureau of Standards, Journal of Research, Vol. 29, pp. 409–436, 1952.

[165] Hewson J.C. and Bollig M. *Reduced Mechanisms for $NO_x$ Emissions from Hydrocarbon Diffusion Flames.* Twenty-Sixth Symposium (International) on Combustion, The Combustion Institute, pp. 2171–2179, 1996.

[166] Heyerichs K. and Pollard A. *Heat transfer in separated and impinging turbulent flows.* International Journal of Heat and Mass Transfer, Vol. 39, No. 12, pp. 2385–2400, 1996.

[167] Heywood J.B. *Internal Combustion Engine.* Automotive Technology Series. McGraw-Hill Book Company, New York, 1988.

[168] High Fuel-Efficient Diesel Engine with Significantly Increased Peak Pressure (HEDE). *Periodic Progress Report, 12 Months.* Contract No. BRPR-CT97-0451, Project No. BE 96-3929, August 1997 – July 1998.

[169] High Fuel-Efficient Diesel Engine with Significantly Increased Peak Pressure (HEDE). *HEDE Project Meeting Minutes, Athens, Greece.* Contract No. BRPR-CT97-0451, Project No. BE 96-3929, 8–9 September, 1999.

[170] High Fuel-Efficient Diesel Engine with Significantly Increased Peak Pressure (HEDE). *HEDE Project Meeting Minutes, Bradford, United Kingdom.* Contract No. BRPR-CT97-0451, Project No. BE 96-3929, 23–24 March, 2000.

[171] High Fuel-Efficient Diesel Engine with Significantly Increased Peak Pressure (HEDE). *HEDE Project Meeting Minutes, Bad Boll, Germany.* Contract No. BRPR-CT97-0451, Project No. BE 96-3929, 28–29 September, 2000.

[172] Hill S.C. and Smoot L.D. *Modeling of nitrogen oxides formation and destruction in combustion systems.* Progress in Energy and Combustion Science, Vol. 26, No. 4-6, pp. 417–458, 2000.

[173] Hinze J.O. *Fundamentals of the Hydrodynamic Mechanism of Splitting in Dispersion Processes.* AIChE Journal, Vol. 1, No. 3, pp. 289–295, 1955.

[174] Hinze J.O. *Turbulence,* 2nd ed. McGraw-Hill Book Company, Inc., New York, 1975.

[175] Hiraiwa T., Ono N. and Niioka T. *High-Pressure Combustion Characteristics of Liquid Fuel in the Stagnation-Point Flow.* Twenty-Fourth Symposium (International) on Combustion, The Combustion Institute, pp. 239–245, 1992.

[176] Hiroyasu H. *Diesel Engine Combustion and Its Modeling.* In International Symposium on Diagnostics and Modeling of Combustion in Reciprocating Engines, COMODIA 85, Tokyo, Japan, The Japan Society of Mechanical Engineers, pp. 53–75, 4-6 Sept., 1985.

[177] Hiroyasu H. and Kadota T. *Fuel Droplet Size Distribution in Diesel Combustion Chamber.* SAE Technical Paper Series,, No. 740715, 1974.

[178] Hiroyasu H., Kadota T. and Arai M. *Development and Use of a Spray Combustion Modeling to Predict Diesel Engine Efficiency and Pollutant Emissions, Part 1: Combustion Modeling.* Bulletin of the JSME, Paper No. 214-12, Vol. 26, No. 214, pp. 569–575, April, 1983.

[179] Hiroyasu H., Shimizu M. and Arai M. *The Breakup of a High Speed Jet in a High Pressure Gaseous Atmosphere.* In Proceedings of the Second International Conference on Liquid Atomization and Spray Systems, ICLASS-82, Univ. of Wisconsin, Madison, WI, USA, pp. 69–74, 1982.

[180] Hirsch C. *Numerical Computation of Internal and External Flows,* Vol. 2. John Wiley & Sons, Chichester, 1990.

[181] Hishida M., Nagano Y. and Tagawa M. *Transport Processes of Heat and Momentum in the Wall Region.* In Heat Transfer 1986, Proceedings of The Eighth International Heat Transfer Conference, San Francisco, CA, USA, August 17-22, 1986, Washington, C. Tien, V. Carey, and J. Ferrell, editors, Vol. 3, Hemisphere Publishing Corporation, pp. 925–930, 1986.

[182] Hohenberg G.F. *Advanced approaches for heat transfer calculations.* SAE Technical Paper Series, Vol. 88, No. 790825, pp. 2788–2806, 1979.

[183] Hohmann S, Klingsporn M. and Renz U. *An Improved Model to Describe Spray Evaporation Under Diesel-Like Conditions.* SAE Technical Paper Series, No. 960630, 1996.

[184] Hong C.W. and Tarng S.D. *Direct measurement and computational analysis of turbulence length scales of a motored engine.* Experimental Thermal and Fluid Science, Vol. 16, pp. 277–285, 1998.

[185] Horrocks R.W. *Light-duty diesels – an update on the emissions challenge.* In Journal of Automotive Engineering, London, UK, Vol. 208, Proceedings of the Institute of Mechanical Engineers, pp. 249–255, 1994.

[186] Hountalas D.T. and Anestis A. *Effect of pressure transducer position on measured cylinder pressure diagram of high speed diesel engines.* Energy Conversion and Management, Vol. 39, No. 7, pp. 589–607, 1998.

[187] Hsiang L.P. and G.M. Faeth. *Near-Limit Drop Deformation and Secondary Breakup.* International Journal of Multiphase Flow, Vol. 18, No. 3, pp. 634–652, 1992.

[188] Hsieh K.-C., Shuen J.-S. and Yang V. *Numerical Study of Multicomponent Droplet Vaporization at Near Critical Conditions.* In AIAA 26th Aerospace Sciences Meeting, AIAA Paper 88-0637, Reno, NV, 11-14 Jan., 1988.

[189] Hsieh K.-C., Shuen J.-S. and Yang V. *Droplet Vaporization In High-Pressure, Environments, I: Near Critical Conditions.* Combustion Science and Technology, Vol. 76, pp. 111–132, 1991.

[190] Hüppelshäuser H. *Experimentelle Untersuchung der Strömung und des Wärmeübergangs im Kolbenmotor.* Ph.D. thesis, Rheinisch-Westfälische Technische Hochschule Aachen, Fortschritt-Berichte VDI, Reihe 6: Energieerzeugung, No. 278, Düsseldorf, May, 1992.

[191] Huh K.Y., Chang I.-P. and Martin J.K. *A Comparison of Boundary Layer Treatments for Heat Transfer in IC Engines.* SAE Technical Paper Series, No. 900252, 1990.

[192] Huh K.Y. and Gosman A.D. *A phenomenological model of diesel spray atomization.* In Proceedings of The International Conference on Multiphase Flows, Tsukuba, Vol. 2, pp. 515–518, 1991.

[193] Iacovides H. and Launder B.E. *PSL – An Economical Approach to the Numerical Analysis of Near-Wall, Elliptic Flow.* ASME Journal of Fluids Engineering, Vol. 106, pp. 241–242, 1984.

[194] Ikegami M. *Role of Flows and Turbulent Mixing in Combustion and Pollutant Formation in Diesel Engines.* In Proceedings of the International Symposium on Diagnostics and Modeling of Combustion in Internal Combustion Engines,

COMODIA 90, Kyoto, Japan, Engine Systems Division, The Japan Society of Mechanical Engineers, pp. 49–58, 3-5 September, 1990.

[195] Ikegami M., Kidoguchi Y. and Nishiwaki K. *A Multidimensional Model Prediction of Heat Transfer in Non-fired Engines.* SAE Technical Paper Series, No. 860467, 1986.

[196] Ikonomou E. *A Computational Study of Diesel Sprays and Combustion.* Ph.D. thesis, Imperial College of Science, Technology and Medicine, University of London, October, 1995.

[197] Incropera F.P. and DeWitt D.P. *Fundamentals of Heat and Mass Transfer,* $4^{th}$ ed. John Wiley & Sons, Inc., New York, 1996.

[198] Ishii M. *Two-Fluid Model for Two-Phase Flow.* In Multiphase Science and Technology, G. Hewitt, J. Delhaye, and N. Zuber, editors, Vol. 5. Hemisphere Publishing Corporation, New York, 1990, Chapter 1, pp. 1–63.

[199] Issa R.I. *Solution of the Implicitly Discretised Fluid Flow Equations by Operator-Splitting.* Journal of Computational Physics, Vol. 62, pp. 40–65, 1985.

[200] Isshiki N. and Nishiwaki N. *Study on Laminar Heat Transfer of Inside Gas with Cyclic Pressure Change on an Inner Wall of a Cylinder Head.* In Heat Transfer 1970, Papers presented at the Fourth International Heat Transfer Conference, Paris-Versaille, Section FC 3.5, U. Grigull and E. Hahn, editors, Elsevier Publishing Company, pp. 1–10, 1970.

[201] Janicka J. and Peters N. *Prediction of Turbulent Jet Diffusion Flame Lift-Off Using a PDF Transport Equation.* Nineteenth Symposium (International) on Combustion, The Combustion Institute, pp. 367–374, 1982.

[202] Jayatilleke C.L.V. *The Influence of Prandtl Number and Surface Roughness on the Resistance of the Laminar Sub-layer to Momentum and Heat Transfer,* $1^{st}$ ed., Vol. 1 of Progress in Heat and Mass Transfer. Pergamon Press Inc., 1969, pp. 193–329.

[203] Jennings M.J. and Morel T. *An Improved Near Wall Heat Transfer Model for Multidimensional Engine Flow Calculations.* SAE Technical Paper Series, No. 900251, 1990.

[204] Jennings M.J. and Morel T. *A Computational Study of Wall Temperature Effects on Engine Heat Transfer.* SAE Technical Paper Series, No. 910459, 1991.

[205] Jia H. and Gogos G. *Investigation of Liquid Droplet Evaporation in Subcritical and Supercritical Gaseous Environments.* Journal of Thermophysics and Heat Transfer, Vol. 6, pp. 738–745, 1992.

[206] Jia H. and Gogos G. *High Pressure Droplet Vaporization; Effects of Liquid-Phase Gas Solubility.* International Journal of Heat and Mass Transfer, Vol. 36, No. 18, pp. 4419–4431, 1993.

[207] Jia H. and Gogos G. *Droplet Vaporization in Subcritical and Supercritical Environments; High Versus Low Pressure Modelling.* Acta Astronautica, Vol. 32, No. 2, pp. 121–129, 1994.

[208] Jiang T.L. and Chiang W.-T. *Droplet Vaporization in Expansible Dense Sprays at Sub- and Supercritical Conditions.* Atomization and Sprays, Vol. 4, No. 5, pp. 523–549, 1994.

[209] Jiang T.L. and Chiang W.-T. *Effects of Multiple Droplet Interaction on Droplet Vaporization in Subcritical and Supercritical Pressure Environments.* Combustion and Flame, Vol. 97, pp. 17–34, 1994.

[210] Jin J.D. and Borman G.L. *A Model for Multicomponent Droplet Vaporization at High Ambient Pressures.* SAE Technical Paper Series, No. 850264, 1985.

[211] Jones A.R. *Light scattering for particle characterization.* Progress in Energy and Combustion Science, Vol. 25, pp. 1–53, 1999.

[212] Jones W.P. and Launder B.E. *The Prediction of Laminarization with a Two-Equation Model of Turbulence.* International Journal of Heat and Mass Transfer, Vol. 15, pp. 301–314, 1972.

[213] Jones W.P. and Launder B.E. *The Calculation of Low-Reynolds-Number Phenomena with a Two-Equation Model of Turbulence.* International Journal of Heat and Mass Transfer, Vol. 16, pp. 1119–1130, 1973.

[214] Jones W.P. and Lindstedt R.P. *Global Reaction Schemes for Hydrocarbon Combustion.* Combustion and Flame, Vol. 73, pp. 233–249, 1988.

[215] Jones W.P. and Whitelaw J.H. *Calculation Methods for Reacting Turbulent Flows: A Review.* Combustion and Flame, Vol. 48, pp. 1–26, 1982.

[216] Kadota T. and Hiroyasu H. *Combustion of a Fuel Droplet in Supercritical Gaseous Environments.* Eighteenth Symposium (International) on Combustion, The Combustion Institute, pp. 275–282, 1988.

[217] Kamimoto T. *Diagnostics of Transient Sprays by Means of Laser Sheet Techniques.* In Proceedings of the International Symposium on Diagnostics and Modeling of Combustion in Internal Combustion Engines, COMODIA 94, Yokohama, Japan, Engine Systems Division, The Japan Society of Mechanical Engineers, pp. 33–41, 11-14 July, 1994.

[218] Kamimoto T. and Kobayashi H. *Combustion Processes in Diesel Engines.* Progress in Energy and Combustion Science, Vol. 17, No. 2, pp. 163–189, 1991.

[219] Kamimoto T., Yagita M., Moriyoshi Y., Kobayashi H. and Morita H. *An Experimental Study of In-Cylinder Air Flow with a Transparent Cylinder Engine.* JSME International Journal, Series II, Vol. 31, No. 1, pp. 150–157, 1988.

[220] Karlsson A., Magnusson I., Balthasar M. and Mauss F. *Simulation of Soot Formation Under Diesel Engine Conditions Using a Detailed Kinetic Soot Model.* SAE Technical Paper Series, No. 981022, 1998.

[221] Kasagi N., Tomita Y. and Kuroda A. *Direct Numerical Simulation of Passive Scalar Field in a Turbulent Channel Flow.* ASME Journal of Heat Transfer, Vol. 114, pp. 598–606, 1992.

[222] Kawatani T., Mori K., Fukano I., K. Sugawara and T. Koyama. *Technology for Meeting the 1994 USA Exhaust Emission Regulations in Heavy-Duty Engine.* SAE Technical Paper Series, No. 932654, 1993.

[223] Kays W.M. and Crawford M.E. *Convective Heat and Mass Transfer*, 3rd ed. McGraw-Hill Book Company, New York, 1993.

[224] Kazakov A. and Frenklach M. *Dynamic Modeling of Soot Particle Coagulation and Aggregation: Implementation With the Method of Moments and Application to High-Pressure Laminar Premixed Flames.* Combustion and Flame, Vol. 114, pp. 484–501, 1998.

[225] Kellerer H., Koch R. and Wittig S. *Measurements of the Growth and Coagulation of Soot Particles in a High-Pressure Shock Tube.* Combustion and Flame, Vol. 120, No. 1-2, pp. 188–199, 2000.

[226] Kennedy I.M. *Models of Soot Formation and Oxidation.* Progress in Energy and Combustion Science, Vol. 23, No. 2, pp. 95–132, 1997.

[227] Kennedy I.M., Kollmann W. and Chen J.-Y. *A Model for Soot Formation in a Laminar Diffusion Flame.* Combustion and Flame, Vol. 81, pp. 73–85, 1990.

[228] Kershaw D.S. *The incomplete Cholesky conjugate gradient method for the iterative solution of systems of linear equations.* Journal of Computational Physics, Vol. 26, pp. 43–65, 1978.

[229] Khalil E.E. and Whitelaw J.H. *Aerodynamic and Thermodynamic Characteristics of Kerosene Spray Flames.* Sixteenth Symposium (International) of Combustion, The Combustion Institute, pp. 569–576, 1977.

[230] Khan I.M., Greeves G. and Probert D.M. *Air Pollution Control in Transport Engines.* Proceedings of the Institution of Mechanical Engineers, Vol. C142/71, pp. 205–217, 1971.

[231] Khan I.M. and Greeves G. *A method for calculating the formation and combustion of soot in Diesel engines.* In Heat Transfer in Flames, N. Afgan and J. Beer, editors, Advances in Thermal Engineering. John Wiley & Sons, New

York, 1974, Chapter 25, Part II: Heat Transfer in Unsteady Confined Flames, pp. 389–404.

[232] Khan I.M., Wang C.H.T. and Langridge B.E. *Coagulation and Combustion of Soot Particles in Diesel Engines.* Combustion and Flame, Vol. 17, pp. 409–419, 1971.

[233] Kim J. and Moin P. *Transport of Passive Scalars in a Turbulent Channel Flow.* In Sixth International Symposium on Turbulent Shear Flows, Toulouse, 7-9 Sept., 1987.

[234] Kim J.S. and Williams F.A. *Structures of flow and mixture-fraction fields for counterflow diffusion flames with small stoichiometric mixture fractions.* SIAM Journal on Applied Mathematics, Vol. 53, No. 6, pp. 1551–1566, 1993.

[235] King C. *Separation Processes,* $2^{nd}$ ed. McGraw-Hill Book Company, New York, 1980.

[236] Kittelson D.B. *Engines and nanoparticles: a review.* Journal of Aerosol Science, Vol. 29, No. 5-6, pp. 575–588, 1998.

[237] Klingsporn M. and Renz U. *Vaporization of a Binary Unsteady Spray at High Temperature and High Pressure.* International Journal of Heat and Mass Transfer, Vol. 37, Suppl. 1, pp. 265–272, 1994.

[238] Knapp H., Döring R., Oellrich L., Plöcker U. and Prausnitz J.M. *Vapor-liquid equilibria for mixtures of low boiling substances.* In Chemistry Data Series, D. Behrens and R. Eckermann, editors, Vol. VI. DECHEMA, Deutsche Gesellschaft für Chemisches Apparatewesen, Frankfurt, 1982.

[239] Kobayashi H., Yagita M., Kamimoto T. and Matsuoka S. *Prediction of Transient Diesel Sprays in Swirling Flows Via a Modified 2-D Model.* SAE Technical Paper Series, No. 860332, 1986.

[240] Kong S.C., Han Z. and Reitz R.D. *The Development and Application of a Diesel Ignition and Combustion Model for Multidimensional Engine Simulation.* SAE Technical Paper Series, No. 950278, 1995.

[241] Kong S.-C. and Reitz R.D. *Modelling Engine Spray Combustion Processes.* In Progress in Astronautics and Aeronautics, K. Kuo, editor, Vol. II of Recent Advances in Spray Combustion, pp. 395–424, 1996.

[242] Koss H.J. and Brüggemann D. *Results from fuel/air ratio measurements in an n-heptane injection spray.* In Periodic Report No. 7 for the Period 01.01.1992 – 30.06.1992, K.-P. Schindler, editor. IDEA, Subprogramme A2, Rheinisch Westfälische Technische Hochschule, Aachen, 1993, pp. 117–124.

[243] Koss H.J., Brüggemann D., Wiartalla A., Bäcker H. and Breuer A. *Results from fuel/air ratio measurements in an n-heptane injection spray.* In Eighth Periodic Report for the Period 01.07.1992 – 31.12.1992, K.-P. Schindler, editor. IDEA, Subprogramme A2, Rheinisch Westfälische Technische Hochschule, Aachen, May, 1993.

[244] Kouremenos D.A., Rakopoulos C.D., Hountalas D. and Kotsiopoulos P. *A Digital-Simulation of the Exhaust Nitric-Oxide and Soot Formation Histories in the Combustion-Chambers of a Swirl Chamber Diesel-Engine.* Forschung im Ingenieurwesen - Engineering Research, Vol. 56, No. 1, pp. 22–32, 1990.

[245] Kouremenos D.A., Rakopoulos C.D. and Yfantis E.A. *A Fortran program for calculating the evaporation rates in diesel-engine fuel sprays.* Advances in Engineering Software, Vol. 15, No. 1, pp. 67–71, 1992.

[246] Kralj C. *Numerical Simulation of Diesel Spray Processes.* Ph.D. thesis, Imperial College of Science, Technology and Medicine, University of London, October, 1995.

[247] Krüger C., Otto F., Wirbeleit F., Willand J. and Peters N. *Incorporation of the Interactive Cross-Sectional Average Methodology for Diesel Spray Simulations into a 3D-Code.* In Proceedings of the $9^{th}$ International Multidimensional Engine Modeling User's Group Meeting at the SAE Congress, Detroit, Michigan, USA, Silicon Graphics Inc. and University of Wisconsin, Engine Research Center, 28 Febr., 1999.

[248] Kummer C. *Private Communication.* Forschungsinstitut Fahrzeugtechnik, Hochschule für Technik und Wirtschaft, Dresden, 1998-2000.

[249] Kuo K.K. *Principles of Combustion.* John Wiley & Sons, Inc., New York, 1986.

[250] Kyriakides S.C., Dent J.C. and Mehta P.S. *Phenomenological Diesel Combustion Model Including Smoke and NO Emissions.* SAE Technical Paper Series, No. 860330, 1986.

[251] Lam C.K.G. and Bremhorst K.A. *Modified Form of the $k - \varepsilon$ Model for Predicting Wall Turbulence.* ASME Journal of Fluids Engineering, Vol. 103, pp. 456–460, 1981.

[252] Lange F. *Berechnung des Strömungsfeldes und der Wärmeübertragung im Zylinder eines geschleppten Motors.* Diploma thesis, Institut für Wärmeübertragung und Klimatechnik, Rheinisch-Westfälische Technische Hochschule Aachen, 1993.

[253] Lapuerta M., Armas O. and Hernández J.J. *Diagnosis of DI Diesel combustion from in-cylinder pressure signal by estimation of mean thermodynamic properties of the gas.* Applied Thermal Engineering, Vol. 19, No. 5, pp. 513–529, 1999.

[254] Latini G. and Baroncini C. *Effect of temperature and pressure on thermal conductivity of organic liquids.* High Temperatures – High Pressures, Vol. 15, No. 4, pp. 407–411, 1983.

[255] Laufer T. *Private Communication.* DaimlerChrysler, Engine Research Department, 20 June, 2000.

[256] Launder B.E. *Numerical computation of convective heat transfer in complex turbulent flows: time to abandon wall functions?* International Journal of Heat and Mass Transfer, Vol. 27, No. 9, pp. 1485–1491, 1984.

[257] Launder B.E. *On the Computation of Convective Heat Transfer in Complex Turbulent Flows.* ASME Journal of Heat Transfer, Vol. 110, pp. 1112–1128, 1988.

[258] Launder B.E. and Sharma B.I. *Application of the Energy-Dissipation Model of Turbulence to the Calculation of Flow near a Spinning Disc.* Letters in Heat and Mass Transfer, Vol. 1, No. 2, pp. 131–137, 1974.

[259] Launder B.E. and Spalding D.B. *The Numerical Computation of Turbulent Flows.* Computer Methods in Applied Mechanics and Engineering, Vol. 3, pp. 269–289, 1974.

[260] Lavoie G.A., Heywood J.B. and Keck J.C. *Experimental and Theoretical Investigation of Nitric Oxide Formation in Internal Combustion Engines.* Combustion Science and Technology, Vol. 1, pp. 313–326, 1970.

[261] Law C.K. *Recent advances in droplet vaporization and combustion.* Progress in Energy and Combustion Science, Vol. 8, pp. 171–201, 1982.

[262] Le Bas G. *The Molecular Volumes of Liquid Chemical Compounds.* Longmans, Green, New York, 1915.

[263] Lebrère L. and Dillies B. *Engine Flow Calculations Using a Reynolds Stress Model in the Kiva-II Code.* SAE Technical Paper Series, No. 960636, 1996.

[264] Leduc J.-F. and Karlsson J.A.J. *Comparison between Different Atomization Models and Experimental Data.* In ICLASS-94, Rouen, France, 18-22 July, 1994.

[265] Lee T.-W. and Faeth G.M. *Structure and Mixing Properties of Combusting Monopropellant Sprays.* Journal of Propulsion and Power, Vol. 8, No. 2, pp. 271–279, 1992.

[266] Lee K.B., Thring M.W. and Beér J.M. *On the Rate of Combustion of Soot in a Laminar Soot Flame.* Combustion and Flame, Vol. 6, pp. 137–145, 1962.

[267] Lei J.-F. and Will H.A. *Thin-film thermocouples and strain-gauge technologies for engine applications.* Sensors and Actuators, A: Physical, Vol. 65, No. 2–3, pp. 187–193, 1998.

[268] Leskovšek D. *Predictions of Combustion in Spark-Ignition Engines.* Ph.D. thesis, Imperial College of Science, Technology & Medicine, University of London, July, 1996.

[269] Letsou A. and Stiel L.I. *Viscosity of Saturated Nonpolar Liquids at Elevated Pressures.* AIChE Journal, Vol. 19, No. 2, pp. 409–411, 1973.

[270] Leung K.M., Lindstedt R.P. and Jones W.P. *A Simplified Reaction Mechanism for Soot Formation in Nonpremixed Flames.* Combustion and Flame, Vol. 87, pp. 289–305, 1991.

[271] Libby P.A. and Williams F.A. *Chapter 1: Fundamental Aspects.* In Turbulent Reacting Flows, P. Libby and F. Williams, editors, Vol. 44 of Topics in Advanced Physics, pp. 1-43. Springer-Verlag, Berlin, 1980.

[272] Lindstedt P. *A simple reaction mechanism for soot formation in non-premixed flames.* In Aerothermodynamics in Combustors: IUTAM Symposium, Taipei, Taiwan, 3-5 June 1991, Berlin, R. Lee, J. Whitelaw, and T. Wung, editors, Springer-Verlag, pp. 145–156, 1992.

[273] Lindstedt P.R. *Simplified soot nucleation and surface growth steps for non-premixed flames.* In Soot Formation in Combustion, Berlin, H. Bockhorn, editor, Springer-Verlag, pp. 417–439, 1994.

[274] Liu Y. and Reitz R.D. *Modeling of heat conduction within chamber walls for multidimensional internal combustion engine simulations.* International Journal of Heat and Mass Transfer, Vol. 41, No. 6-7, pp. 859–869, 1998.

[275] Lucas K. *Die Druckabhängigkeit der Viskosität von Flüssigkeiten – eine einfache Abschätzung.* Chemie Ingenieur Technik, Vol. 53, No. 12, pp. 959–960, 1981.

[276] Lyford-Pike E.J. and Heywood J.B. *Thermal boundary layer thickness in the cylinder of a spark-ignition engine.* International Journal of Heat and Mass Transfer, Vol. 27, No. 10, pp. 1873–1878, 1984.

[277] Lykov A.V. and Mikhailov Y.A. *Theory of Heat and Mass Transfer.* Israel Program for Scientific Translations, Jerusalem, 1965. (Translation of: Teoriya Teplo- I Massoperenosa, Gosudarstvennoe energeticheskoe izdatel'stvo, Moskva-Leningrad, 1963).

[278] Macleod D.B. *On a relation between surface tension and density.* Transactions of the Faraday Society, Vol. 19, pp. 38–42, 1923.

[279] Magnussen B.F. and Hjertager B.H. *On Mathematical Modeling of Turbulent Combustion with Special Emphasis on Soot Formation and Combustion.* Sixteenth Symposium (International) on Combustion, The Combustion Institute, pp. 719–729, 1976.

[280] Majer V. and Svoboda V. *Enthalpies of Vaporization of Organic Compounds: A Critical Review and Data Compilation.* Blackwell Scientific Publications, Oxford, 1985.

[281] Maly R.R., Stapf P. and König G. *Progress in Soot Modeling for Engines.* In The Fourth International Symposium on Diagnostics and Modeling of Combustion in Internal Combustion Engines, COMODIA 98, Kyoto, Japan, Engine Systems Division, The Japan Society of Mechanical Engineers, pp. 25–34, 20-23 July, 1998.

[282] Mao C.-P., Wakamatsu Y. and Faeth G.M. *A Simplified Model of High Pressure Spray Combustion.* Eighteenth Symposium (International) on Combustion, The Combustion Institute, pp. 337–347, 1981.

[283] Marble F.E. and Broadwell J.F. *The Coherent Flame Model For Turbulent Chemical Reactions.* SQUID Report; Technical Report TRW-9-PU, Purdue University, 1977.

[284] Matlosz R.L., Leipziger S. and Torda T.P. *Investigation of liquid drop evaporation in a high-temperature and high-pressure environment.* International Journal of Heat and Mass Transfer, Vol. 15, pp. 831–852, 1972.

[285] Mauss F. *Entwicklung eines kinetischen Modells der Rußbildung mit schneller Polymerisation.* Ph.D. thesis, RWTH Aachen, Aachen, Germany, 1997.

[286] Mauss F. and Bockhorn H. *Soot Formation in Premixed Hydrocarbon Flames: Prediction of Temperature and Pressure Dependence.* Zeitschrift für Physikalische Chemie, Vol. 188, pp. 45–60, 1995.

[287] Mauss F., Keller D. and Peters N. *A Lagrangian Simulation of Flamelet Extinction and Re-Ignition in Turbulent Jet Diffusion Flames.* Twenty-Third Symposium (International) on Combustion, The Combustion Institute, pp. 693–698, 1990.

[288] Mauss F., Schäfer T. and Bockhorn H. *Inception and Growth of Soot Particles in Dependence on the Surrounding Gas-Phase.* Combustion and Flame, Vol. 99, pp. 697–705, 1994.

[289] Mauss F., Trilken B., Breitbach H. and Peters N. *Soot formation in partially premixed diffusion flames.* In Soot Formation in Combustion, Berlin, H. Bockhorn, editor, Springer-Verlag, pp. 325–349, 1994.

[290] Merryman E.L. and Levy A. *Nitrogen oxide formation in flames: The role of $NO_2$ and fuel nitrogen.* Fifteenth Symposium (International) on Combustion, The Combustion Institute, pp. 1073–1083, 1975.

[291] Miller D.G. *Graphical Methods for determining a nonlinear constant in vapor pressure equations.* Industrial and Engineering Chemistry Fundamentals, Vol. 2, No. 1, pp. 68–73, 1963.

[292] Miller J.A. and Bowman C.T. *Mechanism and modelling of nitrogen chemistry in combustion.* Progress in Energy and Combustion Science, Vol. 15, pp. 287–338, 1989.

[293] Miller J.A. and Melius C.F. *Kinetic and Thermodynamic Issues in the Formation of Aromatic Compounds in Flames of Aliphatic Fuels.* Combustion and Flame, Vol. 91, pp. 21–39, 1992.

[294] Milton B.E. *Thermodynamics, Combustion and Engines,* 1$^{st}$ ed. Chapman & Hall, London, 1995.

[295] Missenard F.A. *Conductivité thermique des liquides organiques d'une série ou d'un "groupe de liquides".* Révue Générale de Thermique, Vol. 9, No. 101, pp. 649–660, May, 1970.

[296] Missenard F.A. *A propos de la conductivité thermique des séries de liquides organiques.* Révue Générale de Thermique, Vol. 12, No. 141, pp. 751–759, Sept., 1973.

[297] Missenard A. *Conductivité thermique des solides, liquides, gaz, et de leurs mélanges.* Editions Eyrolles, Paris, 1965.

[298] Miwa K., Ohmija T. and Nishitani T. *A Study of the Ignition Delay of Diesel Fuel Spray Using a Rapid Compression Machine.* JSME International Journal, Series II, Vol. 31, No. 1, pp. 166–173, 1988.

[299] Miyamoto N., Ogawa H., Shibuya M., Arai K. and Esmilaire O. *Influence of the Molecular Structure of Hydrocarbon Fuels on Diesel Exhaust Emissions.* SAE Technical Paper Series, No. 940676, 1994.

[300] Monaghan M.L. *High-speed direct injection diesels – present and future perspectives.* In Lean Burn Combustion Engines, London, No. S433/012/96 in IMechE Seminar Publication 1996-20, The Institution of Mechanical Engineers, Mechanical Engineering Publications Ltd., pp. 189–199, 3-4 December, 1996.

[301] Moon Y.W., You Y.W., Kim Y.M. and Kim S.W. *Numerical Modeling for Evaporating Spray Dynamics in High-Pressure Environment.* In The Fourth International Symposium on Diagnostics and Modeling of Combustion in Internal Combustion Engines, COMODIA 98, Kyoto, Japan, Engine Systems Division, The Japan Society of Mechanical Engineers, pp. 417–422, 20-23 July, 1998.

[302] Morel T. and Keribar R.A. *A model for predicting spatially and time resolved convective heat transfer in bowl-in-piston combustion chambers.* SAE Technical Paper Series, No. 850204, 1985.

[303] Moss J.B., Stewart C.D. and Syed K.J. *Flowfield modelling of soot formation at elevated pressure.* Twenty-Second Symposium (International) on Combustion, The Combustion Institute, pp. 413–423, 1988.

[304] Moss J.B., Stewart C.D. and Young K.J. *Modeling Soot Formation and Burnout in a High Temperature Laminar Diffusion Flame Burning under Oxygen-Enriched Conditions.* Combustion and Flame, Vol. 101, No. 4, pp. 491–500, 1995.

[305] Mostafa A.A. and Mongia H.C. *On the Modeling of Turbulent Evaporating Sprays: Eulerian Versus Lagrangian Approach.* International Journal of Heat and Mass Transfer, Vol. 30, pp. 2583–2593, 1987.

[306] Mühlbauer A.L. and Raal J.D. *Computation and thermodynamic interpretation of high-pressure vapour-liquid equilibrium — a review.* The Chemical Engineering Journal, Vol. 60, pp. 1–29, 1995.

[307] Müller U.C. and Peters N. *Development of Reduced Reaction Schemes for the Ignition of Diesel Fuels in a Non-Premixed Turbulent Flow Field. Subprogramme B2.* CEC/NUTEK/JCR IDEA Project (JOUE-0008-D), Final Report, January, 1993.

[308] Müller U.C., Peters N. and Liñán A. *Global Kinetics For n-Heptane Ignition at High Pressures.* Twenty-Fourth Symposium (International) on Combustion, The Combustion Institute, pp. 777–784, 1992.

[309] Musculus M.P. and Rutland C.J. *Coherent Flamelet Modelling of Diesel Engine Combustion.* Combustion Science and Technology, Vol. 104, pp. 295–337, 1995.

[310] Naber J.D. and Siebers D.L. *Effects of Gas Density and Vaporization on Penetration and Dispersion of Diesel Sprays.* SAE Technical Paper Series, No. 960034, 1996.

[311] Nagle J. and Strickland-Constable R.F. *Oxidation of Carbon between 1000-2000° C.* In Proceedings of the Fifth Conference on Carbon, Pennsylvania State University, 1961, New York, Vol. 1 of Symposium Publications Division, Pergamon Press, pp. 154–164, 1962.

[312] Najjar Y.S.H. *Combustor liner temperatures in the gas turbine using heavy fuels.* Journal of the Institute of Energy, Vol. 55, pp. 187–194, 1982.

[313] Najjar Y.S.H. and Goodger E.M. *Soot oxidation in gas turbines using heavy fuels, 2.* Fuel, Vol. 60, pp. 987–990, October, 1981.

[314] N. V. Nederlandse Gasunie. *Physical Properties of Natural Gases.* Groningen, The Netherlands, 1980.

[315] Neufeld P.D., Janzen A.R. and Aziz R.A. *Empirical Equations to Calculate 16 of the Transport Collision Integrals $\Omega^{(l,s)^*}$ for the Lennard-Jones (12-6) Potential.* The Journal of Chemical Physics, Vol. 57, No. 3, pp. 1100–1102, 1972.

[316] Newman J.A. and Brzustowski T.A. *Behavior of a Liquid Jet near the Thermodynamic Critical Region.* AIAA Journal, pp. 1595–1602, 1971.

[317] Nicholls J. *Stream and Droplet Breakup by Shock Waves.* In NASA SP-194. Harrje, D.T. and Reardon, F.H., editors, 1972, pp. 126–128.

[318] Nigmatulin R.I. *Dynamics of Multiphase Media*, revised and augmented edition ed., Vol. 1. Hemisphere Publishing Corporation, New York, 1991. Originally published by Nauka Moscow under the title *Dinamika mnogofaznykh sred.*

[319] Nishida K. and Hiroyasu H. *Simplified Three-Dimensional Modeling of Mixture Formation and Combustion in a D.I. Diesel Engine.* SAE Technical Paper Series, No. 890269, 1989.

[320] Nishiwaki K. *Modeling Engine Heat Transfer and Flame-Wall Interaction.* In The Fourth International Symposium on Diagnostics and Modeling of Combustion in Internal Combustion Engines, COMODIA 98, Kyoto, Japan, Engine Systems Division, The Japan Society of Mechanical Engineers, pp. 35–44, 20-23 July, 1998.

[321] Nusselt W. *Der Wärmeübergang in der Verbrennungskraftmaschine.* Zeitschrift Verein Deutscher Ingenieure, Vol. 67, pp. 692–708, 1923.

[322] O'Rourke P.J. *Collective Drop Effects on Vaporizing Liquid Sprays.* Ph.D. thesis, University of Princeton, 1981.

[323] O'Rourke P.J. and Amsden A.A. *The TAB Method for Numerical Calculation of Spray Droplet Breakup.* SAE Technical Paper Series, No. 872089, 1987.

[324] Overbye V.D., Bennethum J.E., Uyehara O.A. and Myers P.S. *Unsteady Heat Transfer in Engines.* SAE Technical Paper Series, Vol. 69, pp. 461–494, 1961.

[325] Patankar S.V. *Numerical Heat Transfer and Fluid Flow.* Hemisphere Publishing Corporation, 1980.

[326] Patankar S.V. and Baliga B.R. *A new finite-difference scheme for parabolic differential equations.* Numerical Heat Transfer, Vol. 1, pp. 27–37, 1978.

[327] Patel V.C., Rodi W. and Scheuerer G. *Turbulence Models for Near-Wall and Low Reynolds Number Flows: A Review.* AIAA Journal, Vol. 23, No. 9, pp. 1308–1319, 1984.

[328] Patterson M.A., Kong S.C., Hampson G.J. and Reitz R.D. *Modeling the Effects of Fuel Injection Characteristics on Diesel Engine Soot and $NO_x$ Emissions.* SAE Technical Paper Series, No. 940523, 1994.

[329] Payri F., Desantes J.M. and Arrègle J. *Characterization of D.I. Diesel Sprays in High Density Conditions.* SAE Technical Paper Series, No. 960774, 1996.

[330] Peng D.-Y. and Robinson D.B. *A New Two-Constant Equation of State.* Industrial and Engineering Chemistry. Fundamentals, Vol. 15, No. 1, pp. 59–64, 1976.

[331] Perić M. *A Finite Volume Method for the Prediction of Three-Dimensional Flow in Complex Ducts.* Ph.D. thesis, Imperial College of Science, Technology & Medicine, University of London, August, 1985.

[332] Peters N. *Laminar Diffusion Flamelet Models in Non-Premixed Turbulent Combustion.* Progress in Energy and Combustion Science, Vol. 10, pp. 319–339, 1982.

[333] Peters N. *Laminar Flamelet Concepts in Turbulent Combustion.* Twenty-First Symposium (International) on Combustion, The Combustion Institute, pp. 1231–1250, 1987.

[334] Peters N. and Rogg B. *Reduced kinetic mechanisms for applications in combustion systems.* Lecture notes in physics. Springer-Verlag, Berlin, 1993.

[335] Pfahl U., Fieweger K. and Adomeit G. *Self-ignition of Diesel-relevant hydrocarbon-air mixtures under engine conditions.* Twenty-Sixth Symposium (International) of Combustion, The Combustion Institute, Vol. 1, pp. 781–789, 1996.

[336] Pflaum W. *Wärmeübergang bei Dieselmaschinen mit und ohne Aufladung.* Motortechnische Zeitschrift MTZ, Vol. 22, No. 3, p. 70, 1961.

[337] Pinchon P. *Modelling of Fluid Dynamics and Combustion in Piston Engines.* In Proceedings of the International Symposium on Diagnostics and Modeling of Combustion in Internal Combustion Engines, COMODIA 90, Kyoto, Japan, Engine Systems Division, The Japan Society of Mechanical Engineers, pp. 31–47, 3-5 September, 1990.

[338] Pischinger S. *Fahrzeugantriebe der Zukunft: Die Verbrennungskraftmaschine und ihre Alternativen.* Sonderheft 60 Jahre MTZ, Motortechnische Zeitschrift, pp. 10–14, 1999.

[339] Pitsch H., Barths H. and Peters N. *Three-Dimensional Modeling of $NO_x$ and Soot Formation in DI-Diesel Engines Using Detailed Chemistry Based on the Interactive Flamelet Approach.* SAE Technical Paper Series, No. 962057, 1996.

[340] Pitsch H., Chen M. and Peters N. *Unsteady Flamelet Modeling of Turbulent Hydrogen-Air Diffusion Flames.* Twenty-Seventh Symposium (International) on Combustion, The Combustion Institute, pp. 1057–1064, 1998.

[341] Pitsch H. and Peters N. *A Consistent Flamelet Formulation for Non-Premixed Combustion Considering Differential Diffusion Effects.* Combustion and Flame, Vol. 114, pp. 26–40, 1998.

[342] Pitsch H. and Peters N. *Investigation of the Ignition Process of Sprays Under Diesel Engine Conditions Using Reduced n-Heptane Chemistry.* SAE Technical Paper Series, No. 982464, 1998.

[343] Pitsch H., Wan Y.P. and Peters N. *Numerical Investigation of Soot Formation and Oxidation Under Diesel Engine Conditions.* SAE Technical Paper Series, No. 952357, 1995.

[344] Plee S.L. and Ahmad T. *Relative Roles of Premixed and Diffusion Burning in Diesel Combustion.* SAE Technical Paper Series, No. 831733, 1983.

[345] Pohlmann H.C. *Strömung und Wärmeübergang im Zylinder eines geschleppten Kolbenmotors.* Ph.D. thesis, Rheinisch-Westfälische Technische Hochschule Aachen, April, 1988.

[346] Pollutant Reduction In Diesel Engines (PRIDE). *2nd Periodic Progress Report.* Contract No. JOF3CT950011, September 1996 – February 1997.

[347] Pollutant Reduction In Diesel Engines (PRIDE). *Periodic Progress Report.* Contract No. JOF3CT950011, September 1997 – August 1998.

[348] Poplow F. *Numerical Calculation of the Transition from Subcritical Droplet Evaporation to Supercritical Diffusion.* International Journal of Heat and Mass Transfer, Vol. 37, pp. 485–492, 1994.

[349] Prausnitz J.M. and Chueh P.L. *Computer Calculations for High-Pressure Vapor-Liquid Equilibria.* Prentice-Hall, Inc., Englewood Cliffs, New Jersey, 1968.

[350] Press W.H., Flannery B.P., Teukolsky S.A. and Velterling W.T. *Numerical Recipes – The Art of Scientific Computing (FORTRAN Version).* Cambridge University Press, Cambridge, 1992.

[351] Quayle O.R. *The parachors of organic compounds: an interpretation and catalogue.* Chemical Reviews, Vol. 53, pp. 439–589, 1953.

[352] Raine R.R., Stone C.R. and Gould J. *Modeling of Nitric Oxide Formation in Spark Ignition Engines with a Multizone Burned Gas.* Combustion and Flame, Vol. 102, No. 3, pp. 241–255, 1995.

[353] Rakopoulos C.D. and Giakoumis E.G. *Simulation and exergy analysis of transient diesel-engine operation.* Energy, Vol. 22, No. 9, pp. 875–885, 1997.

[354] Ranz W.E. and Marshall, Jr. W.R. *Evaporation From Drops, Part I.* Chemical Engineering Progress, Vol. 48, No. 3, pp. 141–146, 1952.

[355] Ranz W.E. and Marshall, Jr. W.R. *Evaporation From Drops, Part II.* Chemical Engineering Progress, Vol. 48, No. 4, pp. 173–180, 1952.

[356] Redlich O. and Kwong J.N.S. *On the Thermodynamics of Solutions. V. An Equation of State. Fugacities of Gaseous Solutions.* Chemical Reviews, Vol. 44, pp. 233–244, 1949.

[357] Reid J.K. *On the Method of Conjugate Gradients for the Solution of Large Sparse Systems of Linear Equations.* In Large Sparse Sets of Linear Equations, J. Reid, editor. Academic Press, New York, 1971.

[358] Reid R.C., Prausnitz J.M. and Poling B.E. *The Properties of Gases and Liquids.* McGraw-Hill Book Company, New York, 1987.

[359] Reitz R.D. *Modeling Atomization Processes in High-Pressure Vaporizing Sprays.* Atmosation and Spray Technology, Vol. 3, pp. 309–337, 1987.

[360] Reitz R.D. and Bracco F.V. *Mechanism of Atomization of a Liquid Jet.* Physics of Fluids, Vol. 25, No. 10, pp. 1730–1742, 1982.

[361] Reitz R.D. and Bracco F.V. *Global Kinetics and Lack of Thermodynamic Equilibrium.* Combustion and Flame, Vol. 53, pp. 141–143, 1983.

[362] Reitz R.D. *Computational fluid dynamics.* In Diesel Engine Reference Book, B. Challen and R. Baranescu, editors, 2nd ed. Butterworth-Heinemann, Oxford, 1999, Part 2: Engine design practice. Chapter 7, pp. 153–171.

[363] Reitz R.D. and Diwakar R. *Effect of Drop Breakup on Fuel Sprays.* SAE Technical Paper Series, No. 860469, 1986.

[364] Reitz R.D. and Diwakar R. *Structure of High-Pressure Fuel Sprays.* SAE Technical Paper Series, No. 870598, 1987.

[365] Reitz R.D. and Rutland C.J. *Development and Testing of Diesel Engine CFD Models.* Progress in Energy and Combustion Science, Vol. 21, pp. 173–196, 1995.

[366] Reitz R.D. *Assessment of Wall Heat Transfer Models for Premixed-Charge Engine Combustion Computations.* SAE Technical Paper Series, No. 910267, 1991.

[367] Renksizbulut M., Bussmann M. and Li X. *A Droplet Vaporization Model for Spray Calculations.* Particle-Particle System Characterization, Vol. 9, pp. 59–65, 1992.

[368] Renz U., Hüppelshäuser H., Schneemann A. and Lange F. *Strömung und Wärmeübergang im Zylinder eines geschleppten Motors.* In Kolloquium des Sonderforschungsbereichs 224 der RWTH Aachen, "Motorische Verbrennung" Teilprojekt A7, pp. 181–201, 11-12 March, 1993.

[369] Réveillon J. and Vervisch L. *Spray vaporization in nonpremixed turbulent combustion modeling: a single droplet model.* Combustion and Flame, Vol. 121, No. 1–2, pp. 75–90, 2000.

[370] Reynolds O. *On the Dynamical Theory of Incompressible Viscous Fluids and the Determination of the Criterion.* Philosophical Transactions of the Royal Society of London, Series A, Vol. 186, p. 123, 1895.

[371] Reynolds W.C. *Modeling of fluid motions in engines – an introductory overview.* In Proceedings of the Symposium on Combustion Modeling in Reciprocating Engines held November 6-7, 1978 at the General Motors Research Laboratories, Warren, Michigan, New York, J. Mattavi and C. Amann, editors, Plenum Press, pp. 41–68, 1980.

[372] Ricardo Consulting Engineers. *Exhaust emissions.* In Diesel Engine Reference Book, B. Challen and R. Baranescu, editors, $2^{nd}$ ed. Butterworth-Heinemann, Oxford, 1999, Part 4: Environmental aspects. Chapter 19, pp. 471–484.

[373] Ricardo Consulting Engineers. *Exhaust smoke, measurement and regulation.* In Diesel Engine Reference Book, B. Challen and R. Baranescu, editors, $2^{nd}$ ed. Butterworth-Heinemann, Oxford, 1999, Part 4: Environmental aspects. Chapter 18, pp. 459–470.

[374] Richter H. and Howard J.B. *Formation of polycyclic aromatic hydrocarbons and their growth to soot — a review of chemical reaction pathways.* Progress in Energy and Combustion Science, Vol. 26, No. 4-6, pp. 565–608, 2000.

[375] Riedel L. *Wärmeleitfähigkeitsmessungen an Zuckerlösungen, Fruchtsäften und Milch.* Chemie Ingenieur Technik, Vol. 21, No. 17/18, pp. 340–341, 1949.

[376] Riedel L. *Die Wärmeleitfähigkeit von wäßrigen Lösungen starker Elektrolyte.* Chemie Ingenieur Technik, Vol. 23, No. 3, pp. 59–64, 1951.

[377] Riedel L. *Neue Wärmeleitfähigkeitsmessungen an organischen Flüssigkeiten.* Chemie Ingenieur Technik, Vol. 23, No. 13, pp. 321–324, 1951.

[378] Riedel L. *Wärmeleitfähigkeitsmessungen an Mischungen verschiedener organischer Verbindungen mit Wasser.* Chemie Ingenieur Technik, Vol. 23, No. 19, pp. 465–469, 1951.

[379] RIF Fortran Version 2.0. *Manual.* Institut für Technische Mechanik, RWTH Aachen, Aachen, 1997.

[380] Rowlinson J.S. *Liquids and Liquid Mixtures*, 2nd ed. Butterworth, London, 1969.

[381] Ruszalo R. and Hallett W.L.H. *A Model for the Autoignition of Single Liquid Droplets at High Pressure.* Combustion Science and Technology, Vol. 86, pp. 183–197, 1992.

[382] Saad Y. and van der Vorst H.A. *Iterative solution of linear systems in the 20th century.* Journal of Computational and Applied Mathematics, Vol. 123, No. 1-2, pp. 1–33, 2000.

[383] Sahetchian S., Champoussin J.C., Brun M., Levy N., Blin-Simiand N., Aligrot C., Jorand F., Socoliuc M., Heiss A. and Guerassi N. *Experimental Study and Modeling of Dodecane Ignition in a Diesel Engine.* Combustion and Flame, Vol. 103, pp. 207–220, 1995.

[384] Said R., Garo A. and Borghi R. *Soot Formation Modeling for Turbulent Flames.* Combustion and Flame, Vol. 108, No. 1-2, pp. 71–86, 1997.

[385] Sanchez-Tarifa C., Crespo A. and Fraga E. *A Theoretical Model for the Combustion of Droplets in Super-critical Conditions and Gas Pockets.* Astronautica Acta, Vol. 17, pp. 685–692, 1971.

[386] Sandler S.I. *Chemical and Engineering Thermodynamics*, 3rd ed. John Wiley & Sons, Inc., New York, 1999.

[387] Satoh K., Zhang L., Hatanaka H., Takatsuki T. and Yokota K. *Relationship between $NO_x$ and SM emissions from DI diesel engine with EGR.* JSAE Review, Vol. 18, No. 4, pp. 369–375, 1997.

[388] Sato J. *Studies on Droplet Evaporation and Combustion in High Pressures.* In AIAA 31st Aerospace Sciences Meeting & Exhibit, AIAA Paper 93-0813, Reno, NV, 11-14 Jan., 1993.

[389] Saxon A. and Diaz-Sanchez D. *Review: Diesel exhaust as a model xenobiotic in allergic inflammation.* Immunopharmacology, Vol. 48, No. 3, pp. 325–327, 2000.

[390] Sazhina E.M., Sazhin S.S., Heikal M.R. and Marooney C.J. *The Shell autoignition model: applications to gasoline and diesel fuels.* Fuel, Vol. 78, No. 4, pp. 389–401, March, 1999.

[391] Scheinert H. *Private Communication.* Daimler-Benz AG, Stuttgart, June, 1998.

[392] Schlichting H. *Boundary Layer Theory*, 7th ed. McGraw-Hill Classic Textbook Reissue Series. McGraw-Hill Book Company, New York, 1979.

[393] Schmidt T., Esser-Schmittmann W., Roosen P., Hassel E., Xu H., Reuter U. and Scheid E. *Pressure chamber experiments for fuel spray model development.* Final Report. JRC, Contract No. EN3E-0102-D, Rheinisch Westfälische Technische Hochschule Aachen, October, 1988.

[394] Schubert K. *Die Bedeutung des Dieselmotors als Antriebsmaschine für Kraftfahrzeuge.* Sonderheft 60 Jahre MTZ, Motortechnische Zeitschrift, pp. 86–89, 1999.

[395] Schulte H.S.-H. *Passenger car engines.* In Diesel Engine Reference Book, B. Challen and R. Baranescu, editors, 2nd ed. Butterworth-Heinemann, Oxford, 1999, Part 5: Applications. Chapter 22, pp. 523–551.

[396] Shyy W. and Krishnamurty V.S. *Compressibility effects in modeling complex turbulent flows.* Progress in Aerospace Sciences, Vol. 33, No. 9-10, pp. 587–645, 1997.

[397] Sirignano W.A. *The Formulation of Spray Combustion Models: Resolution Compared to Droplet Spacing.* ASME Journal of Heat Transfer, Vol. 108, pp. 633–639, 1986.

[398] Sirignano W.A. *Fluid Dynamics and Transport of Droplets and Sprays.* Cambridge University Press, Cambridge, 1999.

[399] Smith O.I. *Fundamentals of Soot Formation in Flames with Application to Diesel Engine Particulate Emissions.* Progress in Energy and Combustion Science, Vol. 7, pp. 275–291, 1981.

[400] Smoluchowski M. van. *Versuch einer mathematischen Theorie der Koagulationskinetik kolloider Lösungen.* Zeitschift der Physikalischen Chemie, Vol. 92, pp. 129–168, 1917.

[401] Soave G. *Equilibrium Constants From a Modified Redlich-Kwong Equation of State.* Chemical Engineering Science, Vol. 27, pp. 1197–1203, 1972.

[402] Soo S.L. *Fluid Dynamics of Multiphase Systems.* Blaisdell, Waltham, MA, 1967.

[403] Soo S.L. *Multiphase Fluid Dynamics.* Science Press, Beijing, 1990.

[404] Sornek R.J., Dobashi R. and Hirano T. *Effect of Turbulence on Vaporization, Mixing, and Combustion of Liquid-Fuel Sprays.* Combustion and Flame, Vol. 120, No. 4, pp. 479–491, 2000.

[405] Spalart P.R. *Strategies for turbulence modelling and simulations.* International Journal of Heat and Fluid Flow, Vol. 21, No. 3, pp. 252–263, 2000.

[406] Spalding D.B. *A Single Formula for the "Law of the Wall".* ASME Journal of Applied Mechanics, pp. 455–458, Sept., 1961.

[407] Spalding D.B. *Mixing and chemical reaction in steady confined turbulent flames.* Thirteenth Symposium (International) of Combustion, The Combustion Institute, pp. 649–657, 1970.

[408] Spalding D.B. *Development of the eddy-break-up model of turbulent combustion.* Sixteenth Symposium (International) of Combustion, The Combustion Institute, pp. 1657–1663, 1976.

[409] Stainback P.C. and Nagabushana K.A. *Review: hot-wire anemometry in transonic and subsonic slip flows (data bank contribution).* ASME Journal of Fluids Engineering, Vol. 119, No. 1, pp. 14–18, 1997.

[410] STAR-CD Version 3.1. *Methodology.* Computational Dynamics Limited, London, 1999.

[411] Stokes G.G. *On the theories of internal friction of fluids in motion.* Transactions – Cambridge Philosophical Society, Vol. 8, pp. 287–305, 1845.

[412] Stone R. *Introduction to Internal Combustion Engines,* 3rd ed. Macmillan Press Ltd., London, 1999.

[413] Stull D.R., Westrum Jr. E.F. and Sinke G.C. *The Chemical Thermodynamics of Organic Compounds.* John Wiley & Sons, Inc., New York, 1969.

[414] Stumpp G. and Ricco M. *Common Rail – An Attractive Fuel Injection System for Passenger Car DI Diesel Engines.* SAE Technical Paper Series, No. 960870, 1996.

[415] Subramaniam S. and O'Rourke P.J. *The KIVA Stochastic Spray Model: Convergence Issues and Implications for Modeling.* In Proceedings of the 9th International Multidimensional Engine Modeling User's Group Meeting at the SAE Congress, Detroit, Michigan, USA, Silicon Graphics Inc. and University of Wisconsin, Engine Research Center, 28 Febr., 1999.

[416] Subramanian C.S. and Antonia R.A. *Effect of Reynolds number on a slightly heated turbulent boundary layer.* International Journal of Heat and Mass Transfer, Vol. 24, No. 11, pp. 1833–1846, 1981.

[417] Svehla R.A. *Estimated Viscosities and Thermal Conductivities of Gases at High Temperatures.* NASA Technical Report R-132, Lewis Research Center, Cleveland, Ohio, 1962.

[418] Syed K.J., Stewart C.D. and Moss J.B. *Modelling soot formation and thermal radiation in buoyant turbulent diffusion flames.* Twenty-Third Symposium (International) on Combustion, The Combustion Institute, pp. 1533–1541, 1990.

[419] Tabata M., Arai M. and Hiroyasu H. *The Sauter Mean Diameter of a Diesel Spray in an Elevated Pressure Environment.* In Proceedings of the Fourth International Conference on Liquid Atomization and Spray Systems, ICLASS-88, Sendai, Japan, pp. 405–410, 22-24 August, 1988.

[420] Tabrizi B.S. *Three-Dimensional Diesel Spray Predictions in Combustion Chamber Flows.* Ph.D. thesis, Imperial College of Science, Technology & Medicine, University of London, June, 1991.

[421] Takahashi S. *Preparation of a Generalized Chart for the Diffusion Coefficients of Gases at High Pressures.* Journal of Chemical Engineering of Japan, Vol. 7, No. 6, pp. 417–420, 1974.

[422] Tennekes H. and Lumley J.L. *A First Course in Turbulence,* $15^{th}$ ed. The MIT Press, Cambridge, Massachusetts, 1994.

[423] Tesner P.A. and Tsibulevsky A.M. *Gasification of Dispersed Carbon in Hydrocarbon Diffusion Flames. III. Flames of Acetylene-Hydrogen and Acetylene-Water Vapor Mixtures.* Combustion, Explosion and Shockwaves, Vol. 3, pp. 163–167, 1967.

[424] Thangam S. and Speziale C.G. *Turbulent Flow Past a Backward-Facing Step: A Critical Evaluation of Two-Equation Models.* AIAA Journal, Vol. 30, No. 5, pp. 1314–1320, 1992.

[425] Theobald M.A. and Cheng W.K. *A Numerical Study of Diesel Ignition.* ASME Paper 87-FE-2, Energy-Sources Technology Conference and Exhibition, Dallas, TX, February 15-20, 1987.

[426] Theodoropoulos T. *Prediction of Three-Dimensional Engine Flow on Unstructured Meshes.* Ph.D. thesis, Imperial College of Science, Technology & Medicine, University of London, June, 1990.

[427] Theodossopoulos P. *Multidimensional simulation of combustion and pollutant formation in diesel engines.* Ph.D. thesis, Imperial College of Science, Technology & Medicine, University of London, March, 1999.

[428] Thomson G.H., Brobst K.R. and Hankinson R.W. *An Improved Correlation for Densities of Compressed Liquids and Liquid-Mixtures.* AIChE Journal, Vol. 28, No. 4, pp. 671–676, 1982.

[429] Thring M.W. and Newby M.P. *Combustion Length of Enclosed Turbulent Jet Flames.* Fourth Symposium (International) on Combustion, The Combustion Institute, pp. 789–796, 1953.

[430] Travis J.R., Harlow F.H. and Amsden A.A. *Numerical Calculation of Two-Phase Flows.* Nuclear Science and Engineering, Vol. 61, pp. 1–10, 1976.

[431] Tree D.R. and Foster D.E. *Measurements of Soot Particle Size, Number Density, and Temperature in a Direct Injection Diesel Engine as a Function of Speed and Load.* SAE Technical Paper Series, No. 940270, 1994.

[432] Tsukamoto T. and Niioka T. *Numerical Simulation of Fuel Droplet Evaporation and Ignition under High Temperature and High Pressure.* Progress of Astronautics and Aeronautics, Vol. 152, pp. 263–279, 1993.

[433] Tsukamoto T. and Niioka T. *Numerical Simulation of Fuel Droplet Combustion Under High Pressure.* Microgravity Science and Technology, Vol. 6, No. 4, pp. 219–222, 1993.

[434] Turns S.R. *Understanding $NO_x$ formation in nonpremixed flames: experiments and modeling.* Progress in Energy and Combustion Science, Vol. 21, No. 5, pp. 361–385, 1995.

[435] Umemura A. *Supercritical Liquid Fuel Combustion.* Twenty-First Symposium (International) on Combustion, The Combustion Institute, pp. 463–471, 1986.

[436] Umemura A. *The Fundamental Theory of Supercritical Evaporation.* Heat Transfer - Japanese Research, Vol. 17, pp. 82–94, 1988.

[437] Umemura A., Chang X.-Y. and Fujiwara T. *Supercritical Droplet Evaporation.* In Proceedings of the Fifth International Conference on Liquid Atomization and Spray Systems, ICLASS-91, Paper 4, Gaithersburg, MD, USA, NIST Special Publication, No. 813, pp. 89–96, July, 1991.

[438] Van den Vorst H.A. *BI-CGSTAB: a fast and smoothly converging variant of BI-CG for the solution of non-symmetric linear systems.* SIAM Journal on Scientific and Statistical Computing, Vol. 13, pp. 631–644, 1992.

[439] Vander Wal R.L., Ticich T.M. and Stephens A.B. *Can Soot Primary Particle Size be Determined Using Laser-Induced Incandescence.* Combustion and Flame, Vol. 116, pp. 291–296, 1999.

[440] Van Driest E.R. *On Turbulent Flow Near a Wall.* Journal of the Aeronautical Sciences, Vol. 23, pp. 1007–1011, November, 1956.

[441] Van Gerpen J. and Reitz R. *Diesel combustion and fuels.* In Diesel Engine Reference Book, B. Challen and R. Baranescu, editors, 2nd ed. Butterworth-Heinemann, Oxford, 1999, Part 1: Theory. Chapter 4, pp. 89–104.

[442] Varnavas C. and Assanis D. *A High Temperature and High Pressure Evaporation Model for the KIVA-3 Code.* SAE Technical Paper Series, No. 960629, 1996.

[443] Versteeg H.K. and Malalasekera W. *An Introduction to Computational Fluid Dynamics - The Finite Volume Method.* Longman Scientific & Technical, Essex, 1995.

[444] Volino R.J. and Simon T.W. *Velocity and Temperature Profiles in Turbulent Boundary Layer Flows Experiencing Streamwise Pressure Gradients.* ASME Journal of Heat Transfer, Vol. 119, No. 3, pp. 433–439, 1997.

[445] Wallis G.B. *One-Dimensional Two-Phase Flow.* McGraw-Hill, New York, 1969.

[446] Wan Y.P. *Numerical Study of Transient Fuel Sprays with Autoignition and Combustion Under Diesel-Engine Relevant Conditions.* Ph.D. thesis, RWTH Aachen, Aachen, Germany, 1997.

[447] Wan Y.P. and Peters N. *Application of the Cross-Sectional Average Method to Calculations of the Spray Region in a Diesel Engine.* SAE Technical Paper Series, No. 972866, 1997.

[448] Wan Y. and Peters N. *Scaling of spray penetration with evaporation.* Atomization and Sprays, Vol. 9, No. 2, pp. 111–132, 1999.

[449] Wan Y.P., Pitsch H. and Peters N. *Simulation of Autoignition Delay and Location of Fuel Sprays Under Diesel-Engine Relevant Conditions.* SAE Technical Paper Series, No. 971590, 1997.

[450] Wark K.Jr. and Richards D.E. *Thermodynamics*, $6^{th}$ ed. McGraw-Hill Companies, Inc., Boston, USA, 1999.

[451] Warnatz J. *The structure of laminar alkane-, alkene-, and acetylene flames.* Eighteenth Symposium (International) on Combustion, The Combustion Institute, pp. 369–384, 1981.

[452] Warsi Z.U.A. *Conservation Form of the Navier-Stokes Equations in General Nonsteady Coordinates.* AIAA Journal, Vol. 19, pp. 240–242, 1976.

[453] Watkins A.P. *Flow and Heat Transfer in Piston/Cylinder Assemblies.* Ph.D. thesis, Imperial College of Science and Technology, London, September, 1977.

[454] Weller H.G. *The Development of a New Flame Area Combustion Model Using Conditional Averaging.* Thermofluids Section Report TF/9307, Department of Mechanical Engineering, Imperial College of Science, Technology and Medicine, 1993.

[455] Weller H.G., Uslu S., Gosman A.D., Maly R.R., Herweg R. and Heel B. *Prediction of Combustion in Homogeneous-Charge Spark-Ignition Engines.* In The Third International Symposium on Diagnostics and Modeling of Combustion in Internal Combustion Engines, COMODIA 94, Yokohama, Japan, Engine Systems Division, The Japan Society of Mechanical Engineers, 11-14 July, 1994.

[456] Wendt J.F. *Computational fluid dynamics : an introduction.* Springer-Verlag, Berlin, 1991.

[457] Westbrook C.K. and Dryer F.L. *Simplified Reaction Mechanisms for the Oxidation of Hydrocarbon Fuels in Flames.* Combustion Science and Technology, Vol. 27, pp. 31–43, 1981.

[458] Westbrook C.W. and Dryer F.L. *Chemical Kinetics Modelling of Hydrocarbon Combustion.* Progress in Energy and Combustion Science, Vol. 10, pp. 1–57, 1984.

[459] Westenberg A.A. *Kinetics of NO and CO in Lean, Premixed Hydrocarbon-Air Flames.* Combustion Science and Technology, Vol. 4, pp. 59–64, 1971.

[460] Westerweel J. *Fundamentals of digital particle image velocimetry.* Measurement Science and Technology, Vol. 8, No. 12, pp. 1379–1392, 1997.

[461] White F.M. *Viscous Fluid Flow*, $2^{nd}$ ed. McGraw-Hill Book Company, New York, 1991.

[462] Wilcox D.C. *Turbulence modelling for CFD.* DCW Industries, Inc., La Cañada, California, 1993.

[463] Wilke C.R. and Lee C.Y. *Estimation of Diffusion Coefficients for Gases and Vapors.* Industrial and Engineering Chemistry, Vol. 47, No. 6, pp. 1253–1257, 1955.

[464] Williams F.A. *Combustion Theory: The Fundamental Theory of Chemically Reacting Flow Systems*, $2^{nd}$ ed. Benjamin/Cummings Publishing Company, Inc., Menlo Park, 1985.

[465] Wolfshtein M. *The Velocity and Temperature Distribution in One-Dimensional Flow With Turbulence Augmentation and Pressure Gradient.* International Journal of Heat and Mass Transfer, Vol. 12, pp. 301–318, 1969.

[466] Woschni G. *Beitrag zum Problem des Wärmeüberganges im Verbrennungsmotor.* Motortechnische Zeitschrift MTZ, Vol. 26, No. 4, pp. 128–133, 1965.

[467] Woschni G. *A Universally Applicable Equation for the Instantaneous Heat Transfer Coefficient in the Internal Combustion Engine.* SAE Technical Paper Series, Vol. 76, No. 670931, pp. 3065–3083, 1967.

[468] Woschni G. *Die Berechnung der Wandverluste und der thermischen Belastung der Bauteile von Dieselmotoren.* Motortechnische Zeitschrift MTZ, Vol. 31, No. 12, pp. 491–499, 1970.

[469] Xin J., Montgomery D., Han Z. and Reitz R.D. *Multidimensional modeling of combustion for a six-mode emissions test cycle on a DI diesel engine.* ASME Journal of Engineering for Gas Turbines and Power, Vol. 119, No. 3, pp. 683–691, 1997.

[470] Yakhot V. and Orszag S.A. *Renormalization group analysis of turbulence. I. Basic theory.* Journal of Scientific Computing, Vol. 1, pp. 1–51, 1986.

[471] Yang J. *Convective Heat Transfer Predictions and Experiments in an IC Engine.* Ph.D. thesis, University of Wisconsin, Madison, 1988.

[472] Yang V., K.C. Hsieh and Shuen J.S. *Supercritical Droplet Combustion and Related Transport Phenomena.* In AIAA 31st Aerospace Sciences Meeting & Exhibit, AIAA Paper 93-0812, Reno, NV, 11-14 Jan., 1993.

[473] Yang J. and Martin J.K. *Approximate Solution - One-Dimensional Energy Equation for Transient, Compressible, Low Mach Number Turbulent Boundary Layer Flows.* ASME Journal of Heat Transfer, Vol. 111, pp. 619–624, 1989.

[474] Yang J. and Martin J.K. *Predictions of the Effects of High Temperature Walls, Combustion, and Knock on Heat Transfer in Engine-Type Flows.* SAE Technical Paper Series, No. 900690, 1990.

[475] Yi Y., Hessel R., Zhu G.-S. and Reitz R. *The Influence of Physical Input Parameter Uncertainties on Multidimensional Model Predictions of Diesel Engine Performance and Emissions.* SAE Technical Paper Series, No. 2000-01-1178, 2000.

[476] Yoshihara Y., Kazakov A., Wang H. and Frenklach M. *Reduced mechanism of soot formation — application to natural gas-fueled diesel combustion.* Twenty-Fifth Symposium (International) on Combustion, The Combustion Institute, pp. 941–948, 1994.

[477] Yoshizaki T., Yamamoto O., Nishida K., Hiroyasu H. and Suzuki M. *Evaporating spray and flame distributions in the combustion chamber of a direct injection diesel engine.* JSAE Review, Vol. 18, No. 9733611, pp. 219–224, 1997.

[478] Young K.J. and Moss J.B. *Modelling Sooting Turbulent Jet Flames Using an Extended Flamelet Technique.* Combustion Science and Technology, Vol. 105, pp. 33–53, 1995.

[479] Yuen M.C. and Chen L.W. *On Drag of Evaporating Liquid Droplets.* Combustion Science and Technology, Vol. 14, pp. 147–154, 1976.

[480] Zeldovich Y.B. *The Oxidation of Nitrogen in Combustion Explosions.* Acta Physicochimica U.S.S.R., Vol. 21, pp. 577–628, 1946.

[481] Zellat, M. Rolland T. and Poplow F. *Three Dimensional Modeling of Combustion and Soot Formation in an Indirect Injection Diesel Engine.* SAE Technical Paper Series, No. 900254, 1990.

[482] Zellbeck H. *Dresdner Schule.* Sonderheft 60 Jahre MTZ, Motortechnische Zeitschrift, p. 48, 1999.

[483] Zhang G., Filipi Z.S. and Assanis D.N. *Flexible, reconfigurable, transient multicylinder diesel engine simulation for system dynamics studies.* Mechanics of Structures and Machines, Vol. 25, No. 3, pp. 357–378, 1997.

[484] Zhao H. and Ladommatos N. *Optical diagnostics for soot and temperature measurement in diesel engines.* Progress in Energy and Combustion Science, Vol. 24, pp. 221–255, 1998.

[485] Zhao H. and Ladommatos N. *Optical diagnostics for in-cylinder mixture formation measurements in IC engines.* Progress in Energy and Combustion Science, Vol. 24, pp. 297–336, 1998.

[486] Zheng Q.P., Jasuja A.K. and Lefebvre A.H. *Influence of air and fuel flows on gas turbine sprays at high pressures.* $26^{th}$ Symposium (International) on Combustion, The Combustion Institute, Vol. 2, pp. 2757–2762, 1996.

[487] Zhu G.S. and Aggarwal S.K. *Transient supercritical droplet evaporation with emphasis on the effects of equation of state.* International Journal of Heat and Mass Transfer, Vol. 43, No. 7, pp. 1157–1171, 2000.